europhysics
conference
abstracts

17th EPS Conference on

# *Controlled Fusion and Plasma Heating*

Amsterdam, 25-29 June 1990

Editors: G. Briffod, Adri Nijsen-Vis, F.C. Schüller

Contributed Papers
Part IV

Published by: European Physical Society

es Editor: Prof. K. Bethge, Frankfurt/M.

aging Editor: G. Thomas, Geneva

**VOLUME 14 B Part IV**

# XVII FUSION AMSTERDAM 1990

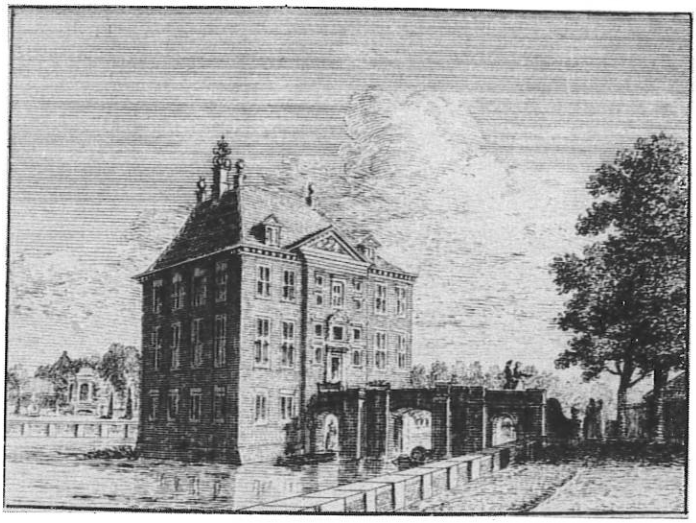

Het HUIS RYNHUIZEN.

17th
FUSION
AMSTERDAM
1990

| I |
|---|
| J |
| K |
| |

17th European Conference on

# *Controlled Fusion and Plasma Heating*

Amsterdam, 25-29 June 1990
Editors: G. Briffod, Adri Nijsen-Vis, F.C. Schüller

Contributed Papers
Part IV

# PREFACE

The 17th European Conference on Controlled Fusion and Plasma Heating was held in Amsterdam, the Netherlands, from the 25th to the 29th of June 1990 by the Plasma Physics Division of the European Physical Society (EPS).

The Conference has been organized by the FOM-Instituut voor Plasmafysica Rijnhuizen, which is part of the Foundation for Fundamental Research on Matter (Stichting Fundamenteel Onderzoek der Materie). FOM is supported by the Dutch Research Organization NWO and Euratom.

The Conference has been sponsored by the Koninklijke Nederlandse Academie van Wetenschappen (KNAW) and by the Foundation Physica.

The programme, format and schedule of the Conference are determined by the International Programme Committee appointed by the Plasma Physics Division of the EPS.

The programme included 18 invited lectures; from the contributed papers 24 were selected for oral presentation and 470 for poster presentation.

This 4-volume publication is published in the Europhysics Conference Abstract Series and contains all accepted contributed papers received in due time by the organizers. The 4-page extended abstracts were reproduced photographically using the manuscripts submitted by the authors. The invited papers will be published in a special issue of the journal "Plasma Physics and Controlled Fusion" and sent free of charge to each registered participant.

The editors would like to acknowledge the skillful and dedicated support given by Laura van Veenendaal - van Uden, Rosa Tenge - Tjon A Tham and Cora de Bruijne in preparing the manuscripts for reproduction in these four volumes.

May 1990

The Editors

## INTERNATIONAL PROGRAMME COMMITTEE

G. Briffod, Chairman, CEN, Grenoble, France
K. Appert, CRPP, Lausanne, Switzerland
R. Balescu, Université Libre de Bruxelles, Belgium
F. De Marco, Euratom-ENEA, Frascati, Italy
C. Gormezano, JET Joint Undertaking, Abingdon, United Kingdom
L. Laurent, Association Euratom-CEN, St. Paul-lez-Durance, France
S. Ortolani, Association Euratom-CNR, Padova, Italy
D.D. Ryutov, Academy of Sciences, Novosibirsk, USSR
F.C. Schüller, FOM-Rijnhuizen, Nieuwegein, The Netherlands
S.E. Segre, Euratom-ENEA, Frascati, Italy
P.E. Stott, JET Joint Undertaking, Abingdon, United Kingdom
H. Wobig, Max-Planck-Institut für Plasmaphysik, Garching bei München, FRG

## LOCAL ORGANIZING COMMITTEE

M.J. van der Wiel, Chairman, FOM-Rijnhuizen, Nieuwegein
F.C. Schüller, Vice-Chairman, FOM-Rijnhuizen, Nieuwegein
A. Nijsen-Vis, Scientific Secretary, FOM-Rijnhuizen, Nieuwegein
J.T. van den Hout, Treasurer, FOM-Rijnhuizen, Nieuwegein
A.J.H. Donné, FOM-Rijnhuizen, Nieuwegein
N.J. Lopes Cardozo, FOM-Rijnhuizen, Nieuwegein
J. Rem, FOM-Rijnhuizen, Nieuwegein
H. Hopman, FOM-AMOLF, Amsterdam
D.C. Schram, Technical University, Eindhoven

CONTENTS

## PAPER IDENTIFICATION

All contributed papers are listed with their title and responsible author. In those cases where no author was underlined the first author mentioned was taken. The day of the poster presentation of each paper, followed by the number of the poster board, is given under the title in the list of contributed papers. The four poster sessions will be held on:

Monday afternoon indicated as Mo,
Tuesday afternoon indicated as Tu,
Thursday afternoon indicated as Th,
Friday afternoon indicated as Fr.

The poster boards are numbered from 1 to 130. From the 494 contributed papers, 24 were selected for oral presentation. The authors of those orally presented papers were requested to give also a poster presentation. Most of them confirmed that they were prepared to do so.

## TITLE LIST OF CONTRIBUTED PAPERS

### A. TOKAMAKS

* This paper will also be presented orally on Friday 29 June at 9.40 hrs.

* This paper will also be presented orally on Tuesday 26 June at 14.30 hrs.

* This paper will also be presented orally on Tuesday 26 June at 14.10 hrs.
** This paper will also be presented orally on Tuesday 26 June at 13.30 hrs.
*** This paper will also be presented orally on Tuesday 26 June at 13.50 hrs.

* This paper will also be presented orally on Friday 29 June at 9.00 hrs.
** This paper will also be presented orally on Friday 29 June at 9.20 hrs.

## B. STELLARATORS



* This paper will also be presented orally on Tuesday 26 June at 14.50 hrs.

* This paper will also be presented orally on Tuesday 26 June at 15.10 hrs.

## C. ALTERNATIVE MAGNETIC CONFINEMENT SCHEMES



---

* This paper will also be presented orally on Thursday 28 June at 13.30 hrs.
** This paper will also be presented orally on Thursday 28 June at 13.50 hrs.

## D. MAGNETIC CONFINEMENT THEORY AND MODELLING



* This paper will also be presented orally on Thursday 28 June at 14.10 hrs.

* This paper will also be presented orally on Thursday 28 June at 14.50 hrs.
** This paper will also be presented orally on Thursday 28 June at 15.10 hrs.

* This paper will also be presented orally on Thursday 28 June at 14.30 hrs.

## E. HEATING BY NEUTRAL BEAM INJECTION

## F. RF HEATING



* This paper will also be presented orally on Monday 25 June at 13.45 hrs.

* This paper will also be presented orally on Monday 25 June at 14.05 hrs.

## G. CURRENT DRIVE AND PROFILE CONTROL

* This paper will also be presented orally on Monday 25 June at 14.25 hrs.

* This paper will also be presented orally on Monday 25 June at 14.45 hrs.
** This paper will also be presented orally on Monday 25 June at 15.05 hrs.

## H. IMPURITY AND EDGE PHYSICS



* This paper will also be presented orally on Friday 29 June at 11.00 hrs.

* This paper will also be presented orally on Friday 29 June at 11.20 hrs.

## I. DIAGNOSTICS



* This paper will also be presented orally on Friday 29 June at 10.00 hrs.

Project of magnetic fluctuation measurement by cross polarization scattering in the TORE SUPRA tokamak.
**First author:** M. Paume et al.

Fr 40 I 62 IV-1721

## J. BASIC COLLISIONLESS PLASMA PHYSICS



* This paper will also be presented orally on Monday 25 June at 16.00 hrs.

## K. INERTIAL CONFINEMENT FUSION

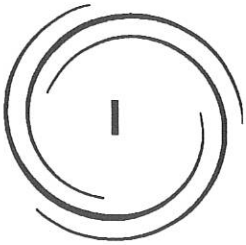


# DIAGNOSTICS

## I1 RESULTS

# TOKAMAK T-10 SOFT X-RAY IMAGING DIAGNOSTIC.

P.V.Savrukhin, G.A.Bobrovskij, D.A.Kislov, E.S.Lyadina.

Kurchatov Institute of Atomic Energy,P.O.Box3402,Moscow,USSR.

## I. DIAGNOSTICS.

The T-10 soft X-ray imaging system consists of three pin-hole cameras arranged at one toroidal location (Fig.1). The "vertical" array (a) ($\theta$=90°), the "middle" camera (b) ($\theta$=+30°) and the "bottom" camera (c) ($\theta$=-30°) consist of 20, 19 and 19 channels, accordingly. The field of view r/a<0.7. The spatial resolution and the spatial step are 2-2.5 cm for each array. The detectors are Si surface-barrier diodes arranged in each camera in two or three rows (1) (Fig.1.).

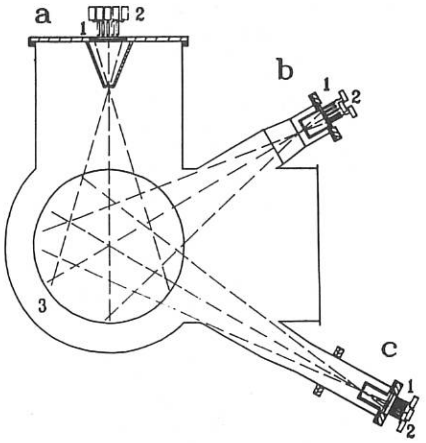


Fig.1. Shematic veiw of the T-10 soft X-ray imaging system.

The system allows to register the emission with intensity $10^5$-$10^9$ $cm^{-2}c^{-1}$ in the photon energy range between 2.5 and 15 keV. For this energy range the soft X-ray spectrum is Maxwellian and the $K_\alpha$ line radiation from Cr, Fe, Ni ions is negligible (less than 10%) in the ohmic stationary stage of the T-10 discharge. The relative calibration of the channels was made by the comparison with the soft X-ray intensity profiles measured with two Si(Li) detectors scanning the plasma in vertical and horizontal directions at the stationary stage of the discharge.

Temporal resolution of the system is up to 10 μsec.

The local structure of the soft X-ray intensity perturbations is reconstructed by the use of the 2D-tomographic technique based on modified Cormack method [1].

## II. RESULTS.

The T-10 soft X-ray imaging system was used to study the plasma perturbation at minor and major disruptions [2] and during the sawtooth crashes. This paper was restricted only for the sawtooth mechanisms investigation. [The m=1 harmonic of the perturbations at the sawtooth crash is dominated, therefore data of only two array (14 channels in "a" and 5 in "c") were used for sawtooth mechanism investigation in the case.]

SAWTOOTH CRASH MECHANISMS. Experimental study of sawteeth at many tokamaks seems to point out that the mechanisms of the sawtooth crash are different in various conditions. Analysis of

the soft X-ray emission from the JET plasmas by tomographic reconstruction technique indicated a quasi-interchange motion during the sawtooth crash [3]. This behavior agrees quite well with the Wesson model of the ideal m=1 mode [4]. But recent experiments on TFTR [5] shown that in some cases the time evolution of the magnetic surfaces agrees with the Kadomtsev reconnection model [6]. The sawteeth on Alcator-C [7] and JIPP TII [8] may have rather complex character. Is this difference caused by a real distinctions in mechanism of the sawtooth crash in different experiments or it is the result of using different reconstruction methods?

To answer the question, the sawtooth crash was investigated in two different T-10 regimes but with the same tomographic technique. The main parameters of the regimes are presented in Table.I. The regimes under study are characterized by the different Te profiles in the central region of the plasma. At the stationary stage of the ohmically heated discharge it can indicate a quite different value of the shear S=rdq/dr in the central region. According to the theoretical and experimental results [9,10] one can expect different mechanisms of the crash in such conditions.

Regime.I. with low-Ip (high-qL) value is a typical for the experiments on the small tokamak or for the high-qL on the big machines. The soft X-ray signals and the series of the tomographic images for the case are displayed on Fig.2. A flattered crescent-like region appears at the X-ray image at the beginning of the crash. During the crash this plateau grows in size and rotates in "poloidal" direction which looks like sinusoidal oscillations on the chord signal. The perturbation has the m=1 poloidal structure. The flat region may be interpretated as magnetic island proposed by the Kadomtsev theory but it does not occupy all the central region during the crash. The maximum size of the island is up to 0.5 r(q=1). This partial reconnection may be connected with large stochastisity generated during the crash [9].

The typical growth rate of m=1 mode during the crash in the the low-Ip regime is $t=(1-2)10^{3}sec^{-1}$. It is consistent with the growth rate of the internal resistive mode but it is too small for the ideal mode.

A quite different mechanism of the sawtooth crash was obtained for the Regime.II. with high-Ip (low-qL) value (flat Te profile in the central region). There is no precusor oscillations on the soft X-ray signals and the symmetrical structure of the counter line at the X-ray image just before the crash is the typical feature of this regime (Fig.3.A.). At the first stage of the crash "cavity-like" perturbations start from the q=1 surface and simultaneously heat flows outside from the "hot" core and spreads in poloidal direction (Fig.3.B.).

Later (the second stage), the cold cavities lengthen in poloidal direction and the "cold" valleys appear at the X-ray image (Fig.3.C.). In some cases this valleys expend and tends to surround the core from either two or one side. The core itself becomes "cool" for the moment.

At the final stage of the crash, the "cold" valleys surround the core and new hot island sometimes appears

(Fig.3d). All the structure slowly rotates in poloidal direction. (Sometimes the valleys contract instead of surrounding the central zone and symmetric uniform structure reappears after the crash.)

It should be pointed out that in all cases under study the hot core (the region with maximum X-ray intensity) does not displace during the crash in opposite to the results of JET[3].

Duration of the crash in this regime is typically 100-200 μsec which is much smaller then the growth time of the resistive m=1 mode but agrees with the growth time of the quasi-interchange mode . Indeed, the time evolution of the tomographic images in $q_L$~2 regime is something like to the plasma motion induced by the ideal MHD m=1 mode in plasma with small shear. (The central zone remains unperturbed if q(0)>1.)

In conclusion , the results of the 2D tomographic reconstruction of the soft X-ray profiles in the T-10 plasmas with the modified Cormack method show that the different sawtooth mechanisms can be realized in tokamak. The realization depends on the Te-profile in the central region.

This work was usefully supported by S.Hokin,MIT,Mass.,USA.

FIG.2. X-ray image for Regime I.

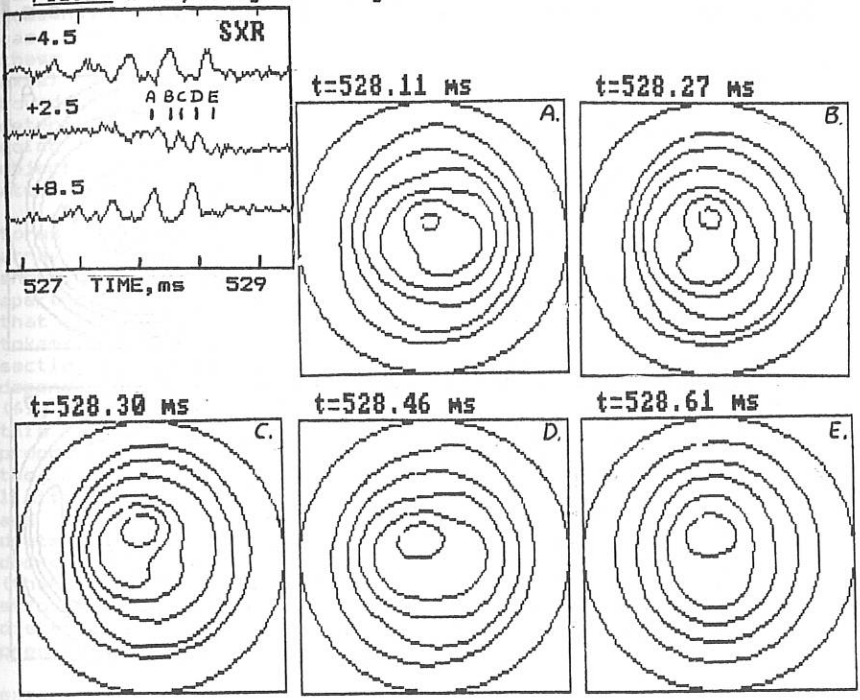

[1] Dnestrovskii Yu.N., et al. This Conference.
[2] Kislov D.A., et al. This Conference.
[3] Granetz R.S., et al. Nucl. Fusion 28 (1988) 457.
[4] Wesson J.A. Plasma Phys. 28 (1986) 243.
[5] Kuo-Petravich G.PPPL-2556(1988).
[6] Kadomtsev B.B. et al. Fizika Plazmy 1 (1975) 710
[7] Granetz R.S. et al Nucl. Fusion 28(1985) 727.
[8] Nagayama Y.,et al. Jpn. J. Appl. Phis. 20, L779 (1981).
[9] Lichtenberg A.J. Nucl. Fusion 24(1984) 1277
[10] Bobrovskii G.A. et al. 15th Europ. Conf.on Controll. Fus. and Plasma Phys.,1988, Dubrovnik, v.1., p.55.


Tabel.I.

| Regime | I | II |
|---|---|---|
| I,MA | 0.22 | 0.44 |
| BtT | 2.8 | 3.0 |
| aL,m | 0.32 | 0.32 |
| qL | 4.5 | 2.1 |
| $\langle ne \rangle$, $10^{19}$ m-3 | 2.75 | 4.5 |
| ne(0),$10^{19}$ m-3 | 4.5 | 6.5 |
| Usur,V | 1.3 | 1.25 |
| Te(0),keV | 1.2 | 1.3 |
| Ti(0),keV | 0.6 | 0.8 |
| Zeff | 2.5 | 2.0 |
| Sawteeth: | | |
| period,ms | 6 | 7-10 |
| inv.radius,cm | 6 | 9 |
| crash time,ms | 0.5-1.0 | 0.1-0.5 |

FIG.3. X-ray image for Regime II.

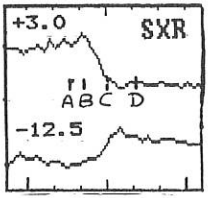


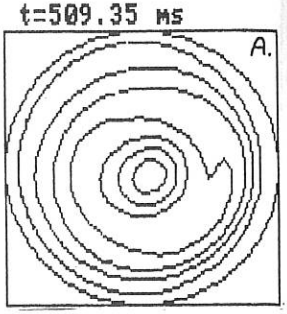


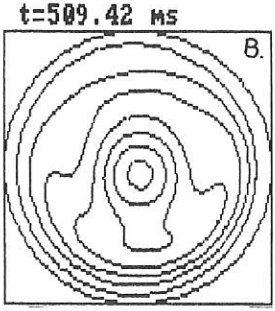


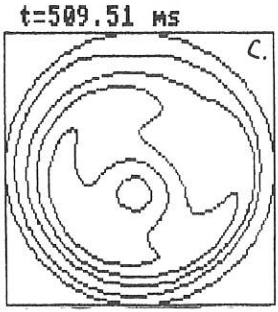


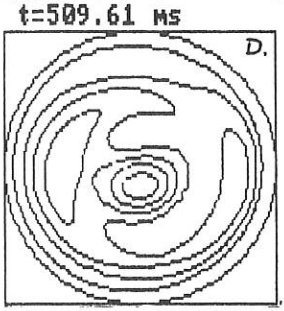

# MEASUREMENT OF NEUTRAL DEUTERIUM FLUXES ON T-10 PERIPHERY.

E.L.Berezovsky, V.P.Vlasov, A.A.Medvedev, V.Yu.Mirensky, A.B.Pimenov
I.V.Kurchatov Institute, Moscow, USSR
U.Wenzel, C.Grunov,
Central Institute of Electron Physics, Academy of Science, GDR

Recently, great attention is devoted to neutral balance study on large tokamaks. This steady interest is explained by the facts: in the first place working gas atoms affect the energy balances of electron (radiation losses) and ion (charge-exchange)components; secondly, neutral density data allow us to create the plasma particle balance models and to calculate particle fluxes and corresponding diffusive energy losses. Commonly, the information about energy and density of working gas atoms in every point of plasma is necessary for solving these problems. However, in many cases data, obtained using axial symmetry penetration models with so called equivalent boundary conditions, are sufficient. Boundary conditions are determined by poloidal and toroidal averaging atoms fluxes, going from different sources (commonly three dimensional). Main object of given study was to get an information of energy and atoms fluxes from different sources.

At first, the distribution of Dα-line intensity along the torus was measured (fig.1). For that purpose, the photodiode array with simple optics and filters (FWHM=9 nm) were used. As shown on figure, line intensity at section, where the rail and aperture limiters were placed, several tens times greater than that at other sections. Similar situation was observed on other tokamaks [1]. Line intensity ratio between "limiter" and "wall" sections depends upon discharge parameters. The limiter signal dependencies on limiter radius (fig.2a),on plasma current (fig.2b) and on density (fig.2c) give some information about this ratio. Scaling for the Dα-intensity on the wall isn't so pronounced. To answer the question about limiter source value, the measurements of toroidal line intensity distribution in limiter section were made. For that,periscope optical system and CCD-array with interference filter were used. Examples of distributions observed are shown on fig.3. As shown, the decrease constants at the boundaries of observed zone (therefore, deposit of limiter atoms in neutral balance) strongly depend upon plasma parameters. More details in spatial distributions of line intensities at limiter zone will be presented in a next paper.

Gas puffing deposit into total atom flux was measured in experiments when at first the valve worked at section of these measurements (fig.4a), then in identical discharge the valve

was replaced in another section at 45° along the torus (fig.4b). As shown on figure, the intensity increase at puffing section wasn't greater than 2.5 and fully disappeared after the displacement. Simulations showed that at this case valve atom fluxes were small enough.

Energy of atoms appearing on the wall and limiters was measured by Doppler broadening of Dα-line. Monochromator with CCD-array camera was used for this purpose. At the wall sections experimental curves were well fitted by three energy components (fig.5a), one of which was connected with the rest amount of hydrogen, and two others were determined by deuterium energy distribution. Cold component energy was 4-7 eV (taking into account Zeeman splitting and instrumental width). Energy and amplitude of high energy component depend upon discharge parameters and give (30-250) eV and (10-40) % consequently. For limiter zone Doppler profiles had more complex structure (fig.5b). "Blue" wing increase seems to be in connection with existence of reflected atoms [2]. We intend to provide detailed analysis of Doppler profile for this case, using a model, accounting experimental geometry and limiter zone parameters.

Problems, connected with poloidal neutral flux distributions will be presented in a future paper. However, as experiments showed, in many cases the value of poloidal asymmetry of fluxes from the wall and limiter isn't great. Obtained data are quite sufficiently to find radial distributions of energy and atom fluxes, using models of penetrations. The distributions founded will be used to determine the role of ion energy losses in diffusion and charge exchange processes.

1.W.L.Rowan,C.C.Klapper et al. Nuclear Fusion,vol.27,No.7, (1987),1105.
2.P.Bogen, D.Rusbuldt et al. 8-th Plasma-Surface Interactions, 1988, Julich, A20.

Fig.1. Toroidal distribution of Dα-line intensity. Opened points - OH, closed - ECRH.
$I_p$=220 kA, $B_\theta$=28 kOe, Ne=3.$10^{13}$cm$^{-3}$, $r_1$=28 cm.

Fig.2. Dα-line intensity on the top of the movable limiter versus:
a) the movable limiter radius;
b) plasma current;
c) averaged electron density.

Fig.3. The example of toroidal distribution of Dα-line intensity near by the movable limiter. Lower curve - OH; upper - ECRH.
Ip=250kA, $B_\theta$=28 kOe, Ne=2.2.$10^{13}$cm$^{-3}$, $r_1$=28 cm.

Fig.4. The examples of Dα-line profiles:
a) on the wall,
b) on the movable limiter.
Ip=250 kA, $B_\theta$=28 kOe, Ne=3.$10^{13}$cm$^{-3}$, $r_1$=28 cm.

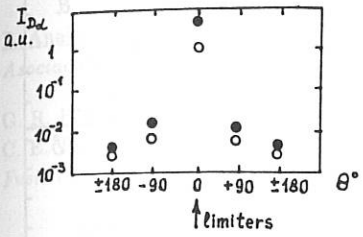


Fig. 1

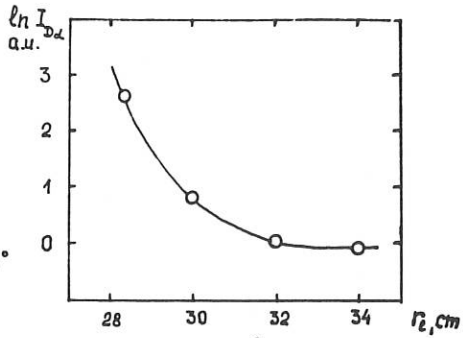


Fig. 2 a

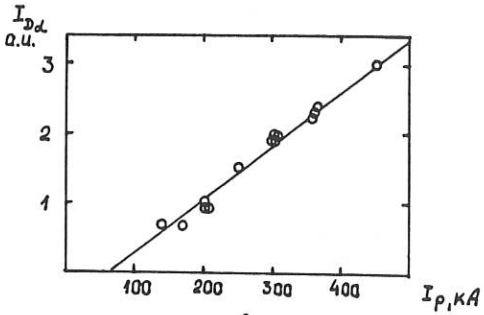


Fig. 2 b

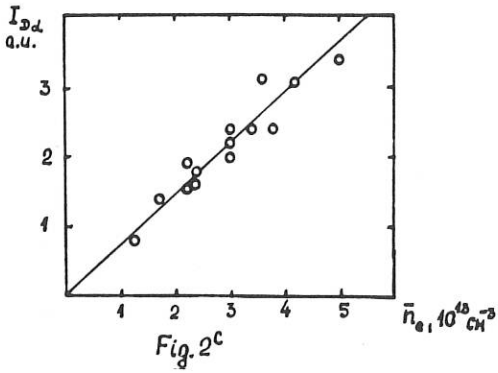


Fig. 2 c

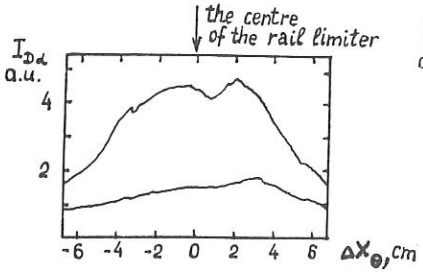


Fig. 3

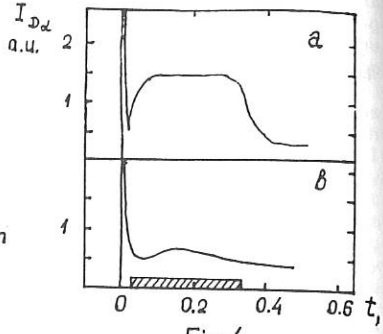


Fig. 4

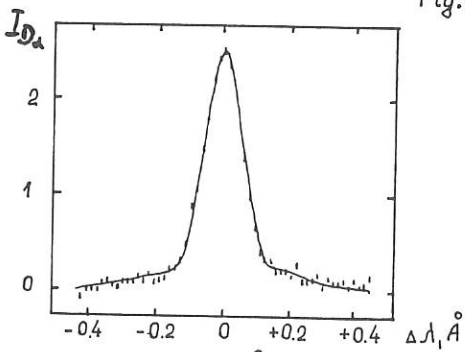


Fig. 5 a

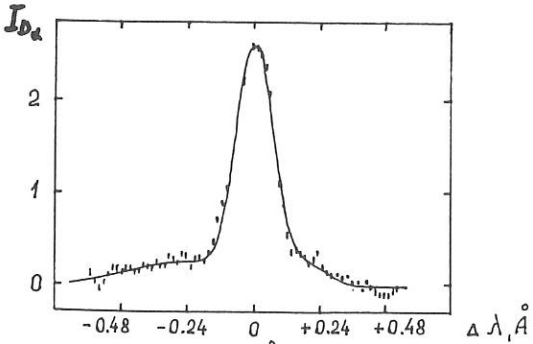


Fig. 5 b

# DENSITY FLUCTUATION MEASUREMENTS ON ATF USING A TWO-FREQUENCY REFLECTOMETER*

E. Anabitarte
*Asociación EURATOM/CIEMAT, Madrid, Spain*

G. R. Hanson,[a] J. H. Harris, J. B. Wilgen, J. D. Bell,[b] J. L. Dunlap, C. Hidalgo,[c] C. E. Thomas,[a] and T. Uckan
*Fusion Energy Division, Oak Ridge National Laboratory, Oak Ridge, Tennessee, U.S.A.*

## Introduction

A microwave reflectometer system has been installed and operated on the Advanced Toroidal Facility[1] (ATF) to measure density fluctuations. This system consists of two individual reflectometers that use the same antenna system and operate in the 30- to 40-GHz band. This arrangement allows operation at two frequencies along the same radial chord so that radial coherence measurements are possible. During the initial operating period of the reflectometer, a correlation was observed between a change in the edge density fluctuation spectrum and a transition to improved confinement. Recently, local measurements of the density fluctuation spectra in electron-cyclotron-heated (ECH) plasmas has been shown to agree with Langmuir probe measurements at the edge. Furthermore, structure in the spectra has been observed in some ECH plasmas.

## System Description

The ATF reflectometer system operates at two frequencies simultaneously in the same dual antenna system.[2] Two tunable microwave sources allow continuous operation between 30 and 40 GHz with separation frequencies from 10 MHz to 10 GHz. Homodyne quadrature phase detection is used to measure the phase fluctuations in the reflected signal. Quadrature phase detection allows decoupling of the amplitude and phase fluctuations in the reflected signal. Because of the low operational RF frequency band of the present reflectometer and the nearly flat density profiles in ATF, the radial extent of the plasma that has been covered to date is limited to the outer third of the minor radius for both O-mode and X-mode operation. A higher-frequency system operating between 65 and 85 GHz is planned to allow internal probing of higher-density plasmas.

*Research sponsored by the Office of Fusion Energy, U.S. Department of Energy, under contract DE-AC05-84OR21400 with Martin Marietta Energy Systems, Inc.

[a] Georgia Institute of Technology, Atlanta, Georgia.

[b] Computing and Telecommunications Division, Martin Marietta Energy Systems, Inc.

[c] Asociación EURATOM/CIEMAT, Madrid, Spain.

## Radial Coherence Measurements

The capability of the ATF reflectometer to operate at two frequencies simultaneously along the same radial chord with a frequency separation as low as 10 MHz provides a simple means of making radial coherence measurements. The coherence between the signals reflected at the two critical layers is calculated using standard cross-correlation techniques and is determined as a function of the frequency separation of the two signals. Conversion to a radial distance is dependent on knowing the density gradient. It has been found that, for coherence measurements, the amplitude fluctuations in the reflected signal have only a minor effect on the coherence.

Figure 1 is a plot of the radial coherence of the density fluctuations measured by the reflectometer versus the separation frequency of the two probing beams in the edge of a plasma heated with neutral beam injection (NBI). The coherence length is estimated to be 0.1–0.2 cm using the density profile obtained by the 15-channel Thomson scattering system.[3] The radial position of the cutoff layer is at $r/a \simeq 1.1$, i.e., outside the last closed flux surface. The radial coherence length in plasmas heated only by ECH is about 0.5–1.0 cm with some fluctuation peaks (similar to the one in Fig. 2) having coherence lengths up to 3 cm. The density profile obtained by Thomson scattering indicates that the position of the cutoff layers for this measurement varies from $r/a \simeq 0.85$ to $r/a \simeq 0.9$.

The fast reciprocating Langmuir probe (FRLP) on ATF can measure the poloidal coherence length of floating potential fluctuations. FRLP measurements have been made for $r/a \geq 0.9$ in ECH plasmas and $r/a \geq 1.0$ in NBI plasmas. In both cases, the frequency-averaged poloidal coherence length increases from approximately 0.2 cm in the velocity shear layer to about 0.5–1.0 cm inside the plasma. The shear layer is consistently measured to be at $r/a \simeq 1.1$. Thus, the radial coherence measurements of the reflectometer in the edge of NBI plasmas and inside ECH plasmas are of the same order of magnitude as the FRLP measurements and seem to follow the same radial trend.

## Density Fluctuation Spectra

The ability to probe the plasma internally in order to measure density fluctuations is one of the important advantages of microwave reflectometry as a fluctuation diagnostic. The ATF reflectometer has been used to measure the density fluctuation spectra in the outer third of ECH plasmas at 0.95 T and in the edge of NBI plasmas at 0.95 T and 1.9 T.

During the initial operating period of the reflectometer, a clear transition in the fluctuation spectra was observed in some NBI plasmas. In these discharges, the plasma stored energy $W_{eq}$ rises quickly when the NBI was started and then decreases slightly for about 50 ms (see Fig. 3). During this time, the density fluctuations at the edge of the plasma measured by the reflectometer have a broadband spectrum with a maximum at low frequencies (below 10 kHz). The line-averaged density measured by the 2-mm interferometer also shows large fluctuations in the same frequency range.

After decreasing for 50 ms, the stored energy then increases by a factor of 2 or more (the NBI power remains approximately constant), corresponding to an increase in $\tau_E$. During this interval, the density fluctuation spectrum changes dramatically. The low-frequency fluctuations observed by both the reflectometer and the 2-mm interferometer rapidly diminish and practically disappear, while the higher-frequency fluctuations seen by the reflectometer increase. In many shots, a narrow frequency peak grows and dominates the spectrum during this period. In Fig. 3, a three-dimensional plot of the density fluctuation spectrum, showing the time evolution of the spectrum, is given. A large 25-kHz peak dominates the spectrum in the valley created by the decrease in low-frequency fluctuations. This fluctuation peak is coherent with a Mirnov loop signal located at a bottom port 15° toroidally away. It is not clear whether the sudden change in the density fluctuation spectrum is a cause or a result of the improved confinement, but it is clear (as can be seen in Fig. 3) that the change in the behavior of the edge fluctuations is related to a change in the stability of the plasma and/or the turbulence characteristics. The main characteristic of this change in the fluctuation spectrum (for both the reflectometer and the Mirnov loops) is the drastic decrease in the low-frequency fluctuations and an increase in the high-frequency fluctuations.

Figure 2 shows detailed structure in the density fluctuation spectra obtained by the reflectometer in a sequence of ECH discharges. In this experiment, the reflectometer frequency was varied to scan the reflecting layer in radius from $r/a \simeq 0.83$ to $r/a \simeq 0.95$. At the edge, the density fluctuation spectra agree well with the FRLP measurements for frequencies below 200 kHz. As the reflecting layer of the reflectometer probing beam is moved further into the plasma, structure around 20 kHz and 40–60 kHz appears in the spectra. As the radial position of the cutoff layer is moved still farther into the plasma, the peak in the spectra decreases and then disappears. The reflectometer's ability to scan across such a large structure in the density fluctuation spectra and observe its disappearance, even though the probing beam is passing through the fluctuation to get to the reflecting surface, is an important indication that reflectometry can be used for local measurements of density fluctuations.[4]

## References

[1]J. F. Lyon et al., Fusion Technol. **10**, 179 (1986).

[2]G. R. Hanson et al., "The ATF Two-Frequency Correlation Reflectometer", accepted for publication, Rev. Sci. Instrum. (1990).

[3]R. R. Kindsfather et al., Rev. Sci. Instrum. **57**, 1812 (1986).

[4]J. Sanchez et al., "Reflectometry Observations of Density Fluctuations Associated with the Resonant q = 2 Surface in WENDELSTEIN VII-AS Stellarator", submitted to Nucl. Fusion.

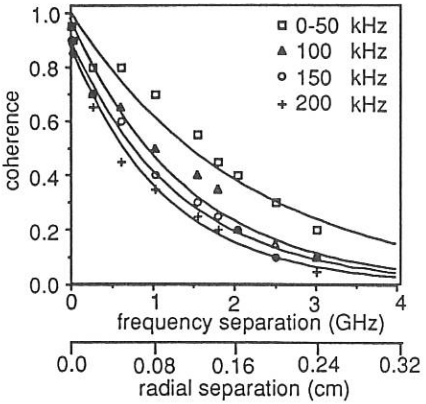


Fig. 1. Radial coherence of density fluctuations in the edge of an NBI plasma measured by two-frequency reflectometry.

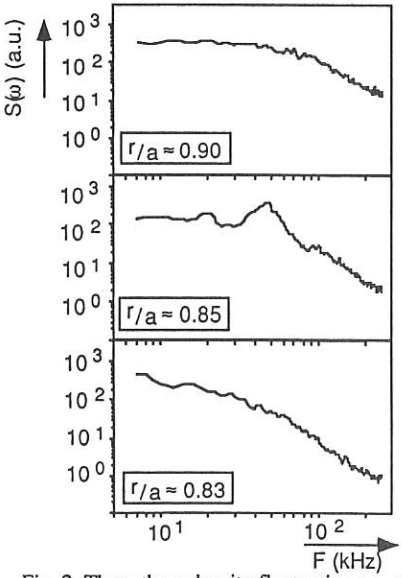


Fig. 2. These three density fluctuation spectra from an ECH plasma obtained by reflectometry show the radial dependence of structure at 20 kHz and 40−60 kHz at three consecutive radial positions.

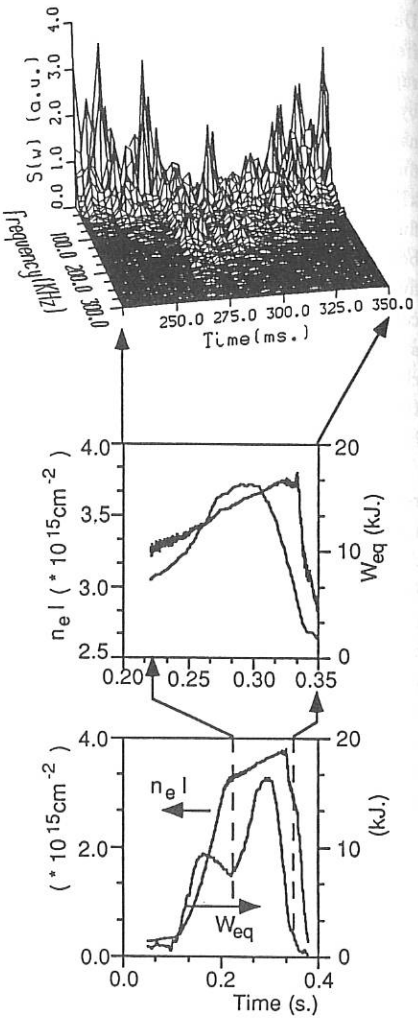


Fig. 3. This 3-D plot shows the rapid decrease in the low-frequency fluctuations and increase in the higher-frequency fluctuations as the plasma stored energy peaks. Also visible is the frequency peak that dominates the spectrum at the stored energy peak.

# MEASUREMENTS OF DEUTERON DENSITY PROFILES IN JET

W.Mandl, M.von Hellermann, P.D.Morgan, H.P.Summers, H.Weisen
M.Olsson[1], P.van Belle, T.Elevant[1], G.Sadler
JET Joint Undertaking, Abingdon, UK
[1]Royal Institute of Technology, Stockholm, Sweden

Introduction:
The plasma purity, deuteron density $n_D$ and deuteron temperature $T_D$ are the governing parameters in determining the rate of thermonuclear fusion. The Lawson criterion $n_D \tau_E T_D > 5 \times 10^{21}$ $m^{-3}$keV sec ($\tau_E$=energy confinement time) is usually applied to assess the fusion product needed for a nuclear reactor. In practice, the electron density and temperature are frequently used in the above criterion because they are the more easily measured. However, in high power neutral beam heated discharges, the ion temperature can exceed the electron temperature by more than a factor of two. Additionally, the high power density on material surfaces can lead to a considerable impurity influx.

At JET a number of diagnostics are applied to measure these quantities [1]. Three different spectroscopic methods are employed to derive profiles of the deuterium density and ion temperature of the bulk plasma. A further independent technique of obtaining the deuteron density relies on measurements of neutron emission.

## CXRS with light impurities

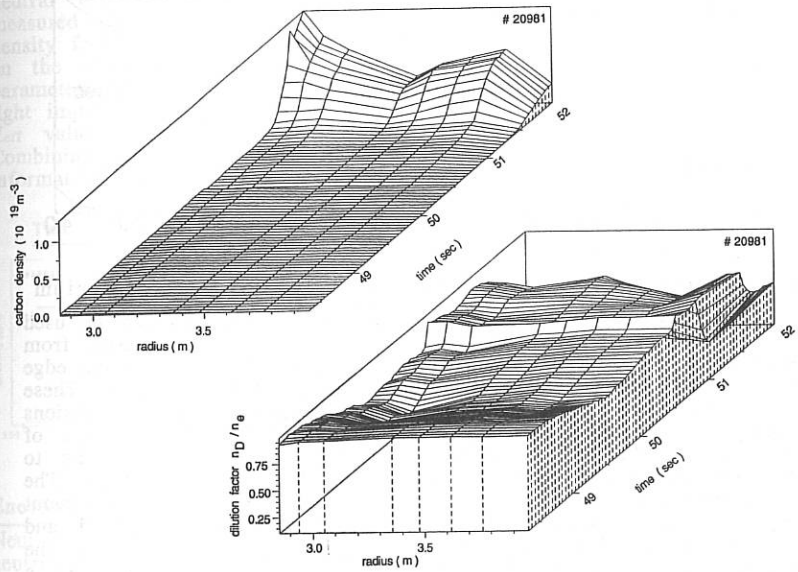

Densities of the main light impurities, namely helium, beryllium, carbon and oxygen, are obtained from absolutely-calibrated charge-exchange recombination spectroscopy (CXRS), using the neutral-particle heating beams as probes. A fan of fifteen nearly-horizontal viewing lines intersects the beams at different radial positions. Simultaneously-recorded optical spectra give radial profiles of ion temperature, impurity concentration and plasma rotation at a temporal resolution of the order of 50 msec [2]. Additionally, the concentrations of up to two further impurities can be monitored with a temporal resolution of 8 to 10 msec at the plasma centre [3]. The deuterium density can then be calculated from the electron density profile, assuming charge neutrality.

$Z_{eff}$ profiles from Abel inverted visible bremsstrahlung

Measurement of visible bremsstrahlung is routinely used at JET to obtain the line-averaged effective plasma charge, $Z_{eff}$. Abel inversion of measurements along 14 lines-of-sight are used to derive the $Z_{eff}$ profile. For this method one has to make assumptions about the plasma geometry and the symmetry of the $Z_{eff}$ profile. It turns out, that the result depends sensitively on the electron density profile used for the inversion. The example shown below illustrates the transition from a peaked to a hollow $Z_{eff}$ profile during increased impurity influx due to intense additional heating.

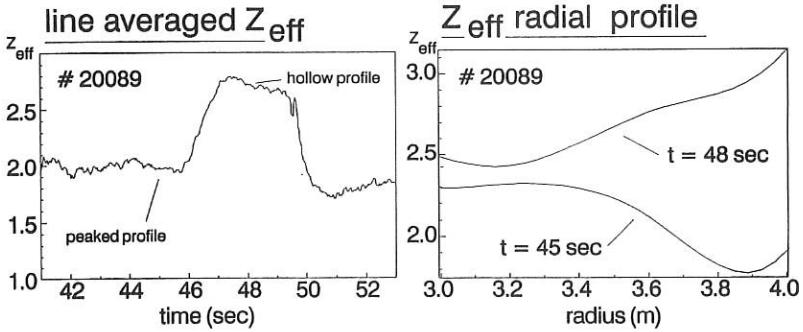


Charge exchange recombination spectroscopy (CXRS) with deuterium

CXR light emitted by deuterons rather than by impurity ions can be used directly. In the past, it proved difficult to distinguish the signal from CX reactions in the bulk plasma from that emerging from the plasma edge due to resonant charge exchange with thermal deuterium atoms. These problems, which have prevented the use of deuterium spectral emissions for density measurements so far, are now being tackled. The use of passive viewing lines and of beam modulation techniques allows us to monitor the background radiation during neutral beam injection. The energy dependence of the CX cross sections has to be taken into account carefully. The atomic data base at JET has recently been updated and extended to meet this requirements. The figure below shows the CXR-emission cross sections for 80keV deuterium neutral beams and a

plasma target with $Z_{eff}$ = 2.5 and $n_e = 3*10^{19}$ $m^{-3}$ as a function of the plasma temperature. It includes l- and n-shell redistribution due to collisional and radiative processes and averaging over the energy distribution of the plasma ions.

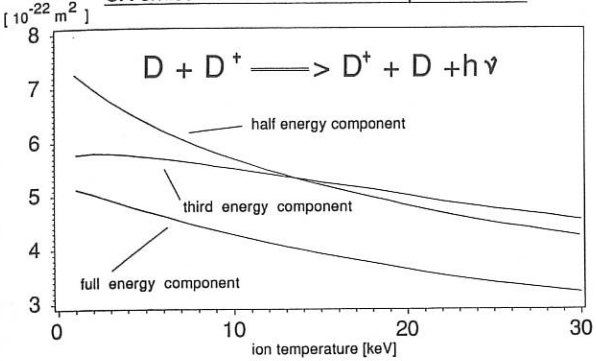


## Active Balmer-alpha spectroscopy (ABAS)

A third, very powerful technique, active Balmer-alpha spectroscopy (ABAS), uses light from the CX reaction with plasma deuterons together with the relaxation radiation from excited fast deuterium atoms in the neutral heating beams [4,5]. The local neutral-particle density can be measured directly and can be used to calculate the plasma deuteron density from the CX line intensity. In this way one does not have to rely on the electron density from the beam emission as an external input parameter. The line ratio of CX to beam radiation and the species mix of light impurities as measured by CXRS enables the determination of a local $Z_{eff}$ value, without recourse to Abel inversion or absolute calibration. Combining the species mix of light impurities and radial $Z_{eff}$ profile information gives the deuterium dilution profile.

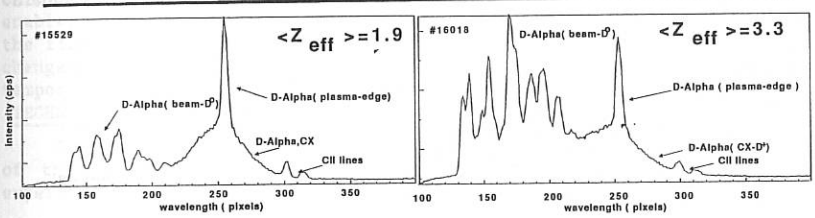


## Energy resolved neutron diagnostics

Neutron spectra measured with a time-of-flight spectrometer during neutral beam injection are analyzed to determine the fractional neutron

yields from the thermonuclear, beam-thermal and beam-beam reactions. For cases in which the thermonuclear fraction is substantial it is possible to determine its value with sufficient accuracy for further analysis. The neutron emission strength and energy spectrum have been used to deduce the deuterium to electron density ratio $n_D/n_e$ at the plasma centre. The temporal resolution depends on the absolute neutron flux and is for most JET pulses of the order of one second.

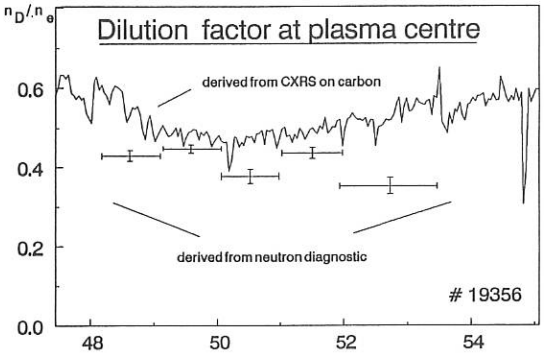


## Summary and error assessment

A number of diagnostic techniques which allow the measurement of deuteron density profiles are available at JET. Plasma dilution measurements with CXRS are performed routinely. The error arising from uncertainties in the instrument calibration and from photon statistics depends on the actual plasma purity. It is estimated to be less than 30% at a plasma dilution $n_D/n_e > 50\%$. The uncertainty decreases for cleaner plasmas. Methods which are independent of calibration (ABAS) have been developed and tested. Independently-measured dilution factors from Abel inverted visible bremsstrahlung and neutron diagnostics provide the means for extensive consistency checks and are generally in fair agreement. Error estimates depend on the plasma conditions in such a way as to make a 'standard' error meaningless.

References

[1] Jarvis O.N. et al.,Nuclear Fusion, Vol.30, No.2 (1990)
[2] Weisen H. et al.,Nuclear Fusion, Vol.29, No 12 (1989)
[3] Boileau A. et al.,Nuclear Fusion, Vol.29, No 9 (1989)
[4] Boileau A. et al.,J.Phys.,B 22 (1889) L145
[5] Mandl W. et al.$Z_{eff}$ profile measurements in JET by Active Balmer-$\alpha$ Spectroscopy, to be submitted to Plasma Phys. Controll. Fusion

# FIRST MEASUREMENTS OF ELECTRON DENSITY PROFILES ON JET WITH A MULTICHANNNEL REFLECTOMETER

R Prentice, A C C Sips[+], J A Fessey and A E Costley

JET Joint Undertaking, Abingdon, Oxon, OX14 3EA, UK

[+] FOM Institute for Plasmaphysics "Rijnhuizen", The Netherlands

## INTRODUCTION

Microwave reflectometry offers the possibility of continuous localized measurements of the electron density with both good spatial and temporal resolutions. Recent applications of the technique to moderate size tokamaks have been successsful [e.g.1,2] but the technique employed,i.e. broad band sweep, is difficult to apply to larger machines because of the need to locate the sources and detectors remote from the torus: complicated waveguide systems in oversized guide are required and mode conversion can lead to spurious signals when the frequency is swept over a broad range. To overcome this problem we have developed a novel technique, multichannel narrow band sweep, and applied it to JET and in this paper we present the first profile measurements. An advantage of this approach is that, by keeping the the probing frequencies constant, the same instrument can be used to measure fast density transients, and data obtained in this way are also presented.

The JET multichannel reflectometer [3,4] probes the plasma with radiation in the ordinary mode along the mid-plane with frequencies in the range 18 - 80 GHz, which corresponds to a critical density range of 0.4 - $8\times10^{19}$ $m^{-3}$. When used in the swept mode a new data correction procedure enables profiles to be determined with a time resolution of ~ 5 ms. In the fixed frequency mode, the system is sufficiently sensitive to monitor changes of ≤ 1mm in the position of the critical density layers with a temporal resolution of ~ 1 ms.

## TECHNIQUE FOR PROFILE DETERMINATION

Fig.1 shows schematically the parameters of interest in a measurement of the profile by the reflectometer. The two parameters determined experimentally are $\tau_w$ and $\tau_x$, the group delay differences between the arms of the reflectometer for reflections from the inner wall and the plasma respectively. For a given channel, the group delay into the plasma, $\tau_p$, from an arbitrarily placed reference plane is given by:

$$\tau_p = \tau_x + \tau_{ref} - \tau_w$$

$$\text{where } \tau_{ref} = 2(R_{ref} - R_w)/c$$

The value of $\tau_x$ for each channel is derived from the simple expression:

$$\tau_x = f_B / \dot{f}_s$$

where $f_B$ is the beat frequency at the detector and $\dot{f}_s$ is the rate of change of source frequency. Values for $\tau_w$ are found using the same relationship.

Simulation studies [5] have shown that the values of $\tau_p$ are required to an accuracy of $\simeq$ 0.1 ns to produce profiles accurate to $\simeq$ 1 cm after inversion. To achieve accuracies of this order it is necessary to carry out a rigorous analysis of the phase detector signals which are used to monitor the phase excursions when the source frequencies are swept up and down. An example of phase detector signals for four channels of the system are shown in Fig.2 Note that the fixed frequency signals evolve and even change direction over the period of the measurements. An accurate value for $f_B$ is found from the phase detector data in the following way. The fixed frequency data, on either side of a swept frequency period, are used in a non-linear fitting procedure (cubic spline) to produce, by interpolation, an accurate 'baseline' over the duration of the sweeps. This 'baseline' is then used to correct the swept frequency data. A further correction is applied to account for the non-linear voltage/frequency characteristics of the Gunn oscillator sources. Linear regression is then applied to the corrected signals to obtain $f_B$. It is worth noting that this procedure makes use of all the data recorded when the source frequencies are swept. The $\tau_p$ values are finally inverted to generate a density profile referenced to the inner wall.

The reflectometer profile shown in Fig.3(a) was obtained in this way for an ohmically heated plasma and is seen to be in good agreement with the profile obtained with the FIR interferometer on JET (dashed line). It should be noted that the radial location of the reflectometer profile is fixed by internal calibration and is completely independent of the interferometer profile. The lower section of a profile obtained under H-mode conditions is shown in Fig.3b. It is clear that the gradient at the edge of the plasma can be very steep: a vertical profile is within the measurement uncertainties. The minimum gradient through the reflectometer data is $\simeq 4\times10^{20}$ $m^{-4}$.

## PROFILE EVOLUTION AND DENSITY TRANSIENTS

By keeping the source frequencies fixed, it is possible to use the phase detectors to monitor the evolution of the density profile, starting from a reference profile obtained, say, from the FIR interferometer. Fig.4 shows some density contours, for each probing frequency, produced in this way. In this case the reference profile was taken at the time of 12.4 s and the variations in the profile were computed, both backwards and forwards in time. The profile derived in this way can then be compared at any time with that available from the FIR interferometer. Checks of this type show that over the time interval of Fig.4 the radial discrepancies between the two profiles are always < 5 cm. During the period when the RF power was applied to the plasma (Fig.4), large sawteeth are clearly visible. Detailed analysis of these density pulses has enabled values for the particle diffusion coefficient to be determined and these are used in

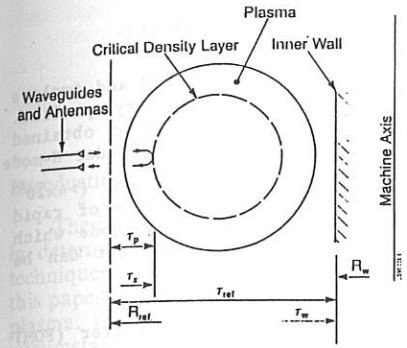


Fig.1 Schematic showing the relationship between relevant parameters for a profile measurement. $R_{ref}$ is chosen to be ~ 200 mm outside of the last closed flux surface.

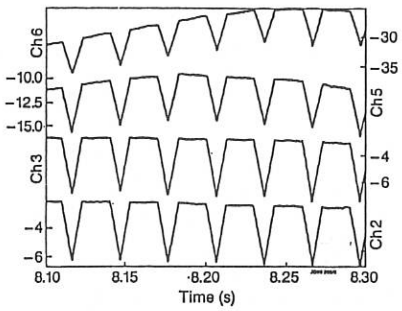


Fig.2 Phase detector signals showing the quasi-stationary fixed frequency signals and the 'V' shaped swept frequncy data. The vertical scales are in units of fringes

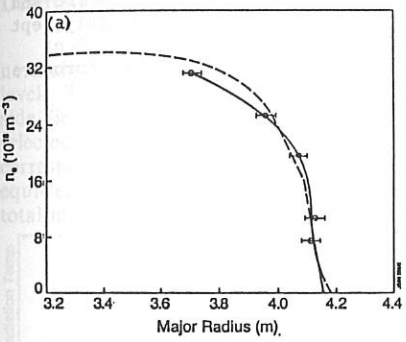


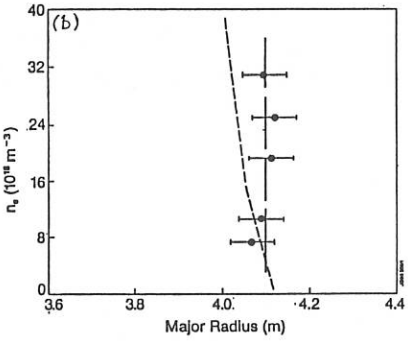


Fig.3 (a) Profile for ohmic pulse # 20982 with $I_p$ = 4.1 MA and $B_T$ = 2.8 T
(b) Section of H-mode profile for pulse # 20994. $I_p$ = 3.1 MA, $B_T$ = 2.2T and NBI power = 8.5 MW. The peak density for this pulse was ≈ $6.3 \times 10^{19}$ $m^{-3}$.

combined studies of localized particle and thermal transport[6].

## CONCLUSIONS

A multichannel reflectometer has been implemented on JET and employs a novel narrow band sweep technique to obtain the density profile. Measured profiles are generally in good agreement with those obtained with the FIR interferometer. The profile information obtained under H-mode conditions confirms the existence of a very steep edge gradient (>$4\times10^{20}$ $m^{-3}$). With the probing frequencies held constant, measurements of rapid density perturbations can be made and, utilizing a transport code which simulates these measurements, the particle diffusion coefficient can be determined.

## ACKNOWLEDGEMENTS

We would like to acknowledge Mr C A J Hugenholtz and Mr A J Putter (FOM) for their work on the sources, receivers, reference waveguides and data acquisition system and Miss K Slavin for developing the control and analysis software.

## REFERENCES

[1] M E Manso et al. 16th European Conf. on Controlled Fusion and Plasma Physics. Venice, 1989. Vol 13B,Pt.IV, p.1517

[2] E Doyle. Bulletin of the Am. Phys. Soc. (Div. of Plasma Phys.) 34,No 9,p.2116 (1989)

[3] R Prentice, A E Costley, J A Fessey and A E Hubbard. Course and Workshop - 'Basic and Advanced Diagnostic Techniques for Fusion Plasmas',Varenna,Italy,Sept 1986. EUR 10797 EN,Vol II,p.451

[4] C A J Hugenholtz and A J Putter. Course and Workshop - 'Basic and Advanced Diagnostic Techniques for Fusion Plasmas',Varenna,Italy,Sept 1986. EUR 10797 EN,Vol II,p.469

[5] A E Hubbard. 'Measurement of Electron Density on JET by Microwave Reflectometry'.Ph.D. Thesis, University of London 1987

[6] G H D Hogeweij et al. This conference

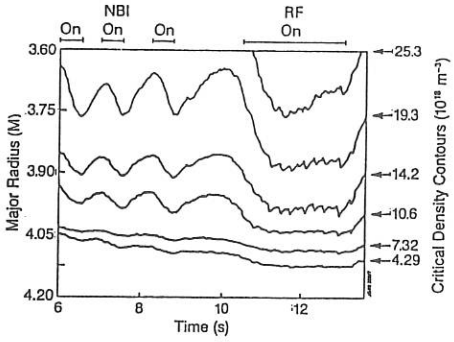


Fig.4 Density contours for pulse # 19596. The powers for NBI and RF were ~ 2.5 MW and ~ 4MW respectively.

# A METHOD FOR THE DETERMINATION OF THE TOTAL INTERNAL MAGNETIC FIELD IN JET

L Porte*, D V Bartlett, A E Costley, C W Gowers

JET Joint Undertaking, Abingdon, Oxon. OX14 3EA, UK
*University of Strathclyde, Glasgow G4, UK

## Introduction

The internal magnetic fields in tokamak plasmas are of paramount importance in determining the plasma confinement and stability. There are, however, few techniques available for making spatially resolved measurements of these fields. In this paper we describe a new method for determining the total magnetic field in the plasma. Combined with data from other diagnostics it is possible, under some circumstances, to derive the spatial distribution of the paramagnetic component of the internal field.

The method combines measurements from two independent electron temperature diagnostics: **E**lectron **C**yclotron **E**mission (**ECE**) which gives temperature as a function of cyclotron frequency, and time-of-flight **LI**ght **D**etection **A**nd **R**anging (**LIDAR**) Thomson scattering which measures temperature as a function of major radius directly. ECE frequencies are identified with the spatial locations which the LIDAR shows to have the same electron temperature. Conversion of the cyclotron frequency scale to magnetic field then gives the total field profile.

## Description of the Method

In detail, the procedure is as follows. The ECE and LIDAR temperatures are normalised to eliminate spurious effects due to any small difference in absolute level. The low frequency side of the ECE spectrum (Figure 1a) and the low field side (ie outer half) of the LIDAR electron temperature profile (Figure 1b) are selected. For peaked profiles, these curves are monotonic, ensuring a one-to-one correspondence between equi-temperature points on the two curves. Linking these equi-temperature points (Figure 1c) gives cyclotron frequency (or equivalently, the total magnetic field) as a function of major radius (Figure 1d).

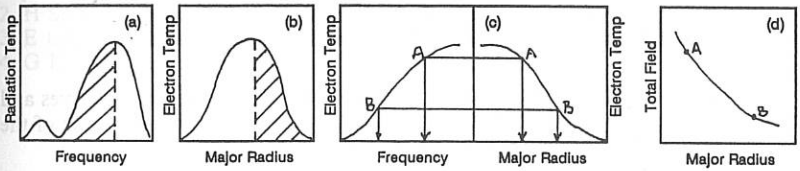


**Figure 1** (a)Select low frequency side of ECE spectrum (b)Select outer half of LIDAR Te profile (c)Link equi-temperature points (d) Deduce total field as a function of major radius.

In this work the ECE spectrum is measured by an absolutely calibrated, rapid-scan Michelson interferometer {1}. It has a spectral resolution of 10GHz ($\approx$15cm spatial resolution), time resolution of 15 ms and relative systematic uncertainty of the measured spectral shape of $\pm$ 5%. The LIDAR diagnostic {2} uses 180° Thomson backscattering to measure the electron temperature profile as a function of radial position. It has a spatial resolution of $\lesssim$10cm and the errors are dominantly statistical, at typically $\pm$ 7%.

**Numerical Simulation**

To determine how the main sources of error and the measurement limits affect the accuracy of the field determination, an error analysis has been performed by applying the method to simulated ECE and LIDAR data. Idealized ECE spectra and idealized LIDAR profiles were perturbed in various ways, representative of the known measurement limitations and uncertainties. The method was then applied to various combinations of the idealized and perturbed data. By examining the effects of the ECE and LIDAR errors separately, and in combination, the relative importance of the different measurement uncertainties and limitations was determined.

Uncertainties in the relative calibration of the ECE system were modelled by applying to the ideal spectrum a sinusoidal perturbation of amplitude $\pm$ 5%, random phase and periodicity similar to that of the estimated calibration errors. The statistical errors in the LIDAR measurements were modelled by multiplying the ideal profile points by random numbers with a suitable Poisson distribution. When field profiles were calculated from these perturbed data and compared with those calculated from the ideal spectra and profiles, it was found that the magnitude of the errors were strongly dependent on the temperature profile shape and that peaked profiles give the most accurate field determination.

The dashed lines in Figure 2 show the relative error in the deduced total field for four different sets of combined simulated ECE and LIDAR errors. The input temperature profile was similar in shape to measured peaked profiles. The envelope curves (solid lines) are calculated by applying a Taylor expansion to an analytic model of the method. This shows that the field error ($\delta$B) resulting from a temperature error ($\delta$T) in one of the measurements can be approximated as:

$$\delta B \approx \frac{\partial B}{\partial R} \Big/ \frac{\partial T}{\partial R} \times \delta T + \frac{1}{2} \times \frac{\partial^2 B}{\partial R^2} \Big/ \left(\frac{\partial T}{\partial R}\right)^2 \times (\delta T)^2$$

The envelope curves give a good indication of the maximum of the error curves and enable the errors to be estimated simply. Figure 2 shows that the magnitude of the total field can be determined to $\approx$3% across most of the minor radius.

It was found that for typical temperature profile shapes, improving the spectral resolution of the Michelson interferometers by up to 30% changed the field

profile by less less than 1% while an improvement of the spatial resolution of the LIDAR system of ≈40% changed the temperature profiles negligibly.

**Experimental Results and Analysis**

The internal fields of JET plasmas during strong additional heating have been determined and compared with those calculated by the JET magnetic equilibrium code {3}. Figure 3 is an example of the results. It shows consistency within the experimental uncertainties shown on the figure.

The poloidal field is known from independent measurements with a far-infrared polarimeter and so it is possible to estimate the paramagnetic field in this case. The known vacuum field and the measured poloidal field are removed from the measured total field. Figure 4 compares the paramagnetic field so obtained with that calculated by the magnetic equilibrium code. Since the paramagnetic and poloidal fields are about an order of magnitude less than the total field, the uncertainty in the deduced paramagnetic field is dominated by the uncertainties in the ECE/LIDAR method: the uncertainties in the poloidal field measurement are not significant. The uncertainty in the deduced paramagnetic field is large, (≈30%), and the two curves agree to within this limit.

Figure 5 displays the total field at a later time during the same plasma pulse, while Figure 6 shows the corresponding paramagnetic field, which is larger than in Figure 4 because the plasma current is higher.

**Conclusions**

A method has been developed to determine the total magnetic field in JET, using two independent electron temperature diagnostics which is accurate to typically 3% to 8% across most of the plasma profile. By introducing the poloidal field measured by the JET polarimeter it is possible to estimate the paramagnetic field to an accuracy of typically 30% to 80%. The results generally agree with the fields calculated by the JET magnetic equilibrium code.

The authors would like to thank Dr. J O'Rourke for making available the polarimetry data used in this work.

**References**

1. D V Bartlett et al, Proc. of Sixth Joint Workshop on ECE and ECRH (Oxford, Sept 1987)
2. H Salzmann et al, Nucl. Fusion 27, 1925 (1987)
3. E Lazzaro and P Mantica, Plasma Physics and Cont. Fusion, 30, 1735 (1988)
4. G Braithwaite et al, Rev. Sci. Instrum. 60, 2825 (1989)

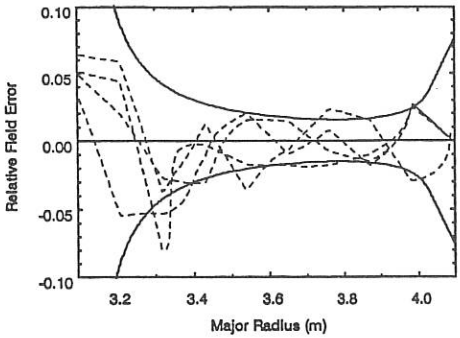


**Figure 2** Numerical simulation of relative error in deduced total field (broken lines) and the error envelopes from the analytical model.

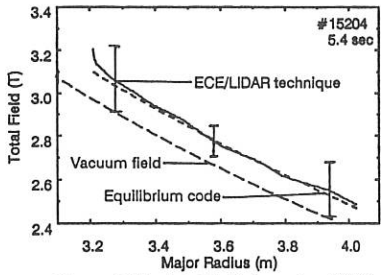


**Figure 3** The total field for pulse 15204 at t = 5.4s. Ip = 4.4MA

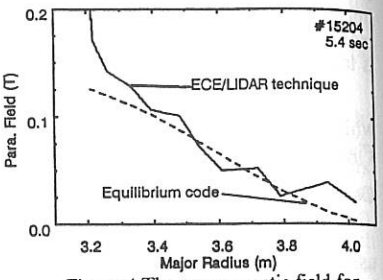


**Figure 4** The paramagnetic field for pulse 15204 at t = 5.4s.

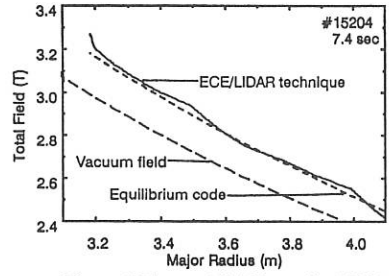


**Figure 5** The total field for pulse 15204 at t = 7.4s. Ip = 5MA

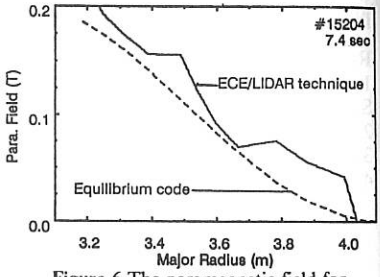


**Figure 6** The paramagnetic field for pulse 15204 at t = 7.4s.

# CURRENT PROFILE MEASUREMENT USING NEUTRAL He BEAM IN JT-60 TOKAMAK

H.Kubo, T.Sugie, N.Nishino*, A.Sakasai, N.Akaoka, T.Itoh,
Y.Tsukahara, H.Takeuchi and JT-60 Team

*Naka Fusion Research Establishment, Japan Atomic Energy Research Institute*
*Naka-machi, Naka-gun, Ibaraki, 311-01, JAPAN*

## 1. INTRODUCTION

For establishment of a steady state tokamak reactor, techniques of noninductive current drive should be obtained. The current profile measurement is of great importance in order to control the current profile in the steady state tokamak reactor. As the current profile can not be directly measured, a variety of methods measuring the poloidal magnetic field have been used to estimate the current profile. The Faraday rotation measurement using a FIR laser gives the average of the density times the component of the field along the sight-line[1]. In medium tokamaks, the Zeeman polarimeter using a Li beam has been used for the directly measurement of the local poloidal field[2]. However, because the Li beam attenuates severely in large tokamaks, the diagnostics is in need of a high energy Li beam such as MeV range which is difficult to obtain. Therefore, a current profile measurement system using a He beam has been constructed for the diagnosis in the discharges with lower hybrid current drive (LHCD) on JT-60[3]. Purposes of this paper are descriptions of the system and its application to the current profile measurement in LHCD discharges on JT-60.

## 2. EXPERIMENTRAL SETUP

Figure 1 shows the outline of the current distribution measurement system consisted of a neutral He beam injector and 4 spatial channel detection system. The beam intensity is equivalent to 0.6A and the maximum energy is 200keV[4]. The neutral beam is also used to measure ion temperatures by Ratherford scattering[5]. The neutral beam is generated from positive ion beam by charge-exchange reaction in a gas cell. The neutral beam contains about 30% metastable ($2s^3S$) atoms which are ionized in the peripheral region of plasma. The component was estimated by a beam attenuation measurement using a Faraday cup and a spectroscopic measurement. Four beam pulses with the durations of 100ms can be injected during 1sec in a discharge. The neutral He beam attenuates to about 1/2 at the electron density of $3\times10^{19}m^{-3}$ and Zeff of 2.5 in the JT-60 plasma.

The spectral line of He beam atoms following collisional excitation with electrons is split into three components by normal Zeeman effect. The line with $\Delta M=0$ transition ($\pi$-component) is polarized to the magnetic field. The local pitch angle $\theta=\tan^{-1}(B_p/B_T)$ of the magnetic field lines can be determined by measuring the polarization angle of the $\pi$-component[2].

Figure 2 shows the schematic diagram of viewing optics layout. The collected light is converted into a parallel beam by a condensing lens. In order to increase the sensitivity of the angle measurement, the polarization direction is rotated 45 degrees by a $\lambda/2$ plate. A Wollaston prism with its axis parallel to the toroidal field separates the incident light into two beams whose polarization directions are perpendicular each other. After converting both beams into circularly polarized lights with a $\lambda/4$ plate, the image is rotated by a prism so that the two beams enter the slit of a Littrow type spectrometer. The wavelength band of the spectrometer is 0.1Å, because the wavelength separation of the Zeeman components is about 0.3Å. The accuracy of the wavelength of the spectrometer is checked remotely using an Ar laser.

The intensity of light emitted from the He beam is estimated to be $10^{16}$ photons $m^{-3}$

$sec^{-1}$. Accordingly, considering the solid angle, the intensity of light coming to the system becomes $10^6$ $sec^{-1}$. The transmittance of each optical component is higher than 0.96 except the Wollaston prism and the spectrometer whose transmittances are 0.6 and 0.4, respectively. Therefore, the total light throughput is estimated to be 0.2. As a result, the intensity of the light coming into the detector becomes about $5x10^4 sec^{-1}$. In order to recover the difficulty of the low intensity, we have developed a high efficiency avalanche photo diode detector whose detection efficiency is 30-32% at the wavelength of 5015Å. As a result, the count rate is estimated to be several times $10^3 sec^{-1}$.

The spatial distribution of the poloidal magnetic field is measured at four points as shown in Fig.1. The sight lines intersect the He beam at angles of 50-70 degrees. The pitch angle $\theta$ relates to the measured polarization angle ($\theta_M$) as $\tan\theta_M=\cos\gamma \tan\theta$, where $\gamma$ is the angle between the normal line to the magnetic surface and the sight line as shown in Fig.3. For estimation of the current profile, MHD equilibrium should be calculated from the polarization angle and the external magnetic data.

## 3. EXPERIMENTAL RESULTS

The measurement system was applied to estimate the current profile in LHCD discharges with 2MW LHCD applied from a new multi-juction launcher. In the experiment, the current drive product became up to $12x10^{19}$ MA $m^{-2}$. And H-mode was also realized in the limiter discharges with low threshold power (1.2MW)[4].

Before the application to LHCD experiment, the dependences of the polarization angle on the surface safety factor $q_s$ were investigated in order to confirm the performance of the measurement system. The Zeeman pattern was distorted by Stark effect in the electric field originating from the product of He beam velocity and magnetic field. The observed Zeeman spectrum and the calculated spectrum considering the Stark effect are shown in Fig.4. Therefore, we observed the blue wing of the $\pi$-component which was not influenced by the $\sigma$-components. The line intensity was obtained subtracting noise signal due to the bremsstrahlung from the raw signal. The observed count rate is the order of $10^4$cps, and the ratio of the signal to noise was 2-3. The polarization angle was determined from the ratio of the intensities of the separate light beams. The accuracy for determination of the poloidal angle depends on the statistical error coming from the count rate. And the accuracy also depends on the installation accuracy of each Wollaston prism. In $q_s$ scanning experiments, the measurement of the polarization angle suggested that the lower $q_s$ operation formed the broader current distribution. However, the absolute current profile could not be deduced because of the difference between the directions of the polarization axes of the channels. Therefore, a relative change of the current distribution was estimated in the LHCD experiment. Figure 5 shows the comparison of polarization angle between L-mode and H-mode phase in the LHCD discharges; $I_p$=1MA, $B_T$=4.5T, $\overline{n_e}=3x10^{19}m^{-3}$, $P_{LH}\geq$1.2MW, and the LH frequencies were 1.74 and 2.23 GHz. The H-mode continued during several seconds, and the polarization angles were measured at 2 sec after the H transition. Channel numbers of 1-4 correspond to the spatial points of 16.5, 35.0, 57.5 and 76.0 cm from the plasma center, respectively. The angle did not indicate absolute one, because the axes of the Wollaston prisms were not calibrated to the toroidal field direction. However, the change of the signal of each channel indicates a change of the poloidal magnetic field. It is inferred from the figure that the poloidal field becomes larger in the outer region and a broader current distribution is realized in the H-mode. The detailed investigation of the current distribution needs an elaborate calibration of the polarization axis of the Wollaston prism.

## 4. SUMMARY

The measurement system of the poloidal magnetic field using He beam was newly developed. It was realized by adopting a high-transmittance spectrometer. And the avalanche photo diode with the detection efficiency of 0.3 was also developed. As a result, the measurement of the poloidal magnetic distribution in the large tokamak such as JT-60 become

possible. Applying to the measurement of LHCD experiment, it suggested that the current density distribution became broader in the H-mode. However, because the offset angels were not known at present time, elaborate calibration must be performed to obtain a more detailed information of current profile.

**Acknowledgements**

The authors would like to thank people of Nikon Corporation and Hamamatsu Photonics K.K for their collaboration to develop the spectroscopic system. The authors would like to acknowledge Drs. A.Funahashi, H.Kishimoto, S.Tamura and M.Yoshikawa for their continuing support.

**REFERENCES**

[1]H. Soltwisch, Rev.Sci.Instrum. 57, 1939 (1986).
[2]P.West, D.M.Thomas, E.S.Ensberg, J.S.deGrassie, and J.F.Baur, Rev.Sci.Instrum. 57, 552 (1986).
[3]S. Tsuji, et al., Phys.Rev.Lett. 64, 1023 (1990).
[4]K. Itoh, et al., Proc. 4th Intern.Symp. on Heating in toroidal Plasma, Roma, Italy (1984) 1081.
[5]H.Takeuchi, K.Tobita, Y.Kusama, M.Nemoto, T.Itoh, Y.Tsukahara,and JT-60 Team, Rev. Sci. Instrum. 59 (1652) 1988.

*Hitachi Ltd., Hitachi-shi, Ibaraki, Japan

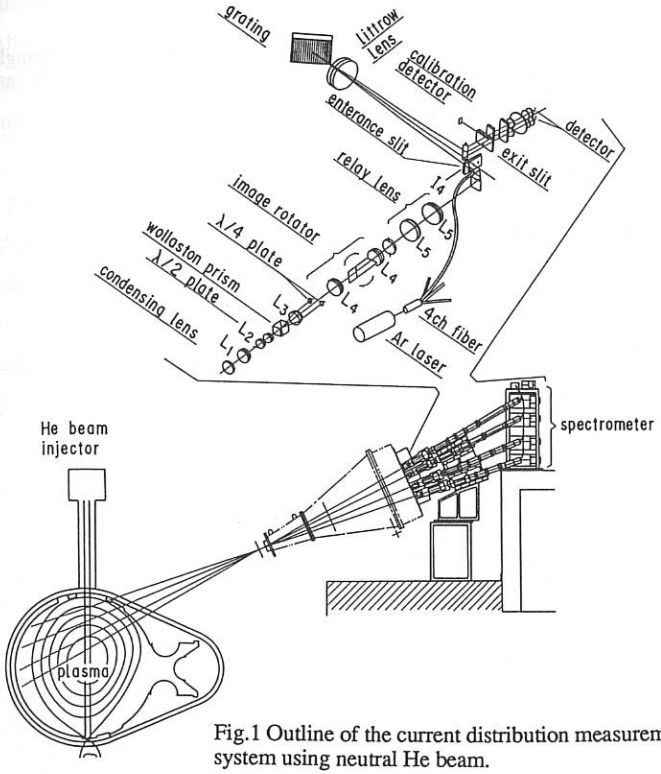


Fig.1 Outline of the current distribution measurement system using neutral He beam.

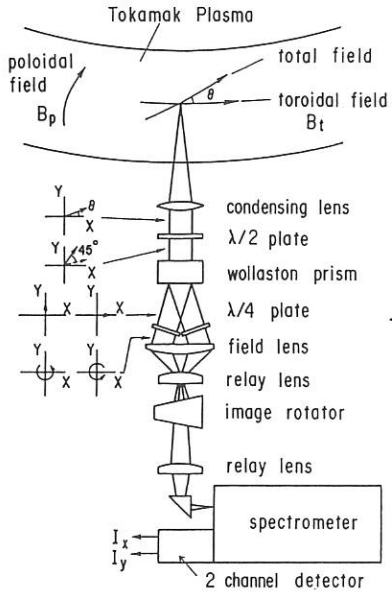


Fig.2 Viewing optics layout.

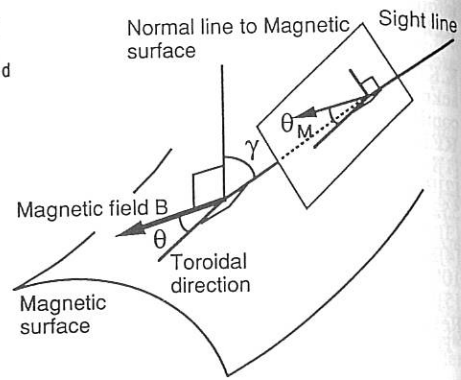


Fig.3 Relation between the pitch angle of the field and the polarization angle measured by the polarimeter.

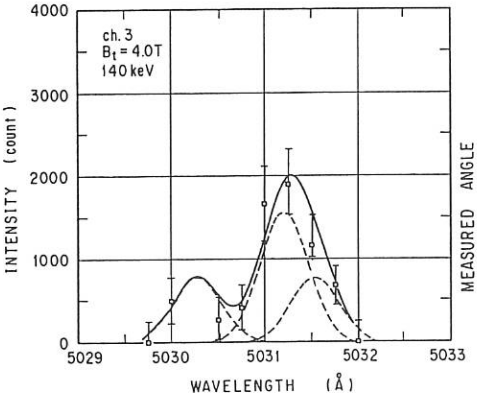


Fig.4 Measured Zeeman pattern. The pattern was distorted by the Stark effect originating from the electric field of VxB.

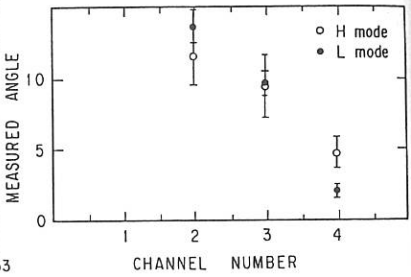


Fig.5 Change of polarization angle in H-mode of LHCD experiment. Numbers of channel 1, 2, 3, and 4 correspond to 15, 25, 55, and 75 cm, respectively.

Mo 34

# REAL TIME PROFILING OF TOTAL RADIATION IN THE TJ-I TOKAMAK BY A FLUORESCENT DETECTOR

B. Zurro and TJ-I Team

Asociación EURATOM/CIEMAT para Fusión. E-28040 Madrid. Spain

Excellent detectors have been developed or borrowed from other fields for radiation diagnostic in tokamaks. Most of these systems involve tens of channels to provide an almost continuous in time and discrete in space, mapping of the plasma radiation in defined spectral ranges. All of them involve sophisticated electronics and data acquisition hardware which are not justified for small plasma experiments, but where similar information must be gathered for machine operation and plasma experiment documentation.

In this paper we describe a detector capable of obtaining global radiation profiles in a hot plasma every 0.5 ms, by spatially scanning the fluorescence of a phosphor. The phosphor chosen, sodium salicylate (ss) when unfiltered responds to a very broad spectral range (x-rays - 3500 Å), which is the relevant region for radiation losses in many hot plasmas. Thus it is a good alternative for bolometry and moderate size experiments and for studying impurity problems so long as high spectral and time resolution are not required.

A simplified schematic diagram of the detector is shown in Fig. 1. The global plasma radiation passing through a diaphragm shines into a quartz window where a uniform layer of ss has been deposited. Its fluorescent band emission, which peaks around 420 nm, is scanned by means of a galvanometric mirror (M1) which focuses the light onto a quartz fiber bundle (3x5 $mm^2$) by means of a quartz lens working with a magnification of 1. The light is guided to a filtered photomultiplier. The spatial resolution in the plasma equatorial plane is around 2.5 cm, which could been improved by deconvolving the profile with a function taken into account the finite size of the fibre bundle.

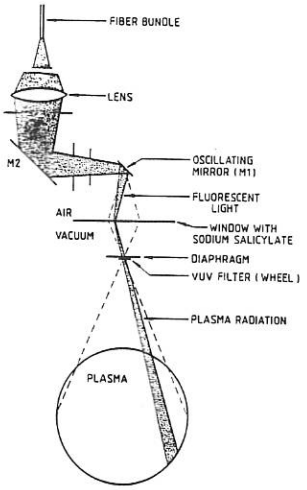


Fig. 1. Schematic diagram of the ss detector. The system is installed at a top flange.

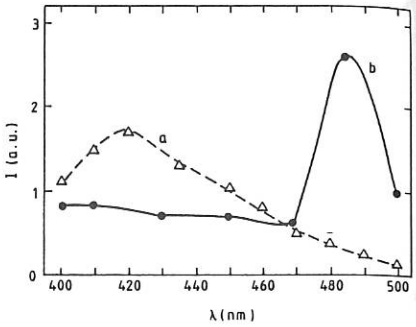


Fig. 2. Spectrum of ss fluorescent light, curve a), excited by cleaning discharges of spectrum b).

The behaviour of ss as a phosphor converter of x-ray and UV radiation into light has been extensively studied and a good review is given in (1). The quantum yield is approximately constant up to 80 eV (155 Å), whereas in the x-ray region (above 12 keV) the energy yield is constant. In the intermediate region is not constant but is well known. The absolute quantum yield depends on, in addition to wavelength, the layer thickness and age. For our application the layer thickness was chosen of around 6 mg/cm$^2$, in order to not have stray light problems due to the strong plasma light, and to reduce the influence of a non uniform deposition on the detector spatial response.

The stray light rejection capability of the detector has been assessed by measuring the fluorescent spectrum of ss excited by periodic tokamak cleaning discharges. This spectrum, curve a), is shown along with the discharge spectrum, curve b), in Fig. 2. Since the most prominent plasma line lying within the ss fluorescent band is the $H_\beta$ (4861 Å), as is evident in b), and this is not visible in the ss fluorescent spectrum we can conclude that the system has good stray light rejection capabilities.

The absolute calibration of the detector has been performed by an in situ procedure and the deduced detector sensitivity is in excellent agreement with that deduced from basic detector parameters. The procedure, explained in more detail in (2), is based in comparing the response of this detector to a tokamak discharge with that of an absolutely calibrated pyroelectric detector, by assuming poloidal and toroidal symmetry in the total radiated power. The sensitivity of the detector so obtained is of 2.7 V/mW, which must be corrected by the observation geometry to get the total radiated power. Since the most important uncertainty in absolute bolometry in tokamaks stems from the existence of radiation asymmetries, the calibration method is good enough for practical applications.

Results obtained with this detector using ohmically heated discharges of the TJ-I tokamak are presented. This toroidal device ($R_0$ = 30 cm; a= 10 cm) was operated with a plasma current around 40 kA and a toroidal field ranging from 0.8 to 1.5 T. The detector can be operated in two modes: when the scanning mirror is at rest, the detector is sensitive to the central line integrated plasma radiation along a vertical chord; turning on the oscillating mirror we can get line integrated radiation profiles. In Fig. 3, the ss detector signal, when the scanning mirror is at rest, is shown along with the trace of a central pyroelectric detector which is sensitive to the whole plasma radiation spectral range (from x-rays to infrared) and the $H_\alpha$ monitor; whereas in Fig. 3a we do not use any type of filter in front of the ss layer, in Fig. 3b a hard UV filter was used. One observes the good agreement between the two radiation detectors, ss and pyroelectric, when the former is unfiltered. The ss detector exhibits some fine structure which is not due to noise but reflects rapid plasma fluctuations. The ss detector tends to underestimate the total radiated power when the visible light is important, like at the beginning of some discharges, but it responds better than the pyroelectric to hard x-rays which are significantly produced in very low density discharges. In fig. 4a, the trace of the modulated detector signal, showing the space-time evolution of plasma radiation, is depicted along with the plasma current, pyroelectric detector and $H_\alpha$ traces in a typical TJ-I tokamak discharge. In Fig. 4b, an expanded view of a particular radiation profile obtained with the detector, in the scanning mode, is shown. This profile exhibit small wings at the plasma edge and a slight hollowness at the plasma centre. Peaked, skewed and hollowed radiation profiles

have been observed, with this detector, in the TJ-1 tokamak which correlate with the global behaviour of the discharge. Typical radiation profiles on varying the plasma density and toroidal field will be shown, as well as the observation of deeps in the profiles, supposedly due to the presence of magnetic island in the plasma.

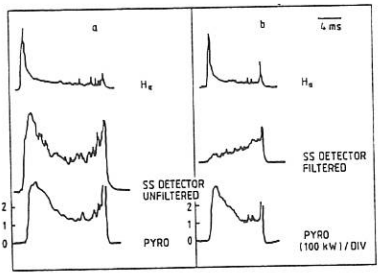


Fig. 3 Typical continuous signature of ss detector along with $H_\alpha$ and central pyroelectric traces.

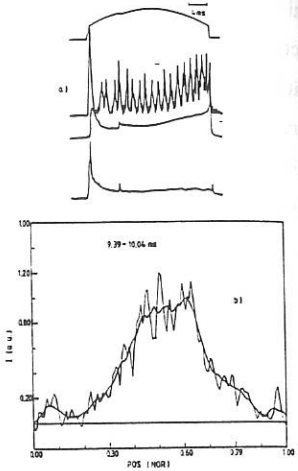


Fig. 4. a) Typical time evolution of radiation profiles in TJ-I ohmically heated discharge; b) Expanded view of a particular profile.

In conclusion, a simple detector capable of presenting in real time the line integrated plasma radiation profiles has been developed. A reasonable method for absolute calibration has been work out. It seems a reasonable alternative to standard bolometers as long as the plasma visible emission is not a significant part of the total radiated power.

REFERENCES

(1) J. A. R. Samson, Techniques of Vacuum Ultraviolet Spectroscopy (John Wiley & Sons Inc., New York, p. 212) (1967).

(2) B. Zurro, Submitted for publication to Rev. Sci. Inst. (1990).

# ION TEMPERATURE DETERMINATION FROM NEUTRON RATE MEASUREMENTS DURING DEUTERIUM INJECTION

B. Wolle, B. Bomba

Max-Planck-Institut für Plasmaphysik, EURATOM Association, D-8046 Garching

K. Hübner

Institut für Angewandte Physik, Universität Heidelberg, D-6900 Heidelberg

## ABSTRACT

Neutron rate measurements are often used to determine the ion temperature or the deuteron density in tokamak fusion plasmas. This can be done easily during ohmic heating or $H^0$-injection, since the velocity distribution function of the plasma deuterons is Maxwellian. However, during $D^0$-injection the distribution function is highly non-Maxwellian and thus needs to be calculated explicitly to perform a temperature or density determination. A parameter study for neutron rate calculations during deuterium injection, using a classical relaxation-time ansatz or a simplified Fokker-Planck model to evaluate the distribution function of the injected particles, shows good agreement of the results obtained from both models for temperatures below 4 keV. As an example for application, calculated ion temperatures are presented for an ASDEX discharge.

## RELAXATION-TIME MODEL

Assuming classical energy relaxation for the injected particle:

$$\frac{dW}{dt} = - \frac{W}{\tau_w} \qquad /1/$$

where W is the particle energy and $\tau_w$ the classical relaxation time as given by Trubnikov, the stationary energy distribution function of the fast particles is:

$$F_b(W) = \dot{S} \frac{\tau_w}{W} . \qquad /2/$$

Here, $\dot{S}$ is the number of local injected particles per second. Now, the local neutron rate in a plasma containing ion species of type (i) and (j), e.g. deuterons or deuterons and tritons, is given by:

$$Q = \frac{n_i \, n_j}{1 + \delta_{ij}} \iint \sigma(|v - v'|) \, |v - v'| \, f_i(v) \, f_j(v') \, d^3v \, d^3v' \qquad /3/$$

where $n_i$ and $n_j$ are the densities of the interacting particles, $\sigma$ is the fusion cross section and $f_i(v)$ and $f_j(v')$ are the normalised distribution functions. From this, the local beam-target neutron rate $Q_{BT}$ follows as:

$$Q_{BT} = n_D \dot{S} \int_0^\infty F_b(W) \langle \sigma v \rangle_{BT} \, dW. \qquad /4/$$

Here, $n_D$ represents the deuterium density of the bulk plasma and $\langle \sigma v \rangle_{BT}$ the fusion reactivity of a target-plasma with the temperature kT and a particle with the energy W.

## FOKKER-PLANCK MODEL

The pitch angle averaged distribution function F(v) is calculated using a steady-state solution of the Fokker-Planck equation:

$$\frac{\partial F}{\partial t} = C(F) + S - L = 0 \qquad /5/$$

where C(F) is the collision operator (see for instance Stix [1]), S is the source of injected particles represented by a delta function at the injection velocity and L is a particle loss term which is needed to calculate the low energy part of the distribution function. From the above given equation, Anderson [2] obtained an analytical expression for a first order differential equation for F(v) which can be solved quickly with numerical methods. The particular solution of this equation is just the distribution function $F_b(v)$ for the injected particles, while the homogeneous solution $F_t(v)$ represents the one of the bulk plasma particles.

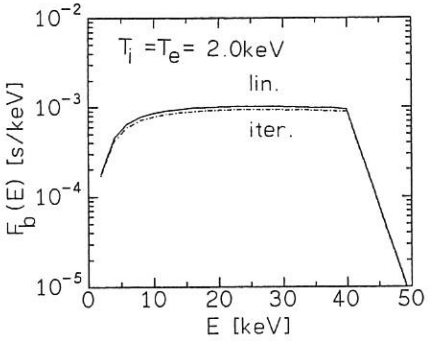


FIG. 1: *Distribution functions calculated using Rosenbluth potentials (solid) and by iteration (dashed).*

Usually, a linearised collision operator is used in which the diffusion coefficients are calculated with the classical Rosenbluth potentials. To estimate the error on neutron rate calculations due to linearisation, a self-consistent solution which takes into account the distribution function itself in the collision potentials was calculated. The non-linear integro-differential equation was solved using an iteration technique, taking the initial distribution as Maxwellian. Fig. 1 shows the calculated distribution function $F_b(E)$ from the linearised (solid line) model and the iterated solution (dashed line) for $T_e = T_i = 2$ keV and plasma data as used for the parameter study below. The final difference in the calculated neutron rates was 6%, which justifies the use of the linearised model.

## PARAMETER STUDY

For this study, the plasma data used was as follows: $n_e = 4 \cdot 10^{13}$ cm$^{-3}$, $n_D/n_e = 0.65$, $S = 5.96 \cdot 10^{13}$ cm$^{-3}$s$^{-1}$, $E_{inj} = 40$ keV. The plasma ion composition was: 18.1% $H^+$, 78.45% $D^+$ and 3.45% $^{14}N^{7+}$ (average of $^{12}C^{6+}$ and $^{16}O^{8+}$).

Fig.2 shows the distribution functions calculated with the two different models /2/ and /5/ for $T_e = T_i = 2.5$ keV. The relaxation time model does not take energy diffusion into account so that $F_b = 0$ if $E > E_{inj}$, while the Fokker-Planck solution shows a Maxwellian tail in this energy range. Because there is no loss model at low energies in the

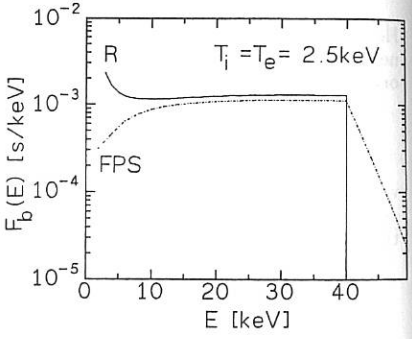


FIG. 2: *Distribution functions calculated with the relaxation-time ansatz (R) and the Fokker-Planck model (FPS).*

relaxation-time ansatz, this distribution function is wrongly calculated at low energies. If the ion temperature is just a few keV, the error on the beam-target neutron rate is small, because the cross-section, which is several orders of magnitude smaller for energies below 10 keV than for energies near the injection energy, compensates this sufficiently.

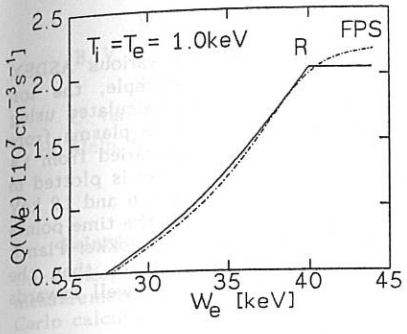


FIG. 3: *Neuton rate plotted as a function of the upper integration limit in eq. /4/.*

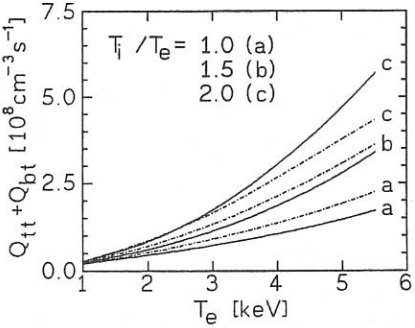


FIG. 4: *Neutron rates for $T_i/T_e$-ratios 1.0 (a), 1.5 (b), 2.0 (c) versus $T_e$. Solid: relax.-time model, dashed: F.-P. model.*

The energy diffusion affects the neutron rate as shown in fig. 3. Here $Q_{BT}+Q_{TT}$ is plotted as a function of the upper integration limit in /4/ for $T_e = T_i = 1$ keV. The relaxation time model overestimates the neutron rate for energies lower than the injection energy, but the final neutron rate is about 6% smaller than the Fokker-Planck result where energy diffusion is included. This effect becomes more important with increasing temperatures but since in ASDEX the temperatures are below 3 keV, the error in neutron rate calculation using the relaxation-time ansatz can be neglected.

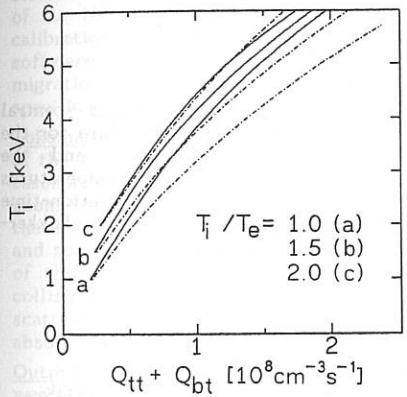


FIG. 5: *Ion temperature versus neutron rate for different $T_i/T_e$-ratios. Dashed: F.-P. model, solid: relax.-time model.*

Fig. 4 shows this in more detail. Here, the neutron rates for different $T_i/T_e$-ratios (a: 1.0; b: 1.5; c: 2.0) obtained from the two models are plotted versus $T_e$. Both electron and ion temperature have an influence on the number of particles in the tail. If the temperature ratio $T_i/T_e$ is greater than 1.0, the number of particles in the tail decreases with increasing electron temperature because the plasma becomes less collisional. Thus, in the plotted temperature range, the calculated neutron rates based on the Fokker-Planck model are greater than the ones using the relaxation-time model if the $T_i/T_e$-ratio is 1.0 or 1.5, but they are smaller above 2.5 keV for the case $T_i/T_e = 2.0$.

Fig. 5 shows the dependence of $T_i$ on the neutron rate. The temperature determination with the two models gives the same results at very low temperatures, but for temperatures occurring in ASDEX discharges, ion temperatures determined using the Fokker-Planck model are mostly lower than the ones calculated with the relaxation-time model.

## ION TEMPERATURE DETERMINATION

Neutron interpretation calculations have been carried out for various ASDEX discharges with deuterium injection. As a representative example, the ion temperature for some time points of the discharge #30953 was calculated using both models. This shot had 1.25 MW $D^0$-injection into deuterium plasma from 0.9-1.9 sec. The central electron density was $5\text{-}7 \cdot 10^{13} cm^{-3}$, $Z_{eff}$ varied from 1.4 to 2.0. The measured neutron rate for the time window 0.8-1.8 sec is plotted in fig.6. The measured central electron temperature varied between 0.6 and 1.2 keV and is plotted in fig. 7. The calculated deuteron temperatures for the time points 1.0, 1.3 and 1.65 sec are plotted as well in fig. 7. As expected, the Fokker-Planck solution (FPS) gives due to energy diffusion smaller temperatures than the relaxation-time model (R), but the calculated temperatures agree well towards the middle and the end of the discharge.

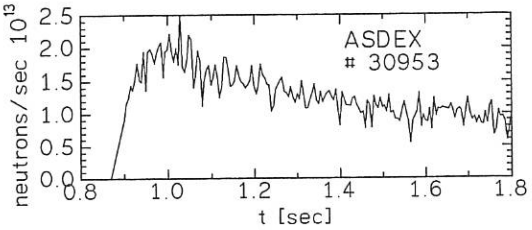


FIG. 6: Measured neutron rate for the ASDEX shot #30953.

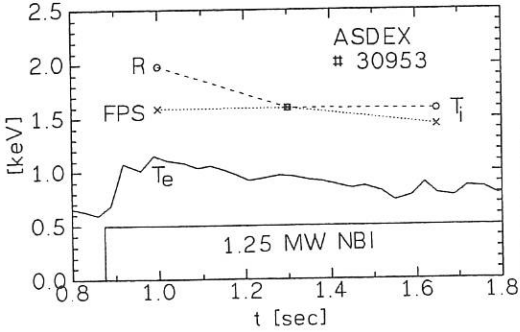


FIG. 7: Measured central electron temperature for the discharge #30953 and the calculated ion temperatures (R: using the relaxation-time model, FPS: using the Fokker-Planck model).

## REFERENCES

[1] T.H. Stix, Nuclear Fusion 15, 737 (1975)
[2] D. Anderson, W. Core, L.-G. Eriksson, H. Hamnen, T. Hellsten, M. Lisak, Physica Scripta 37, 83-88 (1988)

# ABSOLUTE DETERMINATION OF HIGH NEUTRON YIELDS FOR ASDEX

R. Bätzner, K. Hübner, L. Ingrosso, R. Wagner
Institut für Angewandte Physik, Universität Heidelberg
B. Bomba, S. Bosch, J. Kucinski
MPI für Plasmaphysik, EURATOM-Assoziation, Garching
B. V. Robouch, Associazione EURATOM-ENEA sulla Fusione, Frascati
J. S. Brzosko, Stevens Institute of Technology, Hoboken
C. van Calker, Institut für Experimentalphysik, Universität Düsseldorf
H. Klein, S. Guldbakke, Physikalisch-Technische Bundesanstalt, Braunschweig

## 1. Principle

Our concept for absolute calibration at high neutron yields is based on absolute measurement of the neutron fluence $\Phi$ at a suitable position and on a Monte Carlo calculation of the specific fluence $\varphi$, i.e. the ratio between the fluence $\Phi$ and the total neutron production Y in the plasma. These two results immediately give the absolute yield Y.

Absolute measurement of a neutron fluence requires an absolutely calibrated detector and unfolding of the response of the detector or an additional Monte Carlo simulation of its response to the specific fluence $\varphi$. At present, we are using nuclear emulsions and indium activation; though the treatment of emulsions is very time-consuming, they enable us to restrict the procedure to an appropriate interval of the neutron energy spectrum.

## 2. Numerical treatment

General procedure Monte Carlo calculation of the specific fluence $\varphi = \Phi/Y$ is started from the spectral local neutron birth rate, which is determined by means of our NR code [1] from the measured plasma data for the discharges used for calibration. Starting from this plasma neutron source, the VINIA-3DAMC software [2] is used to generate stochastically neutrons, to follow their migration and scattering through the full tokamak device, and to determine the specific neutron fluence arriving in the active detector volume.

Tokamak model The Monte Carlo calculations use a full 3-dimensional model of the tokamak. The intention in preparing our models is always to distribute all essential masses as realistically as possible without taking into account all minor geometrical details except in the vicinity of the detectors. As many details from there as possible are included in the model in order to make sure that absorption and scattering near the detector are properly taken into account. The constituents of the detector device are always absorbing but are usually considered to be collisionless. In fact, their masses are very small and they contribute little to the scattered neutron flux, but their absorption is essential in determining the absolute neutron fluence arriving in the detecting volume.

Output The output files from the VINIA-3DAMC software (PTO files) are very detailed. They contain the coordinates of each point of neutron emission or collision, the coordinates of the corresponding point of detection in the active volume of the detector, and the energy and weight of each contribution to the specific fluence.

Nuclear emulsion response The response of the nuclear emulsion plates (NEP) to the contributions stored in the PTO files is simulated by the special Monte Carlo software NEPMC [3]. Owing to off-axis incidence of the neutrons - which also exists to a small degree in collimated measurements - and to the limited energy resolution of the emulsion the apparent neutron spectrum is broadened in relation to the incoming specific neutron fluence $\varphi$. Thus the integrated neutron fluence in a certain energy interval is somewhat changed by the emulsion response function.

Indium activation response The treatment of the response of the indium sample is very simple. From the data in the PTO files just the absorption in the sample and the total number of activated nuclei $^{115}In^{m}$ is calculated.

## 3. Measurements

We are using nuclear emulsions for spectrally resolved measurements and indium activation for spectrally integrated measurements. We have done measurements at a sequence of different positions with stepwise improvement of the ASDEX model, the software and the evaluation of the results. These positions are located at ASDEX as follows:

*position 1:* horizontal radial measurement in front of the quartz window for the Thomson scattering system,
*position 2:* horizontal radial measurement in front of vacuum vessel,
*position 3:* tangential measurement near the quartz window (co-emission),
*position 4:* tangential measurement near the quartz window (counter-emission),
*position 5:* measurement near the quartz window,
*position 6:* measurement inside the vessel.

Positions 1 to 4 were used for collimated emulsion measurements in the energy range 2.1 to 3.0 MeV, positions 5 and 6 for uncollimated emulsion measurements in the energy range 2.3 to 3.0 MeV and for indium activation measurements.

For collimated measurements some basic aspects concerning a suitable choice of position of the collimator and the orientation of its line of sight have to be considered. First of all, tangential orientation of the collimator does not seem to be recommendable, because the observed section of the plasma is rather complicated and the results would be very sensitive to the plasma neutron emission profile. However, our results for position 3 and 4 demonstrate that even such positions could be used, provided that the neutron plasma source is well known.

In radially orientated measurements, the full cross-section of the plasma neutron source should be observed in order to make the measurements insensitive to the details of emission profiles. The ideal position for the collimator would be above (or below) the tokamak, because in such measurements radial motions of the plasma would not affect the results. Unfortunately, it is practically impossible on large tokamaks to obtain such access to the device. Usually, vertical observations must be restricted to a small part of the plasma cross-section and can thus become sensitive to the emission profile and plasma position.

The best solution in practice is horizontal radial observation, which, in principle, is what we are doing at ASDEX. As the plasma position is well measured, problems due to the radial Shafranov shift of the plasma need not be expected.

Uncollimated emulsion measurements and indium activation measurements should be made as near the plasma as possible. Positions near the vessel or a port are usually easily accessible, but our experience shows that such positions cause trouble in the form of large contributions from collided neutrons scattered in the vicinity of the detector. For this reason we have now installed at ASDEX the new measuring position 6, using a tube inside the vessel and a transport system for both the emulsions and the indium samples.

## 4. Calibration of the detectors

Nuclear emulsion The absolute response of the nuclear emulsion is simply determined by the cross-section of the n-p collision and the total number of protons in the emulsion, which itself is calculated from the quotations of the suplier Ilford for the hydrogen density and the emulsion thickness. Nevertheless, we calibrated one emulsion at the accelerator of the PTB and got an agreement within 3% with the data from Ilford.

Indium activation The calibration of the activation measurements was also done at the PTB. Infact it is a calibration of the Ge detector used for the $\gamma$ counting. Thereby two essential problems arise. Firstly, the counter efficiency depends on the position of the point of $\gamma$ emission inside the indium sample. Secondly, the sample is not homogenously activated and the situation inside the tokamak vessel could not be simulated with an accelerator. Therefore we used different orientations of the sample at the accelerator and a reproducible positioning of the sample above the counter, but it seems not to be possible to get the efficiency by this way with an error smaller than 10%. Finally, we will take advantage of our emulsion measurements done at the same position in ASDEX like the activation and calibrate the indium measurements by the emulsion.

## 5. Results for absolute neutron yield

The tables 1 and 2 summerize the results obtained so far for ASDEX. For all of them the ratio of the neutron yield Y determined by our procedure and the neutron yield $Y_c$ obtained by the counters is between 0.9 and 1.2 with an error between 20% and 30%. Thus, within the error bars the two results are in good agreement. We want to mention here, that this ratio $Y/Y_c$ is always the result of three completely independent procedures: the measurements with the in-situ calibrated counter array, the measurement of the absolute value of the local neutron fluence or the corresponding activity, and the Monte Carlo simulation including the measured plasma data. Thus the good result demonstrates the quality of all three procedures.

Table 1: Results from nuclear emulsion measurements

| Pos. | $\Phi$ from NEP neutr./cm$^2$ | $\varphi$ from VINIA cm$^{-2}$ | $Y = \Phi/\varphi$ neutrons | $Y_c$ from count. neutrons | $Y/Y_c$ |
|---|---|---|---|---|---|
| 1 | $3.0\times10^{5}\pm12\%$ | $2.2\times10^{-8}\pm 2\%$ | $1.4\times10^{13}\pm12\%$ | $1.3\times10^{13}\pm25\%$ | $1.1\pm28\%$ |
| 2 | $2.7\times10^{6}\pm12\%$ | $7.5\times10^{-8}\pm 7\%$ | $3.6\times10^{13}\pm14\%$ | $3.2\times10^{13}\pm25\%$ | $1.1\pm29\%$ |
| 3 | $4.0\times10^{5}\pm11\%$ | $6.4\times10^{-8}\pm12\%$ | $6.3\times10^{13}\pm14\%$ | $5.7\times10^{13}\pm25\%$ | $1.1\pm30\%$ |
| 4 | $5.2\times10^{5}\pm11\%$ | $7.5\times10^{-8}\pm 8\%$ | $6.9\times10^{13}\pm16\%$ | $5.7\times10^{13}\pm25\%$ | $1.2\pm28\%$ |
| 5 | $6.7\times10^{6}\pm11\%$ | $6.2\times10^{-7}\pm12\%$ | $1.1\times10^{13}\pm16\%$ | $1.0\times10^{13}\pm20\%$ | $1.1\pm26\%$ |
| 6 | | $5.8\times10^{-6}\pm 7\%$ | | $6.2\times10^{13}\pm15\%$ | |

Table 2: Results from indium activation measurements

| Pos. | A/Y from Vinia Bq/g neutron | $A/Y_c$ from counters Bq/g neutron | $Y/Y_c$ |
|---|---|---|---|
| 5 | $3.5\times10^{-14}\pm15\%$ | $3.9\times10^{-14}\pm20\%$ | $1.1\pm25\%$ |
| 6 | $1.6\times10^{-13}\pm15\%$ | $1.4\times10^{-13}\pm15\%$ | $0.9\pm21\%$ |

In position 6 the neutron fluence is high enough to measure the activity for single discharges with D-injection and to compare this with the result of the counter array. By this way we get a direct check of the calibration of the less sensitive counter which is the most problematic one in the calibration procedure. For example we got for the ASDEX discharge 31135:

| | | | | |
|---|---|---|---|---|
| yield from the counters | $Y_{count.}$ | $= 6.2 \times 10^{13}$ | ± 15% | neutrons |
| count rate per gramm indium | $C_0/m$ | = 0.476 | ± 4% | counts/s g |
| efficiency of $\gamma$ counter | $\varepsilon$ | = 0.055 | ± 10% | counts/s Bq |
| activity of indium sample per g | $A_0$ | = 8.65 | ± 11% | Bq/g |
| specific activity from VINIA | a | $= 1.58 \times 10^{-13}$ | ± 10% | Bg/g neutron |
| yield from activity and VINIA | $Y_{act.}$ | $= 5.5 \times 10^{13}$ | ± 15% | neutrons |

## 6. Numerical Results

Table 3 gives for illustration the two distances between detector and plasma axis resp. observation port and the scattered fraction of the specific fluence in the respective energy interval of the emulsion and the activation measurements as well as the fraction of specific activity caused by this scattered fluence.

The indium activation integrates over the full neutron energy spectrum, and therefore over a much larger scattered fraction of the neutron fluence than the emulsion measurement. But owing to the strong decrease of the activation cross-section below 2 MeV the relative contribution of the scattered fluence to the activation is reduced. On the other hand for the uncollimated emulsion measurements in position 5 and 6 the contribution of the scattered fluence is essentially reduced by the response function of the emulsion.

Table 3:

| Pos. | $d_{plasma}$ [cm] | $d_{port}$ [cm] | $\varphi_{scatt.}$ NEP | $\varphi_{scatt.}$ In | $a_{scatt.}$ |
|---|---|---|---|---|---|
| 1 | 282 | 174 | 32% | -- | -- |
| 2 | 163 | 99 | 41% | -- | -- |
| 3 | 129 | 48 | 30% | -- | -- |
| 4 | 129 | 48 | 30% | -- | -- |
| 5 | 110 | 8 | 39% | 73% | 55% |
| 6 | 45 | -- | 16% | 54% | 35% |

## References


[1] K. Hübner, et al., 14th Europ. Conf. on Controlled Fusion and Plasma Physics, Madrid 1987, part 3, pp 1298-1301, and Report IPP III/122, August 1987

[2] K. Hübner, et al., 15th Europ. Conf. on Controlled Fusion and Plasma Heating, Dubrovnik 1988, part 3, pp 1191-1194

[3] K. Hübner, et al., 16th Europ. Conf. on Controlled Fusion and Plasma Physics, Venice 1989, part 4, pp 1453-1456

# PLASMA DIANOSTICS IN INFRARED AND FAR-INFRARED RANGE FOR HELIOTRON E

S.Sudo, H.Zushi, K.Kondo, H.Suematsu, T.Obiki, K.Muraoka[1)], K.Matsuo[1)], T.Tsukishima[2)], M.Nagatsu[2)], T.Okada[3)], Y.Tsunawaki[4)], S.Okajima[5)]

Plasma Physics Laboratory, Kyoto Univ., Gokasho, Uji Kyoto 611, Japan
1)Dept. of Energy Conversion, Kyushu Univ., Kasuga, Fukuoka 816, Japan 2)Faculty of Engineering, Nagoya Univ., Nagoya 464, Japan 3)Dept. of Electrical Engineering, Kyushu Univ., Hakozaki, Fukuoka 812, Japan 4)Dept. of Electrical Engineering & Electronics, Osaka Sangyo Univ., Daito, Osaka 574, Japan 5)Dept. of Applied Physics, Chubu Univ., Kasugai, Aichi 487, Japan

**ABSTRACT:** Diagnostics in infrared and far-infrared range for Heliotron E are described: (a) FIR interferometer for measuring electron density profile and (b) ECE for electron temperature profile as routine work, and (c) Fraunhofer diffraction method with a $CO_2$ laser for density fluctuation and (d) Thomson scattering with a $D_2O$ laser ($\lambda = 385\mu m$) for ion temperature, as new methods.

## I. INTRODUCTION

As for diagnostics in infrared and far-infrared range for Heliotron E, (a) Far-Infrared (FIR) interferometer for measuring electron density profile and (b) 2nd harmonic Electron Cyclotron Emission (ECE) for electron temperature profile have been routinely used, and these have been powerful methods for studying plasma properties. These characteristics are described in chapter 2. In addition to these, new diagnostics in infrared and far-infrared range for Heliotron E are being developed: (c)Fraunhofer diffraction method with a $CO_2$ laser for measuring density fluctuation and (d)Thomson scattering with a $D_2O$ laser for ion temperature measurement. These are described in chapters 3 and 4, respectively.

Heliotron E[1] confines a toroidal plasma by nested magnetic fields, but it does not need plasma current for plasma confinement in contrast with tokamak. It has high rotational transform ( 0.5 at the center and 2.5 at the edge ) and thus high shear which is favorable for stability. The major and minor radii are 2.2m and 0.2m (averaged), respectively. A plasma is initially produced by electron cyclotron resonance heating (ECRH: 53.2 GHZ, B = 1.9T), and additionally heated by neutral beam injection (NBI: 30kV max., 4MW max.).

## II. FIR and ECE

For electron density profile measurement, a 7-chord interferometer using a FIR laser (a 30mW cw methyl alcohol laser with $\lambda = 119\mu$ m)[2] is equipped. The laser beam is split into 3 parts, and 3 chords are simultaneously measured. Thus, 7-chord data are obtained in similar 3 plasma shots at least by shifting the laser beam, and the density profile is reconstructed from the chord density. An example of chord density of FIR is shown in Fig.1, where 5 hydrogen pellets are injected into a NBI heated plasma. A rapid density rise due to pellet injection is correctly counted, as shown in the figure, while a $2mm$ microwave interferometer failed due to losing fringes. Moreover, from FIR signals, density fluctuation with low frequency ($\sim 2kHz$) in the time interval from D1 to D2 indicated in Fig.1 can be observed, and an internal disruption which occurs just after the timing D2 is revealed. The plasma is not collapsed completely by the disruption. It should be noted that the central chord density decreases at the internal disruption, while the outer-chord density increases. This indicates particle flow in the radial direction or rapid profile change. Thus, FIR is useful for measuring density profile, density fluctuation in low frequency range, and dynamic particle flow.

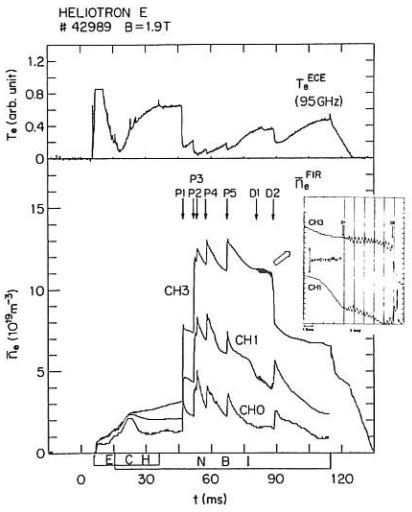


Fig.1 FIR and ECE signals in case of 5 pellets injection.

For electron temperature profile, 2nd harmonic electron cyclotron emission (ECE) from a plasma in range of 75-110 $GH_Z$ is measured by a heterodyne radiometer with a sweepable local oscillator. An example of ECE signal is shown in Fig.1. In this case, frequency is fixed at 95 GHz, which corresponds to the location of $r \sim a/2$. The rapid temperature decrease due to pellet injection is clearly observed. In the phase of higher density than about $n_e = 7 \times 10^{19} m^{-3}$, the ECE value is not correct because of ECE cutt-off condition, but it can be used as a monitor as shown in the figure. For instance, the temporal change of the ECE signal in the interval from D1 to D2 in Fig.1 is interested, comparing with FIR signals.

## III. FRAUNHOFER DIFFRACTION METHOD FOR DENSITY FLUCTUATION

For measuring density fluctuation in high frequency range of up to 400kHz, the Fraunhofer diffraction method[3] with a 50 W cw $CO_2$ laser ($\lambda = 10.6\mu m$) beam is used. A beam waist ($W_o = 1.9mm$), which is adjusted with lens, is located in the plasma center. The essential point is that the mixing signal of the scattered light due to density fluctuation and the non perturbed incident beam is detected. Thus the only one pair of ports opposite to each other for one chord observation is necessary, which is adequate for Heliotron E configuration. The schematic view of experimental set-up is shown in Fig.2. The detectors are 16 channels of $H_gC_dT_e$ photovolatatic type with a frequency response of 100 MHz. By detecting the mixed beam profile in perpendicular to the laser beam, the Fraunhofer diffraction profile in the $k_\perp$ direction ( $k_\perp$ is the wave number, and $\perp$ denotes the direction perpendicular to the magnetic field line) can be obtained. One example of a Fraunhofer diffraction profile is shown in Fig.3.

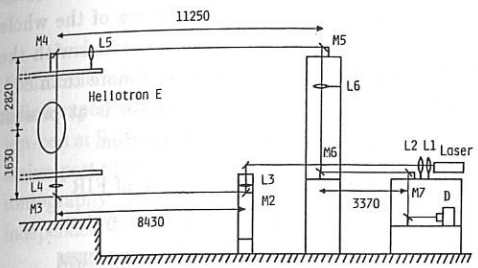


Fig.2 Experimental set-up for Fraunhofer diffraction method.

The points are measured ones, and the solid lines are fitted theoretical curves with adjusting $k$ values for each frequency. With this system, preliminary results of density fluctuation are obtained; frequency spectra ($0 \sim 400kHz$) and wave number ($k_\perp \lesssim 1.5mm^{-1}$) of fluctuation. The preliminary results show that the fluctuations roughly agree with drift wave type. Their effect on particle confinement is also being studied.

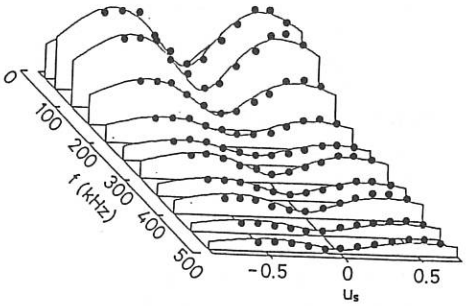


Fig.3 Example of Fraunhofer diffraction profile.

## IV. FIR THOMSON SCATTERING FOR ION TEMPERATURE MEASUREMENT

For new ion temperature measurement, the far-infrared collective Thomson scattering method using a $D_2O$ laser($\lambda = 385\mu m$) system is being developed. A pulsed single-mode $CO_2$ laser for pumping the $D_2O$ laser is constructed and tested for achieving high power with the wavelength ($\lambda = 9.26\mu m$) efficient for pumping the $D_2O$ laser. From the viewpoint of obtaining enough signal to noise ratio, a 200kW output power of the $D_2O$ laser with a pulse duration longer than $1\mu s$ is required. For that, $CO_2$ laser energy of more than 60 J with pulse width longer than 1 $\mu s$ is required. The schematic drawing of the whole system is shown in Fig.4. The wave form of the pumping $CO_2$ laser operated with the injection locking technique[4] is shown in Fig.5a). The energy is achieved more than 80J. The $D_2O$ laser waveform is shown in Fig.5b). The mode of the $D_2O$ laser is at present multi-mode. This point should be improved by better resonator configuration.

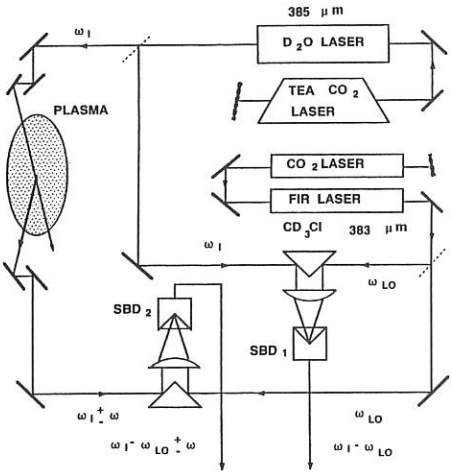


Fig.4 Schematic diagram of FIR Thomson scattering system.

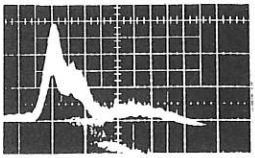

a) $CO_2$ laser (500ns/div)

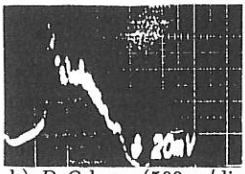


b) $D_2O$ laser (500ns/div)

Fig.5 Wave forms of the lasers.

## ACKNOWLEDGMENT

The authors would like to thank all Heliotron staff for valuable discussions and for supporting operation of Heliotron E.

## REFERENCES

[1] K.Uo, et al., in Controlled Fusion and Plasma Physics (Proc. 10th Europ. Conf. Moscow, 1981), USSR Acad. Sci., Moscow(1981) E-1.

[2] H.Zushi, et al., Rev. Sci. Instrum., **56** (1985) 919.

[3] K.Matsuo, et al., J.Phys. Soc. Japan, **56** (1987) 150.

[4] T.Okada, S.Inoue, et al., Int. J. Infrared Millimeter waves, **6** (1985) 883.

# NEUTRAL BEAM PROBE DIAGNOSTIC AT TEXTOR

A.A.E. van Blokland, E.P. Barbian, T.W.M. Grimbergen and T. Oyevaar

FOM-Instituut voor Plasmafysica Rijnhuizen, Association Euratom-FOM,
3430 BE Nieuwegein, The Netherlands

## INTRODUCTION

A neutral beam probe diagnostic for measurements of the ion temperature in a defined volume element of a hot plasma has been developed for application at the TEXTOR tokamak. In a first experimental set-up the main components of the diagnostic have been investigated in a test-bed at Rijnhuizen. The performance of the ion source and the gas neutralizer, which are the active part of the beam line, has been tested by a beam parameter diagnostic with computer tomography analysis. The time-of-flight spectrometer has been tested and calibrated by an independent beam source.

## ELASTIC SCATTERING OF BEAM NEUTRALS

The diagnostic method uses the elastic (Rutherford) scattering of mono-energetic (20-35 keV) He of H atoms on the plasma ions of a hot plasma. By momentum and energy transfer at single encounters with the nuclei of the ions, the velocity distribution of the scattered particles becomes broadened and is then a direct measure of the local ion temperature. Scattering of light neutrals with beam energies $E_b >> T_i$ on plasma ions occurs preferentially in forward direction. A $\sin^{-4}\theta$ dependence of the differential cross-section for Rutherford scattering [1] determines also the intensity of scattered particles observed with an observational solid angle of the analyser.

A scattering angle $\theta$ of about $7^o$ combines the advantage of still an appropriate spatial resolution (~ 0.2 m) and a time resolution at the 10 ms range [2] and has entered the design for the application of the diagnostic at TEXTOR [3, 4].

The shape of the velocity distribution of scattered particles observed at angle $\theta$ is caused in first instance by the randomly moving ions in the chosen scattering volume. In this case the distribution is nearly gaussian and broadened in respect to the narrow distribution of the incoming beam probe particle. From the observed half width $\Delta E_{1/2}$ of the distribution which depends on the beam energy and the mass ratio $\gamma = m_b/m_p$ of the beam and plasma particles, the $T_i$-value can be determined from

$$\Delta E_{1/2} = 4 \sin\theta \sqrt{\gamma E_b T_i \ln 2} \quad [eV]$$

with $E_b$ and $T_i$ in units [eV].

The $T_i$-value is not dependent on the intensity of the probing beam. Due to the straight-on observation, the scattering process is strictly one-dimensional and related to the ion velocity component situated in the scattering plane rectangular to the beam axis only. This opens the opportunity observing the ion velocity distribution separately in poloidal or toroidal direction. A non-thermal distribution of the plasma ions appears as a shift of the measured distribution or causes a deviation from a gaussian shape.

## THE TEST-BED EXPERIMENT

The beam line to carry the neutral beam probe through the core of the plasma is positioned vertically in respect to the torus equatorial plane of TEXTOR and has been mounted in a preliminary configuration simulating the TEXTOR environment. A multipole reflex discharge source CORDIS produces with a single extraction aperture of 10 mm diameter an ion beam of 40 mA at 35 keV. This beam passes a focusing magnet and the triangular shaped pressure profile of a gas neutralizer (He, $p_{max} = 5 \times 10^{-3}$ mbar) which produces with a 50% efficiency the neutral beam. Scraping diaphragms limit the beam to a diameter of 16 mm and a permanent deflection magnet takes away the residual ion component.

A scanning beam diagnostic is inserted above the ion source and again beyond the neutralizer to measure the intensity and divergence of the probing beam. A wedge-formed target rotates at constant angular velocity and cuts successively in x- and y-direction through the beam. Secondary electrons are collected by a ring-shaped auxiliary electrode and the time derivative of the current is processed by a tomographic analysis [5] to attain a two-dimensional beam profile.

By proper setting of the ion source parameters a narrow beam profile can be attained as shown in Fig. 2. From the scans with the upper beam diagnostic a total neutral beam current equivalent of 10 mA and a 1/e-width of 4 mm in either dimension can be derived.

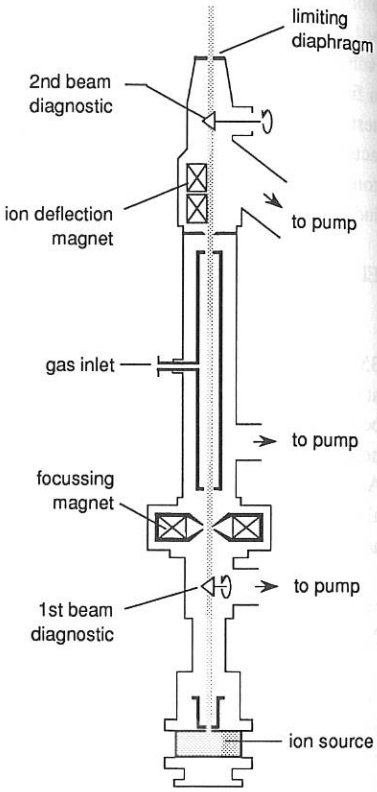


Fig. 1.
Schematic view on the beam line guiding the neutral probing beam to the torus.

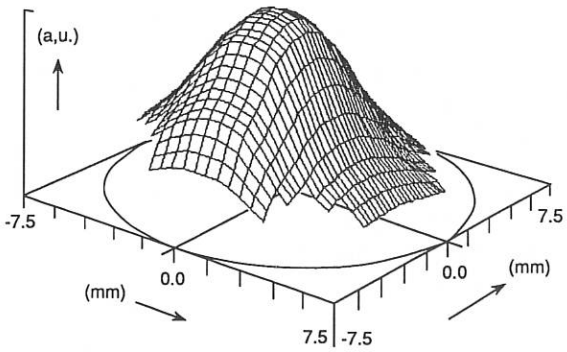


Fig. 2.
Two-dimensional profile of the beam probe measured by a scanning beam diagnostic and processed by tomographic analysis.

## CALIBRATION AND EFFICIENCY OF THE ANALYSER

The spectrum of scattered particles can be measured by a time-of-flight analyser (Fig. 3) for single particle detection and coincidence technique. To cover the expected spectral width $E_b$ ± 25%, a triple magnet preselector has been integrated into the analyser. The impact of low energy charge-exchange neutrals or plasma radiation can therefore be excluded. An ionizing carbon foil (1 to 4 $\mu g/cm^2$) has been used behind the entrance aperture to produce ions which are guided through the achromat to hit the likewise thin start foil. There, at the front and at the rear side, secondary electrons are released, which are guided to well-separated micro channel plate start detectors. Particles clearly identified by coincidence circuitry follow the flight path to hit the MCP stopping detector. Flight times of individual particles can be determined within the processing time of 1 µs, which allows to take spectra at a rate of 1 kHz [4].

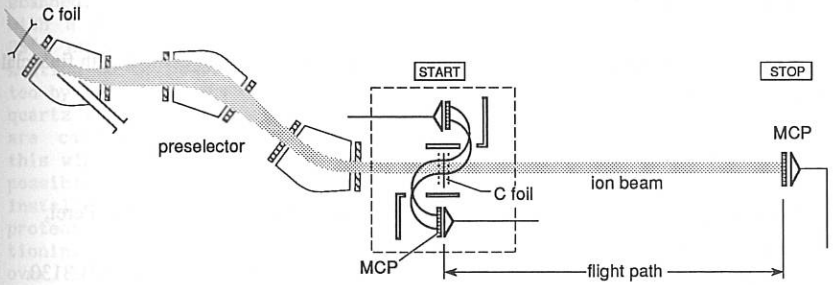


Fig. 3.
Elements of the time-of-flight analyser.

Performance tests and energy calibration were carried out with an independent ion source in the extended energy range between 10 and 65 keV. The instrumental width dE/E decreases

with rising energy values of the probing beam and is smaller than 0.03 in the working region (Fig. 4). The main contributions come from straggling effects inside the foils (A), the spread of pathlengths of secondary electrons (C), and the variational width of flight paths of atoms due to the finite transversal size of start foil and stop detector (B).

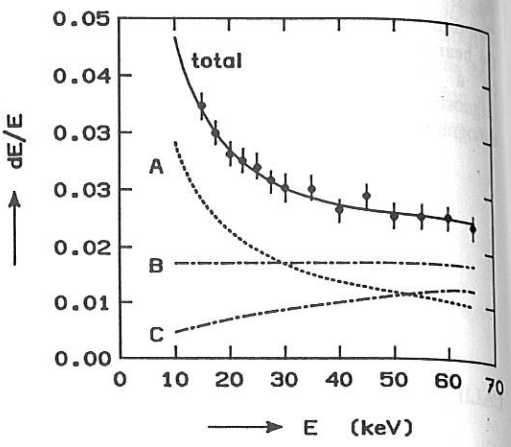


Fig. 4.
Instrumental width for He-atoms. Thickness for the ionization and start foils: 1.9 $\mu g/cm^2$.

The triple achromat proved to be very sensitive to the angular variation of trajectories as expected from numerical calculations. Foil ionization, transmission of the achromat, and time-of-flight measuring section contribute each with a 10% efficiency to a total of 1 out of 1000 recording probability for 35 keV He atoms, which might be compared with a 1% value for H-atoms as probing particles.

After the test-bed investigation the diagnostic has been integrated into the TEXTOR environment and put successfully into operation.

ACKNOWLEDGEMENT

This work was performed under the Euratom-FOM association agreement with financial support from NWO and Euratom.

REFERENCES

[1] V.G. Abramov, V.V. Afrosimov, J.P. Gladkovskii, A.I. Kislyakov and V.I. Perel, Sov. Phys.-Tech. Phys. **16** (1972) 1520.
[2] A.J. H. Donné, E.P. Barbian and H.W. van der Ven, J. Appl. Phys. **62** (1987) 3130.
[3] A. Cosler, H.W. van der Ven, E.P. Barbian, G. Bertschinger, A.A.E. van Blokland, E. Kemmereit, Proc. 15th Symposium on Fusion Technology, Utrecht (1988) p. 347.
[4] A.A.E. van Blokland, M.K. Korten, F.D.A. de Winter, E.P. Barbian, H.W. van der Ven, Proc. 15th Symposium on Fusion Technology, Utrecht (1988) p. 1702.
[5] A. Holland, G.A. Navratil, Rev. Sci. Instrum. **57** (1986) 1557.

# VISIBLE BREMSSTRAHLUNG MEASUREMENTS ON TEXTOR FOR THE DETERMINATION OF $Z_{eff}$ UNDER DIFFERENT DISCHARGE AND HEATING CONDITIONS.

J.Ongena, N.Schoon†, G.Van Oost, J.Schwarz‡, G.Telesca

Laboratoire de Physique des Plasmas - Laboratorium voor Plasmafysica
Association EURATOM-Etat Belge - Associatie EURATOM-Belgische Staat
Ecole Royale Militaire - Koninklijke Militaire School
B-1040 Brussel, Belgium

†Laboratorium voor Natuurkunde, Rijksuniversiteit Gent
Rozier 44, B-9000 Gent, Belgium

‡Institut für Plasmaphysik, Forschungszentrum Jülich,
Association EURATOM-KFA, D-5170 Jülich, Federal Republic of Germany

## 1. INTRODUCTION

A diagnostic has been developed on TEXTOR to measure the intensity of the bremsstrahlung radiation in the visible range, allowing the study of the temporal behavior of $Z_{eff}(r)$ - the radial profile of the average ion charge in the plasma. First results of $Z_{eff}$ profiles for different TEXTOR plasmas ( ohmic and ICRH, as well as co- and counter NBI-heated plasmas ) are reported.

## 2. EXPERIMENTAL SETUP

A block diagram of the experimental setup is shown in Fig.1. The plasma is scanned, using an oscillatory mirror with a field of view of approximately 35°, enabling 90% of the plasma cross section to be observed. The light emitted by the plasma is collected through a quartz window. As absolute measurements are carried out, the transmission of this window must be kept as constant as possible. To this end a shutter has been installed in front of the window to protect it from sputtering during conditioning discharges in the tokamak. Moreover, the space between window and shutter can be pumped and vented separately from the tokamak operation. In this way the transmission of the window can be checked at regular time intervals, and if necessary the window can be exchanged. To eliminate reflections from the liner, a viewing dump was installed consisting of small graphite tiles covering that part of the liner, which is

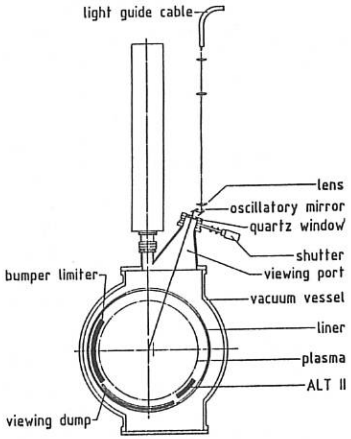


FIGURE 1 : EXPERIMENTAL SETUP

directly seen by the mirror. With an array of optical fibers ( Quartz & Silice, PCS600W, core diameter 0.6 mm, length ± 30 m ) the light is carried outside the tokamak hall to a photomultiplier ( Thorn EMI 9658R ). In this way the influence of neutrons and electric or magnetic fields on the PM is easily avoided. An interference filter with peak transmission at 5230.1 Å and a FWHM of 21.9 Å ( Barr Associates, Inc ) isolates a spectral region which is relatively free of line emissions [1].

The absolute calibration of the whole system is performed using a calibrated tungsten ribbon lamp and precision metallic neutral density filters ( Melles Griot ) to attenuate the light reaching the detector to levels which are normally measured during tokamak operation.

The time resolution of the diagnostic is determined by the time needed to scan the plasma once and is presently 150 ms.

Advantages of this diagnostic are: 1) no relative calibration of different detectors is needed, 2) a complete profile of the line-integrated emissivity is recorded, 3) insensitive to perturbations of magnetic fields, RF or neutrons.

## 3. ANALYSIS OF THE DATA

The local emissivity of the bremsstrahlung continuum is given by [2] :

$$\varepsilon(r) = \frac{1.50 \times 10^{-29}\ n_e^2(r)\ Z_{eff}(r)\ \bar{g}_{ff}\ e^{-\frac{12400}{\lambda\ T_e(r)}}}{\lambda^2\ \sqrt{T_e(r)}} \quad \left[\frac{W}{cm^3\ Å\ sr}\right]$$

where $\bar{g}_{ff}$ is the averaged free-free Gaunt factor, $T_e(r)$ in eV, $n_e(r)$ in $cm^{-3}$, and $\lambda$ in Å. Provided $T_e(r)$ and $n_e(r)$ are known from other measurements, a measurement of $\varepsilon(r)$ results in a profile of $Z_{eff}(r)$.

For the Gaunt factor $\bar{g}_{ff}$, several approximations can be found in the literature [2-5]. Among these different formulae, the formula of Elwert for $\bar{g}_{ff}$ is the best approximation to the calculations of Karzas et al.[6] for values of $Z_{eff}$ between 1 and 3, which are usually found in TEXTOR. Therefore, this approximation of $\bar{g}_{ff}$ has been used in all subsequent calculations. Electron density profiles are obtained from interferometric measurements and the electron temperature profiles from the ECE diagnostic.

The measured line-integrated emissivities have to be abel inverted in order to obtain a profile of the local emissivity $\varepsilon(r)$. There exist several procedures to perform an abel inversion. However, in the present case, the application of these methods is not straightforward. As one of the principal objectives of TEXTOR is the study of plasma-wall interactions, various limiters ( ALT II, poloidal-, RF antenna-, bumper- and test limiters ) are present inside the vacuum vessel. Their presence perturbs in most cases the measured line-integrated emissivity, due to line radiation, recombination radiation, etc [1] in their immediate vicinity. These perturbations of the measured data have to be dealt with in the analysis. An abel inversion procedure has been used [7], which assumes that the surfaces of constant emissivity are circular but not necessarily concentric. The emissivity profile is developed as a linear combination of orthonormal polynomials and the line-integration of this expression along different chords is fitted to the unperturbed part of the measured signal by the method of adjustment of elements [8]. Implicit in this method is the determination of the error on the inverted profile $\varepsilon(r)$ and thus on the obtained $Z_{eff}(r)$ profile, provided the errors on $n_e(r)$ and $T_e(r)$ are

known. In Fig.2, curve A shows an example of a measured line-integrated emissivity profile; curve B shows the line-integrated emissivity profile, which has been fitted to that part of the signal where no perturbations are seen. The examples shown in the next section pertain to discharges under boronized wall conditions.

## 4.RESULTS AND DISCUSSION

### 4.1.OHMIC DISCHARGES.

During the ohmic phase of a discharge, following the establishment of a stationary density profile, $Z_{eff}(r)$ is usually peaked in its central part and the shape of this profile remains practically unchanged during the whole stationary phase of the discharge; the central peaking is more pronounced for low density discharges. Figure 3 shows typical $Z_{eff}$ profiles for four different values of the line-averaged central electron density $\bar{n}_{e0}$ in ohmically heated deuterium plasmas. For one of the curves we indicate representative error bars. These curves also show the increase of $Z_{eff}$ with decreasing densities. Good agreement with $Z_{eff}$ values from soft-X ray measurements has been found for these shots.

### 4.2.AUXILIARY HEATED DISCHARGES ( ICRH, NBI-CO, NBI-COUNTER )

The analysis of several ICRH heated discharges shows that in general $Z_{eff}$ is slightly increased with respect to the ohmic phase. At the same time the perturbing radiations from ALT II and the bumper limiter increase, indicating enhanced interaction with the plasma at these locations [9]. Figure 4 shows the evolution of $Z_{eff}(r)$ during the different phases of a discharge heated with 660 kW ICRH during 0.7 s. The peaking of $Z_{eff}$ in the central part of the profile, which is clearly seen during the ICRH phase, almost disappears after this phase and the $\bar{Z}_{eff}$ approaches its pre-ICRH ohmic level.

Preliminary results show also a peaking of the $Z_{eff}$ profile during most co- and counter neutral beam heated plasmas, and it seems to be more pronounced as compared to ICRH heated plasmas. After the NBI phase the peaking decreases and $\bar{Z}_{eff}$ returns close to its ohmic value. Figure 5 gives an example of this evolution for a TEXTOR deuterium plasma heated by hydrogen co-injection at a power level of 0.9 MW. Figure 6 finally gives an example of a deuterium plasma heated with 1.60 MW of hydrogen counter-injection. The behaviour is more or less the same as for co-injection. However, one should be careful in drawing general conclusions from these curves, because the heating power is different for each case. A systematic study will be undertaken in the near future.

## REFERENCES

[1] Pospieszczyk A. et al., J.Nucl.Mat. 145-147, 574 (1987)
[2] Griem, H., "Plasma Spectroscopy", Mc Graw Hill, New York (1964)
[3] Brussaard, P.J., Van de Hulst, H.C., Rev.Mod.Phys. 34, 507 (1962)
[4] Ramsey A. et al., Rev.Sci.Instr. 58, 1211 (1987)
[5] Elwert, G., Z.Naturforschung 9a, 637 (1954)
[6] Karzas, J., Latter, R., Astrophys.J., Suppl.Ser. 6, 167 (1961)
[7] Diesso, M., PPPL Princeton, private communication
[8] Wilks, S.S., "Mathematical Statistics", John Wiley & Sons, New York (1963)
[9] Van Oost G. et al., IAEA Technical Committee Meeting on ICRH/Edge Physics, Garching Oktober 2-5 1989, Fusion Engineering and Design (1990), in press

FIGURE 2 : line-integrated emissivity profile

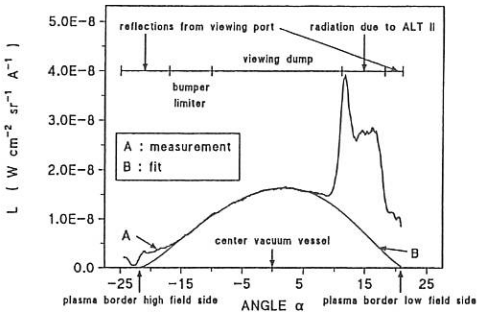


FIGURE 3 : $Z_{eff}$ PROFILES FOR OHMIC DISCHARGES

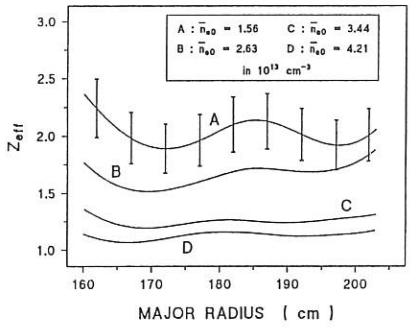


FIGURE 4 : $Z_{eff}$ PROFILES FOR AN ICRH HEATED DISCHARGE

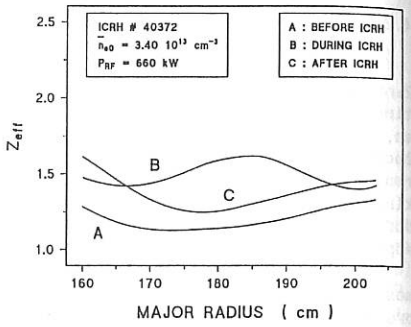


FIGURE 5 : $Z_{eff}$ PROFILES FOR A NBI HEATED DISCHARGE

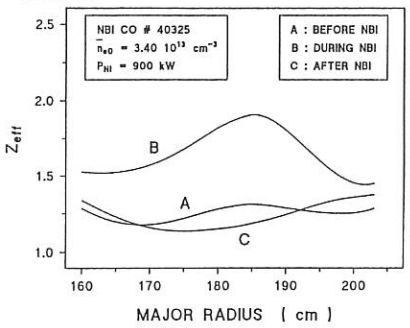


FIGURE 6 : $Z_{eff}$ PROFILES FOR A NBI HEATED DISCHARGE

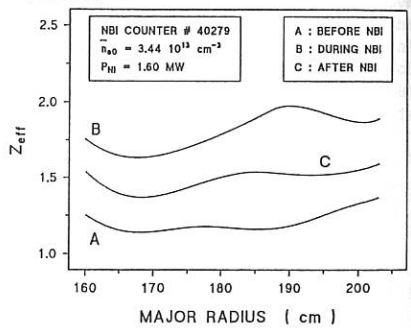

# ELECTRON DENSITY PROPAGATION ON MAGNETIC SURFACE IN T-10 DURING PELLET INJECTION

N.L.Vasin*, S.M.Egorov, B.V.Kuteev, I.V.Miroshikov, P.V.Reznichenko, V.Yu.Sergeev, S.N.Ushakov, V.V.Chistijkov*

Kalinin Polytechnical Institute, Leningrad, USSR
* Kurchatov Institute of Atomic Energy, Moscow, USSR

The main purpose of this paper is to describe poloidal and toroidal symmetrization of the electron density perturbation created by the pellet injection.

In the experiment carbon pellets with diameter $d_p$ = 350 $\mu$m and velocity $V_p$ = 120 m/s were injected in direction of T-10 chamber core. Electron density perturbations were measured using 6-channel rf-interferometer. It was placed $(+\pi/2)$ toroidally away from the injection plane in the direction of the plasma current. The ablation rate of the pellet and interferometer data were registered with 10 $\mu$s time resolution. Interferometer data for shot # 47015 with $I_p$ = 209 kA, $B_t$ = 2.9 T, $a_l$ = 32 cm, $\bar{n}_e = 2.1 \cdot 10^{13}$ $cm^{-3}$ are presented in Fig.1 (open circles).

We analyzed the evolution of the electron density outflow on magnetic surface using the following model.

The source of perturbation was calculated using the ablation rate $\dot{N}(r)$. We supposed that the quantity of carbon atoms evaporated between magnetic surfaces with radii r and r+dr is equal to $N_a(r) = \dot{N}(r) \cdot dr/V_p$. The poloidal length of the electron source was taken equal to ionization length of ablated atoms $l_i = V_a \cdot \tau_a^{ion} \sim$ 1 mm [1].

The propagation of electron perturbation along magnetic field line was described as outflow with fixed ion-sonic velocity $V_\parallel = ( 2 \cdot T_{cold} / m)^{1/2}$ corresponding to the temperature of secondary cold plasma $T_{cold}$. The radial density transport was neglected. We used the following expression for the longitudinal distribution :

$$n(l,t)=\frac{N_a(t)\cdot Z_i(t)}{2\cdot S_\perp\cdot V_\parallel\cdot t}\cdot\exp\left(-\frac{|l|}{V_\parallel\cdot t}\right)$$

This form of density perturbation conserves particle number in the magnetic tube. Here, l - the length along magnetic field line from the injection plane; $S_\perp$ - the area of cross-section of magnetic tube; $Z_i$ - ion charge of secondary plasma. In the model $Z_i(t)$ values were sequent increased from $Z_i = 1$ to 6 in accordance with the condition $t > \tau_i^{ion}$, where $\tau_i^{ion}$ is Lotz's ionization time [2] of carbon ions evaluated using electron density $n_e(r)$ and temperature $T_e(r)$ profiles.

In the poloidal direction the motion of electron perturbation is determined by a projection of toroidal motion $V_\vartheta(r) = (V_\parallel(r)\cdot r)/(q(r)\cdot R)$ and a poloidal plasma rotation velocity $V_o(r)$. We assumed that density perturbation takes the undisturbed value of the poloidal velocity $V_o(r)$ immediately. It's clear that due to velocities $V_\vartheta(r)$, $V_o(r)$ originally rectangular cross-sections of the magnetic tube ( in calculations) deforms into parallelogram without area changing $S_\perp = dr\cdot 2\cdot l_i$. This deformation of magnetic tube cross-section was taken into account in calculations of simulated interferometer signals.

The profile of safety factor q(r) was obtained using the plasma current value $I_p$ and $T_e(r)$ in the assumption that Spitzer conductivity being low and radially independent of the effective plasma charge. The shape of plasma poloidal velocity $V_o(r)$ was approximated by a triangle form with maximum value $V_{omax}$ at $r = a_l/2$ . This radial profile is similar to a neoclassical [3] and measured [4,5] profiles of $V_o(r)$. The change of value and sign of $V_{omax}$ were provided in simulations.

Interferometer signal simulation results are presented in Fig.1 for $T_{cold}$ = 10 eV, $V_{omax}$ = 0 (dotted line) and $3\cdot 10^5$ cm/s (solid line). The sign of $V_{omax}$ is opposite to the neoclassical one. It is necessary to emphasize that for the range of $V_{omax}$ = 0 - $3\cdot 10^5$ cm/s the interferometer experimental data disagree with calculated ones for both signs of plasma poloidal

rotation. On the other hand, the rotation sign isn't valuable for the agreement of experimental and calculated results at high values $V_{\theta max} > 10^6$ cm/s. As can be seen from Fig.1 a significant difference between model interferometer signals for different $V_{\theta max}$ values is observed for the chord with r = +15 cm. This can be easily understood taking into account tracks of pellet trajectories for the injection plane and for planes situated $(+\pi/2)$ and $(-3\pi/2)$ away from injector. These tracks are shown in Fig.2. For fast poloidal plasma rotation the agreement of experimental and simulated interferometer signals seems to be good enough. A variation of $T_{cold}$ in the range of 5 - 20 eV weakly changes the results of simulation for fast rotation velocity.

Thus the behavior of interferometer signals during carbon pellet injection in T-10 can be reasonably described as the outflow of the cold secondary plasma with $T_{cold} \sim 5 - 20$ eV and the fast plasma poloidal rotation with $V_{\theta max} \sim 10^6$cm/s.

References.

1. S.M.Egorov et al., 12th European Conference on Controlled Fusion and Plasma Heating, Budapest, September 1985, V.12F,Part 2, p.47.
2. W.Lotz, Reprint IPP-1/62, May 1967.
3. F.L.Hinton, R.D.Hazeltine, Rev. of Modern Phys., 1976, V.48, No.2, Part 1, p. 239.
4. A.P.Zhilinsky et al., 10th European Conference on Controlled Fusion and Plasma Physics, Moscow, September 1981, V.1, Paper A-3A.
5. S.M.Egorov et al., ibid, Paper A-3B.

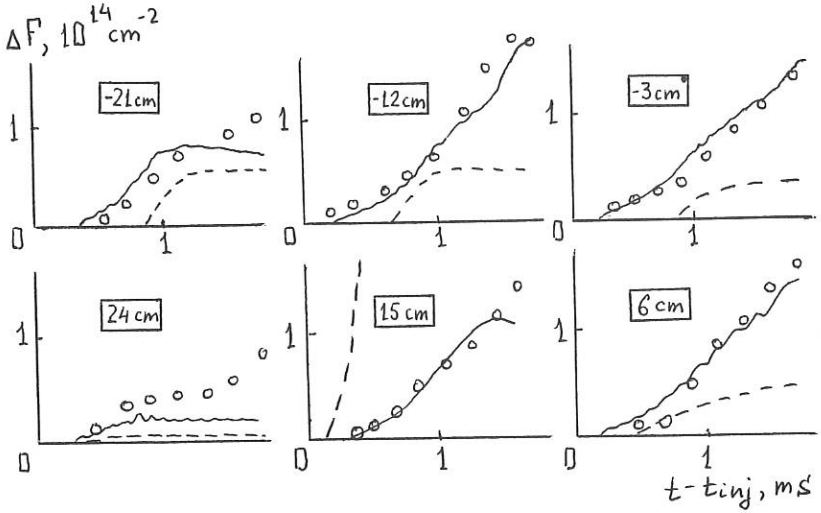


Fig.1 Time evolution of interferometer data at chords with radii r = -21, -12, -3, 6, 15, 24 cm.
° ° ° ° experimental data
– – – – calculation results for $V_{0max}$ = 0 cm/s
——— calculation results for $V_{0max}$ = $3 \cdot 10^5$ cm/s

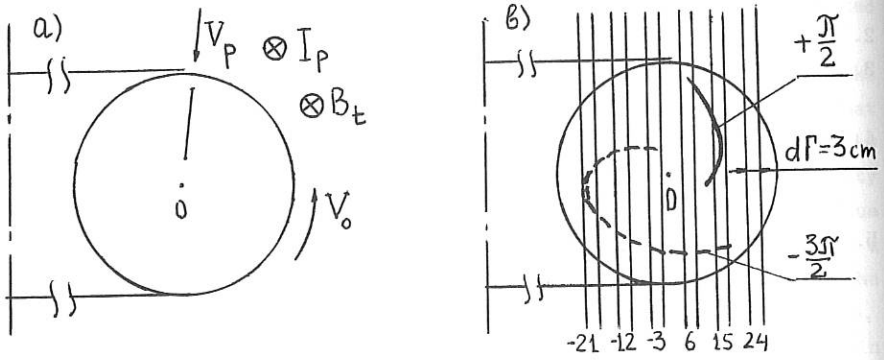


Fig.2 The geometry of a poloidal cross section at the injector plane (a) and the interferometer one (b). Tracks of the pellet trajectory for the injection plane ( solid line in Fig.2a) and for planes situated $\pi/2$ ( solid line in Fig.2b) and $-3\pi/2$ ( dashed line in Fig.2b) away in the toroidal direction from injector are shown.

# MEASUREMENTS OF ION CYCLOTRON EMISSION AND ICRF-DRIVEN WAVES IN TFTR

G.J. Greene and the TFTR Group

Plasma Physics Laboratory, Princeton University
Princeton, New Jersey 08543, U.S.A.

**Introduction** The TFTR RF probe array is a general purpose diagnostic consisting of seven probes that can be used for detecting or launching waves in the frequency range of 1 - 500 MHz. The system is being used to study ion cyclotron harmonic emission from ohmic and neutral beam-heated discharges with an aim of evaluating the utility of the spectrum as a fusion product diagnostic. Waves excited by the ICRF heating antennas are being investigated in order to determine the nature of the excited fields in the edge region and their possible correlation with impurity production and heating efficiency. The RF probes are also being used as broadband launching antennas for ICRF wave propagation experiments in the edge region. This paper presents some initial measurements relating to these topics.

**Experimental Arrangement** Previous studies of ion cyclotron emission on TFTR [1] utilized a small moveable double-loop probe that was located near the outer midplane of the vessel. That probe has been replaced with seven larger fixed probes (loop area = 12 cm$^2$) positioned 10 cm inside the vessel wall. Four probes at toroidal angles ($\phi$) of 0°, 18°, 90°, and 126° (where the Bay M ICRF antenna is located at $\phi = 0$) comprise a toroidal array and are located slightly on the high-field side of the vessel center at poloidal angles ($\theta$) of 6°–9° (where $\theta = 0$ represents the top of the vessel). At the Bay M location, two additional probes are located at $\theta = 158°$ and 176°, while the seventh probe is located at $\phi = 90°$, $\theta = 171°$. Each probe consists of two orthogonal, balanced loops that measure $B_\phi$ and $B_\theta$; the data presented here utilized only the $B_\phi$ loops. Processed RF signals are transmitted out of the machine area using wideband analog optical links and are directed to spectrum analyzers or fixed-frequency amplitude and phase detectors. Broadband wave propagation experiments are performed using an RF network analyzer that is coupled to a pair of probes via two RF optical links [2].

**RF Emission during Beam-Heated Discharges** During deuterium neutral beam (NB) injection into deuterium plasma, a sequence of harmonically-related narrow peaks in the frequency spectrum was observed. A spectrum taken 100 msec after the start of a 30 MW NB pulse, using the probe at $\phi = 0°$, $\theta = 6°$, is shown in Fig. 1; as in the previous study on TFTR, the frequencies of the peaks corresponded closely to $n\omega_{CD-edge}$, where $\omega_{CD-edge}$ is the deuteron cyclotron frequency evaluated at the outermost plasma edge ($R_p + a_p$). It should be noted that the probe in the earlier study was located near the outer midplane, while the probes used for data presented here were located on the top and bottom of the vessel at a major radius near that of the plasma center. It thus appears that the source of the emission is spatially localized near the outer midplane and that the waves propagate poloidally in the region between the plasma and the vessel wall (a result also found on PDX [3]).

During intense neutral beam heating, a new feature of the emission was observed: a broadband increase in the spectrum appeared, beginning near the fifth cyclotron harmonic and extending for ~200 MHz. A spectrum taken at a time near the peak of the neutron flux is shown in Fig. 2 (for the same discharge as in Fig. 1). A waveform representative of the time evolution of this component of the spectrum was obtained by averaging the power over a band of frequencies (200 - 240 MHz) for each sweep of the analyzer. The result, plotted together with the time evolution of the neutron flux,

is shown in Fig. 3. The waveforms are similar, with the rise of the RF probe power trace delayed by some 100 msec with respect to the neutron signal. The turnover in the neutron flux (arising from a carbon bloom) is mirrored in the RF probe trace, as is the pedestal during the latter part of the trace. The lag between the signals is suggestive of the rise time of a confined fast ion population and it is speculated that this component of the spectrum may be driven by charged fusion products.

In contrast, the amplitude of the ion cyclotron harmonic peaks during beam injection did not show a clear relation to the neutron flux. Examination of the time evolution of a single harmonic peak revealed that the emission consisted of short bursts (Fig. 4). Similar bursts of RF emission were found previously by Buchenauer, et al., on PDX [3] and were correlated with expulsion of fast ions and with fishbone instabilities.

**Harmonic Emission during Ohmic Plasmas** Previous work on TFTR using the outer midplane probe revealed two weak, broad peaks in the emission spectrum of ohmic plasmas, occurring in the 200-300 MHz range and separated by a frequency corresponding to $\omega_{CH-edge}$ (the proton cyclotron frequency evaluated at the outer plasma edge). The new probes and signal processing electronics were sufficiently sensitive that all of the ohmic emission spectrum was above the noise floor. A sequence of five or more evenly spaced peaks was observed throughout the discharge, and the frequencies of the peaks corresponded to $(n + 1/2)\omega_{CH-edge}$; an example of this spectrum in shown in Fig. 5. The peaks shifted in frequency appropriately during the toroidal field ramp-up at the beginning of the discharge. Note that these results differ from observations on JET [4] where an ICRF antenna was used as a receiver and the frequencies of the peaks in the spectrum occurred at $n\omega_{CD-edge}$.

**Waves Driven by ICRF Heating Antenna** During ICRF heating experiments (D-majority, H-minority, $f$ = 47 MHz, $P_{RF}$ = 2-3 MW, Bay M antenna energized alone, 0-$\pi$ antenna element toroidal phasing), waves were detected on all of the RF probes. The spectra of the received signals showed no sign of parametric decay or of sub-harmonic components to a level of 40 db below the pump amplitude. In general, the wave amplitude was not significantly greater on probes located closer to the heating antennas, suggesting that the observed waves were in fact propagating globally. In high-power experiments where the density varied significantly during the RF pulse, large amplitude modes were seen on the probe signals with minima and maxima occurring at different densities for the different probes (Fig. 6). Small modes were also seen on the loading resistance ($\Delta R/R$ <20 %), but in general these did not appear to be related to the probe signal modulation. The large-scale structure of the modulation was also uncorrelated with sawteeth (which were frequently suppressed), edge density, $H_\alpha$ light, and MHD activity. The mode structure is likely a result of RF wave propagation and interference and may represent high-$m$ fast Alfvén modes that can be excited by radial antenna currents and propagate in the plasma as surface waves [5].

**Waves Driven by RF Probes** The above observations suggest that propagating waves exist in the low-density region between the plasma boundary and the vacuum vessel wall. The nature of the propagation in this region is of importance as it may govern both the distribution of potentially undesired wave fields from the RF antennas (e.g., during in-phase antenna strap excitation) as well as the global propagation of RF emission from poloidally localized sources. An effort has begun to directly examine the characteristics of these waves by using one RF probe as a launching antenna and detecting propagating waves with the other probes. In addition, these experiments allow study of the vacuum toroidal eigenmodes that have been proposed as a possible means for tile bakeout in a tokamak [6]. An example of the vacuum transmission over the range of 1-150 MHz, using two $B_\phi$ probe loops separated toroidally by 120°, is shown in Fig. 7. The toroidal cavity is cut off below about 70 MHz, while above that frequency the modes quickly take on the form of a continuum (possibly due to mode broadening from damping by the significant amount of resistive graphite in the vessel).

The analogous trace for a typical deuterium plasma discharge is shown in Fig. 8. At high frequencies there is significant communication between the two probes. However, there is a large decrease in the transmitted signal over a band of frequencies for which the proton cyclotron resonance layer is located between the center and outer edge of the plasma. Both transmitting and receiving probes were located at the same major radius (close to that of the vessel center), and the apparent asymmetric absorption is suggestive of the expected difference in absorption and reflection coefficients for waves launched from the high-field or low-field side of a resonance-cutoff layer in an H-minority deuterium plasma [7]. Further experiments will use phase detection, multiple probes, and varying $B_{TF}$ and the minority concentration in order to elucidate the nature of the waves being excited and determine the utility of this technique for investigating ICRF wave physics.

**Acknowledgement** This work was supported by US DOE Contract No. DE-AC02-76-CHO-3073.

**References**

[1] G.J. Greene, et al., in *Proc. 15th Eur. Conf. on Cont. Fus. and Plasma Heating* (Dubrovnik, 1988) Vol. 12B, Part 1, pp. 107–110.

[2] G.J. Greene, in *Proc. 8th Top. Conf. on High Temp. Plasma Diagnostics* (Hyannis, 1990), to be published in Rev. Sci. Instrum. (1990).

[3] D. Buchenauer, et al., in *Proc. 4th Int. Symp. on Heating in Toroidal Plasmas* (Rome, 1984), pp. 111–118. Also D. Buchenauer, Ph.D. Thesis, Princeton University (1985).

[4] G.A. Cottrell and R.O. Dendy, Phys. Rev. Lett. **60**, 33 (1988).

[5] M.J. Ballico and R.C. Cross, *Phys. Fluids* **B2**, 467 (1990).

[6] P.L. Colestock, private communication (1989).

[7] O. Sauter, et al., in *Proc. 14th Eur. Conf. on Cont. Fus. and Plasma Physics* (Madrid, 1987), Vol. 11D, Part III, pp. 958-961. Also M. Bures, private communication (1990).

**Figure Captions**

1. RF emission spectrum early during 30 MW NB heating pulse, showing harmonically related peaks.
2. RF emission spectrum at time of peak neutron flux, showing rise of broadband component.
3. Time evolution of averaged broadband RF power (200–240 MHz) and the neutron flux.
4. Time-resolved amplitude of the sixth harmonic peak during shot with 11 MW NB injection.
5. RF emission spectrum during ohmic discharge. Peaks occur at $\omega = (n + 1/2)\omega_{CH-edge}$.
6. Time evolution of amplitude of four RF probe signals during 2 MW ICRF heating pulse.
7. Transmission between two probes separated toroidally by 126°, from 1-150 MHz, in vacuum torus.
8. Transmission as in Fig. 7, but during typical ohmic deuterium plasma discharge.

FIGURE 1

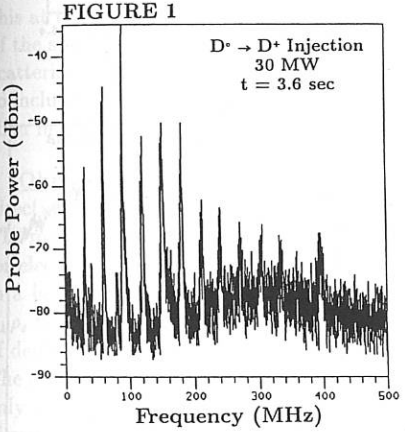


FIGURE 2

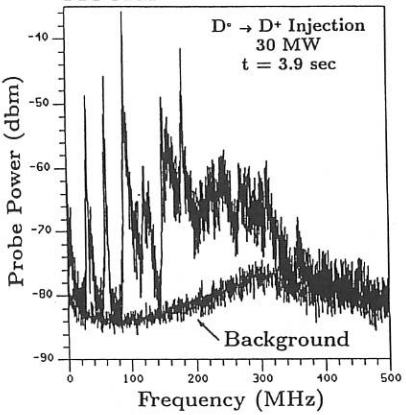

FIGURE 3

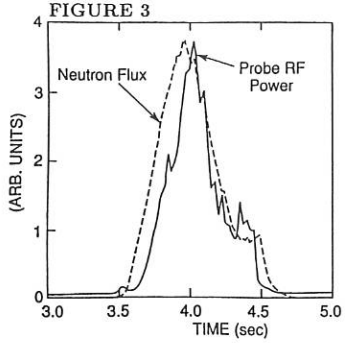


FIGURE 4

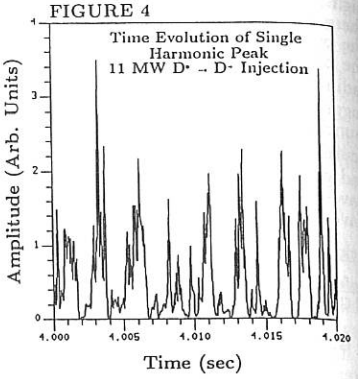


FIGURE 5

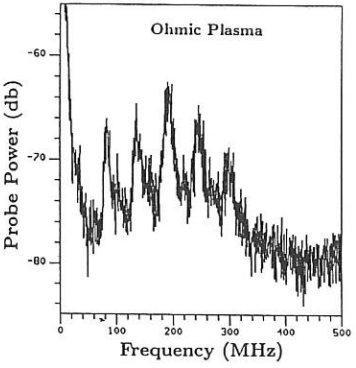


FIGURE 6

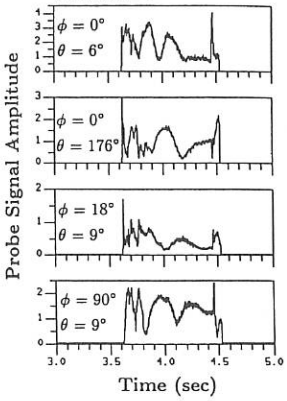


FIGURE 7

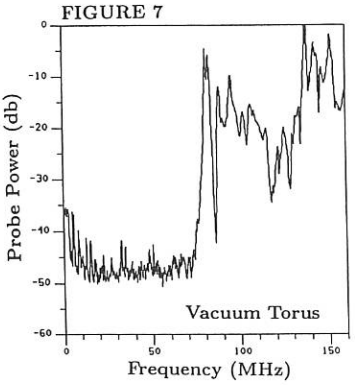


FIGURE 8

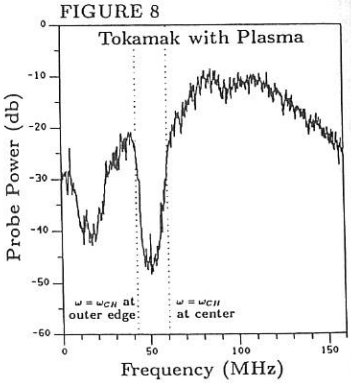

# Density Fluctuation Measurements from Microwave Scattering on TFTR

N.L. Bretz, R. Nazikian, and K.L. Wong

Princeton Plasma Physics Laboratory, Princeton, NJ 08543 USA

**Introduction:** A spatially scanning microwave scattering system operating in the extraordinary mode at 60 GHz is used to study small scale density fluctuations in TFTR plasmas [1]. Heterodyne measurements of density fluctuation in the wave number range $2.0cm^{-1} \leq k_\perp \leq 25cm^{-1}$ are made at various radial and poloidal locations. Power spectra at $r/a \approx 0.3$ for linear and saturated ohmic, L-mode, and supershot plasmas have stong similarities. In all cases the highest fluctuation amplitude occurs at the longest resolvable scale lengths corresponding to $k_\perp \rho_s < 0.5$. Estimates of the local density fluctuation level shows general agreement with the mixing length estimates, $\delta n_e \approx 1/(k_\perp L_n)$. However, direct comparisons of ohmic and L–mode plasmas with the same, $I_p, B_T, n_e(r)$, and $T_e(r)/T_e(0)$ indicate that $\delta n_e/n_e$ for strongly heated L–mode plasmas is several times higher than the ohmic level. In ohmic plasmas no features have been observed propagating in the ion diamagnetic direction; however, plasma rotation is probably shifting all spectral features substantially toward the electron side.

Density fluctuation spectra in ohmic and L–mode plasmas in TFTR share most features observed on other tokamak plasmas [2,3]. Observations in the central plasma region for similar supershot plasmas indicate that for $k_\perp \gtrsim 2cm^{-1}$ these fluctuation spectra are also very similar to L-mode and ohmic spectra. Comparisons have been made with shot-by-shot scans of $k \approx k_\perp \approx k_\Theta$ at $z/a \approx 0.3$ with a scattering volume of dimensions (at the 10 dB power level) of $(\pi \Delta R^2)(2\Delta z) \approx (\pi 5^2)(150/k)cm^3$. No quantitative comparisons are made between $k_r$ and $k_\Theta$ because the beam geometry is not flexible enough to do this at the same location and because the rotationally and diamagnetically shifted parts of the spectra are used to distinguish scattering from the central region from anomalous scattering at low frequency. For values of $k_\perp$ less than $2cm^{-1}$ the spatial resolution begins to include the edge region where scattered intensities are approximately ten times higher than in the plasma interior.

**Ohmic:** In ohmic plasmas we observe frequency shifts in the electron diamagnetic direction whose sign is determined by $\boldsymbol{v}_{De} \cdot \boldsymbol{k}$ where $\boldsymbol{v}_{De} \equiv kT_e/eBL_n$ and $\boldsymbol{k} \equiv \boldsymbol{k}_{scat} - \boldsymbol{k}_{inc}$. The measured shift is usually larger than that predicted by the linear dispersion relation for electron drift waves. For example, Fig. 1 shows a typical spectrum for $k_\perp = 4.2cm^{-1}$ in a helium plasma with $I_p = 1.4MA, B_T = 3.8T$, and $n_e(0) = 4.2 \times 10^{19}cm^{-3}$ where $k_\perp \rho_s \approx 0.5$. This plasma is in the confinement saturation regime where $\tau_E$ is independent of density. The spectrum is dominated by an electron diamagnetic feature at -130 kHz. The electron drift wave estimate, $\omega \equiv \omega_{scat} - \omega_{inc} = k_\perp v_{De}/(1 + k_\perp^2 \rho_s^2)$, predicts a shift of only -20 kHz. We interpret the difference as bulk plasma rotation in either the (electron diamagnetic) poloidal direction or the (counter) toroidal direction. The feature near zero

frequency is probably caused by low level wings in the transmitting and receiving antenna patterns which sample low values of k from a larger plasma volume [4]. This feature is unaltered when the plasma is rotated with neutral beams whereas the diamagnetic feature is further shifted (negative for counter or positive for co-injection). In comparison, spectra in helium and deuterium plasmas in the linear confinement regime at $n_e(0) = 2.3$ x $10^{19} cm^{-3}$ show no significant features in the ion (positive frequency) direction and no substantial differences in the spectra themselves. Similarly, higher density helium plasmas with $n_e(0) = 6.4$ x $10^{19} cm^{-3}$ show no feature in the ion direction. Except in the highest density helium plasma where $T_i$ profile measurements cannot be made, charge exchange recombination $T_i$ profiles give $\eta_i \equiv L_n/L_{Ti} = 1$ to 2 in the scattering volume ($L_{ne} = L_{ni}$ has been assumed). The anomalous feature at low frequency and the apparent width of the electron feature make it difficult to identify an ion feature on the negative frequency side of the line. The expected separation of the electron and ion features is considerably less than the observed shift or width of the spectra. TFTR scattering data can thus neither exclude nor confirm the observtions of Brower [4].

If the width of the fluctuation spectrum perpendicular to **B** is assumed to fall within the instrumental resolution, $\Delta k_{\|} \approx 0.4 cm^{-1}$, is isotropic in this plane, and is cut off at $k_\perp = 2cm^{-1}$ then $\delta n_e/n_e \approx 5.0$ x $10^{-3}$ when $n_e(0) = 2.3$ x $10^{19} cm^{-}3$, and $\delta n_e/n_e \approx$ 1.6 x $10^{-3}$ when $n_e(0) = 4.2$ x $10^{19} cm^{-3}$. In both cases the mixing length estimate gives $\delta n_e/n_e \approx 1/(k_\perp L_n) = 5.0$ x $10^{-3}$. These estimates rely on a calculation of the extraordinary mode single particle cross section [5] and on ray tracing estimates of the scattering volume and its distortion by refractive effects. The instrumental uncertainty in the absolute measurement of $\delta n_e/n_e$ is estimated to be +100%, -50%. The power spectrum shown in Fig. 3a reaches its maximum at the lowest resolvable value for $k_\perp \approx 2cm^{-1}$. For $k_\perp \geq 8cm^{-1}$ the signal level is below the instrumental sensitivity.

L-mode: A typical wave number spectrum in a deuterium L-mode plasma with the same $n_e, I_p$, and $B_T$ as the ohmic case of Fig. 2a but with heating power $P_B = 9MW$ is shown in Fig. 2b. The shifted electron feature is due to counter beam rotation and the spectral broadening is primarily due to radial variations in rotational velocity across the scattering volume. The $k_\perp$ spectrum is shown in Fig. 3b and has the same general structure and magnitude as the ohmic spectra at the same density. With the same symmetry assumptions we estimate $\delta n_e/n_e \approx 4.0$ x $10^{-3}$. The mixing length estimate (5.0 x $10^{-3}$) is the same as in the ohmic helium case. Within the measurement accuracy the fluctuation amplitudes of the ohmic and L-mode of Figs. 2a and 2b are the same. More accurate relative measurements are presented below.

Supershot: A k spectrum for a supershot is shown in Fig. 3c. For this case $I_p = 1.0MA, B_T = 4.6T, n_e(0) = 3.4$ x $10^{19} cm^{-3}$, and $P_B = 16MW$. A supershot with a weakly peaked density profile (i.e., one formed using the full aperture with $R/a = 2.58/0.93m$) is used to avoid complications arising from beam refraction. For this case, the nominally

balanced injection was altered for 100 ms to separate scattering which originates from the crossover region of the main lobes of the transmitter and receiver antennas from the anomalous feature at low frequency. The fluctuation amplitude is $\delta n_e/n_e \approx 3.0 \times 10^{-3}$ and $1/(k_\perp L_n) \approx 4.5 \times 10^{-3}$.

**L-mode/ohmic comparison:** The change in spectra from ohmic to L-mode ($P_B = 9.1 MW$) is examined in a set of discharges in which the density was kept constant at $n_e(0) = 4.1 \times 10^{19} cm^{-3}$ in both the ohmic and L-mode phase of the discharge. The density profiles are also indistinguishable. The wave number spectrum is shown in Fig. 5. The L-mode spectrum has a higher amplitude and is more peaked at low k, leading to an increase in the $\delta n_e/n_e$ ratio between ohmic and L-mode of 3.3. Fig. 6 shows the scattered power increasing steadily with total heating power [$P_{HEAT} = P_{OH} + P_B$] at a fixed $k_\perp = 4.2 cm^{-1}$. However, the shot-to-shot variations are substantial. The scattered power in ohmic plasmas at $k_\perp = 4.2 cm^{-1}$ can be as large as in L-mode plasmas for $P_{HEAT}/P_{OH} \lesssim 6$.

**Conclusion:** The $k_\perp$ spectra of all types of TFTR discharges look very similar as long as the profile shapes and other external parameters ($B_T, I_p, n_e(0)$) are kept the same. This strongly suggests that the fluctuation are caused by drift waves which are dominated by long wavelength modes. However, based on current data TFTR scattering cannot distinguish $\eta_i$ modes from electron magnetic drift waves. To do this parametric studies of distinctly different density profile shapes are needed. Differences between ohmic and L-mode fluctuation levels for similar plasmas with nearly identical density profiles indicate that other factors are influencing the measurement — the $k_\perp$ spectrum below $2 cm^{-1}$ may be important or differences in $T_e/T_i$ or $\eta_i$ may be affecting our results.

**Acknowledgements:** The authors wish to acknowledge the assistance of B.C. Stratton, E.J. Synakowski, E. Mazzucato, H. Park, P.C. Efthimion, E.D. Fredrickson, K. McGuire, F. Perkins, S.J. Zweben, D. Mueller, T.S. Hahm, W. Tang, and G. Rewoldt. This work was supported by U.S. DOE Contract No. DE-AC02-76-CHO-3073.

**References:**

1. N. BRETZ, P. EFTHIMION, J. DOANE, A. KRITZ, Rev. Sci. Instrum., 59 (1988) 1538.
2. E. MAZZUCATO, Phys. Fluids 21 (1978) 1063.
3. T. CROWLEY and E. MAZZUCATO, Nucl. Fusion 25 (1985) 507.
4. D.L. BROWER, W.A. PEEBLES, *et al.*, Phys. Rev. Let. 59 (1987) 48.
5. N. BRETZ and R. NAZIKIAN, Rev. Sci. Instr. (to be published).
6. N. BRETZ, J. of Plasma Physics 38 (1987) 79.

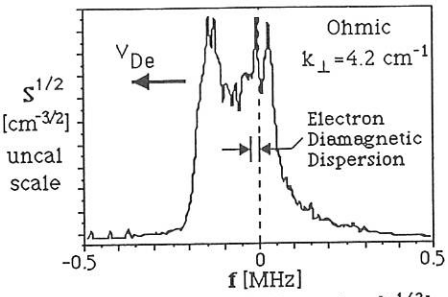


**Fig. 1** The scattered field spectra [$S^{1/2}$] versus frequency [f] shows the electron diamagnetic feature in an ohmic plasma.

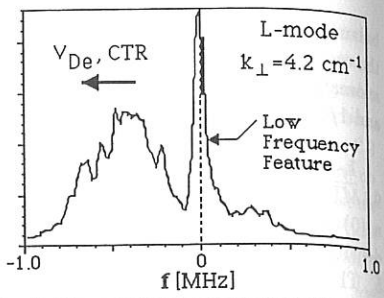


**Fig. 2** The scattered field for a typical counter rotating L-mode plasma shows a shift of $f=v_\psi k_\perp B_\theta/B_\psi/2\pi$.

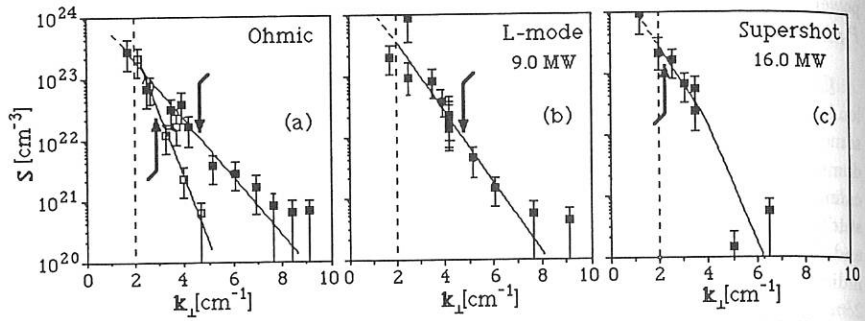


**Fig. 3** Power spectra [S] versus wave number [$k_\perp$] are shown for (a) linear ohmic [□], saturated ohmic [■], (b) L-mode at the same density as the saturated ohmic case, and (c) supershot plasmas. The arrow shows the position of $k\rho_s$=0.5.

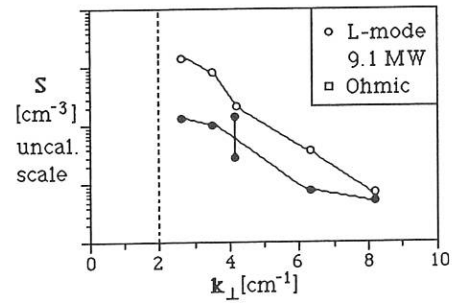


**Fig. 4** Power spectra [S] versus wave-number [$k_\perp$] for L-mode [○] and ohmic [●] plasmas at $n_e(0)=4.0\times10^{19}$cm$^{-3}$.

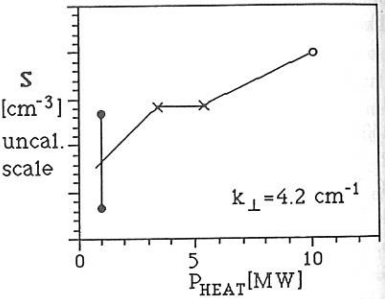


**Fig. 5** Scattered power versus heating power [$P_{HEAT}$] for $k_\perp$=4.2 cm$^{-1}$ using part of the data of Fig. 4.

# INFLUENCE OF NEUTRON SCATTERING ON MEASURED TFTR NEUTRON PROFILES

J.D. Strachan, A.L. Roquemore, M. Diesso, S.L. Liew, and J. Roberts

Princeton Plasma Physics Laboratory
Princeton, New Jersey 08543

The TFTR multichannel neutron collimator [1] consists of ten vertical channels which view the plasma from below. The detectors are hydrogen/ZnS (NE 451) scintillators located 6.3 meters from the plasma midplane. The detectors are shielded by 80 tons of lead and concrete. The collimation of each channel has been tested with a Cf neutron source at the vessel midplane. The detectors are primarily sensitive to neutrons which originate within the 7 cm diameter field-of-view. It has been established by a series of experiments where sets of channels were blocked [1] that the signal in each detector arises from neutrons which travel down its associated flight tube.

The scattered neutron flux can originate both from neutrons which scatter from components that are in the collimator sightline above the plasma, and from neutrons which scatter from the neutron collimator aperture. The local neutron emissivity is usually small near the plasma edge so that signals from channels that observe the outer plasma region are dominated by the scattered component. However, the virgin flux is $\approx 95\%$ of the signal in the channel which views the plasma center.

Several design features of the TFTR multichannel neutron collimator were intended to reduce the flux of detected scattered neutrons. These include: (a) the NE 451 scintillator responds to higher energy recoil protons. Thus, the neutron energy degradation caused by neutron scattering tends to make the detectors less sensitive to scattered neutrons. Also, the detector is relatively insensitive to gammas; (b) the vacuum window at the bottom of the vessel was recessed approximately 0.5 meters into the shielding; (c) the vacuum window at the top of the vessel was thinned to be 3 mm of steel located 1.25 or 1.45 m above the vessel midplane. The next observable neutron scattering centers are located above the machine or approximately 5 m above the horizontal midplane. Thus, the vertical viewing TFTR multichannel neutron collimator was arranged to directly view a minimum of scattering centers; and (d) the collimating tubes were extended 3.3 m beyond the scintillators.

Plasmas with small minor radius [2] were used to evaluate the effect of neutron scattering. For these plasmas, many of the channels do not have any plasma above them and their entire count rate arises from scattered radiation. The detected neutron fluxes (Fig. 1) exterior to the plasma are $1 \rightarrow 5\%$ of the fluxes detected from the plasma center (Table 1). The magnitude of the scattered signal is comparable to that obtained from MCNP calculations [3] of the neutron scattering from some typical scatters (Table 2), such as thin steel plates (windows) and the entrance aperture to the collimator.

The data in Table 1 was used to subtract the scattered component from each channel's signal by assuming that the neutrons originate from a line source located at the plasma magnetic axis, and that the scattering occurred from material components located $\pm$ 1.4 m above the horizontal midplane. This means that the scattered signal in each channel for a plasma with a Shafranov

shifted magnetic axis of $R_{SHAV}$ and a total volume-integrated neutron intensity $I_{neut}$ is for channel $i$ (located at major radius, $R_i$):

$$I_i^{SCATT} = C_i \frac{1.4\, I_{neut}}{\sqrt{1.4^2 + (R_{SHAF} - R_i)^2}} \,. \quad (1)$$

where $C_i$ (Table 1) is the experimentally determined scattered fraction projected to occur when the plasma is located directly above the channel (i.e., is maximum).

The above model reasonably describes the signal in exterior channels which are proportioned to the volume-integrated neutron emission and insensitive to the small changes in $R_{SHAF}$ that actually occur in TFTR (Fig. 3). Such validation is only available for channel 10, since most channels are usually interior to the plasma.

In summary, neutron scattering is a small ($\approx 5\%$) component of the neutron flux detected in the TFTR multichannel neutron collimator and comprises the entire flux in the outer channels (Fig. 3). The magnitude of the scattered component is in agreement with simple neutron streaming calculations for typical scattering centers.

Efforts to further reduce the scattered component do not yet seem necessary but could be made by: (a) shaping of the collimator aperture to reduce the influence of scattering from the collimator entrance throat, and (b) reduction of material that can be observed above the plasma.

The techniques of using small minor radius plasmas to experimentally evaluate the neutron scattering has been valuable and should be considered for CIT and ITER where horizontally mounted collimators may have a larger scattered component. So far, Eq. (1) has been used to subtract the scattered signal from about 2,000 TFTR plasmas and always predicts an edge neutron emissivity near zero (e.q., Fig. 3).

**Acknowledgments** - The authors thank K. Young, and L.C. Johnson for their support. This work was supported by the U.S. Department of Energy Contract No. DE-AC02-76-CHO-3073.

## References

1. L. Roquemore et al., Proceedings of the Topical Conference on High Temperature Plasma Diagnostics (1990), to be published Rev. Sci. Instrum.
2. L. Grisham, Proceedings this conference.
3. Los Alamos National Laboratory Report No. LA-7396-M, Rev. 2 (1986).

Table 1

| Channel | Major Radius $R_i$(m) | Sensitivity $10^{10}\ \frac{n/sec}{cps}$ | (Fig. 1) Scattered $\frac{Signal}{CentralChannel}$ | (Used in Eq. 1) $C_i$ $(10^{-13})\frac{cps}{n/sec}$ |
|---|---|---|---|---|
| 1 | 1.80 | 6.3 | 0.049 | 2.1 |
| 2 | 1.94 | 7.1 | 0.037 | 1.3 |
| 3 | 2.08 | 3.5 | 0.033 | 2.1 |
| 4 | 2.23 | 5.3 | 0.051 | 1.8 |
| 5 | 2.47 | 3.1 | 0.006 | 1.08 |
| 6 | 2.68 | 3.8 | 0.021 | 1.25 |
| 7 | 3.00 | 1.6 | 0.040 | 5.3 |
| 8 | 3.16 | 1.4 | 0.035 | 6.3 |
| 9 | 3.32 | 3.6 | 0.002 | 1.5 |
| 10 | 3.48 | 4.2 | 0.018 | 0.95 |

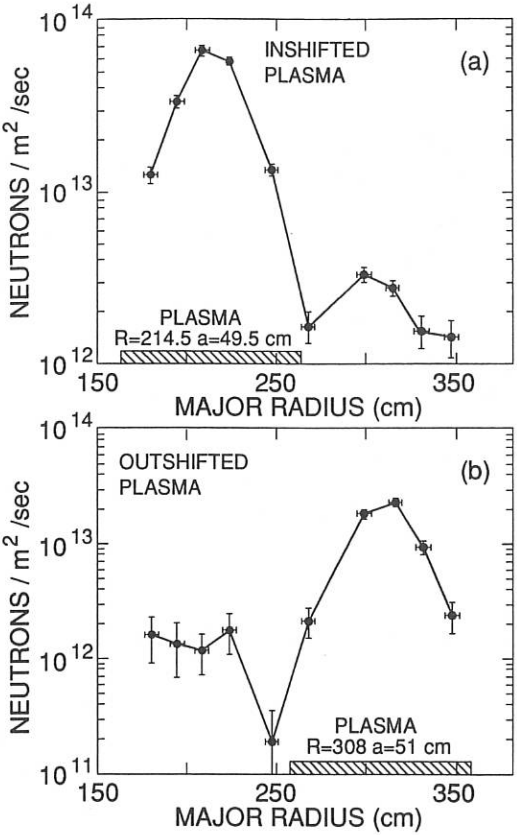


FIG. 1. The calibrated line-integrated neutron emission for (a) inshifted and (b) outshifted TFTR plasmas. The signal in the channels which view outside the plasma are interpreted to be scattered neutrons originating near the TFTR vacuum vessel.

| Typical Scatterer | Edge Scattered Signal/Central Signal |
|---|---|
| Mouth of aperture | 0.008 |
| 1 cm Fe plate 1.3 m below plasma | 0.03 |
| 5 cm Fe plate 2.5 m above plasma | 0.019 |
| 0.5 cm Fe plate 2.5 m above plate | 0.01 |

Table 2

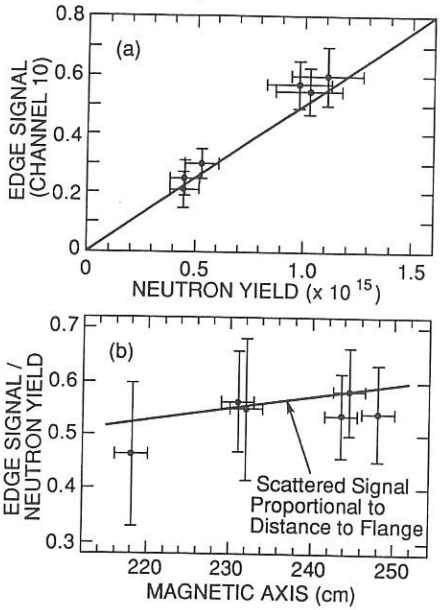


FIG. 2. The dependence of the magnitude of the scattered neutron signal upon (a) the neutron emission from the plasma and (b) the major radius of the plasma. These measurements are for a single channel viewing outside the edge of the plasma.

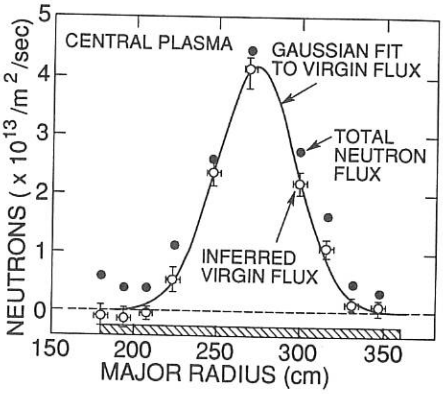


FIG. 3. The line-integral neutron profile for a central TFTR plasma (R = 260 cm, a = 93 cm) heated by deuterium neutral beams. The closed points are the measured neutron flux and the open circles are the inferred virgin neutron flux with a scattering compoent subtracted by use of Eq. (1). The error bars include calibration uncertainties, statistical uncertainties, and uncertainties in the scattering subtraction.

# EDGE DENSITY X-MODE REFLECTOMETRY OF RF-HEATED PLASMAS ON ASDEX

R. Schubert, F. Braun, J. Gernhardt, F. Hofmeister, F. Leuterer, M. Münich, J.-M. Noterdaeme, F. Wesner, ASDEX Team

Max-Planck-Institut für Plasmaphysik
Euratom Association - D 8046 Garching - Fed.Rep.Germany

## Introduction

RF heating methods need special diagnostics to help better understand the interaction of the wave with the plasma. Of particular interest is the influence of the wave on the edge plasma in the direct vicinity of the RF heating antenna. One important parameter in this context is the electron density, which can be measured by means of microwave reflectometry.

In this paper we describe a fast X-mode reflectometer installed on ASDEX. We present measurements of the edge density profile in the range $10^{11}cm^{-3} < n_e < 1.5 * 10^{13}cm^{-3}$.

## Principle of the measurement and experimental set-up

Reflectometry has been used previously to measure electron density profiles (s. e.g. [1], [2]). We extended the range to the very edge (to 2.5 cm behind the limiter) and installed two system at different toroidal positions to give the density profile, which might be different at toroidally different positions in the SOL. Fig. 1 shows the principle, which is the same at the two positions. The microwaves from the generator (BWO) are split by a directional coupler (DC) into a signal branch (emitted to the plasma and reflected at the cut-off, the point in the plasma beyond which a propagation is not possible) and a reference branch. Changes in the relative phase of these two branches lead to maxima and minima (fringes) in the output signal of the phase detector. Due to the use of the X-mode (E perp. B) it is possible to follow the location of the cut-off from $r=r_{ant}$, the position of the antenna mouth, to about 20 cm into the plasma and consequently to calculate the density profile by sweeping the microwave frequency up from $f_1 < f_{ec}(r = r_{ant})$ to $f_2$. In the final configuration a sweep from 60 - 80 GHz was performed in 150 µs, which gives a fringe frequency of about 1 MHz. A repetition time of about 2.5 ms together with a data acquisition of 2 x 100 ms at 10 MHz allowed to sample about 2 x 40 sweeps per shot. The two sets of microwave antennas we installed are located in the equatorial plane on the lowfield side of ASDEX. The first one consists of a hornantenna (opening: 8 mm x 10 mm, emitter) and an open-ended waveguide (1.9 mm x 3.8 mm, receiver) and is inserted in a diagnostic opening of the faraday screen of an ICRF-antenna. The second one consists of two hornantennas (16 mm x 10 mm, emitter, and 8 mm x 10 mm, receiver) and is placed about 6 cm toroidally away from the LH-grill antenna.

Influence of the electron density fluctuations

In first tests with a slow sweep and an expected fringe frequency of 6 kHz no clear fringe pattern could be seen. Experiments at fixed frequency showed that the fringes were blurred out by strong intensity modulations of the reflected signal (fig. 2, fig. 3). Similar problems have also been reported in an O-mode system with much bigger antennas [3]. These strong modulations (factor of 10 and larger) cannot be explained by radial movements of the cut-off layer due to electron density fluctuations and are probably caused by interference effects due to poloidally inhomogeneous electron density fluctuations [4]. Our way to make possible the fringe counting despite these perturbations, was to reduce the sweep time and thus to increase the fringe frequency to values higher than that of most fluctuations. Fig. 3 shows that the bulk of the fluctuations are below 500 kHz, so that fringes at 1 MHz can clearly be distinguished from the fluctuations by frequency.

Results

Fig. 4 shows the raw data of the first 40 μs of a sweep. The reflection begins only at $f_0$, which is, within the error bars, identical to the electron cyclotron frequency at the antenna mouth. This is a particularity of the X-mode, and allows to give the location of the first reflection, which is not possible in an O-mode system (s. e.g.[5]). In an O-mode system the very low densities at the edge demand the use of very low microwave frequencies, which give a very poor spatial resolution. The fringes in the mixed signal (upper trace, fig. 4) are clearly seen. As a sweep is performed on the time scale of the fluctuations, one single sweep gives a momentary profile, which is not constant during the time of the sweep. Fig. 5 shows the momentary profiles of 35 sweeps during a stationary plasma phase. Averaging over these sweeps gives reproducible electron density profiles. Fig. 6 shows the profiles measured in two stationary phases, where the plasma has been moved 5.3 cm horizontally. The measured shift of only about 4 cm in the edge may be explained by toroidal asymmetries and by edge profile changes due to the bulk movement. From the momentary profiles we can also calculate absolute and relative fluctuation levels (fig. 7; comparison to other fluctuation measurements on ASDEX: [6], [7]). A comparison to Thomson scattering data shows good agreement (fig. 8). Reflection coefficients for the LH-waves calculated from density values we measure in the plane of the LH-grill (typically: $n_e = .5\ 10^{12}\ cm^{-3}$ and $dn_e/dr = .5\ 10^{12}\ cm^{-4}$) are in good agreement with experimental ones.The influence of the LH can be seen in fig. 9. This steepening of the electron density profile at the very edge during LH is also reported on Castor [8].

Conclusions

We demonstrated that reflectometry is applicable to measure electron density profiles at the very edge of the plasma. This was only possible by the use of the X-mode, which has in contrary to the O-mode, even at very low densities a finite cut-off frequency ($f_{cut\text{-}off\text{-}X} > f_{ec}$). The perturbations by the density fluctuations could be overcome by increasing the fringe frequency to over 1 MHz. The very limited access to the plasma it requires (a few $cm^2$) and its good spatial resolution makes

reflectometry an ideal diagnostic for the measurement of local effects during HF-heating. As it can measure the absolute edge electron density profile independently of other diagnostics and because of the possibility of a further improvement of the sweep and the data acquisition it can be considered as candidate for standard diagnostic.

References

[1] Simonet F., thèse de doctorat d´état, Nancy, France 1985
[2] Bottollier-Curtet H., thèse de doctorat, Paris, France, 1986
[3] Busankin V.V., Vershkov V.A., Dreval´ V.V., Zhuravlev V.A. Voprosy atomnoj nauki i tekhniki, ser. termojadernyj sintes, vyp. 2 s. 63-65 ( Questions of nuclear science and technology, series of nuclear fusion; Russian) [ Post deadline paper Madrid 87 ]
[4] Zhuravlev V.A., Kurchatov Institute of Atomic Energy, Moscow, private communication
[5] M.E. Manso et al., conf. rep. Controlled Fusion and Plasma Physics,13B, IV,p.1517,Venice 1989
[6] H.Niedermeyer et al.,conf. rep. Controlled Fusion and Plasma Physics,13B, I, p.27,Venice 1989
[7] A. Rudyj et al., this conference
[8] Journal of Nuclear Materials 162-164 (1989) 562-567, North-Holland, Amsterdam

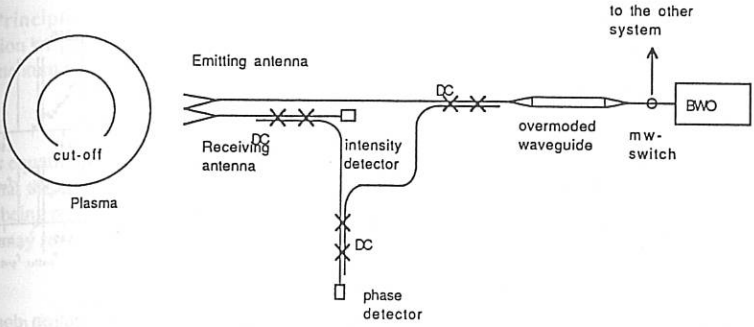


fig. 1 Principle of the reflectometer

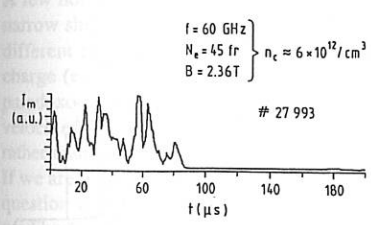


fig. 2 Intensity of the reflected signal from the plasma, fixed frequency; The launched signal has been chopped, so that the right part of the trace gives the baseline.

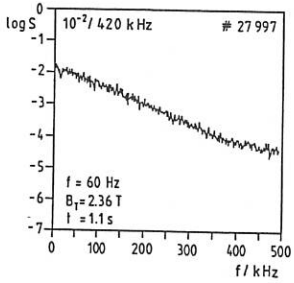


fig. 3 A typical power spectrum of the reflected intensity (fixed frequency launched)

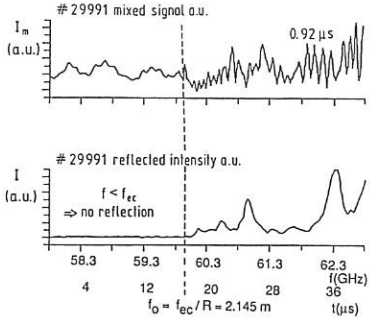


fig. 4 Raw data in sweep operation; upper tr.: mixed signal containing the phase information; lower tr.: intensity of the reflected signal ( B =2.8T, $I_p$ =320kA, $n_e$=2.0 x $10^{13}$/cm$^{-3}$)

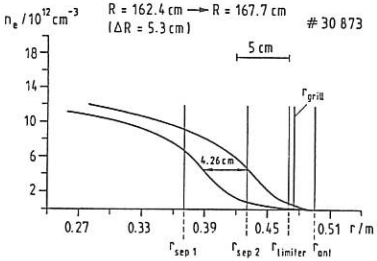


fig. 6 Density profiles measured in two stationary plasma phases in one shot, where the plasma has been moved horizontally 5.3 cm ( B =2.8T, $I_p$ =420kA, $n_e$=1.3 x $10^{13}$/cm$^{-3}$)

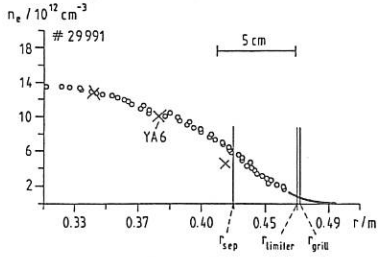


fig. 8 Comparison of the density profile measured with the reflectometer to the densities obtained with outermost channels of the Thomson scattering system (YAG). ( B =2.8T, $I_p$ =320kA, $n_e$=2.0 x $10^{13}$/cm$^{-3}$)

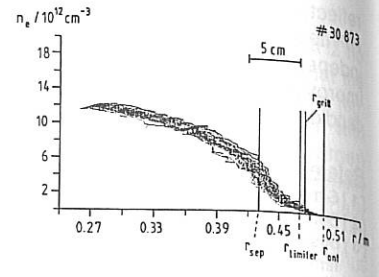


fig. 5 momentary profiles from 35 sweeps in a stationary plasma phase, superimposed (same plasma phase as in fig. 6, R = 167.7 cm) ( B =2.8T, $I_p$ =420kA, $n_e$=1.3 x $10^{13}$/cm$^{-3}$)

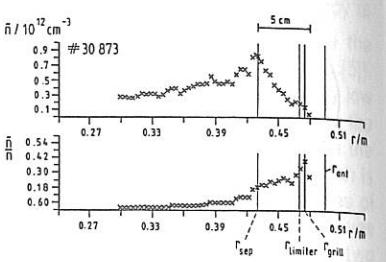


fig. 7 Absolute and relative electron density fluctuations as calculated from the data shown in fig. 5

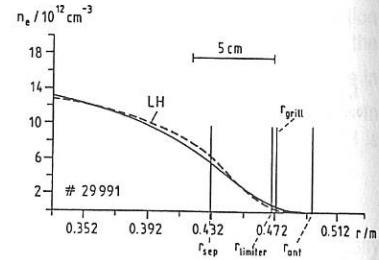


fig. 9. Profile change measured during LH experiments ( B =2.8T, $I_p$ =320kA, $n_e$=2.0 x $10^{13}$/cm$^{-3}$, $P_{LH}$=1.3MW)

# MEASUREMENT OF POLOIDAL ROTATION ON ASDEX

J. V. HOFMANN, A. R. FIELD, G. FUSSMANN and the ASDEX team
*Max-Planck-Institut für Plasmaphysik*
*EURATOM-IPP Association D-8046 Garching, FRG*

**1. Introduction:** Measurements of the poloidal drift velocities of the ion species in a Tokamak plasma are of fundamental importance for investigating a number of physical processes involving momentum sources and sinks, viscosity and radial electric fields. In particular, various authors have hypothesized marked changes in the radial electric field near the separatrix during the L → H transition in NI heated plasmas. Experimental investigations on the DIII-D Tokamak have revealed line shifts of a 'warm' component of the He II (4686 Å) line corresponding to poloidal rotation velocities of $v_{pol} = 1.8 \cdot 10^4\ ms^{-1}$[1]. From this the existence of a negative radial electric field of $2.7 \cdot 10^4\ Vm^{-1}$ during the H-phase is inferred. Analogous measurements have been performed on the ASDEX Tokamak in the visible spectral range where the required resolution is easily achieved. Code calculations and measurements show that the lines of C III (4647.4 Å), B IV (2821.7 Å) and He II (4686 Å) are emitted from radially localized shells near the separatrix.

**2. Principle of electric field measurements:** The basic relation between the perpendicular motion of particles and the radial electric field is obtained from the radial component of the momentum equation:

$$\frac{\partial p_z}{\partial r} = e_z\, n_z \left[ E_r + (\vec{v_z} \times \vec{B})_r \right] \qquad (1)$$

This equation pertains for all charged particles provided the radial velocities are sufficiently small so that the corresponding friction forces can be neglected. The perpendicular velocity component $v_{z\perp}$ being relevant in equ. (1) is tangent to the magnetic surface and nearly in the poloidal direction. We may rewrite equ.(1) as

$$E_r + v_{z\perp} B = \frac{p_z'}{e_z\, n_z} \qquad (2).$$

Only in the case that the right hand side of this equation, with $p_z' = d(n_z T_z)/dr$, is small compared to the two terms on the left hand side, the electric field can be directly determined by measuring the perpendicular velocity.

A few notes appear appropriate in this context. First, choosing low-z impurity ions existing in narrow shells in the boundary region, we notice that in the case of $E_r = 0$, the velocity will have different sign on the inner and outer sides of the shell. In fact, different ions but of the same charge (e. g. C IV and O VI ) may have opposite velocities at the same radial position. This paradoxon is solved by realizing that the velocities ocuring in the above equations are macroscopic velocities of diamagnetic kind; for $E_r = 0$ these are solely produced by the gyration of the particles rather than by a motion of the gyro-centres.

If we are going to determine $v_{z\perp}$ by the shift of spectral lines some attention must be paid to the question whether the photons emitted from a particular point in the plasma do virtually reflect the gradients of $n_z$ and $T_z$ over a distance of the order of the gyro-radius as it is assumed in a microscopic derivation of the above equations. This is the case if the life time $\tau = 1/A$ of the excited ions is small compared to the reciprocal gyro-frequency $\omega_z^{-1}$ (i.e. $\omega_z \tau << 1$). In the opposite case $\omega_z \tau \approx 1$ or $\omega_z \tau > 1$, the spectral shift is in addition influenced by the gradient of the excitation rate and the measured velocity $v_{z\perp}^*$ is obtained from an equation of type (2) with the density $n_z$ being replaced according to

$$n_z \rightarrow n_z^* A = \left\{ \begin{array}{l} n_z\, n_e\, X_{ex}, \text{ elec. excitation} \\ n_{z+1}\, n_0\, X_{cx}, \text{ cx -recombination} \end{array} \right\} \qquad (3)$$

This effect may be of importance in particular in case of charge exchange recombination of low Z-ions (He II) in the boundary region. In this case the recombination and cascading from high quantum numbers can result in relatively large life times on one hand, and on the other hand the neutral hydrogen density $n_0$ is characterized by large gradients.
The decay length $\lambda = ( n_z T_z)/ ( n_z T_z)'$ or $\lambda^* = ( n_z^* A T_z)/ ( n_z^* A T_z)'$, respectively, allows us to estimate the electric field being equivalent to the right hand side of equ. (2)

$$E_\lambda = T_z / ( e_z \lambda) \quad (4).$$

For a typical case $T_z = 50$ eV, $\lambda = 5$ cm, and $z = 2$ for instance we obtain $E_\lambda = 0.5$ kVm$^{-1}$. In a magnetic field of B = 2 T this corresponds to a diamagnetic velocity of 250 ms$^{-1}$.

**3. Experiment and accuracy:** Light emitted from the edge region of the plasma is collimated into a 1m Czerny-Turner spectrometer using a lens, a rotatable mirror at the port entrance and two edge mirrors above and below the plasma mid-plane. This provides two nearly anti-parallel lines of sight; the lower mirror looking upward in a vertical poloidal plane; and the upper mirror looking downward at 5° to the vertical plane opposite to the direction of the plasma current. By scanning the rotatable mirror the lines of sight may be scanned from 3 cm inside to 7 cm outside the separatrix at the horizontal mid-plane. By using a prism to rotate the slit image by 90° a radial resolution of 0.1 cm was achieved. The spectrometer was equipped with a 2400 lmm$^{-1}$ grating and a 1024 channel photo-diode array detector providing spectra at 20 ms intervals. The dispersion of the instrument at this wavelength is 3.11 Åmm$^{-1}$ or 0.078 Åpix$^{-1}$. Contributions to the spectra from lower wavelength lines in second order were suppressed using a filter and additional broadening due to Zeeman splitting by cutting out the circularly polarized σ-components with a polarizer.
The accuracy with which the line centroids could be determined was estimated using two techniques. Firstly, the C III triplet was deconvolved using a FFT technique and then fitted with a 3-Gaussian line profile. The weighted mean of the shift of the centroids of these Gaussians from a reference wavelength could be determined to an accuracy of ± 0.005 Å corresponding to a velocity of ± 300 ms$^{-1}$. Secondly, spectra of a line from a Cd lamp were recorded as the grating was turned in steps of 0.01 Å. A plot of the line shift determined from the spectrometer setting versus the shift of the centroid of the fitted Gaussian is shown in fig.1. Assuming that the spectrometer settings were perfect yields an accuracy of 0.012 Å in determining the line centroid. Any inaccuracies in these settings would result in this estimate being too large. An estimate of the accuracy of determining the line centroids is thus between ± 0.005 Å and ± 0.012 Å corresponding to velocities of ± 300 ms$^{-1}$ and 800 ms$^{-1}$ respectively.
The radial emission profile of the C III multiplet ($2s3s\ ^3S_1$ - $2s3p\ ^3P_{0,1,2}$: 4647.40 Å, 4650.16 Å and 4651.35 Å) could be measured either by shifting the plasma radially or by scanning the rotatable mirror.

**4. Results:** From measurements of the C III multiplet performed whilst shifting the plasma and measurements performed whilst scanning the rotatable mirror we determined the maximum of the emissivity of the C III shell being located at the separatrix to an accuracy of ±1cm. The radial extent of the shell is about 6 cm FWHM. This shell moves radially outward during NI and broadens to 8 cm FWHM. Numerical code calculations predict a radial position 2 cm outside the seperatrix during the OH phase. The B IV shell is predicted to be located further inside the separatrix and was not fully accessible to our measurements. For this reason these measurements concentrated on the C III multiplet.
Figs.2(a) and (b) show the spectra of the C III triplet measured during the OH and Co-NI heated phases (ASDEX # 31199 $D^o \rightarrow D^+$, 2.7 MW), respectively. The instrument profile is deconvolved from these profiles using a FFT technique. The corresponding intensity profile fitted to the sum of

3 Gaussians and a constant background is shown in figs. 2(c) and (d). The estimated errors in the determination of the fit parameters are propagated through subsequent calculations of the derived parameters.

The intensities, intensity ratios, separations and shifts of the three lines as a function of time are shown in figs. 3(a)-(d); note the increase in intensity at the onset of NI at 1s (NI: 1 - 2.6 s, H-phase: 1.2 - 1.8 s). As a consistency check of our measurements we find that the line ratios in fig. 3(b) remain equal, within the estimated uncertainties, to the line ratios determined from the statistical weights of the upper level of the transition of 1:0.6:0.2, indicated by the dashed lines. The ion temperatures derived from the widths of the line profiles agree to within the estimated uncertainties and are about 45 ± 5 eV. This may be understood in terms of an equilibration time longer than the ionisation time for C III. The separations of the lines, fig. 3(c), also remain constant at values close to those tabulated (dashed lines) of 1-2: 2.76 ± 0.007 Å and 1-3: 3.95 ± 0.007 Å. Fig. 3(d) shows the shifts in the centroid positions of the 3 fitted Gaussians relative to their mean positions determined over the first four time points. The weighted mean shift of the triplet is indicated by the solid line. The estimated uncertainty of this mean shift during the sustained phase of the plasma is ± 0.005 Å.

The corresponding velocities derived from these shifts are shown in fig. 4. The data presented here were measured using the upper edge mirror viewing downward at r = a - 0.02 m = 0.38 m. There is a statistically consistent increase in the poloidal drift velocity on the onset of NI at 1 s and a decrease in this velocity at the termination of the H-phase at 1.8 s. In contrast to our expectations, however, we do not observe a decrease with the end of NI heating at 2.6 s during the plasma ramp-down phase. The sign of the velocity corresponds to a downward flow of the C III ions at the outer edge of the plasma. When viewing with the lower edge mirror a blue shift is observed of the same magnitude. These results are thus consistent with a poloidal compo- nent of the C III drift velocity of 1600 ± 300 $ms^{-1}$. Data from OH and LH heated plasmas do not show statistically significant drift velocities.

The typical toroidal rotation velocities for this parameters on ASDEX are about $4 \cdot 10^4$ $ms^{-1}$ at a minor radius of 0.38 m during NI [2]. With q = 3 and taking into account the 5° angle of the line of sight to the vertical poloidal plane the found poloidal rotation velocities are explicable as the poloidal component of the ion flow parallel to the magnetic field.

**4. Conclusions:** Measurements of the drift of the C III ions located near the plasma seperatrix show poloidal velocities of 1600 ± 300 $ms^{-1}$ during Co-NI heating in the direction of $B_{pol}$. The estimated accuracy of this measurement is of the order of magnitude of the diamagnetic drift velocity. The C III ions in the ASDEX tokamak certainly do not exhibit as high poloidal drift velocities as measured on DIII-D. The consistency of the line intensity ratios, separations and ion temperatures of the C III triplet lend credence to our measurements.

**References:**

[1] Groebner, R.J., Gohil, P., Burrell, K.H., et al., Proceedings of 16th European Conference on Controlled Fusion and Plasma Physics, Venice, Italy, Vol. 1 (1989) 245-248.

[2] Kallenbach, A., Mayer, H.M., Fussmann, G., et al., "Momentum Transport Studies on ASDEX", this conference.

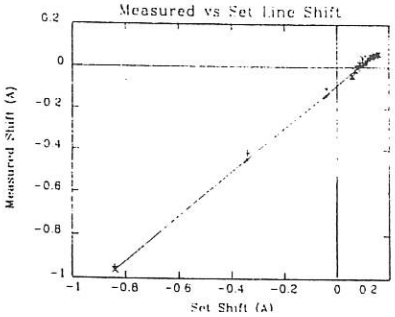


Fig. 1: Check of accuracy in line shift measurements using a Cd-lamp. The grating was turned in steps of 0.01 Å. Data evaluation by double-Gaussian fits.

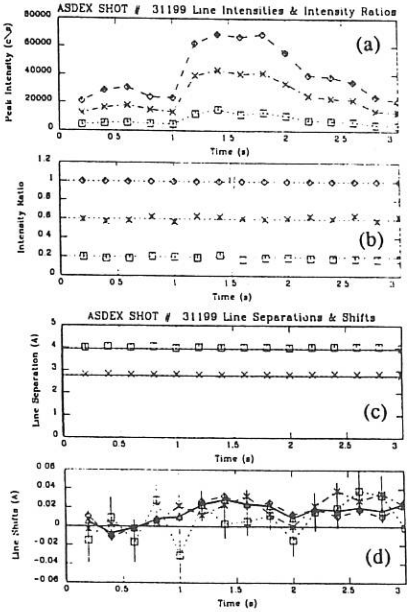


Fig. 3: C III triplet line intensities (a), ratios (b), separations (c) and shifts (d). NI from 1.0-2.6s. H-phase from 1.2-1.8s.

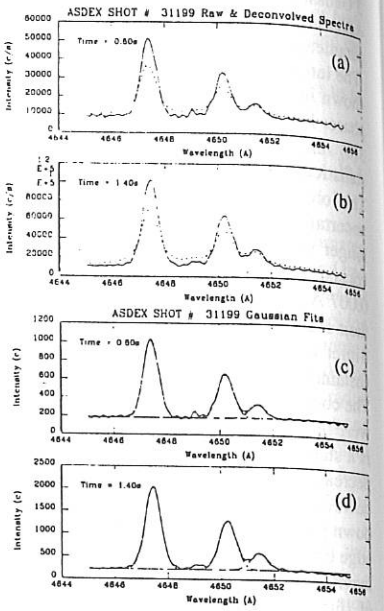


Fig. 2: C III triplet. Above: raw (dashed) and deconvolved data (solid line) for OH (a) and NI phase (b). Below: deconvolved data and triple-Gaussian fit (c,d).

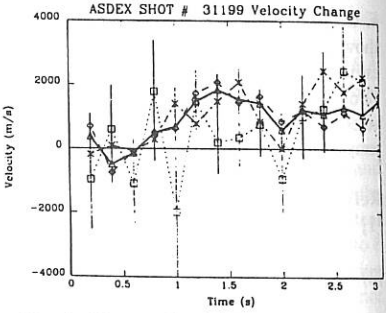


Fig. 4: Measured poloidal velocity: solid line: weighted mean of whole multiplet, dashed lines: single spectral lines (symbols as in Fig. 3).

# LOCALIZED DENSITY MEASUREMENTS ON ASDEX USING MICROWAVE REFLECTOMETRY

M. Manso, F. Serra, A. Silva, J. Matias, F. Nunes,
J. Leitao, J. Mata, P. Varela, S. Vergamota
Instituto Superior Tecnico, Lisboa, Portugal

J. Neves, J. Pereira, L. Cupido
Universidade de Aveiro, Aveiro, Portugal

F. X.- Söldner, G. Siller
Max-Planck-Institut fur Plasmaphysik, Garching, FRG

## 1. Introduction

Reflectometry is based on the propagation and reflection of probing waves in the inhomogeneous fusion plasma. For O-mode propagation the density of a reflecting plasma layer ne(Xc) is determined by the microwave frequency (F) which equals the local plasma frequency; the position Xc is evaluated from the phase delay $\Phi(F)$ between the incident and reflected waves. If the frequency is swept, a density profile can be obtained from the phase shift $d\Phi/df$ the wave undergoes in the plasma, integrated from f=0 to f = F:

$$X_c(F) = \frac{c}{2\pi^2} \int_0^F \frac{d\Phi}{df} (F^2 - f^2)^{-1/2} \, df$$

In fixed-frequency, global plasma movements and local plasma density fluctuations can be studied from the phase shift $d\Phi/dt$ resulting from the movements of the reflecting layer.

Broadband swept systems have been recently developed for TORE SUPRA /1/, ASDEX /2/ and DIII-D /3/, and a multichannel narrowband system for JET /4/. The ASDEX reflectometric system consists of three reflectometers (O-mode) in the frequency bands 18-26.5 (K-band), 26.5-40 (Ka-band) and 40-60 GHz (U-band), as described in /2,5/; electron densities measurements can be performed in the region starting from the plasma radius close to the magnetic separatrix on to the gradient region, (from 0.4 to $4.45*10^{13}$ $cm^{-3}$). Broad band experiments were made with simultaneous swept operation of three reflectometers (2ms). Plasma density profiles and density perturbations have been measured for several plasma scenarios. Results are presented and the scope and the limitations of the evaluating techniques are discussed.

## 2 - Experimental results

As an example of typical broadband reflectometric measurements, we show in Fig.1 a K-band signal obtained (a) during shot 27328 (ohmic, $\bar{n}e = 3.9*10^{13}$ $cm^{-3}$) and (b) before the plasma discharge. Clear fringes due to the plasma can be observed; the frequency minima are automatically detected

(as indicated below the horizontal axis of the figure). The phase shift $\Delta\Phi/\Delta f$ is evaluated from the minima for each frequency band and fitted to a unique curve as shown in Fig.2(a); the curve exhibits oscillations that result from the plasma density fluctuations. The corresponding density profile is shown in Fig. 2(b); the data from both HCN (- - -) and YAG (o) lasers is also presented.

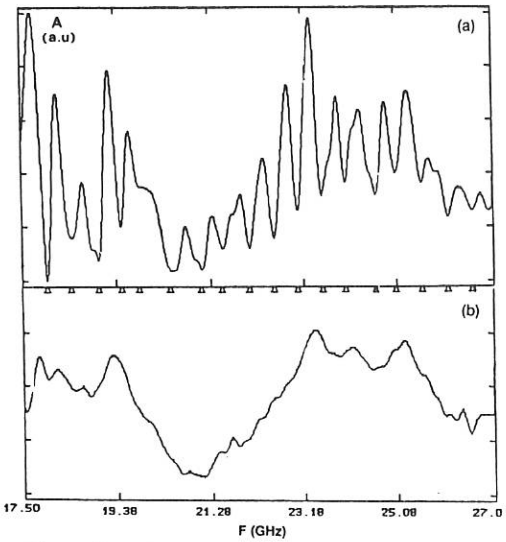


Fig. 1: Output signal of the K band reflectometer obtained (a) during ASDEX shot 27328 (1100 ms - 1102 ms), and (b) before the plasma discharge.

Several numerical analysis techniques were developed in order to smoothing and/or filtering the perturbations /6/. These techniques aim at obtaining the nondisturbed density profile. Figure 3 shows the profile of shot 27328 after smoothing (a); it can be seen that the shape (Fig.2b) has not been changed. In Fig.3 it is also plotted (b) the profile concerning shot 27294 (LHCD, $\bar{n}e=1.3*10^{13}\ cm^{-3}$), in order to illustrate the wide range of densities measured with the reflectometric system.

The influence of the non-measured part of the phase shift curve (below $F_1$ =18 GHz) on the evaluation of the profiles was studied, by assuming different profile shapes between X0(ne=0) and the first reflecting layer X1($F_1$). The study showed that the shape of the nonmeasured part of the pedestal affects mainly: (i) the outer part ( $\Delta X \lesssim 1$ cm) of the evaluated density profiles, (10-20%); (ii) profiles concerning high density plasmas ($\bar{n}e > 3x10^{13}\ cm^{-3}$).

Two similar shots, 27327 and 27328, (with the plasma radially displaced by 1.7 cm), were analyzed; a linear shape for the pedestal was considered. The measured density profiles for $ne < 2*10^{13}\ cm^{-3}$, are presented in Fig. 4. The radial shift of ~ 1.7 cm between the two profiles is recovered, showing both the validity of the assumed linear shape for this case, (from the point of view of profile evaluation), and the accuracy of the reflectometric system in measuring radial movements of the plasma.

In some situations significant modifications of the plasma reflected waves are observed. An example is presented in Fig. 5, for shot 29285 when a m=2 tearing mode is present. The output signal of the Ka band reflectometer shows both amplitude and phase modulations due to the rotating ($f_{rot}$) mode (Fig.5). The period of the modulations can be determined, namely from the time interval $\Delta t$ = 700 $\mu$s between two beat frequency maxima, as indicated in Fig.5; the mode frequency can be

estimated: $f_{rot} \sim \Delta t^{-1} \sim 1.4$ kHz, this beeing in agreement with the magnetic data . Broadband reflectometry can therefore give the time scale of localized modifications of the profile occuring during the 2 ms measuring time; amplitude information can also be obtained. A detailed study of this example is done in an accompanying paper /7/

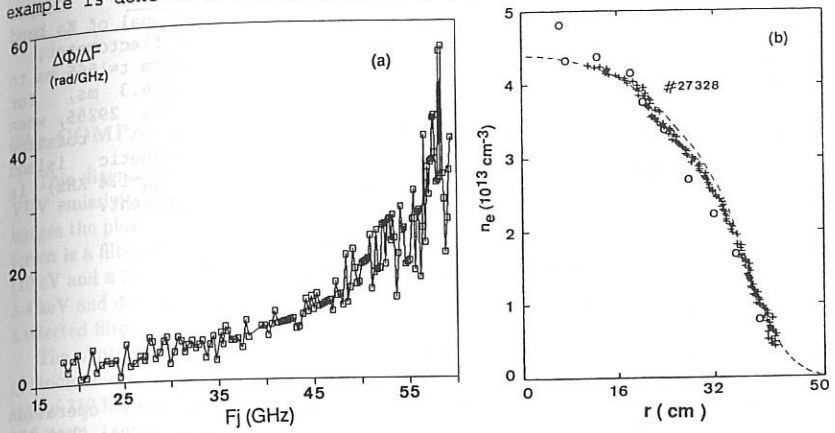


Fig. 2: (a) Phase shift curve including the phase information from the three reflectometers, with the minima obtained from raw data, for shot 27328; (b) density profile evaluated from phase shift curve (a).

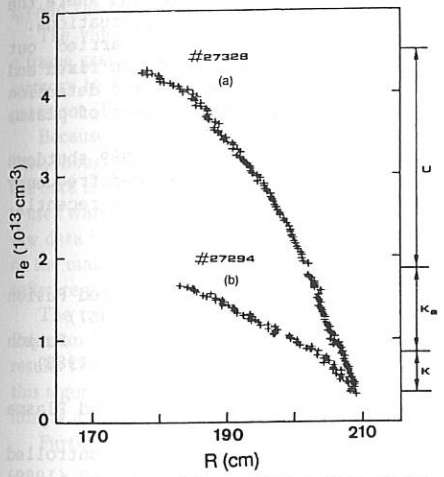


Fig.3: Density profiles for shots (a) 27328 (t=1100 ms), after smoothing of the phase characteristic, and (b) 27294 (t=1100 ms), direct from raw-data

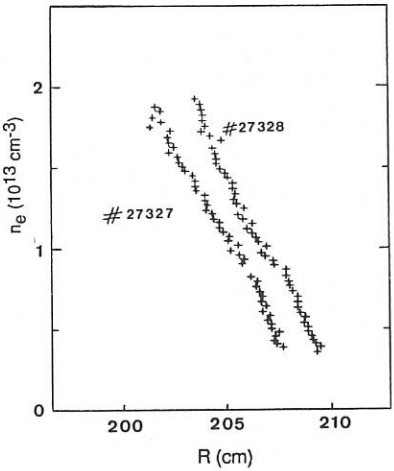


Fig. 4: Density profiles (K and Ka bands), for shots 27327 (Ro = 164.9 cm) and 27328 (Ro = 166.6 cm), at t = 1300 ms.

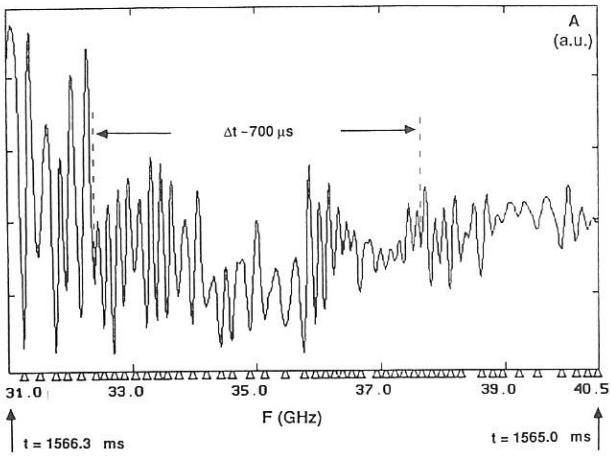


Fig.5: Output signal of Ka band reflectometer, from t=1565 ms to 1566.3 ms, for shot 29285, when a rotating magnetic island ($f_{rot}$~1.4 KHz) is present.

3 - Concluding remarks

The ASDEX reflectometric system had started swept-frequency operation by mid-December 1988. The analysis of the broad band data reveal that the difficulty of profile evaluation comes from the errors in the phase shift resulting from the plasma density fluctuations. Nonlinear stochastic numerical filters have been develloped (now being tested) that may provide a useful tool for routine evaluation of the data, for situations where the reflectometric signals are strongly disturbed by the plasma fluctuations.

Fixed frequency measurements (homodynic detection) were carried out and the study of plasma density fluctuations, based both on fixed and broadband experimental results, was initiated. A new heterodynic detection is beeing developed that will allow more sensitive measurement of plasma density fluctuations.

The reflectometric system was upgraded during the summer 1989 shutdown of ASDEX by installing three new reflectometers, aiming at fixed-frequency correlation reflectometric measurements; experiments have started recently.

References

/1/ P. Millot, F. Simonet, Proc. 14th Eur. Conf. on Controlled Fusion and Plasma Heating, Madrid, Vol. 11D, Part III, p. 1303 (1987)
/2/ M. Manso, F.Serra et al., Proc. 15th Eur. Conf. on Cont. Fusion and Plasma Heating, Dubrovnik, Vol. 12B, Part III, p. 1127 (1988)
/3/ T. Lehecka et al., Rev. Sci. Instrum. 59, 1620 (1988)
/4/ R. Prentice et al., 15th Eur. Conf. on Controlled Fusion and Plasma Heating, Dubrovnik, Vol. 12B, Part III, p. 1115 (1988)
/5/ M. Manso, F. Serra et al., Proc. 16th Eur. Conf. on Controlled Fusion and Plasma Heating, Venice, Vol. 13B, Part IV, p. 1517 (1989)
/6/ F. Nunes, Internal Report CAPS/IST (1989)
/7/ M. E. Manso, A. Silva et al. This conference.

Th 35

# Tangential Soft X-Ray/VUV Tomography on COMPASS-C

R.D. Durst, P.G. Carolan, B. Parham, the COMPASS Group

AEA Fusion/Euratom Association
Culham Laboratory, England

## The COMPASS Tangential Soft X-Ray Camera (TAN SOX)

This diagnostic exploits toroidal symmetry to tomographically reconstruct soft x-ray or VUV emissivity contours from a tangential view of the plasma [1,2,3]. A 0.4 mm pinhole images the plasma onto a P-11 (ZnS:Ag) scintillator screen [3]. Between the pinhole and this screen is a filter wheel with two soft x-ray edge filters (1 keV and 2 keV) and two VUV filters (10 eV and a 140 nm, 10 nm FWHM interference filter). The efficiency of the system peaks at 3-4 keV and decreases monotonically thereafter so that the effective energy range lies between a selected filter edge to about 15 keV.

The phosphor screen is fiber optically coupled to a Microchannel Plate (MCP) intensified photodiode camera. The camera has a resolution of 128x128 pixels and a maximum framing rate of 330 Hz. The MCP gain is externally controllable from $10^3 - 10^6$ and can be gated down to 5 nsec.

The camera control and data acquisition are managed by an IBM AT compatible PC which is linked to the camera via fiber optics. An add-in board containing an Intel 8253 programmable timer provides the camera with the frame timing (synchronized to the plasma $t_0$) and the MCP gate commands. This board also controls the MCP gain.

The video data is sent to the PC via a 50 MHz analog optical link and is digitized by a frame grabber board (Data Translation 2861). The frame grabber has sufficient on-board memory to acquire up to 256 frames per shot and is coupled to a fast (8 MFLOPS) array processor (DT7020) which is used to tomographically invert some of the raw data.

Because of the very large amounts of data that this diagnostic can generate (up to 4 MB per shot, though the typical data load is presently $< 1$ MB) on-line data compression is used before the data is stored in the main COMPASS data archive. Differential run length compression [4] is used which results in a compression factor of about 4 with no loss of information content. The raw data is compressed by the PC processor at 30 sec/MB and then sent to the data archive on the main COMPASS VAX via Ethernet. The PC-VAX link is controlled by Digital's PCSA software which allows the PC to directly access VMS files.

The techniques used for the tomographic reconstructions are Maximum Entropy [5] and Bayesian Regularized Least Squares Optimization [6]. The two techniques produce similar results though the latter is preferred for on-line processing because of its greater speed. Using this algorithm a 32x32 pixel inversion typically takes 10-15 seconds to converge. Thus, several images may be reconstructed between shots.

Further details on the system and the inversion techniques used will be presented in [7].

## Results from Ohmic Discharges

Figure 1 shows reconstructions of two typical COMPASS discharges. Parameters for these shots were, respectively, 100 kA, 1.0 T, $1.7\text{x}10^{19} m^{-3}$ and 100 kA, 1.2 T, $1.7\text{x}10^{19} m^{-3}$. The frame times were, respectively, 13 and 14 msec while the filters were

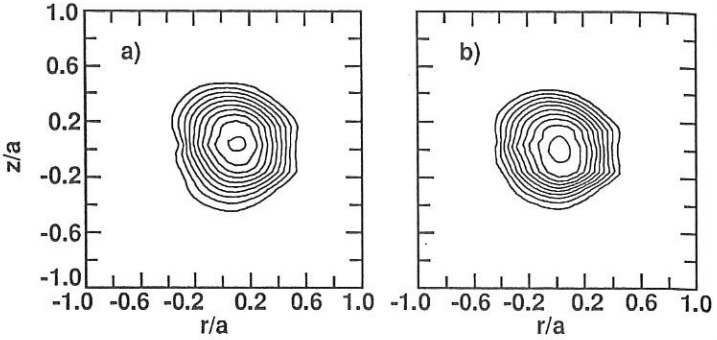


Figure 1: Reconstructions of typical ohmic discharges (shots 1640 and 1796).

1 keV and 2 keV. Both distributions are basically circular (within the uncertainties of the reconstruction).

## Results from Runaway Discharges

The TAN SOX diagnostic was designed to image the bulk, thermalized plasma but it is also useful for studying the behavior of suprathermal electrons. Suprathermals generate hard x-rays which are not imaged (since the pinhole plate is transparent to hard x-rays they cause a spatially uniform increase in the background level of the image) but they also generate soft x-rays which are imaged. Assuming that the suprathermal bremsstrahlung spectrum is given by the Kramer approximation [8] and that the thermal bremsstrahlung is consistent with the enhanced free-free form [9], then the ratio of the soft x-ray power at the photon energy E produced by the suprathermal electrons ($W_{se}$) to that produced by the thermal electrons ($W_e$) is

$$\frac{W_{se}}{W_e} = \frac{0.67}{\xi}\frac{n_{se}}{n_e}\left(\frac{E_{se}}{T_e}\right)^{1/2} e^{E/T_e} \qquad (1)$$

where $n_{se}$ and $E_{se}$ are the density and energy of the suprathermal electrons, $n_e$ and $T_e$ are the density and temperature of the thermal electrons and $\xi$ is the enhancement factor due to recombination. $E$ is in the range 1-15 keV for TAN SOX while a typical central $T_e$ for ohmic discharges on COMPASS is about 700 eV. The suprathermal electrons can emit significant amounts of soft x-ray radiation, e.g., for $T_e = 700$ eV, $E = 3.5$ keV, $E_{se} = 100$ keV, $n_{se}/n_e = .005$ and $\xi = 10$, the ratio of suprathermal to thermal radiation is of order unity. Accordingly, during runaway discharges TAN SOX will image both thermal and suprathermal electrons.

Figure 2 shows a COMPASS poloidal diverter discharge with interesting suprathermal activity. At about 40 msec the shaping circuit is activated to produce an inboard x-point. This initiates an immediate decrease in the density which continues until the x-point moves into the vacuum vessel (as indicated by the inboard $B_\theta$ coil) at 65 msec when the density begins to recover. This density drop is possibly due to a decrease in recycling at the edge but is currently not well understood. The density drop is expected to cause an increase in the runaway production rate [10] as $E/E_D$ rises from 0.045 at 40 msec to 0.076 at 55 msec consistent with the hard x-ray monitor signals in 2b. The upper curve represents emission at 0.05-1 MeV and the lower 0.5-2 MeV.

The two hard x-ray traces begin to rise together. However, at 55 msec the high energy

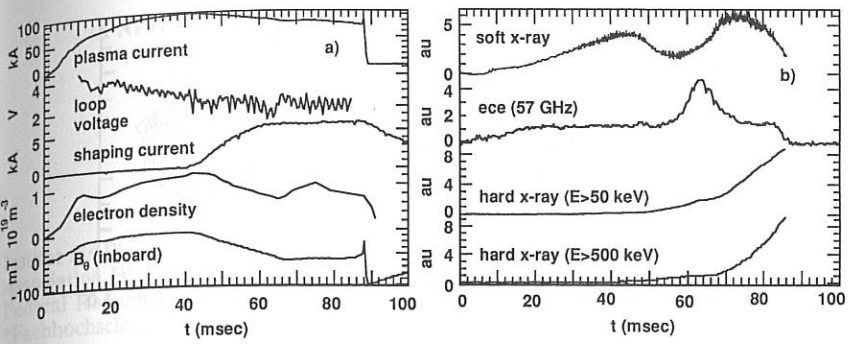


Figure 2: Discharge 1861, an ohmic shot with an inboard x-point.

x-ray signal from detector two enters a plateau while the medium energy signal continues to climb for about 7 msec. This is significant because it indicates that after 55 msec electrons continue to run away but that some process is interfering with their free fall acceleration to higher energy.

The electron cyclotron emission (ECE) trace (2nd harmonic x-mode, $B_T$=1.1 T) in 2b shows a dramatic increase which begins at 55 msec. This increase is seen on all the low field side (54-60.5 GHz) ECE channels. This rise would seem to be too large to represent a change in the over all bulk temperature and is probably due to suprathermal ECE emission. This type of broad band enhancement is characteristic of suprathermal activity and especially runaway instabilities (e.g., Parail-Pogutse) [10,11]. The ECE and loop voltage data were digitized at too slow a rate (2 kHz) distinguish the fast spikes normally associated with this instability. However, the presence of a velocity space instability could explain the behavior of the hard x-ray signals since it effectively damps the free fall acceleration of the runaways as parallel momentum is periodically converted into perpendicular momentum.

After 65 msec (when the density begins to rise again) the enhanced ECE emission dies away and the hard x-ray signals begin to rise together. It would thus seem that at this point the instability may be suppressed by the rise in density [11].

Figure 3 shows TAN SOX reconstructions before and during the suspected runaway instability. The images were taken with the 1 keV SXR filter with a frame time of 14 msec. Figure 3a shows an exposure from 28-42 msec. It is typical of ohmic, circular discharges. Figure 2b shows the exposure taken from 56-70 msec. Here the distribution is dramatically different. The distribution is broader (though the peak emissivity has decreased by 40% from figure 1a). A clear cresent shaped feature is apparent which is shifted outwards from the geometric plasma center by 4 cm. No known systematic error could account for this non-circular feature which is only seen in shots with runaway activity and then only while there is enhanced ECE emission. It is therefore thought to represent the actual plasma emissivity distribution despite the fact that it is very different from the expected central flux surface geometry (though the outer surfaces remain consistent with the reconstructions from magnetic data).

## Discussion

It is thought that in figure 3b suprathermal soft x-ray emission is important. During a runaway microinstability (Parail-Pogutse) the density of trapped suprathermal electrons is

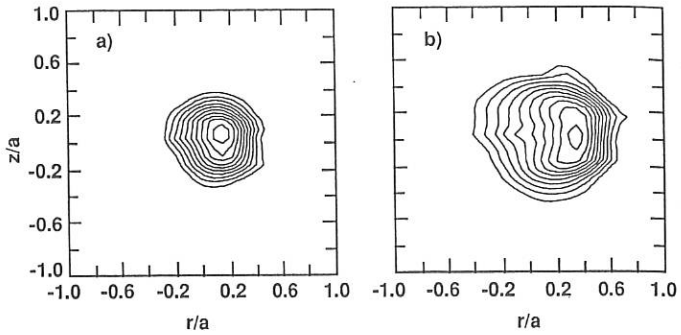


Figure 3: Reconstructions of SXR emissivity before and during the runaway activity at 55-70 msec. Each plot is normalized to unity at the peak and the contour interval is 0.1.

enhanced due to pitch angle scattering [9]. The distribution shown in 3b may represent the emission from banana trapped suprathermal electrons superimposed on the thermal soft x-ray emission. Such an effect was reported on TOSCA [12] and CLEO [13] where trapping was enhanced by ECRH.

This image is somewhat difficult to interpret since it contains information from both the thermal plasma and the runaways. However, it shows that with suitable filtering (e.g., using a filter edge at $4 - 5\ T_e$) a tangential scintillation camera can be used to study the spatial distribution of suprathermal electrons in a tokamak discharge as a function of time, an area in which little experimental data is available.

## Acknowledgements

The input of T. Edlington, J. Hugill, A.W. Morris and T.N. Todd is gratefully acknowledged. Thanks go also to K.B. Axon for hard x-ray data.

## References

[1] SCHIVELL, J., IEEE Trans. Plasma Sci. PS-8 (1980), 226.
[2] TAKAMURA, S. et al, Plasma Phys. and Cont. Fusion 28, 11 (1986), 1717.
[3] FONCK, R. et al , Rev. Sci. Instrum. 59, 8 (1988), 1831.
[4] PRATT, W.K., Digital Image Processing, John Wiley and Sons (1978).
[5] GULL, S.F., and NEWTON, T.J., Appl. Opt. 25 (1986), 156.
[6] ARTZY, E. et al, G.T., Comp. Graph. Image Process. 11 (1979), 242.
[7] DURST, R.D. et al, Proc. of the 8th Topical Conf. on High Temp. Plasma Diagnostics, Hyannis, to be published in Rev. Sci. Instrum. (1990).
[8] BUSSARD, P. and VAN DE HULST, M., Rev. Mod. Phys. 34 (1962), 507.
[9] GILL, R.D. el al, Nuclear Fusion 19, 8 (1979), 1003.
[10] KNOEPFEL, H. and SPONG, D.A., Nuclear Fusion 19, 6 (1979), 785.
[11] PARAIL, V.V. and POGUTSE, O.P., Rev. of Plasma Phys. 11, ed. Leontivich (1986).
[12] ROBINSON, D.C. et al, Heating in Tor. Plas. (Proc. 3rd Joint Varenna-Grenoble Int. Symp., Grenoble (1982), 647.
[13] ROBINSON, D.C., Turb. and Anom. Trans. in Magnetized Plasmas, Cargese, Corsica, (1986), 21.

# A NEW PROBE TO DETERMINE THE MACH NUMBER OF PLASMA FLOW IN A MAGNETIZED PLASMA

K. Höthker, W. Bieger* and H.-J. Belitz

Institut für Plasma Physik, Forschungszentrum Jülich GmbH,
Association EURATOM-KFA, Postfach 1913, D-5170 Jülich,
Federal Republic of Germany
*Fachhochschule Aachen, Abt. Jülich, Ginsterweg 1, D-5170 Jülich, Federal Republic of Germany

Electrical probes are widely used to determine the electron temperature, density and electrical fields in magnetized plasmas such as in the scape-off layer of tokamaks. In addition to that a rotatable electrical double probe can be used to determine the ion temperature in such a plasma as we have shown recently /1/. Besides these parameters the measurement of the plasma flow is important to understand the transport and the plasma wall interaction in the scape-off layer of machines like tokamaks. In this contribution we demonstrate that the rotating electrical double probe is also well suited to measure the plasma flow speed parallel to the magnetic field.

## EXPERIMENTAL SET-UP

The measurements have been performed in the scape-off layer of the tokamak TEXTOR. Parameters of the machine and details of the probe have been describes in reference /1/. The probe head consists of two cylindrical probe pins with a diameter of 5 mm, and a length of 5 mm. Their distance is 10 mm, Fig. 1. The axis of the probe is perpendicular to the magnetic field and rotates around this axis, cf. Fig. 2, during the tokamak discharge with a frequency of ca. 2 Hz.

## RESULTS

During the rotation of the probe the pins remain on the same flux surface. Simultaneously the probe measures a characteristic every 2.5 ms from which the electron temperature and density can be deduced in the usual way. The envelope of the probe

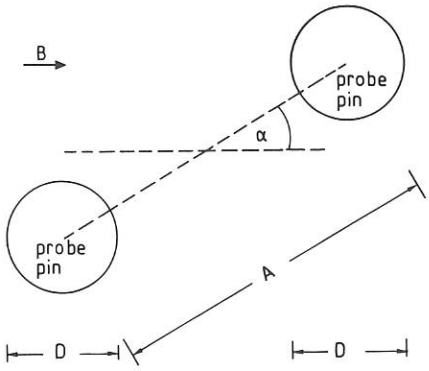


Fig. 1 Probe pin configuration in the magnetic field

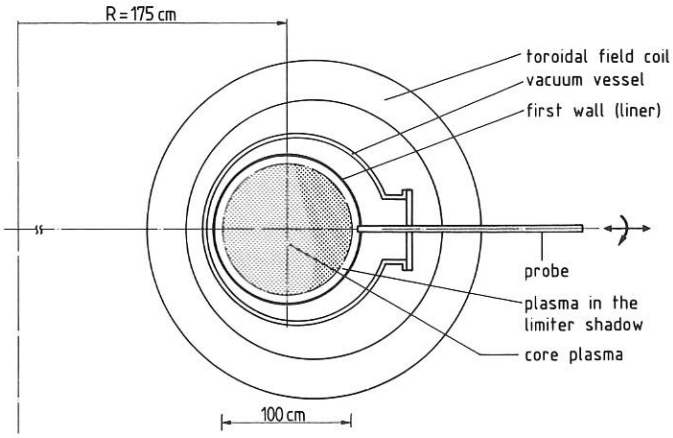


Fig. 2 Position of the rotating probe on the tokamak TEXTOR

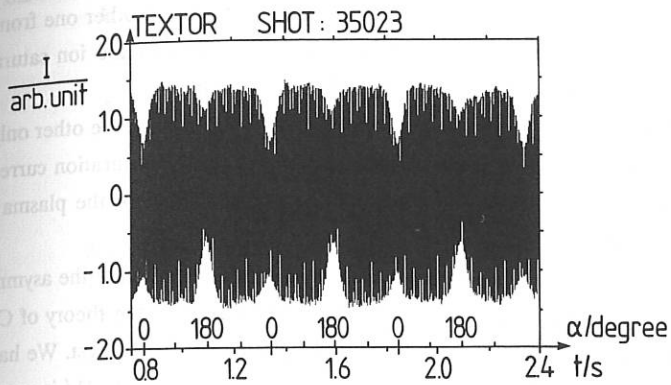


Fig. 3 Ion saturation current as a function of the rotation angle $\alpha$

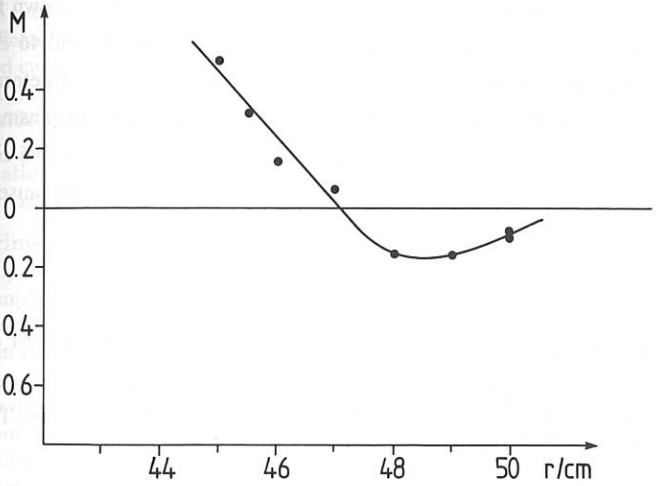


Fig. 4 Mach number of the plasma flow parallel to the magnetic field as a function of the radius in the scape-off layer

current gives the ion saturation currents to the two probe pins as a function of the angle of rotation $\alpha$, Fig. 3. At the angle $\alpha = 0$ one probe pin screens the other one from the flow from one side. For a non-streaming plasma the envelope of the ion saturation current is symmetric to $I = 0$ for all angles $\alpha$. For a streaming plasma at the angle $\alpha = 0$ one probe pin collects only the up-stream, the other only the down-stream flux, which are different. This asymmetry of the ion saturation current to the two probe pins at $\alpha = 0$ is a measure for the Mach number of the plasma flow parallel to the magnetic field.

Among the different models which have been proposed to relate the asymmetry of the upstream/downstream probe currents to the Mach number the theory of Chung and Hutchinson /2/ seems to describe the present plasma conditions best. We have to keep in mind, however, that the ion temperature in the present plasma /1/ is not small in the sense of ref. /2/. This entails that the values of the Mach numbers which are quoted here are lower limits. Larger probe pins would give more accurate results for the present plasma conditions, cf. /1/.

In Fig. 4 the Mach number of the plasma flow parallel to the magnetic field as determined from this procedure for the scrape-off layer of TEXTOR is shown for an Ohmic discharge. In the layer adjacent to the core plasma between 44 and 46 cm the direction of the plasma flow is the same as that of the plasma current, not determined by the distance to the nearest limiter. Further outward the direction of the plasma flow reverses. Here in the shadow of the toroidally symmetric ALT II limiter, $r \geq 46$ cm, the results are in qualitative agreement with numerical calculations of Gerhauser and Claaßen /3/.

/1/ K. Höthker, H.-J. Belitz, W. Bieger and H. Amemiya Rev. Sci. Instr. 61 (1990) 114
/2/ K. S. Chung and H. I. Hutchinson, Phys. Rev. A38 (1988) 4721
/3/ H. Gerhauser and H. A. Claaßen, Workshop on Plasma Edge Theory, Augustusburg (DDR), Sept. 1989

# REFLECTOMETRY OBSERVATIONS OF DENSITY FLUCTUATIONS IN WENDELSTEIN VII-AS STELLARATOR

J. Sanchez, H.J. Hartfuß, WVII-AS Team, NBI Team
Max-Planck-Institut für Plasmaphysik
EURATOM Ass., 8046 Garching, FRG

E. Anabitarte, A.P. Navarro
Association EURATOM/CIEMAT, 28040 Madrid, Spain

ECRH Group
Institut für Plasmaforschung der Universität Stuttgart
7000 Stuttgart, FRG

## Introduction

In the almost shearless stellarator WENDELSTEIN VII-AS strong correlation between the confinement properties and the rotational transform iota has been found [1,2]. Reduced confinement was observed for the low order rational values 1/2 and 1/3. In their vicinity best confinement is observed. In general optimum confinement is obtained in the low shear configuration if the "resonant" iota values can be excluded from the plasma column. The iota profile inside the plasma is affected by toroidal currents and beta effects. Although the global net current can be kept at zero level using a small OH induced current opposed to the gradient driven bootstrap current, the different currents flow at different radial positions affecting the iota profile. Tools for configuration control inside the plasma are besides OH current vertical fields and the currents driven by the NBI and most promising the ECH heating systems. In this context experimental information on the iota profile is highly needed. The localization of rational surfaces by reflectometry seems possible.

## Experiments

Radially resolved density fluctuation measurements have been carried out by means of a simple microwave reflectometry system. The method is based on the reflection of microwave radiation in the millimeter range at the plasma cutoff layer. The phase delay between the launched and the reflected waves gives information on the location and the movement of the reflecting layer. The use of electronically tunable oscillators allows to probe radially different reflecting points. As the simplest approach a homodyne receiver has been used. In this case the microwave beam is launched and received by using the same antenna. The wave reflected at the plasma and that reflected at some reference (the vacuum window) are mixed in a square law detector diode.The output voltage at the detector is:

$$v(t) = p_0 + p_1 + 2\sqrt{p_0 p_1}\cos[\delta(t)]$$

$p_0$ is the power coming from the reference, $p_1$ that one coming from reflection at the

plasma cutoff layer and $\delta(t)$ is the phase delay of interest. The variation in the output of the diode responds to changes both in the phase $\delta$ and in the amplitude $p_1$ of the signal coupled from the plasma. If no coherent MHD activity is present, $v(t)$ shows a broadband spectrum. When a density fluctuation with a well defined frequency $\Omega$ exists, the reflecting layer will have an oscillating movement too. So the phase shift can be written as:

$$\delta(t) = \delta_0 + \Delta\Phi \sin \Omega t$$

Thus the amplitude spectrum of the signal shows harmonics of the density fluctuation frequency $\Omega$. The number of harmonics with significant amplitude is the higher the bigger $\Delta\Phi$ is. An analysis of the ratio of amplitudes for the harmonics of the same parity leads to a determination of $\Delta\Phi$. For 1.25 T operation the relevant cutoff frequencies for the X-mode wave lie in the range 40 - 85 GHz. A system in the microwave V-band has been used covering the range 47 - 80 GHz. The accessible density range is: $7\text{x}10^{18}$ - $4\text{x}10^{19}$ $m^{-3}$. This gives access to the whole gradient region up to the separatrix. The measurements were performed in a special NBI heated discharge with pellet injection at 1.25 T. Currentless plasma was produced by applying a 10 ms ECH pulse of 200 kW power that gives place to a 1.5 MW NBI (45 keV) heating period with tangential injection. The two neutral beams used are balanced to minimize the driven Ohkawa currents. The rotational transform at the edge, $\iota$(a), is kept constant slightly above 0.5. A series of reproducible shots has been produced under these conditions. During this series the beam frequency of the reflectometer was changed shot by shot to reflect at different radial positions. Six different frequencies were chosen to cover the density range of interest. Electron density and temperature profiles have been measured by Thomson scattering. Fig. 1 gives the density profile and the location of the 6 reflection points. The accessible range is between about 0.17 m and 0.09 m. For each of the 6 different frequencies, reflectometry data where taken during 3 - 4 shots. The output voltage from the detector was digitized with a sampling rate of 1 MHz during the time interval 0.11 - 0.16 s ($5\text{x}10^4$ points are taken).

**Results And Discussion**

The amplitude spectrum of the reflectometer signal which is obtained by fast Fourier transform technique is given in fig.2 for channel 5 as an example. In the spectrum a monochromatic density perturbation with a frequency of 22 kHz is observed. The harmonic structure agrees with what is expected. The determination of the phase oscillation amplitude can be achieved by the analysis of amplitudes at different harmonics. Fig.3 shows the radial distribution of the phase oscillation amplitude $\Delta\Phi$ along the radius for 0.122 s, the time of maximum activity. A well defined mode is observed located at 0.105 m. In addition strong oscillation at the plasma edge outside the separatrix is present. An estimation of the amplitude of the density fluctuation can be done using the expression:

$$\delta n/n = (\Delta\Phi/2\pi)\lambda_0 \nabla n/n$$

resulting in about 3 per cent relative fluctuation level at 0.105 m. In the following we only concentrate on the instability at r = 0.105 m and its configurational implications: The vacuum iota profile of WENDELSTEIN VII-AS for this series of discharges shows a low positive shear which brings iota close to 0.5 at the plasma center. As mentioned

above a small OH current is induced to compensate the bootstrap current keeping the net current at zero level. Nevertheless the bootstrap current and the induced current flow at different radial positions resulting in local net currents. Small deviations from the balanced heating and beta effects (Pfirsch-Schlüter-currents) modify the iota profile additionally. Under these conditions the rational value $\iota = 0.5$ (q = 2) can be reached inside the plasma giving place to island formation and pressure driven instabilities. The most likely interpretation for the origin of the MHD activity observed is therefore the location of the resonant surface q = 2 at the radial position r = 0.105 m.

Additional information about the position of the rational q = 2 surface can be derived for the same series of discharges from the time evolution of the reflectometer signals. The OH transformer used to keep the total plasma current at zero level shows a small 300 Hz ripple. This ripple modulates the plasma current around its average zero level, resulting in a 300 Hz modulation of the rotational transform $\iota$. The oscillating current must flow in the external cold region where the resistivity is high enough to allow for short skin times. The amplitude of the iota oscillation around the controlled value is small ($4x10^{-3}$) but the high sensitivity of the plasma properties to iota changes in the vicinity of rational values generates 300 Hz modulation in different plasma parameters. In fig.4 the time evolution of the rms value of the reflectometer signal is shown for two extreme radial points. The rms signal of the detector output gives information about its ac components. The 300 Hz component is a modulation of the amplitude of the broadband turbulence. A clear synchronization between iota and reflectometer signals exists exhibiting a phase jump as function of radial position. For the channels probing at radial positions $r \geq 0.11$ m, iota minima correspond to increasing turbulence. The phase is opposed for $r \leq 0.11$ m : high turbulence appears at the iota peaks. The signals are in phase for $r \leq 0.10$ m (channel 6) and in opposed phase for $r \geq 0.11$ m (channels 1-4). The phase jump appears just at the position where stronger MHD activity is observed.

The observed effects can be used to obtain information on the iota profile even when no well defined MHD activity or coherent fluctuation is present. This can be an effective tool to be used in current control experiments. If a receiver measuring directely the phase delay is used (heterodyne system with sin/cos detector), no iota modulation is needed: the local turbulence at different radial positions can be compared directely. Such a system is now under construction. In any case the iota modulation helps to show clearly the configurational origin of the local enhanced turbulence.

**References**

[1] H. Renner, WVII-AS Team, NBI Team, ECRH Group, ICRH Group,
Plasma Phys. Contr. Fus. 31, 1579 (1989)

[2] H.Renner, WVII-AS Team, NBI Team, ICRH Group, ECRH Group,
"Configurational effects on the confinement in the stellarator WENDELSTEIN VII-AS".
7th International Workshop on Stellarators, April 10 - 14, Oak Ridge, TN, 1989

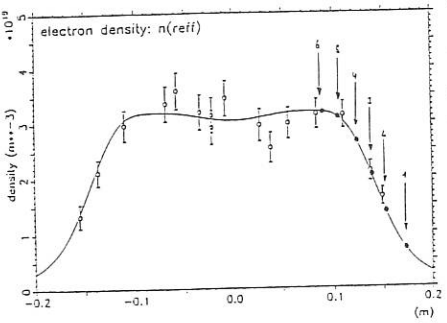


Fig.1: Density profile as measured by Thomson scattering. Reflection points for the different frequencies used are marked.

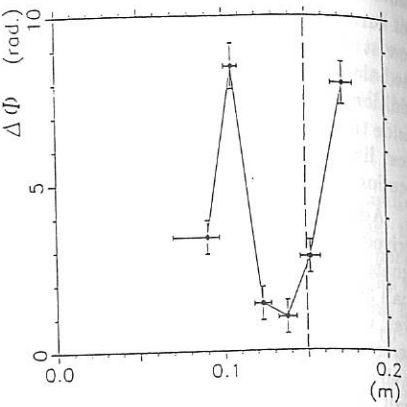


Fig.3: Radial distribution of the phase oscillation amplitude $\Delta\Phi$ for the coherent fluctuation at 22 kHz, taken at 0.122 s.

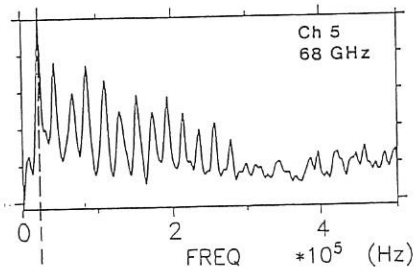


Fig.2: Normalized amplitude spectra of the reflectometer signal for the different incident frequencies showing a dominant perturbation at 22 kHz with harmonic structure at 0.122 s.

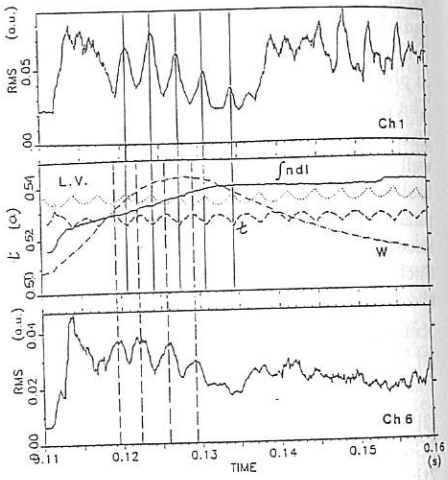


Fig.4: Modulation of the rms reflectometer signal and synchronization with the iota modulation. Upper frame: outermost, lower frame: innermost channel.

# ON DENSITY AND TEMPERATURE FLUCTUATIONS OBSERVED BY ECE DIAGNOSTICS IN WENDELSTEIN VII-AS STELLARATOR

H.J. Hartfuß, M. Tutter, WVII-AS Team, NBI Team
Max-Planck-Institut für Plasmaphysik
EURATOM Ass., 8046 Garching, FRG

ECRH Group
Institut für Plasmaforschung der Universität Stuttgart
7000 Stuttgart, FRG

## Introduction

A multichannel heterodyne radiometer system with two times 12 channels is used on WVII-AS to measure the electron cyclotron emission (ECE) both time and space resolved [1]. In this paper we report about sporadic observations of density and temperature fluctuations using this system. The observations are made under different operation conditions concerning field, rotational transform, and heating scenario. In the case of density fluctuations no direct measurement is possible using ECE diagnostics. The conclusions are drawn from observations near the cut off conditions and are of qualitative character. The fluctuation level necessary to explain the observed phenomena seems to be model dependent.

## Density Fluctuations

During neutral beam injection (NBI) heating the electron density usually reaches the cut off density resulting in a breakdown of the EC emission. Because cut off conditions are reached at first in the plasma center, the EC emission spectrum becomes hollow in that part which corresponds to the emission from the central region. Simulations of the EC spectrum based on temperature and density profiles as measured by Thomson scattering show sharp edges of the central hole in contrast to the experimental observations where flat slopes are found. The observations can be understood if density fluctuations are taken into account, which are treated as follows:

Plasma density and temperature are specified in 3-dimensional space. For given magnetic coil currents and plasma profile parameters density and temperature values are calculated at meridional torus planes in a quadratic pattern. The distance between the matrix points is 1.5 cm, the meridional planes are separated by 2.25 degrees in toroidal direction. Between the points linear interpolation is used. Density fluctuations are included by multiplying the density value n at each matrix point by $1+F\delta n/n$, where F is a random function varying between -1 and +1. Fig.1 gives a density distribution generated in this way which is a momentary picture of the fluctuating plasma. After running the ray tracing code about 30 times the results are averaged.

Fig.2 gives an example of the result obtained during 1.25 T operation. As can be seen the simulated "profile" clearly shows the flat slope of the central hole as indicated by the 7 channel ECE data. At 1.25 T only 7 channels are available. They all correspond

to the high field side of the profile and monitor the 2nd harmonic X mode ECE. The absolutely calibrated spectral data have been converted to radiation temperatures as function of plasma radius in the usual way. Thomson scattering data are included for comparison.
The concept of fluctuating density can also serve to explain the power deposition profiles during electron cyclotron heating (ECH). They are found to be broader at densities near cut off than obtained by ray tracing calculations for given non fluctuating stationary profile. Fig.3 gives an example.
A further case which confirms the concept is its application to the spatial power distribution of ECH power after passing the plasma. With an antenna array which is mounted opposite to the launching antenna rather high power levels have been observed at large angles which cannot be understood assuming an unperturbed static plasma. Simulations on the basis of scattering in the presence of density fluctuations lead to good agreement with the observations.
It should be mentioned that the fluctuation level $\delta n/n$ necessary to explain the data must be of the order of 10 per cent. This high level is not confirmed by other diagnostics. Investigations on the influence of the pattern used in the simulation code are being carried out.

**Temperature Fluctuations**
Two examples may demonstrate in which way temperature fluctuations reflect the confinement properties of WENDELSTEIN VII-AS. In general good confinement is obtained if the edge value $\iota$(a) of the rotational transform is slightly above or below the low order rationals 1/2 and 1/3. Confinement is strongly reduced in the shearless configuration when $\iota$(a) reaches these values [2].
Strong temperature fluctuations were observed during EC heated transient plasma discharges conducted at 2.5 T which cross $\iota$(a)=1/3 due to the monotonic development of a bootstrap current.
The low field side of the electron temperature profile was monitored with the ECE radiometer system at 12 different radii. When the resonant iota value is reached, the confinement time collapses to about 15 per cent, accompanied by a shrinking of the hot core of the plasma column. It takes about 100 ms until the regime of poor confinement is crossed. This interval was analyzed by applying autocorrelation techniques to determine the relative level $\delta T_e/T_e$ of the temperature fluctuations. Fig.4 gives the result as a function of the plasma radius. About 3 per cent are found in the central confinement region of the plasma with a strong increase towards the plasma edge.
After the $\iota$ range of poor confinement is crossed, the high fluctuation level almost completely disappears: Fig.4 for comparison gives $\delta T_e/T_e$ as determined from the same discharge about 150 ms later. The central value is reduced by about a factor of 3, while the edge value drops to at least 1/15.
The whole phenomenon can be suppressed by controlling the plasma current to zero level with the aid of a small counterdirected OH current. The results obtained in a different shot conducted under these conditions are included in the figure too. Within the estimated experimental errors they are identical to results obtained in the unperturbed phase of the discharge discussed before.
Two fundamental difficulties in the measurement of temperature fluctuations with ECE

diagnostics should be mentioned. A fundamental fluctuation level always exists observing an incoherent, thermal light source. The level observed depends on the detection method applied i.e. coherent or incoherent detection, and the input and video bandwidth of the radiometer involved [3]. Below this fundamental lower limit of temperature fluctuations no source fluctuation can be detected. The fluctuation level of 1 per cent which is reached in the plasma center corresponds to this limit for the parameters of the ECE radiometer in use. Therefore the true temperature fluctuation in the plasma center cannot be measured in this case. Crossed sightline correlation techniques may overcome the fundamental difficulties.
The second difficulty deals with the optical depth of the plasma at its edge. It depends both on the electron temperature and density. Because the radiation temperature depends on the optical depth, the measured ECE signal is not only determined by the electron temperature but becomes dependent on the electron density at the plasma edge too. In this way density fluctuations can be converted to apparent temperature fluctuations. The total fluctuations observed are a combination of density and temperature fluctuations and are always higher than the temperature fluctuations alone.

Cross correlation between channels monitoring at different radial positions shows that the strong fluctuations as found during the $\iota$=1/3 crossing are coherent over a large part of the profile whereas in the current controlled case spatial coherence is clearly below 1 cm.
The dominating part of the fluctuation spectrum is restricted to below about 3 kHz, reflecting the timescale of rearrangement of the bootstrap current in the plasma column.

In a second example the relative fluctuation level has been measured near the plasma center (1 ECE channel evaluated only) during a series of shots in which $\iota$(a) has been scanned around 1/2. As mentioned above confinement maxima are found in close vicinity to the sharp confinement minimum at 1/2. In this series of shots the line density has been kept constant. No stationary discharge could be established at the resonant iota value 1/2.
Fig.5 shows $\delta T_e/T_e$ as function of $\iota$(a). A broad minimum in the fluctuation level is observed which corresponds to the maxima of confinement near $\iota$=1/2 and its flat decrease with increasing distance to this value. Because no stationary discharge was possible at $\iota$=1/2 the expected sharp peak in the fluctuation level cannot be observed. Again the central fluctuation level at optimum confinement is about 1 per cent identical to the radiometric fundamental level. At poor confinement in the wings of the curve about 3 per cent are found as before in the transient discharge.

**References**

[1] H.J. Hartfuß et al.,"ECE Diagnostic for the new Stellarator Wendelstein VII-AS", Proc. of EC-6, Joint Workshop on ECE and ECRH, September 16-17, Oxford, 1987

[2] H. Renner, WVII-AS Team, NBI Team, ICRH Group, ECRH Group, "Configurational effects on the confinement in the stellarator WENDELSTEIN VII-AS". 7th International Workshop on Stellarators, April 10 - 14, Oak Ridge, TN, 1989

[3] H.J. Hartfuß, "Coherent Versus Incoherent Detection Schemes", Proc. Joint IAEA Technical Committee Meeting On ECE and EC-7 Meeting, May 8-11, Hefei PR China, 1989

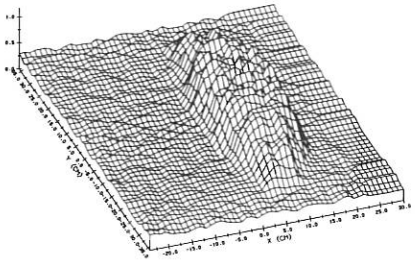

Fig.1 Snapshot of the fluctuating plasma as used for the ray tracing calculation.

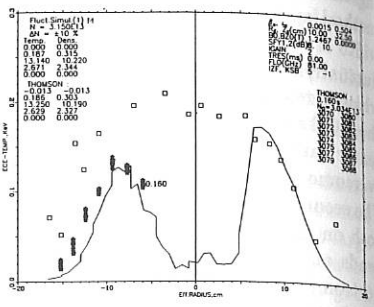

Fig.2 Breakdown of the experimental ECE "profile" (dots) at plasma density near cut off. The line is the result of a simulation, squares give the temperature profile as measured by Thomson scattering.

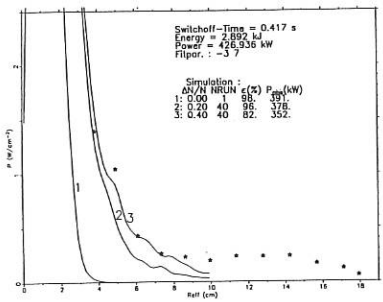

Fig.3 Power deposition profiles: Dots are derived from the slope of ECE temperature signals at ECH switch off. Lines are from simulations using $\delta n/n = 0$, 0.2 and 0.4 resp.

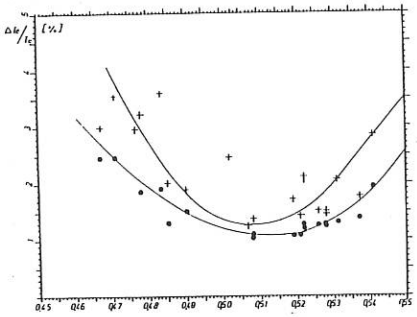

Fig. 5 Temperature fluctuations of central temperature as function of the edge value of the rotational transform.

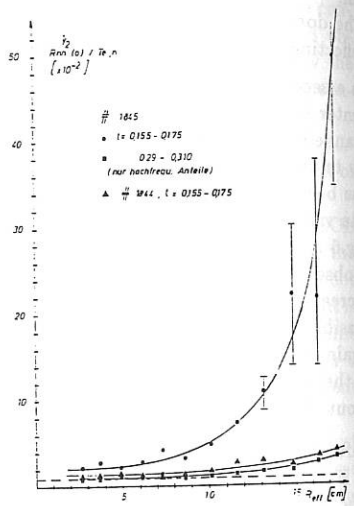

Fig. 4 Temperature fluctuations as function of plasma radius as derived from ECE data during the crossing of $\iota$=1/3 and for comparison without perturbation from resonant surface.

# FAST SCANNING FIBER-MULTIPLEXER USED FOR PLASMA-EDGE VISIBLE SPECTROSCOPY ON TORE SUPRA

W.HESS,M.DRUETTA*,T.FALL,D.GUILHEM,C.KLEPPER**,M.MATTIOLI

Association EUR-CEA
DRFC CEN/Cadarache, 13108 St PAUL LEZ DURANCE, FRANCE
* Université de St Etienne, FRANCE
** ORNL, Oak-Ridge, Tenn., USA

## INTRODUCTION

In this paper we describe a versatile tool which is used to scan a number of optical fibers in front of the entrance slit of a multichannel spectrometer. It is now a common technique, especially on Tokamaks with high radiation level, to use fibers with good transmission (T=70% for 60m length) in the visible spectral range (250-800nm) which transport the radiation flux to the detection system behind the biological shield. In long duration discharges as in Tore Supra (10 sec) radial scans with a single diode array (OMA) are an alternative to a 2-dimensional CCD where all the fibers can be viewed simultaneously.

Instead of using a moving mirror, sweeping the cross- section of the plasma, we preferred a fixed multifiber configuration: each of the 9 fibers corresponds to a precisely mapped viewing line. Five groups of 9 fibers are installed on Tore Supra for Bremsstrahlung,Hα and other measurements, but we will concentrate here on the 9-fiber system located in the equatorial plane since it intersects at 9 points the lower half of the plasma diameter; the first fiber being about central (r~0) and the last one in the scrape off layer (r=80 cm) fig.:1. Light is collected from a cone expanding from 25 mm at the entrance pupil (EP) of the specially designed triplet lens (f/2,f=50 mm,wide angle 30°) to a spot of 60 mm at the inner carbon bumper limiter. A rotating dichroic sheath polarizer mounted at the EP allows analysis of the σ and π polarized Zeeman pattern emitted by light impurities [1]. In Tore Supra the toroidal field increases from the outer edge to the inner wall from 3 to 6 Tesla, which results in a complete separation of the Zeeman pattern of some selected lines (e.g. Hα, HeI, CII). This simplifies the line spectrum, especially in the π (parallel to Bt) position. As is shown in detail in fig.:2, reliable ion-temperatures can thus be calculated once the instrumental function I.F. of the Czerny-Turner (f/5, f=640mm, 2400gr/mm) spectrometer is deconvoluted from the measured profil (I.F.=0.5 Å ;entrance slit=50 μm). All components of the optics are made of UV-grade fused Silica. The PCS-1000 (Quartz and Silice) fiber (core diameter=1mm) shows good transmission at 280nm for a fiber length of 60m. An interesting feature of our fiber-multiplexer is that fiber bundles can be

interchanged very quickly with fiber connectors, allowing a selection of the viewing region. As an example we show the Hydrogen and Carbon recycling at the front face of the pump limiter (fig.:3).

DESCRIPTION OF THE FIBER MULTIPLEXER

It is essentially composed of a quick scanning stepping motor at the front face of the spectrometer (fig.:4). A typical step-time of 4msec can be achieved with an adjustable brake. The shaft bears a light-weigthed wheel with a convenient diameter, so that one step corresponds at the circumference of the wheel to an arc of 1.5mm which is the external diameter of the fibers. 10 of them are closely spaced at the rim of the wheel and 2 quartz lenses (f/2;f=50,100mm) form the image of one fiber at the center of the entrance slit with 2.5 x magnification ($\Phi$(image)=2.5 mm). This is the heigth of the 1024 pixel CCD-array. An important feature is that the intersection between the fiber-image and the slit (width=50$\mu$m) is insensitive to the oscillations of the braked wheel at the end of each step. In fact we are limited by the intensity of the spectral lines, using CCD-scan times of at least 32 msec. At the end of this scan, the stepping motor is triggered and the diode-array is zeroed during one dummy scan (t=32 msec). The whole cycle takes in this case 9x32x2=576 msec, which produces about 10 complete radial scans during a typical current plateau of Tore Supra. Wavelength calibration and instrumental function measurement are done with an auxiliary fiber, which superposes the radiation of a spectral lamp to the plasma emission.

EXPERIMENTAL RESULTS

When the plasma is limited by the inner Carbon wall, strong recycling is observed, which depends poloidally on the distance between the Carbon wall and the last closed flux surface (LCFS). This emission is so strong that the contribution from the remaining viewing chord can be neglected. This is true for fibers 1 to 6 , since the Zeemann splitting (strong-field approximation) shows the 1/R dependence of the Tokamak field. Due to the Zeeman splitting, the emission can be localized with respect to the major radius R with an incertainty of ±5 cm (fig.:1). As in the case of the outside limited plasmas, the remaining fibers show a splitting which is the sum of the emission of the two intersections of the viewing chord with the radiating layer. In fig.:2 we show three OII lines close to H$\gamma$ in the $\pi$ and $\sigma$ polarization. A Mercury line yields the I.F. for the deconvolution of the central $\pi$ components. Within the error bars no poloidal dependence of the edge in temperature appears. We find: Ti(H)=4.6 ±0.8 eV, Ti(O)=40 ±3 eV, Ti(C)= 19 ± 2 eV. These ion temperatures are characteristic for the cold influxes at the very edge.

Figure 3, shows the recycling of H,D and C at the front face of

the pump-limiter. Deuterium is continuously injected. Hydrogen comes mostly from the dissociation of the $H_2$ contained in the graphite of all plasma facing surfaces. The increase of the Hα signal may be due to outgasing of the pump-limiter heating up during the plasma shot.

Figure 5, shows the strong increase of Hydrogen and Carbon recycling during $D_2$ pellet fuelling. The Carbon emission can be localized due to the Zeeman splitting (weak field approximation). We can see that it corresponds to a major radius R=1.73m (Btot=5.3T) at the inner Carbon wall. Small σ-components are visible due to a misalignment of the polarizer with respect to the total magnetic field.

[1] P.G. CAROLAN and al. Plas. Phys. Contr. Fus. 27, 1101 (1985)

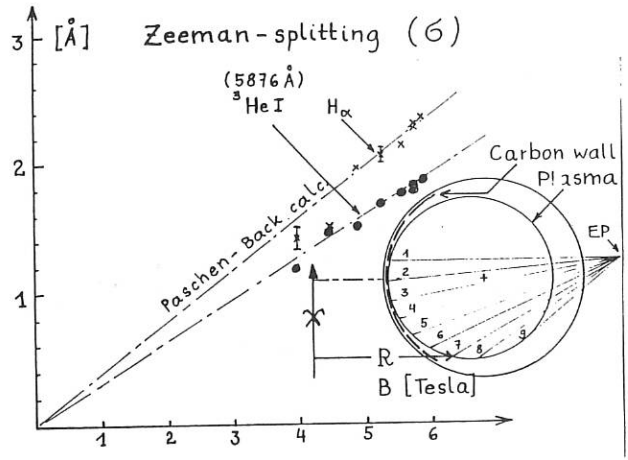


Figure 1

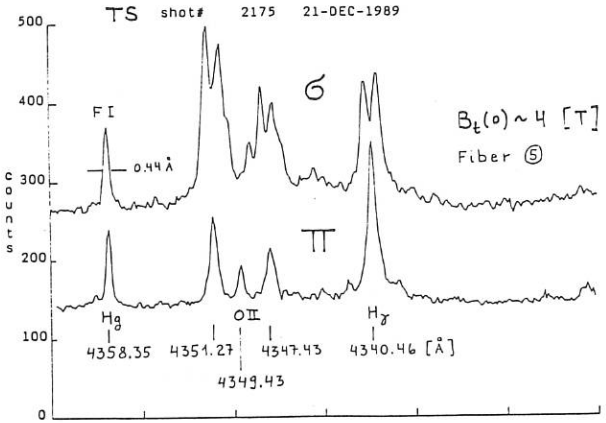


Figure 2

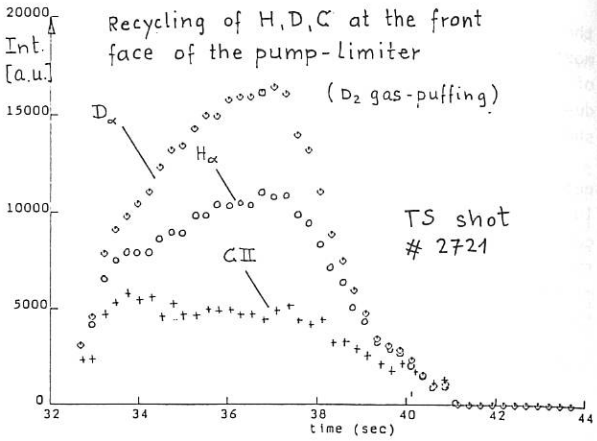


Figure 3

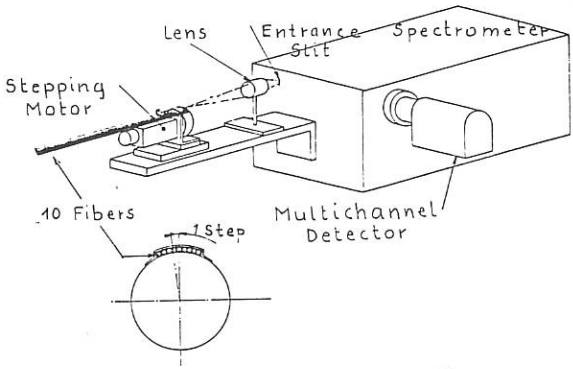


Figure 4

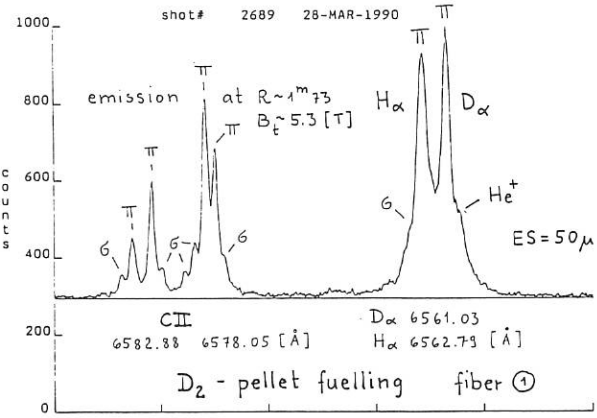


Figure 5

# FUSION PROFILE MEASUREMENT ON TORE-SUPRA

G. MARTIN , P. GILLES , P. JOYER

Association EURATOM-CEA sur la fusion / C.E.N. CADARACHE
13108 SAINT-PAUL-LEZ-DURANCE CEDEX / FRANCE

A new diagnostic has been recently set on TORE-SUPRA , to observe charged fusion particles . Both 3 MeV ( $D + D \rightarrow P + T$ ) and 14.7 MeV protons ( $D + He^3 \rightarrow P + He^4$ ) can be measured .

## DETECTOR ASSEMBLY

The detector is located in a vertical port . It has been installed in a tube separated from the plasma vaccuum by a 6 µm stainless steel foil . It allows us to modify the detector configuration more easily , but limit the measurement to the protons only . Active cooling is necessary ; the 190°C of the vessel are too hot for the detector .

The detector is a multiple silicon strip chips : it is equivalent to 16 small detectors , placed close to one other . The entrance window , which support the 6 µm foil , is used as a collimator . Each strip is looking at particles with different pitch-angle ( angle between the particle velocity and the magnetic field ) .

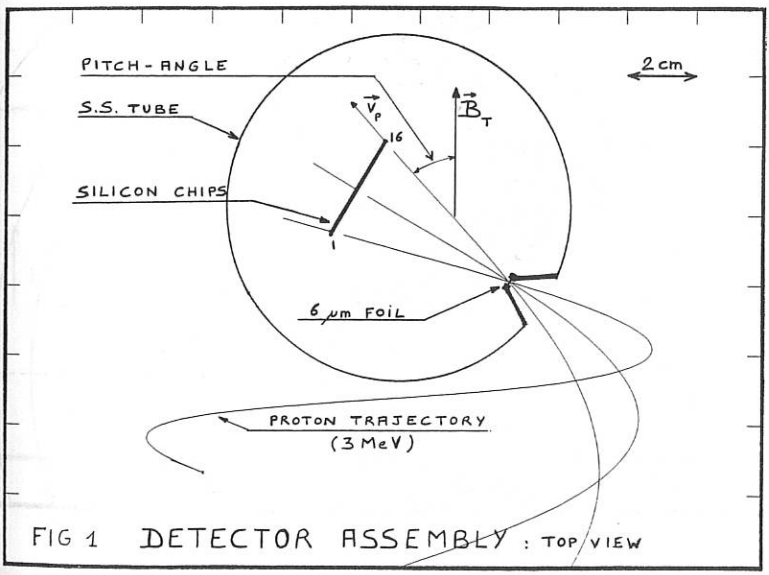


FIG 1 DETECTOR ASSEMBLY : TOP VIEW

## PROTONS TRAJECTORIES

For given toroidal and poloidal fields , the knowledge of the pitch-angle permits to calculate the particles trajectories : each detector strip is then looking at the plasma on a different chord . Figure 2 shows three examples ( projection in a poloidal plane ) . They correspond to the three values of pitch-angle from figure 1 . The proton flux on the detector is highest for the most central trajectory .

These complex lines of sight , can be used exactly in the same way as more classical straight chords ( e.g. optical diagnostics ) : it is possible to calculate the proton emission profile from the integral fluxes received on the detectors . The spatial resolution is then related to the angular resolution of the detector/collimator assembly , and to the knowledge of the magnetic fields .

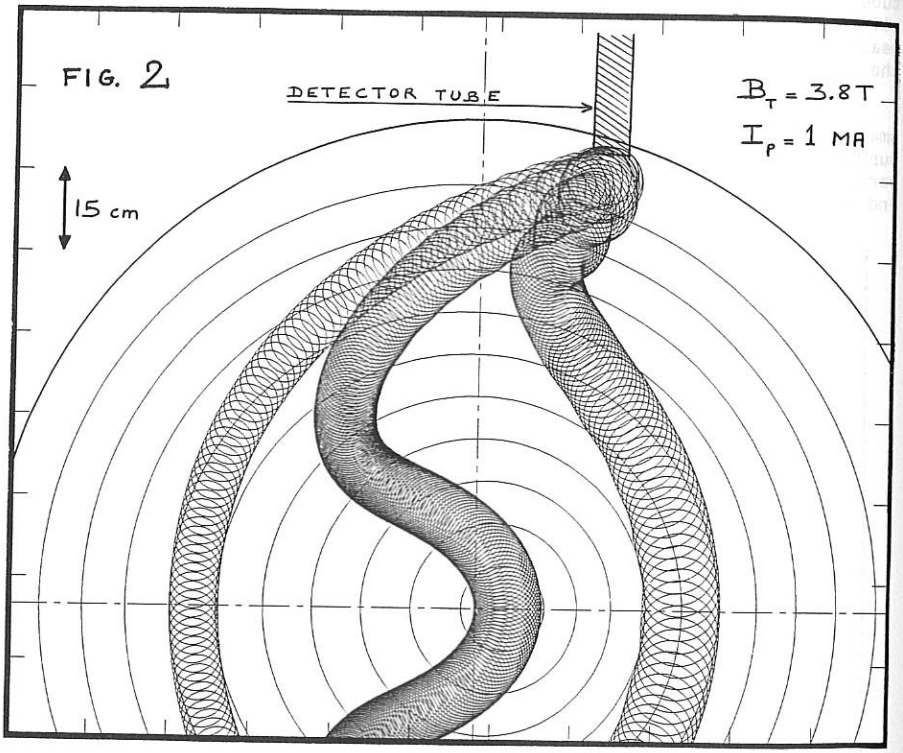

## DETECTOR EFFICIENCY AND RESOLUTION

Due to the width of both the detector and the window , and Rutherford scattering in the foil , the pitch-angle resolution of the system is about 3 degrees , corresponding to a spatial resolution of 5 cm ; this value does not take account of the uncertainties on the magnetic fields , mainly on the current profile . Pitch-angle efficiencies of eight detector strips are given on figure 3a .

Figure 3b shows a calculated proton flux versus pitch-angle for parabolic temperature and deuterium density profile . The right-hand side of the curve ( high angles ) corresponds to banana trajectories , and the left-hand side ( small angles ) to passing trajectories . The modulation is due to the ripple : each peak can be correlated to a toroidal field coil .

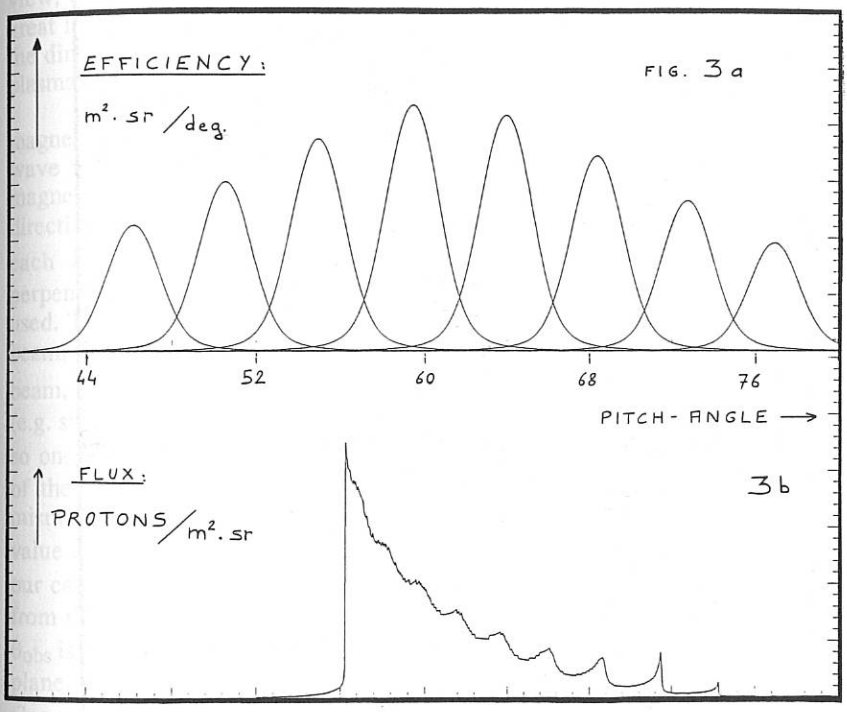

## FIRST EXPERIMENTAL RESULTS

A measured proton signal is plotted on figure 4a , with plasma current ( 4b ) and neutron flux ( 4c ). During that shot , four deuterium pellets have been injected in the plasma . The last peak on the neutron signal is due to runaway electrons ( photo- neutrons ) produced during the disruption. So , it does not appear on the proton signal .

Direct measurement of the Doppler broadening of the proton line ( Width $\Delta E = 91.6 \sqrt{T}$ ) has been performed , but with a bad temporal resolution , due to the weakness of the fluxes ( countig time of ≈ 200 ms ) . However , it shows the cooling of the plasma due to the pellets ( see figure 4d ) : measurements made just after the injection are lower than later ones .

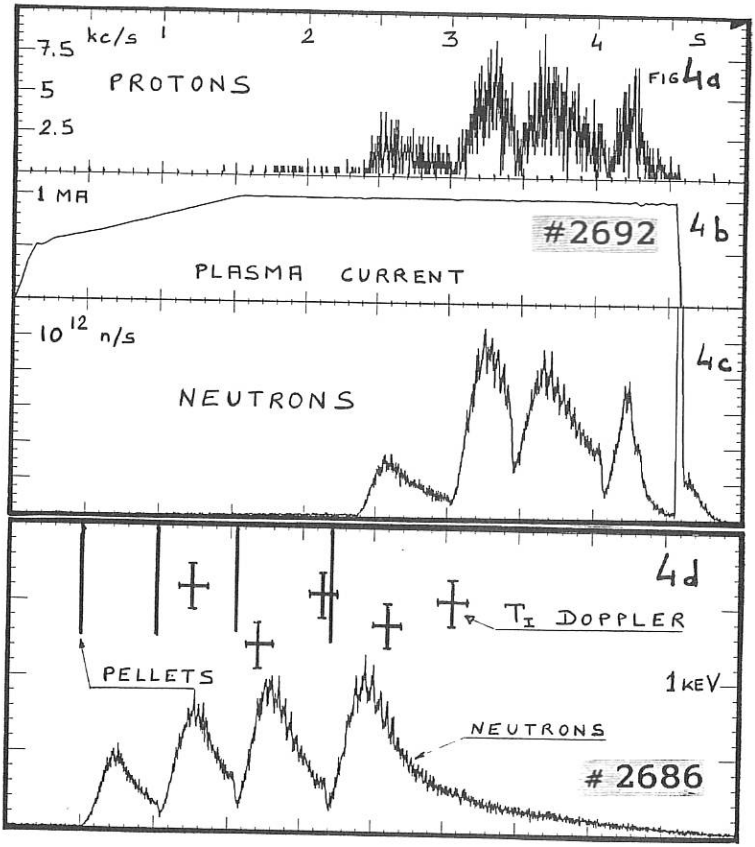

# FIRST DENSITY FLUCTUATIONS OBSERVATIONS BY $CO_2$ SCATTERING IN TORE SUPRA

C.LAVIRON, X.GARBET, J.OLIVAIN
Association EURATOM-CEA, CEN Cadarache (France)
and
A.TRUC, A.QUEMENEUR, P.HENNEQUIN, D.GRESILLON, F. GERVAIS
PMI- Ecole Polytechnique- Palaiseau (France)

## Introduction

A new $CO_2$ scattering experiment has been conceived and recently installed on the Tore Supra tokamak.

Using a 10.6 μm electromagnetic wave to observe electronic density fluctuations has several advantages compared to microwave radiations: easy propagation in open air, negligible refraction effects (letting the possibility to probe high density plasmas), large sensitivity and, from the technical point of view, easy plasma interface. Unfortunately the $CO_2$ usual apparatus suffers a great limitation: the scattering angles are so weak that no spatial resolution in the direction of the probing beam remains. All the fluctuations issued from a plasma chord are observed.

On Tore Supra, we take advantage of the existence of a variable magnetic shear along the plasma radius to get a finite spatial resolution.The k wave vector of the natural turbulence is mainly perpendicular to the local magnetic field. For a probing beam following a vertical diameter, the local direction of the magnetic field ($\overline{B} = \overline{B}_{tor} + \overline{B}_{pol}$) varies along the beam. For each $\delta y$ element of a diameter, the natural turbulence is located perpendicularly to the local magnetic direction. An heterodyne technique is used. The local beam is fixed. The main beam can rotate $2\pi$ around the local beam, so that the optical $\overline{k}_\Delta$ vector, which is always perpendicular to the local beam, can explore all directions ($\theta_{obs}$) perpendicular to the vertical direction (e.g. successively exploring a poloidal direction, then the toroidal direction and so on...). Presently, during one experiment, $\theta_{obs}$ is fixed and so each element of the vertical diameter contributes with a weighting factor related to the mismatch between the azimuthal location of the turbulence and the azimuthal value of $\theta_{obs}$. For one particular position of the main rotator ($\theta_{obs} \sim 90°$ in our case), the $\overline{k}_\Delta$ is located in the meridian plane and the turbulence arising from the centre of the discharge, where the shear vanishes, is detected. When $\theta_{obs}$ is increased, (~ 95 to 100°), the analyzing vector $\overline{k}_\Delta$ has left the meridian plane. Fluctuations stemming from a positive ordinate ($y>0$) are detected. Conversely, $\theta_{obs}$ ~ 80 to 85° coincides with negative y ordinates. By this $\theta_{obs}$ analysis, it is possible to have a finite spatial y resolution.

A further advantage of the existence of a spatial resolution results in the use of an heterodyne receiving technique. Two acousto-optic crystals are used in serial to modulate the main beams in such a way that the complex spectrum of the fluctuations is accessible. So it would be possible to determine the direction of rotation of the turbulence in the various domains of the plasma (centre, gradient zone, periphery plasma and scrape off layer).

## II.Experiment

The apparatus is able to silmultaneously measure the fluctuations associated to two wave vectors $\bar{k}_1$ and $\bar{k}_2$ .The beam issued of a $CO_2$ laser is splitted into three beams using two acousto-optic deflectors. Two of these beams have the same power and constitute the main beams, the third one, of weak power, is used as a common local oscillator for an heterodyne detection (one of the main beams and the local oscillator are respectively modulated at frequencies $f_1$=42 MHz and $f_0$=80 MHz).The two scattering signals superimposed on the local oscillator are collected on a photovoltaic detector. The radius of the beams in the plasma is about 3cm; it corresponds to a k resolution $\Delta k$=0.7 $cm^{-1}$. The modulus of the accessible wave numbers are between 3 and 40 $cm^{-1}$.

## III Spatial resolution

For a fixed $\bar{k}_\Delta$ observation vector, wich makes an angle $\theta_{obs}$ with the toroidal direction, each element $\delta y$ of the vertical plasma diameter contributes to the scattered signal, with a weighting factor related to the mismatch between $\theta_{obs}$ and the azimuthal direction of the fluctuation k vector.

The $\delta y$ element of the scattering diameter, located at the y ordinate , is assumed to have a gaussian azimuthal turbulence distribution around the angle $\xi(y) = Arctg\ (\bar{B}_{pol}(y) / \bar{B}_{tor})$. The probing beams have a gaussian angular resolution around the value $\theta_{obs}$ of the form $\exp-((\theta-\theta_{obs})/\Delta k/k_\Delta))^2$ where $\theta$ is the azimuthal angle.The density fluctuations are inhomogeneous along the probing beams . A radial turbulence profile can be assumed, as given in ref(1), for instance: $\delta n/n = ( 3\ 10^{-3} +0.1\ (y/a)^3)$, where a is the radius of the plasma.

The power scattered by an unit element of the scattering volume is proportional to the quantity

$$S(\theta_{obs},y,k_\Delta) = \delta n^2(y) \int \exp-((\theta-\xi(y))/\Delta\theta))^2\ \exp-((\theta-\theta_{obs})/\Delta k/k_\Delta))^2\ d\theta,$$

where $\Delta\theta$ is the turbulence spectrum width. Fig(1) and Fig(2) give some examples of this calculation and of the expected radial resolution for different values of $k_\Delta$ and $\theta_{obs}$. Fig(1) shows that for the chosen values of $k_\Delta$ and $\theta_{obs}$

he scattered signal mainly originates from the central region whereas in Fig.2 t corresponds to the upper part of the plasma. Typically, for $k_\Delta \geq 9$ cm$^{-1}$ in arying $\theta_{obs}$ we can separate the contribution coming from the upper,the entre and the lower part of the vertical diameter. For $k_\Delta \geq 15$ cm$^{-1}$ the ertical spatial resolution is better than 15 cm (FWHM) e.g.~ a/5. The cattered detected signal $S(\theta_{obs},k_\Delta)$ has to be proportional to the integral of uch a curve (y varying between $\pm y_{max} = \pm 1.2$ r/a to include the turbulence of he scrape off layer).

V Experimental results

Preliminary experimental observations herewith reported confirm the otentiality of the diagnostic as a tool to detect the fluctuations issued from a ocalized radial domain and to estimate the sense of rotation of the turbulence n the Laboratory frame.

For instance, Fig.3 corresponds to a $k_\Delta$=12 cm$^{-1}$ wave number analysis or $\theta_{obs} = 95°$. A significant negative shift in the turbulence spectrum is oticed ($\Delta F \sim 120$ kHz corresponding to a rotation velocity of 0.6 $10^5$ cm/s). Conversely in Fig.4, for $k_\Delta$= 6 cm$^{-1}$ and $\theta_{obs}$=85° a positive shift is observed $\Delta F \sim 50$ kHz corresponding to a velocity of 0.5 $10^5$ cm/s). These emissions pproximately originate from the gradient zone of the plasma.

Fig.5 is an illustration of a numerical simulation of the expected zimuthal variation of the peak amplitude of the turbulence and its associated requency integrated value as a function of the azimuthal coordinate for $k_\Delta = 6$ cm$^{-1}$ in standard working conditions of Tore Supra. Fig.6 is the result of a set of experiments with $\theta_{obs}$ variations. Crosses refer to the positive frequencies of the maximum amplitude (F ~ 100 kHz) of the fluctuations and dots to the egative values. In this case, we successively detect the upper, the central and he lower part of a vertical diameter. The turbulence spectrum is broad but we evertheless notice a shift in the frequency spectrum corresponding to a otation of the plasma.

V Conclusion

It has been experimentally shown that the scattering apparatus on TS llows a spatial resolution of the turbulence and a determination of the direction of propagation of this turbulence. A more accurate determination of he localization domain sizes is in progress and the possibility of simultaneous measurements for two different wave numbers will be explored.

Reference:(1) J. OLIVAIN in Proceedings of the Cadarache Worshop on Electrostatic Turbulence,EUR-CEA-FC 1381 Report (1989).

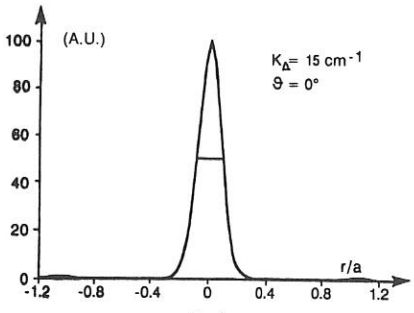

Fig.1

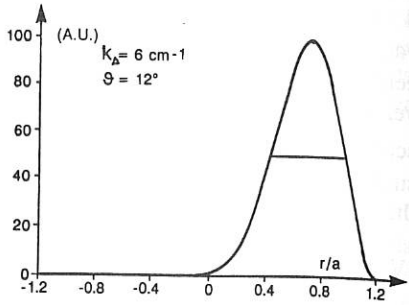

Fig.2

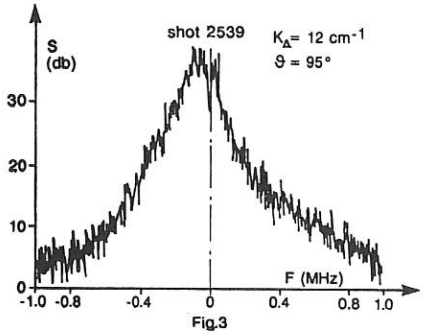

Fig.3

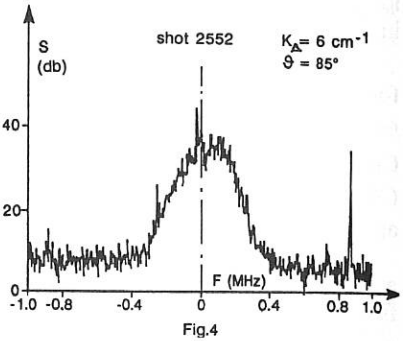

Fig.4

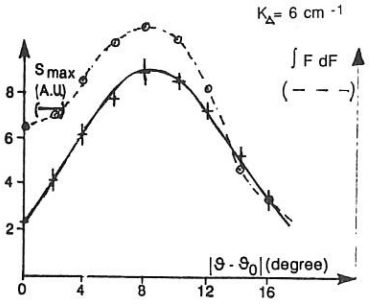

Fig.5

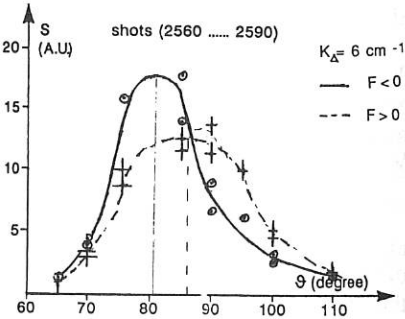

Fig.6

# TURBULENCE STUDIES IN TJ-I TOKAMAK BY MICROWAVE REFLECTOMETRY

T. Estrada, A.P. Navarro, J Sanchez, B Brañas

Asociacion EURATOM/CIEMAT 28040-Madrid, SPAIN

## Introduction

The analysis of density turbulence in the plasma bulk with microwave reflectometry contributes to the program on turbulence studies and anomalous transport which is being conducted in the TJ-I tokamak (R=0.30 m, a=0.10 m, Ip<50 kA, Bt<1.5 T).

The microwave reflectometer installed in TJ-I operates in the x-mode and covers the frequency range 33 to 50 GHz with homodyne detection. The system uses a single antenna for launching and receiving the microwave beam (1).

In this paper we present experimental results on density fluctuations taken in the radial range from the plasma center to r/a=0.7 (3 cm from the plasma edge), operating in standard discharges at 1T and central density about $1\text{-}2\times10^{19}$ $m^{-3}$. Operation in frequency sweeping mode enabled to obtain this radial scan of the turbulence level in a single shot.

Operation at higher field (1.4 T) allowed us to reach the plasma edge and compare reflectometer and Langmuir probes results.

In addition a new method to study coherence lengths is presented.

## Radial sweeping

Most of the reflectometers use direct homodyne detection techniques. This method has the major advantage of simple broadband operation but in the other hand suffers from ambiguity in the determination of the phase delay between the reference and the reflecting layer. Heterodyne methods or quadrature phase detection can be used but they are essentially narrowband and a complete radial scan is very difficult.

In the homodyne system the phase delay $\phi$ of interest is measured indirectly trough an interferometric method: the interference term which carries the phase information is:

$$V = E_1 E_2 \cos\phi \qquad [1]$$

Where $E_1$ is the field amplitude of the reference beam and $E_2$ the field amplitude of the beam reflected from the plasma.

Two problems arise: first, $\cos\phi$ and not $\phi$ is determined, the sensitivity of V to an oscillation in $\phi$ will depend on the point around which the phase is oscillating. Second, due to the characteristic of the microwave equipment, $E_1$ and $E_2$ are functions of the incident frequency with a sharp structure which cannot be easily precalibrated and, in addition, $E_2$ can be time dependent due to the changes in the plasma geometry during the discharge.

A method must be used to bring into a comparable scale the turbulence levels which have been measured at different radial positions with different frequencies of the microwave beam.

We have used frequency sweeping with this aim: If we make a frequency sweeping during the discharge the phase $\phi$ will increase monotonously and, according to the expression [1], V will have a senoidal shape as a function of the frequency . For a given frequency point, the difference between neighboring maximum and minimum is a good on-line estima-

tion of 2 x $E_1$ $E_2$. This is true if the "beat" frequency of the senoidal structure in V(t) is higher than that of the changes in $E_1$ and $E_2$.

The resulting waveform V(t) has a senoidal shape which carries as a ripple the oscillations due to the turbulence. To obtain the radial distribution of phase turbulence we proceed on steps: First the raw signal is filtered around the beat frequency to get the normalizing function, then the raw signal is normalized and the RMS of the signals with frequencies above the beat frequency is taken.

In addition the method shows the periodic sensitivity of the reflectometer as $\phi$ is increasing and some averaging can be performed, which is not possible in fixed frequency experiments.

The procedure can only work if the oscillations in $\phi$ due to turbulence are below $2\pi$, which is the usual situation for microturbulence.The observation of the microscopic oscillation of V around the senoidal function can give thus a direct estimation on the phase oscillation magnitude. On the other hand a higher dynamic range in the detection system is needed in the sweeping experiment to observe with good accuracy the turbulence ripple around the senoidal variation in V(t). A good linearity in the detector diode is also necessary.

The speed of the displacement of the reflecting layer (7 m/s in the experiment in TJ-I) will produce a Doppler-like effect on the observed plasma waves. To minimize this effect the sweeping must be slow. Radial coherence lengths play also some role. Simulation experiments show that the effect of the traveling reflecting point is not severe and that the radial distribution and spectrum of the density turbulence can be reproduced in a similar way as fixed frequency experiments can do.

The rate of frequency change and the subsequent beat frequency must be then carefully chosen to fulfill all the requirements.We can play with the delay paths in the reflectometer to have a suitable $\delta\phi/\delta f$.

For one-antenna reflectometers the path lengths must be also chosen in such a way that the parasitic reflections can be spectrally separated from the relevant signals. In this sense is always easier to apply the present method to reflectometers with separated antennas to launch and receive the beam.

The experiment was performed in TJ-I by sweeping from 33 to 46 GHz in 10 ms, fig 1 shows the frequency spectrum of the recorded signal. Around 3-4 kHz we have the plasma to reference beat frequency and turbulence is taken for f > 10kHz. The peak around 0.5 kHz

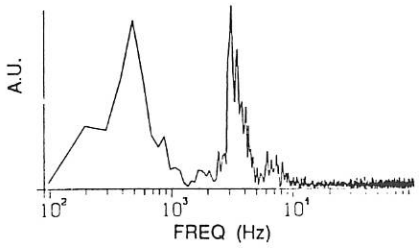


Fig.1 Spectrum of the reflectometer signal in a frequency sweeping experiment

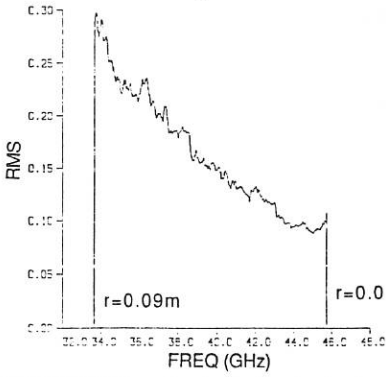


Fig.2 RMS of the normalized reflectometer signal in a slow frequency sweeping (10 ms)

is due to the beating between the reference beam and the reflected one at the vacuum window. Fig 2 shows the normalized turbulence level for the different incident frequencies ( 33 GHz corresponds to r=7 cm and 46 GHz are close to the plasma center for this discharge).The fine structure in the turbulence which appears on fig 2 is non-significant since it is in the order of the present accuracy of the method. Further improvements in the dynamic range of the detection and in the normalization procedure could give meaningful pictures of the turbulence fine structure ( rational surfaces).

A normalization of the radial density fluctuation level for this experiment can be obtained by taking into account the vacuum wavelength and density gradient for the different reflecting points. This will still enlarge the magnitude of the edge fluctuations (lower microwave frequencies). The result is consistent with previous reflectometric measurements and with the probe results at the edge: strong density fluctuations are present at the plasma edge and they decay very fast when moving to deeper radial positions (2), (3).

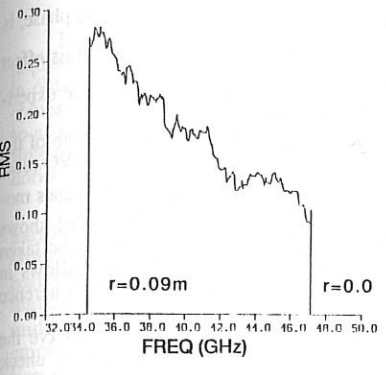


Fig.3 RMS of the normalized reflectometer signal for a fast frequency sweeping (1 ms).

A similar experiment was taken with a faster sweeping (33 to 48 GHz in 1 ms) which is more convenient for the short plateau times (10 ms) in TJ-I but has the disadvantage of a higher beat frequency ( 40 kHz) and a higher Doppler shift. Only turbulence frequencies above $f_{beat}$ can be taken into account. Fig. 3 shows the distribution of turbulence in this experiment for frequencies higher than 60 kHz. The radial behavior is similar to that obtained in the slow sweeping experiment.

Turbulence with frequencies below the beat frequency will appear as a phase modulation effect. If we make a very fast sweeping the density profile with the local perturbations due to the turbulence could be obtained. Then the analysis of density fluctuation on time could be changed to the analysis of a density variation on space. Some simulation studies will be accomplished to evaluate whether a local density profile reconstruction process could bring the high accuracy needed to observe density variations in the 1% range.

The spectra of the density fluctuations for different radial positions have been obtained, no major changes in the spectra structure were found for standard discharges without strong MHD activity. Comparison with probe measurements were performed in discharges at 1.4 T were the reflecting layer for 33 GHz goes closer to the plasma edge. Fig 4 shows the amplitude spectra taken by a Langmuir probe and by the Reflectometer in fixed frequency operation. The spectra are very similar, mainly at low frequencies, the maximum amplitude appears at 70 kHz for the reflectometer and at 100 kHz for the probe. The decay of the power spectrum fits $f^{-\alpha}$ with $\alpha$= 2.8 for the reflectometer and $\alpha$=2.9 for the probe. Coherence between both signals is very low ( < 0.2), this is consistent with the distance between the probing points: 1cm in radial direction and 3 cm

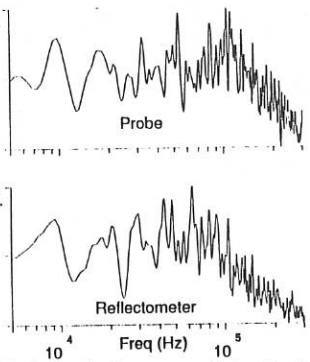


Fig.4 Amplitude spectra of the density turbulence from reflectometric and probe measurements.

in poloidal direction for the same toroidal position.

**Coherence studies**

One of the most interesting features of reflectometry is the ability to obtain radial correlation lengths of the density turbulence by the use of systems with two simultaneous frequencies. The spatial resolution needed and the line integrated effects as well as the possibility of poloidal and toroidal correlation measurements have been discussed elsewhere (2), (4).

Again the use of homodyne receivers is very convenient for broadband operation (which allows the complete radial mapping of correlation lengths) but some new problems are involved: The coherence of $\cos \delta(t)$ and $\cos (\delta(t)+\delta_0)$, where $\delta(t)$ is the oscillating phase, is only equivalent to 1 for $\delta_0=n\pi$ and goes to very low values for $\delta_0=(2n+1)(\pi/2)$, this effect depends on the amplitude of the oscillation of $\delta(t)$. Thus fixed frequency homodyne experiments could produce errors in the determination of the coherence.

We propose a slow frequency sweeping method to overcome this problem : one of the oscillators remains at fixed frequency ( a fixed gunn will be used) and the other ( BWO tube) makes the slow sweeping, then $\delta_0$ increases monotonously and the coherence measured shows maxima and minima, the maxima will be taken as significant coherence values. This allows in addition the determination of the coherence length in a single shot.

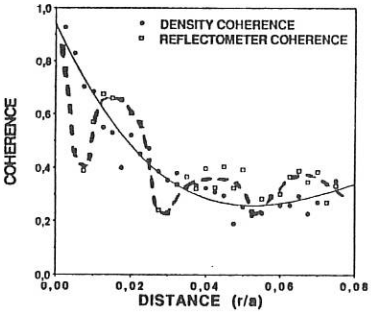


Fig.5 Simulation of coherence measurements. Solid line: fitting of the coherence of the density fluctuation for the different distances between points, dashed line: fitting of the coherence as determined by a homodyne reflectometer in frequency sweeping.

A simulation has been done to observe the swinging effect in the coherence and check whether the correlation length determined in the dynamical process corresponds to the physical one for the density fluctuations.

The density turbulence was generated by a random distribution of magnetic islands (2). The results are shown in fig.5: following the model, the coherence of the density turbulence decays to 0.3 in 4 mm . This is very similar to the behavior of the reflectometer coherence which shows the expected maxima and minima. We can also see that strong errors could arise if only a few discrete points are chosen with the reflectometer. The number of swinging periods can be increased by increasing the delay paths in the reflectometer.

**References**

(1) E. Anabitarte, E.G. Bustamante, M.A.G. Calderon, J.M. Senties, A.P. Navarro and J.Sanchez, J. Phys. D: Appl. Phys 21, 1384-1390 (1988).

(2) A.P. Navarrro, T. Estrada, J.Senties, E. Anabitarte, and J.Sanchez, "Turbulence studies using microwave reflectometry". Proceedings of the Workshop on Electrostatic Turbulence, Report EUR-CEA-FC-1381, 231-38 (1989).

(3) C. Hidalgo,M.A. Pedrosa, A.P. Navarro, F.L. Tabares, E. Ascasibar and F . P. Murano. " Electrostatic turbulence in the TJ-I tokamak". Accepted for publication in Nuclear Fusion. (1990).

(4) A. E. Costley, P. Cripwell. " Correlation reflectometry: a possible new technique for diagnosing density microturbulence". Proceedings of the Workshop on Electrostatic Turbulence, Report EUR-CEA-FC-1381, 89-96 (1989).

# X-MODE BROADBAND REFLECTOMETRIC DENSITY PROFILE MEASUREMENTS ON DIII-D*

E.J. Doyle, T. Lehecka, N.C. Luhmann, Jr., W.A. Peebles, and The DIII-D Group†

Institute of Plasma and Fusion Research, UCLA, CA 90024, U.S.A.

In recent years, there has been a resurgence of interest in reflectometric techniques for density profile measurements. This interest has been driven by difficulty in obtaining sufficient access for interferometer systems, especially on D-shaped machines such as DIII-D and JET, while most Thomson scattering systems are limited to at most a few pulses per discharge. Reflectometry, by contrast, can generate multiple profiles per discharge and requires only minimal vessel access, preferably on the horizontal plasma centerline.

Two alternative approaches to reflectometric profile measurements are available; narrowband and broadband techniques. Narrowband systems, employing modulated Gunn sources, are attractive because of the simple source technology and low capital cost.[1,2] However, in practice on DIII-D and JET, actual machine performance has not matched that of laboratory tests, though more sophisticated schemes are currently under investigation.[3] By contrast, both O- and X-mode broadband systems, which employ frequency tunable BWO sources to sweep through a range of critical densities, have obtained satisfactory results on a variety of tokamaks.[4,5,6] However, none of these results were obtained with H-mode or high beam power L-mode discharges, such as are frequently encountered on DIII-D. O-mode systems have the advantage that the refractive index depends solely on the plasma density, while X-mode systems cover a larger portion of the density profile for a given frequency range, thus requiring fewer sources. In addition, due to the magnetic field dependence, X-mode systems can penetrate beyond the plasma centre. Taking these factors into account, a 50 to 75 GHz, X-mode, broadband reflectometer system was installed and is now operational on DIII-D. Profiles have been obtained under a wide range of conditions, including Ohmic, L- and H-mode operation.

## SYSTEM DESCRIPTION

The system utilizes a 50 to 75 GHz BWO as source and X-mode propagation. Thus, the density coverage is dependent on the toroidal field strength; at full field (2.1 T) the density coverage is $\approx 2.0 \times 10^{18}$ to $3.5 \times 10^{19}$ $m^{-3}$. A schematic of the microwave circuit is shown in Fig. 1. Overmoded waveguide is used to reduce attenuation, while mode generation at bends is minimized by the use of reduced height, DeRonde, bends. As shown, a bistatic arrangement is utilized, with separate transmit and receive horns viewing the plasma through a vacuum window and an adjustable mirror. The tube can be swept full band in as little as 200 $\mu$s and, allowing for the reset time of the tube, density profiles can be measured every 2.5 ms. Currently, the minimum sweep time employed is 500 $\mu$s, due to the data rates at higher sweep speeds being beyond the bandwidth of the electronics. Fringes are measured using an automated fringe detection, timing and counting system employing a zero crossing detector and a DSP model 2904 timer/counter module. Profiles are currently obtained

* This work was sponsored by General Atomics Subcontract SC120536 under U.S. Department of Energy Contract No. DE-AC03-89ER51114.

† General Atomics, San Diego, California.

at seven selectable times per discharge, expandable to 132 profiles per discharge. Fluctuation data can also be obtained, simply by using the tube in CW mode, and directly digitizing the mixer output.

## PROFILE INVERSION

The measured data, $\phi_m(f)$, the phase of the reflected signal as a function of BWO frequency, have three components; $\phi_m = \phi_v + \phi_w + \phi_p$, where $\phi_v$, $\phi_w$ and $\phi_p$ are, respectively, the contributions from the air/vacuum path length, waveguide, including dispersion, and plasma density profile. The air/vacuum and waveguide contributions can be determined by an in-vessel calibration, so the desired plasma contribution can be obtained by subtraction. $\phi_p(f)$ are line integrated quantities related to the density profile through the same expression as for interferometry, viz:

$$\phi_p(f) = 2\,k_o \int_{r_a}^{r_c(f)} \mu(r,f)dr - \pi/2$$

where $k_o$ is the wavenumber of the probing beam, $\mu$ the plasma refractive index, and $r_a$ and $r_c$ are the limiter and cutoff radii, respectively. For O–mode propagation, this integral can be analytically solved for the density profile using an Abel inversion. For X–mode propagation, however, no analytic solution exists and numerical methods must be used. A numerical algorithm has been developed to invert the data which is similar in outline to that given in Ref. 5. However, it does not suffer from the numerical instability problems encountered with that work.[5,7]

Consider an arbitrary step in the profile inversion process. Assume the profile is known up to the n'th frequency, $f_n$. Then,

$$\phi(f_n) = 4\,\pi f_n/c \int_{r_a}^{r_c(f_n)} \mu\,(r, f_n)\,dr$$

For the next frequency, $f_{n+1}$, the measured phase can be represented as:

$$\phi(f_{n+1}) = 4\,\pi f_{n+1}/c \int_{r_a}^{r_c(f_{n+1})} \mu\,(r, f_{n+1})\,dr + \frac{1}{2}\,\Delta r[\mu\,(r_n, f_n) - \mu\,(r_{n+1}, f_{n+1})]$$

where $\Delta r$ is the extra distance propagated by increasing the frequency from $f_n$ to $f_{n+1}$. Now, by definition, $\mu\,(r_{n+1}, f_{n+1}) = 0$, and all the other quantities, except $\Delta r$, are known because the profile for $f_n$ is known. Thus, it is possible to solve for $\Delta r$, whence $r_{n+1} = r_n + \Delta r$, and the density at this radius is known from the cutoff condition. The density profile can thus be extended in a step by step manner using the above algorithm. However, the edge profile up to the density corresponding to 50 GHz must be modelled.

## EFFECT OF DENSITY FLUCTUATIONS

In measuring $\phi_p(f)$, the largest experimental problem is the effect of the intrinsic plasma density fluctuations. These impart a random Doppler shift to the frequency of the measured fringes and can distort or entirely mask the desired profile information. While this Doppler shift is determined by the plasma conditions and cannot be

modified, its effect on the measured fringes can be minimized by utilizing the fastest possible sweep time. This can be understood as follows: If the IF frequency is low, the signal voltage will be close to zero for an appreciable time turing each half period. Thus, only relatively small fluctuations are necessary in order to generate additional, spurious, zero crossings, increasing the measured phase. These spurious counts can only increase the measured phase, and their number is directly proportional to t, the sweep length. If the sweep is sufficiently fast to minimize these spurious counts, the fluctuations can still modulate the counting rate by both advancing and retarding the time of the zero crossings. In this case, using a random walk type argument, the rms deviation from what the count would be in the absence of fluctuations is proportional to $\sqrt{t}$. Therefore, the influence of both forms of phase distortion can be minimized by reducing the sweep length, while the desired profile induced phase shift, $\phi_p$, is independent of t. As density fluctuations are largest during L–mode discharge phases, it is immediately apparent that L–mode profiles are the most difficult to measure. On DIII–D, sweep lengths of 500–750 $\mu$s have been employed and this will be further decreased to 200 $\mu$s in order to cater for the most turbulent discharges encountered.

## RESULTS

Using the techniques described above, good agreement has been found with Thomson profiles in Ohmic, L– and H–mode discharges under a variety of conditions. Examples of reflectometer density profiles, and comparison Thomson profiles, are shown in Fig. 2. An example of the fringe quality during an Ohmic discharge phase is shown in Fig. 3. Fringes obtained during H–mode are similar, while those for L–mode are considerably more distorted during high beam power discharge phases. One unexpected observation is that the plasma VSWR can change such as to affect the measurements. During H–mode, the plasma can become a very good reflector, with signal levels comparable to those of actual mirrors. Under these conditions, a spurious second harmonic signal component can be generated due to multiple reflections, which can cause distortion unless filtered out.

## SUMMARY

Reflectometric density profiles are obtained on DIII–D which are in good agreement with Thomson profiles, but only with the use of fast sweeps. The large changes in plasma profile which occur between ohmic and H–mode operation are observed to change the plasma VSWR. The system is still under development: By adding an additional 50–75 GHz BWO and mixers, the present system will be reconfigured to act as a correlation reflectometer, while still retaining the capability to measure density profiles. These alterations are currently underway, and it is hoped to obtain preliminary data by the time of the EPS conference.

## REFERENCES


1. Lehecka, T., et al., Rev. Sci. Inst. **59**, (1988) 1620.
2. Hugenholtz, C.A.J., and Putter, A.J., Rijnhuizen Report 86-170, Association EURATOM-FOM, The Netherlands.
3. Stek, P.C., et al., Bull. Am. Phys. Soc., Series II, Vol. 34, Abstract 2R15, (1989), 1953.
4. Simonet, F., Rev. Sci. Inst. **56**, (1985), 664.
5. Bottollier-Curtet, H., and Ichtchenko, G., Rev. Sci. Inst. **58**, (1987) 539.
6. Anabitarte, E., et al., J. Phys. D: Appl. Phys. **21**, (1988) 1384.
7. Schubert, R., ASDEX, private communication.

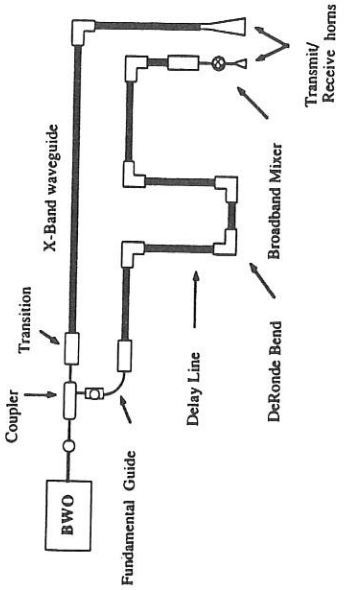


Fig. 1. A schematic of the broadband reflectometer microwave circuit.

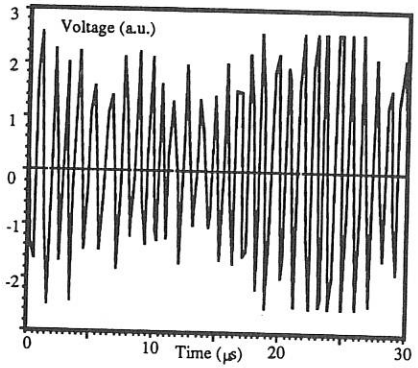


Fig. 2. Measured fringes from a portion of a 500 $\mu$s long sweep in an Ohmic discharge plasma.

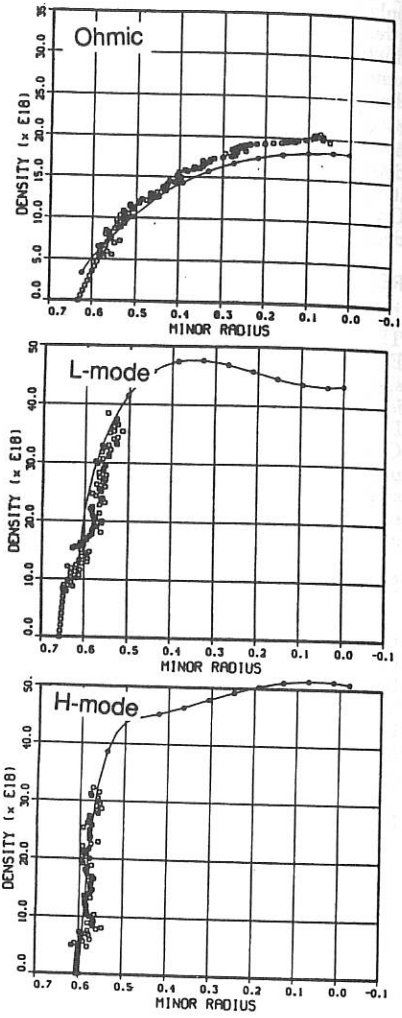


Fig. 3. Compaison of reflectometer and Thomson profiles in Ohmic, L–mode, and H–mode discharges. The solid curve represents a fit to the Thomson data.

# STRONGLY NON-MAXWELLIAN ELECTRON VELOCITY DISTRIBUTIONS OBSERVED WITH THOMSON SCATTERING AT THE TORTUR TOKAMAK

C.J. Barth, A.C.A.P. van Lammeren, Q.C. van Est,
G.C.H.M. Verhaag and A.J.H. Donné

FOM-Instituut voor Plasmafysica Rijnhuizen,
Association Euratom-FOM, P.O. Box 1207, 3430 BE Nieuwegein, The Netherlands

TORTUR is a small tokamak (R = 0.46 m, a = 0.085 m, $B_T$ = 2.9 T) in which a plasma current $I_p \leq 55$ kA is confined during ~ 30 ms. At the plasma centre $T_e \leq 1$ keV and $n_e \leq 10^{20}$ $m^{-3}$. Fast current ramping at plasma formation induces a state of weak turbulence, which is maintained during the plateau stage [1]. Additional heating is performed by superimposing a fast ($\tau \approx 10$ μs) current pulse ($\Delta I_p \approx 30$ kA) on the plateau current [2]. The Thomson scattering diagnostic of TORTUR [3] enables us to measure $T_e$ and $n_e$ at r = 5 and 60 mm. At r = 5 mm scattered light can be collected perpendicular (⊥) and parallel (//) to the toroidal axis: radial and tangential scattering, respectively. According to the scattering geometry (Fig. 1) tangential scattering makes it possible to observe components of v//.

The scattered light is spectrally resolved with a high transmission 20-channel polychromator [3] and is detected with GaAs photomultipliers. At $n_e = 5\times10^{19}$ $m^{-3}$ the observational error is less than 1%; the signals of individual spectral channels have an error of ~ 3%. In Fig. 2 typical spectra are depicted along with the deviations with respect to the fitted gaussian after correction for relativistic effects: $\delta y_i = \{y_i - f(\lambda_i)\}/A$, where $y_i$ is the measured signal, $f(\lambda_i)$ is the value of the fit and A is the amplitude of the gaussian. Under some plasma conditions - which will be presented later - $\delta y_i$ is very small (Fig. 2a) but during the current flat-top distortions with respect to the expected gaussian are found on radial (Fig. 2b) and tangential (Fig. 2c) spectra. The value of $\delta y_i$ amounts up to 5 times the observational error and is therefore substantial. The typical shape of the distortions is found by averaging $\delta y_i$ over 30 observations (Fig. 3a and b). At $|\Delta\lambda| > 30$ nm all data points match the fitted gaussian accurately. Observational errors of tangential spectra are larger than those of radial spectra, due to a smaller collection efficiency. The deviation spectra $\delta y(\lambda)$ for radial and tangential observations are characterized by two symmetrical dips at $\Delta\lambda = +/- 15$ nm with an amplitude $\langle\delta y\rangle$ of ~ 7%.Correlation studies concerning the largest negative deviations in the 4 innermost channels of the red and the blue wing of the spectrum show four combinations with a total probability of 80%. The four channels involved have a wavelength shift $\Delta\lambda = \lambda - \lambda_0$ of -17.2, -11.4, +16.1 and +22.6 nm. When the position of these minina was purely a matter of statistics a total probability of 25% is expected.

Due to the gyration of the electrons around the toroidal magnetic field lines the electron velocity distribution for a tokamak plasma is given by $f(v) = f(v_\perp, v_{//})$. So, in principle it is possible to determine f(v) from the spectra observed in the radial, $f(\lambda_\perp)$, and tangential, $f(\lambda_{//})$ direction. However, straightforward determination of f(v) from $f(\lambda_\perp)$ and $f(\lambda_{//})$ is not possible since both measured spectra represent a projection of f(v) on the radial and tangential scattering vector, respectively. Further complications arise from relativistic effects [4]. Therefore, a computer code [5] has been written to calculate for any anisotropic electron velocity distribution the corresponding Thomson scattering spectra for each scattering geometry. Application of this code demonstrates that the congruence between the observed spectra can be well explained by an isotropically distorted velocity distribution. In that case the velocity distribution is proportional to the derivative of the spectrum: $f(v) \propto df(\lambda)/d\lambda$ [6]. A typical spectrum is obtained by superimposing the mean deviation spectrum on a thermal distribution of 600 eV, as is shown in Fig. 4a. The corresponding f(v) is shown in Fig. 4b. From this it is clear that the small spectral deviations (~ 7%) correspond to large deviations (~ 50%) in the electron velocity distribution. Calculations showed that the collisional relaxation time of such a distorted distribution is of the order of 0.5 μs [7], which is much larger than the duration of one measurement (20 ns). To get an idea of the number of electrons involved in the distortions, a partial density, $\Delta n_e$, is defined as:

$$\Delta n_e = N \times RF \frac{\sum |\delta y_i| \, \delta\lambda_i / \sigma_i}{\sum 1/\sigma_i},$$

where RF is the calibration factor for Rayleigh scattering, N is the number of channels within the wavelength interval from -30 to +30 nm, $\delta\lambda_i$ is the channel width and $\sigma_i$ is the observational error of channel i. It was found that $\Delta n_e$ scales proportional with $n_e$ [3] resulting in $\Delta n_e/n_e \approx 5\%$ and 9% for the radial and tangential direction. A typical evolution in time is found for $\Delta n_e$ just after the injection of the fast heating pulse. The time dependence of the main plasma parameters is depicted in Fig. 5, using a logarithmic timescale for demonstrating the μs- and ms-phenomena in one picture. The smooth spectrum of Fig. 2a was observed at $\Delta t = 1.0$ ms, after the fast current pulse. Correlation in time between $\Delta n_e(t)$ and $\tilde{n}(t)$ was found. The latter was obtained from $\lambda_o = 4$ mm collective scattering measurements [3, 8] in the frequency interval of 0.7-3 MHz (Fig. 5g).

Similar phenomena were found shortly after minor disruptions which appeared as a result of strong gaspuffing. The time dependence of $\Delta n_e/n_e$ as a function of the relative time $\Delta t$ after the start of a minor disruption is shown in Fig. 6. There is a similarity in this time development compared to that after the fast current pulse (Fig. 5). Here the collective scattering signals showed strong bursts in the frequency ranges between 0.7 and 3 MHz and between 5 and 50 MHz [9]. In both cases - fast current pulse and minor disruption - $\Delta n_e$ reduces when a redistribution in $T_e(r)$, $j_\phi(r)$ and $n_e(r)$ takes place.

In conclusion, Thomson scattering measurements at the TORTUR tokamak demonstrate that f(v) is strongly distorted. The partial density involved in the distortions varies in time after the injection of a fast current pulse and after minor disruptions. Some interesting questions arise: do these distortions also exist in other tokamak discharges or are they a specific result of the state of weak turbulence? What is the impact of such distortions on the particle and energy transport?

This work was performed under the Euratom-FOM association agreement with financial support from NWO and Euratom.


1 H. de Kluiver et al., Phys. Lett. **94A** (1983) 156

2. H. de Kluiver and N.J. Lopes Cardozo,Comments Plasma Phys. Contr. Fusion, **11** (1988) 211

3 C.J.Barth,"Thomson-scattering measurements of the electron velocity distribution function in the TORTUR tokamak", Thesis State University of Utrecht, 1989

4. M. Mattioli and R. Papoular, Plasma Phys. **17** (1975) 165

5. Q.C. van Est, "Computation of Thomson spectra for anisotropic relativistic electron velocity distributions", Rijnhuizen Internal Report 89/003, 1989

6 J.H. Williamson and M.E. Clarke, J. Plasma Phys. **6** (1971) 211

7 E. Westerhof, private communication, 1989

8 H. de Kluiver, C.J. Barth and A.J.H. Donné, Plasma Phys. and Contr. Fusion **30** (1988) 699

9 G.J.J. Remkes and F.C. Schüller, This conference.


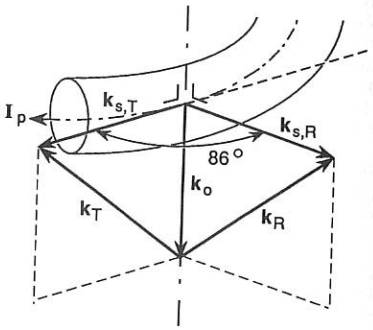


Fig. 1 Scattering geometry for radial and tangential scattering at r = 5 mm.

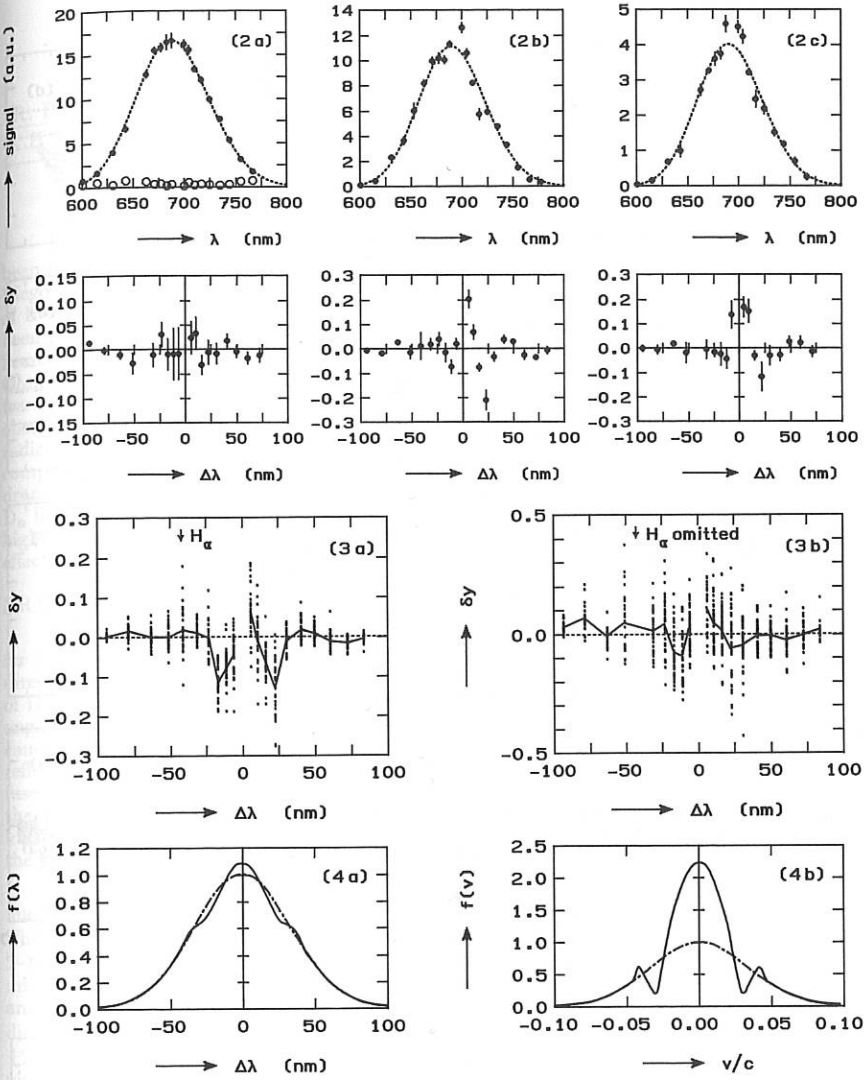


Fig. 2. Scattered spectra at r = 5 mm, with relative deviations, $\delta y_i$ : (a) a smooth and (b) a distorted radial spectrum and (c) a tangential spectrum. Conditions: $T_e \approx 600$ eV and $n_e \approx 5\times10^{19}$ m$^{-3}$. Dots: scattered light, open circles: plasma light.

Fig. 3. Relative deviations for an ensemble of ~ 30 observations in the radial (a) and tangential (b) direction. The solid line indicates the mean value.

Fig. 4 (a) The distorted spectrum compared to the unperturbed 600 eV-spectrum
(b) Electron velocity distributions corresponding to the perturbed and unperturbed spectra, when an isotropic distortion is assumed.

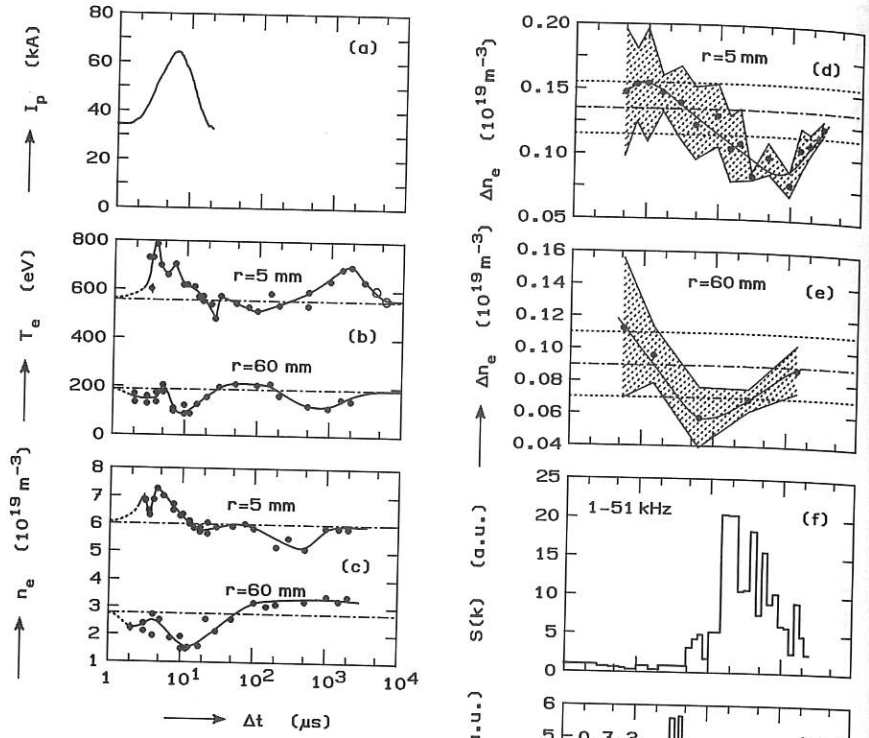


Fig. 5 Evolution in time of plasma parameters after the injection of the fast current pulse:
(a) plasma current; (b) and (c): $T_e$ and $n_e$, respectively; (d) and (e) $\Delta n_e$ at r = 5 (radial) and 60 mm, respectively; (f) and (g) scattered power of density fluctuations in different frequency intervals at r = 65 mm.

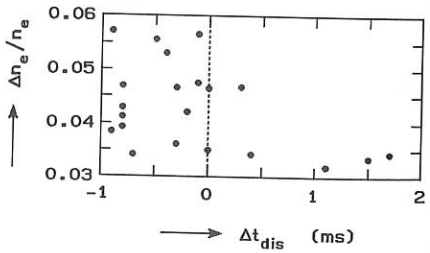


Fig 6. Time development of $\Delta n_e/n_e$ at r = 5 mm (radial) after minor disruptions.

# MICROTURBULENCE STUDIES ON DIII–D VIA FAR INFRARED HETERODYNE SCATTERING

R. PHILIPONA, E.J. DOYLE, N.C. LUHMANN, JR., W.A. PEEBLES, C. RETTIG
K.H. BURRELL,† R.J. GROEBNER,† H. MATSUMOTO,‡ AND THE DIII–D GROUP

Institute of Plasma and Fusion Research, UCLA, CA 90024, U.S.A.

A far infrared collective scattering system, to measure density fluctuations, has been installed and is operational on the DIII–D tokamak at General Atomics in San Diego. The primary goal of the present measurements is to determine the effect of H–mode operation on fluctuation spectra. In addition, particular emphasis has been placed on identifying $\eta_i$ mode turbulence in Ohmic, L– and H–mode operation. Search for the existence of $\eta_i$ modes has initially been conducted in the saturated Ohmic regime which occurs at relatively low densities in DIII–D. Fluctuation spectra were found dependent on plasma conditions with both electron and ion features observed. However, large toroidal rotation velocities (20 km/s) possessing strong radial dependence were measured which, together with possible poloidal rotation, complicate a clear identification of $\eta_i$ mode turbulence. During H–mode operation a dramatic drop of low frequency fluctuations is observed coincident with the drop in $D_\alpha$ light and the $k$ spectrum appears to narrow. This is followed by a gradual rise of a high frequency component possibly connected with profile modification and rotation effects.

## FIR COLLECTIVE SCATTERING

The scattering system consists of a 245 GHz ($\lambda = 1.22$ mm) twin frequency far infrared laser. In the equatorial plane of the tokamak, the laser probe beam is directed radially into the vessel and reflects from a special carbon tile on the centerpost of DIII–D. The laser beam enters slightly above the midplane of the tokamak and is angled downward by 1.5° in order to isolate the probe laser cavity from modulation caused by feedback laser radiation. Scattered light from the returning probe beam is reflected out of the machine by a large metallic mirror and through two 25 cm diameter fused quartz windows. A vertically mounted optical table close by the machine holds the optical components for the receiver channels, while the probe laser beam and the local oscillator are transmitted by two overmoded circular dielectric waveguides from the laser, which is located outside the machine pit.

At present three receiver channels are available to study poloidally propagating fluctuations along the entire midplane of DIII–D in the range of $0.2 \leq k_\perp \rho_s \leq 2$. The system is currently limited to wavenumbers of 2.5–16 $cm^{-1}$ at the outside edge, 2–10 $cm^{-1}$ at the center and 2–7 $cm^{-1}$ at the inside edge because of the required misalignment described above. Simultaneous measurements of different wavenumbers and or different spatial locations can be made. The beam geometry of the system dictates a wave-number resolution of $\Delta k \approx 0.7$ $cm^{-1}$ and a radial spatial resolution of $\pm 20$ cm at $k = 10$ $cm^{-1}$. The propagation direction of the fluctuations is determined via the use of heterodyne detection techniques. Quasi optical biconical GaAs Schottky Barrier Diode Mixers are used for the optical mixing of the local oscillator and the scattered light. The mixed signal is amplified and digitized at a sampling rate of 5 MHz using Le Croy Model 6810 digitizers which provide a measuring time window of 100 ms per channel.

† General Atomics, San Diego, California 92138-5608, U.S.A.

‡ Japan Atomic Energy Research Institute.

## DENSITY FLUCTUATIONS IN THE OHMIC REGIME

Fluctuation studies were initially made in the Ohmic regime of DIII–D plasmas. Measurements at the outside edge of the plasma ($R = 220$ cm) show strong, narrow, frequency spectra with fluctuations in the range of 50–250 kHz, predominantly at small wavenumbers in the range of 2–5 $cm^{-1}$. The measured spectra extend to higher frequencies but decrease strongly in scattered power at larger wavenumbers (drop of two orders of magnitude in power from $k = 2.5$ to 7.5 $cm^{-1}$). Depending on plasma parameters and plasma shape, heterodyne measurements show a detached peak from the intermediate frequency (IF) or a rolloff in frequency space which can be observed in either the ion or electron diamagnetic drift direction. In general, the characteristics of density fluctuations in Ohmic DIII–D plasmas are in accord with observations made on other tokamaks.[1–3] Frequency range and wavenumber spectra are comparable as well as the level of density fluctuations which scale with the mean density ($\tilde{n}/n \simeq$ constant). However, the propagation direction is found to depend on plasma parameters and plasma shape and seems to be correlated with toroidal rotation.

Simultaneous measurements with three receiver channels are shown in Fig. 1. Two channels measuring wavenumbers of 3 and 6 $cm^{-1}$ respectively are set up in the outside edge of the plasma ($R = 220$ cm) while a third channel is set to measure fluctuations at 6 $cm^{-1}$ at the inside edge ($R = 120$ cm). Spectra from the outside edge show fluctuations predominantly shifted to positive frequencies which indicate fluctuations propagating downwards in the tokamak corresponding to the ion diamagnetic drift direction. The spectrum measured at the inside edge shows its main signal shifted to negative frequencies which indicate an upwards propagation and hence reveals the same ion diamagnetic drift direction. These measurements were made in a low density double null divertor deuterium plasma at 2.1 Tesla and 1 MA.

As mentioned earlier, the propagation direction of density fluctuations has been found to be dependent on plasma parameters and plasma shapes. In limiter plasmas density fluctuation spectra show throughout a dominant electron diamagnetic drift for all plasma conditions except the locked mode which shows an ion feature. Divertor plasmas, however, show ion or electron features depending on magnetic field, plasma current and density. At low current, low density and low magnetic field (0.5 MA; $1.5 \times 10^{19}$ $m^{-3}$; 1.1 T) the spectra show predominantly an ion drift while at high field (2.1 T) an electron feature is observed. Maintaining the high field and low density but increasing the current (1 MA) switches the propagation direction back to the ion side. At high field and high current but increasing now the density ($4 \times 10^{19}$ $m^{-3}$), brings the propagation direction again back to the electron side. Together with these observations, a large toroidal rotation velocity (up to 20 km/s) possessing strong radial dependence was measured using CER[5] spectroscopy. In all of the above mentioned cases, changes in propagation direction of density fluctuations were measured to be consistent in sign and magnitude with changes of toroidal rotation. Figure 2(a) and 2(b) show toroidal rotation and scattering measurements respectively from the outside midplane in the case of a plasma current scan. High currents show an important positive toroidal rotation at $\rho = 0.6$–$0.8$ where turbulence is strongest and fluctuations are predominantly in the ion direction. At low currents, rotation is decreased and the fluctuation spectra show an electron feature. For positive toroidal rotation (i.e. direction of neutral beams) a Doppler shift of scattered signals towards the ion side is expected. As regards $\eta_i$ mode turbulence, scattering data in saturated Ohmic operation appear to be entirely consistent with spectral shifts resulting from the observed large toroidal rotation effects. Therefore, no clear supporting evidence has, so far, been found for the existence of $\eta_i$ modes on DIII–D.

## FLUCTUATION SPECTRA IN L–MODE, H–MODE AND ELMs

The narrow low frequency fluctuation spectra measured in the Ohmic regime are typically enhanced in amplitude and broadened in frequency with injected beams. During the L–mode phase preceding the H–mode, frequency spectra are slightly shifted in the ion diamagnetic drift direction. Strong low frequency turbulence is observed at low wavenumbers ($k$ = 2–4 cm$^{-1}$) which seems to evolve depending on beam power and duration of the L–mode phase. At the transition into H–mode, a dramatic drop of the low frequency fluctuations is observed coincident with the drop in $D_\alpha$ light.[4] This is followed by a gradual rise of a high frequency component shifting further to the ion direction. The high frequency component evolves typically in the first 10 to 50 ms of the quiescent H–mode phase before settling to a frequency several hundred kHz on the ion side. At larger wavenumbers ($k$ = 6 cm$^{-1}$) the reduction of the integrated scattered power is greater, which seems to indicate a narrowing of the poloidal wavenumber spectra in H–mode. Figure 3(a) shows the photodiode trace and the FIR time slices of a single null deuterium discharge at 2 Tesla, 1 MA and a density of $3.8 \times 10^{19}$ m$^{-3}$. Co-injected deuterium beams at a power of 8 MW are injected at 2000 ms and the H–mode transition occours at 2085 ms. Density fluctuation spectra measured in the outside midplane at $k$ = 3 cm$^{-1}$ are shown in Fig. 3(b) during the Ohmic, L–mode, H–mode phase and during an ELM. The evolution of the frequency shift again is in accord with rotation effects as shown from CER measurements.[5] Co-injected beams enhance positive toroidal rotation which in the H–mode phase is strongly increased and which may be responsible for the frequency shift to the ion direction measured with the scattering diagnostic. ELMs basically show very similar fluctuation characteristics to those measured in L–mode, supporting the hypothesis that ELMs represent a transient return to L–mode.[6]

## SUMMARY

Although fluctuations have been observed to propagate in the ion diamagnetic drift direction in the laboratory reference frame, no clear evidence for $\eta_i$ mode turbulence in Ohmic DIII–D plasmas has been established thus far. Links found between scattering measurements and toroidal rotation measurements strongly suggest shifts in frequency space due to rotation effects. Much larger frequency shifts have been measured in the H–mode phase where plasma rotation is known to be well above Ohmic levels.

This work is sponsored by the U.S. Department of Energy under contracts DE-FG03-86ER53225 and DE-AC03-89ER51114.

## REFERENCES

1 Crowley, T. , and Mazzucato, E., Nucl. Fusion **25**, (1985), 507.

2 Brower, D.L., et al. , Nucl. Fusion **27**, (1987), 2055.

3 Dodel, G., and Holzhauer, E., in Proceedings of Fifteenth European Conference on Controlled Fusion and Plasma Heating, Dubrovnik, (1988) 43.

4 Doyle, E.J., et al., "Density Fluctuation Measurements Via Reflectometry on DIII–D During L– and H–mode Operation," this conference.

5 Groebner, R.J., et al., in Proceedings of Sixteenth European Conference on Controlled Fusion and Plasma Heating, Venice, (1989) 245.

6 Burrell, K.H., et al., Plasma Physics and Controlled Fusion **31** (10), (1989) 1649.

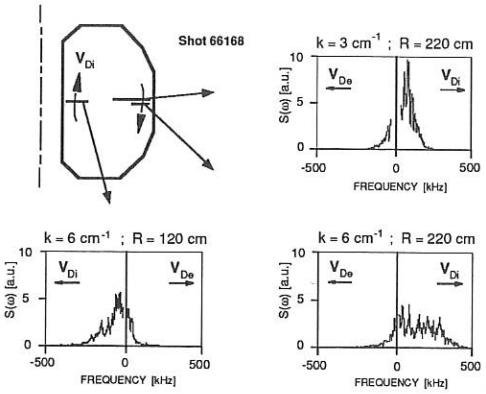


Fig.1 Single shot poloidal frequency spectra.

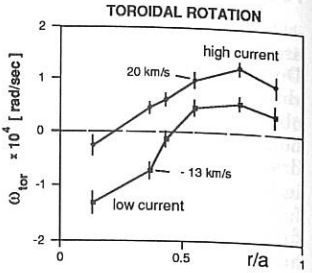


Fig. 2a CER toroidal rotation vs. r/a.

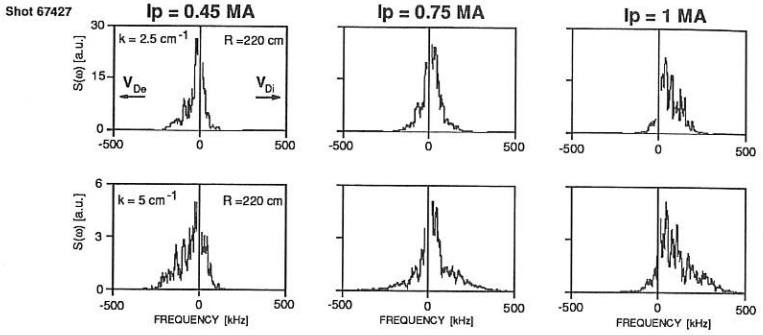


Fig. 2b Change of propagation direction during current ramp.

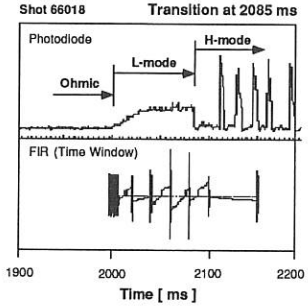


Fig. 3a Photodiode and FIR time slices.

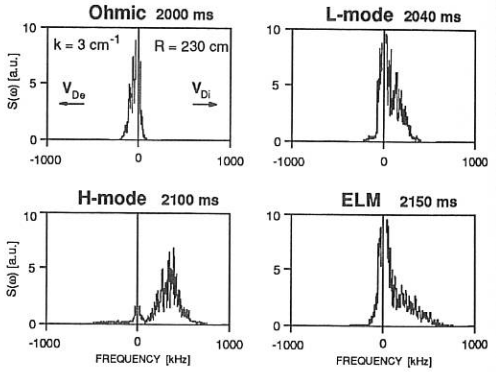


Fig. 3b Frequency spectra of ñ during four plasma phases.

# ION TEMPERATURE MEASUREMENTS AT JET

H.W.Morsi, M.von Hellermann, R.Barnsley, J.J.Ellis,
R.Giannella, W.Mandl, G.Sadler, H.Weisen, K-D.Zastrow*

JET Joint Undertaking, Abingdon, Oxfordshire, UK
*Royal Institute of Technology, Stockholm, Sweden

## Introduction

Record performances of the JET tokamak in 1989 are reflected in a significant increase of the product of ion temperature and deuteron density and the length of time for which those values were sustained. The measurement of a radial ion temperature profile and its peak values on axis play a key role in the assessment of fusion performances. We address in this paper the reliability of ion temperature measurements and compare the diagnostic techniques at the JET tokamak.

## Instrumentation

The measurement of ion temperatures at JET is based on four independent diagnostics (Fig.1), a high resolution X-ray spectrometer [1] and two active beam charge exchange diagnostics [2,3] using visible recombination radiation, and a neutron yield monitor measuring the total neutron rate[4].

The X-ray spectrometer (KX1) views the plasma at a single horizontal line of sight along the mid plane of the JET torus intersecting the plasma centre twice. The instrument is of Johann type with a bent crystal of long focal length (25m) providing high resolution ($\lambda/\Delta\lambda$=20000) and a geometry with crystal and detector placed outside the torus hall. The maximum time resolution is 20ms.

The multi chord charge exchange diagnostic (KS4) uses a fan of horizontal viewing lines intersecting the neutral beams in the torus mid plane at radii between plasma centre and plasma boundary taking spectra at up to 12 discrete radial positions. An additional charge exchange diagnostic (KT3) uses a single vertical viewing line intersecting these neutral beams at a major radius of 3.1m (plasma centre). The collected light of both CX diagnostics is transferred by quartz fibres to remote spectrometers and multi-channel detection systems. A UV optical link without fibres is presently comissioned. Splitting the light into different spectrometers enables the simultaneous ion temperature analysis of the main light impurities and that of the bulk plasma deuterons.

The neutron yield monitor diagnostic (KN1) consists of 3 pairs of fission chambers (detectors) attached to the magnetic limbs at the torus mid plane. Since the neutron production is concentrated to the plasma core, the observed neutron yield is representative for the central thermal ion temperature and deuteron density. The yield is recorded continously with a sampling rate of 10ms.

## Data analysis and results

The spectroscopic ion temperature measurements are based on the Doppler broadening of spectral lines emitted by either highly ionized medium Z impurity atoms, e.g. $Ni^{26+}$ in the case of high resolution X-ray

spectroscopy [5], or in the case of charge-exchange-spectroscopy by fully stripped light impurity ions, e.g. $Be^{4+}$ or $C^{6+}$ [2,3]. The passive emission of the resonance line of $Ni^{26+}$ represents the hot plasma core, whereas the locations of the active CX emission are defined by the intersection of neutral beam and respective viewing lines giving a spatial resolution of the order of 1% of the major radius (±3cm).
During ohmic heating the neutron production can be assumed to be entirely thermal and central ion temperatures can thus be derived from observed absolutely calibrated neutron yield, and a deuteron density derived from an averaged value of $Z_{eff}$, measured by visible bremsstrahlung.
Fig.2 gives an example of a JET pulse (#20934) showing results of the 3 ion temperatures in the various heating phases. In the ohmic phase the values of Ti(neutron) and Ti(X-ray) agree typically within 20%. The latter depending on the concentration of nickel in the centre of the plasma required for a minimum signal-to-noise ratio. In the additional heating phase, characterised usually by an enhancement of nickel concentrations and light impurity levels of the order of 1 to 5% of the electron density, the X-ray and CXS diagnostics measure the ion temperature with typical 20ms time resolution.
The sensitivity of the X-ray diagnostic and the analysis procedure has recently been improved enabling the retrieval of central ion temperature even at photon fluxes as low as $3\ 10^{13} \frac{photons}{m^2\ sr\ s}$ corresponding to nickel concentrations of the order of $n(Ni)/n(e)=10^{-6}$. The resonance line of helium-like nickel ($Ni^{26+}$,w) is fitted with a Voigt-function which is truncated on the long wavelength side of the line to avoid unresolved dielectronic satellites.

At high electron temperatures (Te(0) > 8keV) inferred central ion temperatures have to be corrected for profile effects induced by the broadening and central burn-out of the emission profile of helium-like nickel in the plasma centre. As a result of a broad emission profile the uncorrected ion temperature presents an averaged value weighted toward the plasma centre. In contrast to this, an apparent Doppler broadening can result from a velocity shear across the line of sight or a rapidly changing toroidal velocity during a sampling time interval. These effects are taken into account by a new model which creates a synthetic spectrum [6] and fits it to the observed spectrum with the central ion temperature being one of the fit parameters, thus providing $Ti^{corr}(0)$.

The synthetic spectrum is based on atomic physics data, actual profiles of electron temperature and density, and on the assumption of proportionality of the radial profiles of ion and electron temperature $Ti(r) \propto Te(r)$ and the flatness of the toroidal rotation frequency profile of the plasma (i.e. $\gamma(\omega) < 0.5$). If this assumption is not valid , for instance during a hot-ion-mode plasma, with high toroidal velocities and highly peaked radial profiles, it is replaced by the model functions $Ti(r)=Ti(0)\exp(-\gamma(T)\Psi(r)^{3/4})$ and $\omega_{rot}(r)=\omega_{rot}(0)\exp(-\gamma(\omega)\Psi(r)^{3/4})$, where $\Psi(r)$ is the flux surface index and $\gamma(i)$ the respective peaking factors taken form the charge-exchange-spectroscopy data [7]. The results in Fig. 3 and 4 show that even in extreme cases with ion temperatures of 30keV and central angular frequencies of the order $5\ 10^5$ rad/sec, the observed spectra can be matched by the calculated emission profile, and lead to consistent values of central ion temperatures.

For ion temperatures derived from Doppler broadened charge-exchange -spectra, several errors sources are considered. Statistical errors

increase from the edge (typ.3%) to the plasma centre (typ.10%), as a result of beam attenuation. This also results in an increased ratio of emission of edge lines at the CX wavelength to the CX lines, and can cause additional uncertainties when the CX signal is low. Effects from 'plume emission' from hydrogen-like ions produced outside the observation volume and drifting into the line of sight, are estimated to down-bias central temperatures by less than 5%. Distortions of the observed emission spectra due to the energy dependence of the CX cross sections have been systematically investigated using the recent up-date of atomic cross-sections of He(4-3) and C(8-7) [8]. For the JET viewing geometry, ion temperatures and toroidal velocities the decrease of observed central ion temperatures is calculated to be less than 5% for the n=8 to 7 transition of $C^{6+}$ in the centre of a 20keV plasma. Overall uncertainties are therefore typically between 5% (near the edge) and 15% (centre).

## Conclusions

Generally the diagnostics agree within 10 to 20% and provide values for the central ion temperatures which appear to be consistent with predictions of neutron rates based on radial profiles of CX ion temperature and deuteron density [9]. In hot-ion-mode plasmas with highly peaked rotation profiles and broad $Ni^{26+}$ emission profiles the observed X-ray spectra need to be modelled. On the other hand in high density plasmas, typical for pellet fuelling or long pulse H-modes, beam penetration can be rather poor and CX spectra difficult to analyse. For future JET operations it is planned to investigate the options of using hydrogen-like nickel emission spectra, or in the case of of CX analysis to explore the enhanced beam penetration of neutral He beams.

## References

[1] Bartiromo R., Bombarda F. et al., Rev.Sci.Instrum., **60**, 237 (1989)
[2] Weisen H., von Hellermann M. et al., Nucl.Fusion, **29**, 2187 (1989)
[3] Boileau A., von Hellermann M. et al., Plasma Phys., **31**, 779 (1989)
[4] Jarvis O.N. et al., Proc. 12th EPS Conf.,Budapest, **1**, 223 (1985)
[5] Bombarda F., Gianella R. et al., JET-P(88)36 (1988)
[6] Zastrow K-D., Källne E., Summers H.P., Phys.Rev.A, **41**, 1427 (1990)
[7] Zastrow K-D., Källne E., Morsi H.W. et al., in preparation
[8] Summers H.P., von Hellermann M. et al., in preparation
[9] Mandl W., von Hellermann M. et al., this conference

## Figure captions

**Fig.1** Layout of the ion temperature diagnostics at the JET torus. KX1=high resolution X-ray spectrometer, KS4=multichord (horiz.) CX-spectrometer, KT3=single-chord (vertical) CX-spectrometer, KN1=neutron yield monitor, KH2=pulse height analyser, NBI=neutral beam injector.

**Fig.2** Comparison of ion temperature measurements in ohmic and combined NBI and RF heating phases. During additional heating a non-Maxwellian deuteron velocity distribution does not allow the derivation of an ion temperature from the measured neutron yield.

**Fig.3** Hot-ion-mode pulse #20983. Comparison of central $Ti(C^{6+})$, $Ti(Ni^{26+})$ and corrected value of $Ti(Ni^{26+})$, taking into account profile effects.

**Fig.4** Radial profile of ion temperatures.

**Fig.1**

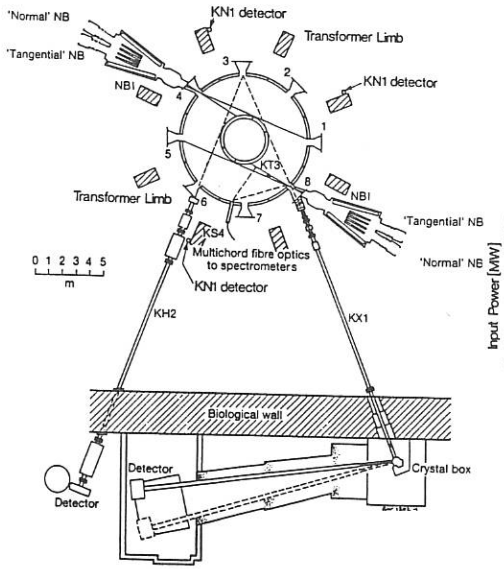


**Fig.2**

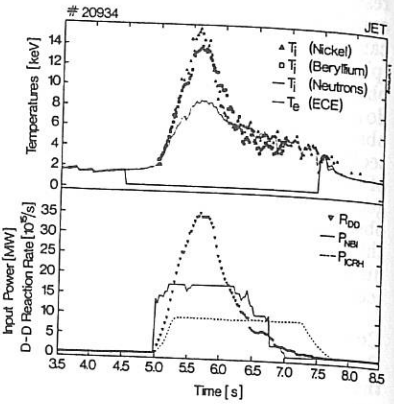


**Fig.3**

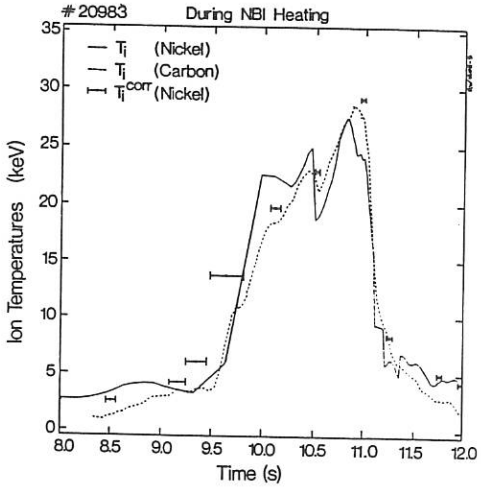


**Fig.4**

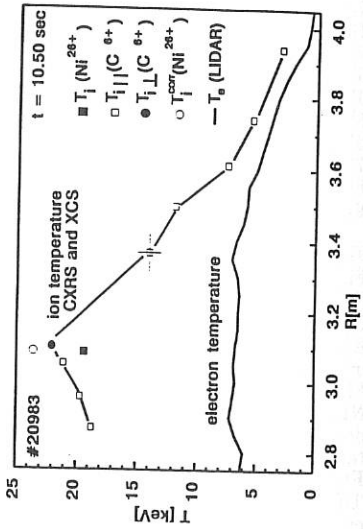

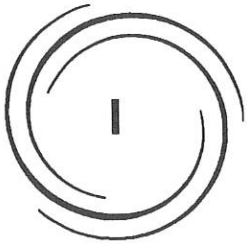


# DIAGNOSTICS

## I2 TECHNIQUE / NEW METHOD

# A SIMPLE AND SENSITIVE INSTRUMENT FOR PLASMA ELECTRON TEMPERATURE DETERMINATION.

Yu.V.Gott, V.A.Shurygin
I.V.Kurchatov Institute of Atomic Energy, Moscow, U.S.S.R

The results of designing and application of a simple and sensitive integral photoelectron spectrometer, (PES-I), allowing one to study the evolution of temperature $T_e$ and plasma electron energy distribution in time are given in the paper.

The photoelectron method of $T_e$ measuring [1,2] is based on the fact that the thermal X-ray continuum of Maxwellian plasma

$$\frac{dN_\gamma}{dE_\gamma} \sim \frac{n_e^2}{\sqrt{T_e}} \exp(-E_\gamma / T_e), \qquad (1)$$

where $E_\gamma$ is the X-ray quantum energy, is transformed, as a result of photoeffect, into a photoelectron spectrum

$$\frac{dN_e}{dE_e} \sim \frac{n_e^2}{\sqrt{T_e}} \Phi(E_e, T_e) \exp(-E_e/T_e), \qquad (2)$$

where $E_\gamma$ and $E_e$ are related by $E_\gamma = E_e + E_i$ where $E_e$ is the energy of photoelectron knocked out from the $i$-th atomic shell, $E_i$ is the electron binding energy in this shell, $n_e$ is the plasma electron density, $\Phi(E_e, T_e)$ is the function representing some details of X-ray spectrum transformation into the photoelectron one. The function $\Phi(E_e, T_e)$ has a weak dependence on $E_e$ and it allows one to find $T_e$ directly from the experimental spectrum.

Such an exponential form of photoelectron spectrum for a Maxwellian plasma is retained in the integral photoelectron spectrum, $N_e$, too. Indeed, from (2) it follows that

$$N_e = \int_E^\infty \frac{dN_e}{dE_e} dE_e \sim \exp(-E/T_e), \qquad (3)$$

Thus, the slope of integral photoelectron spectrum represented in semi-logarithmic scale can also be used for $T_e$ determination.

The PES-I sketch is given in Fig.1. The X-rays enter through a filter 1 ( carbonic foil, 500Å thick) a thin ( 100Å) carbonic target 2, located at 45° towards the incident radiation. The photoelectrons emitted from the target are energy analysed in the retarding electric field concentrated between the target unit 3 and the unit, where the microchannel plate detector 4 is located. The grounded grid 5 increases the signal contrast range . Venetian blinds 6 reduce the probability of the fluorescent target radiation registering with a detector. The fast photoelectrons passing through retarding field incident upon the venetian blinds and knock out the low-energy secondary electrons which are accelerated by the potential $\sim$50 V and are registered with the detector.

The filter 1 was used to suppress the background produced by an ultra-violet plasma radiation. The PES-I has a magnetic screen 7 and a lead shield against a hard X-ray radiation effect.

The PES-I calibration was done with a monochromatic X-ray radiation in the energy range 1.5 - 8 keV.

The developed instrument was used for determining of the plasma electron temperature in the experiments on a small tokamak with plasma density $10^{12}$-$10^{13}$ $cm^{-3}$, discharge current 20-50kA, minor radius 6 cm, major radius 37 cm, discharge duration 10-20 ms.

The integral photoelectron spectra measurements were performed in the current mode of operation in the energy range 0.1 - 2 keV by two methods:

a) by changing of analyzing voltage during the time interval determined by the X-ray radiation intensity. In these experiments it was equal to 1-2 ms;

b) by changing of analyzing voltage from one discharge to another. This method allows one to follow a change in the photoelectron flux with the energies higher $E$ ( see(3)) during the

whole discharge. At the good reproducibility of plasma parameters, it is possible to determine its temperature, $T_e$, at any time with the resolution higher than that in a).

The results obtained by both methods for a stationary phase of discharge coincide with each other. The spectra obtined for different discharge currents are given in Fig.2.The temperature of a main, $T_{th}$, and superthermal part, $T_{sth}$, of plasma electron energy distribution function and a relative amount of superthermal electrons, $\alpha$, are given in the Table:

| curve in Fig.2 | I, kA | $T_{th}$, eV | $T_{sth}$, eV | $\alpha$, % |
|---|---|---|---|---|
| 1 | 25 | 94 | 280 | 9 |
| 2 | 40 | 100 | 433 | 4 |
| 3 | 48 | 132 | 1170 | 2.6 |

In conclusion one should emphasize the main advantages of the technique under discussion:

1. The PES-I is a simple instrument with the sensitivity sufficient for spectral measurements in the current mode of registration. The absence of loading limits is an essential advantage of the PES [1,2] and PES-I over traditional X-ray PHA systems.
2. The spectrum scanning in a wide energy range, with high time resolution, essentially simplifies ( in comparison with the filter method) the delivery of information on the evolution of plasma electron energy distribution.
3. The detector of the PES-I, as well as in that of PES, does not face the plasma directly. It is especially valuable for diagnostics of the D-D and D-T plasmas.

References

1. Yu.V.Gott, A.N.Silaev, R.R.Chistyakov, V.A.Shurygin, Nucl. Instrum. Meth. Phys. Res., 1983, v.214. p.463
2. Yu.V.Gott, V.A.Shurygin, Nucl. Fusion, 1988, v.28. p.543

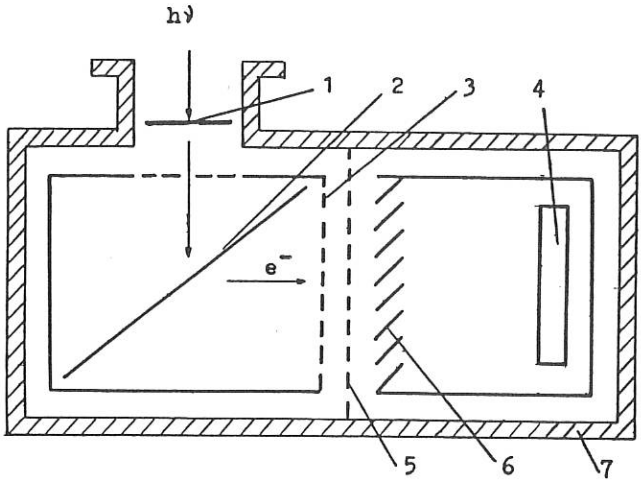


*Fig. 1*

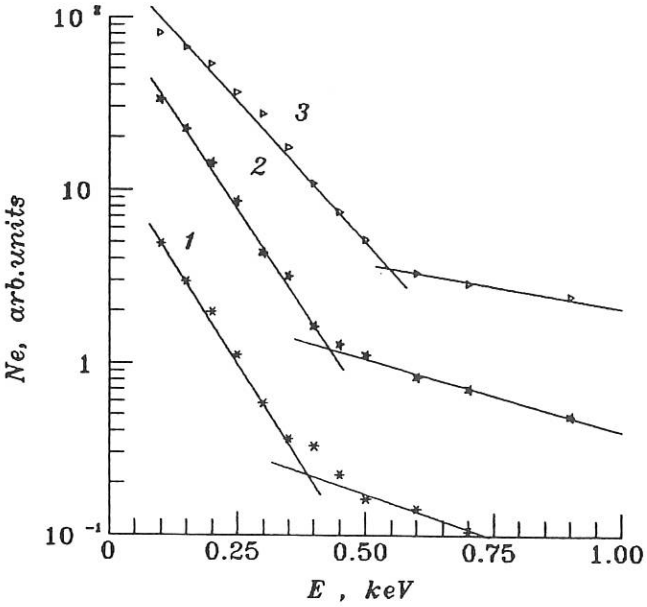


*Fig. 2*

# DETERMINATION OF POLOIDAL FIELDS BY THE PECULARITIES OF ELLIPTICALLY POLARISED PROBE WAVE IN TOKAMAK

Yu.N.Dnestrovskij, E.S.Lyadina, V.V.Chistjakov

I.V.Kurchatov Institute of Atomic Energy, Moscow, USSR

A technique of poloidal field distribution reconstruction by the characteristics of a probe wave with an arbitrary elliptic polarization has been developed. This technique is a generalization of poloidal field diagnostics by the Faraday effect. This technique allows one to carry out the measurements under operatins conditions, when the relationship

$$\lambda^3 B_T^2 \bar{n}_e \Delta l \ll 1$$

necessary for the diagnostics based on the Faraday effect, is not satisfied. In this case the following opportunity emerges:

1) to increase the wave length of a probe radiation;

2) to include the regimes with high density and with a strong toroidal field into the range of the regimes accessible to measurements;

3) to rise the magnitude of a registered signal, thus improving the signal-to-noise ratio.

The model of S.E.Segre [1] has been used for representing the evolution of electromagnetic wave polarization in plasma. The point on the Poincare sphere with longitude $2\psi$ and latitude $2\chi$ represents uniquely the state of the polarization ellipse: orientation $\psi$ and the ellipticity $\varepsilon=b/a$, $tg\ \chi = \pm b/a$.

The evolution of the polarization state for a plane electromagnetic wave propagating through the plasma is accompanied by the moving of the polarization vector S on the Poincare sphere and is described by the following differential vector equation:

$$\frac{d\bar{S}}{dl} = \bar{\Omega}(l) \otimes \bar{S}(l) \qquad (1)$$

where $$\bar{\Omega} = \frac{\omega}{c} (\mu_1 - \mu_2) \cdot \bar{S}_{c_2}$$

$\omega$ is the wave frecuency, $\mu_1$ and $\mu_2$ are the refractive indices of the slow and fast characteristic waves in local space point.

$\bar{S}_{c_2}$ is the polarization vector of the fast characteristic wave.

Vector $\bar{\Omega}$ depends on the wave length, total toroidal plasma current and toroidal magnetic field, on the magnitude and profiles of plasma density and poloidal magnetic field. Electromagnetic wave propagating through the plasma provides the information about local distributions of the poloidal field and plasma density which can be used for the reconstruction of these parameters.

An algorithm for solving a direct problem (1) allows to calculate several parameters of outcome elliptically polarised wave as a function of the position of the view chord at different initial probe wave polarizations. Such parameters are: Stokes parameters $s_1$, $s_2$, $s_3$, ellipticity $\varepsilon$, orientation $\psi$, the fraction of the output radiation power in the polarization orthogonal to the input polarization and the projection $E$ of the polarization ellipse into one of the coordinate axis which is experimentally registered.

The dependences of these characteristics on:

1) probe wave length;
2) magnitude and profile of plasma density;
3) direction and magnitude of toroidal magnetic field;
4) direction and magnitude of toroidal plasma current

have been studied.

The sensitivity of the registered signal to the variations of the current density profile is studed also (Fig.1).

The optimal relationship between the current direction in the plasma, toroidal field and the probe beam direction, providing the best sensitivity of the method, have been found. Fig.1 shows that the measurements are informative only at that side of plasma cross section where the probe wave and the vertical component of poloidal magnetic field have the same direction. Therefore the real diagnostic experiment should guide probe wave in two opposite directions inside/outside the plasma center.

It has been found that an elliptically polarized wave

provides a greater information about the poloidal field distribution near the plasma center , than a linear polarized wave. Fig.1 shows that for different plasma current profiles the magnitudes of the registered signals at (X=0) are different too. This fact allows to correct q-value determination in plasma center. For the linear polarized wave used by the Faraday effect diagnostic and for the axial symmetric model of plasma the different current density profiles have the same value of registered signal at (X=0). Therefore q(0)-value may be determined only from the gradients of the experimental curves. At the measurements of the elliptically polarized wave the different values of registered signal at (X=0) give absolut (but nonlinear) scale for q(0) determination. In this case the connections between registered signal and internal plasma parameter distributions are more complex (in particular, nonlinear), than for linear polarized wave, but these connections are not degenerated in plasma center.

The multichannel electromagnetic wave probing with known initial polarization allows to reconstruct the local space distribution of poloidal magnetic field with the using of pecularities of the outcome elliptically polarized wave.

An algorithm for solving a non-linear inverse problem on the recovery of a poloidal field, current density and q profiles has been developed. The distribution of the poloidal field belongs to the functional class:

$$B(r)=B_0(r)+B_1(r)$$

where $B_0(r)=2\ b\ r\ (1-r^2/2)$ corresponds to the parabolic distribution of the current density,

$$B_1(r)=r\ (1-r^2)^2 \sum_{i=0}^{m} c_i r^{2i}$$

simulates the deviation of the solution from $B_0(r)$.

Natural physical conditions

$B(0)=0$, $B(a)=b=0.2I_0/a$, $j'(0)=0$, $j(a)=0$ are satisfied.

The coefficients $c_i$ are determined by approximation of experimental data. The special regular algorithm for minimization of nonlinear discrepancy functional is designed.

The numerical simulation allows to study the processing accuracy and stability. Processing consists in the sequential solution of two inverse problems:

the first step: electron density profile reconstruction from phase measurement with the certain level of noise;

the second step: B(r) -profile nonlinear reconstruction with noisy profile n(r) and noisy value of registered signal E(x).

The variations of B(r),j(r),q(r)-profiles with the many realizations of experimental perturbations are studied. It has been found that j(r) reconstruction accuracy by elliptically polarized probe wave has some advantages in relation to the Faraday effect diagnostic.

Developed procedure for solving of nonlinear inverse problem allows to avoid some experimental problems and moves the difficulties from experimental into processing area.

Reference.

1.S.E.Segre, Plasma Physics, Vol.20,1978,p 295-307.

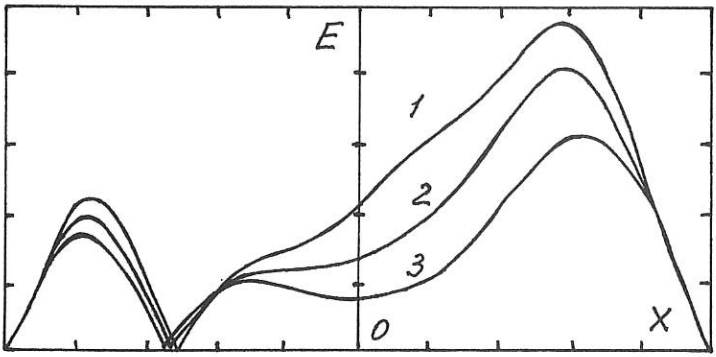


Fig.1. Registered signal functions for different current density profiles (1-peaked,2-parabolic,3-hollow profile), normalised to the same toroidal current value $I_0$. Initial probe wave has linear polarization orthogonal to the toroidal magnetic field, $\lambda$ =1mm ; T-10 plasma.

# SPACE-TIME TOMOGRAPHY PROBLEM FOR PLASMA DIAGNOSTIC

Yu.N.Dnestrovskii, E.S.Lyadina, P.V.Savrukhin

I.V.Kurchatov Institute of Atomic Energy, Moscow, USSR

## 1. INTRODUCTION.

Tomographic reconstruction of plasma parameters local space distributions is effective instrument for study of tokamak plasma internal structure.

The adaptation of the tomographic methods to fusion diagnostic has some difficulties. The main of them is limited number of chords and view directions. However physical tomography has an additional opportunity for use of different 'a priori' information, in particular the condition of continuous time evolution of reconstructed image.

If some fusion diagnostic maintaines rather high time resolution, it is possible to use the whole statistic information contained in total 3-D experimental data array for procedure regularization and reliable space-time image reconstruction. The multichannel 3-direction measurements of the soft X-ray emission from the T-10 plasma with high time resolution are the example of such a diagnostic.

## 2. METHOD.

The combined algorithm for tomographic reconstruction of 2-D emissivity space structure and for investigation of its time evolution is designed. It is based on classic Cormac inversion [1] using the expansion of the solution into trigonometric Furier series in angular component and expansion into orthogonal Zernicke polinomials $R_{ml}(r)$ in radial component:

$$g(r,\theta,t) = \sum_{m=0}^{M} \left[ g_m^{cos}(r,t)\, Cos\, m\theta + g_m^{sin}(r,t)\, Sin\, m\theta \right]$$

$$g_m(r,t) = \sum_{l=0}^{L} a_{ml}(t) R_{ml}(r)$$

The number of angular harmonics $(M+1)$ is equal to the number of view directions.

The central point of the processing is the determination of the optimal number $L$ in radial expansions, consistent with number of chords and with level of measurements errors. Unfortunately the adequate statistic estimations given by standard regression analysis at separate time cross-section are very sensitive to noises if number of chords is small (N=5-15) and plasma structure is rather complex.

The combined algorithm uses the universal method of stabilizing factors [2] for known ill-posed problem of summation of Furier series with noisy coefficients.

In this case the stabilized solution has radial component:

$$g_m(r,t)= \sum_l q_{ml}(t) a_{ml}(t) R_{ml}(r)$$

where $q_{ml}(t)$ factors ($0 \leqslant q_{ml}(t) \leqslant 1$) ensure the stable summation of the spatial expansion.

The optimal values of stabilizing factors can be obtained by the statistic analysis of time dependences $a_{ml}(t)$ of the spatial expansion coefficients (Fig.1). We use the smoothing spline approximation of noisy functions $a_{ml}(t)$ by cross validation method [3] without 'a priori' noise variances giving. It allows us to obtain some statistical estimation for variance $\sigma^2_{ml}$ of each noisy coefficient $a_{ml}$ and to construct optimal stabilizing factors

$$q_{ml}(t)=\left[1-(\sigma^2_{ml}/\bar{a}^2_{ml}(t))\right]\cdot\left[1+(\sigma^2_{ml}/\bar{a}^2_{ml}(t))l\right]^{-1}$$

These factors are consistent with the level of measurement errors. With increase of spatial harmonic number $l$ variance $\sigma^2_{ml}$ increases also and stabilizing factor $q_{ml}(t)$ tends to zero. The stabilizing factors procedure realizes the adaptive filter selecting the valid signal and surpressing the noisy component. In fact this method takes into account the real spectral characteristics of signal and noise. In comparison with abrupt limiting of spatial harmonics number this method allows to surpress artifact osciillations of reconstructed image at plasma edge.

The use of the spline approximation for the time dependences of the coefficients $a_{ml}(t)$ ensures the smooth time evolution of the reconstructed image.

Numerical simulation have defined the processing accuracy and insensitivity to noise at real detector configuration.

Space-time numerical procedure is realized on IBM PC-XT/AT. Grafic service allows one to show the continious film on time evolution of contour plots and profiles for total reconstructed emissivity (Fig.2) and for several perturbation modes.

## 3. CONCLUSION.

The study of time dependences of the Fourie-Zernicke expansion coefficients gives the criterion for optimal regularization of the processing procedure and allows to get the smooth time evolution of the reconstructed image.

## REFERENCES.


1. Cormac A.M., J.Appl.Phys.,1963,V.34,N.9
2. Tichonov A.N., Arsenin V.J., Metodi reshenija nekorrektnich zadatsh, Nauka,1979.
3. Graven C., Wahba G., Numer.Math.,1979,V.31,N.3,p.377-403.


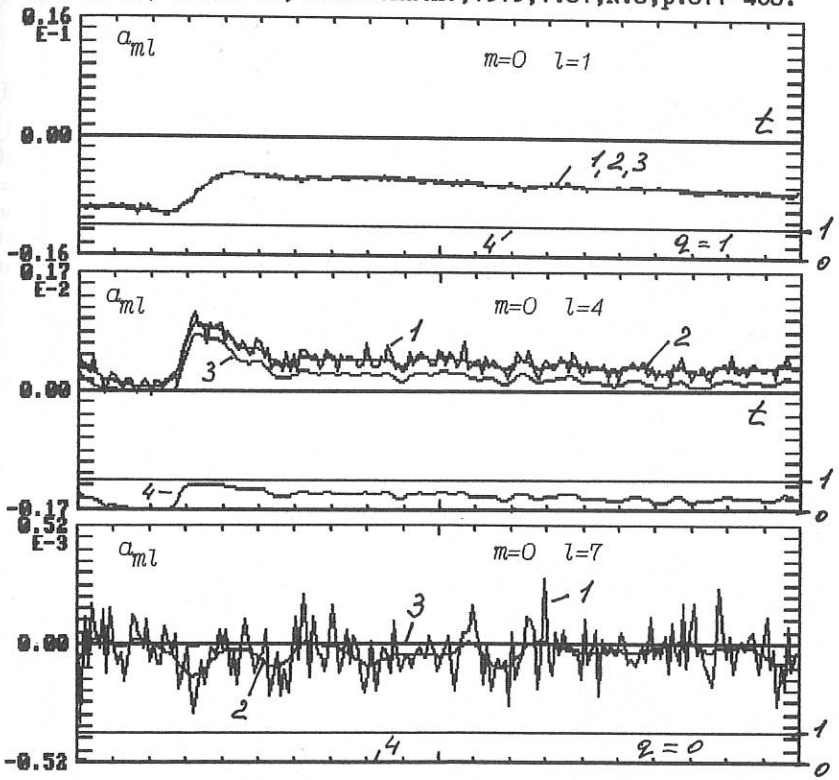


Fig.1 Typical time dependence of the coefficients $a_{ml}$ of the solution spatial expansion at several $l$:

1- noisy value of the coefficient
2- spline fitting,
3- stabilized value of the coefficient
4- stabilizing factor $0 \leq q_{ml}(t) \leq 1$

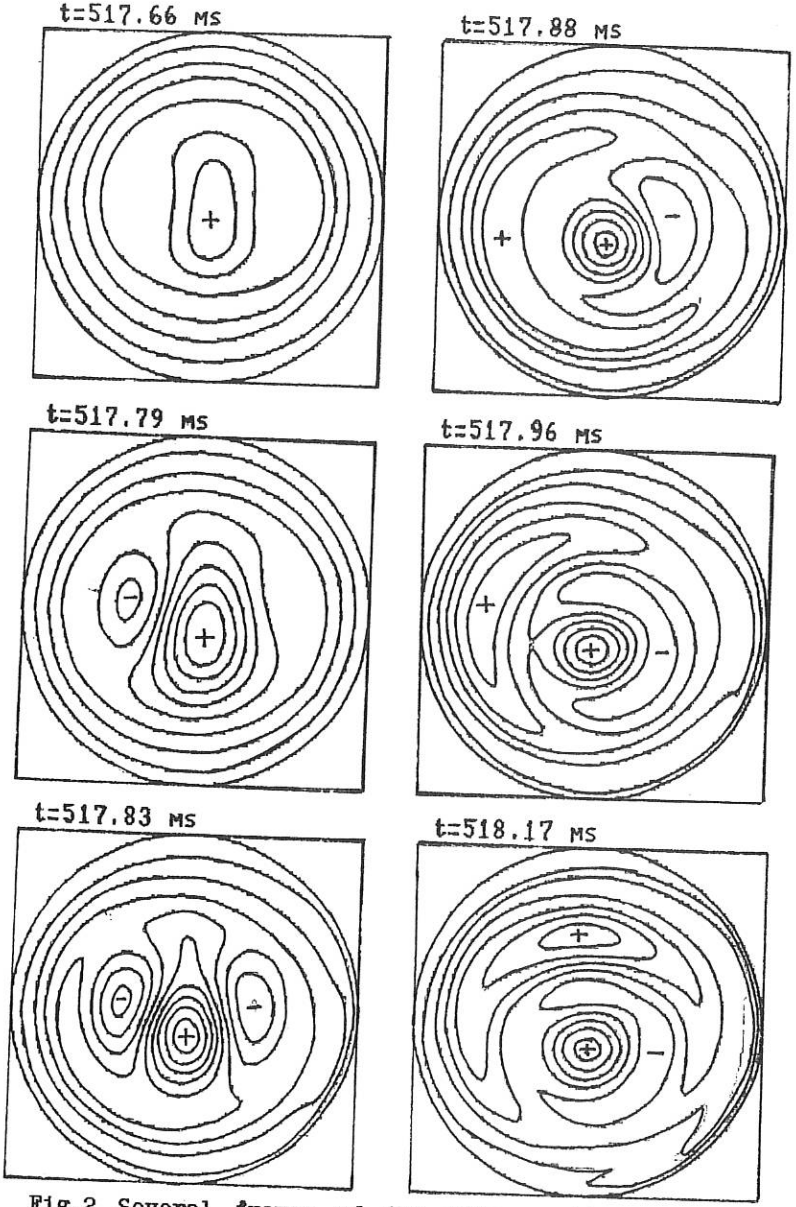


Fig.2 Several frames of the film on time evolution of contour plots for reconsructed soft X-ray emissivity during the sawtooth crash in the T-10 plasma.

# ELECTRON AND ION TAGGING DIAGNOSTIC FOR HIGH TEMPERATURE PLASMAS

F. Skiff, D. A. Boyd and S. C. Luckhardt*

Laboratory for Plasma Research
University of Maryland, College Park, MD, USA

*Plasma Fusion Center
Massachusetts Institute of Technology, Cambridge, MA, USA

## I. Introduction

Progress in experimental science is closely linked to the development of measurement techniques which not only address the appropriate variables but also provide sufficient precision. Especially in the study of complex systems, such as tokamak plasmas, the issue of thorough diagnostics is essential in order to test the validity of theories as well as to define the parameters for improved theories. Unfortunately, the study of plasma transport processes has, for many years, been impeded by the fact that theoretical and experimental studies typically involve discussions of different variables. Theory and experiment are only indirectly related. Measurements of the variables necessary to discriminate between different theories are frequently not available.

A second difficulty in the study of transport has to do with the nature of the processes themselves. Transport is inherently a nonlocal process. If some physical quantity is transported, then it is moved from one location at one time to some other location at a later time. Therefore, neither point measurements nor global average measurements directly measure transport. Global measurements may provide the bounds or the scaling properties of transport, and point measurements may give an indication of the state of the plasma, but neither approach indicates how transport has actually occurred. This is particularly true in collisionless plasma where the macroscopic observables may be influenced by a variety of microscopic processes. For this reason, the development of new and appropriate diagnostics is of vital concern to the understanding of transport. In particular, diagnostics are needed which address the processes of transport as directly as possible.

Relatively recently, the study of ion transport processes has made significant process through the introduction of test-particle techniques.[1–3] Test particles usually are chosen to be identical to a given component (ions or electrons) as regards their dynamics, but somehow distinguishable from the bulk plasma for the purposes of diagnostics. In the case of the ion transport experiments, test particles are selectively produced in space, time, and velocity by means of laser-optical pumping of ions into stable or metastable quantum states. Since the dynamics of ions, in collisionless plasma, depends only on

the ratio of charge to mass, these test ions have the same dynamics as the bulk ions and are distinguishable through laser fluorescence on transitions from the test particle quantum state. This technique is also known as "tagging" because the test particles are effectively labeled. Since the plasma is "seeded" with test-particles at one location and the position and velocity of test particles is subsequently detected, test particle methods provide a direct measure of particle transport. Depending on the method of detecting test particles, information on the transport of energy and momentum may also be available.

Due to the appropriateness of test particle methods to the study of transport, it would be advantageous to extend their application to electrons and to high temperature plasmas. Unfortunately, electrons have no known internal structure. Furthermore, both spin states are reasonably stable in magnetized plasma, and the spin orientation is very difficult to measure. Collisionless (high temperature) plasmas do, however, support ballistic (free streaming) perturbations which may be generated so as not to significantly produce macroscopic fields.[4] Furthermore, these perturbations may be selectively excited and detected through wave-particle interaction.

## II. Theoretical Basis

Ten years after Vlasov began the kinetic theory of plasma waves, Van Kampen showed that collisionless plasmas support both wave-like and free-streaming perturbations.[4] Because fields and waves depend on the moments of the particle velocity distribution function, perturbations $\delta f$ of the distribution functions which have very small moments (e.g., $\int \delta f dv \sim 0$) will propagate with the unperturbed particle motions. The particle motions themselves will be unperturbed because there is no self-consistent field generated.

In many presentations of plasma wave theory, ballistic perturbations tend to "fall through the cracks" because only the Fourier space dielectric $\epsilon(\omega, k)$ is considered. Recently, there has been theoretical work which naturally includes ballistic perturbations (or "modes") and which demonstrates their role in wave absorption.[5-6] Wave absorption may be viewed, in this context, as a mode conversion to ballistic modes. Such a formulation avoids the usual problems of the linear theory which does not conserve energy (thus the need for quasilinear theory). With the advent of these more appropriate theoretical formulations, the analysis of ballistic mode excitation through wave absorption is made clear. In general, the particles which are involved in the ballistic mode created by a ("pump") wave satisfy the wave-particle resonance condition

$$\omega - k_{\|} v_{\|} - n\omega_c/\gamma.$$

The detection of ballistic modes may be performed by approximately the inverse process of their excitation. Wave absorption, as measured via the transmission coefficient of a "search" wave, is a sensitive measure of the phase space density of resonant particles. These are the particles which satisfy the resonance condition

$$\omega' - k'_{\|} v_{\|} - n'\omega'_c/\gamma \sim 0$$

with $\omega'$ and $k'_{\|}$ corresponding to the search wave. The harmonic number of the search interaction $n'$ need not be the same as for the pump interaction and the local electron cyclotron frequency $\omega'_c$ (given by the magnetic field) may also be different. A Vlasov tagging signal is obtained if ballistic modes generated by the absorption of the pump wave travel to the location of the search wave and also satisfy the corresponding resonance condition. Three conditions are important, therefore, for the diagnostic signal. Firstly, the spatial separation of the beams will imply spatial transport. Secondly, if the resonance conditions are tuned so as not to overlap, then velocity space diffusion is indicated. Finally, the time of flight or time delay between the pump and search signal indicates the speed of transport. In practice, the transfer function between the pump and search beams is the measured quantity as a function of the wave frequencies $(\omega, \omega')$, wavenumbers $(k_{\|}, k'_{\|})$ and the spatial separation.

An analogy can be drawn here between the laser-induced transitions used in ion test-particle techniques and the free-free transitions produced by wave particle interaction which produce and detect ballistic modes. The concept of a transfer function is also central to the interpretation of ion tagging.[3,7] Figure 1 illustrates a possible combination of wave-particle resonance conditions for electron Vlasov tagging. For perpendicular propagation ($k_{\|} = 0$) of, say, the pump beam the resonance condition is a circular arc in velocity space. For an oblique search beam various curves are obtained depending on the angle of propagation. Different sets of curves are obtained for different wave frequencies. If pump and search curves intersect (as in Fig. 1) then velocity space diffusion may not be necessary to obtain a signal.

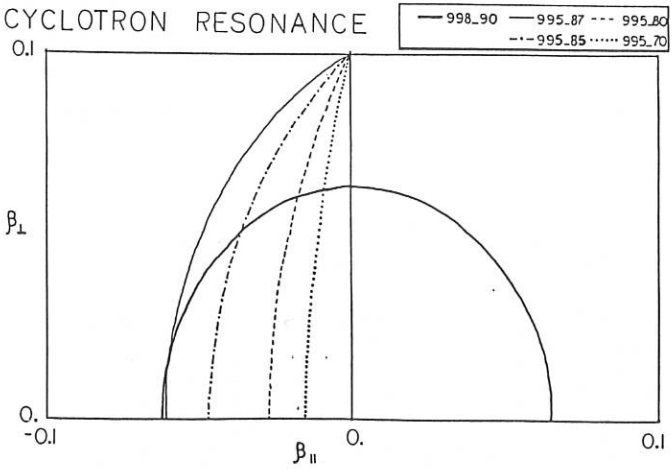


Figure 1. Resonance condition in velocity space. Circular arc, $\theta = 90°$, $\omega/\omega_c = .998$; other curves $\omega/\omega_c = .995$ and $\theta$ as indicated.

III. Experiments

A schematic view of Vlasov tagging is shown in Fig. 2. The first objective is to create and detect ballistic perturbations. Experiments are planned for the Versator tokamak involving the lower-hybrid system, an ECRH system, and the electron cyclotron transmission diagnostic. The first experiments will use short pulses of lower hybrid waves or electron cyclotron waves to generate ballistic perturbations and the transmission diagnostic to detect them.[8]

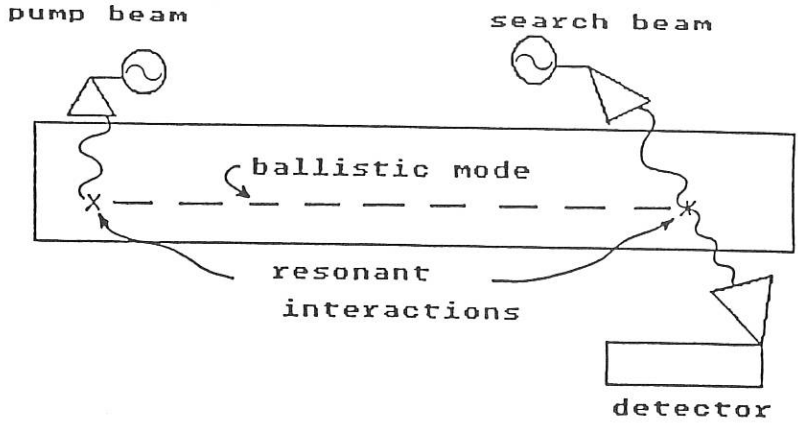


Figure 2. Experimental set-up for electron Vlasov tagging.

References

1. R. A. Stern, D. N. Hill, and N. Rynn, Phys. Lett. A **93** (1983) 127.
2. R. McWilliams, D. N. Hill, N. S. Wolf, and N. Rynn, Phys. Rev. Lett. **50** (1983) 836.
3. F. Skiff, T. N. Good, F. Anderegg, and P. J. Paris, Phys. Lett. A **137** (1989) 57.
4. N. G. Van Kampen, Physica **27** (1955) 949.
5. L. Friedland and G. Goldner, Phys. Fluids **29** (1986) 4073.
6. H. Ye and A. N. Kaufman, Phys. Rev. Lett. **60** (1988) 1642.
7. F. Skiff et. al., Plasma Phys. Contr. Fus. **31** (1989) 1569.
8. R. K. Kirkwood, Ph.D. Thesis, M.I.T., Cambridge, Mass., August 1989.

# TRANSIENT INTERNAL PROBE DIAGNOSTIC

Dr. R.J. SMITH, E.J. LEENSTRA

AERP, University of Washington, Seattle, Wa.

## INTRODUCTION

Internal probing of laboratory plasmas on a transient time scale is becoming popular without its generality being fully realized. What is meant by "transient internal probing" is the introduction of foreign material into a plasma for a time interval much less than the plasma's lifetime and in such a manner that unperturbed properties of the plasma state can be measured. In general, the plasma survives this intrusion. Examples are: retractable Langmuir probes to study the edge region of tokamaks involving the mechanical insertion and withdrawal of a probe, the injection of low Z pellets such as carbon, lithium or deuterium to study transport, internal magnetic fields from Zeeman splitting of ablated material and heat loading, and, if the plasma is translatable, the insertion of a probe array in the plasma's path to map the equilibrium.[1,2,3] This paper investigates a transient internal probe (TIP) that encompasses all of the above in principle and is of greater generality. The proposed device is a diamond projectile that is fired through the plasma at high speeds and capable of measuring some properties of the plasma state along its path.

## THE TRANSIENT INTERNAL PROBE

Table 1 details the properties of materials that are commonly considered for plasma probe jackets. Diamond isn't usually included in the list but for projectile size probes, diamond is a possibility. The figure of merit for diamond, as shown in the last column of Table 1, is 6000 times better than that of quartz. Diamond has the highest thermal conductivity of any material, a very high boiling point, high dielectric strength, introduces only low Z impurities into the plasma, and is transparent over a wide optical range. Diamonds, of the size needed for projectiles, are not expensive, are synthetically produced as single crystals and can be appropriately machined to carry a payload.

A translating probe in a laboratory plasma is akin to a satellite that would be used to study astrophysical plasmas such as the earth's ionosphere or magnetosphere. The TIP could contain microcircuits and a laser diode that would relay analog signals from its sensors to the lab. Even an energy source is present via magnetic induction from the spatially inhomogeneous fields and the probe's velocity.

**Table 1.**
**Properties of some common probe materials.**

| Material | $T_B$(°K) | ρ | κ | C | $t_BP^2$ |
|---|---|---|---|---|---|
| Quartz | 1900 | 2.65 | .015 | .74 | $9x10^{4b}$ |
| Inconel | 1700 | 8.25 | .3 | .2 | $1x10^{6b}$ |
| Alumina | 2300 | 2.6 | .26 | .26 | $1x10^{6b}$ |
| Diamond | 4000[a] | 3.5 | 26[a] | .52 | $5.8x10^{8}$ |

[a] CRC Handbook of Chemistry and Physics, 1984-5, 65th Ed.
[b] Reference 5.

In order to measure magnetic fields along the TIP's trajectory, a magneto-optic material of high Verdét constant can be placed on the TIP as shown in Fig. 1. By shining laser light from the lab to the TIP, retro-reflecting the light back to the lab and detecting the rotation of the plane of polarization of the laser light, a magnetic field measurement can be made. To give one an idea of what is possible, the properties of the semi-magnetic semiconductor $Cd_xMn_{1-x}Te$ are briefly detailed.[5,6,7] By changing x, this crystal can be tailored to the laser's frequency, for HeNe at 633nm, x would be .42. A high Verdét constant of 15° per cm-gauss is obtained. The temperature dependence of the Verdét constant can also be zeroed to first order for a given frequency. Such sensitivities would allow the measurement of sub-milliTesla fields using miniature crystals of the order of 1 mm in size with the use of known detection schemes. The bandwidth of the crystal is greater than 3 GHz allowing the characterization of RF heating and many low frequency instabilities appearing in the magnetic field.

Using laser light of three different frequencies, three components of the field can be simultaneously measured as shown in Fig. 2. The diamond's surface is angled to the laser beam due to light reflected from the the diamond-vacuum interface. The TIP is of 1 carat size and would be mounted in a sabot as shown. This is necessary since the diamond will ruin the muzzle of the gun, being much harder than the steel. A sabot is also advantageous for a number of reasons, first the jerk from the acceleration of the TIP can be very high and some of this can be absorbed in the sabot, second, the diamond does not have to be made cylindrical in shape or used to seal the muzzle, third, the sabot being made from soft material can easily be spun up from the rifling of the barrel allowing the TIP to fired with high rotational speeds, and fourth, the sabot can be used to block some of the blast from

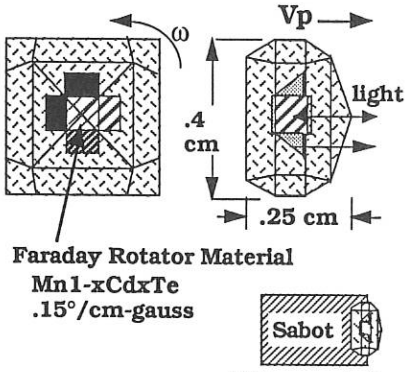


**Fig. 2**
**Schematic of a TIP with a magneto-optic sensor to measure 3 orthogonal field components.**

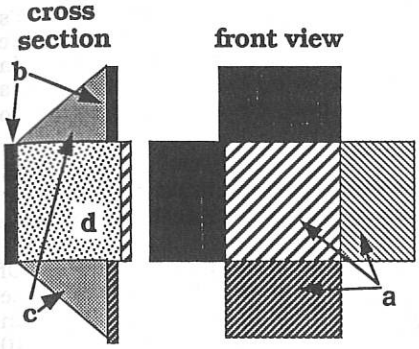


a: Bandpass filters.
b: Dielectric mirrors (3x)
c: 45° reflectors (4x)
d: Verdét material

**Fig. 2**
**Detailed view of sensor.**

following the TIP. The velocity of the probe is expected to be in excess of 5 km/sec. This is accomplished using a two stage light-gas gun and presents no significant demands on the technology. The light-gas gun would use helium or deuterium gas so that the vacuum system would not be compromised. It may be hard to control the flight characteristics of the TIP. Tumbling can be circumvented by spinning the TIP and wobble can perhaps be minimized or tolerated.

A measurement of local plasma density along the probe's trajectory can also be measured optically. Many electrical signals can be converted to optical signals using this crystal as an electo-optical conversion device. If microcircuits are incorporated then various sensors can be added to the TIP, for instance, Langmuir probe, capacitive probes, etc. Not only can measurements taken, but tasks can be performed. Impurities can be deposited on the TIP using diamond deposition, allowing either low Z impurities that would be better tolerated by the plasma or high Z impurities that would radiate longer to be deposited in specific regions of the plasma. Deuterium ice payloads can be loaded into a diamond shell. The shell would offer some protection and greater injection speeds allowing the deposition of the deuterium at much deeper regions than is presently possible, possibly allowing fueling of the plasma at the magnetic axis, for instance.

ELECTROSTATIC SHEATH DEVELOPMENT AND HEAT LOADING

A characteristic time for probe effects to become important is the time required for the surface of the probe to reach its boiling point, $t_B$. The heat loading is strongly dependent on the plasma's temperature, T and density, n and is given by[4]

$$P(n,T) = \frac{n}{\sqrt{2\pi m_i}} \sqrt{T}\, T \left(\ln \sqrt{\frac{m_i}{m_e}} + 4\right).$$

For a deuterium plasma this expression gives $P = 3.6\times10^{-13}\ n(cm^{-3})\ T^{3/2}(eV)\ W/cm^2$. The energy loading of the probe is essentially the particle collision rate times the average energy per particle incident on the probe's surface. However the electrostatic potential of the probe is the floating potential, $V_f$, which is negative with respect to the plasma's potential due to the higher mobility of the

electrons. The probe is essentially shielded from most of the electron's heat flux. The probe is further thermally insulated by strong magnetic fields and a sheath of colder particles in the vicinity of the probe. In general the calculations may be considered to be conservative. $t_B$ has been calculated from the one dimensional heat equation and found to be[7]

$$t_B P^2 = \frac{T_B^2(\pi\kappa\rho C)}{4},$$

where $\kappa$ is in W/°K-cm, $\rho$ in g/cm$^3$, C in J/°K-g, $T_B$ in °K is the boiling temperature and P is the heat flux incident on the probe's surface in W/cm$^2$. Table 1 details these values for the four probe materials.

Fig. 3 shows the probing time in some contemporary devices. Of significance, are the 400 μsec time in DIII-D and the 40 μsec time in LSX. Both are considered to be exemplary plasmas in their class. More detailed results on internal probing of magnetically confined plasmas will be presented and possible studies concerning the LSX-FRC and the DIII-D tokamak will be discussed from the point of view of a TIP diagnostic.

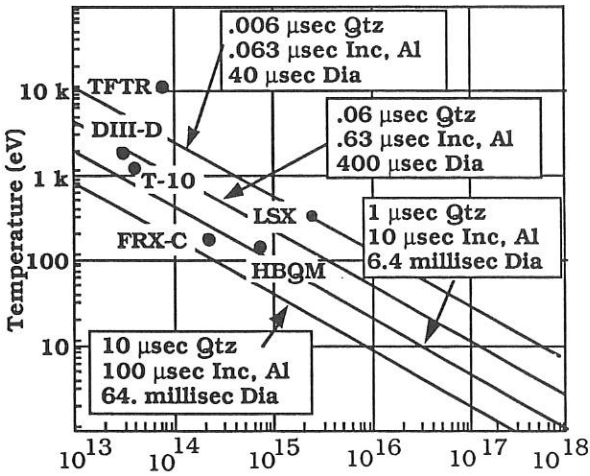


**Fig. 3**
**Boiling times for probe materials in various magnetic fusion devices.**

REFERENCES


(1) M. Lenoci, G. Haas, IPP (Garching) Report III/113 (July 1986)
(2) M. Tuszewski, Phys. Rev. Letters, **63**, 2236 (1989)
(3) E.S. Marmar, Bulletin of the A. P.S., (1987)
(4) R.H. Lovberg, Plasma Diagnstics, Edited by K. Huddlestone et. al., Academic Press, 69 (1968)
(5) N. Kullendorff and B. Hok, Applied Physics Letters, **46**, 1016 (1987)
(6) J.A. Gaj, et. al., Solid State Communications, **25**, 193 (1978)
(7) S.J. Martin and M.A. Butler, SPIE, **566**, 197 (1985)

# ON THE POSSIBILITY OF LASER DIAGNOSTICS OF ANISOTROPICALLY SUPERHEATED ELECTRONS IN MAGNETIC FUSION SYSTEMS

A.B.Kukushkin
I.V.Kurchatov Institute of Atomic Energy,Moscow,USSR

The anisotropically superheated electrons (ASE) are known to be generated by a resonance interaction of high-frequency electromagnetic waves with electron plasma. Under definite conditions the ASE energy may essentially exceed ( by the order of magnitude or even more) thermal energies of background electron plasma, the ASE distribution in pitch-angle being concentrated around definite directions. This situation is typical for, e.g., the electron cyclotron heating of magnetic mirror plasmas (generation of "sloshing" electrons) [1] and for current drive in tokamaks by means of lower-hybrid or,sometimes, electron cyclotron waves [2].

In this work, an analysis of the possibility of the ASE laser diagnostics is based on the calculations of Thomson scattering of laser radiation by plasma electrons. The model electron velocity distribution functions, which provide qualitative description of the ASE peculiar features, were used in calculations. The analysis of the resulted spectral and angle distributions for scattered radiation leads to following conclusions:

1) if ASE effective temperature exceeds the temperature $T_e$ of background plasma by a factor of only few units , the ASE give negligible contribution to "red" wing of scattered radiation spectrum even for relative concentration of the ASE in background plasma $\Delta=10\%$ . This fact, in turn, allows

1a) to determine $T_e$ by applying of conventional "maxwellian" procedure to "red" wing of Thomson spectrum (see,e.g.,[3] and cited there references);

1b) to separate ASE contribution to total spectrum by means of the subtraction of background plasma spectrum from "blue" wing of total spectrum;

2) the availability of adequate interpretation of ASE

Thomson spectrum depends on $\Delta$, laser wavelength $\lambda_o$ and scattering geometry:

2a) the choice of scattering geometry (the directions of incident $\vec{n}_o$ and scattered $\vec{n}$ radiation) should be based on the fact that an increase on electron energy leads to the shift of scattered spectrum towards larger radiation frequencies $\omega$ and to concentration of scattered radiation angular distribution around the directions (in velocity space) of ASE formation . Since scattered intensity with fixed $\omega$ is determined by the electrons located within the definite plane in velocity space $(\omega - \omega_o)=\vec{v}/c*(\omega \vec{n} - \omega_o\vec{n}_o)$, favourable scattering geometry corresponds to the intersection of ASE velocity distribution by a mentioned planes at as large angle between the plane and ASE direction as possible. Most favourable conditions for the determination of ASE velocity distribution occurs when the ASE are formed along one definite direction (e.g.,for lower-hybrid heating). In this case one has most strict correlation between $\omega$ and the mean energy of the corresponding cross-section of ASE distribution function.

2b) The ASE Thomson spectrum may be allocated within a desirable interval of the values of scattered radiation wavelength $\lambda$ by means of an adequate choice of $\lambda_o$. Thus, an operation on the first harmonic of neodimium glass laser leads to the values of $\lambda$ which are typical for "blue" wing of the spectrum corresponding to scattering by background plasma of usually used second harmonic radiation of the same laser.

In what follows, described approach is applied to the diagnostics of "sloshing" electrons which are generated by electron-cyclotron heating of plasma in mirror magnetic trap OGRA-4 (see [4]). The distribution function of sloshing electrons may be considered as localized ( in velocity space) in the vicinity of two (symmetrical with respect to magnetic axis) cones with opening angle $\vartheta_{SL}= \arcsin((B_o/B_s)^{1/2})$, where $B_s$ is magnetic field value on the resonance surface, $B_o$ is minimal value of B on a given force line [1]. The vector $\vec{n}_o$ is orthogonal to magnetic axis and to vector $\vec{n}$, the angle between

$\vec{n}$ and magnetic axis $\vartheta_n=60^o$, polarization vectors of incident and scattered radiation are coincident, both being orthogonal to the "scattering plane" which contains $\vec{n}$ and $\vec{n}_o$.

Fig.1 gives exact relativistic Thomson scattering cross-section $\sigma$ which is differential with respect to $X=(\lambda/\lambda_o-1)$ and solid angle, and is expressed in terms of squared electron classical radius. The curve (1) corresponds to Maxwellian distribution function with $T_e=5$ keV (no particles in the loss cone $\vartheta<45^o$). Some deviation from conventional Maxwellian spectrum (curve (2)) prevents from using of universal "Maxwellian" procedure for the determination of $T_e$,which relies on existing approximate analytic formulas (see,e.g.,[3]). Therefore, the temperature dependence of the signal ratio for arbitrary pair of spectral channels should be calculated and then compared with corresponding experimental value to give finally $T_e$. Repetition of this procedure for different pairs of spectral channels allows to evaluate the accuracy of the result obtained, and ,moreover, permits to verify the very fact of one-parametrical (namely,temperature) dependence of ASE distribution function. Other curves on Fig.1 corresponds to ASE Thomson scattering cross-section weighted by the relative concentration of the ASE plasma:$\sigma=\sigma_{ASE}\Delta/(1-\Delta)$. Here $\Delta=0.1$, $\vartheta_{SL}=60^o$ (probing of magnetic trap central point), ASE effective temperature $T_{SL}=15,30,50$ keV (curves 3,4,5). Applying then a procedure, which is in general analogous to that described above for the determination of background plasma temperature $T_e$, one may find $T_{SL}$. For the ASE Thomson spectrum to be detected, the requirements of 2b item should be satisfied; as to item 2a ,existing scattering geometry described above is found to be quite satisfactory.

Investigation of the dependencies of Thomson spectrum on ASE parameters reveals that it is the peculiar features of ASE distribution function that permit to estimate the main parameters of the ASE without solving the "ill-posed" problem of a reconstructing the electron velocity distribution

function( in general case, non-maxwellian, non-one-parametrical ) from it´s functional ( scattered radiation spectrum, which is an integral over electron velocities ).

The author is indebted to A.A.Skovoroda and V.A.Zhiltsov for valuable stimulating discussions.

REFERENCES

1. Timofeev A.V.// In.: Voprosy teorii plasmy. Moscow, Energoatomizdat, 1985,Vol.14,P.56-226.
2. Kolesnichenko Ya.I., Parail V.V., Pereverzev G.V.// Ibid., 1988, Vol.17,P.3-156.
3. Kukushkin A.B.,Leneva A.E.,Pergament V.I.// In.:Diagnostika plasmy. Moscow, Energoatomizdat, 1986, Vol.5, P.70.
4. Belavin M.I. et.al.// Voprosy atomnoi nauki i techniki, seriya Termoyadernii sintez. Moscow, CNIIatominform, 1988, Vol.1,P.51.

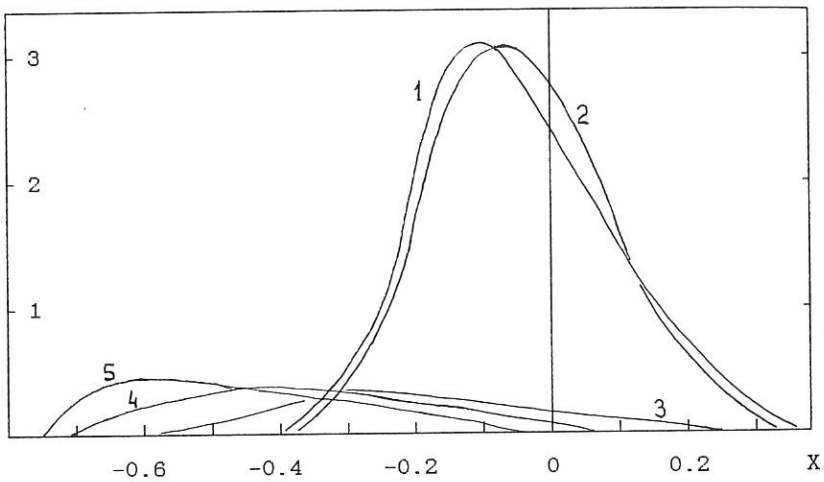


Fig.1

# COLLECTIVE SCATTERING SPECTRA WITH ANISOTROPIC DISTRIBUTIONS OF FAST IONS AND ALPHA PARTICLES

*Galbiati S., Lontano M., Tartari U.*

*Istituto di Fisica del Plasma, EURATOM-ENEA-CNR Ass., Milano, Italy*

Collective Thomson Scattering (CTS) is known to be strongly influenced by fast ion and/or alpha particle populations. This taking into account, it has seemed interesting to investigate the effects of the anisotropies often involved in the production, heating, confinement and slowing down of these populations as concerns both the amount of additional information made available by CTS measurements and the possibly conflicting role of the different non-thermal features. We present preliminary results on two kinds of anisotropies: a) that associated with the perpendicular acceleration of the (minority) ions in ICRH /1/ and LHRH /2/, leading to high temperature ratios $R_T = T_\perp/T_\parallel$ for the heated species, and b) that associated with transverse particle losses due to orbits intersecting the walls /3/ and/or due to the magnetic field ripple /4/. Anisotropies of the former type are expected to be dominant in the heated region of the plasma, usually the central one; that of the latter will be mainly significant off-axis. A kind of complementarity therefore exists, while the above mentioned anisotropies in principle can involve both fast ions and alpha particles.

**Anisotropy induced by external heating** - The non-isothermal and anisotropically-distributed (minority) population has been modeled by assuming a bimaxwellian distribution in a otherwise thermal plasma. For not too low magnetic angles $\phi$ ( $\sin\phi = (\underline{k} \cdot \underline{B})/kB$, k being the fluctuation wave vector), the spectral density function $S(\underline{k}, \omega)$ can be obtained simply by defining an *effective temperature* for the species (i), given by

$$T_{eff}^{(i)} = T_\perp^{(i)} \cos^2\phi + T_\parallel^{(i)} \sin^2\phi \,, \qquad (1)$$

where $T_\perp^{(i)}$ and $T_\parallel^{(i)}$ are the perpendicular and parallel temperatures, with an associated unidimensional velocity distribution. The energy spread due to $T_\perp^{(i)}$ and to $T_\parallel^{(i)}$ will determine the shape of the CTS spectra at large and small $\phi$ -values, respectively.

Numerical simulations of $S(\underline{k}, \omega)$ have been performed with reference to JET, where NB+ICR heating has been applied to D plasmas with H or $He^3$ minority species, leading to an estimated mean energy of the fast ions of $\simeq$ 1MeV with $R_T$ up to 50 /5/. Fig. 1 shows simulated CTS spectra for JET with a ICR-heated $He^3$ population and $R_T = 50$. It is seen that the effect of the suprathermal population largerly dominates in the $\omega_{pD}$ region and above ($f \geq 2GHz$), while it extends for a range $\Delta f \simeq 10\ GHz$. The spectral level is 1 ÷ 3 orders of magnitude lower than that of the thermal ion feature. In many respects the spectra are similar to that produced by a population of alpha particles of comparable concentration /6/; the general conditions for diagnosability are therefore also quite similar. Even taking into account that the suprathermically heated species can be selectively chosen (for instance, D ions in a D-T plasma) and thus that the anisotropy induced by external heating does not

directly affect the alpha particles, it is apparent that the two conflicting populations can be discriminated only if the anisotropy associated with the lower-mass heated ions is evidenced by CTS measurements at two sufficiently different $\phi$ -angles.

**Anisotropies due to transverse losses** - In a D-T toroidal plasma the energetic ($\mathcal{E}_\alpha \leq 3.52 MeV$) alpha particles (and eventually, although at a lower extent, the anisotropically heated minority ions) can escape from the confinement region since large perpendicular energies favour trapping in the magnetic field ripples, with consequent drift towards the wall, and/or make the drift surfaces "touch" either the chamber wall or the limiter /7/.

The effect of ripple-induced transverse losses mainly consists in a symmetric depletion of the fast ion distribution function at small $v_\parallel$ values. We represent this situation by an *inverse loss-cone distribution* of the form

$$f_{r,\alpha}(v,\theta) = \frac{1}{1-\eta_0} f_{0,\alpha}(v)\, H(|\eta| - \eta_0), \tag{2}$$

where $f_{0,\alpha}$ is the isotropic alpha distribution, solution of the unidimensional Fokker Planck equation for the collisional slowing down; $\eta = \cos\theta$ , $\eta_0 = \cos\beta_0$, $\beta_0$ defining the inverse loss-cone region : $-\eta_0 < \eta < +\eta_0$. Being interested in the high frequency part ($\omega \gg k V_{t,D}$) of the spectra, we shall neglect the isotropic low energy part of the alpha distribution (for $\mathcal{E}_\alpha < E_r$, where $E_r$ is defined in /4/).

The asymmetric (in $v_\parallel$) losses due to the intersection of the alpha drift surfaces with the walls can be approximated by generalizing eq.(2) in the form:

$$f_{so,\alpha}(v,\theta) = \frac{1}{1-\dfrac{\eta_1-\eta_2}{2}} f_{0,\alpha}[H(\eta-\eta_1) + H(\eta_2-\eta)]\,. \tag{3}$$

Eq.(2) is recovered for $\eta_2 = -\eta_1$. Since we are interested in the effects of the anisotropies and asymmetries, we can describe the alpha particle distribution merely by a high temperature Maxwellian, $f_{0,\alpha}(v) = f_{M,\alpha}(v)$.

The unidimensional distribution $F_\alpha(u) \equiv \int d^3v \delta(u - \underline{k}\cdot\underline{v}/k) f_\alpha(v,\theta)$ , directly involved in the unmagnetized $S(\underline{k},\omega)$, is given by $F_\alpha(u) = (n_\alpha/\pi^{3/2}V_\alpha^3)F(u/V_\alpha)$, where

$$F(x) = \frac{2e^{-x^2}}{1-\dfrac{\eta_1-\eta_2}{2}} \int_{-\infty}^{+\infty} d\xi e^{-\xi^2} \left[ H(v_\parallel)\, erf\left(\sqrt{X_1(\xi,x)}\right) + H(-v_\parallel)\, erf\left(\sqrt{X_2(\xi,x)}\right)\right],$$

$$X_i(\xi,x) \equiv \xi^2(t^2 t_i^2 - 1) - 2\xi x t(1+t_i^2) + x^2(t_i^2 - t^2), \tag{4}$$

and $t = \tan\psi$, $\psi = \pi/2 - \phi$, $t_i = \tan\beta_i$, $i = 1, 2$. Being very energetic ($T_D \ll \mathcal{E}_\alpha \leq 3.5 MeV$), the alpha particles can be taken as unmagnetized. Further, for sufficiently high values of the Salpeter parameter $\alpha$ , provided that:

$$\alpha^4 \sin\phi > \frac{1}{4\sqrt{\pi}} \frac{n_e}{n_\alpha} \frac{V_\alpha}{V_{Te}}\,, \tag{5}$$

in the range $\omega \geq \omega_{pi}$ the ratio between the alpha and the electron feature, $S_\alpha/S_e$, can become large /6, 8/. Thus $S(\underline{k}, \omega)$ can be approximated by $F_\alpha(u)$ alone, obtaining

$$S(\underline{k}, \omega) \simeq \frac{8\pi}{kn_e} F_\alpha(\omega/k). \tag{6}$$

Figs. 2 and 3 show the approximated CTS spectra obtained under the assumptions mentioned above and refer to the distributions (2) and (3), respectively, for different values of the magnetic angle $\phi$ . A thermal ion component has been included to represent the frequency range covered by the ion feature. For $\phi > 10°$, in the range $1.5 < f < 4.2$ GHz, $S_\alpha$ directly determines the shape of the spectral density function. The density fluctuations propagating at small $\phi$ angles turns out to be particularly sensitive to the transverse losses. Fig. 2 shows the effect of the symmetric anisotropy of eq. (2) for $\beta_0 = 75°$. The CTS signal is depressed in the low frequency part with decreasing $\phi$ . Two measurements at different $\phi$ values therefore in principle can give information on the symmetric inverse loss-cone in the alpha particle (or even the energetic minority ion) distribution. Fig. 3 refers to the case of the asymmetric loss region described by eq. (3). For $\beta_1 = 90°$ and $\beta_2 = 120°$ a strong asymmetry in the two "wings" of the spectrum appears, which again is better observed for $\phi \geq 80°$. Information on this kind of asymmetry therefore can be obtained if both wings of the CTS spectrum are spectrally resolved and compared.

*References*

/1/ Stix, T.H. (1975), Nucl. Fus., **15**, 737.

/2/ Schuss, J.J., Antonsen, T.M., Porkolab, N. (1983), Nucl. Fus., **23**, 201.

/3/ Whang, K.W., Morales, G.J., Fried, B.D. (1980), *2nd Joint Grenoble-Varenna Int. Symp. on Heating in Toroidal Plasmas* (Como,1980), vol. 1, 613.

/4/ Anderson, D., Lisak, M. (1984), Phys. Fluids, **27**, 2477.

/5/ JET Team (1989), *12th Int. Conf. on Plasma Phys. and Contr. Nucl. Fus. Res.* (Nice, 1988), Nucl. Fus. Suppl., vol. 1, 41.

/6/ Hughes, T.P., Smith, S.R.P. (1988), Nucl. Fus., **28**, 1451.

/7/ Belikov, V.S., Kolesnichenko, Ya.I., Fursa, A.D. (1979), *7th Int. Conf. on Plasma Phys. and Contr. Nucl. Fus. Res.* (Innsbruck, 1978), Nucl. Fus. Suppl., vol. 1, 561; Tani, K., Takizuka, T., Azumi, M., Kishimoto, H., (1983), Nucl. Fus., **23**, 657.

/8/ Vahala, L., Vahala, G., Sigmar, D.J. (1988), Nucl. Fus., **28**, 1595.

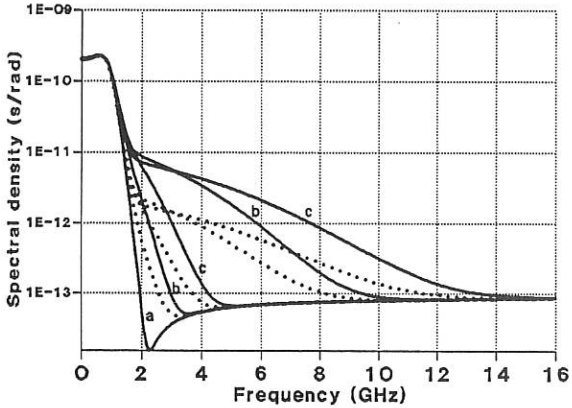


FIG. 1 - $S(\underline{k}, \omega)$ with anisotropically heated $He^3$ minority ions; $n_e = 1.2 \times 10^{14} cm^{-3}$, $T_e = T_i = 10\ keV$, $\theta_{scatt} = 90°$. Curve a) is a reference spectrum for an isothermal plasma with $He^3$ concentration $c = 4\%$. Solid curves of type b) and c) refer to $T_\perp = 0.5$ and $1 MeV$, with $R_T = 50$, $\phi = 5°$ (upper curves) and $\phi = 85°$ (lower curves). The associated dotted curves are for the same parameters with $c = 1\%$.

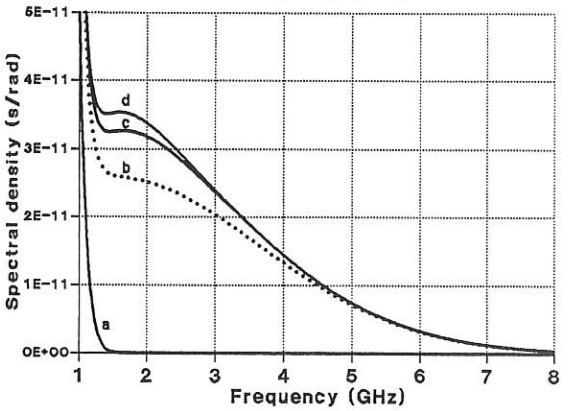


FIG. 2 - Approximate $S(\underline{k}, \omega)$ with a symmetric inverse loss-cone distribution of alpha particles, with concentration $c = 5\%$ and $T_\alpha = 1 MeV$, $\beta_0 = 75°$, $\alpha = 4$. a) Reference curve with $c = 0$; b) $\phi = 60°$; c) $\phi = 80°$; d) $\phi = 87°$.

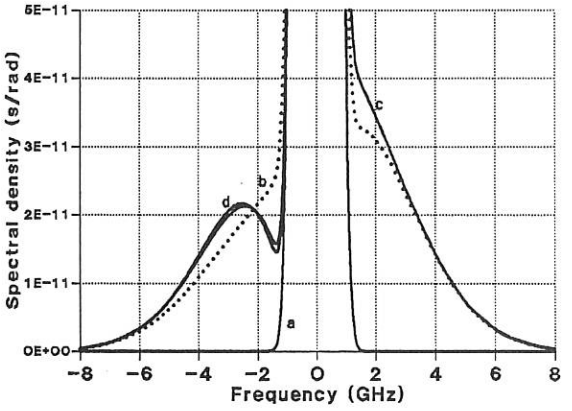


FIG. 3 - Approximate $S(\underline{k}, \omega)$ with an asymmetric inverse loss-cone distribution of alpha particles. Parameters are as in Fig. 2 with the aperture of the loss-cone defined by $\beta_1 = 90°$ and $\beta_2 = 120°$.

# FEASIBILITY STUDY OF BULK ION TEMPERATURE MEASUREMENT ON JET BY MEANS OF A COLLECTIVE SCATTERING OF A GYROTRON RADIATION

F. Orsitto

Associazione EURATOM-ENEA sulla Fusione, Centro Ricerche Energia Frascati, C.P. 65 - 00044 Frascati, Rome, Italy

In the proposal for a Thomson scattering diagnostic of fast ions and alpha particles in JET [1], using a gyrotron ($\lambda_o$ = 0.214 cm), the possibility of measuring the plasma ion temperature was considered briefly and a preliminary conclusion was that the signal to noise in this type of experiment should be large enough, provided plasma turbulence effects do not affect the spectrum.

In this report we discuss the possibility of the measurement of the bulk ion feature in detail, because the proposed diagnostic could give detailed information on the ion dynamics through the measurement of the spatial ion temperature profile, possibly resolved in time.

The predicted error on the ion temperature as measured by this diagnostic is of the order of 15%, the spatial resolution should be a few cm, and the temporal resolution is of the order of 10 ms.

The recent results of the Lausanne collective scattering experiment [2] give concrete support to these ideas, because the general understanding is that the theory at our disposal and the signal to noise ratio evaluation are in broad agreement with the experimental findings, at least in conditions in which strong refractive effects are not present.

In the present work we give a brief report of the study of the bulk ion feature in the scattered spectrum, made considering various geometries $\theta_s$ = 20°, 40°, 90°, 148°, for the plasma parameters given in Table I and we calculate the scattering structure function S (**k**, $\omega$) at a given **k** = $4\pi(\sin\theta_S/2)/\lambda_O$, and frequency $\omega/2\pi$, for a deuterium plasma, and related signal to noise ratio for a measurement in these plasma conditions. It is found that the scattered power received by a heterodyne detector at a given angle is:

$$P_S(k,\omega=0)=3.6\ 10^{-18}\ n_{e13}(P_O(kW)/400)T_i(keV)^{-1/2}\ \alpha^4$$

$$\sin^{-1}(\theta_S)\ \sin^{-1}(\theta_S/2)\ (1+\alpha^2(1+ZT_e/T_i))^{-2}\ \ (W/Hz)$$

where $n_{e13}$ is the electron density in units of $10^{13}$ cm$^{-3}$, $P_O$ the incident power which is supposed focused into the plasma at a waist radius of 5 cm and $\alpha = 1/k\lambda_D$ is the

TABLE I

| PLASMA PARAMETERS USED IN THE CALCULATIONS | IMPURITIES PRESENT IN THE DEUTERIUM PLASMA | CHARGE | MASS NUMBER A |
|---|---|---|---|
| $n_e$=3×10$^{13}$-1×10$^{14}$ cm$^{-3}$ | $^{1}H_1$=10% = n(H)$\Sigma$n$_j$ | $Z_O$ = 8 | Deuterium A=2 |
| Te = 5-10 keV | $^{16}O_8$ = 6% | $Z_C$ = 6 | Oxygen A=16 |
| Ti = 5-25 keV | $^{12}C_6$ = 5% | | Carbon A=12 |

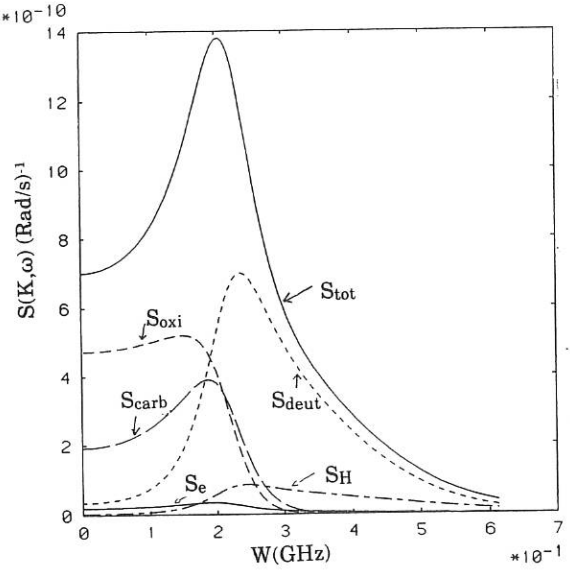


Fig. 1 - $\phi = 0°$, $T_e/T_i = 1.0$; Mass = 2; z = 1.0; $\theta = 40.0°$
$T_e$(keV) = 10.0; $n_e = 3.0\ 10^{13}\ cm^{-3}$; $B_T = 3.4T$

collective parameter ($\lambda_D$ = Debye length). For example at 40° the scattered power is $5\ 10^{-18}$ W/Hz.

The signal to noise ratio S/N is given by:

$$S/N(k,\omega=0)=11\ n_{e13}(P_O(kW)/400)T_i(keV)^{-1/4}\sin^{-1}(\theta_S)\ \sin^{-1}(\theta_S/2)$$

where $a > 4$, $T_e = T_i$ and Z = 1 are supposed , the noise temperature assumed is $T_B$=500 eV, the integration time 10 ms, and the spectrum full bandwidth at half maximum is divided in 5 channels. For example at a $\theta_S = 40°$, $n_{e13} = 4$, $P_O$ = 400 kW, $T_e = T_i$ = 10 keV, we obtain and S/N=66 on a central channel ($\omega$=0), with a bandwidth of 100 MHz: at 100 ms, which is significant for the JET plasma the S/N is of the order of 200.

The calculation of S(k, $\omega$) for a plasma with impurities, mainly, C, O, is carried out and a strong modification of spectra comes out from the presence of these impurities.

Typical fractions of impurities used are: $n(H)/n_{ion,total}$=10%, $n(oxygen)/n_{ion,total}$=6%,$n(carbon)/n_{ion,\ total}$= 5%. The presence of the impurities changes the deuterium feature because the dielectric function of the plasma changes the deuterium feature and the cross section is enhanced by a factor 2-3 for frequencies $\omega/\omega_D < 0.8$ ($\omega_D/2n$ is the halfwidth at 1/e of the maximum of the deuterium thermal feature) at $\theta_S = 20°$ and $n_e = 10^{14} cm^{-3}$. Figure 1 is typical example of the deuterium spectrum with impurities, the individual ion features are also shown.

The form factor S(k, $\omega$) is calculated (Fig. 2) also taking into account the

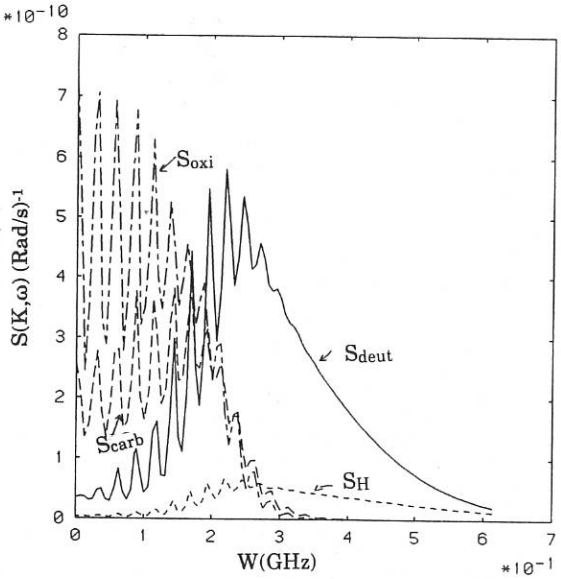


Fig. 2 - $\phi$ = 85.0°, $T_e/T_i$ =1.0; Mass = 2; z = 1.0; $\theta$ = 40.0° $T_e$(keV) = 10.0; $n_e$ = 3.0 $10^{13}$ $cm^{-3}$; $B_T$ = 3.4T

magnetic field effect, and a general condition on the angle $\phi$ (between the k vector and the magnetic field direction) is given in order to avoid the spectrum modulation at the ion cyclotron frequency induced by the magnetic field and the depression in the electron responce at low $\phi$ [3]. We find that at $\theta_s$= 40° the angle between the magnetic field and the k wavevector must be less than 80° in order to avoid the magnetic field effects on the form factor.

The role of turbulence in the modification of the scattered spectrum is analyzed [4], in order to establish the signal level due to the scattering on non-thermal density fluctuations and the expected range of the mean wavenumber typical of the JET turbulence is $\bar{k}$ = 0.2-3 $cm^{-1}$, while the frequency characteristic of turbulence is of the order of 200-600 kHz, i.e. the diamagnetic electron frequency. This means that the turbulence affects heavily only the central channel where presumably a notch filter should be used. A well accepted fit of the behaviour of the non-thermal form factor based on gaussian behaviour in **k** and $\omega$ gives the conclusion that the turbulence has no effect on the ion spectrum, but a power law fit, also compatible with the available data base, should attenuate that conclusion: so an experimental measurement of turbulence in the range of k and $\omega$ typical for the ion feature could be useful.

It is important to determine the influence of turbulence on scattering volume definition. The signal to noise ratio (S/N) degradation due to this effect must be included in the calculations. It is found that the plasma density fluctuation at the edge, which is of the order of 0.1-0.5 could decrease the S/N by the same fraction because it determines a fluctuation of the principal beam waist into the plasma.

Spectrum asymmetries are caused by the mass motion of the plasma [5]. It turns out that the drift of the electrons causes an asymmetry of the collective spectrum. Such asymmetry is given by

$$R-1 = S_{ion}(-x_i)/S_{ion}(x_i) = (4\ T_i/ZT_e)(x_{dk}/x_i)$$

where $x_{dk}=V_{drift}\ \cos\chi/V_{the}$ ($\chi$ is the angle between k and $V_D$), and $x_i = \omega/\omega_i$. If we choose the geometry in order to have $\chi = O$, the $x_{dk} = 0.1$ for JET plasma. It turns out that in order to measure an $x_{dk} = 0.01$ in a plasma with $T_i=2.5\ T_e$ and $Z=2.5$ at $x_i=1$, an S/N=50 must be achieved.

The frequency instability of the central gyrotron frequency must be taken into account in the design of the detection system and frequency tracking could be useful. Furthermore the presence of gyrotron spurious modes in the frequency region of the ion feature spectrum must be considered. As consequence the upper limit on the tolerable gyrotron power present in these modes must be determined. For 400 kW of incident power, we can tolerate on the detector a stray power radiation of $6\ 10^{-19}$ W/Hz, when we measure at 40° scattering angle. This figure must be respected in each channel of the spectrum.

Because the extraction of the ion feature from the measured spectrum depends upon the knowledge of the electron temperature, density and $Z_{eff}$, a fitting procedure is necessary in order to determine the contributions of the various ions present into the plasma. The experimental errors on the measurements of $T_e$, $n_e$, $Z_{eff}$ affect the error of ion temperature measurement. A preliminary analysis [following Ref. 6] leads to the conclusion that, for an error on the electron temperature and density in the range of 10%-20%. The possibility of an ion temperature spatial profile, resolved in time, could be realized tilting the collecting mirror. It turns out that if we arrange the collecting optics in order to collect the light at a scattering angle of 40° at the plasma center, we have at half radius an almost doubled bandwidth and half signal to noise ratio. The S/N decrease to 1/10 from the centre to the plasma edge. Correspondingly the spatial resolution improves in the spatial scan.

## REFERENCES


[1] A.E. Costely et al.: Jet Report R(88)08

[2] R. Behn et al.: PRL Report 62 (89)2833

[3] F. Orsitto and P. Buratti: ENEA Report RT/FUS/88/30

[4] P.C. Liewer: Nucl. Fusion **25**, 543 (1985); C.M. Surko and R.E. Slusher: Science **221**, 817 (1983); P. De Simone, D. Frigione, F. Orsitto: Plasma Phys. **28**, 751 (1986); T. Crowley, E. Mazzucato: Nucl. Fusion **25**, 507 (1985); C.M. Surko: Comm. Plasma Physics Controlled Fusion **10**, 265 (1987)

[5] D.E. Evans, M.J. Forrest, J. Katzestein: Nature **212**, 21 (1966)

[6] L.E. Sharp, A.D. Sanderson, D.E. Evans, Plasma Phys. **23**,357 (1981)

# ON THE POSSIBILITIES OF SPECTROSCOPIC MEASUREMENTS OF VARIOUS ELECTRIC FIELDS AND RELATED PLASMA PARAMETERS FOR TOKAMAK CONDITIONS

E. Oks

Ruhr-Universität, Institut für Experimentalphysik 5, Postfach 102148,
D - 4630 Bochum 1, FRG

1. Analyze the possibilities of corpuscular-spectroscopic diagnostics of quasimonochromatic electric fields (QEF) $\vec{E}(t) = \vec{E}_0 \cos\omega t$ in tokamaks. These fields may represent microwaves from the external source used for additional heating or some regular waves exited in a plasma (as it was experimentally revealed in the T - 10 tokamak /1/).But for the conditions in which a beam of neutral atoms with velocity $\vec{v}$ is injected across a magnetic field $\vec{B}$ the beam atoms experience a strong Lorentz field $\vec{F} = \vec{v} \times \vec{B}/c$ of order 10-100 k V/cm. It was already experimentally demonstrated that this strong static field $\vec{F}$ leads to a significant shift /2/ and/or splitting /3/ of spectral lines (SL).The question arises whether it is possible to detect relatively weak QEF $|\vec{E}(t)| \ll F$ in spite of a strong field $\vec{F}$ by analysis of spectra of beam atoms.Our main idea is to use some spectroscopic manifestations which may be caused only by joint action of a static field $\vec{F}$ and a dynamic field $\vec{F}(t)$.

The first proposal is to utilize a lithium beam and then to observe the profile of SL Li I 4603 A (2P - 4P,D,F).As a starting point recall the results of oup previous papers /4,5/, devoted to the revision of the problem of Baranger-Mozer satellites of dipole-forbidden SL /6/ (appearing in spectra of helium- or alkali-atoms under the action of QEF) caused by the allowance for additional static field $\vec{F}$. It was shown in /4,5/,that even relatively

weak field $F \lesssim 10^{-1} E_0$ drastically changes the spectra; in particular, the field $\vec{F}$ leads to the appearance of intense satellites separated by $\pm\omega$ from dipole-allowed SL (this type of satellites was formerly known only in spectra of hydrogen SL under the action of QEF).

In our present case the strong field $\vec{F}$ completely mixes the states 4F,4D,4P of Li atom and they respond to a weak field $\vec{E}(t)$ as a hydrogen-like structure displaying pronounced satellites separated by $\pm\omega$ from the line components 2P-4D and 2P-4F. The numerical example: the Li-beam with the energy 100 keV is injected across the magnetic field B=2.8T (so that F=46 kV/cm). If $\vec{E}(t)$ represent the oscillations at electron-cyclotron frequency, then the satellites appear separated by $\pm\lambda_\omega = \pm\omega\lambda_0^2/(2\pi c)$ from the position $\lambda_0$ of main components. Their relative (with respect to a main component) intensity is $S/I_a \approx [0.2\ E_0(\mathrm{kV/cm})]^2$. Thus upon $E_0 \gtrsim 1.5$ kV/cm we have $S/I_a \gtrsim 0.1$, i.e. the quite observable effect. In order the Doppler width of all features (controlled by a beam divergence) to be smaller than $\lambda_\omega$, the angular divergence of the beam should be $v_\perp/v_\parallel < 10^2$.

The second proposal is to use a hydrogen beam and then to observe the profile of the SL $H_\beta$ 4861 A. A strong field $\vec{F}$ essentially splits hydrogen degenerate states and they may respond to a weak field $\vec{E}(t)$ by appearance of a pronounced forbidden components (unresolved satellites) in the line centre. Recall that under the action of static field only ($E_0$=0) the SL $H_\beta$ has no central Stark components. The numerical example: the H-beam with the energy 40 keV is injected across the magnetic field B=1.4 T (so that F=40 kV/cm). The separation between Stark components of $H_\beta$ is $\Delta\lambda_F$ =0.030 F(kV/cm)=1.2 A. The relative increase of intensity in the centre of $H_\beta$ (with respect to main maxima) after switching on a microwave field $\vec{E}(t)$ is $I_f/I_a \sim (6\ E_0/F)^2$. Thus upon $E_0 \gtrsim 2$ kV/cm we have $I_f/I_a \gtrsim 0.1$, i.e. the rather observable effect. In order the Doppler broadening to be smaller than the Stark one, the angular

divergence of the beam should be $V_\perp/V_\parallel < 2.2\ 10^{-2}\ B(T) \approx 0.03$.

In the both proposals it was assumed that the splitting of a multiplet in the Lorentz field dominates over the pure Zeeman splitting. This is the case under the condition, that a beam velocity $v > c/(205.5\ n)$. For the principal quantum number $n=4$ the corresponding condition for a beam energy is $E_{beam} > E_{cr}$, where $E_{cr}=4.9$ keV for Li and $E_{cr}=0.7$ keV for H.

2. A new spectroscopic method for local determination of the effective charge $Z_{eff}$ in tokamaks was theoretically proposed /7/ and recently experimentally realized/8/. The method was based on the two ideas. The first one is that for tokamak conditions the broadening of hydrogen SL by protons and by impurity ions is not quasistatic but impact, the impact with $\Gamma$ being proportional to $Z_{eff}$. But $\Gamma$ is approximately one order of magnitude smaller than a Doppler width $\Delta\omega_{1/2}^{D}$. The second idea was to use laser saturation of excited transition (with laser line width $\Delta\omega_{1/2}^{L} \ll \Delta\omega_{1/2}^{D}$) in order to extract a small value of $\Gamma$ in spite of a large value of $\Delta\omega_{1/2}^{D}$. As the strength of laser light $E_0$ increases, occurs an increase of fluorescene SL width (so-called energy broadening): $\Gamma_B = \Gamma(1+G)^{1/2}$, $G \equiv (d_{12}E_0/\hbar)^2/(\gamma\Gamma)$, where $\gamma$ is the radiative level width. This means that Doppler and energy broadenings may be distinguished from the profiles of hydrogen fluorescence line, so that the values of $\Gamma$ and $Z_{eff}$ can be measured.

Our third proposal is to improve this method by carrying out the analogous laser saturation spectroscopy measurements but on hydrogen atoms of beam injected into a plasma. The advantages are the following : 1) the uncertainties intrinsic to the method /8/ vanish, since the proportionality coefficient between $\Gamma$ and $Z_{eff}$ is now controlled by the well-known beam velocity $v_{beam}$ (instead of hydrogen atom mean velocity $\langle v_a \rangle$, which is not usually well-known); 2) the Doppler width is drastically reduced (since it is now controlled by the beam diveregence $v_\perp/v_\parallel \ll 1$); it becomes possible to carry out the laser satu-

ration experiment on isolated Stark components of SL and the response of components widths to the laser field action will essentially increase.

The formula for $\Gamma$ in this case significantly differs from /7,8/ and may be expressed as follows:

$$\Gamma = \left\{12(\hbar/m_e)^2 f(n,n') N_e v_{beam}^{-1} \ln\left[2em_e^2 c v_{beam}/(3n^3\hbar^2 B)\right]\right\} Z_{eff},$$
$$f(n,n') \equiv n^2\left[n^2+(n_1-n_2)^2-m^2-1\right]+n'^2\left[n'^2+(n_1'-n_2')^2-m'^2-1\right]-4nn'(n_1-n_2)(n_1'-n_2'), \quad (1)$$

where $n_1, n_2, m$ and $n_1', n_2', m'$ are parabolic quantum numbers of upper and lower levels correspondingly; $N_e$-electron density.

Our fourth proposal is to combine the saturation technique not with H- but with He- or Li-beams. The suitable SL are He I 4471 A, He I 4922 A or Li I 4603 A (all transitions are 2P-4D). The general expressions for $\Gamma$ is

$$\Gamma = \left\{\left[8\pi N_e/(3\langle v_{rel}\rangle)\right]\left[\hbar r_{12}/(m_e a_o)\right]^2 \ln\left[\max(1, m_e a_o \langle v_{rel}\rangle^2/(\hbar r_{12}\Delta\omega_{12}))\right]\right\} Z_{eff}, \quad (2)$$

where $r_{12}$ and $\Delta\omega_{12}$ are a dipole matrix element and a distance between the states 4D, 4F. For thermal He- or Li-atoms the relative perturber-radiator velocity $\langle v_{rel}\rangle \approx v_{Ta}$, so that the logarithm in (2) equal to zero (no impact broadening). But for He- or Li-atoms in a beam $\langle v_{rel}\rangle \approx v_{beam}$, so that the ratio $m_e a_o \cdot \langle v_{rel}\rangle^2/(\hbar r_{12}\Delta\omega_{12})$ increases in $E_{beam}/T_a \sim 10^2$-$10^3$ times, what leads to an essential value of $\Gamma$. In other words, a beam may change to mechanism of He- or Li-lines broadening by impurity ions from quasistatic to impact. Due to the strong Lorentz field the allowed and forbidden components have comparable intensities. Hence laser saturation measurements of $Z_{eff}$ may be carried out on both 2P-4D and 2P-4F components.

The author express his sincere gratitude to the Alexander von Humboldt Foundation for the sponsoring his work.

References.

1. Gavrilenko V.P., Oks E.A., Rantsev-Kartinov V.A., JETP Lett. 1986, 44, 4o4. 2. Dullni E., Leismann P., Mau mann S., v.Reventlow C., Kunze H.-J., Physica Scripta 1986, 34, 405. 3. Boileau A., v.Hellerman M., Mandl W., Summers H.P., Weisen H. Zinoviev A., J.Phys.B 1989, 22, L145. 4. Oks E.A., Gavrilenko V.P., Optics Communications 1986, 56, 415. 5. Volod'ko D.A., Gavrilenko V.P., Oks E.A., "Spectral line Shape", 9th Int.Conf., Torun, Poland, 1988, v.5, A 25. 6. Baranger M., Mozer B., Phys.Rev. 1961, 123, 25. 7. Abramov V.A., Lisitsa V.S., Sov.J.Plasma Phys. 1977, 3, 451. 8. Bychkov S.S., Ivanov R.S., Stotskii G.I. Sov.J.Plasma Phys. 1987, 13, 769.

# MODELLING OF NON-THERMAL ELECTRON CYCLOTRON EMISSION DURING ECRH

V. Tribaldos and V. Krivenski

Asociación EURATOM/CIEMAT para Fusion, CIEMAT, Madrid

The existence of suprathermal electrons during Electron Cyclotron Resonance Heating experiments in tokamaks is today a well established fact. At low densities the creation of large non-thermal electron tails affects the temperature profile measurements obtained by 2nd harmonic, X-mode, low-field side, electron cyclotron emission.[1] At higher densities suprathermal electrons can be detected by high-field side emission.[2] In electron cyclotron current drive experiments a high energy suprathermal tail, asymmetric in $v_{\parallel}$, is observed.[3]

Non-Maxwellian electron distribution functions are also typically observed during lower-hybrid current drive experiments.[4] Fast electrons have been observed during ionic heating by neutral beams as well.[5]

Two distinct approaches are currently used in the interpretation of the experimental results: simple analytical models which reproduce some of the expected non-Maxwellian characteristics of the electron distribution function are employed to get a qualitative picture of the phenomena ( see for example Ref. 6 ); sophisticated numerical Fokker-Planck calculations give the electron distribution function from which the emission spectra are computed.[7] No algorithm is known to solve the inverse problem, i.e., to compute the electron distribution function from the emitted spectra. The proposed methods all relay on the basic assumption that the electron distribution function has a given functional dependence on a limited number of free parameters,[4] which are then "measured" by best fitting the experimental results.

Here we discuss the legitimacy of this procedure as follows. We consider as "experimental" result the emission spectra obtained from the distribution function computed numerically by a Fokker-Planck code and try to fit this result by a model distribution function which depends only on a few parameters: non-thermal population, current, parallel and perpendicular energy.

The following tokamak parameters are considered:

$$T_e = T_e(0) \exp( -( ( r/a ) / 0.371 )^{1.2} ) \ , \quad T(0) = 1.3 \text{ keV} \ ,$$
$$n = n(0) (1- ( r/a )^2 ) \ , \quad n(0) = 2.5 \times 10^{13} \text{ cm}^{-3} \ ,$$

$B=B_0/(1+x/R)$ , $B = 2.16$ T , $f = 60$ GHz , $P_{EC} = 500$ kW , $a = 26$ cm , $R = 100$ cm , $V_l = 1.5$ , $Z_{eff} = 1.9$ .

Oblique, low-field side injection of ordinary mode electron cyclotron waves is considered in an ohmic discharge. In Fig. 1a the level lines of the Fokker-Planck distribution function are presented at $r = 0$ ( $u = p/p_{th}$ ). Note that during ECRH the distribution function has a complex bidimensional form. We then fit the numerical result with the following analytical model:

$$f = \frac{1}{(2\pi)^{3/2}}\left[(1-\eta)\exp\left(-\frac{u^2}{2}\right)+\eta(T_e)^{3/2}/\left(T_\perp\sqrt{T_\parallel}\right)\exp\left(-\frac{T_e}{2}\left(\frac{(u_\parallel-u_0)^2}{T_\parallel}+\frac{u_\perp^2}{T_\perp}\right)\right)\right] .$$

We consider the direct problem: the knowledge of the local current, non-thermal population, parallel and perpendicular energy, as given by the Fokker-Planck solution, allows us to determine the free parameters of the model. For comparison the level curves of the model distribution function at $r = 0$ are shown in Fig. 1b and $n(E)$ ( ≡ fraction of non-thermal particles with energy larger than E ) in Fig. 2 . The high field side cyclotron emission is presented in Fig. 3 for the Fokker-Planck solution, the previous model and for the corresponding model with $T_\parallel = T_\perp$. We observe that the model is in fair agreement with the Fokker-Planck result when the radiation is emitted by relatively low energy electrons. In the case of vertical emission, where high energy electrons give an important contribution, the agreement is poor.

We next consider the inverse problem, i.e., the uniqueness of the parameters giving the same temperature profile. The radiative temperature for a given frequency is the result of the contribution of electrons with different energy, as determined by the spatial dependence of the resonance condition ( $E_{res}(x) = m_e c^2 ( ( 2f_c(x)/ f )^2 - 1 ) )$ ; as an example the local radiative temperature and the power deposition are shown in Fig. 4 for $f = 2 f_c$( $x = 1.4$ cm ) . The lines of constant radiative temperature vs the model parameters are shown for the same frequency in Figs. 5 : (a) for a relatively low resonant energy ( $x = -0.6$ cm , $E_{res} = 14$ keV ) and (b) for a high resonant energy ( $x = -1$ cm , $E_{res} = 25$ keV ). It appears that the same local radiative temperature ( which labels the curves in keV units ) can be obtained by different sets of parameters.

In conclusion, we have discussed on the basis of a simple example the possibility of modelling the non-thermal electron cyclotron emission during ECRH. Specifically, we have shown that a simple analytical model based on the knowledge of the suprathermal population, current and energy distribution, can fairly well reproduce the low energy non-thermal emission as given by the numerical solution of the kinetic equation. On the other hand higher energy emission, which depends on higher momenta of the distribution function, cannot be reproduced by the model: reproduction of this part of the spectrum could be obtained only by using parameters which does not correspond to the actual distribution function. As far as the inverse

problem is concerned, we have shown that even a simple model does not allow a unique inversion of the free parameters that "measure" the distribution function.

## References


1 A. Cavallo et al., Nucl. Fusion **25**, 335 (1985). R. M. J. Sillen et al., Nucl. Fusion **26**, 303 (1986).

2 M. E. Austin et al., Bull. Am. Phys. Soc. **34**, 2157 (1989).

3 A. Ando et al., Phys. Rev. Lett. **56**, 2180 (1986). H. Tanaka et al., Phys. Rev. Lett. **60**, 1033 (1988). B. Lloyd et al., Nucl. Fusion **28**, 1013 (1988).

4 K. Kato and I. H. Hutchinson, Phys. Rev. Lett. **56**, 340 (1986). S. Ide et al., Nucl. Fusion **29**, 1325 (1989).

5 G. Taylor et al., Plasma Phys. Controll. Fusion **31**, 1957 (1989).

6 I. Fidone et al., Phys. Fluids **23**, 1336 (1980) and **26**, 3284 (1983). G. Giruzzi et al., Phys. Fluids **27**, 1704 (1984).

7 G. Giruzzi, Nucl. Fusion **28**, 1413 (1988).


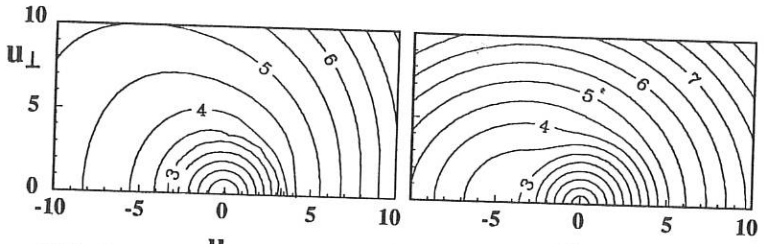


FIG. 1a FIG. 1b

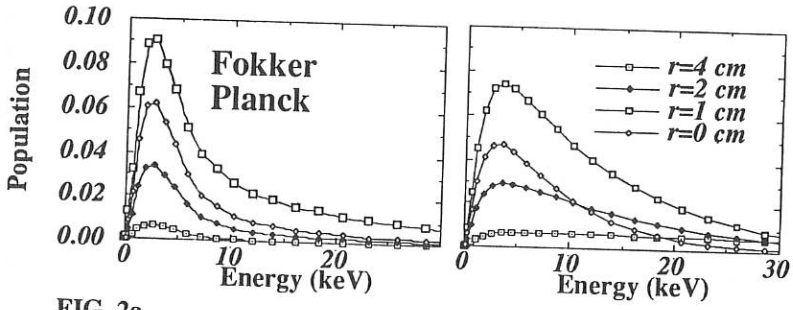


FIG. 2a FIG. 2b

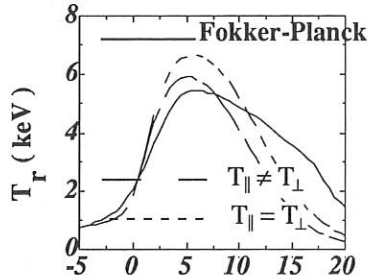


FIG. 3

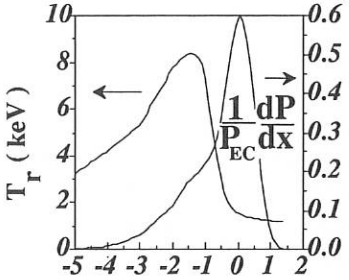


FIG. 4

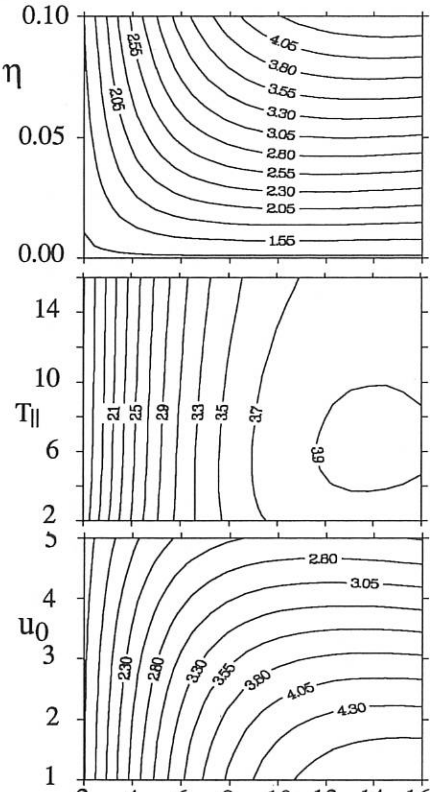


FIG. 5a

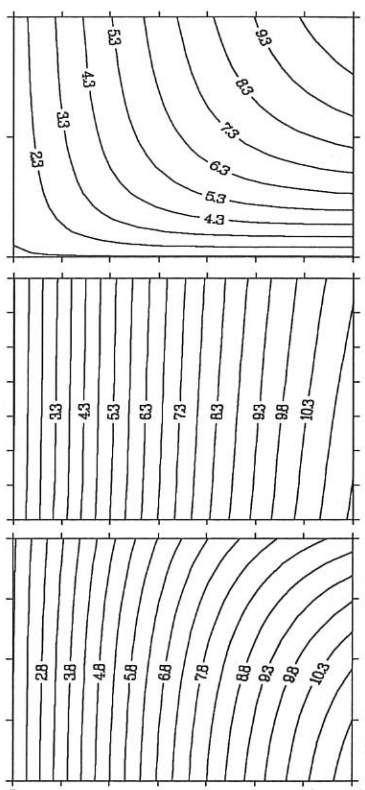


FIG. 5b

# PHYSICS STUDIES OF COMPACT IGNITION PLASMAS USING NEUTRON MEASUREMENTS

G.Gorini, J.Källne♦, S.Rollet*

*Istituto di Fisica del Plasma, Associazione EURATOM- ENEA-CNR, via Bassini 15, 20133 Milano, Italy*
*♦Department of Neutron Physics, Uppsala University, S-75121 Sweden*
**Fellow of Associazione per lo Sviluppo Scientifico e Tecnologico del Piemonte, Torino, Italy*

**INTRODUCTION-** This contribution deals with the plasma physics studies that can be performed based on neutron measurements with new techniques. In particular, we discuss the use of the magnetic proton recoil (MPR) spectrometer as a basic instrument for neutron measurements in compact ignition D-T plasmas. Parallel exists with present diagnostic systems in use, for instance, at JET for the detection of D-D neutrons. Therefore, we use the JET results both as guidance for system design and to predict what kind of physics studies could be performed with a diagnostic system exploiting the high neutron production of D-T burning plasmas.

**NEUTRON MEASUREMENTS IN COMPACT EXPERIMENTS-** The first proposal of a compact ignition experiment was made in 1975 [1]. Since that time, the basic premises of these experiments have been essentially confirmed, and the design of these devices has been optimized. In this work we take the Ignitor device as an example (see Table for a list of the Ignitor design parameters assumed in this work).

Neutron diagnostics stand to gain in importance in fusion burning experiments for two reasons. First, measurements of 14-MeV neutrons can provide crucial information on $\alpha$-particle issues and partially replace direct $\alpha$-particle observations (which are rather difficult). Second, the higher neutron fluxes and neutron energies of D-T plasmas are intrinsic advantages for neutron measurements and can be exploited even if the associated high background radiation levels (in the form of backscattered neutrons and $\gamma$-rays) require effective background insensitivity of the measurements.

The main parameter determining the choice of possible neutron detectors for measurements in compact experiments is the expected fusion neutron flux at the detector location, F, and the width, W (FWHM), of the neutron spectrum. The former will largely depend on the fusion performance of the experiments. For instance, the Ignitor device is expected to produce D-T plasmas with ion densities ($n_D \approx n_T$)of the order of $10^{15}$ cm$^{-3}$, confinement times $\tau_E \approx 0.4$ s and ion temperatures ($T_D \equiv T_T$) of 4 keV at the beginning of the current flat top. Having achieved these plasma conditions, the $\alpha$-particle heating would increase rapidly and the plasma would reach the ignition condition at an ion temperature $T_D \approx 13$ keV in about 2 s [2]. The neutron spectrum is expected to be of a Gaussian shape with $W(keV) = 177 T_D(keV)^{1/2}$. The fusion power level at ignition would be 150 MW or more. The neutron yield in the self-heating phase would be in the range $5 \cdot 10^{18}$-$5 \cdot 10^{19}$ n/s.

**COLLIMATION GEOMETRY-** Assuming the Ignitor biological protection wall to be at a distance of about 7.5 m from the plasma, a neutron detector located just outside the wall would record rather high neutron fluxes in collimators with reasonable apertures. In particular, we consider a collimation geometry consisting of a 9-channel camera (see Fig.1) with $A_{ap}$=10 cm$^2$, $A_{eff}$= 100 cm$^2$, D= 750 cm, $\Delta \lesssim$ 12.5 cm (here $A_{ap}$ is the collimation aperture, $A_{eff}$ is the effective plasma cross section area viewed, D is the detector distance from the plasma centre and $\Delta$ is the distance between two adjacent channels at the plasma centre). This choice of parameters gives a spatial resolution (relative to the vertical minor radius) similar to the resolution of one of the two collimators in use at JET; the latter is found to be adequate for detailed profile studies [3]. For a central line of sight and for peaked emissivity profiles, the neutron flux at the detector per unit total neutron production rate ($\Phi$) is found to be about $4 \cdot 10^{-10}$ cm$^{-2}$, corresponding to a neutron flux of $2 \cdot 10^{10}$ ncm$^{-2}$s$^{-1}$ for a total neutron production rate of $5 \cdot 10^{19}$ n/s. Since $\Phi$ in a central line of sight can vary at most by a factor of 2 in JET [3], we also expect the central value of $\Phi$ to be fairly insensitive to the shape of the Ignitor emissivity profile. This is not the case for the peripheral lines of sight. Using again the results of Ref.[3], we see that the central to peripheral (i.e, at 2/3 of the plasma vertical minor radius) brightness ratio is $\approx$10 for broad profiles and $\gtrsim$100 for peaked profiles. These reference values are used in the following discussion of neutron measurements in Ignitor plasmas.

**THE MPR DETECTORS-** MPR detectors [4] can be designed having high ($\Delta E/E \approx 2.5\%$ FWHM) to modest ($\Delta E/E \approx 20\%$) energy resolution and corresponding efficiencies in the range $2 \cdot 10^{-5}$ to $10^{-3}$ cm$^2$, respectively; this makes them suitable for use as high resolution spectrometers (MPRs) as well as neutron counters (MPRc). Here we consider a neutron diagnostic system for Ignitor based on these detectors, consisting of one horizontal neutron camera for neutron brightness profile measurements, and one or more spectrometers for measurements of the ion temperature at different locations in the plasma.

The reference MPRs considered here is schematically shown in Fig.2. It consists of a Quadrupole-Dipole-Quadrupole (QDQ) magnetic spectrometer which momentum-analyzes the recoil protons from n+p reactions in a 10 mg/cm$^2$ thick, 10 cm$^2$ large $CH_2$ target located at the collimator aperture. The acceptance of the QDQ system is 10 msr corresponding to a neutron detection efficiency of $2 \cdot 10^{-5}$ cm$^2$. The protons are detected by a hodoscope consisting of an array of plastic scintillation counters. The energy resolution is 2.6% as determined essentially by target (1.9%) and optics (1.8%) contributions.

Since the detection takes place in proton *counters* placed out of view from the direct neutron and $\gamma$ flux, this spectrometer has excellent count rate capabilities and background rejection. The time resolving power ($1/\Delta t$) of the MPRs, defined as the inverse of the collection time resulting in a $\pm$10% statistical accuracy in $T_D$ measurements, is plotted in Fig.3 as a function of the total neutron yield in Ignitor plasmas. The upper limit corresponds to a maximum expected count rate of 400 kHz, i.e., $\Delta t \lesssim 1$ ms.

MPRc's can be used in the neutron camera. High efficiency and small dimension are the main requirements for this application, whilst a modest energy resolution is sufficient for discrimination against backscattered neutrons. The optimization of the MPRc design has not been attempted yet, but it should be possible to achieve an efficiency of $\approx 10^{-3}$ cm$^2$ and an energy resolution of ±20% with detectors of vertical dimension ≈50 cm. The time resolving power of an MPRc camera for profile measurements, defined as the inverse of the collection time resulting in a ±10% statistical accuracy in the peripheral channels for a ratio of central to peripheral brightness of 100, is similar to that of the MPRs spectrometer and is shown in Fig.3.

**PHYSICS STUDIES USING NEUTRON MEASUREMENTS-** The excellent time resolution of the MPR instruments opens new possibilities in terms of physics studies of fusion burning D-T plasmas. By use of the same methods applied in Ref.[3] to representative JET data, the $T_D$ profile could be derived from 14-MeV neutron brightness measurements with the assumption of a known fuel concentration $n_D n_T / n_e^2$. This would be determined experimentally at the plasma centre with the spectrometer measurement, and can be assumed to be constant along the plasma radius if the plasma impurity content is not large; this could be checked by a second MPRs measurement along a peripheral line of sight. The main uncertainty comes from using the $n_e$ profile in lieu of the ion density profile, but this should have a small effect as long as the temperature profile is steeper than the density profile. Therefore the total (absolute and statistical) uncertainty on the ion temperature profile derived from neutron brightness measurements and central temperature measurement should not exceed ±10% for plasmas with a low impurity content. This uncertainty would allow to determine the $\eta_i$ profile [3] with sufficient accuracy, and is marginally sufficient to separate the ion and electron temperature profile in the plasma. This is essential for studying the ion heat transport. More precisely, it would allow to determine the ion heat flux $q_i$ from power balance analysis, and hence the ion heat transport coefficient $\chi_i$ (defined as $\chi_i = -q_i / \nabla T_i$). In fact, the excellent time resolution of the measurements allows to study other phenomena related to the topic of ion heat transport. An example is the heat pulse following a sawtooth crash. The interpretation of the observed brightness pulse, however, needs to be discussed in more detail than it can be done in this general discussion.

Apart from ion temperature profile information, the neutron camera measurements provide a direct determination of the α-particle birth profile. Again this has an important application in the power balance analysis, since it allows to determine the α-heating profile. We also mention that the good space and time resolution of these measurements makes them also suitable for studying the consequences of possible α-particle driven instabilities on the plasma temperature and/or density.

Finally, a different application of the MPR detectors can be considered, where the 14-MeV neutron emissivity profile from Ignitor D-plasmas is measured to determine the triton burn-up fraction [5]. This measurement would have a modest time resolution ($\gtrsim$1s), sufficient to provide information on the burn-up fraction profile under quasi-stationary plasma conditions.

**CONCLUSION-** We conclude that the use of new techniques allows neutron measurements to take on the role they are expected to play in future ignition experiments, especially with regards to studies of the physics of plasma ions and of α-particle heating.

**References**


[1] Coppi,B., Rep. PRR 75/18, MIT, Cambridge, MA (1975).
[2] Englade,R., Nucl. Fusion 29 (1989) 999.
[3] Gorini,G., Gottardi,N., Rep. JET-R(90)03, JET, Abingdon, Oxon (1990).
[4] Källne,J., Comments Plasma Phys. Control. Fusion 12 (1989) 235.
[5] Källne,J., Batistoni,P., Gorini,G., et al, Nucl.Fusion 28 (1988)7, 1291.


| Main Parameters of Ignitor | |
|---|---|
| Plasma minor radius (horizontal) | 45.5 cm |
| Plasma minor radius (vertical) | 82.5 cm |
| Plasma major radius | 126.5 cm |
| Total magnetic field at plasma centre | 13.2 T |
| Toroidal plasma current | 12 MA |
| Volt seconds available to drive plasma current | 31.5 |
| Additional ion cyclotron frequency heating | ~10 MW |
| Duration of plasma discharge | 10 s |

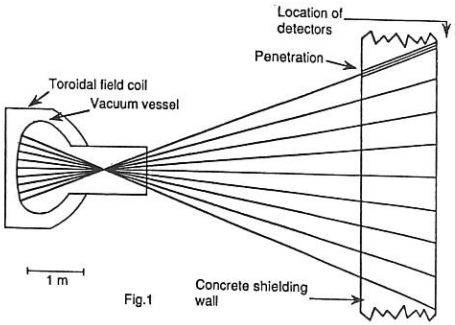


Fig.1

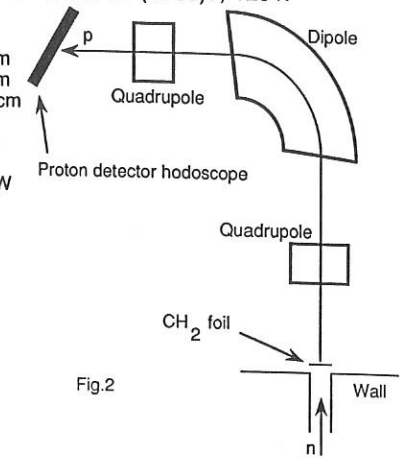


Fig.2

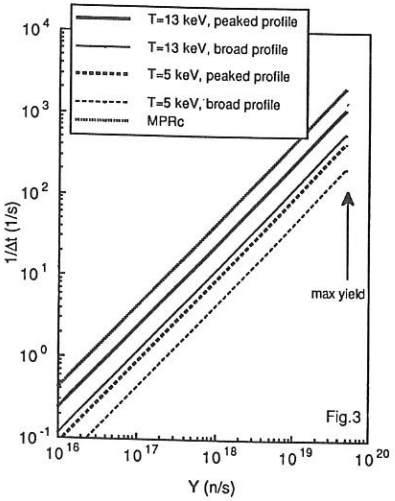


Fig.3

*Fig.1-Schematics of the neutron camera viewing the Ignitor plasma through a horizontal port.*

*Fig.2-Schematics of the MPR neutron spectrometer. The protons are momentum analyzed in the dipole and their momentum determined from the counter struck in the hodoscope.*

*Fig.3-Time resolving power ($1/\Delta t$) of the reference MPRs for extreme emissivity profile shapes and $T_D$ values (the resolving power depends weakly on $T_D$ for R≈W). Also shown is the time resolving power of the reference MPRc,.*

# THE MULTI-CHANNEL INTERFEROMETER/POLARIMETER FOR THE RTP TOKAMAK

A.C.A.P. van Lammeren, S.K. Kim and A.J.H. Donné

*FOM-Instituut voor Plasmafysica Rijnhuizen, Associatie EURATOM-FOM, P.O. Box 1207, 3430 BE Nieuwegein, The Netherlands.*

## Introduction

A sophisticated interferometer and polarimeter system was designed for the medium-sized RTP tokamak (Rijnhuizen Tokamak Project); a = 16 cm, R = 72 cm, $B_0$ = 2.5 T and plasma pulse duration 200 ms. RTP is specifically dedicated to transport and fluctuation studies. For electron heat transport studies two 60 GHz, 200 kW gyrotrons will be used.

The multi-channel interferometer system is dedicated to the study of plasma transport such as electron density pulse propagation induced by sawteeth, oscillating gaspuff, pellet injection and density effects of (modulated) ECRH, as well as routine density profile measurements.

## Interferometer

A sketch of the multi-channel interferometer is given in Fig. 1. The system uses a dual-beam optically-pumped FIR (Far Infra-Red) laser [1]. At a wavelength of $\lambda = 432$ μm the laser system produces a total power of 65 mW. By detuning the cavities, an IF (Intermediate Frequency) of 1 MHz can be obtained between the two beams. The two beams are both expanded to a slab-like beam by a set of two parabolic mirrors. This, in combination with the large diagnostic ports of RTP, makes it possible to observe nearly the complete minor plasma cross-section. After one beam has passed through the plasma, the two beams are recombined on an array of 9 corner-cube mixers with Schottky diodes. The positioning of the detectors can be changed on a shot-to-shot base. The number of interferometer channels can be increased to a maximum of 19. This set-up gives the opportunity to optimize the detector positions according to the plasma parameters.

The outputs of the mixers at the IF frequency are fed into phase detectors which determine the phase differences between the signals from the probing beam and the reference channel. The accuracy of this phase detector is $1^o$. The overall accuracy is expected to be better then $2\times10^{16}$ $m^{-2}$ for a line density of $2\times10^{19}$ $m^{-2}$.

## Polarimeter

The interferometer system will be extended in the near future with a polarimeter. This can be done by replacing the beam splitter by a polarizer and placing a second array of corner-cube detectors perpendicular to the interferometer array [2]. One has to keep in mind, however, the polarization dependence of the mixers, which complicate this simple set-up.

Calculations show that the expected Faraday-rotation angle for a standard RTP discharge is in the order of a few degrees (see Fig. 2). Earlier experiments showed that it is hard to obtain an accuracy better than $0.15^o$ if one uses the above scheme of Soltwisch [2]. Another detection scheme is that of Kunz and Dodel [3]. In their scheme the polarization of the probing beam is modulated over a few degrees. By using lock-in

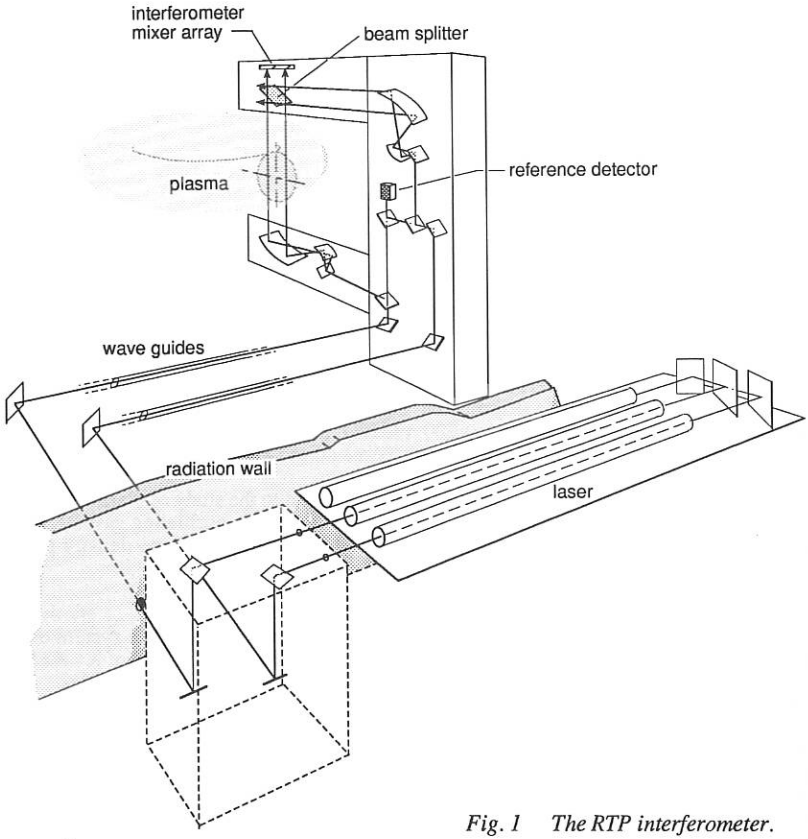


*Fig. 1* *The RTP interferometer.*

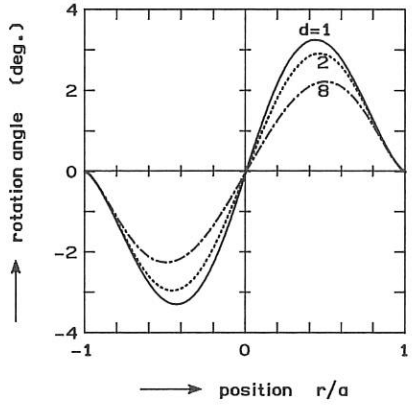


*Fig. 2* *Calculated Faraday-rotation angles as a function of the minor radius for a standard RTP plasma ($B_T$ = 2.5 T, $I_p$ = 150 kA, $n_e(0)$ = $5\times10^{19}$ $m^{-3}$) for different current density profiles $j_\phi$ = $j(0) \times (1-r^d)$ with d = 1, 2 and 8.*

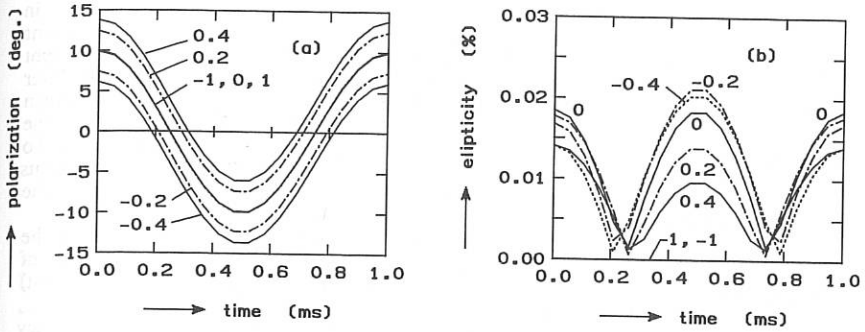


*Fig. 3 Calculations done for a standard RTP plasma (see legend of Fig. 2) for different positions (r/a = -1, -0.4, -0.2, 0, 0.2, 0.4, 1). The polarization angle of the incoming beam is modulated with an amplitude of 10°, the offset angle of the polarization is 0°. The ellipticity of the incoming beam is 0.*
*a) The polarization angle of the probing beam after propagation through the plasma, b) the ellipticity of the probing beam.*

techniques one can determine the Faraday-rotation angle. The major drawback for this detection scheme was the difficulty to modulate the polarization of the beam over a few degrees. We will now discuss some aspects of this scheme.

Suppose that we are able to modulate the polarization angle of the probing beam sinusoidally. If plasma is present, the Faraday-rotation angle will add a dc-level to the sine wave. Figure 3a shows the output polarization of the probing beam for several chords through the plasma as a function of time for a standard RTP discharge. The amplitude of the modulation is chosen to be 10°. In Fig. 3b the corresponding ellipticity is shown. From the calculations it is clear that the ellipticity remains acceptably small. No problems are expected if the modulation amplitude is kept small.

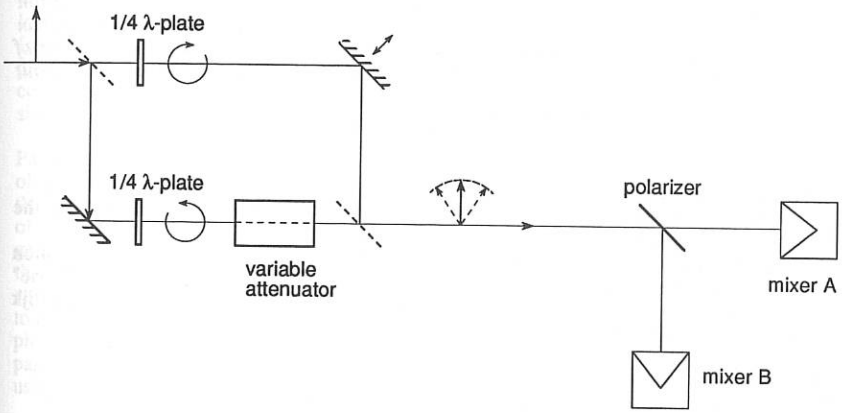


*Fig. 4 Test set-up for polarization modulation of the probing beam. The mixers A and B are used to analyse the beam polarization.*

Our scheme for modulating the polarization is rather straightforward and is shown in Fig. 4. The probing beam is split by a beam splitter into two parts. Each part is sent through a quarter wave plate. Both beams are now circularly polarized but with different orientations. In one of the paths a time-varying path length difference is introduced. After this the two beams are recombined. If the two beams have the same amplitude, which can be tuned with the variable attenuator, the recombined beam will be linearly polarized. The polarization angle is proportional to the phase difference between the two beam paths. To analyse the beam, two mixers are used which observe the different polarization components of the beam. To modulate the path length we used a loudspeaker with a small mirror in the centre. This limited the maximum modulation frequency to 1 kHz.

An example of polarization modulation is shown in Fig. 5. In this case the modulation amplitude was chosen to be larger than $45^{o}$ at a modulation frequency of 500 Hz. One can clearly see the inversion of the signals at the largest (and smallest) polarization angles. The first results of the test set-up are promising.

Next, we will compare the results of different detection schemes considering accuracy and time resolution in a test set-up. If possible the RTP polarimeter will be constructed in such a way that one can easily switch between one detection scheme and another. In this way we hope to measure accurately the current density distribution in RTP.

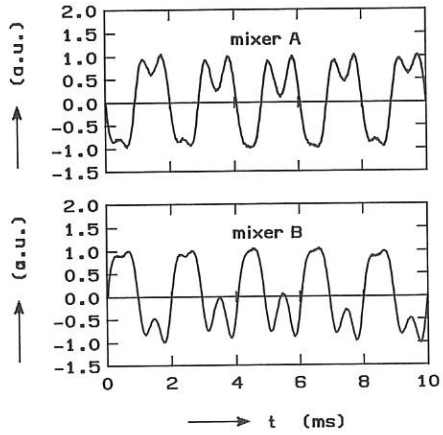


*Fig. 5* *Signals of the mixers A and B. The modulation amplitude was larger than $45^{o}$. The offset angle of the polarization is about $40^{o}$.*

**Acknowledgement**

The authors want to thank R. Lendvai and P. Zandbelt for their work on the polarization modulation experiment.

This work was performed as part of the research programme of the association agreement of Euratom and the "Stichting voor Fundamenteel Onderzoek der Materie" (FOM) with financial support from the "Nederlandse Organisatie voor Wetenschappelijk Onderzoek" (NWO) and Euratom.

**References**

[1] Lehecka T. et al. (1986) Rev. Sci. Instrum. **57**, p. 1986.
[2] Soltwisch H. (1986) Rev. Sci. Instrum. **57**, p. 1939
[3] Kunz W., Dodel G. (1978) Plasma Phys. **20**, p. 171.

# APPLICATION OF FUNCTION PARAMETRIZATION TO THE ANALYSIS OF POLARIMETRY AND INTERFEROMETRY DATA AT TEXTOR

B.Ph. van Milligen*, H. Soltwisch**, N.J. Lopes Cardozo*

* FOM Instituut voor Plasma Fysica 'Rijnhuizen', Association EURATOM-FOM, P.O.Box 1207, 3430 BE Nieuwegein, The Netherlands
** Institut für Plasmaphysik der KFA Jülich GmbH, 5170 Jülich, Postfach 1913, F.R. of Germany

**Abstract**
Function Parametrization (FP) provides a way to do complex data analysis in a fast and reliable manner that allows inter-shot analysis. The method has been used to analyze polarimetry and interferometry data at TEXTOR. A standard TEXTOR discharge is investigated, allowing comparison of the results obtained by FP analysis with results obtained previously. Agreement between results of the two methods is good. FP allows easy incorporation of additional data into the analysis.

We have determined the value of $q_0 = 0.8 \pm 0.09$. This is in close agreement with the value obtained by other methods from the same data.

## 1. Introduction

In a tokamak, the total toroidal plasma current can be programmed, but it is not possible to control the distribution of the current over the plasma column. In fact, it is not even possible to make direct, accurate measurements of the current density profile. The only measurements available are indirect, such as the magnetic fields outside the plasma (which give very little information on the current density in the plasma centre) and the Faraday rotation a polarised laser beam experiences when passing through the plasma. To construct the current distribution from those measurements, it is in general necessary to parametrize the plasma state (i.e. the profiles of density and current, or the MHD equilibrium) and to simulate the measurements corresponding to that plasma state. The problem is to find a set of parameters for which the simulated measurements match the experimental values within the measuring accuracy.

This type of problem is very well suited to be tackled with a method known as Function Parametrization (FP) [1]. In general terms, this method provides a direct mapping of the observables onto the state parameters of a physical system. For the problem at hand, this means that the current density profile is parametrized, and the profile parameters are expressed in terms of the magnetic fields or faraday rotation measurements. To achieve this, a database is generated containing a large number MHD equilibria. The equilibria are chosen in such a way that all normal plasma conditions are covered by the variation in the database. Along with each equilibrium, a set of simulated measurements is computed and stored. The database is subjected to a statistical analysis procedure that results in a direct mapping of the measurements onto the physical parameters. This mapping is a set of simple functions which express the plasma parameters in terms of the observables. These functions can be evaluated for experimental data using a minimum of CPU time. Thus, the advantages of FP are twofold:

- once set up, the analysis is very fast,
- the analysis is internally consistent, i.e. one always finds results within the class of parametrized MHD equilibria.

## 2. Interpretation of interferometry and polarimetry data at TEXTOR

At TEXTOR, the plasma is intersected by nine linearly polarized Far Infrared laser beams, vertically aligned in a poloidal cross-section. A more detailed description is given in Ref. [2].

The plasma equilibrium is computed by means of a fixed boundary ideal MHD equilibrium code: HBT [3]. The code has been extended to perform polarimetry simulations. In this computer model, a state of the plasma $p$ is identified by the following set of quantities:

1) Main plasma parameters:
   $I_p$ (plasma current) and $B_0$ (toroidal magnetic field on torus axis)
2) Flux surface geometry parameters specifying the location of the magnetic axis and parameters specifying the shape of the plasma boundary
3) Profile parameters specifying the equilibrium profiles $p'(\psi)$, $FF'(\psi)$
4) Electron density parameters specifying the electron density $n_e$

The profiles are represented in parametric form.

To get an indication whether the parametrization chosen is sufficient to describe real data, interferometry and polarimetry data of a prototypical TEXTOR shot (# 14214) were compared to data simulated by the equilibrium program HBT. The data were taken at time t = 1.33 s., when the plasma was in steady-state. The plasma state parameters were adjusted until satisfactory agreement with the measurements was obtained. We found that satisfactory reproduction of the measurements was possible using the parametrizations selected. A database of equilibria was created by varying the plasma state parameters around this typical state.

The database thus obtained was analysed by means of the function parametrization analysis program FP. The result of this was a mapping of the interferometry, polarimetry, plasma current and toroidal field measurements onto several interesting plasma parameters.

We performed an extensive error analysis on the mapping obtained. Quantities related to the outer plasma regions such as $a_{min}$ are indeterminate, as can be expected from this type of measurement. Use of magnetic diagnostics should improve the latter. Likewise, $\delta$ cannot be estimated accurately, due to the fact that the polarimetry/interferometry probing beams are 0.1 m apart in the central region. However, the plasma boundary position, $R_{geo}$, can be determined with an accuracy of 1 cm.; $n_{e0}$ with $9 \cdot 10^{17}$ $m^{-3}$; and $q_0$ with 0.09. This accuracy is comparable to the accuracy obtained with the iterative analysis method now in use at TEXTOR (Method I): 2.5% for $n_{e0}$ for FP against 3% for Method I; 11% for $q_0$ for FP against 15% for Method I [4].

## 3. Application to TEXTOR data and comparison to Method I

We have performed the analysis as described above. Here we present results for TEXTOR shot # 14214. We have selected a small number of plasma parameters from the large array available as being indicative of the possibilities of the reconstruction method: $R_{geo}$, $n_{e0}$ and $q_0$.

Figure 3.1 shows the time trace of the plasma current. There is a minor disruption at t = 0.79 s.

Figure 3.2 shows the time trace of $R_{geo}$ as computed using FP. The plasma performs a fast inward movement followed by a fast outward movement during the disruption. This behaviour is confirmed by the plasma position signal $\Delta$ that is computed using the method described in [5]. However, the fast outward movement could be an artefact due to the non-fulfillment of the assumption $n_e = n_e(\psi)$.

Figure 3.3 shows the time trace of $n_{e0}$ from FP. A steep drop in central electron density at the disruption is followed by a recovery shortly after. The recovery is not complete. The negative density spike is reflected on the Shafranov shift, showing a sharp drop followed by a rapid increase to its original value.

Figure 3.4 shows the time trace of $q_0$. After the start of the discharge, the signal steeply decreases to a value of around 0.8, crossing the $q_0 = 1$ line. Prior to the disruption the value increases slightly but stays below 1. During the disruption it drops slightly. It is interesting to see that both prior to the disruption, when sawteeth are absent, and after the disruption, when sawteeth are observed, $q_0 = 0.8 < 1$.

## 4. Results for discharge # 14214

The value of $q_0$ obtained with FP ($q_0 = 0.8 \pm 0.09$) compares well with the value obtained with Method I ($q_0 = 0.7 \pm 0.1$). We stress that this result is obtained by means of a self-consistent method employing ideal MHD equilibria as the basis for the analysis. Given the plasma model we have chosen, we are able to devise a $\chi^2$-test, and reject the hypothesis $q_0 \geq 1$ with 95% certainty. In other words, $q_0 \geq 1$ would require a more complex model than the one adopted here. The data presently available are well represented by the model used here, however, and therefore the need for a more complex model is not apparent.

Time traces for several important plasma parameters for the typical discharge # 14214 have been obtained using FP analysis. These traces satisfactorily reproduce the traces obtained by method I.

## Acknowledgements

The authors would like to thank Bas Braams and Patrick McCarthy for providing many useful insights into the subject of Function Parametrization. The latter is also responsible for some of the algorithms used in the polarimetry simulations. Guido Huysmans has been of great help in adapting the MHD equilibrium code HBT to our purpose. We are endebted to Chris Schüller for many fruitful discussions on the theme of this paper. This work was performed under the Euratom-FOM Association agreement with financial support from NWO and Euratom.

## References

[1] BRAAMS, B.J., JILGE, W., LACKNER, K., Nucl. Fusion **6** (1986) 699

[2] SOLTWISCH, H., *Interferometry and Faraday rotation on tokamaks, Part I: Experimental techniques; Part II: Data analysis,* Proc. course and workshop on basic and advanced plasma diagnostic techniques, Varenna, EUR 10797 EN, Vol. II (1986) 343

[3] GOEDBLOED, J.P.: *Some remarks on computing axisymmetric equilibria*, Computer Phys. Commun., **2&3** (1984) 123

[4] SOLTWISCH, H., STODIEK, W., MANICKAM, J., SCHLÜTER, J., *Current density profiles in the TEXTOR tokamak,* Proc. 11th International Conf. on Plasma Phys. and Contr. Fusion Research, Kyoto, Vol. 1 (1987) 263

[5] SOLTWISCH, H., *Plasma position detection and control in the TEXTOR tokamak by means of a far-infrared interferometer/polarimeter*, Nucl. Fusion **23** (1983) 1681

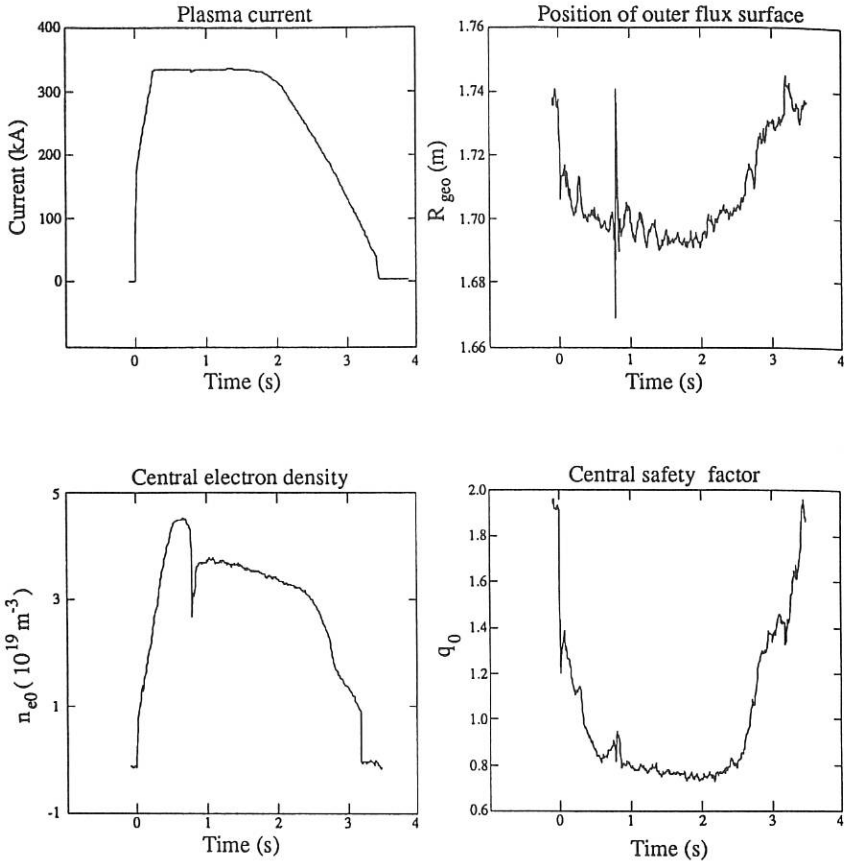


Left to right, top to bottom:
TEXTOR plasma parameters as a function of time for discharge 14214
Fig. 3.1 - Plasma current
Fig. 3.2 - Geometrical centre of the outer flux surface
Fig. 3.3 - Central electron density
Fig. 3.4 - Central safety factor

# Feasibility of alpha particle diagnostics for the active phase of JET, using Charge Exchange Recombination Spectroscopy

G.J. Frieling, R. Hoekstra, F.J. de Heer:
*FOM Institute for Atomic and Molecular Physics, Amsterdam;*
W. Mandl, A. Boileau, H.P. Summers, M. von Hellermann:
*JET Joint Undertaking, Abingdon.*

## Introduction

Observations of spectral emission from impurity ions in fusion plasmas following charge transfer from neutral deuterium or hydrogen beams has made great impact on deduction of impurity ion temperature, ion density and plasma rotation in recent years. The reactions are:

$$\begin{aligned} X^{z+} + D^0_{beam}(1s) &\longrightarrow X^{(z-1)+}(n\,l) + D^+ \\ X^{(z-1)+}(n\,l) &\longrightarrow X^{(z-1)+}(n'l') + h\nu, \end{aligned} \qquad (1)$$

where $X^{z+}$ is a fully ionised impurity ion of nuclear charge $z$.
In JET, transitions $n \rightarrow n'$ in the visible spectral region $\lambda > 3500$ Å are observed and the $D^0$ source is the neutral heating beams with primary particle energy in the range 40 - 80 keV/amu. The experimental arrangements, diagnostic methodology and deductions of the JET plasma behaviour have been reported previously [1,2,3]. In this paper, attention is focussed specifically on He II ($n = 4$ - 3) emission at $\lambda = 4686$ Å.

## Experiment

The emitted photons from the plasma are observed through several windows in the tokamak (figure 1). A multi-cord system containing 15 quartz fibres is mounted at point *A*.

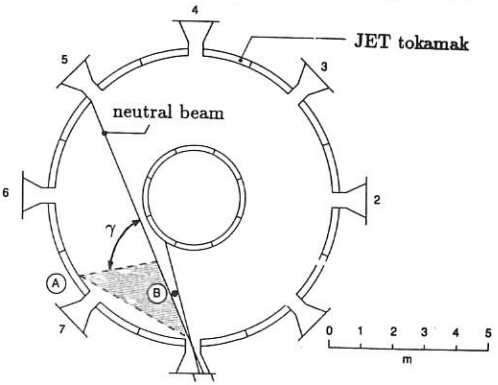


*Figure 1: Arrangement of viewing lines. Location A: collection optics mutichord system with horizontal viewing lines; Location B: single vertical viewing line.*

Each fibre provides the possibility to 'look' with a small solid angle into the plasma. Together these fibres form a fan of horizontal viewing lines intersecting with the injected neutral beams at major radii between 2.7 and 4.0 m. The relevant Charge Exchange (CX) processes (eq. 1) only occur at two locations: a) near the plasma wall where neutral

deuterium desorbes from the surface, and b) in the plasma bulk along the injected neutral deuterium beams. Generally the measured He II ($4 \rightarrow 3$) Doppler broadened spectrum is fitted with two Gaussians: a narrow feature corresponding with CX-processes at relatively low temperature near the plasma edge, and a broad feature coming from the hot plasma bulk due to charge transfer between impurities and the injected neutral beam. Analysis of these observations allow space and time resolved deduction of many plasma parameters e.g. absolute impurity ion density, ion temperature and plasma rotation [1,2,3], which is performed at JET routinely.

## Simulation He II ($4 \rightarrow 3$) emission at JET, and diagnostic implications

The Charge Exchange spectrum $I(\lambda)$ $[photons \cdot s^{-1}(sr)^{-1}m^{-3}\text{Å}^{-1}]$ of He II ($n = 4$ - 3), due to charge transfer between alpha particles in the plasma and injected neutral deuterium has been calculated as a function of the plasma temperature and for various observation angles $\gamma$ between the horizontal viewing lines and the injected neutral beam. The principle of the simulation is illustrated starting by defining a spherical coordinatesystem at observationpoint $O$ in the plasma (fig. 2).

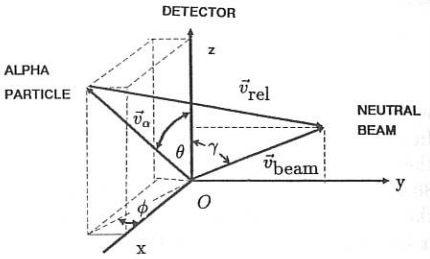


*Figure 2: Coordinatesystem and velocities at observationpoint O in the plasma.*

The alpha particles have a certain velocity distribution function $f_\alpha(v_\alpha)$. The crucial factor in the calculation is $v_{rel}$ (the speed of the alpha particle relative to the injected neutral beam), since it can take all values and it is directly linked with the ratecoefficient $k(v_{rel}) = \sigma(v_{rel}) \cdot v_{rel}$ for emission of photons. Both theoretical and experimental CX-cross sections have been collected [4,5,6,7], examined and stored in the JET atomic database. $I(\lambda)$ is expressed in the following analytic equation:

$$I(\lambda) = \frac{1}{4\pi} \int_{v_\alpha} \int_{\phi} \int_{\theta} \delta(v_\lambda - v_\alpha \cos\theta) \cdot k(v_{rel}) \cdot n_{D^0} \cdot f_\alpha(v_\alpha) \cdot v_\alpha^2 \sin\theta \, dv_\alpha \, d\theta \, d\phi \,, \quad (2)$$

which can be solved numerically.
The importance of this simulation is to investigate the influence on the shape and position of the observed spectrum due to the variation in the ratecoefficient $k$ as a function of $v_{rel}$. A measured spectrum is usually fitted with Gaussians, which implicitely assumes a *constant* ratecoefficient (chosen at the collision speed equal to the velocity of the injected beam), whereas in reality the ratecoefficient changes with all possible values of $v_\alpha$ relative to the velocity of the injected neutral beam. Therefore the shape of the real spectrum is *not* identical to a Gaussian. The consequences for deduction of ion temperature, ion density and plasma rotation velocity are briefly discussed in the next paragraph.

## Conclusions on emission of thermalised and slowing down alpha particles

*Thermal populations:*

When a simulated emissionspectrum obtained with equation 2 is compared with a Gaus-

sian spectrum corresponding with the same temperature and plasmaconditions, differences are observed. This is illustrated in figure 3 for the case of a 20 keV ion temperature plasma, half energy component (20 keV/amu) of the injected neutral beam and observation angle $\gamma = 45$ degrees.

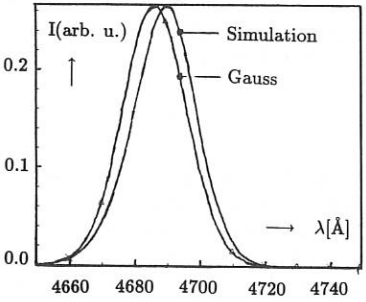


*Figure 3: Predicted Gaussian and simulated emission spectrum corresponding with identical plasma conditions (scaled on maxima).*

The simulated spectrum represents a realistic prediction of the spectrum to be observed. Fitting this spectrum with a Gaussian yields a 'measured' temperature smaller than 20 keV; the appeared shift $\Delta\lambda$ from the atomic wavelength at 4686 Å gives rise to an artificial plasma rotation velocity and from the difference in the areas underneath the curves, an incorrect $He^{2+}$ ion density is deduced. Corrections for the 'measured' quantities have been calculated as a function of the plasma temperature and for all beam energy components and for various observation angles $\gamma$ with respect to the injected neutral beam. A few typical results are presented in figure 4 (corresponding with full beam energy component of deuterium, and observation angles $\gamma$ in steps of 10° plus additional 45° as indicated).

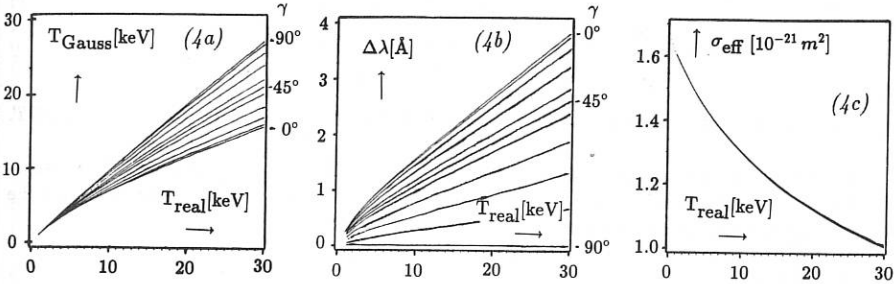


*Figure 4: Results for a) corrected temperature, b) induced red shift $\Delta\lambda$, and c) effective cross section.*

Generally speaking the slope in the cross section curve determines the displacement $\Delta\lambda$ of the peak and the curvature causes the change in the width of the spectrum affecting the 'measured' temperature. Since a simulated spectrum is still very well described by a Gaussian, the real spectral observations can still be analysed by the conventional procedure with Gauss fittings, taking into account the corrections for ion temperature and rotation velocity afterwards. The correct ion density is obtained by introducing an *effective* ratecoefficient $k_{eff} = \sigma_{eff} \cdot v_{beam}$, taking $\sigma_{eff}$ from figure 4c.
Analogue corrections have been obtained for other ion species e.g. carbon and oxygen, but for these cases the introduced corrections are significantly smaller.

*Slowing Down alpha particles:*

Concerning future measurements at JET, simulations have been done for alpha particles produced by fusion of deuterium and tritium. Initially created at 3.5 MeV with a source rate $S_\alpha\,[s^{-1}m^{-3}]$, the alpha particles slow down by electron collisions to a critical speed $v_c$ ($\simeq$ 100 keV/amu) at which point ion collisions become important. The slowing down velocity distribution [8], $f_{sd}(v_\alpha)$, of this population is written as:

$$f_{sd}(v_\alpha) = \left(\frac{S_\alpha\,\tau_s}{4\,\pi}\right)\left(\frac{1}{v_c^3 + v_\alpha^3}\right), \qquad (3)$$

with $\tau_s$ the slowing down time, usually in the order of a few seconds. With the extensive knowledge of the cross section behaviour required for the simulation, substitution of (3) in equation (2) produces the emission that is expected from this population.
In figure 5 an illustration is presented for an expected typical future case of JET (an ion temperature $T_i$ = 20 keV, a power production to input ratio $Q$ = 1 and an energy confinement time $\tau_E$ = 1 s).

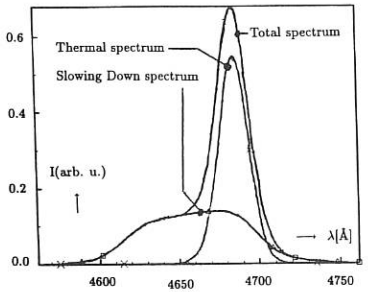


*Figure 5: Expected thermal and slowing down spectra of $He^{2+}$ in the tritium phase of JET.*

Extraction of the slowing down feature provides a unique future tool for local measurements of alpha particle source rate $S_\alpha$, slowing down time $\tau_s$, critical velocity $v_c$ and the slowing down velocity distribution function.

## References

[1] Boileau A., von Hellermann M.G., Horton L.D., Spence J., Summers H.P., Plasma Physics of Controlled Fusion **31** (1989) 779.
[2] Boileau A.,von Hellermann M.G., Horton L.D., Summers H.P., Morgan P.D., Nucl. Fusion **29** (1989) 1449.
[3] Weisen H., von Hellermann M.G., Boileau A., Horton L.D., Mandl W., Summers H.P., Nucl. Fusion **29** (1989) 2187.
[4] Fritsch W., Phys. Rev. **A38** (1988) 2664; J. Phys. Coll. **50** (1989) 87 and private communication.
[5] Belkic D., Institute of Physics, Belgrade, Yugoslavia, private communication.
[6] Hoekstra R., Frieling G.J., de Heer F.J., FOM-AMOLF, Amsterdam, private communication.
[7] Hoekstra R., Thesis (1990), Rijksuniversiteit Groningen, The Netherlands.
[8] Post D.E. et al., J. Fusion Energy **1**, No. 2, (1981) 129.

# POLARIZATION ROTATION AND ION THOMSON SCATTERING

D. A. Boyd

Laboratory for Plasma Research
University of Maryland
College Park, MD 20742
U. S. A.

In the ion Thomson scattering diagnostic[1] proposed for JET a 140 GHz beam of radiation will be injected from the top of the machine and travel downwards at various selected angles to the vertical on its way to the observed scattering volume. The beam will be launched as an ordinary mode at the plasma edge and it is assumed that most of the power will remain in the ordinary mode as the beam propagates across the plasma to the scattering volume. Likewise, the scattered ordinary mode is presumed to propagate toward the receiver preserving its state of polarization and emerge at the plasma edge as an ordinary mode.

It has been shown[2] that if an ordinary mode is launched so that it propagates exactly perpendicular to the magnetic field all the way across the plasma it preserves its state of polarization. This restricted condition matches a situation in which the beam propagates vertically and perpendicular the the magnetic surfaces in the discharge. Naturally the proposed diagnostic seeks to probe at a variety of launched beam angles to obtain a greater spatial range for the location of the scattering volume. Consequently this study seeks to investigate the evolution of the polarization state of a beam launched as an ordinary mode as it propagates across the plasma at an arbitrary angle to the vertical.

For simplicity the calculation uses a "circularized" description[3] of the JET plasma. A ray is launched at $R=R_o$, the major radius, and $z=+a$, the minor radius, at an arbitrary angle to the vertical. The ray propagates rectilinearly. No refraction is allowed although the ray propagates at an angle to the density gradient. Both the extraordinary and ordinary modes are constrained to propagate along the same ray path. A formulation of the problem due to Segre[4] is used as a basis for a computer code which integrates the propagation equation for the evolution of the three Stokes' parameters which describe the polarization state along the ray.

The parameters of the "circularized" JET are: $R_o=2.96m$, $a=1.25m$, $B_o=3.5T$, $n_e=(n_e(0)-n(a))(1-(r/a)^2)+n(a)$. $n(a)=2x10^{17}\ m^{-3}$. The poloidal magnetic field is defined by $q=q(0)+(q(a)-q(0))(r/a)^s$. For this study $q(0)=1$ and $q(a)=3$ with $S=2$ or 4. The results of the calculation are expressed in terms of the properties of the polarization ellipse. This ellipse is shown in figure 1a. Since it is the divergences of the ellipse parameters from those of the local ordinary mode that are of concern, it is

these differences which are plotted in the figures.

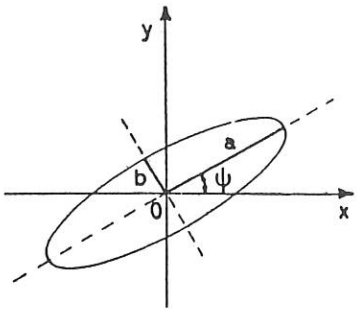


figure 1a

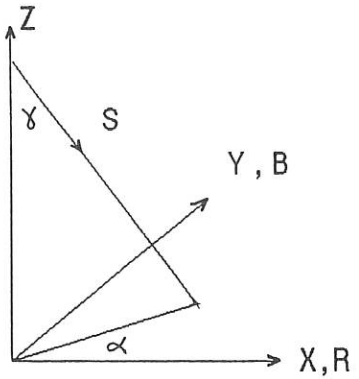


figure 1b

The geometry of the system is described in figure 1b. The origin is at the major radial coordinate $R_o$. x is in the major radius direction and y is in the toroidal direction. z is vertical. S measures the length along the wave propagation path, whose direction is specified by the angles alpha and gamma, from the injection point (0.0.a). The Stokes' parameters are evaluated in another coordinate frame. In this frame z is in the S direction and y is parallel to the magnetic field at the injection point.

The orientation of the polarization ellipse is given by the angle Psi and the ellipticity is given through an angle Chi by b/a=tan(Chi). Computation of the evolution of the Stokes' parameters allows the evolution of the angles Psi and Chi to be followed as the wave propagates. The difference between the evolved values of Psi and tan(Chi) and the values of these parameters for the local ordinary mode are evaluated at chosen points.

The electron density profile is shown in figure 2a. The q profiles for the two values of the shape parameter, s, are shown in figure 2b.

Results

If alpha is fixed at zero and gamma is scanned S lies in the z,R plane. A typical set of results is shown in figure 3a and 3b. Psi nutates about the local ordinary mode orientation. The nutation angle is about ± 3°. The ellipticity, tan(Chi), also fluctuates about the local ordinary mode value. As gamma is increased from 0° to 20° the fluctuation amplitudes increase nearly linearly. At 0° the nutation angle and ellipticity fluctuations are very small and rise to about 6° and ±0.1 at gamma=20°. If the central electron density is raised from $2\times10^{19}$ to $8\times10^{19}$ $m^{-3}$ the

fluctuation amplitudes do not change. What does change is the spatial period of the fluctuations. At $2x10^{19}$ the spatial period is about 8 cm, at $4x10^{19}$ about 3 cm, and at $8x10^{19}$ about 1 cm. Changing the shape of the q profile also has only minor effects.

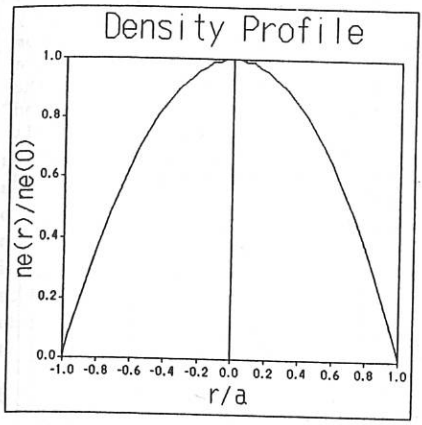


figure 2a

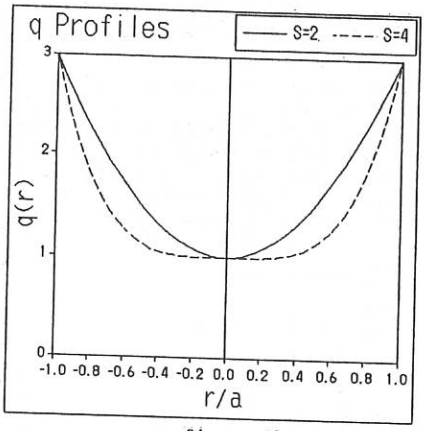


figure 2b

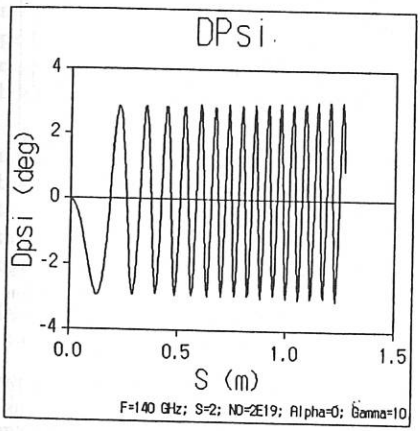


figure 3a

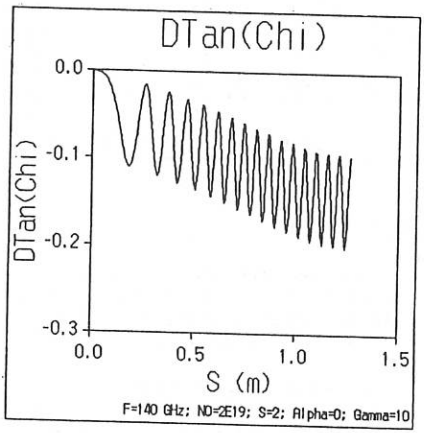


figure 3b

If gamma is fixed at 10° and alpha is varied the launching direction scans out the surface of a cone with half angle equal to 10°. At alpha=0° Psi nutates by about ±3°, at 45°and 225° by about ±18°, at 90° and 270° by about ±22°, and at 135° and 315° by about 13°. As one crosses the angle

alpha=172° and 352°, the phase of the nutation changes by π.

At a fixed alpha=90° an interesting transition occurs as gamma is increased. Up to an angle of gamma≈18° Psi nutates about the local ordinary mode Psi orientation with a steadily growing amplitude as gamma increases. Beyond gamma≈18° psi rotates continously so that there are very large divergences of the propagating wave's polarization properties from that of the local ordinary mode. This transition is clearly visible in the Stokes' parameter space S12:S22. ½Arctan(S22/S12) defines Psi. As the launched wave propagates S12 and S22 are coupled so that they lie on an ellipse in the S12:S22 space. When this ellipse is confined to the left two quadrants of the space, Psi nutates. This is the situation in figure 4a where gamma=10°. When gamma is increased to 20° then the ellipse covers all four quadrants and Psi continuously rotates.

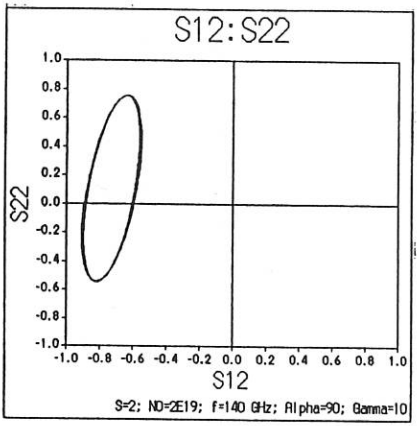


figure 4a

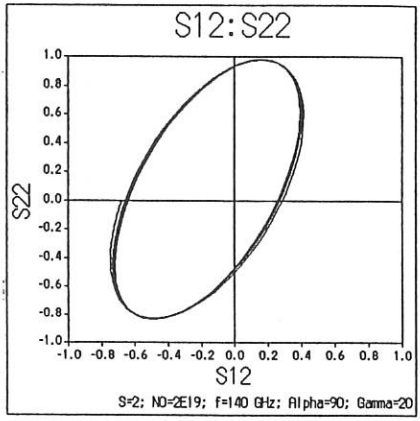


figure 4b

## Conclusions

a) As the angle gamma of the launched wave propagation vector is increased, Psi nutates about the local ordinary mode Psi. This nutaion angle increases linearly with gamma. The nutation angle is not a function of the electron density or q profile shape. It is a strong function of alpha.

b) When alpha and gamma are such there is an appreciable toroidal field component parallel to the propagation vector of the launched wave Psi begins to rotate continuously. This is a complication for the scattering experiment.

## References

1. A. E. Costley et al. JET Report JET-R(88)08
2. T. P. Hughes et al. Proceeedings of 16th EPS-PPD, Venice 1989
3. A. Airoldi, A. Orefice, G. Ramponi FP 88/14 June 1988
4. S. E. Segre. Plasma Phys **20** 295 (1978)

# A POSSIBLE ELECTRIC FIELD MEASUREMENT BY A MOLECULAR HYDROGEN BEAM

W. Herrmann

Max-Planck-Institut für Plasmaphysik, EURATOM Association
D-8046 Garching, Fed. Rep. Germany

## Abstract

A diagnostic method of measuring the static electric field in a plasma is proposed and analyzed. By injecting a neutral molecular beam into a plasma, some of the molecules are ionized and dissociated after some orbital motion. The energy of the neutrals originating from dissociation is determined by the original beam acceleration, energy changes due to atomic processes, and the potential difference between the points of ionization and dissociation. If the first two parts of the energy can be compensated or subtracted by calibration, the potential difference and hence the electric field can be obtained by measuring the energy of the neutral. The analysis shows that fields as low as 40 V/cm might be measurable by this method.

## Introduction

Static or quasistatic electric fields in a plasma result from different confinement times of ions and electrons (if no electric fields are present), which cause deviations from neutrality. Electric fields, although themselves caused by particle transport, influence particle transport and confinement. They also affect plasma equilibrium and stability, cause global poloidal rotation of the plasma, influence the power deposition of neutral beams and may be especially important for the confinement of impurities [1].

This paper proposes a new method of measuring the electric field by means of a molecular hydrogen beam. The availability and effectiveness of molecular hydrogen beams for penetration and detection have been discussed in an earlier paper devoted to measurement of the "local" $q$-profile with molecular hydrogen beams [2]. This paper therefore concentrates on describing the proposed method and discussing the expected measuring accuracy.

## Description of the Method

A beam of neutral hydrogen molecules is assumed to be injected into a plasma in the poloidal plane. Some of them are ionized and start to rotate in the magnetic field (the motion in the toroidal direction is unimportant for this consideration, since it only determines the observation angle of the later-described analyzer). The lifetime of the ionized molecule till dissociation is only of the order of the gyration time[2].In the presence of a radial electric field the energy of the rotating molecule changes with its radial position. The dissociation of the molecule may lead to a proton and a neutral hydrogen atom. Both particles carry just half of the energy of the molecule (the Frank-Condon effect is discussed later). The energy of the neutral therefore depends on the radial position of dissociation. If ionization and dissociation of the molecule occur at different radial positions, measurement of the neutral particle energy reveals the

potential difference between these two points. Figure 1 gives an illustration of this method. A molecular beam is injected from below in the vertical or nearly vertical direction. The energy analyzer views the horizontal plane and the magnetic field is purely perpendicular to the plasma cross-section. The locations of ionization $r_1$ and dissociation $r_2$ are then separated by about one Larmor radius $R$. In any case, this distance can be calculated from the known particle energy, magnetic field, injection geometry, and line of sight of the analyzer.

For 20 keV hydrogen molecules in a 2 T field $R$ is about 1 cm. The largest distance possible is two times the Larmor radius if the injector and analyzer are both below or above the plasma for the measuring location in the horizontal midplane of the plasma. (Because of the toroidal velocity gained by the ionized molecule in interacting with a poloidal field, e.g. in a tokamak, the line of sight of the analyzer generally has to be inclined in the toroidal direction; see ref. [2].) In such an arrangement, however, the space resolution is small. For optimal measurement of the local field value the angle between the injection and line of sight of the analyzer should be about 90°. If the fields vary on a scale shorter than the above-assumed 1cm and a better resolution of the electric field profile is required, the energy of the beam can be reduced or the geometrical arrangement of injection and detection can be changed to get a smaller distance between the ionization and dissociation sites.

An analyzer suitable for measuring the particle energy is a retarding field analyzer coupled with a stripping cell. The toroidal inclination of the analyzer has to be chosen according to the toroidal velocity gained by the molecule from interaction with the poloidal field [2]. This poses the least problem for measurement in the plasma edge, where the poloidal field is best known and the electric fields are probably largest.

### Discussion of the Atomic Processes Involved

Not only is the energy of the neutrals escaping from the dissociation determined by the acceleration voltage of the beam and the potential difference between the points of ionization and dissociation of the molecule, but it may also be affected by the atomic processes involved. Each particle detected has gone through four atomic processes:

- neutralization of the accelerated molecule
- ionization of the molecule in the plasma
- dissociation of the molecule in the plasma
- ionization of the neutral atom in the stripping cell of the analyzer.

If we assume that charge exchange collisions and collisions with electrons do not appreciably alter the energy of the molecule or atom we have to consider the effect of the following collisions on the final particle energy:

- ionization of the molecule by proton impact
- ionization of the atom in the stripping cell of the analyzer.
- dissociation of the molecule (Frank-Condon effect)

According to ref. [3], the energy lost by a proton on impact with electron production in a hydrogen gas is of the order of 40 to 50 eV (this process includes ionization as well as dissociative ionization) and is not negligible. This impact can, however, be avoided if

the energy of the molecule is chosen significantly below the maximum of the ionization cross-section. Charge exchange is then the dominant process. This is the case for a beam with less than or about 20 keV in a plasma with a temperature of a few keV.

The ionizing process in the stripping cell is always an atomic impact on a neutral molecule, and the energy transfer involved is probably as large as the average energy loss for production of an electron and will therefore show up in the measurement.

Dissociation is a process which produces large energy changes, irrespective of whether the collision is ionic or electronic. This is due to the Frank-Condon effect. According to ref. [4], the average energy each particle gains in a dissociative collision is $E_{FC} = 4.3$ eV in the rest frame. (The energy loss of the molecule in the dissociation collision is neglected in this context.) Converted to the laboratory frame, the average energy change $\Delta E_{FC}$ in the direction of motion of the molecule is

$$\Delta E_{FC} = 2 \cdot \sqrt{E_{FC} \cdot E}.$$

$E$ is half the energy of the molecule. The relative energy change $\Delta E_{FC}/E$ is the smaller the larger the original energy of the molecule.

### Discussion of the Measuring Accuracy

As the Frank-Condon effect is usually the dominant one in atomic processes, only this effect is considered in estimating the measuring accuracy. If for the energy measurement, for example, a retarding field analyzer is used, one finds a smeared-out curve as a function of the retarding voltage $U$ (curve 2 in Fig. 2) instead of the sharp limit (curve 1). The measuring curve one would obtain when an electric field is present in the plasma will be shifted according to half the potential difference (the atom gets only half the energy of the molecule) between the points of ionization and dissociation of the molecule, as shown in curve 3 of Fig. 2.

If one assumes that a shift $\Delta E$ of the curves can be measured, which is at least 10 % of the average spread $\Delta E_{FC}$ due to the Frank-Condon effect, then the following relation is found for the minimum field strength $F$ measurable for a separation of the points of ionization and dissociation equal to the Larmor radius $R$:

$$\Delta E = \frac{e \cdot F \cdot R}{2} = \frac{e \cdot F}{2} \cdot \frac{\sqrt{m} \cdot \sqrt{2 \cdot (2E)}}{e \cdot B} = 0.1 \cdot \Delta E_{FC} = 0.2 \cdot \sqrt{E_{FC} \cdot E}$$

$$F = [V/m] = \frac{0.2 \cdot \sqrt{E_{FC}}}{\sqrt{m}} \cdot B[T] \approx 2.8 \cdot 10^3 \cdot B \quad \text{for } H_2\text{beam}$$

$$\approx 2.0 \cdot 10^3 \cdot B \quad \text{for } D_2\text{beam}$$

With a magnetic field of 2 T, electric fields of ~40 V/cm could be measured by means of a deuterium beam. Here it should be mentioned that $\Delta E_{FC}$ is the largest possible spread in the particle direction. The spread is negligible if the Frank-Condon motion is perpendicular to the particle motion, and on the average the spread will be considerably smaller and the lower limit of the measurable electric field may be reduced.

The best way to take the atomic processes into account could be by operating the system in a regime with negligible electric field. A relative measurement then suffices to determine the electric field.

The minimum measurable electric field does not depend on the beam energy. This can be used to obtain good resolution of the electric field profile by appropriately choosing the beam energy.

## Conclusion

An electric field of the order of 40 V/cm and larger may be measured by analyzing the energy of neutral atoms resulting from injected, ionized and then dissociated hydrogen molecules.

## Acknowledgement

The author is grateful to Professor V. Dose for pointing to the Frank-Condon effect as the main effect limiting the measuring accuracy and for critically reading the manuscript.

## References

[1] W. Feneberg, Nuclear Fusion **29** (1989) 1117;

[2] W. Herrmann, 16th EPS Conference, Venice, 1989, Proc. Volume IV, p. 1541; IPP Report 1/249, Sept. 1989, submitted for publication in Plasma Physics and Controlled Fusion;

[3] M. Rudd, H. Jorgenson, Phys. Ref. **131** (1963), 666;

[4] R.K. Janev et al., Elementary Processes in Hydrogen-Helium Plasmas, Springer Verlag Berlin, Heidelberg, New York, London, Paris, Tokyo, 1987.

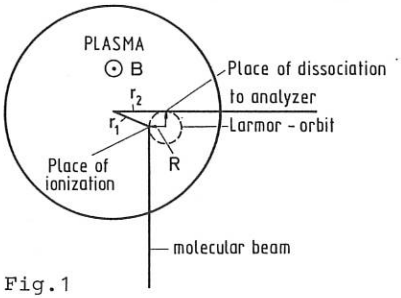


Fig.1

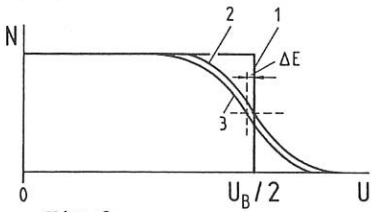


Fig.2

# THE LIMITATIONS OF MEASUREMENTS OF THE LOCAL WAVENUMBER

A. Carlson, A. Rudyj, and the ASDEX Team.

Max-Planck-Institut für Plasmaphysik, 8046 Garching, Fed. Rep. Germany

## I. Introduction

A Langmuir probe consists of a small conductor in a plasma whose current-voltage characteristic is measured. The characteristic can be evaluated to provide density, temperature, and potential. Because the spatial and temporal resolution can be very good, Langmuir probes are often used to study fluctuations of these quantities. Such measurements are straightforward as long as one is only interested in temporal fluctuations of the ion saturation current or the floating potential. If information about the spatial variations of these quantities or the fluctuations of fundamental plasma properties is desired, then at least two probes are required and the measurements and their interpretation become difficult. We are concerned here with two aspects of this problem, estimation of the spatial spectral density function S(k), and measurement of temperature fluctuations.

## II. Two Tip Estimate of S(k)

Measurements with two probes are sufficient to provide an estimate of S(k) /1/. Since a sufficient number of sample times are available, a temporal Fourier transformation can be made without loss of information, and the various Fourier components can be independently analyzed. Each component of the signal from each tip (located at $x_1$ or $x_2$) can be characterized by an amplitude ($A_1$ or $A_2$) and a phase ($\varphi_1$ or $\varphi_2$). There are three independent measurable quantities, the average power P, the usual local wavenumber $k_l$, and a second local wavenumber we call $k_l^*$.

$$P = (A_1^2+A_2^2)/2$$

$$k_l = (\varphi_2-\varphi_1)/(x_2-x_1)$$

$$k_l^* = (1/P)(A_2^2-A_1^2)/(x_2-x_1)$$

In order to investigate the information content of measured values of P, $k_l$ and $k_l^*$, we need to develope a more detailed model. We take a single frequency and assume a particular S(k) to be given. We divide the k-axis into a large number of equally-spaced discrete values, to each of which we assign a Fourier component with an amplitude equal to $\sqrt{S(k)}$. The phases are assigned random numbers between 0 and $2\pi$, a different set for each realization. We then "measure" this function by calculating the amplitude and phase as a function of position.

$$f(x,t) = \Sigma a_k \sin(kx-\omega t+\varphi_k) = A(x)\sin(-\omega t+\Phi(x))$$

We then take the limit $(x_2-x_1)\rightarrow\infty$ and set $x=0$ without loss of generality.

$$P = A^2(0) = [\Sigma\sqrt{S(k)} * \sin(\varphi_k)]^2 + [\Sigma\sqrt{S(k)} * \cos(\varphi_k)]^2$$

$$P\,k_l = P\,d\Phi(0)/dx = [\Sigma\sqrt{S(k)} * \cos(\varphi_k)] * [\Sigma\sqrt{S(k)} * \sin(\varphi_k)] + [\Sigma\sqrt{S(k)} * \sin(\varphi_k)] * [\Sigma\sqrt{S(k)} * \cos(\varphi_k)]$$

$$P\,k_l{}^* = P\,dA(0)/dx = [\Sigma\sqrt{S(k)} * \cos(\varphi_k)] * [\Sigma\sqrt{S(k)} * \sin(\varphi_k)] - [\Sigma\sqrt{S(k)} * \sin(\varphi_k)] * [\Sigma\sqrt{S(k)} * \cos(\varphi_k)]$$

With this formulation of the problem, we are in a position to examine ensemble averages of the above quantities, averages over all possible sets of phases. One can show that

$$\langle P\,k_l \rangle / \langle P \rangle = [\Sigma\, k\, S(k)] / [\Sigma\, S(k)] = \langle k \rangle.$$

We see that <k> may be equivalently defined as the average k in the fluctuations (weighted with S(k)) or as the average of $k_l$ in the measurements (weighted with the measured power). Convenient cancellations of cross-terms also allow an exact calculation of the rms deviations:

$$\langle P((k_l-\langle k\rangle)^2 + (k_l{}^*)^2) \rangle / \langle P \rangle = [\Sigma\,(k-\langle k\rangle)^2\, S(k)] / [\Sigma\, S(k)] = (\delta k)^2.$$

As with <k>, we may define δk in terms of S(k) or in terms of the distribution of measured values.

We see now that the information immediately available from two-tip measurments consists of P, <k>, and δk, each as a function of frequency. If there is any additional information in a set of measurements, then it must be found in the shape of the distributions of the measured quantities normalized as follows:

$$P' = P / \langle P \rangle$$

$$k_l{}' = (k_l - \langle k \rangle) / \delta k$$

$$k_l{}^{*\prime} = k_l{}^* / \delta k$$

We have carried out simulations as described above for several different shapes of S(k), three of which are shown in Fig. 1(a). The first has a Gaussian bell shape and might represent a turbulent spectrum with $\Delta k \approx k$. The second has two well-defined wavenumbers of equal strength, as might be the case for non-turbulent waves which propagate in both directions. The third represents the possibility of an asymmetric spectrum. The three functions have been normalized so that $\langle k \rangle = \delta k = 1$.

If we are looking for an approximation to S(k), the most natural thing to look at is the power-weighted distribution of $k_l$. This distribution for each of the S(k) is plotted in Fig. 1(b). It is clear from the figure that the distributions are indistinguishable and do not retain any of the shape of the input spectral density functions. The fourth curve in the figure is the function $(3/4)(1+k_l{}^2)^{-5/2}$, which was found to be the limiting distribution. If this distribution is interpreted too literally as an approximation to S(k), then one would always come to the erroneous conclusion that the spectrum drops off as $k^{-5}$. It is also worth noting that the distribution of $k_l$ is narrower than the corresponding S(k) by a factor $\sqrt{2}$.

The power-weighted distribution of $k_l$ is only one way to look at the data. It was found that the probability that the normalized measured values lie between P′ and P′+dP′, \klh\ and \klh+d\klh, and \klsh\ and \klsh+d\klsh\ is equal to

$(1/\pi)\ P'\ \exp(-P'(1+k_l'^2+k_l^{*\prime 2}))\ dP'\ dk_l'\ dk_l^{*\prime}$. If this expression is multiplied by $P'$ and integrated over $P'$ and $k_l^{*\prime}$, the power-weighted distribution of $k_l'$ given above is recovered.

We have analyzed ion saturation current measurements from the ASDEX divertor in a similar fashion. The tip separation was 6 mm, and the correlation was about 80%. We analyze 0.84 sec of data as 21 packets, each 40 msec long (40,000 points at 1 MHz sampling rate). For each packet we use the 81 Fourier components from 9 kHz to 11 kHz. Thus the distributions of $k_l$ and $k_l^*$ plotted in Fig. 2 are based on a total of 1701 realizations. Comparison with the $(1+k^2)^{-5/2}$ curves also plotted shows that the ASDEX data fit the theoretical prediction very closely.

## III. Temperature Fluctuations with Two Tips

One method used to investigate temperature fluctuations is to observe the fluctuations in the current through a pair of probes $\langle(\delta I)^2\rangle$ as a function of the bias voltage $V_{bias}$ between the probes /2,3/. The measured curve is fitted with the theoretical curve as a function of six parameters, $\langle(\delta n^2)\rangle$, $\langle(\delta E^2)\rangle$, $\langle(\delta T^2)\rangle$, $\langle(\delta n)(\delta E)\rangle$, $\langle(\delta n)(\delta T)\rangle$, and $\langle(\delta T)(\delta E)\rangle$. There is a serious problem with this method, namely that although fluctuating gradients in plasma potential ($\delta E$) are central to the measurement, gradients in density and temperature are neglected. Since the floating potential is strongly influenced by the temperature ($V_{fl} \approx V_{pl} - 3kT/e$), and it is reasonable to suppose that the temperature fluctuations may be of the same order as the potential fluctuations, the effect of temperature gradients cannot be neglected.

If temperature and density gradients are included on the theory, we are faced with the difficult task of determining not 6 but 15 parameters from a single curve. The important point is that a gradient in temperature has a qualitatively and quantitatively similar effect on the current as an electric field. In particular, both can produce a $\langle(\delta I)^2\rangle$-$V_{bias}$ curve whose minimum is non-zero and shifted away from $V_{bias}=0$.

How can we obtain more information? One possibility is to measure the potential of one of the tips as well as the current. The fluctuations in probe potential $\langle(\delta V_1)^2\rangle$ provide a second curve which can be fitted, and the correlation between the two signals $\langle(\delta I)(\delta V_1)\rangle$ provides a thisrd curve. The information is tripled; the number of parameters to be fitted is increased from 15 to 21 since we can now detect absolute potential fluctuations, not just gradients.

The information content of the measurement can be further increased by allowing a different current to flow in the two probes. The simplest configuration of this sort would be to measure the current fluctuations to two single probes and their correlations, as functions of the two bias voltages.

**References:**

/1/ J.M.Beall, Y.C.Kim, and E.J.Powers. J.Appl. Phys. 53(6), June 1982.
/2/ D.C.Robinson and M.G.Russbridge. Plasma Phys. 11(73), 1969.
/3/ H. Lin, R.D.Bengtson, and C.P.Ritz. Phys. Fluids 1(10), October 1989.

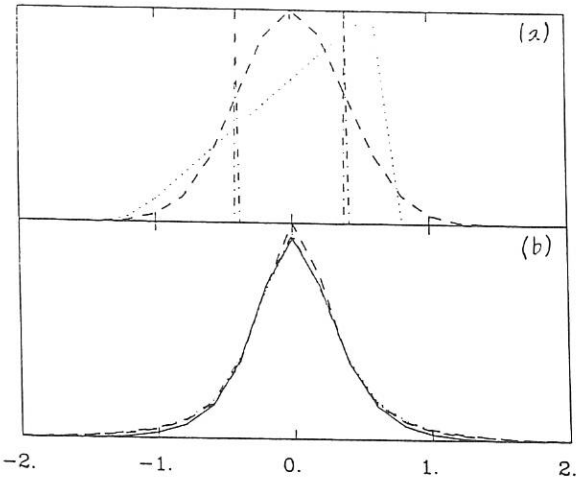


Fig. 1. Results of simulations of measurements of $k_l$ for three qualitatively distinct spectral density functions. (a) The three S(k), normalized so that $\langle k \rangle = 0$ and $\delta k = 1$. (b) The corresponding three power-weighted distributions of $k_l$. They are normalized to have equal areas, but the position and width have not been adjusted. The solid curve is the analytical prediction.

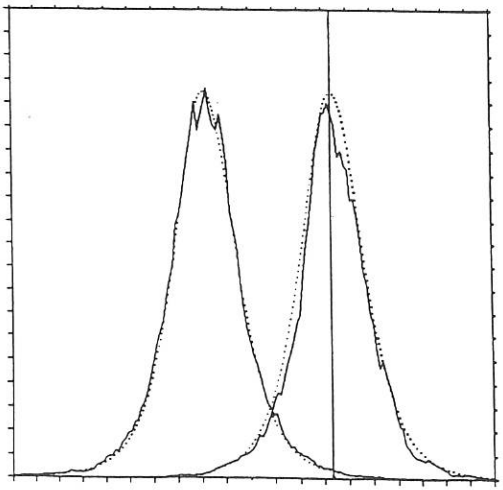

Fig. 2. Results of analysis of ASDEX data. The curve on the left is the power-weighted distribution of $k_l$, on the right, that of $k_l^*$. The dotted curve has the analytically predicted form. The vertical bar is the k=o line.

# ION TEMPERATURE MEASUREMENTS IN THE TCA TOKAMAK BY COLLECTIVE THOMSON SCATTERING

M. Siegrist, R. Behn, D. Dicken*, B. Duval, J. Hackmann,* B. Joye, J. Lister, C. Nieswand, A. Pochelon, G. Soumagne, D.C. Yuan

Centre de Recherches en Physique des Plasmas
Association Euratom - Confédération Suisse
Ecole Polytechnique Fédérale de Lausanne
21, Av. des Bains, CH-1007 Lausanne/Switzerland

*Institut für Laser- und Plasmaphysik, Universität Düsseldorf, West Germany

## ABSTRACT

Collective Thomson scattering, using a high-power pulsed $D_2O$ laser at 385μm and a heterodyne receiver system, has provided local ion temperature ($T_i$) measurements of the plasma in the TCA tokamak. Recent improvements in the noise-equivalent power (NEP) of the Schottky barrier diode mixers permitted us to achieve a typical precision of ±12% for a single shot measurement at densities above $10^{20}m^{-3}$. Even at densities of standard TCA discharges ($5x10^{19}m^{-3}$) the uncertainty is better than ±25%.

For the interpretation of the measured spectra and the evaluation of $T_i$ the local value of the electron temperature ($T_e$) is an important parameter. Therefore, $T_e$ was measured simultaneously by incoherent Thomson scattering at 0.694μm during a series of shots. The density was obtained from a far-infrared interferometer. An independent measurement of $T_i$ on TCA can be obtained from a neutral particle analyzer (NPA). Comparison of the results from the two methods showed good agreement.

The precision of a $T_i$-measurement depends strongly on the plasma density. Since an uncertainty of ±25% at standard densities may still not be regarded as satisfactory, further investigations using a numerical simulation code have been carried out to find ways of improvement.

## INTRODUCTION

Last year we reported the first single shot ion temperature measurements in a tokamak by collective Thomson scattering (CT) [1]. The precision was estimated to be of the order of 25%. This could not yet be considered as sufficient accuracy compared to other $T_i$ diagnostics and hence improvements were required. On the other hand, two important questions still had to be answered: (1) are the observed spectra indeed produced by scattering from thermal velocity distributions and (2) is the ion temperature obtained from collective Thomson scattering in agreement with results from other diagnostics.

In this paper we report measurements which were undertaken to investigate these points.

## APPARATUS

The experimental set-up has been described in detail in ref [1]. We will only briefly recall the main components: A $CO_2$ laser which delivers 600J on the 9R(22) line in a 1.4μs long single mode pulse is used for optical pumping of a 4m long unstable resonator containing 6.5mbar of $D_2O$ vapor. The far infrared laser produces 0.5J during 1.4μs at the wavelength of 385μm.

The $D_2O$ laser emission is focused to a 3mm waist close to the plasma center via a set of off-axis parabolic mirrors. The scattered light is collected at $90^o$ to the incident beam in a solid angle of $4.3 \times 10^{-3}$ sr.

For detection and spectral analysis of the scattered radiation we use a heterodyne receiver with an optically pumped $CD_3Cl$ laser as local oscillator. Its emission is combined with the scattered radiation in an optical diplexer and mixed in a Schottky barrier diode. The resulting IF signal around 3.6 GHz, is amplified and split into twelve channels with a bandwidth of 80 MHz each. Thereafter the signals are integrated and digitized.

A considerable improvement of the sensitivity of our detection system has been achieved through a collaboration with groups at the University of Düsseldorf and the MPI für Radioastronomie, Bonn, which provided the mixer. The double sideband system noise temperature $T_{sys}^{DSB}$ has been measured as a function of the IF frequency. For the diode used for the measurements reported here $5000^oK$, corresponding to a NEP (noise-equivalent-power) of $1.4 \times 10^{-19}$W/Hz, has been obtained in the most sensitive channel.

For the interpretation of spectra obtained from collective Thomson scattering, the electron density and temperature are required. These were measured simultaneously by a far-infrared interferometer and by ruby laser scattering, respectively. An independent measurement of $T_i$ on TCA can be obtained from a neutral particle analyzer with five energy channels with an accuracy of the order of 5%.

## MEASUREMENTS

So far we have analyzed collective scattering data from several hundred plasma discharges. The observed spectra could all be interpreted assuming thermal density fluctuations taking into account the influence of impurity ions and the magnetic field. There is no indication that non-thermal fluctuations contribute to the spectrum in the parameter range of interest ($\Delta k = 230$ cm$^{-1}$, $\Delta\omega > 3 \times 10^9$ s$^{-1}$).

Table I shows the results of 8 plasma shots with fairly reproducible plasma parameters. The diagnostic systems for $n_e$, $T_e$ and the NPA were all operational. It is immediately obvious that while $n_e$, $T_e$ and $T_i^{NPA}$ are very similar, thus proving that the plasmas were indeed reproducible, $T_i^{CT}$ shows large fluctuations. This indicates that the signal-to-noise ratio was not as good as was usually the case for this particular series.

For the centermost channel (400MHz from line center) we show in table I the ratio of the scattered signal S to the standard deviation of acquisitions in the absence of a signal $\sigma(N)$, as obtained from 18 acquisitions immediately before and after the laser pulse. Simulations for the corresponding experimental conditions indicate that this ratio has to be greater than 13 in order to achieve an accuracy of better than 30% in $T_i$. There is a reasonable correlation between the difference $\Delta T_i = T_i^{CT} - T_i^{NPA}$ and the ratio $S/\sigma(N)$.

The last column in table I shows the FIR laser energy in arbitrary units. While the least accurate $T_i$ measurement was obtained at the lowest laser energy, a high laser energy does not necessarily

guarantee good precision. We suspect that the mechanical stability of optical components is partly responsible for shot-to-shot fluctuations of the signal.

Based on the assumption that the plasma conditions for the 8 shots were reproducible, we averaged the measured signals in all channels. Fig 1 shows the resulting spectrum with the standard deviation from the averaging process. The spectrum is now quite smooth and can be fitted with a calculated spectrum based on the measured average plasma parameters ($n_e$ = 1.2 x $10^{20}$ $m^{-3}$, $T_e$ = 415 eV, $z_{eff}$ = 2.5 (estimate)). The resulting ion temperature is 305 eV which is in excellent agreement with the average ion temperature measured by the NPA for these 8 shots: 310 eV.

In Fig 2 we present the results from an individual shot. The shaded area is $\sigma(N)$, the points are the measured signals and the curve is the fit with $T_i$ = 280 eV. For the ratio of $S/\sigma(N) \approx 14$ at 400 MHz we expect an accuracy of ≈ 28% from simulation results. The deviation from $T_i^{NPA}$ is less than this value.

Fig 3 finally shows the expected accuracy of an ion temperature measurement for standard TCA plasmas and the parameters of our collective Thomson scattering system, as obtained from simulation results. In this case, the frequency range covers the region from 640 to 1520 MHz which allows a more accurate determination of $T_i$ by fitting and represents only a minor modification of the filter bank used in the current set-up.

## CONCLUSIONS

Collective Thomson scattering of far-infrared radiation is a powerful tool for the determination of $T_i$ in a tokamak. The measurements with excellent temporal and spatial resolution are based on a direct method and are in good agreement with $T_i$ measurements obtained with other methods. The accuracy is density dependent and approaches 10% for densities around $10^{14}$ $m^{-3}$. Further improvements are still possible, e.g. by using cooled Schottky diodes.

## TABLE I

The measured plasma parameters of 8 reproducible TCA plasma discharges

| shot # | $n_e$ (*$10^{13}$cm$^{-3}$) | $T_e$ (eV) | $T_i^{NPA}$ (eV) | $T_i^{CT}$ (eV) | $\lvert\Delta T_i\rvert/T_i^N$ (%) | $S/\sigma(N)$ (@400MHz) | $E_L$ (AU) |
|---|---|---|---|---|---|---|---|
| 37720 | 12.2 | 450 | 310 | 260 | 16 | 6 | 60 |
| 37721 | 11.7 | 450 | 320 | 290 | 9 | 9 | 80 |
| 37722 | 12.2 | 400 | 315 | 370 | 17 | 16 | 70 |
| 37725 | 12.2 | 450 | 310 | 220 | 29 | 13 | 85 |
| 37726 | 11.9 | 420 | 300 | 160 | 47 | 5 | 55 |
| 37727 | 11.9 | 450 | 310 | 280 | 10 | 9 | 90 |
| 37728 | 11.8 | 380 | 300 | 180 | 40 | 3 | 105 |
| 37730 | 11.3 | 330 | 330 | 300 | 9 | 14 | 105 |
| averaged spectrum | 12.0 | 415 | 310 | 305 | | | |
| average of indiv. shots | 12 | 415 | 310 | 260 | 22 | 9 | 80 |

## REFERENCES

1. Behn R. et al., Physical Review Letters 62, (1989) 2833-36.

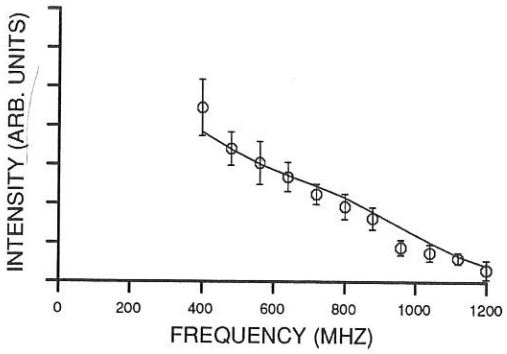


Fig. 1: The average and standard deviation of 8 measured spectra obtained from reproducible plasma discharges. The plasma parameters correspond to table I. The solid line is a least square fit, yielding $T_i = 305$ eV.

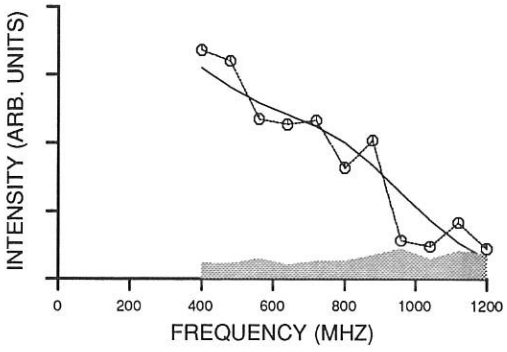


Fig. 2: Fit to an individual spectrum with time resolution of 1.4μs. The shaded region is σ(N) (see text). Measured plasma parameters: $n_e = 7.2 \times 10^{19}$ $m^{-3}$, $T_e = 500$ eV, $T_i^{NPA} = 320$ eV, $z_{eff} = 2.5$. The fit (solid line) yields $T_i^{CT} = 280$ eV.

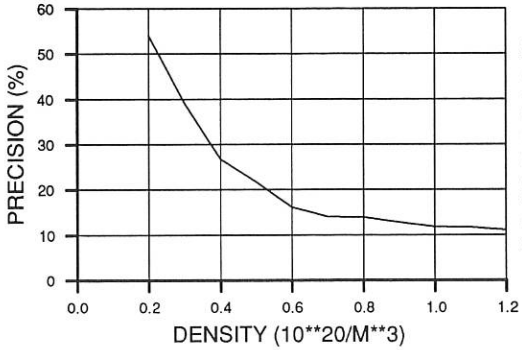


Fig. 3: The accuracy of an ion temperature measurement in D as function of plasma density for $T_e = 700$ eV, $T_i = 400$ eV and $z_{eff} = 2.5$, for 12 optimally placed frequency channels of 80 MHz width. The scattering angle is 90° and the laser frequency 780 GHz. (Simulation results).

# THOMSON SCATTERING DIAGNOSTICS DEVELOPMENT IN FT-1 TOKAMAK FOR THE ELECTRON TEMPERATURE TEMPORAL VARIATION MEASUREMENTS

T.Yu.Akatova, D.G.Bulyginsky, V.M.Zavadsky, M.Yu.Kantor, L.S.Levin, Yu.V.Petrov, G.T.Razdobarin, A.I.Tokunov, N.V.Shustova

A.F.Ioffe Physico-Technical Institute, Leningrad, USSR.

To study the dynamics of ECRH in FT-1 tokamak a proper Thomson scattering diagnostic approach has been developed using the multipulsed ruby laser and the multibeam laser optical system for plasma probing.

The multipulsed laser operation mode was obtained by means of the Q-switcing dye solution cell The oscillator was adjusted to yield the train of 70 ns duration pulses with the spasing between being from 100 up to 200 μs. The overall energy of the 5 to 6 pulse train was near 2.5 J. This energy was increased up to 15-20 J after the amplification.

For additional rise of the energy by approximately one order of magnitude the multibeam plasma probing of tokamak plasms was applied. To build the multibeam laser probing system which is fitted to the tokamak experimental conditions a new optical layout has been designed [1].Its schematic diagram is shown in Fig.1, where 1 and 2 are the spherical mirrors with the tokamak discharge chamber being put between them, $C_1$ and $C_2$ are their curvature centre points, $a$ is the input beam axis, S is the line of observation, $S_1$ and $S_2$ are the points of the input and the first reflected beam intersection with the line of observation, 3 is the focusing lens. The spasing between the two mirror surfases is the sum of both curvature radii. The input beam is pointed to plasma closely to the first mirror edge. After being focused on the line S it is placed on the second mirror reflecting surface. All the reflected beams are lying in the same plane coming through the observation and input beam axes. The coordinate of the (j) mirror beam intersection point for the $n$ reflection is as follows ($n$=0,1..):

$$X_n^{(j)} = X_0^{(j)} + (-1)^j [n^2\Delta - n(C_j - S_0)];$$

$\Delta=C_1-C_2$ is the distance between the curvature centre points.

In the case of the concentric multibeam system ($\Delta=0$) the number of beam transits through the plasma is defined by $N=2(D-d)/d$, where $D$ and $d$ are the diameters of the mirrors and the laser beam section in the vicinty of the first mirror. While taking the optimum distance $\Delta=d^2/16(D-d)$ the number of beam transits became 4 times as large due to more effective light gathering by the mirror reflecting surfases. In this condition the last of the transit probe beams which is leaving out the mirror system is pointed towards the laser body what may be resulting in the laser spontanious generation. Its suppression can be achieved using the dye cell between the oscillator and amplifier.

In FT-1 tokamak the multibeam laser probing system comprises of two spherical mirrors each of 800 mm curvature radius and of 80 mm diameter. As it follows from the experiments on Reileigh scattering the 16 transits of laser beam through the discharge chamber yield the 13 fold scattered power increase. Two scattered signal traces at the same laser output with the multibeam laser probing being on and off are shown in Fig.2 by the curves 1 and 2 correspondingly. A number of peaks which are seen on the curve 1 during the time interval of 500 ns is accounted for the amplification of the consecutive returning to the laser body beams, with the spacing defined by the light travelling time from laser to plasma and back. This helps to use utmost the stored inversion and to give the increment of laser output at a given pumping rate if necessary.

The diagnostic arrangement was used in studies of FT-1 tokamak OH and ECRH discharges. The ECR wave of 100 kW power at frequency of 30 GHz was launched by means of gyrotron from the stronger magnetic field side with the resonance layer being near the discharge axis. The example of the temperature measurements at 4 separate laser pulses with the overall energy of 10 J is shown in Fig.3. The electron temperature measurement statistical error was found to be of near 6% in a single of 3 J laser pulse whenever the electron density was $\cong 10^{13} cm^{-3}$. Within a good accuracy it was happened to be necessary to take into

account the small relativistic corrections in scattered radiation spectrum.

A train of 5 or 6 laser pulses was not large enough to carry out a perfect temporal variation measurements during ECRH. Such measurements are capable only after the storing of number of scattered radiation pulses in different tokamak discharges (see Fig.4). The signal averaging was sometimes performed to decrease the statistical fluctuations. For this purpose the scattered signals in each spectrum channel were summarized inside the taken gate and the resulting integrated signals were used for data processing. The determined averaged temperature value was related to the temporal point which was calculated as the weighted mean value over the all pulse temporal points inside the gate. The weighting coefficients were taken to be propotional to each pulse energy. The gate was shifted step by step. This averaging procedure was performed separately for the time intervals before, at and after the auxiliary heating. The temporal dependence of the averaged temperature values is shown in Fig.5. The gate duration was taken to be 200 μs while the each step was 50 μs.

The temporal variation of the electron temperature spatial profile using the averaged temperature values is shown in Fig.6. The electron energy content time derivative at the moment of gyrotron switching on has been taken to determine the HF absorption rate in bulk electrons. In order to get the more accurate data the local values of electron energy content were determined at the different radial positions in the time before the ECRH and during the first 150-200 μs of gyrotron action. This makes it possible to get the HF absorption rate radial distribution and to obtain the power absorbed throughout the plasma column. This one was found to be of $60^{+}15$ kW which is close to the overall gyrotron power launched into plasma with account of 15% losses in waveguide and discharge chamber walls.

Reference:

1.V.K.Gusev, M.Yu.Kantor, G.T.Razdobarin. Bulletin "Otkrytia i izobretenia",8,I990, aës 142I072. (Invention bulletin, 8, 1990, Aauthor surtification 1421072)

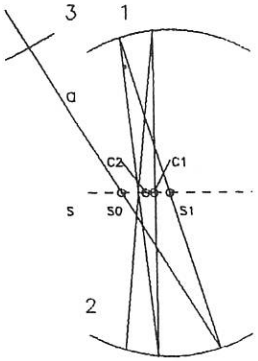


Fig.1

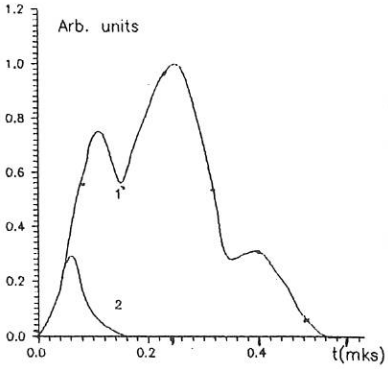


Fig.2

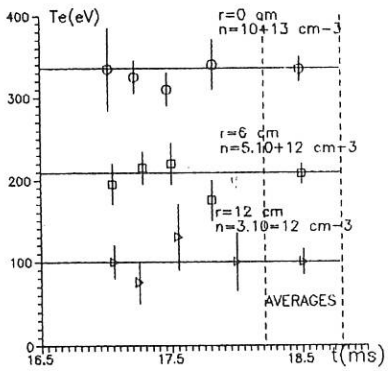


Fig.3

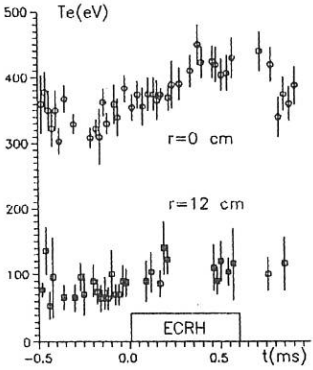


Fig.4

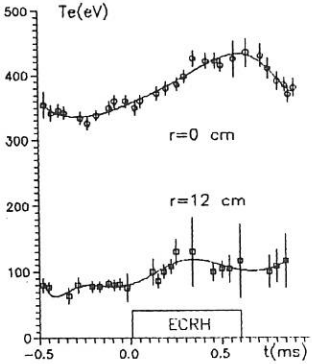


Fig.5

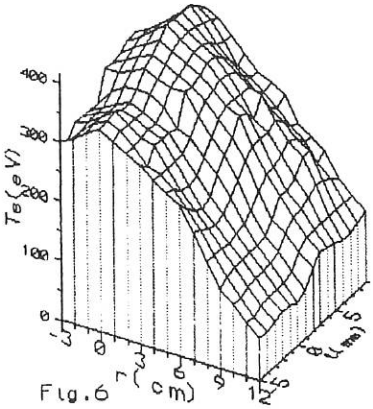


Fig.6

# IN-BEAM STUDY OF $^{9}Be(\alpha\ n_1\gamma)^{12}C$ REACTION, PROMISING AS FAST ALPHA-PARTICLE DIAGNOSTICS IN TOKAMAK PLASMAS.

*V.G.Kiptilyj, A.V.Matjukov, A.S.Mishin, V.O.Najdenov, I.A.Polunovskij, L.A.Rassadin, I.N.Chugunov.*

*A.F.Ioffe Physical Technical Institute, Leningrad, USSR*

The investigation of the behavior of thermonuclear alpha particles in plasma is considered to be one of the main questions on the way of solution of the controlled fusion problem in a tokamak-reactor. A lot of diagnostic methods is being worked out for this purpose [1]. These methods enable to investigate the alpha particle distribution in plasma and the effects connected with a high density of fast alphas.

Atomic collision techniques are considered to be one of the most perspective and worked out diagnostics. Nowadays it is discussed intensively in this connection. It will be informative in the alpha particle energetic range $E_\alpha < 1.5 - 2.0$ MeV in accordance with the conclusions from the report [2]. The method based on the properties of nuclear reaction $^{9}Be(\alpha\ n_1\gamma)^{12}C$ [3] can be used for the diagnostics of alpha particles with $E_\alpha > 1.7$ MeV.

The obtaining of information about the distribution function in this method is based on the measurement and analysis of the spectrum of $\gamma$ rays with energies 4.44 MeV which are as the result of the deexcitation of $2^+$ level of the finite nucleus $^{12}C$. The level lifetime is equal to 0.06 ps and is much less than the slowing down time of the recoiled nuclei in the medium. That's why the measured spectrum of 4.44-MeV $\gamma$ rays is distorted by the Doppler effect. The shape of gamma spectrum is defined by the velocity distribution of the recoiled nuclei, angular distribution of $\gamma$ rays and angular correlation of neutron - $\gamma$ ray cascade. The velocity distribution of the recoiled nuclei depends on the impulse distribution of the incident alpha particles and escaping neutrons (the target can be considered to have negligible velocity). The impulse distribution of neutrons is defined by the energy of alpha particles and angular distribution of neutrons in respect to the direction of the alpha particle

velocity. Angular distribution of neutrons and angular correlation of the neutron - $\gamma$ ray cascade depend on the structure of the excited states of nucleus $^{13}C$ which change together with the excitation energy. So all the factors which determine the shape of 4.44-MeV $\gamma$ ray spectrum depend on the function of the alpha particle velocity distribution. The question is how much their sensitivity to this distribution.

The in-beam spectroscopy investigation of the reaction $^{9}Be(\alpha\ n_1\gamma)^{12}C$ was provided for the estimation of sensitivity of the gamma spectrum on the alpha particle energy and the detection angle in respect to the beam direction. The comparison of spectra with the simultaneously measured angular distribution of neutrons which feed the $2^+$ level of the nucleus $^{12}C$ have shown their adequacy.

Fig.1 shows the example of $\gamma$ ray spectra measured by HpGe detector in two positions $\theta = 0^o$ and $90^o$ (in the direction of the beam and in perpendicular direction). The figure shows that besides the energetic shift of the peak in respect to the non-perturbed position the shape of the spectrum is also distorted. This change can be explained by the anisotropic character of neutron radiation because it is the only factor having an influence on the velocity distribution of recoiled nuclei at so shot lifetimes. In the case of isotropic distribution of neutrons the gamma spectrum would have symmetric shape. The dependence of the line shape on $E_\alpha$ would contain the changes of peak width and center of gravity only. This effect would be practically unnoticeable in the diagnostic experiment.

In the case of single source of the 4.44-MeV plasma radiation the spectrum is connected with the alpha particle distribution function $f(E_\alpha,\theta_\alpha)$ by the formula :

$$S(E_\gamma) \propto \iint n_t\ f(E_\alpha,\theta_\alpha)\ \sigma(E_\alpha)\ v_\alpha\ K(E_\gamma,E_\alpha,\theta_\alpha)\ d\theta_\alpha\ dE_\alpha$$

where $n_t$ - the concentration of $^{9}Be$ in plasma, $\theta_\alpha$ - the angle between the direction of the velocity $v_\alpha$ and the direction of the collimated spectrometer, $\sigma(E_\alpha)$ - cross section of the reaction, $K(E_\gamma,E_\alpha,\theta_\alpha)$ - complex function connecting the energy of detected $\gamma$-ray with energy of the alpha particle and the direction of its

movement. The real diagnostic spectrum of 4.44-MeV γ-rays is the integral $\int_v S\, dv$ through the whole plasma volume observed by the spectrometer.

Obviously, the precise knowledge of function $K(E_\gamma, E_\alpha, \theta_\alpha)$ is necessary for the calculation of the spectrum $S(E_\gamma)$ for given alpha particle distribution. Experimental method of determination of this function is one of simple methods. For this purpose the spectra of 4.44-MeV γ rays were measured carefully and then were organized in the matrix $M(E_\gamma, E_\alpha, \theta_\alpha)$ The energy of the alpha particle beam is varied in the range 1.9 - 4.0 MeV with the step 0.1 - 0.3 MeV. The spectra were registered by the 30% HpGe detector which was located at the angles $\theta = 0^\circ - 150^\circ$ in respect to the beam (the step was equal $15^\circ$). The matrix $M$ was further transformed into the function $K(E_\gamma, E_\alpha, \theta_\alpha)$ by the normalization, interpolation and extrapolation. The accuracy of the transformation was controlled by the comparison of the calculated spectra with the spectra measured in the runs with semi thick targets (0.64 and 1.50 mg/cm$^2$). Good agreement of the compared spectra gives the basis for the modeling of diagnostic spectra using the obtained function $K$.

For calculations the alpha particle distribution based on the classical character of particle slowing down in plasma [4].Fig.2 shows the function $f(E_\alpha)$ and the energetic dependence of cross section $\sigma(E_\alpha$ of the reaction $^9Be(\alpha, n_1\gamma)^{12}C$. Fig.3 shows the calculated spectra of 4.44-MeV γ-rays for the steady state of plasma (*A*) and for the cases when 0.03 s (*B*) and 0.05 s (*C*) have passed after ignition.

The figure shows that the sensitivity of spectra to the different types of the distribution is enough for diagnostic purposes.

It is necessary to mention in the conclusion that the presented calculations were provided on the basis of the simplest model ( the distribution was supposed to be isotropic ). At the NBI and ICRF heating of plasma the anisotropy of the distribution must show itself. As calculation shown, the sensitivity of the spectrum to the anisotropic distribution is enough for diagnostic analysis, too.

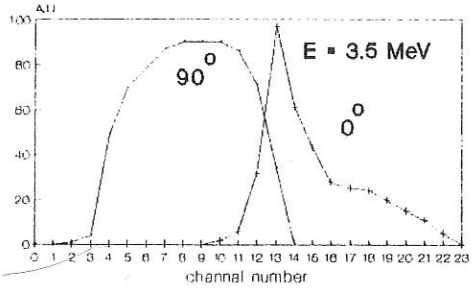


Fig.1

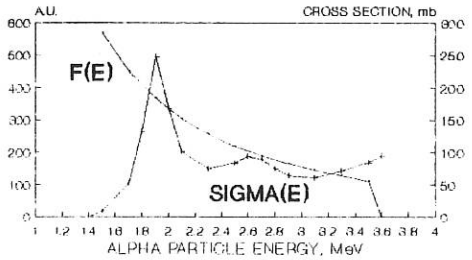


Fig.2

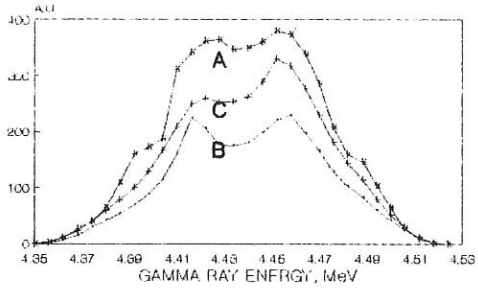


Fig.3

1) D.Post,S.J.Zweben,L.Grisham, in *Proc. of the Cours* 'Basic and Advanced Diagnostic Techniques for Fusion Plasmas', *Italy,* 1986.

2) A.B.Izvozchikov et al., *Report* ITER-IL-PH-7-9-S-07.

3) V.G.Kiptilyj,V.S.Zaverjaev, *Report* ITER-IL-PH-Z-9-S-15.

4) D.Post et al., *J.Fusion Energy*,1981,vol.1,129.

# A High Resolution LIDAR-Thomson Scattering System for JET

H. Fajemirokun, C. Gowers, K.Hirsch, P. Nielsen, H. Salzmann

The spatial resolution achievable with the current LIDAR-Thomson scattering diagnostic at JET is about 8 cm (making use of a fast deconvolution technique to remove some of the detection system response characteristic from the real scattered signal). A LIDAR-Thomson scattering system capable of better than 5 cm spatial resolution is needed to resolve edge electron temperature and density gradients in H-mode operation. This region of the plasma is of interest because it is believed that these gradients determine transport and confinement in the bulk plasma.

The two factors influencing the spatial resolution of a LIDAR-Thomson scattering system are the length of the laser pulse and the integration time of the detection system. To achieve the desired 5 cm level of spatial resolution, it is proposed to use:

- the existing LIDAR ruby laser, operating at 180 ps pulse width (as opposed to the 300 ps pulse currently used);
- the existing input optics, modified to input the beam at .17° above the major radius plane of the torus to optimise the vignetting function for collection of light scattered at the edge;
- one mirror of the existing collection mirror array in conjunction with the rest of the collection optics;
- a new three channel edge filter spectrometer;
- a streak camera to detect incoming light;
- a CCD camera coupled to a personal computer for data digitization and storage.

At present, feasibility tests for the streak camera and the CCD camera are in progress. Measurements made at the expected signal to noise ratio level, using a commercially available streak camera and intensifier unit indicate that the above described scheme is feasible.

A suitable three channel edge filter spectrometer has been designed. The optimum wavelengths of the edges of each channel were determined using simulation software developed specifically for the LIDAR-Thomson scattering system.

# LOCALIZATION OF FLUCTUATION MEASUREMENT BY WAVE SCATTERING CLOSE TO A CUT OFF LAYER

X.L.Zou (1), L.Laurent (1), T.Lehner (2), J.M.Rax(1)

*(1) Association EURATOM-CEA sur la fusion contrôlée*
*CEN Cadarache BP 1 13108 St Paul lez Durance France*
*(2) Laboratoire PMI Ecole Polytechnique 91128 Palaiseau France*

## I. Introduction

In tokamaks several fluctuation diagnostics are based on the scattering of an electromagnetic wave close to a cut off layer. For example measurement of density fluctuations ($\tilde{n}$) by reflectometry [1] and magnetic fluctuations ($\tilde{B}$) by cross polarization scattering [2]. For such a configuration the eikonal approximation does not remain valid to describe the pump wave although it is valid to describe $\tilde{n}(r)$ and $\tilde{B}(r)$[3]. In this paper we shall consider a linear density profile. An unidimensional exact analysis has been performed. Spatial and spectral localization of scattering process close to the cut off layer is investigated and a modified Bragg rule is derived.

## II. Unidimensional Scattering in Critical Layer

II.1) Structure of pump wave

We consider the case of a monochromatic wave of ordinary polarization (O) launched into the plasma perpendicularly to the magnetic surfaces. To have an analytically tractable problem, the density profile is taken linear $n(x)= n_0(1-x/L_n)$ where $n_0$ is the cut off density. The electric field can be expressed using Airy functions Ai, Bi [4] :

$$E_i(\chi) = 2(\pi^3 k_o L_n)^{1/6} E_o \left[ \frac{Ai(-\chi)+i\,Bi(-\chi)}{2} + \frac{Ai(-\chi)-i\,Bi(-\chi)}{2} \right] \qquad (1)$$

where $\chi=x\,(k_o^2/L_n)^{1/3}$. $k_o$, $E_o$ are respectively the wave number and amplitude of pump wave in vacuum. The first term represents an incident wave, and the second term a reflected wave. Far from the cut off layer these fields match with the WKB solutions $Ke^{-i\omega t \pm i\int k dx}$. In a non dissipative medium, energy conservation for each progressive wave yields the group velocity $V_g$:

$$\frac{c}{V_g} = \frac{\pi}{2} (k_o L_n)^{1/3} \left( Ai(-\chi)^2 + Bi(-\chi)^2 \right) \qquad (2)$$

In (2) it can be seen that obviously the amplitude of the field is large close to the cut off layer.

II.2) Structure of scattered wave

Four processes have to be taken into account: the forward and backward scattering of the incident and reflected wave. The wave can interact with either density fluctuations (an ordinary wave is scattered) or magnetic fluctuation (an extraordinary wave is scattered) [3]. Both mechanisms are considered:

a) Process $O_i+\tilde{n}\rightarrow O_s$

Using the fact that the scattered wave in vacuum is simply a reflected plane wave, the solution of scattering equation within the Born approximation is given by:

$$E_s(\chi)=-i\pi[Ai(-\chi)-iBi(-\chi)]\int_{-\infty}^{\chi}Ai(-\xi)G(\xi)d\xi - i\pi Ai(-\chi)\int_{\chi}^{\infty}[Ai(-\xi)-iBi(-\xi)]\,G(\xi)d\xi \qquad (3)$$

where G is the scattering source term $G(\chi) = (k_oL_n)^{2/3}\,\frac{\omega_{pe}(\chi)^2}{\omega_i^2}\,\frac{\tilde{n}(\chi)}{n(\chi)}\,E_i(\chi)$

If $\chi$=a, $\chi$=b are the boundaries of the scattering domain, from Eq.(3), we calculate the spatial autocorrelation function of scattered field as follows:

$$\langle E_s(x,\omega_s)E_s^*(x',\omega'_s)\rangle = |2\pi\,E_o|^2\,(k_oL_n)^{4/3}\left(\frac{r_o\lambda_o^2}{\pi}\right)^2 2\pi\,\delta(\omega_s-\omega'_s)\,e^{ik_o(x-x')}$$
$$\int_a^b d\xi_1\int_a^b d\xi_2 Ai(-\xi_1)^2Ai(-\xi_2)^2\,\langle\tilde{n}\,(\xi_1,\omega_s)\tilde{n}^*(\xi_2,\omega_s)\rangle \qquad (4)$$

where $r_o$ $(=(e^2/4\pi\varepsilon_o m_e c^2))$ is the classical electron radius, $\langle\ \rangle$ stands for statistical average. Through a change of variable $R=(\xi_1+\xi_2)/2$, $r=\xi_1-\xi_2$, and with the Wiener Kinchine theorem [5], the scattered power can be expressed as :

$$P_{\omega_s} = P_{\omega_i}\,(2r_o\lambda_o^2)^2\,(k_oL_n)^{4/3}\int_a^b dR\;n(R)\int_{-\infty}^{\infty}\frac{dk}{2\pi}F_{ab}(k,R)\;S_n(k,\omega,R) \qquad (5)$$

with $F_{ab}(k,R) = \int_{-R_1}^{R_1} dr\left(Ai(-R-\frac{r}{2})Ai(-R+\frac{r}{2})\right)^2 e^{ikr}$ and $S_n = \lim_{T,L\rightarrow\infty}\frac{1}{T,L}\left\langle\frac{\tilde{n}(k,\omega,R)\,\tilde{n}^*(k,\omega,R)}{n(R)}\right\rangle$

$R_1=2(R-a)$, if $R\in[a,(a+b)/2)]$; $R_1=2(b-R)$, if $R\in[(a+b)/2,b]$. $S_n$ is the 1-D form factor of $\tilde{n}$[5]. In the WKB range, $F_{ab}$ is simply given by Dirac functions :

$$F_{ab}(k,R) = \frac{1}{16\pi^2}(k_oL_n)^{-2/3}\;2\pi\,(\delta(k-2k_i(R)) + \delta(k+2k_i(R))) \qquad (6)$$

This corresponds to the standard Bragg relation ($k_i(R)$ is the local wave number of pump wave). In Eq.(5) the integration in R (respectively k) corresponds to the spatial (spectral) distribution of the scattered power. The R variation of $F_{ab}$ describes the "swelling effect " close to the cut off layer. The discussion on the spatial and spectral localization depends essentially on the form factor $S_n$ and the *Bragg function* $F_{ab}$. Fig.1 displays the contour plot of $F_{ab}(k,R)$

with WKB treatment for pump wave. The function $F_{ab}$ is maximum on a parabola corresponding to the usual selection rule $k=2k_{ordinary} = 2\omega/c\sqrt{x/L_N}$. The broadening comes from the finite extension of the scattering zone. Without WKB approximation the main differences are a more complicated structure and spectral broadening around the cut off layer as shown in Fig.2 and forward scattering (corresponding to the straight horizontal line for $k\approx 0$). We find again the parabolic branch outside of the critical layer corresponding to the WKB computation.

b) Process $O_i+\tilde{B}\rightarrow X_S$

It was shown in [3] that using the cut off layer as a polarizing mirror, then combining the reflectometer and forwardscattering technics, we can measure $\tilde{B}$. In this case, the scattered wave ($X_s$) crosses freely the plasma, and the calculation is more simple. The expression of the forwardscattered power per frequency bandwidth is given by :

$$P_{\omega_S}=P_{\omega_i}\frac{(r_o\lambda_o^2)^2}{4\pi}(k_oL_n)\frac{u}{(1-u)^2}\int_a^b n(R)dR\int_{-\infty}^{\infty}\frac{dk}{2\pi}F_{ab}(k,R)\left[S_{bx}(k,\omega,R)+uS_{by}(k,\omega,R)\right] \quad (7)$$

with $u=\left(\frac{\omega_{ce}}{\omega_i}\right)^2$ and $S_{b\mu}(k,\omega,R) = \lim_{T,L\rightarrow\infty}\frac{1}{TL} < \frac{\tilde{B}_\mu(k,\omega,R)\,\tilde{B}^*_\mu(k,\omega,R)}{n(R)B_o^2} >$

A simple expression of $F_{ab}$ can be obtained by using the fact that the scattered wave (X mode) can be treated with the WKB approximation:

$$F_{ab}(k,R) = n(R)^2\frac{K(R)^2}{N_S(R)}\,2\pi\,\delta\left[((L_n/k_o^2)^{1/3}k_oN_S(R)\pm\frac{\partial\theta_o}{\partial R}-k)\right] \quad (8)$$

In Eq.(8), K, $\theta_o$ are respectively the modulus and argument of $A_i+iB_i$, $N_S$ is the refractive index of scattered extraordinary waves. $F_{ab}$ represents a modified Bragg rule for forward and backward scattering processes '+, - ', the Dirac distribution describes a matching with the local wave number. The swelling effect is now expressed by the function $K^2(R)$ in Eq.(8). Finally the spatial localization problem for $\tilde{B}$ depends only of the balance between $K^2$ and $S_b$.

II-3) Numerical application

Let us model the microfluctuations as follows : $S_n$, $S_b\approx \exp(-(k(R)-k_*(\omega))^2/(\Delta k)^2)$ with a maximum at $k_*$ and a width $\Delta k$ equal to the inverse of thermal ion Larmor radius. We define $\tau$ as the ratio between power scattered from the critical layer and WKB domain. We use Tore Supra Tokamak parameters $L_n$=0.7m, $k_*\approx\Delta k\approx 770\ m^{-1}$ ($T_i\approx$1keV, $B_o$=4T), $\omega/2\pi$=60GHz. We find respectively $\tau(\tilde{B})\approx 3.5$, $\tau(\tilde{n})\approx 0.5$. This result is not surprising as we expect, a relative spatial localization for process $O_i+\tilde{B}\rightarrow X_S$ since $k_*$ is met close to the critical layer. On the opposite for process $O_i+\tilde{n}\rightarrow O_S$ the selected wave numbers of fluctuations in the cut off layer are nearly zero and correspond a spectral range far from the maximum of $S_n$.

## III Conclusion

The scattering process is described by a function $F_{ab}(R,k)$ which contains the spectral selection rule through its k variation and the localization effect due to the swelling of the electric

field through its R variation. Numerical application has been made for experimental conditions corresponding to fluctuation measurement by reflectometry. This diagnostic appears to be local and sensitive for low k fluctuations. However only weak swelling and localization effects are expected for higher k turbulence corresponding to standard drift wave spectra. For the magnetic fluctuation measurement by cross polarization scattering, a moderate localization is expected. It has been recently pointed out that the Born approximation may not be valid close to the cut off layer if large fluctuation levels exists ($\tilde{n}/n$ =O(1)) like at the plama edge. In this case that multiple scattering is expected to play a role [6]. It is posssible to describe this mechanism using the same formalism with higher order correlations of density fluctuations as will be shown in a further work.

## References


[1] TFR Group Plasma Physics and Controlled Nuclear Fusion (1985) Vol.27, 11, 1299

[2] M.Paume, X.L.Zou, L.Laurent, T.Lehner, D.Gresillon "Projet of magnetic fluctuation measurement by cross polarization scattering in Tore Supra " in this conference.

[3] Lehner T., Rax J.M., Zou X.L. Europhysic Letters 8,759 (1989)

[4] Ginzburg V.L."Propagation of Electromagnetics Waves in Plasma",Gordon&Breach(1961)

[5] Bekefi G.,"Radiation Processus in Plasma", John Wiley(1966)

[6] L.Laurent, P.Millot, F.Mourgues, J.M.Rax Report EUR CEA FC 1381 (1989) p.247


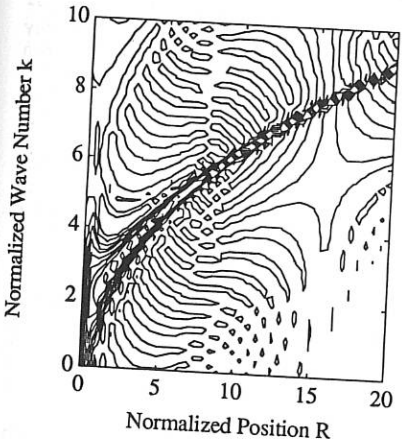


Fig.1 Bragg function diagram with WKB treatment for pump wave in the normalized space.

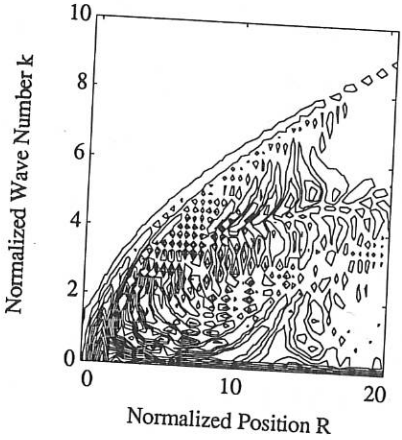


Fig.2 Bragg function diagram with exact treatment for pump wave in the normalized space, including backward and forward scattering.

# POLARIZATION OF HARD X-RAYS, A CONTRIBUTION TO THE MEASUREMENT OF THE NON-THERMAL ELECTRON DISTRIBUTION FUNCTION (L.H.C.D.)

M. HESSE, P. PLATZ, M. LAMOUREUX*

DRFC - CEN/CADARACHE - 13108 St PAUL LEZ DURANCE (France)
*LSAI - Bât 350 - Université Paris Sud 91405 ORSAY (France)

## I - INTRODUCTION

The hard X-ray spectrum emitted by a plasma containing non-thermal electrons generated during Lower Hybrid Current Drive experiments has already been measured on several Tokamaks /1-2/ but the polarization properties of the bremsstrahlung have not yet been studied. The present study starts with the comparison of tractable analytical expressions of cross-sections with more precise computer-calculated values ; then an evaluation of the polarization is carried out under real tokamak current drive situations and finally a proposal of a new diagnostic for the Tore Supra LHCD experiment is presented.

## 2 - ATOMIC PHYSICS OF ELECTRON-ION BREMSSTRAHLUNG

In the medium relativistic range of energy (50 keV - 1 MeV), the only available analytical double-differential cross-section formulae are those obtained in the relativistic Elwert-corrected Born approach (EB) /3/. The EB calculations have already been compared with a numerical Exact-Coulomb (EC) multipole relativistic partial waves approach /4/ for a low-energy electron beam (50 keV) and for a high fraction of emitted energy $h\nu/E_1 = 0.95$. These calculations have now been extented /5/ to electron energies up to 800 keV concerned in LHCD experiments. Figs. 1 and 2 present the Shape-function S $[d^2\sigma/d\Omega d(h\nu)$ normalized to the solid-angle-integrated cross-section $d\sigma/d(h\nu)]$ and polarization versus viewing angle $\theta$ for 2 high electron energies (400 and 600 keV) and for one photon energy, 320 keV ($h\nu/E_1$=.8 and .53) ; a few curves from /4/ are also plotted. At high photon energies ($h\nu$>200 keV) the Shape-functions (cross-sections) decrease very fast with increasing viewing angle $\theta$. EC values are higher than EB values for $0<\theta<10°$.However, this region contributes little to the total emissivity due to the $\sin\theta$-weighting factor. EC and EB polarization values may be quite different in particular ranges of $\theta$ (case $E_1$=600keV,$h\nu$=320keV,$\theta$>50°). They occur in the wings of the Shape-functions and therefore have little contribution in the emissivity. In conclusion, we consider the analytical Gluckstern-Hull /3/ theory appropriate for the present study.

## 3 - POLARIZATION OF LHCD PLASMA CONTINUUM

A detailed study of polarization properties of the continuum emitted by a plasma containing impurity ions and suprathermal electrons has been carried out /6/. The model of electron distribution is a two-temperature Maxwellian with forward and perpendicular temperatures $T_F$ and $T_P$ ; the other plasma relevant parameters of the calculations are : ion and electron profiles, observation angle, cut-off energy of suprathermal electrons and ion charges Z. The most important outputs of this evaluation are :

a) The optimum observation angle for polarization measurements is different from the optimum angle for emissivity measurements ; a good compromise, between polarization sensitivity and emissivity, is a slight forward observation (60°) with respect to the electron toroïdal direction. Line-of-sight integrated volume emissivity is presented fig. 4 in pratical units for the case of Tore Supra experiment.

b) In the range of parameters covered here, the useful X-ray spectrum lies in the 200-600 keV range (fig. 3) where the upper limit is determined by the cut-off energy of the electron distribution.

c) The X-ray spectra and the polarization values are very sensitive to the cut-off energy. Inasmuch as it is physical, this cut-off energy will have to be measured.

d) The polarization value is quite high, up to 0.4. Polarization increases with photon energy but reaches maximum value already at 300 keV.

e) Polarization is almost independent of the forward temperature.

f) Polarization is most sensitive to the perpendicular temperture.

These last two outcomes are the basis of this proposal of polarization measurements aiming to evaluate the transfer of the parallel energy gained from the wave into perpendicular energy.

## 4 - COMPTON POLARIMETER

Relativistic Compton scattering of polarized photons is described by the Klein-Nishina formulae. For the photon energies considered here (200-600 keV) and for low-Z elements the photoelectric effect is negligeable and Compton scattering is greater than pair-production by $\gamma$ radiation up to 10 MeV. A simplified lay-out of a polarimeter is shown in fig. 5. The diffuser-scintillator is equipped with several PM's for the detection of the recoil electron (in a neutron environment the most appropriate Compton scatterer is the hydrogen-free NE 226 scintillator, $\phi$ = 5 cm, L = 10 cm). Pairs of scintillator-analyzers (BGO 10x10x1 $cm^3$) on orthogonal side-arms $S_{11}..S_{22}$ detect the scattered photons. Polarization sensitivity of the polarimeter is given by the contrast C (or asymmetry ratio) for a perfectly linear polarized incident beam, as the ratio of the cross-sections integrated over the scattering solid angles on perpendicular side-arms. C decreases with photon energy and aperture angles as shown in fig. 6. In the 200-600 keV region, a contrast of 10 which is quite sufficient for measurements of $P > 0.1$, is obtained for 10° (half-aperture) angles. For $I_{LH}$ = 1 MA, $n_e = 10^{13}$ $ecm^{-3}$, $\theta = 60°$, $Z_{eff} = 3$ and a plasma resolution of 10 x 10 $cm^2$ a count-rate of $10^3$/keV.s is expected. Reduction of neutron-induced and other non-Compton events will be obtained by use of standard electronics such as coïncidence techniques, pulse height analysis and pulse shape discrimination on the diffuser signal.

## 5 - CONCLUSION

The present study shows that extension of the conventionnal spectrum analysis to polarization measurements permits the determination of the mean perpendicular energy, i.e. a better knowledge of the distribution function of electrons.

1/ VON GOELER and al. RSI 57, 8 (1986) N F, 25, 11 (1985)
2/ TEXTER and al. NF 26, 10 (1985)
3/ GLUCKSTERN, HULL Phys. Rev. 90, 6 (1953)
4/ LAMOUREUX, JACQUET, PRATT Phys. Rev. A. 39, 12 (1989)
5/ LAMOUREUX, PRATT private communication
6/ HESSE, PLATZ EUR-CEA-FC 1376 Report 1989

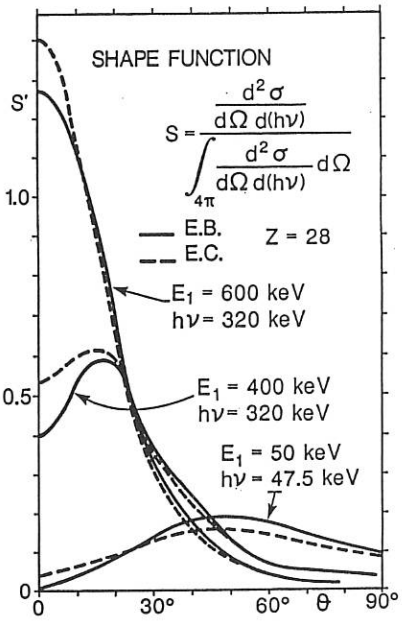


Fig. 1

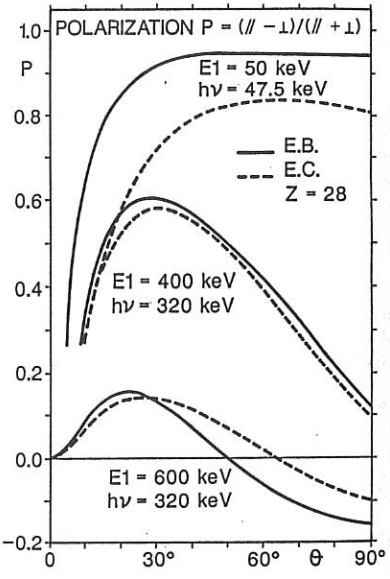


Fig.2

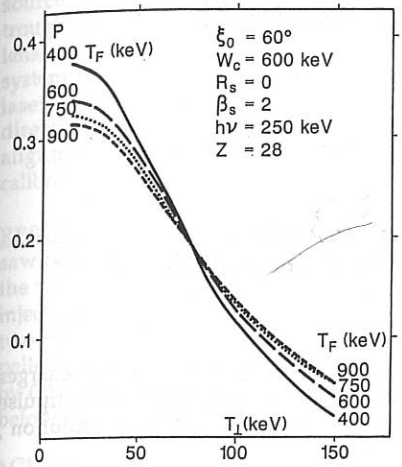


Fig.3

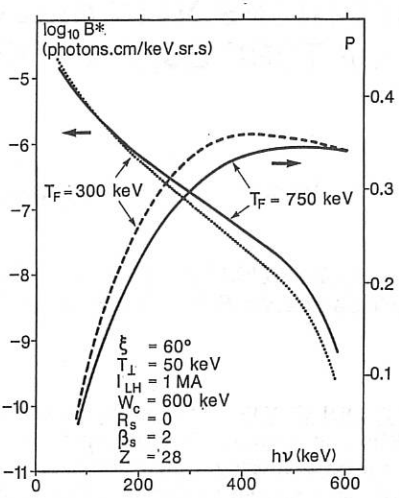


Fig.4

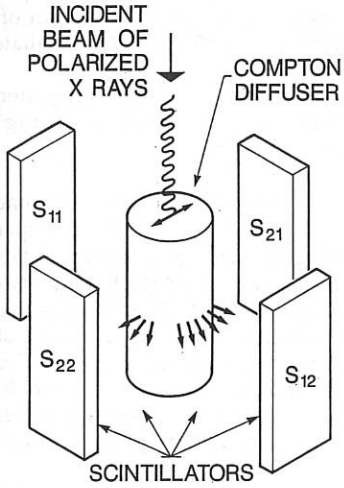


Fig.5

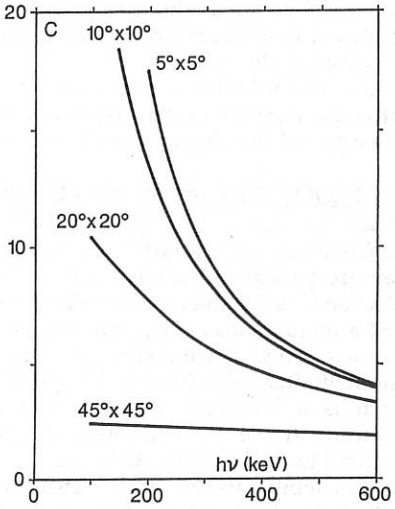


Fig.6

# THE THOMSON SCATTERING SYSTEMS OF TORE SUPRA . FIRST RESULTS.

E. Agostini , T. Chies , J. Lasalle , B. Moulin , P. Platz.

*Association EURATOM-CEA sur la Fusion Contrôlée*
*CEN Cadarache BP1 ,13108 Saint Paul-lez-Durance (FRANCE)*

INTRODUCTION Major objectives of Tore Supra are long-duration discharges (>30s) and ergodic divertor experiments .We have set up a 12-point,multipulse Thomson scattering system for the main plasma and a 3-point,high resolution , single-shot system for the peripheral plasma (Fig1).

LASERS Both lasers are from *B.M.Industries (Evry France)* .The multi-pulse system uses a laser source made-up of 3 Nd:YAG modules (oscillator + amplifier) with a total pulse energy of 2.1J and a combined beam cross-section of 8x33 $mm^2$ ; the pulse FWHM is 15 ns.The mean pulse frequence is 27 Hz. For each pulse , there is a 2 ms time-window for an optional external trigger . The length of the pulse train is unlimited.The single-pulse system uses a 20J Nd:YAG oscillator / Nd : glass amplifier.
Remote controlled mirrors offer complete freedom of beam alignment,in particular parallel beam displacement in the toroidal direction during the discharge (see the alignment and calibration procedures below).

SPECTROMETERS AND DETECTORS. The twelve 3-filter spectrometers (FIG2) for the main plasma , labelled # 1 to 12 , have the spectral characteristics, temperature range and standard radial settings as shown in table 1. They are precision-mounted into four modules , each module having its own collection lens (doublet f=75cm, Ø=22cm) as shown in FIG1. Each module may be tilted around an axis going through its collection lens , allowing for a shift of the three associated space-points by ± 11 cm from the standard position. For the ergodic-limiter experiments the spectrometer # 2 is interchanged with # 2* , which is a low-temperature version with 3 spatial channels of increased resolution (table 1). The detectors are *R.C.A.* avalanche photodiodes,first produced for,and used on Asdex /1/.
Electron temperatures and densities are obtained with the two-channel method developped for T.F.R. /2/. The three-filter lay-out increases the dynamic range and provides , within a reduced range of Te , two redundant measurements , a powerfull indicator of calibration errors.

CALIBRATION PROCEDURES i) in the laboratory , the responsivity functions (volts/nm.watt) of the three channels are measured with a tunable DC light source . ii) on TS , the responsivities are periodically checked with a high-troughput , calibrated DC source (tungsten halogen + diffusing sphere + fresnel lens) mounted in front of the collection lens, iii) the amplifier/data acquisition system is calibrated with a pulse generator, iv) The geometrical coupling of the laser beam to the detectors is measured by scanning the beam in toroidal direction during a stationnary discharge.This also serves to eliminate initial alignment errors, v) Rayleigh scattering in nitrogen for absolute density calibration (not yet done).

RESULTS : FIG3 shows Te(r) profiles 6 ms before (+) and 4 ms after (□) a sawtooth.The high signal-to-noise ratio is demonstrated by FIG4 ,which shows the net output of the acquisition system for the spectrometer #7 during a 4-pellet injection experiment ( 400 laser shots). FIG5 and FIG6 show Ne(t) and Te(t) for two values of r : -5.5 cm and -38.5 cm.The solid lines are eye-guides .Notice that pellet #1 precedes a laser shot by 0.4 ms and that pellet #2 follows a laser shot by 0.1 ms . FIG7 and FIG8 show Ne(r) and Te(r) profiles for 3 lasers shots , before ( □ ) and after ( ■ ; x ) pellet #1.

ACKNOWLEDGMENTS We are grateful to Drs Hirsch [ IPF Stuttgart] , Meisel , Murmann , Röhr , Salzmann and Steuer [IPP Garching] for fruitfull discussions.

REFERENCES

[1] H.Röhr,K.H.Steuer,G.Schramm,K.Hirsch,H.Salzmann : Nuclear Fusion 22 , 1099 (1982).
[2] J.Lasalle and P.Platz Applied Optics , 18 , 4124 (1979)

| SPECTRO | CHANNEL3 (nm) | CHANNEL2 (nm) | CHANNEL1 (nm) | POSITION (cm) | RESOLU--TION(cm) | Te RANGE (KeV) |
|---|---|---|---|---|---|---|
| 1 , 12 | 930-992 | 992-1024 | 1024-1042 | ±60.5 | 6 | 0.1-1.5 |
| 2 , 11<br>3 , 10 | 874-960 | 960-1006 | 1006-1032 | ±49.5<br>±38.5 | 6 | 0.25-3. |
| 4 , 9<br>5 , 8<br>6 , 7 | 850-930 | 930-992 | 992-1024 | ±27.5<br>±16.5<br>±5.5 | 6 | 0.5-5. |
| 2* | 1010-1031 | 1031-1045 | 1045-1054 | 72<br>75 } ±11<br>78 | 2<br>2<br>2 | 0.01-0.20 |

TABLE1

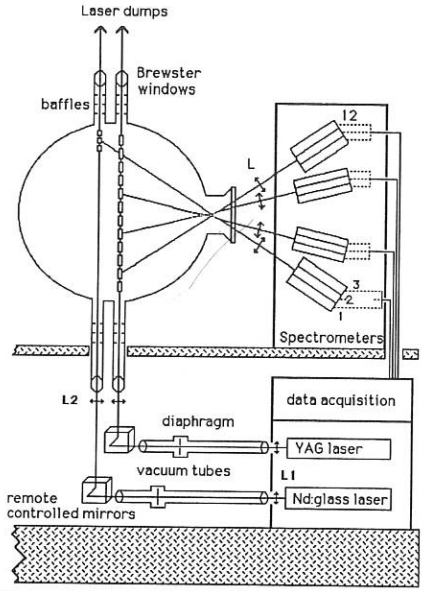


FIG1 : THOMSON SCATTERING ON TORE SUPRA

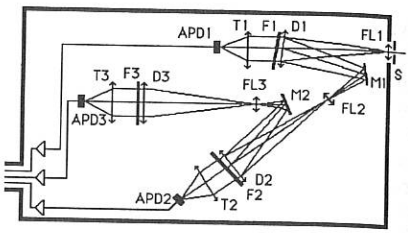


S = entrance slit (21x3 mm$^2$)
D = doublet (f=226 mm , f/3.8)
T = triplet (f=76 mm , f/1.3)
FL = field lens
F = interference filter (Ø = 60 mm)
(F1 and F2 tilted by 7°)
APD = avalanche photodiode ( RCA C30974E)
(2.4 $10^5$ V/W at : 1064 nm , B=25 MHz ,7X1mm$^2$ )
M = dielectric mirror

FIG2 : 3-CHANNEL-SPECTROMETER

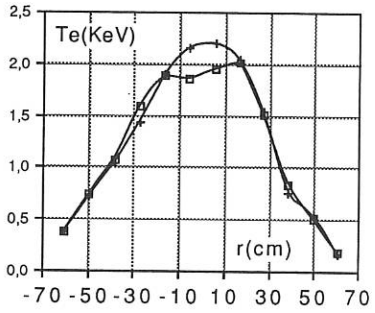


FIG 3 : 2 consecutive laser shots during a sawtooth (Δt=37ms)

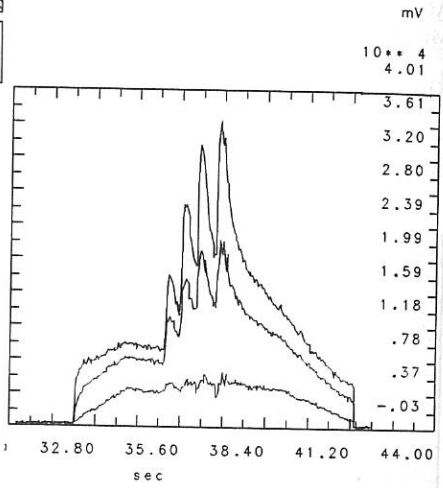


FIG 4 : 3 output-signals (spectro #7) during a 4-pellet injection.

□ 36047. ms
+ 36084. ms

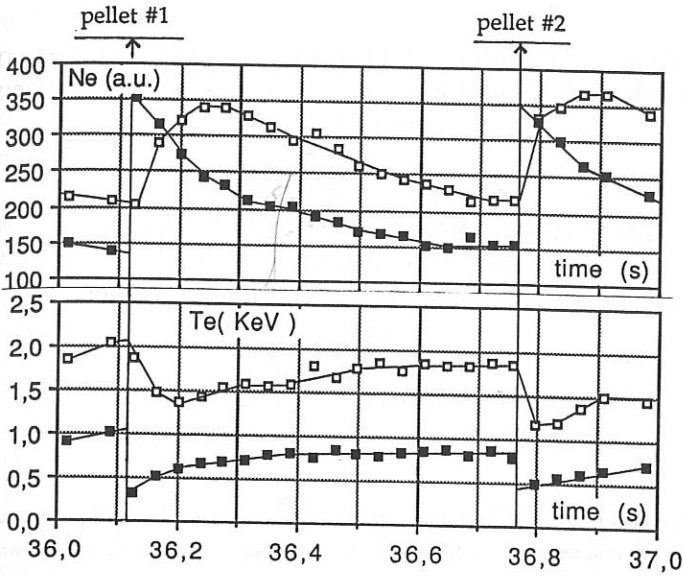


FIG 5 and 6 : Ne(t) and Te(t) during two pellet injection

□ Te(-5,5 cm)
■ Te(-38,5 cm)

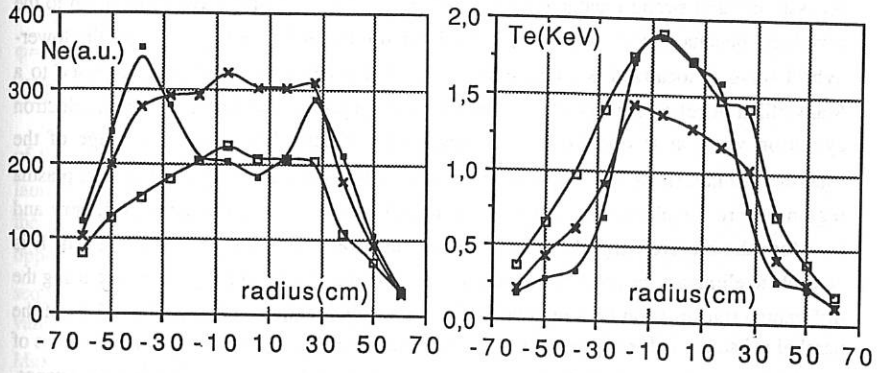


FIG 7 : Ne(r) profile before ( □ ) and after ( ■ , × ) pellet injection.

□ t = 35978 ms
(t = 36125 ms pellet #1 )
■ t = 36126 ms
× t = 36201 ms

FIG 8 : Te(r) profile before (□ ) and after ( ■ , × ) pellet injection.

# DIFFERENTIAL ELECTRON-CYCLOTRON WAVE TRANSMISSION FOR INVESTIGATION OF A LOWER-HYBRID FAST TAIL IN THE REACTOR REGIME

R.L. MEYER, X. CARON
LABORATOIRE DE PHYSIQUE DES MILIEUX IONISES
(URA CNRS 835) UNIVERSITE NANCY I
B.P. 239 - 54506 VANDOEUVRE LES NANCY Cedex FRANCE
and
I. FIDONE, G. GIRUZZI
Association EURATOM-C.E.A. C.E.N. CADARACHE
13108 SAINT PAUL LEZ DURANCE Cedex FRANCE

One method to obtain information on the current carrying fast tail generated by travelling lower-hybrid waves in a tokamak plasma is emission of electron-cyclotron waves. The success of the method [1-3] relies on the fact that in low temperature plasmas the thermal and non-thermal features of the wave frequency spectrum are well separated. In a tokamak device in the reactor regime a new physical situation arises which leads to overlap of the two spectra. We first note that, in a high temperature plasma the combined effects of plasma accessibility and strong Landau damping will restrict lower-hybrid wave penetration to the peripheral plasma region. The electron distribution function in the region where the lower-hybrid wave is localized is characterized by a flat superthermal tail superimposed to a Maxwellian at relatively low electron temperature. This tail can interact with an electron cyclotron wave at frequency $\omega$ if the resonance velocity lies within the range of the superthermal tail. However, it can also interact with the Maxwellian tail in the central plasma region, where the electron temperature is much higher than at the plasma periphery and therefore the received signal is not unambiguously related to the lower-hybrid tail. It is possible to eliminate the contribution due to the thermal electrons in the plasma core using the differential transmission between two equivalent rays with equal and opposite values of the parallel refractive index $N_{\parallel}$ that is two rays characterized by the same sequence of values of the plasma density, magnetic field, bulk electron temperature, and $|N_{\parallel}|$. This is, for instance, the case of wave propagation in the equatorial plane for two modes with equal and opposite launch angles. However, for the same launch from a top position the two rays are not equivalent because the 1/R dependence and the non-zero poloidal component of the tokamak magnetic field produce different effects on the two rays. Two equivalent rays experience

equal plasma refraction and cyclotron damping by a Maxwellian distribution and therefore the differential transmission is totaly unaffected by the hot central plasma and spurious losses due to plasma refraction. On the other hand, the damping of a wave by a fast tail in a given direction is only determined by the resonant value of $N_{||}$ and the differential transmission is unambiguously related to the energetic electrons.

Differential transmission was applied in Versator II to eliminate the effect of plasma refraction [4] on the extraordinary modes launched from a top position. As shown below, the method used is in our case inapplicable since the chosen rays are not equivalent and the values of $|N_{||}|$ along the ray paths differ significantly.

It is easy to show that two rays launched from the same origin with equal and opposite values of $N_z$ (along the toroidal magnetic field direction) will in general describe differents orbits with different values of $|N_{||}|$. This is illustrated by the following example. We consider a torus with circular cross-section with major radius $R_0$=5 m and minor radius a=2 m. The density and temperature profiles are given by $n_e(r)=n_e(0)(1-r^2/a^2)$, $T_e(r)=T_e(0)(1-r^2/a^2)$, and $B_T=B_T(0)/(1+x/R_0)$ where $n_e(0)=10^{14}$ cm$^{-3}$, $T_e(0)$=20 keV and $B_T(0)$=60 kG. The poloidal field results from a central current distribution with a $T_e^{3/2}$ profile ( $I_c$=6 MA ) and a peripheral lower-hybrid current ( $I_{LH}$=6 MA ) located between $r_1$=125 cm and $r_2$=145 cm with a peak near $r_0$=135 cm.This kind of lower-hybrid distribution is predicted by the appropriate lower-hybrid code [5].

We now consider two extraordinary modes at $\omega=0.55\omega_c(0)$ launched from a top position (x=0, y=a) with $N_x$=0, $N_y$=-cos(25°), and $N_z=\sin(\pm\varphi)=\sin(\pm 25°)$. The initial values of $N_{||}=\pm 0.41$. Shown in Fig.1 are the poloidal projections of the two rays with $\varphi$=25° (a) and $\varphi$=-25° (c). It appears that the two trajectories are different that is the two rays experience different plasma refraction.

Two completely equivalent rays with opposite $N_{||}$ are found by exploiting the symmetry of the tokamak configuration with respect to the equatorial plane. We consider two rays launched from two image points with respect to the equatorial plane (i.e., two points having the same x and opposite y), with opposite $N_z$, $N_y$ but the same $N_x$ ,thus, two equal and opposite $N_{||}$ values are obtained. Since the cold dispersion relation depends on $N_{||}^2$ and the sequence of the plasma parameters is the same for the two rays, the two trajectories and local values of $|N_{||}|$ are the same. Consequently, equal absorption is obtained in a plasma with a Maxwellian distribution. For the parameters of Fig.1, the two equivalent rays are labeled by (a) and (b).

We now consider the damping of the these equivalent rays. The lower hybrid-current is carried by a superthermal asymmetric tail. As shown by Fokker-Planck numerical simulations [6], the current carrying tail is represented by a flat distribution in the parallel direction with a

perpendicular temperature $T_\perp \approx 5T_e$, where $T_e$ is the local value of the bulk temperature. The model distribution used here is a Maxwellian at $T_{||} \approx T_\perp \approx 70$keV in the interval $0.45 \leq p_{||}/mc \leq 1.4$. For $p_{||}/mc < 0.45$, the electron distribution tends to the local Maxwellian at $T_e \approx 10$keV. Shown in Fig.2 is the absorption coefficient $\alpha_X$ versus s the arc length along the ray for the two equivalent rays (a) and (b). For the ray (a) the total damping results from the contributions of the Maxwellian plasma centered near s=225 cm and the two satellites due to the lower hybrid tail. For the equivalent ray (b), the contribution to the damping comes from the central Maxwellian only. The bell shaped curve near s=225 cm is then the same for both rays . The total optical depths for the two cases are $\tau_X = 0.69$ and 0.47 respectively, and therefore the transmitted fractions $T_X = \exp(-\tau_X)$ of the initial energies are 50% for the ray (a) and 62% for the ray (b).

Since the effect of the central Maxwellian is the same for the two rays, information on the lower-hybrid current drive is obtained from the differential transmission $\Delta T_X = \exp[-\tau_X(N_{||})] - \exp[-\tau_X(-N_{||})]$. This is presented in Figs.3 and 4 versus $\omega/\omega_c(0)$ ( for $|N_{||}| = 0.41$ ) and $\varphi$ ( for $\omega/\omega_c(0) = 0.55$ ) respectively. It appears that $\Delta T_X$ has a sharp maximum with respect to $\omega/\omega_c(0)$ and $\varphi$. This makes differential transmission a very sensitive diagnostic which is a basic prerequisite for an unambiguous determination of the tail parameters.

In conclusion, we have shown that differential transmission of two equivalent rays with equal and opposite values of $N_{||}$ is a suitable method for obtaining direct information on the superthermal tail generated by lower-hybrid current drive in the reactor regime. The next and by far more difficult problem is how to extract quantitative information on the spatial and energy distribution of the tail from the radiation signal. This can be achieved using adequate interpretation tools based on 2D Fokker-Planck kinetic codes by improving previous algorithms [5] of the lower hybrid current drive.

REFERENCES

[1] Kato , K. , Hutchinson , I.H. , Phys. Fluids 30 (1987) 3809.

[2] Luce , T.C. , Efthimion , P.C. , Fisch , N.J. , Rev. Sci. Instr. 59 (1986) 1593.

[3] Ide , S. , Ogura , K. , Tanaka , H. , et al., Nucl.Fusion 29 (1989) 1325.

[4] Kirkwood , R.K. , Hutchinson , I.H. , Luckhardt S.C. , Squire , J.P. , **Radio-frequency power in plasmas** ( Proc. Eighth Top. Conf. A.I.P., Edited by R. McWilliams , New-York , 1989 ) 146.

[5] Bonoli , P. , Porkolab , M., Nucl. Fusion 27 (1987) 1341.

[6] Karney , C.F.F. , Fisch , N.J. ,Phys. Fluids 22 (1979) 1817.

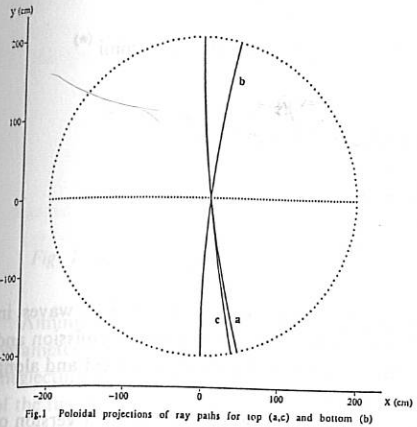


Fig.1 Poloidal projections of ray paths for top (a,c) and bottom (b) launches.

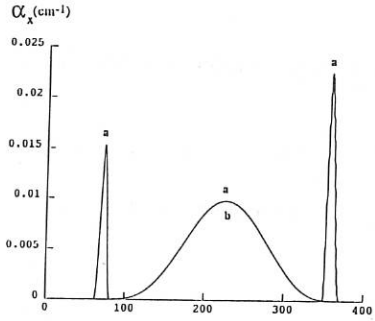


Fig.2 Absorption coefficients $\alpha_x$ vs s for the rays (a) and (b) and the parameters of Fig.1.

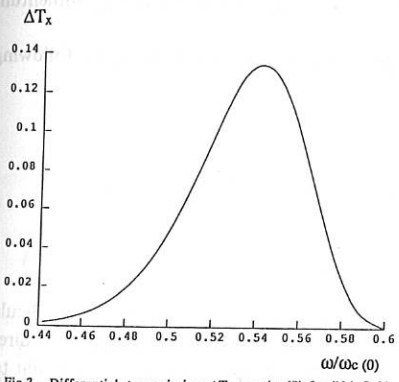


Fig.3 Differential transmission $\Delta T_x$ vs $\omega/\omega_c(0)$ for $|N_{||}|$=0.41.

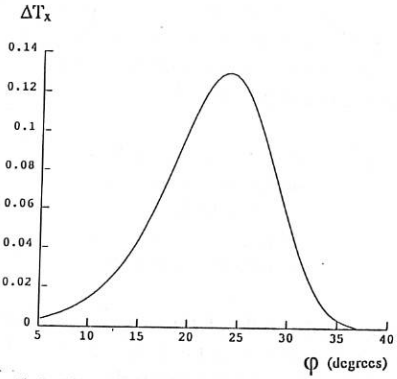


Fig.4 Differential transmission $\Delta T_x$ vs $\varphi$ for $\omega/\omega_c(0)$=0.55.

# DIAGNOSTIC POTENTIALITIES OF ELECTRON CYCLOTRON WAVES IN L.H. CURRENT DRIVE EXPERIMENTS

G.Ramponi, A.Airoldi, D.Bartlett [*], M.Brusati [*], S.Nowak, A.Orefice, F.Rimini [*]

IFP,Euratom-Enea-Cnr Association, Via Bassini 15, 20133 Milano (Italy)

[*] JET Joint Undertaking, Abingdon, Oxon OX14 3EA, UK.

The feasibility of diagnosing the high energy electron tails driven by LH waves in Tokamak plasmas during LHCD experiments is investigated by computing the emission and absorption of electron cyclotron waves both along lines of constant magnetic field and along the usual line of sight parallel to the horizontal midplane.

The modelling and the calculation of the emission spectra are made by using a version of a toroidal ray tracing code /1,2/ which solves the radiation transport equation by evaluating the absorption coefficient given by the computation of the relativistic dielectric tensor and the emission coefficient obtained by a quasi-linear approach /3/. Besides the refractive effects, the effects of plasma diamagnetism, poloidal magnetic field, harmonic overlapping and finite acceptance angle of the antennae are also taken into account.

In order to consider electron distribution functions reproducing those predicted by a quasi-linear Fokker-Plank code for L.H. waves /4/, we superimpose to a Maxwellian bulk plasma a suitable number of Maxwellians drifting in the $p_\parallel$ direction, $p_\parallel$ being the momentum component parallel to the magnetic field /5/.

The simulations shown here refer to a D-shaped JET-like plasma, having the following parameters and profiles:

$$R_o = 3.1 \text{ m} \; ; \; a = 1.03 \text{ m} \; ; \; B(0) = 3.3 \text{ T} \; ;$$
$$n(\overline{\psi}) = (n_o - n_a)(1 - \overline{\psi}^2)^{\beta_n} + n_a$$
$$n_o = 3. \times 10^{13} cm^{-3}; \; n_a = .3 \times 10^{13} cm^{-3}; \; \beta_n = 0.7$$
$$T(\overline{\psi}) = (T_o - T_a)(1 - \overline{\psi}^2)^{\beta_T}$$
$$T_o = 6keV; \; T_a = 0.6keV; \; \beta_T = 3.$$

The radial profile of the electron distribution function integrated over the perpendicular momentum is shown in Fig.1: in the region $\overline{\psi} \geq 0.5$ it exhibits long tails in the positive direction of $p_\parallel$, while it is an unperturbed Maxwellian in the central region $\overline{\psi} < 0.5$ . Each flat tail is constituted by a number of suprathermal electron populations, all Maxwellian in $p_\perp$, but with different values of $T_\perp$ . The maximum value of $T_\perp$, whose profile follows that of the bulk temperature, is around 20KeV.

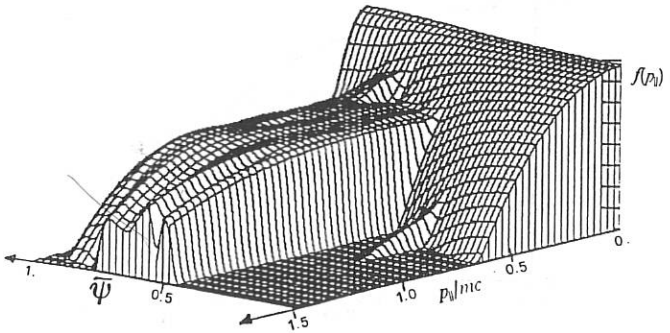


*Fig. 1 - Radial profile of the electron distribution function vs. positive parallel momenta.*

Aiming to evidence the sensitivity of E.C. emission and absorption with respect to the main parameters of the suprathermal population, we show in Fig.2 the emission spectra expected (neglecting reflections) for an X-mode travelling along a vertical line at R = 3.14 m, in the range of the first three harmonics. (These graphs have been obtained without including, for simplicity, the finiteness of the antenna beam, i.e. considering only the central ray propagating perpendicularly to the magnetic field). It is evident that there are sufficiently large ranges of frequency, below the harmonics of the local electron cyclotron frequency, where "only" suprathermal particles emit (or absorb) the radiation.

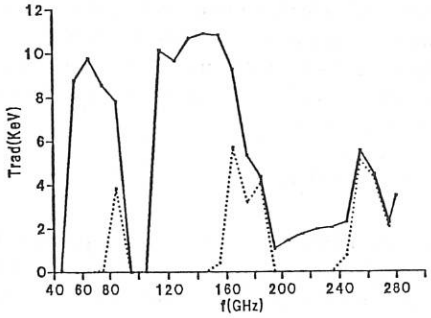


*Fig. 2 - Radiation spectra along a vertical chord at R = 3.14m for the X-mode. The continuous line is obtained when suprathermal particles are present; the dashed line is obtained without suprathermals.*

Fig.3 shows the fraction of transmitted power $P_t$ ( $P_t = e^{-\tau}$, $\tau$ being the optical depth), in the X-mode, in the third harmonic downshifted range where refraction is negligible, for three vertical rays with different values of the component $n_\parallel$ of the refractive index parallel to the magnetic field.

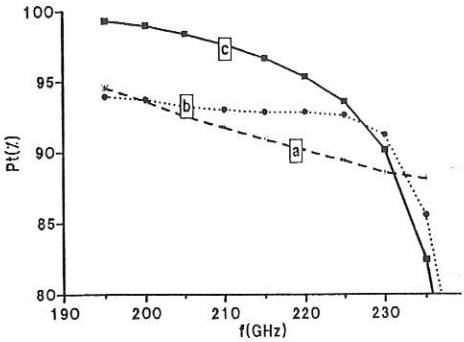


*Fig. 3 - Spectra of the transmitted power for the X-mode in the downshifted third harmonic range and vertical trajectories at $R = 3.14m$ with a)$n_{\parallel} = 0$ , b)$n_{\parallel} = -0.3$ c)$n_{\parallel} = +.3$ .*

In the case of vertically propagating waves, due to the fact that the magnetic field is constant along the ray trajectory (in absence of refraction and if the beam is sufficiently well collimated), the resonance condition

$$\gamma - Y - n_{\parallel} p_{\parallel}/mc = 0 \qquad (1)$$

(where $Y = \nu\Omega/\omega$, $\omega$ is the radiation frequency, $\Omega$ is the local electron cyclotron frequency, $\nu$ the harmonic number, $\gamma = (1 + (p/mc)^2)^{1/2}$ ) , allows a one to one correspondence between the energy of the emitting (or absorbing) particles and the radiation frequency.

If $n_{\parallel} \simeq 0$ , as in the case of curve "a" in Fig.3, the correspondence is between $\omega$ and $\gamma$ , so that no information about the asymmetry of the distribution function can be inferred.

If $n_{\parallel} \neq 0$ , the resonance contours given by eq.(1) are ellipses in the plane $(p_{\perp}, p_{\parallel})$ whose centers are in $(p_{\parallel 0}, p_{\perp} = 0)$ , with $p_{\parallel 0}/mc = Yn_{\parallel}/(1 - n_{\parallel}^2)$, and whose semiaxes parallel to $p_{\perp}$ are $b = \sqrt{Y^2 - 1 + n_{\parallel}^2} \,/\, \sqrt{1 - n_{\parallel}^2}$ . It is easy to see that, if

$$b >> \sqrt{(2T_{\perp}/mc^2)} \qquad (2)$$

$T_{\perp}$ being the perpendicular temperature of the tail, the resonant absorption of E.C. waves shall mainly be due to particles with $p_{\parallel} = p_{\parallel 0,2}$ , $p_{\parallel 0,2}$ being the two intersections of the resonant ellipse with the $p_{\parallel}$ axis. In the present case condition 2) is well satisfied for $Y > 1.2$ and $n_{\parallel} = \pm 0.3$ . Moreover, for large Y, only one of the two intersections will be in the range of $p_{\parallel}$ values where particles are present, so that a "nearly" one-to one correspondence between frequency and $p_{\parallel}$ will exist.

Referring to Fig.3, in the case of curve "b" the attenuation of the wave in the frequency range 195--220 GhZ (corresponding to Y from 1.41 to 1.25) is mainly due to particles with $p_{\parallel}$ ranging from $+0.7$ to $+0.5$, while it comes from particles with opposite values of $p_{\parallel}$ in the case of curve "c". The ratio between the transmitted power in the two cases would give an indication of the asymmetry of the distribution function.

Fig.4 shows the emission spectra which could be measured, from the low field side, along a horizontal line of sight parallel to the equatorial plane. In this case, although the one to one correspondence between frequency and energy is lost because of the dependence on R of the magnetic field, the radiation received at low frequencies is entirely due to the suprathermal electrons in the low field side region. In fact the X-mode cutoff prevents the radiation from bulk particles to escape, and the spectrum of emission, in this frequency range, gives an indication of the spatial localization of suprathermal particles.

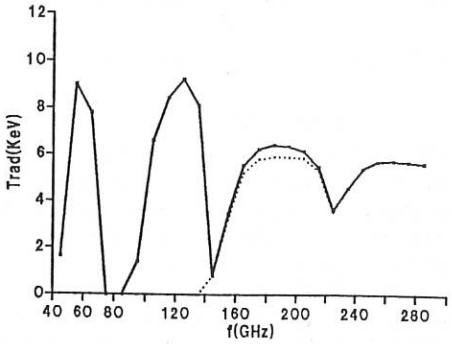


*Fig. 4- Radiation spectra, with (continuous line) and without (dashed line) suprathermals, "viewing" from the low field side parallel to the equatorial plane.*

*References*

/1/ A.Airoldi, A.Orefice, G.Ramponi, Il Nuovo Cimento, **6D** ,527, (1985)

/2/ G.Ramponi, A.Airoldi, D.V.Bartlett, M.Brusati, S.Nowak, A.Orefice, Proc.5th Int. Workshop on ECE and ECH, S.Diego , pg.10, (1985)

/3/ A.Orefice ,Il Nuovo Cimento, **8D** , 318 (1986)

/4/ M.Brusati,C.Gormezano,S.Knowlton,M.Lorentz,N.Gottardi, F.Rimini, Proc. Eighth Topical Conference on Radio Frequency Power in Plasmas, Irvine, Ca., pg.32, (1989)

/5/ A.Orefice, IFP Report FP 89/11 (1989), (to appear on Il Nuovo Cimento D)

# FEASIBILITY OF DIAGNOSTIC OF JET LHCD PLASMAS BY MEANS OF X-RAY CRYSTAL SPECTROSCOPY

F. Bombarda, M. Brusati+, R. Giannella+, F. Rimini+

Associazione EURATOM–ENEA sulla Fusione,
Centro Ricerche Energia Frascati
C.P. 65 – 00044 Frascati, Rome, Italy

+JET Joint Undertaking, Abingdon 0X14 3EA, England

## INTRODUCTION

The interaction of LH waves with the plasma is expected to develop a high energy tail in the electron distribution function. X–ray line emission from highly ionized impurities in the plasma can provide a means to measure the fractional density of the suprathermal electrons. The principle of this measurement, which has already been successfully carried out on FT [1], relies on the relative increase in brightness of a collisionally exited electric dipole transition, like for example the resonance line of He–like ions, and on the observation that, for medium $z$ ions, the impact cross section is fairly constant over the energy range of the fast electrons. The applicability of this method for diagnosing suprathermal tails in JET plasmas is discussed. The general conditions under which a measurement of the suprathermal component fractional density and its localization is expected to be feasible are defined. The set–up of the crystal spectrometers available at JET is outlined.

## I PHYSICS PRINCIPLES

The intensity of a collisionally excited line in a low density plasma is

$$I_R = n_e n_z \int_{E_0}^{\infty} \mathrm{d}E \, \sigma \cdot v(E) f(E)$$

where $n_e$ and $n_z$ are the electron and ion density, $\sigma \cdot v(E)$ is the excitation rate and $f(E)$ is the electron distribution function. The excitation rate is given by the Bethe asymptotic relativistic formula [2], to which an empirical term has been added to correct the departure at low energy from the true values of the cross section, given for example by the Mewe parametric formula. From Fig. 1 it can be seen that for $E \cong 40 - 1000$ $k$eV $\sigma \cdot v$ can be taken as constant; therefore the increase in the line emission rate due to fast electrons is directly proportional to their number.

Excitation rates, and in particular the high energy average value $\langle \sigma v \rangle$ was calculated for the resonant transition $1s2p \rightarrow 1s^2$ of He–like ions of $z$ =18–36. With these values the fraction $N_{s.t.}$ of fast electrons producing an increase in the line intensity of 30% over the thermal value was derived and plotted as a function of the atomic number $z$, for temperatures of the bulk between 1 and 10 $k$eV. The

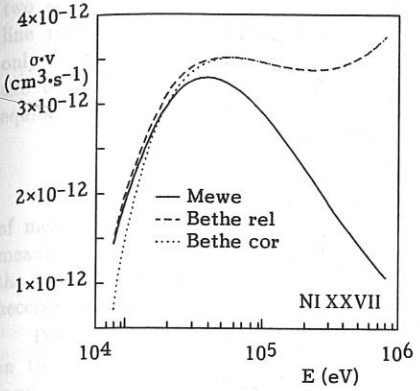


Fig. 1 – Excitation rate of the Ni XXVIII resonance line $w$ as a function of the impact electron energy.

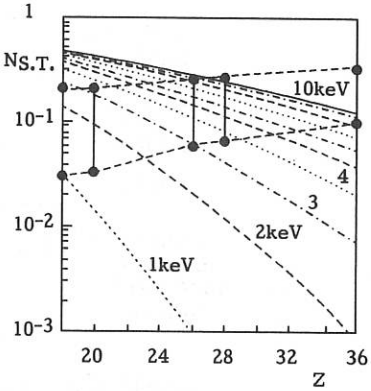


Fig. 2 – Fractional density $N_{s.t.}$ of suprathermal electrons inducing a 30% increase in the emission of the resonance line as a function of atomic number $z$.

curves of Fig. 2 show that ions of higher $z$ are more sensitive to fast electrons, but for all ions an increasingly high fraction $N_{s.t.}$ of suprathermals is needed at increasing temperatures.

The product of the fractional abundance $f_{He}$ of the He–like ionization stage times the line excitation rate $Q(T_e)$ defines the temperature range of maximum emission. This range, also plotted in Fig. 2, roughly determines the fractions $N_{s.t.}$ detectable for each ion. Some of the satellites lines also present in the spectra of He–like ions are the result of the interaction with electrons comprised in a narrow band of energy in the bulk of the distribution function, through the mechanism of dielectronic recombination. Their intensity is therefore not effected by a distortion in the high energy part of the distribution. In thermal conditions their intensity ratio with the resonance line is a function of $T_e$ only. Since $T_e(t,r)$ can be independently measured, from the difference between the experimentally measured ratio $R_{\rm exp}$ and the expected value $R_{th}(T_e)$, the fraction $N_{s.t.}$ of suprathermals can be inferred:

$$N_{s.t.} = (1/R_{exp} - 1/R_{th}(T_e))C_s(T_e)/\langle\sigma \cdot v\rangle$$

where $C_s(T_e)$ is the satellite excitation rate.

## II SIMULATION OF THE JET LHCD EXPERIMENT

The interaction of LH waves with the JET plasma have been simulated by means of a Bonoli–Englade ray–tracing code [3]. The absorption of the 3.7 GHz wave is calculated by solving on a radial grid a steady state, 1D Fokker–Planck equation with an enhanced $T_\perp$ in the resonant region. The output of the code are the parallel electron distribution function $f_\parallel(v_\parallel, r)$, the driven current $J_{RF}(r)$, and the absorbed power $P_{abs}(r)$. These data have been used to calculate the emission

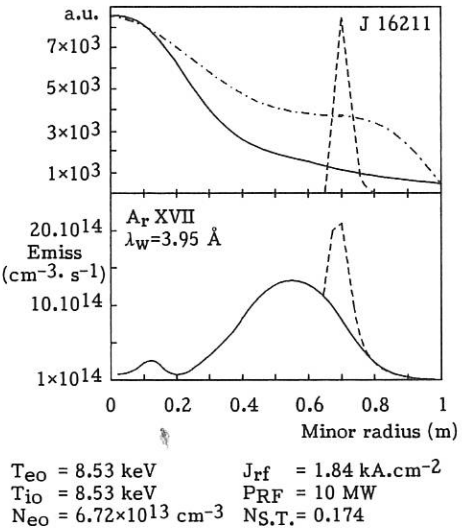


Fig. 3 – Thermal and suprathermal emission profile of Ar XVII in the simulation of a pellet injection JET discharge.

profiles for four impurities, either naturally present or to be injected in the plasma, Ar XVII, Cr XXIII, Ni XXVII , Kr XXXV.

The fraction of fast electrons resulting from the code are generally too small to produce a measurable effect on the line emission of any impurity, but in Fig. 3 is shown for example the relative increase in the emission of the Ar XVII resonance line if the fraction $N_{s.t.}$ were $\sim$15%, in a pellet injection discharge, with very peaked electron and density profiles, $P_{LH} = 10\,\mathrm{MW}$.

In general, when the LH deposition is localized in the outer plasma region, the line radiation of an impurity whose emission is centered in the same region should be selected. The emission of higher $z$ ions is normally dominated by the thermal bulk emission, but for more central deposition a marginally excited line like that of Kr XXXV could be chosen, although even for this element the peak temperature should not be too high. In all the cases considered, the simulations indicate that the local fraction of suprathermals needed to carry out the measurement should be of the order of 10%.

## III EXPERIMENTAL LAY-OUT

On JET three crystal spectrometers are available for X-ray line spectroscopy [4, 5, 6]. One of these, KS2, can perform a radial scan at a fixed wavelength several times during the discharge; the others have a fixed line-of-sight but a broader spectral range. Since at least two lines in the spectrum of the chosen ion need to be monitored, the use of KS2 in conjunction with one of the other

two spectrometers, should provide a good localization of the fast electrons. The line integrated spectra could still be used by themselves, but in this case the only localization would be provided by the definition of the emission region of the observed ion, which can be calculated by means of the existing ionization equilibrium code.

## CONCLUSIONS

In the JET plasmas, characterized by high electron temperatures, the possibility of measuring the fraction of fast electrons produced during LHCD experiments by means of X–ray line intensity ratio techniques is probably limited. In particular, the calculations show that very high fractions, 10% or more, of suprathermals are necessary to produce a measurable effect on the observed line intensities.

Different impurities can be used to monitor different plasma regions, depending on the localization of the resonance layer, with the combined use of the crystal spectrometers available at JET.

This work was performed in the framework of a contract between JET and ENEA on the "Physics support of the LHCD experiment on JET".

## REFERENCES

[1] R. Bartiromo, F. Bombarda, R. Giannella, Phys. Rev. **A 32**, 531 (1985).

[2] M. Inokuti, Review of Mod. Phys. **43**, 297 (1971).

[3] P. Bonoli, R.C. Englade, Phys. of Fluids 29, 2937 (1986).

[4] R. Bartiromo, F. Bombarda, R. Giannella, S. Mantovani, L. Panaccione, G. Pizzicaroli, Rev. Sci. Instrum. **60**, 237 (1989).

[5] U. Schumacher, E. Källne, H.W. Morsi, G. Rupprecht, Rev. Sci. Instrum. **60**, 562 (1989).

[6] R. Barnsley, U. Schumacher, E. Källne, H.W. Morsi, G. Rupprecht, Proc. XVI Europ., Conf. Contr. Fus. and Plasma Phys., Venice, Vol. IV, 1557 (1989).

# THE JET TIME OF FLIGHT NEUTRAL PARTICLE ANALYSER

G.Betello(*),G.Bracco,A.Moleti,B.Tilia,V.Zanza

Associazione EURATOM-ENEA sulla Fusione
Centro Ricerche Energia Frascati
C.P. 65 , 00044 Frascati (Roma) ITALY.

(*) present address IBM-ECSEC (Roma) ITALY

Neutral particle analysers provide a detailed measurement of the ion energy distribution function which can not be obtained by other diagnostics, together with information on neutral density. The standard neutral particle analysers, as the one in [1], have shown to be sensitive to the high neutron fluxes produced in the high temperature deuterium plasma of the large tokamaks as JET [2]. The application of the coincidence tecnique can provide an effective way to discriminate the proper neutral signal from a random background. At the same time it can be used to measure the particle time of flight. A neutral particle analyser with mass rejection capability and low random background sensitivity has been developed and fully calibrated in the energy range between 0.5 and 200 KeV for hydrogen,deuterium and helium neutrals.

In fig.1 the analyser layout is shown. The neutrals are ionized in a gas stripping cell and energy analysed by a cylindrical electrostatic plate system. The inner cylindrical plate has an diameter of 6 cm and the outer diameter is 10 cm. The inner cylinder is terminated at both ends by two flat electrods and is set to a positive potential. This configuration provides focalization of the ion beam from the stripping cell both in the plane parallel and perpendicular to the cylinder axis. The ion trajectories in the electrostatic field of this system have been numerically computed [2].

A set of 15 detectors collect the ion with an energy dynamic range 1:25. Each detector is a time of flight detection system composed by a thin (1ug cm-2) carbon foil and two channeltrons fig.2. The ion produces secondary electrons in the carbon foil which are detected by the first channeltron providing the start trigger for the coincidence while the signal in the second channeltron is the stop signal. The channel length has been choosen in the range from 12 cm to 30 cm in order to have a time of flight of at least 50 ns for each selected energy.

The start pulse triggers a set of three programmed time delays (in the range 10 to 400 ns) and at the end of each delay a time gate of programmed length is generated (in the range 5 to 33 ns). A coincidence event is counted if the stop signal occurs during the programmed gate time. In this way up to three presetted masses can be counted by each detector. The full signal processing for each detector is performed by the CAEN N209 module. Channeltrons have been choosen agaist channelplates as their high gain avoids the need of

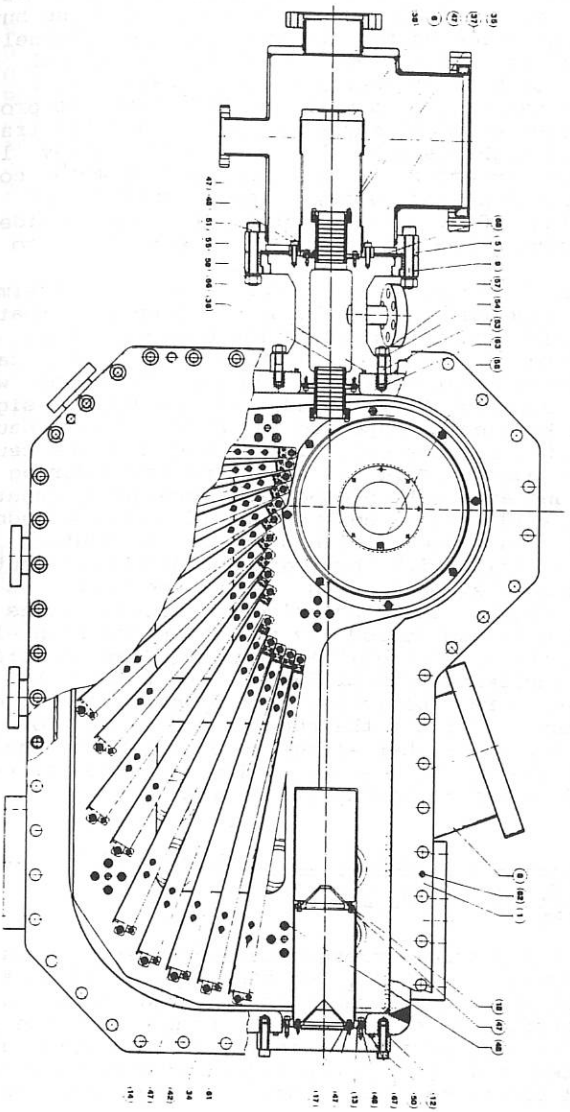

fig.1 Analyser

preamplifiers near to the analyser which can be affected by radiation problems. The channelplates would provide a better time resolution due to their much faster output pulse but in the parameter range selected for the analyser the channeltron time performance is sufficient to obtain a global time resolution (fwhm) of 8 ns at energy greater than 30 kev.

The analyser vacuum box is made in ARMCO steel to provide the shielding agaist external magnetic field. A light trap on the plasma line of sight is set to reduce the stray light background. Each detector is enclosed in a mu-metal box to complete the magnetic and stray light shield of the channeltrons. Two 500 ls-1 turbomolecular pumps provide the vacuum in the analyser box and in the analyser duct to the tokamak.

The neutron background rejection can be estimated assuming a coincidence gate of 10 ns and supposing that the neutron induced background is near to the maximum count rate at which channeltrons can operate (1.10 s-1). In this case a spurious coincidence count rate of 10000 s-1 is found which still provides a dynamic of two decades in the neutral signal. This level of background is expected in JET[2] if the neutron yield exceeds 1.10 neutrons s-1. This means that the neutral particle analyser must be shielded agaist neutrons during the D-T operation and even with present JET results[3] (neutrons yields exceeding 1.10 s-1) a neutron shield is recommended.

The analyser has been calibrated in a neutral beam calibration line [2], with hydrogen and deuterium neutrals bewteen 0.5 and 200 KeV and with helium neutrals up to 100 KeV. In fig.3 the coincidence count rates for hydrogen, deuterium, helium at 100 kev are shown for channel 15 as a function of the programmed time delays in the coincidence module with a coincidence gate of 21 ns. As it can be seen the three masses are resolved with a rejection level of 1% between every mass. In fig.4 the peak delays value for each mass are shown for the higher energy detector of the analyser as a function of the particle energy. The experimental values have been fitted by the following expression:

$$T = \frac{L}{\sqrt{\frac{2}{M}\left(E - D\ EL(E,M,Z)\right)}} + TO$$

where E,M,Z are the particle energy, mass and charge, D is the carbon foil width, L is the detector length, TO is a time offset due to electronics and cable lengths and EL(E,M,Z) is the specific energy loss in carbon foils for the given particles[4]. The free parameters in the fit are D,TO and L and it can be seen that the fitting functions reproduce nicely the experimental values so that they can be used in the analyser tuning.

The detection efficiency of each channel has been found to reach about the 50% of the maximum efficiency which is fixed by the ionization in the stripping cell for energies

greater than 30KeV while it decreeses down to 1% at the very low energies.


1) R.Bartiromo, G.Bracco, M.Brusati, G.Grosso, S.Mantovani B.Tilia and V.Zanza, Rev.Sci.Instrum.,58,788(1987)
2) G.Betello, G.Bracco, S.Mantovani, B.Tilia, V.Zanza Report RT/FUS/88/15
3) JET Team, P.J.Lomas, Plasma Physics and Controlled Fusion, 31,1481(1989)
4) J.F.Janni, Atomic Data and Nuclear Data Tables, 27,147(1982)


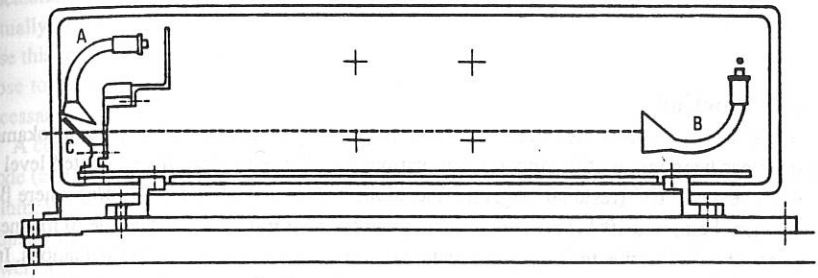


fig.2 Detector

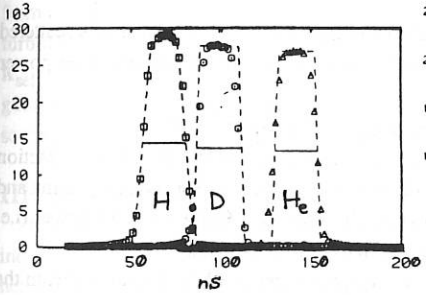


fig.3 Counts versus time delay for H,D and He at 100 KeV

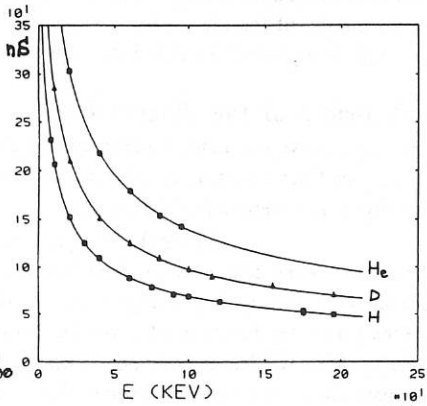


fig.4 Time delay versus neutral energy for H,D,He

# PROJECT OF MAGNETIC FLUCTUATION MEASUREMENT BY CROSS POLARIZATION SCATTERING IN THE TORE SUPRA TOKAMAK

M.Paume[(1)], X.L. Zou [(1)], L.Laurent [(1)], T.Lehner [(2)], D.Grésillon [(2)]

*(1) Association Euratom CEA DRFC/SPPF*
*CEN CADARACHE 13108 St Paul lez Durance France*
*(2) Laboratoire PMI Ecole Polytechnique 91128 Palaiseau France*

## I Introduction

Up to now the direct measurement of the magnetic fluctuations in the core of tokamak plasmas has been impossible. According to various turbulence models, the estimated level of $\tilde{B}/B$ lies between $10^{-6}$ (residual magnetic fluctations due to drift wave i.e. $O(\beta\tilde{n}/n)$ where $\beta$ is the toroidal beta) and $10^{-4}$ (obtained assuming that the heat transport is only due to magnetic turbulence). We describe in this paper a tentative diagnostic to measure these fluctuations. It is based on the cross polarization scattering as suggested in [1]: Magnetic fluctuations scatter an incident electromagnetic wave (with $k_i \perp B$) with a change in polarization. In section II the basic principle of the diagnostic is explained. In section III the experimental set up is described. It will be tested on the Tore Supra Tokamak at the end of 1990.

## II Principle of the diagnostic

It can be shown that an incident electromagnetic wave in the ordinary polarization is scattered by magnetic fluctuations in the extraordinary mode. Far from the cut-off, the scattered power per unity of frequency and solid angle is:

$$dP_s/dfd\Omega = P_i\, r_0^2\, n\, L\, (\omega_{ce}/\omega_i)^2 < |\tilde{B}(k,\omega)|^2 > /B^2$$

where $P_i$ is the incident power, $r_0$ the classical electron radius, L the length of the interaction zone and n the density. Depending on the level of magnetic turbulence, for typical plasma and antenna parameter the scattered power lies between $10^{-9}$ and $10^{-13}$ of the incident power (i.e. typically $10^2$ to $10^6$ less than the power scattered by density fluctuations).

The main difficulty is that one has to excite or detect a pure eigenmode in the plasma from the outside. At the plasma boundary, an incident wave is projected on the plasma propagation modes (ordinary and extraordinary). For not too short wavelengthes (millimetric waves), the two normal modes are distinct enough and the wave propagates across the plasma without mode conversion. Using what is available to the experimentalist i.e. a linearly polarized antenna, it is

possible to excite a pure mode provided the antenna axis is perpendicular to the total magnetic field. In this configuration, when its E plane is aligned ( respectively perpendicular) with the total magnetic field at the edge the antenna is coupled to the ordinary (respectively extraordinary) mode. For other incidence angles normal modes correspond to elliptical polarization and cannot be excited selectively from the outside.

It can be estimated that it is possible to launch or detect a mode with an attenuation of 1000 of the other mode provided: i)the wavelengh is long enough; ii) a high gain antenna is used at normal incidence with a correct orientation of its E plane. This limit comes from spurious elliptical polarization of the antenna, imperfect orientation of the E plane, beam divergence (the incidence angle is not exactly perpendicular).

The geometry of the experiment is so that the emitting and receiving antenna E plane are respectively parallel and perpendicular to the total magnetic field at the plasma edge. The configuration corresponds to pure forwardscattering. The wave vector of the observed fluctuation is in the radial direction and its modulus is the difference $\mathbf{k}_{\text{scattered}}^{\text{extraordinary}} - \mathbf{k}_{\text{incident}}^{\text{ordinary}}$ It actually depends on the plasma parameter through the difference of refractive indices. In our case this formula is only an approximation. As discussed later the scattering process will occur close to a cut off layer where the WKB approximation is not valid. A full wave analysis is necessary [2].

A careful optimization leads to a proportion of $10^{-3}$ emitted/received in the extraordinary mode (assuming that no extraordinary mode generated by wall reflection crosses the scattering volume). There are several spurious effects as shown in figure $1_a$. The mean one is due to the ordinary mode, forwardscattered on density fluctuations (much larger than the cross scattered power) and received by the imperfectly selective receiving antenna. This situation can be made better choosing the probing frequency in such a way that the cut off layer (which is a perfect mode filter) lies between the two antennae as shown in Fig.$1_b$ and Fig.2. This improves the polarization selectivity of the receiver and avoids any direct light on the receiving antenna (when the plasma exists). Now, the only remaining spurious signal is due to the power launched in the extraordinary mode and forward scattered by density fluctuations. It cannot be discriminated from cross polarisation scattering of the ordinary mode. This unavoidable effect is due to low k turbulence, since the selection rule in pure forward scattering without mode conversion is $\mathbf{k}_{\text{selected}} \approx \mathbf{k}_{\text{scattered}}^{\text{extraordinary}} - \mathbf{k}_{\text{incident}}^{\text{extraordinary}} \approx 0$, provided the k resolution of the experiment is good enough (i.e. large width and low divergence beams). According to the results of scattering experiments it should correspond to low level and low frequencies turbulence.

## III Experimental set up

A scheme of this system is given in Fig.2. As the scattered fraction is very small ($10^{-11}$ of incident power for $\delta B/B \approx 10^{-5}$) it is necessary to launch a large power in the plasma and use heterodyne technique as receiver.

The power source is a Varian Extended Interaction Oscillator at f=60 GHz with P=70 Watts CW stabilized in frequency by a feedback loop based on a high Q cavity.

The main part of the power is transmitted to the machine by using a 10 m oversized waveguide WG16. The wave is then launched by a gaussian optic lens antenna consisting in a corrugated

feedhorn antenna coupled to a quartz lens located at the top of the vacuum vessel. The radiation pattern ($HE_{11}$) is characterized by circular symmetry, high gain, and low sidelobes which can be assimilated to a linearly polarized gaussian beam of which the waist is located at the lens ($\phi$= 9.4 cm ). A particularity of this system is that a motorized rotary joint allows to match the direction of the electric field to the total magnetic field at the plasma edge. The vacuum interface is then made of a resonant quartz window ($\phi$=16 cm). The receiver is a similar system located at the bottom of the vacuum vessel. The collected power is sent to a low noise heterodyne receiver. The local oscillator is a Gunn diode (Millitech GDV15) with output power 70 mWatts. Its frequency is stabilized by phase lock loop in order to have an intermediate frequency of 20 MHz. The signal is detected with an AEG balanced mixer with integrated IF amplifier. After amplification the frequency is shifted down by a second mixer and the signal which is proportionnal to $\delta B$ is sent to a fast data acquisition. The spectrum of magnetic fluctuations in the range [0,500 KHz] is then obtained.

The forward scattering geometry allow to use a simple calibration technique: A known power fraction of extraordinary mode is sent to the plasma by a slight oscillating rotation of the top antenna ($10^{-3}$ rad). This simulates a known proportion of forward scattered power. A numerical analysis is then necessary to compute the level of magnetic fluctuations [2] .

## IV Conclusion

A diagnostic which should allow direct measurement of magnetic fluctuations in the plasma core is planned for Tore Supra. The main difficulty is that it is based on the cross scattering process of a pure ordinary mode which competes with the more efficient usual scattering on density fluctuations of spurious incident extraordinary mode. A careful optimization has been made to avoid this second process.

This diagnostic is also equipped with the following systems:

- The top microwave circuit (emitter) is also a reflectometer. The antenna is equipped with a coupler to measure the backscattered signal . This will be useful to discriminate spurious signals.
- The bottom circuit can also be transformed into a reflectometer. The system can then be used as a double reflectometer to detect up down correlation of density fluctuations.
- Quartz prisms located between the lens and the antenna can be inserted and the diagnostic becomes small angle scattering experiment (typically 0.1 radians) useful to study large scale density fluctuations ($k \leq 300\ m^{-1}$).

Acknoledgements: *The authors wish to thank C. Cordier , J.C. Patterlini for technical assistance and P. Goy for useful discussions on the microwave set up.*

## References

[1] Lehner T., Rax J.M. , Zou X.L. Europhysic Letters 8,759 (1989)

[2] X.L. Zou, L.Laurent, T.Lehner, J.M. Rax "Localization of fluctuation measurement by wave scattering close to a cut off layer" in this conference.

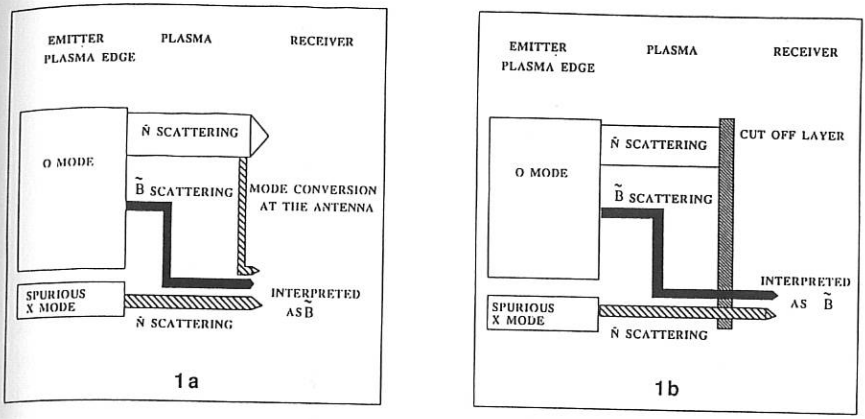


**Figure 1:** *Effect of spurious polarisation with (a) and without (b) cut off layer. The unwanted phenomena are the dashed arrows. Only the relevant scattering processes are shown.*

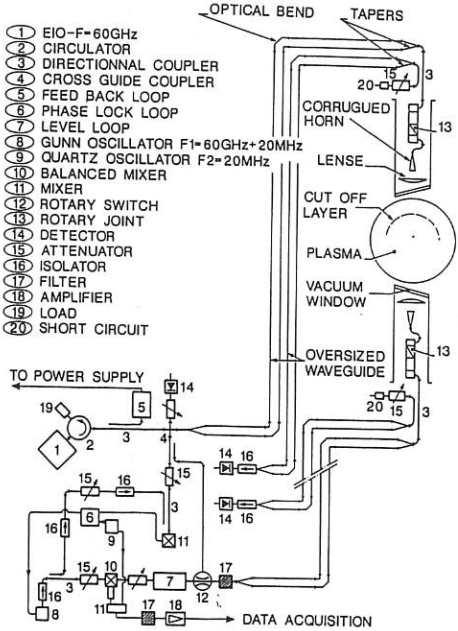


**Figure 2:** *Experimental set up*

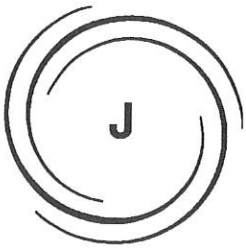


# BASIC COLLISIONLESS PLASMA PHYSICS

# TO THE THEORY OF JUPITER'S DECAMETRIC S-EMISSION

A.G.Boyev, M.Yu.Lukyanov

Institute of Radio Astronomy, Khar'kov

I.So-called Io phase dependent S-emission is observed over all range of Jupiter's decametric radio spectrum up to upper limit frequency $f_{max}$= 39,5MHz. The radiation pattern of this emission was discovered to be a hole cone surrounding the Io flux tube (IFT) and is characterized by specific feature - frequency of emission decreases steadily with increasing of angle between the axis and the formative line of the cone [I].

Previous theories of Jupiters decametric radioemission proceeded from the assumption that frequency of emission corresponds or is close to gyrofrequency in the Jovian ionosphere at the foot of the IFT. However, recent experiments [2] have pointed out on a great discrepancy between the maximum frequency of S-emission and the gyrofrequency on the Jupiter surface as well as on a weak correlationin behaviour of these frequencies with changing of the sattelite Io jovigraphycal longitude.

The proposed mechanism of S-emission generation is based on the next assumptions: a) the electron concentration in the IFT differs from one in the Jovian ionosphere so that the plasma frequency $\omega_p$ can be equal to the gyrofrequency $\omega_B$ or even exceed it slightly ( usually the case $\omega_p \ll \omega_B$ was considered); b) the emission source is supposed to be an electron beam moving along the IFT and exiting plasma waves which have anomalous dispersion ( frequency $\omega$ decreases with increasing wave number k) near the upper-hybrid frequency $\Omega=(\omega_p^2+\omega_B^2)^{1/2}$; c) the plasma waves convert into fast extraordinary waves on the regular unhomogeneity of density arising on the diffusal boundary of the IFT.

2. Assume that the electron beam arises in the polar region

of Jupiter's ionosphere and moves along the IFT in the Io direction. Beam density is much smaller than plasma one. This beam excites a packet of anomalous dispersion plasma waves near the upper-hybrid frequency $\Omega$ owing to beam- type instability. The packet has the width

$$\frac{\Delta\omega}{\omega} \simeq 2\left\{\frac{V_T}{U_o}\ \frac{\omega_p^2\,\omega_B}{\Omega^2(4\omega_B^2-\Omega^2)^{1/2}}\right\}^{1/2} \qquad (2.1)$$

where $U_o$ is the beam velocity, $v_T=(\varkappa T/m)^{1/2}$ is the thermal velocity of plasma particles. The emission is beamed into a wide but hollow cone characterized by the half-angle

$$\theta_o = \arccos\{1/\beta N_{min}\} \qquad (2.2)$$

where $\beta=U_o/c$ ,

$$N_{min}=\left(\frac{c}{V_T}\right)^{1/2}\left\{\frac{(4\omega_B^2-\Omega^2)\,\omega_B^2}{3\,\Omega^4}\right\}^{1/4}$$

is the minimal value of refractive index for anomalous dispersion plasma waves. The width of radiation pattern is determined by the apex angles of external $\theta_{out}$ and internal $\theta_{int}$ cone boundaries

$$\theta_{int} \simeq \arccos\{1,35\cos\theta_o\}$$
$$\theta_{out} \simeq \arccos\{0,94\cos\theta_o\} \qquad (2.3)$$

It should be mentioned that the frequency-angle dependence corresponds qualitatively to the experiment because $\partial\omega/\partial\theta<0$.

The maximum frequency of S-emission $f_{max}$=39,5 MHz can be explained by existing the anomalous dispersion plasma waves in the range from $\omega_B$ to $2\,\omega_B$ . As it follows from the upper-hybrid frequency definition the frequency $f_{max}$ is generated in the auroral regions of Jupiter's ionosphere where magnetic field strength B=7 G. Electron concentration in the IFT must reach the value $n_{tube}= 10^7$ sm$^{-3}$ exceeding the ionosphere maximum $n_{ion}= 5\cdot10^5$ sm$^{-3}$. Such divergence may take place because the IFT is the material formation in ionosphere, with properties differed from ionosphere ones. Increased concentration in the IFT can be explained, for example, by additional ionization of neutrals lifted from the lower lays of

ionosphere .

3. One of the most important features of the decametric emission is the dynamic frequency drift of S-bursts. Whatever observation condition, the frequency drift rate is negative and proportional to frequency $df/dt \simeq -f$ . In the framework of supposed theory, when the source moves along the IFT with velocity U generating waves with frequency $f = \Omega/2\pi$ , the experiment is explained by assuming that the plasma frequency changes along the IFT this way

$$\omega_p^2 = \Omega^2(S_0)\exp\left\{-\frac{2\gamma}{U}(S-S_0)\right\} - \omega_B^2(S) \qquad (3.I)$$

Here $S_0$,S - are coordinates of the source, correspondingly, in the initial and final moments of time, $\gamma = I\ s^{-I}$ is the scale coefficient.

Dependence (3.I) being unverified directly, it was exploited for another experiments explanation. It was the dependence (3.I) which allowed to explain the longitudinal variations of the cone angle and the width of radiation pattern. Figure shows the results of calculation executed accordingly (2.2),(2.3) for frequency f=IIMHz and South hemisphere source location. Here $\Lambda$ is the jovigraphycal longitude of Io in the coordinate system III.1965, the experimental data are taken from [I]

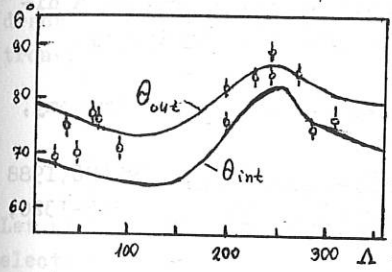


One could see the experiment is explained well in the frame of assumption about distribution of plasma density in the IFT. Small divergencies between theory and experiments can be excepted by variating the model parameters, e.g. the source velocity.

Dependence (3.I) was used also for explanation the maximum frequency behaviour with the change of source longitude. In left figure the circles are marked experimental data [2]. Curves I and 2 show the change of local gyrofrequency at the foot of the IFT on the Jupiter's surface in the North and

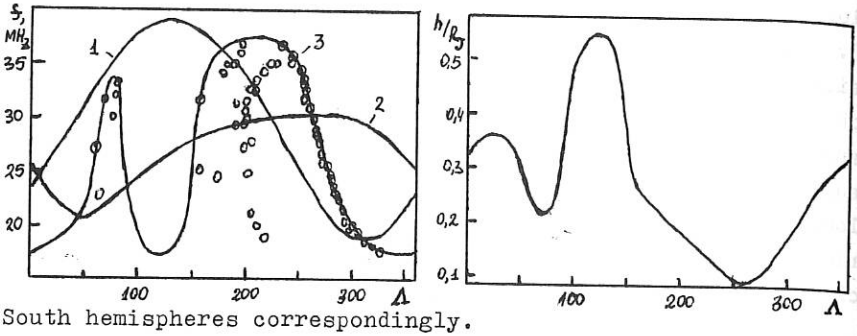


South hemispheres correspondingly.

Supposed mechanism allows to explain this experiment, but the additional assumption about source altitude is needed. To explain the curve 3 extrapolating the experimental data, the source altitude h has to change as it shown in right figure. Here $R_J$=66700 km is the polar radius of Jupiter.

Character of this dependence deal with properties of IFT global instability being responsible for beam occurence and will be investigated in future. But an experimental definition of maximum frequency source localization could provide a direct examination of this dependence predicted by theory.

I. Ryabov B.P., Preprint N°2, Institute of Radio Astronomy, Khar'kov, 1987.

2. Genova F., Calvert W., J. Geophys. Res., 93, 979-986,1988

3. Boyev A.G., Lukyanov M.Yu., Fizika Plasmu, 15, 1315-1320, 1989.

# ON A GAS-DYNAMIC DESCRIPTION OF SCATTERING OF A RAPID ELECTRON CLOUD IN A PLASMA

V.N.Mel'nik

Institute of Radio Astronomy
Ukrainian SSR Academy of Sciences, Kharkov, USSR

A problem of one-dimensional expanding of a cloud of fast electrons with a low number density in a plasma was considered in [1] taking into account generation and absorption of plasma waves. There were got and analyzed quasigas-dynamic equations.

It is shown in the present paper that a closed set of gas-dynamic equations can be obtained for electrons and plasmons, using ideas of [1] and a self-similar solution can be found for the case of abrupt injection.

The system of one-dimensional quasilinear equatios to describe the electron scattering on the one hand and the electron-plasmon interaction on the other has the form

$$\frac{\partial f}{\partial t} + v\frac{\partial f}{\partial x} = \frac{4\pi^2 e^2}{m^2}\frac{\partial}{\partial v}\frac{W}{v}\frac{\partial f}{\partial v}$$
$$\frac{\partial W}{\partial t} = \frac{\hbar\omega_p}{m} v^2 W \frac{\partial f}{\partial v} \qquad (1)$$

Let us consider a problem where an instanteneous source of electrons is introduced at the time t=0 and at x=0 ( i.e. $f_H|_{t=0} = Ng(v)\delta(x)$ , $\int_0^\infty dv\, g(v) = 1$ , with N being the number of rapid electrons). We shall seek the solution for the time $t >> \tau_{q.z} \approx (\omega_p \frac{\hbar'}{\hbar})^{-1}$ . Then it can be assumed that in the zeroth approximation the distribution function takes the form of a 'plateau' at each spatial point over times about $\tau_{q.z}$ [1], viz.

$$f_s(v,x,t) = \begin{cases} p(x,t), & v \le u(x,t) \\ 0, & v > u(x,t) \end{cases} \qquad (2)$$

where p and u are slowly varying parameters. As for the spectral energy density of plasmons, it can only be written

$$W_s(v,x,t)=\begin{cases} W_0(v,x,t), & v<u(x,t) \\ 0, & v\geq u(x,t) \end{cases} \tag{3}$$

Calculating the zeroth, first and second of the kinetic equations (1), we can obtain the following system of gas-dynamic equations:

$$\frac{\partial \rho u}{\partial t}+\frac{1}{2}\frac{\partial \rho u^2}{\partial x}=0$$

$$\frac{1}{2}\frac{\partial}{\partial t}(1+\beta)\rho u^2+\frac{1}{3}\frac{\partial \rho u^3}{\partial x}=0 \tag{4}$$

$$\frac{1}{3}\frac{\partial}{\partial t}(1+\alpha)\rho u^3+\frac{1}{4}\frac{\partial \rho u^4}{\partial x}=0$$

where, instead of the plasmon momentum $\mathcal{P}=\omega_p\int_0^\infty dv\,\frac{W_s}{v^3}$ and energy $\mathcal{W}=\omega_p\int_0^\infty dv\,\frac{W_s}{v^2}$ we have introduced the following dimensionless functions: $\beta(x,t)=\mathcal{P}/\mathcal{P}_{el}$ $\left(\mathcal{P}_{el}=\int_0^\infty dv\,m v f_s=m\frac{\rho u^2}{2}\right)$; $\alpha=\mathcal{W}/E_{el}$ $\left(E_{el}=\int_0^\infty dv\,\frac{mv^2}{2}f_s=m\frac{\rho u^3}{6}\right)$. In order to close the set (4), we shall make use of the equation resulting from (1), i.e.

$$\frac{\partial f_s}{\partial t}+v\frac{\partial f_s}{\partial x}=\frac{\omega_p}{m}\frac{\partial}{\partial v}\frac{1}{v^3}\frac{\partial W_s}{\partial t} \tag{5}$$

Substitution of (2) and (3) into (5) yields [2]

$$\begin{aligned} &\frac{\partial \rho}{\partial t}+v\frac{\partial \rho}{\partial x}=\frac{\omega_p}{m}\frac{\partial}{\partial v}\frac{1}{v^3}\frac{\partial W_0}{\partial t}, && v<u \\ &\rho\left(\frac{\partial u}{\partial t}+v\frac{\partial u}{\partial x}\right)=\frac{\omega_p}{m}\left(-\frac{1}{u^3}\frac{\partial W_0}{\partial t}+\frac{\partial u}{\partial t}\frac{\partial}{\partial v}\frac{W_0}{v^3}\right), && v=u \\ &W_0\frac{\partial u}{\partial t}=0, && v=u \end{aligned} \tag{6}$$

A self-similar solution of the gas-dynamic equation set (4) with conditions (6) has the form [2]

$$\rho = q(\xi)/t \ , \quad q(\xi) = \frac{a}{u|u-2\xi|} \ , \quad u = const, \ a = const, \ \xi = x/t$$

$$\beta(\xi) = -1 + \frac{2}{3}\frac{u}{\xi} + \frac{b}{3u\xi}(2\xi - u), \quad \alpha(\xi) = -1 + \frac{3}{4}\frac{u}{\xi} + \frac{b_1}{4u^2\xi}(2\xi - u), \quad \xi > u/2$$

$$\beta(\xi) = 3 - \frac{4}{3}\frac{u}{\xi} - \frac{b}{3u\xi}(2\xi - u), \quad \alpha(\xi) = 5 - \frac{9}{4}\frac{u}{\xi} - \frac{b_1}{4u^2\xi}(2\xi - u), \quad \xi < u/2 \qquad (7)$$

$$W_0(v,\xi,t) = \frac{mv^2}{\omega_p t}\left[q(\xi)v(1 - \frac{v}{2\xi}) + \varphi(v)/\xi\right]$$

Where $b = 3u + \frac{6}{a}\int_0^u dv\,\varphi(v)$, $b_1 = 6u^2 + \frac{24}{a}\int_0^u dv\,v\,\varphi(v)$. The so far unknown function $\varphi(v)$ is determined by the spectral density $W_0$ at the moment when first particles of the flow arrive to a chosen point. The distribution function of these particles is $f(v) \sim \delta(v-u)$ since the electrons of lower velocities have not achieved this point yet. It is well known, that after the quasilinear relaxation $W_0$ becomes $W_0 \sim v^4$, moreover $W_0 = \frac{am v^4}{\omega_p t u^2}$ (with an account of (7)) and hence $\varphi(v) = \frac{av^2}{2u^2}$, $b = 4u$, $b_1 = 9u^2$.

The solution found describes a beam-plasma structure of a humplike form (Fig.1), moving at a constant velocity $v_{pl} = u/2$ (Fig.2). The electrons slow down in the region of $\xi > u/2$ transferring part of their energy to plasma oscillations (Fig.3),

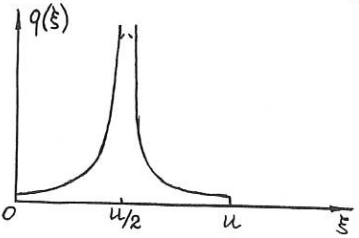


Fig.1. Profile of beam-plasma structure (there is a non-self-similar transition at $\xi = u/2$ of the width $\delta\xi \approx \frac{\tau_{q,z}}{t}u$ ).

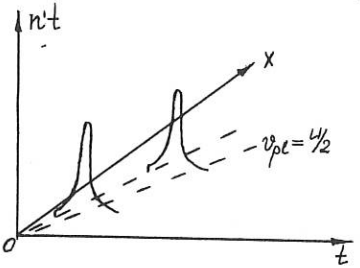


Fig.2. The beam-plasma structure moving at a constant velocity: $v_{pl} = u/2$.

and they accelerate at $\xi < u/2$ absorbing this energy. These two regimes correspond to 2 asymptotic self-similar solutios. There is a non-self-similar transition between them (see Fig.1) of

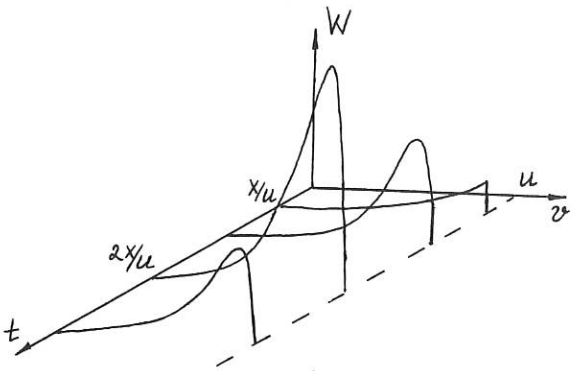


Fig.3. The spectral energy density of the Langmuir waves (7) at the different moments.

width $\delta\xi \approx \frac{\tau_{q.l}}{t} u$ determined by the quasilinear relaxation time. The situation is similar to that arising in gas dynamics, when the front width of a shock wave is determined by the particle free path length.

REFERENCES

1. D.D.Rutov, R.Z.Sagdeev. ZhETPh, 1970, 56, p.739.
2. V.N.Mel'nik. Inst. Radio Astronomy Preprint,No.20,Kharkov, 1988,25p.

# NONEQUILIBRIUM SPECTRA FORMING FOR RELATIVISTIC ELECTRONS INTERACTING WITH MHD - TURBULENCE

A.E. Kochanov

Institute of Radio Astronomy
Academy of Sciences of the Ukrainian SSR, Kharkov, USSR

In this paper the formation of distributions of relativistic electrons propagating through the turbulent cosmic plasma is considered. Interections with different plasma turbulences lead to a spatial diffusion of the electrons and their diffusion in energy space and, consequently, to an acceleration of low energy electrons. We consider that electrons are injected by a point source placed in the centre of the plasma cloud and lose their energy on a synchrotron radiation.

Distribution function of the relativistic electrons $N(p)$ satisfies to the kinetic equation with a source $Q(p)$:

$$\frac{b_1}{p^2}\frac{\partial}{\partial p}p^4 N(p) + \frac{1}{p^2}\frac{\partial}{\partial p}p^2 D_a(p)\frac{\partial N(p)}{\partial p} + D_{\parallel}(p)\Delta N(p) = \\ = -Q(p,z) = -Q(p)\cdot\delta(z), \qquad (1)$$

and the boundary conditions

$$N\Big/_{z=0} < \infty \ , \quad N\Big/_{z=a} = 0. \qquad (2)$$

The first term in equation ( 1 ) describes the synchrotron losses

$$b_1 = \frac{4}{9}\left(\frac{e^2}{mc^2}\right)^2 \frac{H_0^2}{m^2c^2} \ . \qquad (3)$$

The second and the third terms describe energetical and spatial diffusions $D_a(p)$ and $D_{II}(p)$ respectively. $H_o$ is the magnetic field strength, $a$ is the cloud dimension. Boundary condition $N/_{r=a}=0$ corresponds to a free going of the electrons out of the cloud. The diffusion coefficients and the injection spectrum are considered to be power-law function of momentum

$$D_a(p)=D_a\cdot p^{\nu_a}\ ,\quad D_{II}(p)=D_{II}\cdot p^{2-\nu_{II}}\ , \qquad (4)$$

$$Q(p)=Q_o p^{-2-\gamma_o}\theta(p-p_1)\theta(p_2-p)\ . \qquad (5)$$

The equation ( 1 ) have not an analytical solution and should be solved numerically in general case at arbitrary $\nu_a$ and $\nu_{II}$ . However, the equation ( 1 ) becomes the confluent hypergeometric equation in three special cazes, namely, when

$$4-\nu_a-\nu_{II}=n(3-\nu_a)\ ,\quad n=0;1;2\ , \qquad (6)$$

and the solutions can be expressed in terms of Wittekker functions. For example, when $n=0$ the solution has the form ( in one-dimension case)

$$N(p)=\sum_{j=0}^{\infty}\cos\left(\pi\frac{z}{a}\left(j+\frac{1}{2}\right)\right)\varphi_j\ ;$$

$$\varphi_j=\frac{Q_o\exp\left[-(p/p_o)^s\right]p_o^{-2us}p^{-2+us+s/2}}{aD_a\cdot s\,\Gamma\left(u-\kappa+\frac{1}{2}\right)\Gamma\left(u+\kappa+\frac{1}{2}\right)}\left[\left(\int_0^1 dt\cdot t^{u-\kappa-\frac{1}{2}}(1-t)^{u+\kappa-\frac{1}{2}}e^{(p/p_o)^s t}\right)\cdot\right.$$

$$\left.\cdot\int_p^{\infty}dp'p'^{-\gamma_o-2+us+\frac{s}{2}}\int_0^{\infty}dt\,t^{u-\kappa-\frac{1}{2}}(1+t)^{u+\kappa-\frac{1}{2}}e^{-(p'/p_o)^s t}+\right. \qquad (7)$$

$$\left.+\left(\int_0^{\infty}dt\,t^{u-\kappa-\frac{1}{2}}(1+t)^{u+\kappa-\frac{1}{2}}e^{-(p/p_o)^s t}\right)\cdot\int_{p_1}^{p}dp'p'^{-\gamma_o-2+us+\frac{s}{2}}\int_0^1 dt\,t^{u-\kappa-\frac{1}{2}}(1-t)^{u+\kappa-\frac{1}{2}}e^{(p'/p_o)^s t}\right.$$

where

$$P_0^S = \frac{(3-\nu_a)D_a}{b_1}\,, \quad S = 3-\nu_a\,, \quad K = \frac{2}{3-\nu_a}\,,$$

$$u = \frac{1}{2}\sqrt{1+\frac{8(\nu_a-1)}{(3-\nu_a)^2}+\frac{4D_{11}\pi^2(j+\frac{1}{2})^2}{D_a(3-\nu_a)^2a^2}}\,. \qquad (8)$$

Figure 1 represents the electron distribution function ( 7 ) at $\nu_a = \nu_{11} = 2$.

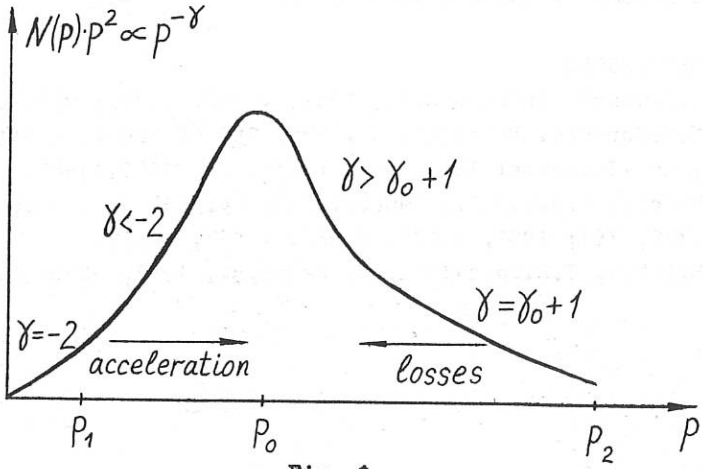


Fig. 1

In the high energy region $p \gg p_0 = D_a/b_1$ the electron spectrum is determined by the synchrotron losses only and has the exponent $\gamma = \gamma_0 + 1$ . In the low energy region $p_1 < p \ll p_0$ the spectrum is determined by the turbulent acceleration and has $\gamma < -2$ . In the region $p \simeq p_0$ the synchrotron losses and the turbulent acceleration became of the same order of magnitude and the spectrum is determined by all three terms in the left-hand side of the equation ( 1 ). The electrons almost do not move along the energy axis in this region. They accumulate near $p = p_0$ and fill in the whole volume of the plasma cloud. The spectrum is much steeper at $p \gtrsim p_0$ than at

$p \gg p_0$.

It is well-known that the spatial ( and energetical ) diffusion of the relativistic electrons in a cosmic plasma may occurs on the Alfven waves [1,2], on the plasma turbulence caused by the hose instability [3], on the ensemble of small scale shock waves [4] etc. The specific values of the indices $\gamma_a$ and $\gamma_{II}$ are determined by the dependences of the turbulence spectra on their wavenumbers. Comparison of the theory with the observational data enables us to estimate the cosmic plasma turbulence parameters.

REFERENCES

1. D.G.Wentzel. Astrophys.J., 1969, v.156, p.303; v.157,p.545.
2. V.N.Fedorenko. Preprints No. 725, 765 of the A.F.Ioffe Physico-Technical Institute, Leningrad, 1981, 1982.
3. A.N.Hall. M.N.R.A.S., 1980, v.190, pp.353, 371, 385; v.191, pp.739, 751; 1981, v.195, p.685; v.197, p.977.
4. A.M.Bykov, I.N.Toptyghin. J. Geophys., 1982, v.50, p.221.

# RESONANT ABSORPTION OF MHD BULK WAVES VIA SURFACE MODES

V.K. Okretic, V.M. Cadez *

University of Belgrade, Mechanical Engineering Faculty, P.O.Box 174, 11000 Beograd, Yugoslavia
* Institute of Physics, P.O.Box 57, YU-11001 Beograd, Yugoslavia

The subject of this paper is to investigate the reflection of magnetohydrodynamic body wave from the inhomogeneous plasma medium in an external magnetic field **B**.

The considered plasma profile consists of three different regions mutually separated by one sharp discontinuity (x=0) and a transitional layer (D≤x≤D+a) with a given parameter distribution. The MHD wave propagates through the medium occupying half-space ($-\infty < x < 0$) and is being reflected from the non-transparent region x≥0.

All the relevant quantities (mass density, temperature, magnetic field) are constants inside each of the regions, sufferring discontinuity at x=0 while continuously changing through the transitional layer.

Starting from standard set of linearized MHD equations for a compressible, perfectly conducting nonuniform plasma at rest in a magnetic field $\mathbf{B}=(0,0,B_0(x))$ the following differential equation for small velocity perturbation (u) perpendicular to the boundary plane, is obtained [1]:

$$\frac{d}{dx}\left\{\varepsilon(x)\frac{du}{dx}\right\} - \beta(x)u = 0 \qquad (1)$$

$$\varepsilon(x)=\rho_0(x)\frac{(k_z^2A^2(x)-\omega^2)(k_z^2c_t^2(x)-\omega^2)(c^2(x)+A^2(x))}{(k_z^2A^2(x)-\omega^2)(k_z^2c^2(x)-\omega^2)+k_y^2(k_z^2c_t^2(x)-\omega^2)(c^2(x)+A^2(x))}$$

$$\beta(x)=\rho_0(x)(k_z^2A^2(x)-\omega^2)$$

where

$$A(x)=(B_0^2(x)/(\mu\rho_0))^{1/2}, \quad c(x)=(\gamma RT_0(x))^{1/2},$$
$$c_t(x)=c(x)A(x)/(c^2(x)+A^2(x))^{1/2}$$

$$\mathrm{Im}\ J = \frac{-\pi}{\left|\dfrac{\partial \varepsilon_r(x)}{\partial x}\right|_{x=x_r}}, \qquad \varepsilon(x)=\varepsilon_r(x)+i\varepsilon_i(x), \quad |\varepsilon_i| \ll \varepsilon_r$$

where $x_r$ is the resonant point ($\varepsilon_r(x_r)=0$).

Numerical calculations of the reflection coefficient show that R is significantly reduced for appropriate parameter values (Fig. 1). On figure 1 the dependence of the reflection coefficient on dimensionless parameter kD/V is drawn. D is the intermediate region width, k is the wave number while V is normalized phase velocity.

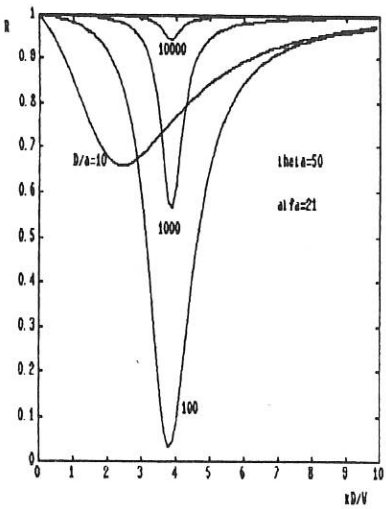


Fig.1 The MHD wave reflection coefficient versus normalized intermediate region width (D)

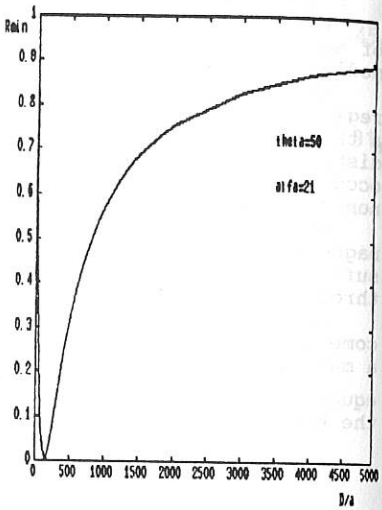


Fig.2 The reflection coefficient minima versus D/a

This phenomenon is equivalent to the increased absorption which we explain as follows.

The incident body wave tunnels through the region located between x=0 and x=D and excites surface modes along the transitional layer. This process is reversed to the MHD surface wave leaking considered by Cadez & Okretic [2]. The presence of

are the Alfven, sound and cusp speeds, respectively.

The solution was assumed to be of the form $f(x)\exp[i(\omega t+k_y y+k_z z)]$

Applying the Fourier analysis, we can easily solve the equation (1) inside separate homogeneous regions: $x<0$, $0\le x\le D$ and $x\ge D+a$. Thus, the related solutions are as follows:

$$u=\begin{cases} e^{i\kappa_1 x}+R\,e^{-i\kappa_1 x} & x\le 0 \\ C_2' e^{\kappa_2 x}+C_2'' e^{-\kappa_2 x} & 0\le x\le D \\ C_4 e^{-\kappa_4(x-D-a)} & x\ge D+a \end{cases} \qquad \kappa_j=(\beta_j/\varepsilon_j)^{1/2} \quad j=1,2,4 \qquad (2)$$

Assuming a relatively thin boundary layer ($ka\ll 1$) so that the total pressure perturbation is nearly constant across it, the equation (1) can be solved in the transition region (index 3) to yield

$$u=C_3'+C_3''\int_D^x \frac{d\xi}{\varepsilon(\xi,\omega)}$$

The boundary conditions for the continuity of both the normal velocity component and the total pressure perturbation give the set of algebraic equations yielding the reflection coefficient of the incident MHD wave

$$R^2=\left|\frac{a_r^2+a_i^2}{b_r^2+b_i^2}\right|,$$

$$a_r=\Delta+(\Delta-2)e^{-2\kappa_2 D}-D_{12}\,\delta(1+e^{-2\kappa_2 D})$$

$$a_i=D_{12}(\Delta-(\Delta-2)e^{-2\kappa_2 D})+\delta(1-e^{-2\kappa_2 D})$$

$$b_r=\Delta+(\Delta-2)e^{-2\kappa_2 D}+D_{12}\,\delta(1+e^{-2\kappa_2 D})$$

$$b_i=D_{12}(\Delta-(\Delta-2)e^{-2\kappa_2 D})-\delta(1-e^{-2\kappa_2 D})$$

$$D_{ij}=\varepsilon_i\kappa_i/(\varepsilon_j\kappa_j), \quad \delta=D_{42}\varepsilon_2\kappa_2\,\mathrm{Im}\,J, \quad J=\int^{D+a}\frac{d\xi}{\varepsilon(\xi,\omega)}, \quad \Delta=1+D_{42}$$

$(i,j=1,2,4)$

To illustrate this phenomenon we shall proceed with a specific parameter distribution inside the boundary layer.

Without loss of generality, we have chosen the quantity $\varepsilon(x)$ to vary linearly and to change sign across the transitional layer.

To calculate the reflection coefficient R for various frequencies with the ratio D/a as a parameter we need to determine the imaginary part of the integral J in a similar way as done in Landau damping derivation:

the boundary layer allows for the resonant transformation of surface waves into local Alfven waves in the region where $\varepsilon=0$. Such a resonant absorption of MHD surface waves alone has been recognized as an efficient damping mechanism and considerable recent investigations have been devoted to this process ([1],[3],[4],[5],[6],[7]).

Now, our investigation shows that the incoming MHD wave is affected too: it loses the energy through the surface wave resonant transformation.

Fig. 2 shows the typical dependence of the reflection coefficient minima on the ratio D/a. Apparently, the total absorption can be reached for appropriate value of D/a.

We point out that the analysis was done for particularly chosen values of the incident angle $\alpha$ and the propagation angle $\theta$. In fact, these are not to be taken arbitrarily because the conditions for surface modes to exist in such a geometry depend strongly on both of them.

In practice, the method could be employed to "detect" the resonant absorption and numerically calculate corresponding slab width, angles and frequencies for any particular physical system.

References

[1] Cadez V.M., Okretic V.K., Proc. 16th EPS Conf. on Controll Fusion and Plasma Physics, Venice, Italy (1989) vol. IV (1337-1340)
[2] Cadez V.M., Okretic V.K., J. Plasma Phys. (1989), vol. 41, part 1, pp. 23-30
[3] Hollweg J.V., Yang G., J. Geophys. Res., vol. 93 (1988) 5423
[4] Hollweg J.V., Ap. J., vol. 312 (1987a) 880
[5] Hollweg J.V., Ap. J., vol. 320 (1987b) 875
[6] Davila J., Ap. J., vol. 317 (1987) 514
[7] Lee M.A., Roberts B., Ap. J. vol. 301 (1986) 430

# NONLINEAR TRANSPARENCY OF UNDERDENSE PLASMA LAYER UNDER THE EFFECT OF INTENSE CIRCULARLY-POLARIZED ELECTROMAGNETIC WAVE

V.V. DEMCHENKO

International Atomic Energy Agency
P.O. Box 100, A-1400
Vienna, Austria

Abstract. Simulation studies have been made of the space-time evolution of the large amplitude circularly-polarized electromagnetic wave normally incident on the plane waveguide filled by nonuniform plasma. It is shown that relativistic electron-mass oscillations plays a crucial role in the evolution process and could lead to a nonlinear transparency of a plasma layer.

1. Introduction. From the linear theory it follows that electromagnetic waves with frequencies $\omega$ less than electron plasma frequency $\omega_{pe}$ cannot propagate in an unmagnetized plasma. However for sufficiently high electric field intensity there exists a redistribution of plasma density under the effect of strictional [1] or relativistic [2] nonlinearities with leads to the downshift of the $\omega_{pe}$ value and violation of the linear theory "opacity" condition ($\omega<\omega_{pe}$). This results in the possibility of electromagnetic wave penetration into the "underdense" plasma (e.g. [3]). However, the effect of "induced" transparency reported before have been restricted by the assumptions of 1) steady-state wave propagation, or 2) homogeneous plasma density profile.

The purpose of this paper is to present the results of numerical simulation of the nonuniform plasma layer transparency in the field of an intense electromagnetic wave.

2. Initial equations. Let us assume that plasma occupy the space bounded by planes x = (0,L). Normally to the plasma boundary (x=0) it is incident circularly-polarized wave electrical field of which could be presented as $E = E_x + i E_y = F(x,t)\exp(-i\omega t) + c.c.$. In modulational approximation $(\partial F/\partial t \ll \omega F)$ the equation for slow varying amplitude F takes the form

$$2i\omega \frac{\partial}{\partial t}(\varepsilon_- A) + \frac{\partial^2 A}{\partial x^2} + \varepsilon_- A = 0, \qquad (1)$$

where

$$\varepsilon_- = 1 - \frac{\omega_{pe}^2(x)}{\omega(\omega - \omega_{ce})} = 1 - \frac{\omega_{po}^2}{\omega^2\left[(1+\gamma^2 A^2)^{1/2} - \beta\right]} \cdot \frac{N_o(x)}{N_p},$$

$$A = \frac{F}{(32\pi N_p T)^{1/2}}, \quad \tau = \frac{\omega_{po}}{\omega} t, \quad \xi = \frac{\omega_{po}}{c} x,$$

$$\Omega = \frac{\omega}{\omega_{po}}, \quad \beta = \frac{\omega_{ce}}{\omega}, \quad \gamma = \frac{2\sqrt{2}\, v_{Te}}{\Omega c},$$

No(x) - profile of equilibrium plasma density schematically presented in Fig. 1.

3. Results of numerical analysis. To demonstrate threshold character of the nonlinear transparency phenomenon let us suppose that the amplitude of incident wave is linearly growing function of time. On Figs. 2-4 the different stages of the electric field amplitude evolution are presented at the following set of parameters: $\gamma^2=5$, $\Omega^2=0,5$, $\beta=0.9$. From Fig. 2 it follows that at small incident wave field intensity the skin-type field amplitude distribution takes place. As the incident field amplitude increases observed depth of field penetration sufficiently exceeds the characteristic scale of the linear skin-layer. After the critical value $A_{cr}^2 \sim 10$ have been achieved, the formation of nonlinear soliton-type structure occurs, which propagetes into the "underdense" region with constant velocity (Fig. 3). On the large time interval the complete plasma layer transparency appears and equilibrium state have been established in the form of a large amplitude standing wave. From Fig. 4 where the temporal evolution of the electric permeability $\varepsilon$ are shown, it follows that function $\varepsilon(A^2)$ have changed it sign under the action of relativistic nonlinearity of $\tau > 220$ which is the cause of "induced" plasma layer transparency.

References


1. B.B. Kadomtsev, V.I. Karpman, Sov. Phys. Usp., 14, 40 (1971)

2. P.K. Shukla, N.N. Rao, M.Y. Yu, N.L. Tsintsadze, Phys. Rep., 138, 1 (1986)

3. A.G. Litvak, Review Plasma Physics, Ed. by M. Leontovich, Consultant Bureau, NY, 10, 294 (1965)

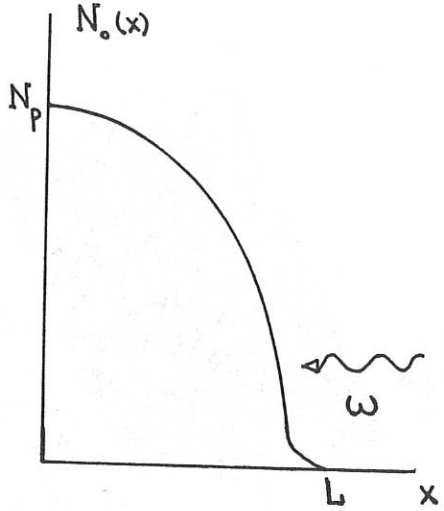


Fig. 1. Equilibrium density profile

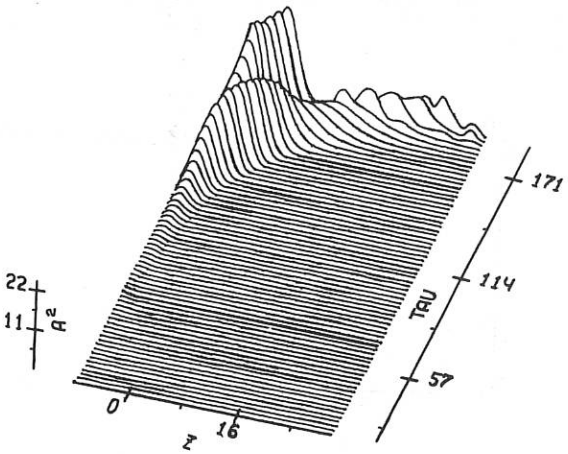


Fig. 2. Time-space evolution of the electric field intensity at the initial time interval.

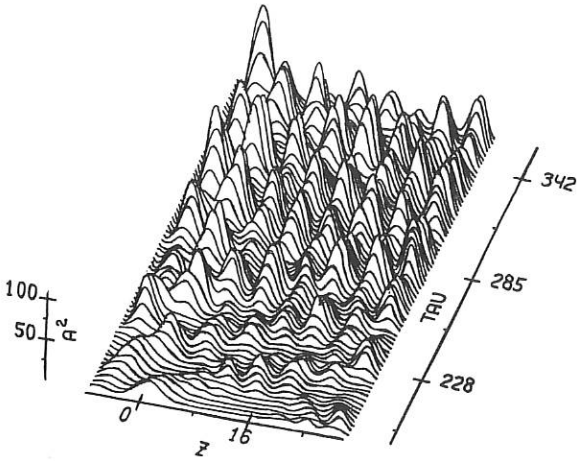


Fig. 3. Establishment of a steady-state standing-wave distribution at the long-time field evolution.

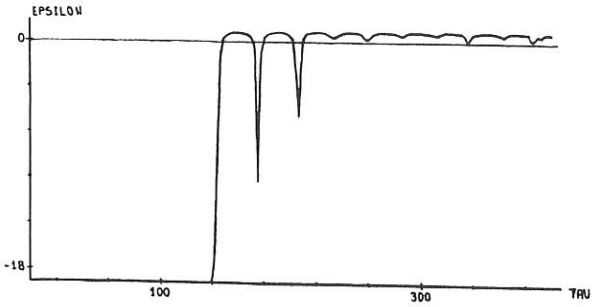


Fig. 4. Time dependence of the plasma dielectric permeability.

# FORMATION AND EQUILIBRIUM OF AN ELECTRON PLASMA IN A SMALL ASPECT RATIO TORUS

Puravi Zaveri, P.I.John and P.K.Kaw

Institute for Plasma Research
Bhat, Gandhinagar 382424, India

## I. Introduction:

Experiments on electron injection and confinement in a toroidal magnetic field were first carried out by J.D.Daugherty et al.[1] and later on by W.Clark et al.[2] in large aspect ratio torii (R/a ~ 5 or 6) for applications related to heavy ion accelerators. Properties of electron plasmas in small aspect ratio toroidal systems have not been studied from the point of view of understanding the formation, equilibrium, instabilities and transport. The present paper deals with the equilibrium. We have designed and built a device having a small aspect ratio (R/a = 1.2) to study those effects which are highly toroidal and their impact on equilibrium.

In ICPP proceedings[3] we published just those results which were obtained using a single electron injector. In this paper we have been able to present equipotential contours obtained using multiple injectors (more uniform injection), electron density profile and a detailed discussion on equilibrium.

## II. Apparatus:

A vertical cross-section of the apparatus is shown schematically in Fig. 1. A toroidal magnetic field is produced by passing current through the central conductor 'A'. 'C' is the vacuum vessel which is placed very close to the central conductor. Experiments are performed at a base pressure of $9 \times 10^{-7}$ Torr and with magnetic field of 150 gauss at the minor axis of the torus. The rise-time of the magnetic field is 75 microseconds and it has a flat top of 800 microseconds.

## III. Observations:

The electron injector located at the outer wall is shown in Fig. 2. 'A' is a semicircular grounded anode having a length of 4 cms. in perpendicular direction to the plane of paper. 'C' is a helical cathode which is applied -200 volts. The cathode-anode gap is ~ 15 mm. The radial electric field E in the gap crossed with $B_{toroidal}$ brings electrons out of the cavity. A mechanism called "inductive charging"[1] is partially responsible for taking electrons into the vessel.

We have used wall probes to measure net charge in the system. These are actually small isolated sections of vessel walls (disks) which measure the charging current (like a capacitor) when charge is introduced into the system. Wall probe signals showed a charging current for the first 12 microseconds which was followed by a quiescent period (of 40-60 μs) and then followed by

a high frequency noise (0.5-1MHz). During 12 microseconds, the magnetic field has risen only to 13.4 gauss. Electrons which are able to go into the vessel have an upper limit of 28 eV to their perpendicular kinetic energies, higher energy electrons being lost to the anode. There is a spread of 12.5 eV in parallel kinetic energy due to an ohmic drop across filaments.

Using a movable high impedance wire probe the potential distribution of the electron cloud was measured at a large number of points in the poloidal plane. The equipotential contours are shown in Fig. 3. The error in shot-to-shot measurements are less than 2%. The fact that we observe these contours all the way up to 800 μsecs supports strongly the case for an equilibrium. The total of grad-B and curvature drift turns out to be $3 \times 10^6$ cms/sec. The electron cloud has its own self electric field $E_r$ in the radial direction. The $E_r \times B$ drift is stronger ($3\text{-}5 \times 10^7$ cm/sec) than the toroidal drifts. The existance of equilibrium in spite of a downward motion of the cloud is not clearly understood.

There is a z-asymmetry in the sense that we observe larger floating potentials in the lower half of the plane than in the upper half. We measured potentials of the order of 320 volts in the lower plane whereas the potentials observed in the upper plane were less than 30 volts. This is also evident from the contours. It could be due to two reasons - very localised nature of the electron injector and secondly, the first order inertial effects, i.e. toroidal drifts. In order to verify the first possibility we put five identical injectors along z-direction as shown in Fig. 4 and the resultant equipotentials are shown in Fig. 5.

We did local density measurements using the wire probe as a charge collector by grounding it through a very small resistance of 100 ohms. These measurements were carried out in a pulsed mode ($\sim$20 microseconds) so that the perturbation is tolerable. The current that was measured was interpreted as to be comprised of two velocities - one being the acceleration of particles because of the local potential difference between the probe and the cloud, And the other contribution comes from the parallel 'thermal' velocities. The density profile obtained using this model is shown in Fig. 6.

IV. Conclusions:

We have formed an electron plasma with an aspect ratio 1.8 lasting for 800 micro seconds which coincides with the duration of the magnetic field. $E \times B$ rotation in the poloidal direction dominates over toroidal drifts and gives an equilibrium, however the first order effects (proportional to $m_e$) are important which are responsible for the downward drift of the cloud. This was further supported when by reversing the magnetic field almost a mirror image of the contours was obtained in the upper half of the poloidal plane. Electron densities are in a range of $8 \times 10^7 - 2 \times 10^8$ per c.c. and their profiles are hollow. High frequency noise (0.5 - 1 MHz) a possible diocotron mode is observed only on the boundaries of the cloud. The particles which are able to go into the vessel have perpendicular kinetic energy less than 28 ev, whereas we have observed floating potentials as large as 320 volts. It indicates that there is an accumulation of the electrons. The extra energy comes

from the work done by the poloidal electric field induced by a rising magnetic field.

References:

1. J.D.Daugherty, J.E.Eninger and G.S.Janes, Physics of Fluids, 12, 2677 (1969).

2. W.Clark, P.Korn, A.Mondelli and N.Rostoker, Physical Review Letters, 37, 592 (1976).

3. Puravi Zaveri, P.I.John and P.K.Kaw, Proceedings of 1989 International Conference on Plasma Physics, India Volume III, 1161.

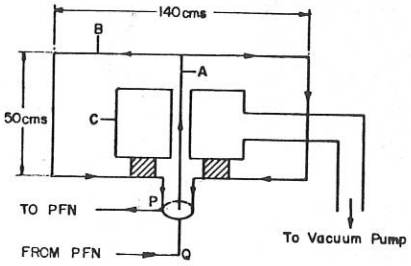


Fig. 1: A vertical cross-section of the apparatus showing the central conductor (A) and the vacuum vessel (C).

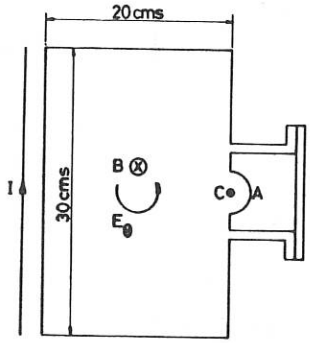


Fig. 2: A vertical cross-section of the vacuum vessel showing the electron injector.

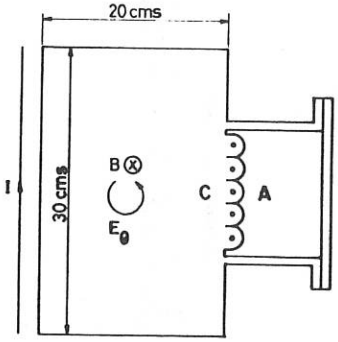


Fig. 4: A vertical cross-section of the vacuum vessel showing the multiple injectors.

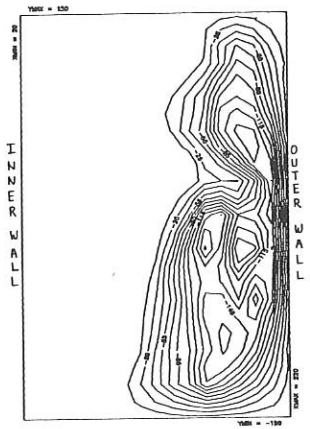


Fig. 3: Contours of equipotentials at 803 microseconds obtained using the single injector configuration

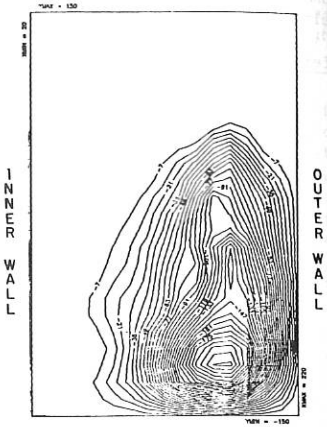


Fig. 5: Contours of equipotentials at 803 microseconds obtained using multiple injectors.

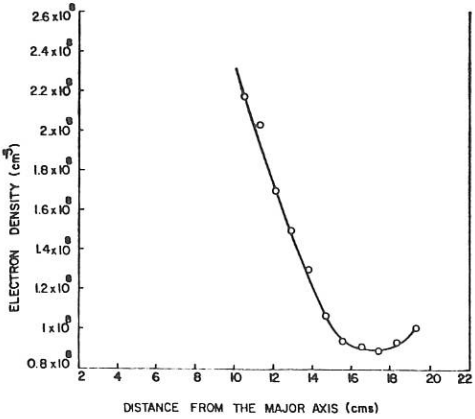


Fig. 6: Electron density profile at midplane.

# FORMATION OF VORTICES IN A TOROIDAL PLASMA

AJAY K.SINGH & Y.C.SAXENA

Institute for Plasma Research
Bhat, Gandhinagar 382 424 INDIA

ABSTRACT

Coherent vortex structures are observed in a toroidal device in which a non uniform plasma is embedded in an inhomogeneous magnetic field. The fluctuating vortex potentials are measured by high impedance Langmuire probes in a poloidal cross section of the plasma column. The contours of equipotentials are found to be closed curves exhibiting a vortex pattern. The vortices are stationary and have negative polarity. They are associated with the fluctuations in the frequency range of 5-9 Khz. It is suggested that the experimentally observed vortices could result from the self organization of fluctuations that are driven by the equilibrium density and magnetic field gradients.

# ARBITRARY-AMPLITUDE ELECTRON-ACOUSTIC SOLITONS IN A TWO ELECTRON COMPONENT PLASMA

R.L. Mace◇ S. Baboolal† R. Bharuthram‡ M.A. Hellberg◇
◇Plasma Physics Research Institute, Department of Physics,
University of Natal, Durban, South Africa
Departments of Applied Mathematics†and Physics‡,
University of Durban–Westville, Durban, South Africa
and Plasma Physics Research Institute, University of Natal

## 1. Introduction

Previous work on nonlinear electron-acoustic waves in two-electron temperature plasmas has often included at least one hot ion species in the plasma model (Yu & Shukla 1983). This usually requires that the ion-electron temperature ratio be very large ($\sim m_i/m_e$), which is not easily fulfilled–especially in the laboratory.

In our investigations, we use a reductive perturbation technique (Washimi & Taniuti 1966) to derive a Korteweg-de Vries equation describing weakly nonlinear electron-acoustic waves in a three component plasma modelled by hot Boltzmann electrons, cold fluid electrons and cold fluid ions. Also, using the arbitrary-amplitude technique of Baboolal, Bharuthram & Hellberg (1988, 1989), we extend the theory of electron-acoustic solitons into the intermediate to large amplitude regime $e\phi/T_h \tilde{>} 1$.

## 2. Arbitrary-amplitude formulation

The normalized fluid and Poisson equations are:

$$\frac{\partial n_j}{\partial t} + \frac{\partial}{\partial x}(n_j u_j) = 0, \tag{1}$$

$$\frac{\partial u_j}{\partial t} + u_j \frac{\partial u_j}{\partial x} + 3\frac{T_j}{m_j}\frac{n_j}{n_{0j}^2}\frac{\partial n_j}{\partial x} = -\frac{Z_j}{m_j}\frac{\partial \phi}{\partial x}, \qquad j = i, c, \tag{2}$$

$$\frac{\partial^2 \phi}{\partial x^2} = n_{0h} \exp \phi + n_c - n_i, \tag{3}$$

where the subscripts $h$, $c$ and $i$ represent the hot electrons, cold electrons and ions, respectively. We have normalized spatial lengths by $\lambda_h = (T_h/4\pi n_{0e}e^2)^{1/2}$, time by $\omega_{pe}^{-1} = (m_e/4\pi n_{0e}e^2)^{1/2}$, densities by $n_{0e}$ the total electron density, potential by $T_h/e$, velocities by $v_h = (T_h/m_e)^{1/2}$, temperatures by $T_h$, masses by $m_e$ and $Z_j \equiv q_j/e$. The assumption of adiabatic ions and cold electrons ($\gamma_{i,c} = 3$) is valid because the phase speed of the electron-acoustic wave is larger than both the ion and cold electron thermal velocities. The plasma is assumed to be undisturbed at $x \to \infty$ and the following

boundary conditions hold

$$\phi, \frac{\partial \phi}{\partial x}, u_i, u_e \to 0, \qquad n_i, n_e \to n_{0i}, n_{0e} \quad \text{as} \quad x \to \infty. \tag{4}$$

We seek travelling wave solutions that are stationary in a frame moving with velocity $\mu$. Transforming the above equations to the frame defined by $\xi = x - \mu t$ and integrating equations (1) and (2) with the above boundary conditions we arrive at the following equations for $n_i, n_e$ (after elimination of $u$)

$$\mu^2 \left(\frac{n_{0j}}{n_j}\right)^2 + 3\frac{T_j}{m_j}\left(\frac{n_j}{n_{0j}}\right)^2 = \mu^2 + 3\frac{T_j}{m_j} - Z_j\frac{2\phi}{m_j}, \qquad j = i, e \tag{5}$$

where for an electron-proton plasma $Z_i = 1$ and $Z_e = -1$. Formally, we can write the first integral of Poisson's equation (Baboolal *et al.* 1988, 1989)

$$\frac{1}{2}\left(\frac{d\phi}{d\xi}\right)^2 + \Psi(\phi, \mu) = 0, \qquad \Psi(\phi, \mu) = -\int_0^{\phi} (n_{0h} \exp \phi + n_e - n_i) d\phi'. \tag{6}$$

For solitons we require (Sagdeev 1966) $\Psi(0, \mu) = \partial\Psi(0, \mu)/\partial\phi = 0$ for all $\mu$, $\Psi(\phi_0, \mu) = 0$ for some $\phi_0$, $\mu$, and $\Psi(\phi, \mu) < 0$ in $0 < |\phi| < |\phi_0|$. The arbitrary-amplitude problem is solved by numerically solving $\Psi = 0$ for $\phi_0$, and integrating (6) as an initial-value problem with $\phi(\xi = 0) = \phi_0$.

## 3. Small amplitude theory

Employing the coordinate stretchings

$$\xi = \epsilon^{1/2}(x - Vt), \quad \tau = \epsilon^{3/2}t, \tag{7}$$

and the expansions

$$n_j = n_j^{(0)} + \epsilon n_j^{(1)} + \epsilon^2 n_j^{(2)} + \epsilon^3 n_j^{(3)} + \cdots, \tag{8}$$

$$u_j = \epsilon u_j^{(1)} + \epsilon^2 u_j^{(2)} + \epsilon^3 u_j^{(3)} + \cdots, \qquad j = i, e, \tag{9}$$

$$\phi = \epsilon\phi^{(1)} + \epsilon^2\phi^{(2)} + \epsilon^3\phi^{(3)} + \cdots, \tag{10}$$

in the reductive perturbation technique, we arrive at the Korteweg de-Vries equation

$$\frac{\partial \phi^{(1)}}{\partial \tau} + a\phi^{(1)}\frac{\partial \phi^{(1)}}{\partial \xi} + b\frac{\partial^3 \phi^{(1)}}{\partial \xi^3} = 0, \tag{11}$$

where

$$A = 3\frac{(V^2 + T_i/m_i)/m_i^2}{(V^2 - 3T_i/m_i)^3} - 3\frac{n_{0e}(V^2 + T_e)}{(V^2 - 3T_e)^3} - n_{0h}, \tag{12}$$

$$B = 2V\left\{\frac{1/m_i}{(V^2 - 3T_i/m_i)^2} + \frac{n_{0e}}{(V^2 - 3T_e)^2}\right\} \tag{13}$$

$$a = \frac{A}{B}, \quad b = \frac{1}{B}. \tag{14}$$

The wave velocity $V$, satisfies

$$n_{0h}V^4 - \left\{3n_{0h}\left(T_c + \frac{T_i}{m_i}\right) + n_{0c} + \frac{1}{m_i}\right\}V^2 + \frac{3}{m_i}\left\{n_{0c}T_i + T_c + 3T_cT_i\right\} = 0, \quad (15)$$

which has the approximate solution $V \simeq (n_{0c}/n_{0h} + 3T_c)^{1/2}$. For $T_c = 0$ this reduces to the linear electron-acoustic sound speed found by Gary & Tokar (1985).

The solution of the Korteweg-de Vries equation in the stationary frame defined by $\eta = \xi - \mu_0\tau$, is given in laboratory coordinates by

$$\phi = \phi_0 \operatorname{sech}^2\left\{\sqrt{\frac{\delta\mu}{4b}}\,(x - \mu t)\right\}, \quad (16)$$

where we have defined the velocity $\mu \equiv V + \epsilon\mu_0 \equiv V + \delta\mu$ and amplitude $\phi_0 \equiv 3\epsilon\mu_0/a = 3\delta\mu/a$ respectively.

The soliton width is given by $(4b/\epsilon\mu_0)^{1/2}$, or, in terms of $\delta\mu$, $(4b/\delta\mu)^{1/2}$. Note also, that in the coefficients $a$ and $b$ of the Korteweg-de Vries equation, the ion terms are at most $O(m_i^{-1})$. Consequently we expect very weak dependence of electron-acoustic wave profiles on ion temperature, which is in accordance with linear theory (Gary & Tokar, 1985). Also, upon ignoring such terms, it is easy to show that $a < 0$ and $b > 0$, which, by inspection of our soliton solution (16), yield the following conditions on $\mu$ and $\phi_0$:

$$\mu > V \quad \text{and,} \quad \phi_0 < 0.$$

The first of the above conditions implies that only supersonic electron-acoustic solitons exist, and the second says that the soliton potential is negative, i.e. only rarefactive solitons exist. This is in contrast to the ion-acoustic wave, where both rarefactive and compressive solitons exist (Baboolal *et al.* 1989) but agrees with the findings of Yu & Shukla (1983) for the modified electron-acoustic wave. The negative potential is associated with a local decrease in the hot electron density and an increase in the cold electron density corresponding to an overall increase in local electron density. The ion density remains virtually constant everywhere.

## 4. Numerical results

In the numerical work we have defined the Mach number by $M \equiv v/(n_{0c}/n_{0h})^{1/2}v_h = \mu/(n_{0c}/n_{0h})^{1/2}$ where $v$ is the soliton velocity and $(n_{0c}/n_{0h})^{1/2}v_h \equiv v_{se}$ is the electron-acoustic sound speed. It is for this reason that we have termed the normalized waveform velocity $\mu$ in what went previously. The figures show the results of numerical solution of (5) and (6) without any approximation (typical soliton profiles shown in fig. 1(d)).

Figure 1(a) illustrates the effect of increasing the Mach number $M$ on the maximum soliton amplitude. The effect is an approximately linear increase in $|\phi_0|$ with $M$. Clearly, the range of Mach numbers over which soliton solutions occur, decreases with increasing temperature. This occurs because above a critical cold electron temperature the cold electron density becomes complex, leading to wave breaking. Also, the threshold Mach

number for solitons increases with increasing cold electron temperature. This is well described by our approximate expression $M > (1 + 3T_c/(n_{0c}/n_{0h}))^{1/2}$.

Figure 1(b) illustrates the monotonic decrease in $|\phi_0|$ with cold electron temperature for various Mach numbers. The effect of a finite cold electron temperature is to increase the phase velocity of the linear electron-acoustic wave which decreases $\delta\mu \simeq \mu - (n_{0c}/n_{0h} + T_h)^{1/2}$ and hence $\delta M$, resulting in weaker nonlinearity and therefore dispersion.

Figure 1(c) illustrates the soliton maximum amplitude as a function of the cold electron number density for a Mach number of $M = 1.2$. The maximum value of $|\phi_0|$ increases with increasing $n_{0c}$. However, it must be borne in mind that because of our definition of $M$ (see above), the absolute velocity of the soliton also increases with progressively larger $n_{0c}$ in order to keep $M$ constant. We have performed some computations (not shown) in which the soliton velocity was kept constant, and find that there is a decrease in the maximum amplitude with $n_{0c}$.

## 5. References


Baboolal, S., Bharuthram, R. & Hellberg, M.A. 1988 *J. Plasma Phys.*, **40**, 163.

Baboolal, S., Bharuthram, R. & Hellberg, M.A. 1989 *J. Plasma Phys.*, **41**, 341.

Gary, S.P. & Tokar, R.L. 1985 *Phys. Fluids*, **28**, 2439.

Sagdeev, R.Z. 1966 *Reviews of Plasma Physics*, vol 4 (ed. M.A. Leontovich) p23. Consultants Bureau. Yu, M.Y. & Shukla, P.K. 1983 *J. Plasma Physics*, **29**, 409.

Washimi, H. & Taniuti, T. 1966 *Phys. Rev. Lett.*, **17**, 996.

Watanabe, K. & Taniuti, T. 1977 *J. Phys. Soc. Japan*, **43**, 1819.


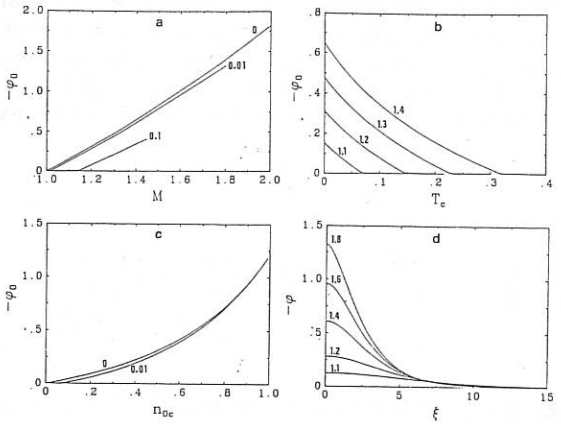


Figure 1 (a)—(c) Maximum soliton amplitude as a function of (a) $M$, (b) $T_c$, (c) $n_{0c}$ for $M = 1.2$. The parameters labelling the curves are (a), (c) $T_c = T_i$, (b) $M$. (d) Arbitrary-amplitude soliton profiles. The parameter labelling the curves is $M$. In (a), (b), (d) $n_{0c} = 0.5$.

# THE OBLIQUELY PROPAGATING ELECTRON-ACOUSTIC INSTABILITY

R.L. Mace M.A. Hellberg
Plasma Physics Research Institute, Department of Physics,
University of Natal, Durban, South Africa

## 1. Introduction

The electron-acoustic mode is a normal mode in a plasma with two electron components provided the temperature of the hot electron component is much larger than that of the cold component (Watanabe & Taniuti 1977). The mode may be driven unstable by a relative drift between the two electron components (Gary 1987) or by a relative drift between two ion components (Schriver & Ashour-Abdalla 1987).

The effect of a magnetic field on the dispersion and growth of the electron-acoustic instability was investigated by Tokar & Gary (1984) (drifting electrons) and Schriver and Ashour-Abdalla (1987) (drifting ions). However, in both cases only a restricted range of the ratio $\Omega_e/\omega_c$ , where $\Omega_e$ is the electron gyrofrequency and $\omega_c$ is the cold electron plasma frequency, was investigated.

In this paper we investigate the magnetized electron-acoustic instability over a wide range of $\Omega_e/\omega_c$ and propagation angles.

## 2. Basic equations

We consider a magnetized plasma consisting of Maxwellian ions, cold electrons and hot electrons. The hot electrons drift with velocity $\mathbf{v}_{0h}$ parallel to an external uniform magnetic field $\mathbf{B}$, relative to stationary ions and cold electrons. The wavevector $\mathbf{k}$ has components $k_\parallel$ and $k_\perp$ parallel and perpendicular to $\mathbf{B}$, respectively, and $\tan\theta = k_\parallel/k_\perp$. The most general dispersion relation for linear electrostatic waves in such a plasma can be written

$$1 + \sum_\alpha K_\alpha = 0, \tag{1}$$

where

$$K_\alpha = \frac{1}{k^2\lambda_\alpha^2}\left[1 + \frac{\omega - k_\parallel v_{0\alpha}}{\sqrt{2}k_\parallel v_\alpha}\sum_{n=-\infty}^{\infty}\exp\left(-\frac{k_\perp^2 v_\alpha^2}{\Omega_\alpha^2}\right) I_n\left(\frac{k_\perp^2 v_\alpha^2}{\Omega_\alpha^2}\right) \times Z\left(\frac{\omega - n\Omega_\alpha - k_\parallel v_{0\alpha}}{\sqrt{2}k_\parallel v_\alpha}\right)\right]. \tag{2}$$

The definitions of symbols are as follows: $\lambda_\alpha = (T_\alpha/4\pi n_\alpha e^2)^{1/2}$ is the Debye length, $\omega_\alpha = (4\pi n_\alpha e^2/m_\alpha)^{1/2}$ is the plasma frequency, $v_\alpha = (T_\alpha/m_\alpha)^{1/2}$ is the thermal speed, $\Omega_\alpha = |q|B/m_\alpha c$ is the cyclotron frequency, $v_{0\alpha}$ is the parallel drift speed, of species $\alpha$, $\alpha = \{i, h, c\}$, $I_n$ is the modified Bessel function of order $n$, and $Z$ is the plasma dispersion function. Temperatures are measured in energy units throughout.

## 3. Results

Figure 1 illustrates the effect of magnetization on the dispersion and growth of the electron-acoustic instability. The resonances at $\Omega_e$ and its harmonics which lie below $\omega_c$, enrich the spectrum of waves for oblique propagation. For oblique propagation these resonances give rise to two modes that lie below $\omega_c$ : one that has an upper frequency of $\Omega_e \cos\theta$ and exhibits an electron-acoustic regime $\omega_r \simeq k(n_c/n_h)^{1/2} v_h \equiv k v_{se}$, at small wavenumbers (fig. 1(a)), and a higher frequency mode that behaves like

$$\omega_r^2 \simeq \frac{\omega_c^2}{1 + 1/k^2\lambda_h^2}$$

for large to intermediate wavenumbers, and which connects to a cyclotron harmonic at small wavenumbers (fig. 1(b)).

If the plasma is strongly magnetized and the ratio $\Omega_e/\omega_c > 1$ then the dispersion of the magnetized electron-acoustic mode (figure 1(c)) differs from its unmagnetized counterpart only by a factor of $\cos\theta$.

Figure 2 shows the threshold $v_{0h}$, as a function of $\theta$, for the electron-acoustic instability, at various values of $\Omega_e/\omega_c$. At $\theta = 0°$ the threshold is the same as that found by Gary (1987) and satisfies $v_{0h} \gtrsim 5v_c$. At larger angles, for $\Omega_e < \omega_c$, we find that maximum growth occurs at two values of $k$, and hence we have two thresholds, corresponding to an electrostatic electron-cyclotron-like instability (lower threshold as $\theta \to 0°$) and an electron-acoustic instability. As the ratio $\Omega_e/\omega_c$ is increased, so the threshold drift velocity of the lower frequency electron-acoustic mode decreases, for $0° < \theta \lesssim 60°$. At $\Omega_e/\omega_c \simeq 1$ the threshold reduces to a single curve corresponding to the strongly magnetized electron-acoustic instability. This curve has local minima at $\theta = 0°$ and $\theta \simeq 40°$. At larger ratios $\Omega_e/\omega_c \gg 1$, the threshold versus $\theta$ curve reduces to $v_{0h} \simeq 4.7v_c$ for $\theta \lesssim 90°$ and illustrates the relative insensitivity of the threshold of the strongly magnetized instability to $\theta$.

In the frequency regime $\Omega_e/\omega_c < 1$ we have two competing instabilities: the electron-cyclotron and electron-acoustic instabilities. The former has lower threshold for small $\theta$ but this behaviour is reversed at larger values of $\theta$. In figure 3 we illustrate the maximum growth rates of the two instabilities at an angle of 20° (a), where the cyclotron-like instability has lower threshold, and at an angle of 40° (b), where the electron-acoustic instability has lower threshold (c.f. figure 2), $\Omega_e/\omega_c = 0.424$. In (a) the electron-cyclotron instability has larger maximum growth rate for all $v_{0h}$. In (b) the electron-acoustic instability has larger maximum growth rate only for $v_{0h} \lesssim 13v_c$.

Lin *et al.* (1985) used particle simulations to investigate the nonlinear development of the hot electron-driven electron-acoustic instability. They demonstrated that the electron-acoustic instability saturates by trapping the beam, by trapping the cold electrons, or by forming a plateau on the beam distribution. If the amplitude of the electron-acoustic waves grows large enough for the beam to become trapped, so that the beam velocity is confined to values near the threshold value for the electron-acoustic instability, and assuming that this eventually leads to saturation of the instability, then, from our previous discussion, it will not be possible to observe the electron-cyclotron

instability for small values of $\theta$. In any real physical situation it will be the electron-acoustic instability that dominates in this regime. At larger $\theta$ values the electrostatic electron-cyclotron instability dominates due to its lower threshold and larger growth rate in this regime. Thus in this sense, the electron-acoustic instability is truly oblique for $\Omega_e/\omega_c < 1$. A further implication of this result is that, in some cone of angles about $\mathbf{B}$, the upper frequency "cut off" of electrostatic noise would be $\omega_c$, which is greater than the gyrofrequency $\Omega_e$. For larger angles the cut off is $\sim \Omega_e$.

In the regime $\Omega_e/\omega_c > 1$ the electron-acoustic instability has lower threshold for all angles $\theta < 90°$ (figure 2). The upper frequency in this case is $\sim \omega_c$ which is less than the gyrofrequency $\Omega_e$ (Tokar & Gary, 1984).

## 4. The hot ion driven instability

In this section we briefly compare the hot electron with the hot ion driven magnetized instability. The ions now consist of two Maxwellian components: a stationary cold ion species and a hot ion species that drifts along $\mathbf{B}$ with speed $v_{0ib}$. The electron species are the same as in §2 but the hot electrons are now stationary. In this model the form of the electron-acoustic wave has become known as the modified electron-acoustic wave (Yu & Shukla 1983).

Figure 4 illustrates the threshold of the instability as a function of $\theta$ for two values of the ratio $\Omega_e/\omega_c$. For the strongly magnetized ($\Omega_e/\omega_c > 1$) curve, the threshold is almost constant with $v_{0ib} \sim 4.1 v_c$. However, in the case of weak magnetization ($\Omega_e/\omega_c < 1$), we observe two instabilities that are related to the modified electron-acoustic instability. The curve for $\Omega_e/\omega_c < 1$ with lower threshold drift velocity at $\theta = 0°$ corresponds to an ion beam-resonant instability (Schriver & Ashour-Abdalla, 1987) for $\theta > 0°$, and the other curve corresponds to the weakly-magnetized modified electron-acoustic instability.

The latter instability, has an upper frequency of $\sim \Omega_e$ as does the hot electron-driven electron-acoustic instability. We note also that in the regime $\Omega_e/\omega_c < 1$, the modified electron-acoustic instability has smallest threshold only at intermediate angles $\theta$, as does the hot electron-driven electron-acoustic instability.

## 5. References


Gary, S.P. 1987 *Phys. Fuids*, **30**, 2745.

Gary, S.P. & Tokar, R.L. 1985 *Phys. Fluids*, **28**, 2439.

Lin, C.S., Winske, D., & Tokar, R.L. 1985 *J. Geophys. Res.*, **90**, 8269.

Schriver, D. & Ashour-Abdalla, M. 1987 *J. Geophys. Res.*, **92**, 5807.

Tokar, R.L. & Gary, S.P. 1984 *Geophys. Res. Lett.*, **11**, 1180.

Watanabe, K. & Taniuti, T. 1977 *J. Phys. Soc. Japan*, **43**, 1819.

Yu, M.Y. & Shukla, P.K. 1983 *J. Plasma Phys.*, **29**, 409.

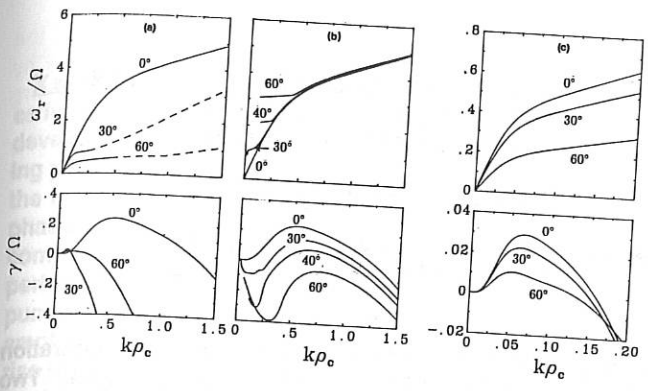


FIGURE 1.

FIGURE 2.

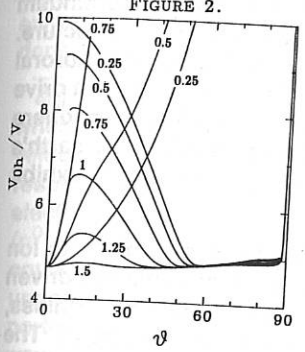


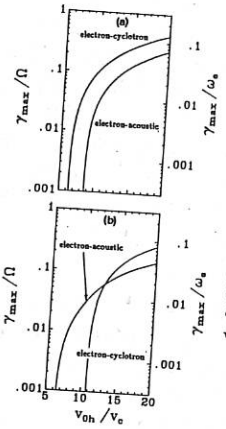


FIGURE 3.

FIGURE 1. The dispersion relation and growth rate of (a), (c) the electron-acoustic-like instability (b) the higher frequency electron-cyclotron-like instability. The parameter labelling the curves is $\theta$. Other parameters are: (a),(b) $\Omega_e/\omega_c = .25$, $v_{0h} = 10v_c$, (c) $\Omega_e/\omega_c = 2$. Unless otherwise stated, in all figures $n_c = n_h$, $T_h = 100T_c$, $T_i = T_c$ and $m_i = 1836m_e$. The dashed section of the curves indicate strongly damped waves where $-\gamma < \omega_r/2\pi$.

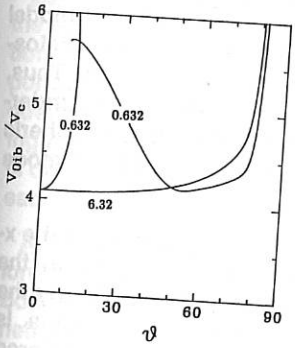


FIGURE 4.

FIGURE 2. The thresholds of the instabilities that arise for various values of $\Omega_e/\omega_c$ and varying $\theta$. The parameter labelling the curves is the ratio $\Omega_e/\omega_c$.

FIGURE 3. A comparison of the maximum growth rate of the electron-cyclotron- and electron-acoustic instabilities. (a) $\theta = 20°$, (b) $\theta = 40°$. $\Omega_e/\omega_c = 0.424$.

FIGURE 4. The threshold ion drift speed for the magnetized modified electron-acoustic instability as a function of $\theta$. The parameter labelling the curves is $\Omega_e/\omega_c$. Other parameters are $n_c = 0.1n_e$, $T_h = T_{ib} = 500T_c$, $T_i = 125T_c$

# GENERATION OF EXTRA-ORDINARY MODE RADIATION BY AN ELECTROSTATIC PUMP IN A TWO ELECTRON TEMPERATURE PLASMA

S.GUHA and ZEHRA HASAN

Department of Physics , Ravishankar University,
Raipur (M.P) INDIA.

There has been a great deal of interest in the study of the generation of the electromagnetic radiation in the earth's magnetosphere. Two types of radio emissions in the range of 10- 80 kHz have been investigated by the IMP 6 satellite [1] The first is the nonthermal continuum radiation which at times also displays a banded frequency structure. The second type of radiation correlates very well with the auroral kilometric radiation. It is also known that an anisotropic flux can drive instabilities more rapidly than an isotropic one. The topside ionosphere is presently known to be a major source of hot plasma within the earth's magnetosphere because here the warm ions and electrons exhibit anisotropic distribution.

In the present paper we have investigated the role of finite ion temperature (thermal ions) on electrostatic plasma instabilities driven by electron temperature anisotropies in a homogeneous, collisionless, charge neutral, nonrelativistic plasma which bears zero current. The problem of radiation emitted by the interaction of upper hybrid waves (UHW) and low frequency wave propogating perpendicularly to the magnetic field has been investigated. We have used standard model [2] with cold ionospheric electrons which is filled with hot magnetospheric electrons and streaming warm ions of ionospheric origin. Thus, in an earth fixed reference frame our analysis could be helpful in understanding the interaction of up flowing ion distribution of ionospheric origin along auroral field lines and also in the generation of the X mode radiation.

A finite amplitude es UH pump is taken to be propagating in the x-z plane in an external magnetic field $B_o\hat{z}$.We are interested in the generation of em radiation$(w_r,\vec{k_r})$and low frequency wave$(w_T,\vec{k_T})$by the pump.The nonlinear interaction of waves in a magnetoplasma is governed by the two fluid and Maxwell's equations.We have considered the dependence of all variables as $\exp.I(k_x\hat{x} + k_z\hat{z}\text{-}wt)$and used perturbation technique.Also $k_nz < k_nx$ and $E_nz < E_nx$ where $n = 0,r,T$.

X mode : The X mode ($w_r, \vec{k_r}$) with $\vec{k_r} \perp \vec{v_r}$, $\vec{E_r} \perp \vec{B_o}$ and $\vec{B_r} // \vec{B_o} \perp \vec{k_r}$ is elliptically polarized and so such a wave while propogating into a plasma develops an es component $E_{rx}$ and an em component $E_{ry}$, thus becoming partly transverse and partly longitudinal ($E_{ry} > E_{rx}$).But at resonance the em component $E_{ry}$ of the X mode approaches zero since both its phase and group velocities approaches zero. On the other hand the es component $E_{rx}$ attains a very high value.This mode has finite density perturbations which also contributes to the coupling strength of the pump, X mode and the decay wave.The nonlinear interaction of a finite amplitude UHW ($w_o, \vec{k_o}$) with the low frequency wave ($w_T, \vec{k_T}$) would give rise to a nonlinear current which becomes the source of the enhanced X mode ($w_r, \vec{k_r}$) radiation propagating perpendicular to $B_o\hat{z}$.The wave equation governing the X mode in the magnetoplasma is $(\partial_{tt} - c^2 \partial_{zz}) \vec{E_r} - 4\pi e n_o \partial_t \vec{v_{er}} = -4\pi \partial_t \vec{J_{NL}}$.(1) Here $\vec{J_{NL}}$ gives the nonlinear electron current density and is given by

$\vec{J_{NL}} = -e(1/2\ n^{l*}_{ec}\ \vec{v^p_{ec}} + n^p_{ec}\ \vec{v^{l*}_{ec}}) - e(1/2 n^{l*}_{eh}\ \vec{v^p_{eh}} + n^p_{eh}\ \vec{v^{l*}_{eh}})$(2) where $n^l_{ec,h}$ and $v^l_{ec,h}$ stands for the perturbed electron density and velocity of the low frequency decay wave for cold and hot electrons respectively and is obtained from the first order equation of motion.The electron quiver velocity ($\vec{v^p_{ec,h}}$) and the electron number density ($n^p_{ec,h}$) in the field of the pump wave are obtained from the zero order equation of motion and continuity.For the three low frequency es waves under consideration $\vec{B_T} = 0$; the expression for electron and ion density perturbation can be obtained using basic fluid equations governing the wave dynamics.

Low frequency waves : Ions having a small gyrofrequency respond to the es fields as an unmagnetized species.The generated X mode radiation beats with the pump thereby generating a low frequency ponderomotive force acting on electrons which amplifies the low frequency wave.The nonlinear dispersion relation is obtained by substituting ion and electron density perturbations in Poisson's equation which is of the form $\epsilon_T \phi_T = \mu_T \phi_o \phi^*_r$ (3) where $\epsilon_T, \phi_T$ and $\mu_T$ are specific for each low frequency wave.

A. ESICW : The parallel phase velocity of this wave lies between the ion and electron thermal velocity, so the inertialess electrons obey the Boltzmann relation.The ions move in a plane perpendicular to the magnetic field.We will get $\epsilon_{IC} = k^2_1 - X_{ec} - X_{eh} - w^2_{pi} X_i$ (4), $X_{ec,h} = 4\pi n_o e^2 / T_{ec,h}$ (5), $X_i = A_i / 1 - 3\ V^2_{thi} A_i$ (6), where $A_{i,ec,eh} = k^2_{1x} / w^2_1 - w^2_{ci,e} + k^2_{1z} / w_1$ (7) and $\mu_{IC} = (X_{ec} + X_{eh}) \phi_{pe}$ (8)

**B. LHW** : The frequency of LHW lies between the electron and ion gyrofrequencies.The magnetized electrons are coupled to the ions by the space charge potential.We get from equation (3) after some algebra $\epsilon_{LH} = k^2_1 - w^2_{pi}\chi_{i2} - w^2_{pec}\chi_{e2c} - w^2_{peh}\chi_{e2h}$ (9) $\mu_{LH} = \phi_{pe}( w^2_{pec}B_c + w^2_{peh}B_h)$ (10) where $B_{c,h} = k^2_{1z}/1-3V^2_{thec,h}A_{ec,h}$(11) $\chi_{i2} = k^2_1/[w^2_1 - 3k^2_1V^2_{thi}$ (12), $\chi_{e2,ch} = A_{ec,h}/1-3V^2_{thec,h}A_{ec,h}$ (13)

**C. EAW** : In a plasma, with electrons of two distinct temperatures, EAW can propagate. The ions follow a Boltzmann distribution. So we get from equation (3) $\epsilon_{EA} = k^2_1 - \chi_{i3} - w^2_{pec}\chi_{e2c} - w^2_{peh}\chi_{e2h}$ (14) where $\chi_{i3} = 4\pi n_o e^2/T_i$ (15).

**Coupled Nonlinear Dispersion Relation** : On finding out the value of JNL from (2) for each low frequency wave and substituting it in (1) we will get the coupled nonlinear dispersion relation as $D_X\epsilon_T = \mu_{rT}$ (16) where $D_X = w^2_r - k^2_r c^2 - w^2_{pe}/P[1 + w^2_{ce}w^2_{pe}/w^2_r P\{w^2_{rc}^2 k^2_r\} - w^2_{pe}w^2_r$ (17) gives the dispersion relation of the X mode.Here $P = w^2_r - w^2_{ce}/w^2_r$ and $\mu_{rT}$ is the coupling constant for the X mode and low frequency wave.Similarly $\epsilon_T = o$ will give the dispersion relation of ESICW, LHW and EAW as in (4 ), ( 9) and (14). $\mu_{rT}$ represents the coupling constant for X mode and low frequency wave and varies with each low frequency wave.

**Growth Rates** : The growth rate, in the absence of linear damping can be determined by the expression [3]

$$\gamma_o^2 = -\mu_r \Big/ \left(\frac{\partial \epsilon_{1r}}{\partial \omega_{1r}}\right)\left(\frac{\partial D_x}{\partial \omega_{xr}}\right) \qquad (18)$$

using some approximations viz, (1)$k^2_{1x}V^2_{thi} > w^2_{pi}, w^2_{ci}, w^2_1$

(2)$w^2_{ce} > w^2_o, w^2_1, w^2_r, w^2_{ci}$ (3)$w^2_{pe} > w^2_{ce}$ (4)$V^2_{thi} > V^2_{theh} > V^2_{thec}$.

**The final expression after some simplification, for the growth rate comes out to be**

$$\gamma_{IC} = \frac{eE_{ox}v_{thi}}{\omega_{ce}}\sqrt{\frac{m_i}{8\omega_o\omega_1 m_e^2 n_i}\left(\frac{n_{oc}}{v^2_{thec}} + \frac{n_{oh}}{v^2_{theh}}\right)\left(\frac{\omega_o k^2_{1x}}{2} + \frac{\omega_1 k_{1x}k_{ox}}{\omega^2_{ce}}(\omega^2_{pec} + \omega^2_{peh})\right)}$$

$$\gamma_{LH} = \frac{eE_{ox}}{\omega_{ce}}\sqrt{\frac{(n_{oc}+n_{oh})\omega_1 k_{ox}/\omega^2_{ce} - \omega_p k_{1x}\left(n_{oc}/(\omega_1^2 - 3k^2_{1x}v^2_{thec}) + n_{oh}/(\omega_1^2 - 3k^2_{1x}v^2_{theh})\right)\left(k_1^2 - \omega^2_{pi}k_1^2/(\omega_1^2 - 3k_1^2v^2_{thi})\right)}{(16\omega_0\omega_1 k_{1x}m_e^2)\left(n_i/(3k_1^2v^2_{thi}) + n_{oc}/(\omega^2_{ce} + 3k^2_{1x}v^2_{thec}) + n_{oh}/(\omega^2_{ch} + 3k^2_{1x}v^2_{theh})\right)}}$$

$$\gamma_{EA} = \frac{eE_{ox}}{\omega_{ce}}\sqrt{\frac{(n_{oc}+n_{oh})\omega_1 k_{ox}/\omega^2_{ce} - \omega_o k_{1x}\left(n_{oc}/(\omega_1^2 - 3k^2_{1x}v^2_{thec}) + n_{oh}/(\omega_1^2 - 3k^2_{1x}v^2_{theh})\right)\left(k_1^2 - 4\pi n_o e^2/T_i\right)}{(16\omega_0\omega_1 k_{1x}m_e^2)^{\frac{1}{2}}\left(n_{oc}/(\omega^2_{ce} + 3k^2_{1x}v^2_{thec}) + n_{oh}/(\omega^2_{ch} + 3k^2_{1x}v^2_{theh})\right)}}$$

Discussion : If we consider the ions to be cold then we see that

$$\gamma_{LH} = \gamma_{EA}.$$

The growth rate depends on the parameters listed in the abstract.The presence of even a small fraction of the low temperature electrons can reduce the growth rate of each of the three waves.These waves are appreciably modified by finite ion temperature also.For EAW, we find that injecting hot electrons will lead to enhancement of growth rate.But for the ion modes the growth rate can be controlled considerably by injecting warm ions.

Our results can be quite useful to the understanding of wave phenomena in the ionosphere, in the earth's magnetosphere at the plasmapause and beyond, as well as in the solar wind.There exist numerous evidence of intense noise band [4] near the upper and lower hybrid resonance frequencies at the plasmapause and beyond.Energetic ions and electron and UH es waves have been observed in source region of transversely accelerated ionospheric ions at altitudes of several hundred kilometres. Analysis of the ion and electron distribution's stability in conjunction with the growth and decay of waves is important to understand the magnetosphere-ionosphere coupling.This coupling undoubtedly plays a major role in forming the dynamics of the aurora.It has been found that the low frequency es turbulence and measured electron fluctuations in aurora are in the range of ion gyrofrequencies at low altitudes [1].

The results of the ion modes should be relevant to the low frequency fluctuations in the solar wind and cometary plasmas.The EAW plays an important role for electron dissipation in collisionless Earth's bow shock.This analysis can also be extended to explain the AKR, weak double layer evolution and formation of both electron and ion conics.A popular mechanism to explain ion conics in the magnetosphere is the perpendicular heating of ions by ESICW and LHW.

References [1] P.C.Filbert & P.J.Kellogg J.Geophys.Res., 94 (1989) 8867 [2] M.A.Abdalla & C.F.Kennel J.Geophys.Res. 83 (1978) 1531 [3]R.R.Sharma & V.K.Tripathi Phys.Rev.B 20 (1979) 748[4]D.A.Gurnett & L.A. Frank J. Geophys.Res.82 (1977) 10311

# PROPAGATION OF ELECTROMAGNETIC WAVES IN A MODULATED DENSITY PLASMA

*M. Lontano (*) and N. Lunin (+)*

*(*) Istituto di Fisica del Plasma, C. N. R., EURATOM-ENEA-CNR Association, Milano, Italy*
*(+) Institute of Applied Physics, Soviet Academy of Sciences, Gorki, USSR*

As it is known, the interaction of high power electromagnetic (EM) waves or relativistic electron beams with a plasma can lead to the onset of a modulation instability which develops spatial periodical (or quasi periodical) structures of the plasma density and of the electric field intensity.

If the spatial pattern consists of a large number of periods and if the modulation is regular enough then an efficient *resonant interaction* between an incident EM wave and the plasma density modulation can occur depending on its relative amplitude and on the wavelength of the incoming radiation /1/.

An analogous situation can happen when a strong density fluctuation is induced in a plasma under RF heating conditions. Around the plasma resonances the heating waves become essentially longitudinal and coherent density fluctuations are excited.

In these conditions the resulting density modulation can strongly increase the reflectivity of the medium, even at relatively low densities ($n_0 < n_{cr}$), for EM waves of particular wavelengths and directions of propagation, leading to a transmitted power spectrum qualitatively different from the incident one. In the unidimensional case (i.e. $\underline{k} \parallel \underline{\nabla} n$) the condition for an efficient backscattering is

$$\frac{\lambda}{\Lambda_n} \simeq \frac{2}{l} \quad , \quad l = 1, 2, 3, \ldots , \tag{1}$$

where $\lambda$ is the radiation wavelength, $\Lambda_n$ is the spatial period of the modulated structure, $l$ is an integer.

In general the spatial scale of the inhomogeneity can be of the order or smaller than the wavelength of the incident radiation, therefore the WKB approximation cannot be used to study the characteristics of the EM wave propagation. Furthermore, in a periodical medium, even if the reflectivity of a single layer is low, when the

number of periods becomes large, the global reflectivity increases substantially and the analysis cannot be performed within a perturbative theory.

The present work/2/ is intended to investigate two main problems:

a) the possibility of computing the transmission coefficient of a single plasma layer when

$$\lambda \geq \left| \frac{1}{n} \frac{\partial n}{\partial z} \right|^{-1};$$

b) the extension of the analysis to a multilayer structure made up of a succession of N identical or slightly different plasma slabs.

Referring to those physical situations based on a unidimensional scalar wave equation:

$$\frac{d^2E(z)}{dz^2} + k^2(z)E(z) = 0, \tag{2}$$

with boundary conditions $E(z_0) = E_0$, $E'(z_0) = E_0'$, we can go to a vector description by introducing the functions $\Phi_{\pm} \equiv \sqrt{k(z)} \left[ E(z) \pm \frac{1}{ik} E'(z) \right]$ and the vector $\underline{\Phi} \equiv (\phi_+, \phi_-)$; eq.(2) becomes

$$\underline{\Phi}'(z) = \hat{P}(z) \cdot \underline{\Phi}(z) \tag{3}$$

where $\underline{\Phi}(z_0) = \underline{\Phi}_0$, $\hat{P}(z) \equiv ik(z)\hat{\sigma}_3 + \frac{k'}{2k}\hat{\sigma}_1$, and $\hat{\sigma}_i$ (i=1,2,3) are the Pauli matrices/3/.

The solution of eq.(3) can be written in terms of the exponential, *time-ordered* operator /4/:

$$\underline{\Phi}(z) = \mathbb{Q}(z,z_0) \cdot \underline{\Phi}(z_0), \tag{4}$$

where

$$\mathbb{Q}(z,z_0) = T \exp\left[ \int_{z_0}^{z} dz' \, \hat{P}(z') \right]. \tag{5}$$

Clearly $\mathbb{Q}(z,z_0)$ acts as a space propagator from $z_0$ to $z$. It is shown that, if $k^2(z)$ is a real function, then the matrix $\mathbb{Q}$ is quasiunitary, i.e. $Q_{11} = \overline{Q}_{22}$, $Q_{12} = \overline{Q}_{21}$. Furthermore, if $z > z_1 > z_2 > \cdots z_{n-1} > z_n > z_0$, the total propagator from $z_0$ to $z$ can be represented as the ordered product of partial propagators:

$$\mathbb{Q}(z,z_0) = \mathbb{Q}(z,z_1) \cdot \mathbb{Q}(z_1,z_2) \cdot \mathbb{Q}(z_2,z_3) \cdot \cdots \cdot \mathbb{Q}(z_{n-1},z_n) \cdot \mathbb{Q}(z_n,z_0). \tag{6}$$

This allows to use at each step of integration different approximations for $\mathbb{Q}(z_i, z_{i-1})$ depending on the steepness of spatial gradients in the $z$-direction. The computation of the propagator relevant to a single plasma layer is accomplished by means of the so called *Magnus approximation* /5/, which preserves the quasiunitarity of the operator at each order of the expansion. It consists of an expansion in successive commutators where the first terms can be written as follows:

$$\mathbb{Q}(z,z_0) = \exp[\int_{z_0}^{z} dz_1 \hat{P}(z_1) + \frac{1}{2}\int_{z_0}^{z} dz_1 \int_{z_0}^{z_1} dz_2 [\hat{P}(z_1), \hat{P}(z_2)] + \tag{7}$$

$$+ \frac{1}{6}\int_{z_0}^{z} dz_1 \int_{z_0}^{z_1} dz_2 \int_{z_0}^{z_2} dz_3 ([\hat{P}(z_1),[\hat{P}(z_2), \hat{P}(z_3)]] + [[\hat{P}(z_1), \hat{P}(z_2)], \hat{P}(z_3)]) + \cdots ].$$

Finally it is easy to show that the transmission and reflection coefficients for the EM wave crossing the plasma layer can be written as follows:

$$T_1 \equiv \frac{1}{|Q_{22}|^2} \quad , \quad R_1 \equiv \left| \frac{Q_{12}}{Q_{11}} \right|^2 , \tag{8}$$

where $R_1 + T_1 = 1$.

Once the matrix $\mathbb{Q}(z_0 + \delta, z_0)$ is known, the extension to a multilayer structure is easily performed by introducing the following representation of the propagator:

$$\mathbb{Q}(z_0 + \delta, z_0) \equiv \exp(\underline{p}\,\underline{\hat{\sigma}}) = \exp(p_1\hat{\sigma}_1 + p_2\hat{\sigma}_2 + p_3\hat{\sigma}_3) \tag{9}$$

where the $p_j$ components can be determined from the matrix elements $Q_{lm}$.

Therefore the propagator relevant to a succession of N identical layers ($z_0 < z < z_0 + N\delta$) can be put in the following form

$$\mathbb{Q}_N(z_0 + N\delta, z_0) = \tag{10}$$

$$= \mathbb{Q}_1[z_0 + N\delta, z_0 + (N-1)\delta] \cdot \mathbb{Q}_1[z_0 + (N-1)\delta, z_0 + (N-2)\delta] \ldots \mathbb{Q}_1(z_0 + \delta, z_0) =$$

$$= [\mathbb{Q}_1(z_0 + \delta, z_0)]^N = \exp(N\underline{p}\,\underline{\hat{\sigma}}),$$

where the $p_j$ components are the same as in the case of a single layer.

The transmission and reflection coefficient relevant to a uniformly modulated plasma can be written as follows:

$$T_N = \frac{1}{\cosh^2(N\,p) - \dfrac{p_3^2}{p^2}\sinh^2(N\,p)}$$

$$R_N = \frac{\dfrac{p_1^2 + p_2^2}{p^2}\sinh^2(N\,p)}{\cosh^2(N\,p) - \dfrac{p_3^2}{p^2}\sinh^2(N\,p)}. \qquad (11)$$

Eq.(10) shows that, for physical parameters describing the wave-plasma system such that $p$ is a real quantity, the dependence of $T_N$ and $R_N$ on the number of periods N has a monotonic character and can give high values of $R_N$ ($\simeq 1$). This happens when the condition (1) is satisfied and is related to the presence of *forbidden zones* in the parameter space/6/. The transmission coefficient has been computed for different kinds of density profiles and the possibility to apply the same techique to a slight non uniform periodical density structure has been exploited.

This work has been performed in the framework of the scientific cooperation agreement between the Soviet Academy of Sciences and the Italian National Research Council (CNR).

*References*

/1/ P.Kaw, A.T. Lin, J.M. Dawson, The Physics of Fluids, **16**, 1967 (1973); H. Figueroa, C. Joshi, *Laser Interaction and Related Plasma Phenomena,* vol.7, edited by H. Hora and G.H. Miley, Plenum Press, New York (1985).

/2/ M. Lontano and N. Lunin, Istituto di Fisica del Plasma, Associazione EURATOM-ENEA-CNR, FP 89/**26.**, (1989).

/3/ V.A. Kolkunov, Soviet Journal of Nuclear Physics, **10**, 734 (1970); V.A. Kolkunov, V.N. Mel'nikov, Soviet Journal of Nuclear Physics, **17**, 452 (1973); V.A. Kolkunov, V.N. Mel'nikov, Soviet Journal of Nuclear Physics, **20**, 322 (1975).

/4/ F.J. Dyson, Physical Review, **75**, 486 (1949); A.L. Fetter, V.A. Walecka, *Quantum Theory of Many-particle Systems,* McGraw Hill, New York.

/5/ W. Magnus, Comm. in Pure and Appl. Mathematics, **7**,649 (1954); P. Pechukas and J.C. Light, The Journal of Chemical Phys., **44**, 3897 (1966).

/6/ L. Brillouin, M. Parodi, *Propagation des Ondes dans les Milieux Periodiques,* Masson et Cie Editeurs, Paris, 1956.

# LASER WAKEFIELD ACCELERATION IN AN EXTERNAL MAGNETIC FIELD

P. K. Shukla

Institut für Theoretische Physik IV
Ruhr-Universität Bochum
D-4630 Bochum 1
F. R. Germany

It has been proposed that the plasma-based particle acceleration schemes, the plasma beat wave accelerator (PBWA), the plasma wakefield accelerator (PWFA) and the laser wakefield accelerator (LWFA), would employ strong electric field gradients of electron plasma waves that have a phase velocity of nearly the speed of light. Large amplitude plasma waves could be excited by the beats of two relatively low power, long pulse laser beams in the PBWA, by a low energy, high current relativistic electron beam in the PWFA, and by a short, intense, single frequency laser pulse in the LWFA. In all these three schemes, a trailing bunch of electrons can then be injected into accelerating phase of the excited plasma waves, so that the energy can be transferred from the plasmons to the electrons.

Recent considerations of the laser propagation issues, along with recent advances in laser technology, indicate that the single frequency, short pulse LWFA might have advantages over the PBWA and PWFA schemes. Accordingly, a number of authors [1,2] has focused attention on the calculation of the electrostatic fields in the LWFA scheme. In the latter concept, the short pulse, intense laser beam provides both a radial and axial (with respect to the laser propagation direction) radiation pressure on the plasma electrons. The radial radiation pressure pushes electrons radially outward while the front (back) of the laser pulse exerts a forward (backward) force on the electrons. In this sense, the short laser pulse behaves roughly like a negatively charged macro-particle propagating through the plasma. The plasma electrons flowing around the laser pulse would then generate large amplitude plasma waves.

In this paper, we present a three-dimensional calculation for the electron plasma wave generation by the circularly polarized short laser pulse propagating along the external magnetic field. Using hydrodynamic and Poisson's equations we derive a driven plasma wave equation including the perpendicular ponderomotive potential as well as the time derivative radiation flux in the longitudinal ponderomotive force. Analytical results for the one-dimensional (parallel to the guide magnetic field) axial wakefield within and behind the laser pulse are obtained by choosing a laser pulse profile of the Gaussian form. It is found that the guide magnetic field has substantial influence on the maximum electric field gradient of the wakefield.

Consider the nonlinear interaction of a pure electron plasma with a short, intense right-hand circularly polarized electromagnetic (CPEM) wave packet whose electric field is represented as $\vec{E} = \vec{E}(\hat{x}+i\hat{y})\exp(i\vec{k}\cdot\vec{r} - i\omega t) +$ compl. conj., where $\hat{x}$ and $\hat{y}$ are the unit vectors in directions perpendicular to the external magnetic field $B_0\hat{z}$. For the CPEM wave propagation along $B_0\hat{z}$, the frequency $\omega$ and the wave vector $\vec{k}=\hat{z}k$ are related by the dispersion

relation $\omega^2 = k^2c^2 + \omega_p^2\omega/(\omega - \omega_c)$, where $\omega_p$ and $\omega_c$ are, respectively, the electron plasma and gyrofrequencies.

The field-aligned short CPEM wave packet interacts with background plasma. As a result, there arises an envelope of high-frequency CPEM wave packet that may propagate at an angle to the external magnetic field. The radial ponderomotive potential reinforces electron motion in a perpendicular plane, whereas the field-aligned ponderomotive force expels the electrons along the magnetic field. The multi-dimensional cold plasma wave dynamics is governed by

$$\partial_t n_1 + n_0 \nabla_\perp \cdot \vec{v}_\perp + n_0 \partial_z v_z = 0 , \tag{1}$$

$$(\partial_t^2 + \omega_c^2)\,\vec{v}_\perp = \frac{e}{m}\,\partial_t \nabla_\perp (\phi + \phi_p) + \frac{e}{m}\,\omega_c\,\hat{z} \times \nabla (\phi + \phi_p), \tag{2}$$

$$\partial_t v_z = \frac{e}{m}\,\partial_z \phi - F_z , \tag{3}$$

and

$$\nabla^2 \phi = 4\pi e n_1 , \tag{4}$$

where $n_0(n_1)$ is the unperturbed (perturbed) electron number density, $\vec{v}$ is the electron fluid velocity, e and m are, respectively, the magnitude of the electron charge and the mass, and $\phi$ is the electrostatic potential. The perpendicular(to $\vec{B}_0$) component of the ponderomotive potential associated with the the CPEM wave packet is

$$\phi_p = - e |E|^2 / m (\omega - \omega_c)^2 . \tag{5}$$

The axial ponderomotive force reads

$$F_z = \left[ \partial_z - \frac{k\omega_c}{\omega(\omega - \omega_c)}\,\partial_t \right] \frac{e^2 |E|^2}{m^2 \omega (\omega - \omega_c)} . \tag{6}$$

The second term on the right-hand side of (6) is the time-derivative of the radiation pressure associated with the CPEM radiation in a magnetized plasma.

Combining (1) to (4), we readily obtain

$$\left[ (\partial_t^2 + \omega_c^2)(\partial_t^2 \nabla^2 + \omega_p^2 \partial_z^2) + \omega_p^2 \partial_t^2 \nabla_\perp^2 \right] \phi = \left\{ (\partial_t^2 + \omega_c^2) \times \left[ \partial_z^2 - \frac{k\omega_c}{\omega(\omega - \omega_c)}\,\partial_{tz} \right] + \frac{\omega}{\omega - \omega_c}\,\partial_t^2 \nabla_\perp^2 \right\} \frac{e^2 |E|^2}{m^2 \omega (\omega - \omega_c)} . \tag{7}$$

Equation (7) governs the excitation of three-dimensional electron plasma waves in the presence of the axial and radial ponderomotive forces of the CPEM waves in an external magnetic field. When all the waves are aligned along the guide magnetic field, then (7) takes the form

$$(\partial_t^2 + \omega_p^2)\,\partial_z \phi = \left[\partial_z - \frac{k\omega_c}{\omega(\omega-\omega_c)}\partial_t\right]\frac{e^2|E|^2}{m^2\omega(\omega-\omega_c)}. \tag{8}$$

On the other hand, in the limit $\partial_t \ll \omega_c$, multi-dimensional electron plasma waves are governed by

$$\left[\left(\nabla^2 + \frac{\omega_p^2}{\omega_c^2}\nabla_\perp^2\right)\partial_t^2 + \omega_p^2\partial_z^2\right]\phi = \left\{\left[\partial_z^2 - \frac{k\omega_c}{\omega(\omega-\omega_c)}\partial_{tz}^2\right] + \frac{\partial_t^2}{\omega_c^2}\,\frac{\omega}{\omega-\omega_c}\,\nabla_\perp^2\right\}\frac{e^2|E|^2}{m^2\omega(\omega-\omega_c)}. \tag{9}$$

For illustrative purposes, we present some specific results for the axial wake electric field assuming that all the waves are aligned parallel to the external magnetic field. We suppose the excitation process to be stationary in the frame moving with a group velocity ($=\hat{z}v_g$) of the CPEM pulse. Thus, in a new frame $\xi = z - v_g t$, (8) becomes

$$(\partial_\xi^2 + k_e^2)\,\phi = \left[1 + \frac{k v_g \omega_c}{\omega(\omega-\omega_c)}\right]\frac{e^2|E|^2}{m^2\omega(\omega-\omega_c)v_g^2}, \tag{10}$$

where $k_e = \omega_p/v_g$ and $v_g = kc^2/[\omega + \omega_c\omega_p^2/2(\omega-\omega_c)^2]$. Equation (10) is solved, giving

$$\phi = -k_e\left[1 + \frac{k v_g \omega_c}{\omega(\omega-\omega_c)}\right]\frac{e^2}{m^2\omega(\omega-\omega_c)\omega_p^2}\int_\xi^\infty |E|^2 d\xi' \sin[k_e(\xi'-\xi)]. \tag{11}$$

Let us assume that the electromagnetic pulse envelope is of the form

$$E = \begin{cases} E_0 \sin(\pi\xi/l)\exp(-r^2/2r_0^2), & 0 \le \xi \le l; \\ 0, & \text{otherwise}, \end{cases} \tag{12}$$

where $l$ is the pulse length and $r_0$ is the spot size. Then, the profile of the axial electrostatic wakefield generated in a pure magnetized electron plasma is given by

$$E_p = k_e\left[1 + \frac{k v_g \omega_c}{\omega(\omega-\omega_c)}\right]\frac{\pi^2 e^2 |E_0|^2 \exp(-r^2/r_0^2)}{m^2\omega(\omega-\omega_c)\omega_p^2(4\pi^2 - k_e^2 l^2)}\left[H\sin(k_e\xi/H) - \sin k_e\xi\right], \tag{13}$$

where $H = (k_e l/2\pi)$ within the laser pulse, $0 \le \xi/l \le 1$, and $H=1$ behind the pulse, $\xi \le 0$. Equation (13) shows that the strength of the wakefield is enhanced in the presence of the external magnetic field.

In order for the LWFA scheme to work, the short laser pulse should be able to propagate without distortion within the plasma. Thus, the laser-driven various parametric instabilities must be suppressed . Therefore, it is instructive to consider the stimulated Raman scattering, the modulational, and the filamentational instabilities in a magnetized plasma. A three-dimensional analysis of these parametric instabilities has yet to be carried out; although the results for one-dimensional problem are available in the

literature. In the following,we summarize some results. The maximum growth rate of the stimulated Raman process ($\Omega/K \gg v_{th}$, where $\Omega$ and K are, respectively, the frequency and the wavenumber of the low-frequency wave in an electron plasma, and $v_{th}$ is the electron thermal velocity) is given by

$$\gamma_R = K v_0 (\omega \omega_p)^{1/2} / 2 A^{1/2} |(\omega - \omega_c)| , \tag{14}$$

where $v_0 = eE_0/m\omega$ , and $A = 1 + \omega_c \omega_p^2 / 2\omega(\omega - \omega_c)^2$. When $\Omega \gg \omega_p$ and $v_0^2/c^2 > (\omega_p/\omega)$, we have a reactive quasi-mode as the scatterer. For this case, one finds the growth rate

$$\gamma_Q = \frac{1}{2} \left[ \frac{K^2 c^2 \omega_p^2 \omega}{2A(\omega - \omega_c)^2} \right]^{1/3} \left( \frac{v_0}{c} \right)^{2/3} . \tag{15}$$

For the stimulated Compton regime, we have $\Omega \sim K v_{th}$, and the maximum growth rate is given by

$$\gamma_C \approx \frac{0.4}{A} \left( \frac{v_0}{v_{th}} \right)^2 \frac{\omega \omega_p^2}{(\omega - \omega_c)^2} . \tag{16}$$

The growth rate of the relativistic modulational instability of the CPEM wave is found to be

$$\gamma_M = (v_g' C_r)^{1/2} K |E_0| , \tag{17}$$

where $C_r |E_0|^2 > K^2 v_g'/4$, $C_r = e^2 \omega^2 \omega_p^2 v_g / 2m^2 c^4 k (\omega - \omega_c)^4$, and $v_g' = \partial v_g / \partial k$.

To summarize, we have developed a three-dimensional model for the laser wakefield acceleration in an external magnetic field. Specifically, we have derived a three-dimensional electron plasma wave equation in the presence of the radial and axial ponderomotive forces of the CPEM waves. Choosing the electromagnetic pulse profile to be of the Gaussian form, we have obtained an expression for the field-aligned wakefield. It is found that the strength of the latter is enhanced in the presence of the guide magnetic field. We have also discussed various parametric instabilities associated with a finite amplitude CPEM wave in a pure electron plasma with fixed ion background.

Acknowledgments: This research was supported by the Deutsche Forschungsgemeinschaft through the Sonderforschungsbereich "Physikalische Grundlagen der Niedertemperaturplasmen".

References

[1] L. M. Gorbunov and V. I. Kirsanov, Sov. Phys. JETP 51(1987) 290.

[2] P. Sprangle, E. Esarey, A. Ting, and G. Joyce, Appl. Phys. Lett. 53(1988) 2146.

# RADIATIVE ENERGY TRANSPORT IN THERMONUCLEAR PLASMAS

Satish Puri
Max-Planck Institut für Plasmaphysik, EURATOM Association,
Garching bei München, Federal Republic of Germany

*Electron thermal diffusivity $\chi$ contributed by the radiative transport of electrostatic electron-Bernstein wave emission in toroidal geometry is computed via accurate ray tracing using the full hot-plasma dielectric tensor. Enhanced values of $\chi \gtrsim \mathcal{O}(.5)$ are found to occur for $T_e \sim 3 \times 10^5\,°K$, $n_e \sim 1 \times 10^{21}\,m^{-3}$ and $B_0 \sim 10\,T$ in a typical Tokamak geometry. The possibility of similarly enhanced values of $\chi$ for other parameter regimes through the introduction of rotational transform is discussed.*

## INTRODUCTION

Energetic electrons in a magnetic field are profuse sources of synchrotron radiation. The collective effects in the plasma channel this radiation into cyclotron-harmonic modes. Using the Rayleigh-Jeans approximation of Planck's formula, Kirchhoff's law generalized to anisotropic media gives the total radiated power density [1, 2]

$$\eta_T = \frac{1}{(2\pi)^3}\int_{\mathbf{k}} \eta(\mathbf{k})\,d\mathbf{k} = \frac{2}{(2\pi)^3} T_e \int_{\mathbf{k}} \mathbf{k}_i(\mathbf{k}) \cdot \mathbf{v}_g(\mathbf{k})\,d\mathbf{k}\ , \tag{1}$$

where $\mathbf{k}$ is the propagation vector, $\mathbf{k}_i = \Im[\mathbf{k}]$ and $\mathbf{v}_g$ is the group velocity. The integration extends over all propagating waves that satisfy the hot-plasma dispersion relation

$$D(\mathbf{k}, \omega(\mathbf{k}, \mathbf{r}), \mathbf{r}) = 0\ . \tag{2}$$

Steady-state Maxwellian distribution and local-dielectric-tensor description are assumed. Since $\eta_T$ scales as the $k$-space volume, radiation in a plasma is dominated by the large-$k$ electrostatic Bernstein [3] waves. The asymptotic ($k_\perp \to \infty$) form of the classical ($k_\parallel = 0$) Bernstein wave dispersion relation near the $n$th-harmonic may be written as

$$k_\perp^3 \approx \frac{2}{\sqrt{\pi}} \frac{\omega_p^2}{\omega \omega_c} \frac{n\omega}{\omega - n\omega_c} \frac{1}{r_{ce}^3}\ . \tag{3}$$

Differentiating Eq.(3) gives the perpendicular group velocity

$$v_{g\perp} = \frac{\partial \omega}{\partial k_\perp} = -\frac{3\pi^{1/6}}{2^{1/3} n^{1/3}} \frac{(\omega - n\omega_c)^{4/3}}{\omega_p^{2/3} \omega_c^{2/3}} v_\perp \sim \omega_p^{-2/3} \omega_c^{2/3} T_e^{1/2}\ . \tag{4}$$

Parallel group velocity along the magnetic field is substantially the electron thermal speed. For finite $k_\parallel$, $k_\perp$ possesses an additional imaginary component in the vicinity of the harmonics, giving rise to the cyclotron-harmonic absorption/radiation.

Figure 1 shows the fundamental-cyclotron emissivity $\eta_\varepsilon = \eta_T/\varepsilon$ normalized with respect to the thermal energy density $\varepsilon = (3/2) n_e T_e$ as a function of electron temperature for $n_e = 10^{21}\,m^{-3}$ and $B_0 = 10\,T$. The corresponding $\eta_T \gtrsim \mathcal{O}(1)\,MW\,m^{-3}$. Large $\eta_\varepsilon$ values imply that a transport of the emitted radiation over a mean square distance of only $< r^2 > \sim \mathcal{O}(10^{-3})\,m^2$ would lead to an electron thermal diffusivity of $\chi = \eta_\varepsilon < r^2 > \sim \mathcal{O}(.5)$.

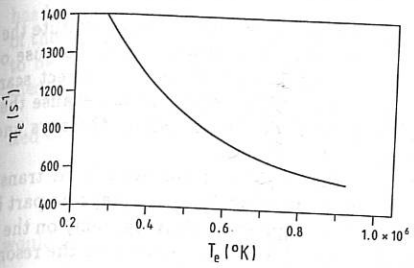


Fig. 1
*Normalized emissivity versus temperature*

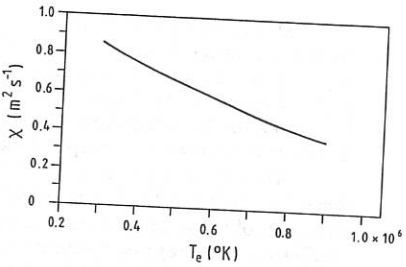


Fig. 2
*Diffusivity versus temperature*

## RAY-TRACING RESULTS

Determination of $\chi$ is accomplished through ray tracing in accordance with the Weinberg [4] approach using the dispersion relation (2). The amplitude of a ray, starting at $r_0$ with the normalized value $\psi(\mathbf{k}, \mathbf{r}_0) = \eta_\varepsilon(\mathbf{k}, \mathbf{r}_0)\, d\mathbf{k}$, at a point $\mathbf{r}$ along the ray path is given by

$$\psi(\mathbf{r}) = \eta_\varepsilon(\mathbf{k}, \mathbf{r}_0)\, d\mathbf{k} \exp\left[-2 \int_{\mathbf{r}_0}^{\mathbf{r}} \mathbf{k}_i(\mathbf{r}) \cdot d\mathbf{r}\right] . \tag{5}$$

The normalized power deposited by the ray in the plasma in distance $\Delta\mathbf{r}$ equals

$$2\psi(\mathbf{r})\mathbf{k}_i(\mathbf{r}) \cdot \Delta\mathbf{r}.$$

The diffusivity contribution of the ray is

$$\chi(\mathbf{k})\, d\mathbf{k} = \int_{\mathbf{r}_0}^{\infty} 2\psi(\mathbf{r})\mathbf{k}_i(\mathbf{r}) \cdot d\mathbf{r}\, |\mathbf{r} - \mathbf{r}_0|^2 . \tag{6}$$

Integrating over all possible rays, gives the total diffusivity at $\mathbf{r}_0$ as

$$\chi(\mathbf{r}_0) = \frac{1}{(2\pi)^3} \int_{\mathbf{k}} \chi(\mathbf{k})\, d\mathbf{k} . \tag{7}$$

The computational parameters consist of: major torus radius $R_0 = 3\,m$, plasma radius $a = 1\,m$, $n_e = n_0(1-\rho^2)$, $T_e = T_0(1-\rho^2)^2$, $n_0 = 10^{21}\,m^{-3}$, and $B_0 = 10\,T$. Rotational transform and relativistic corrections are not included.

Figure 2 shows the computed results for the case of fundamental cyclotron emission as a function of temperature. The starting position of all the rays is assumed to be the plasma axis. Since the emission as well as the absorption of the rays occurs near the cyclotron-harmonic layer, the diffusion takes place primarily in the vertical direction perpendicular to the median plane with $\chi \sim \mathcal{O}(.5)$.

## ROLE OF THE ROTATIONAL TRANSFORM

Despite their considerable import, the foregoing results do not constitute the f verdict on either the magnitude of $\chi$ or its scaling with respect to $T_e$ because of approximations and the limitations of the present model. Even the correct scann of the $k$-space in the integration of Eq.(7) presents delicate problems because the c tributions to the integral are dominated by regions of $k$-space where the rays und large excursions with correspondingly large $< r^2 >$ values.

An important source of inaccuracy is the neglect of the rotational transfo Since the magnetic field lines lie parallel to the singular surface, $v_{g\|}$ plays no part in transport of the emitted radiation away from the singularity. Relying solely on the m smaller $v_{g\perp}$, the rays emanating from the resonant layer tend to stick to the resona Introduction of rotational transform would enable the emitted radiation to move a from the resonant layer along the direction of the magnetic field lines with the la parallel group velocity component $v_{g\|}$. Equation (4) shows that $v_{g\perp}$ grows rapidly one moves away from the resonance. This would cause a corresponding increase $< r^2 >$ and lead to an enhancement of $\chi$. This effect will be most pronounced in hot plasmas since $v_{g\|} \sim T_e^{1/2}$.

As long as the validity of the *local* dielectric tensor is maintained, the ba resonance structure remains intact, although the resonant surfaces are displaced. Th modification requiring the introduction of the poloidal magnetic field component c be readily incorporated into the model.

The concept of *local* dielectric tensor has to be abandoned when dealing with a ho plasma in toroidal geometry. As a matter of fact, the cyclotron harmonic singularit cease to exist with possibly radical consequences on the electrostatic-wave dispersio relation. Absence of singularities would cause a reduction in $k_\perp$, thereby giving ri to larger perpendicular group velocities in the neighborhood of the resonances and enhancing the intensity of radiative emission. This may be seen by rewriting Eq.(4) in the form

$$v_{g\perp} = -\frac{6}{\sqrt{\pi}} \frac{\omega_p^2}{\omega \omega_c} \frac{n\omega}{k_\perp^4} \frac{1}{r_{ce}^3} \,. \qquad (8)$$

An elegant prescription for dealing with the *non-local* dielectric tensor in a large aspect ratio torus has recently been formulated in Ref.[5].

The foregoing conjectures regarding the role of the rotational transform in radiative transport need to be supported through detailed computations.

## DISCUSSION

These results are of fundamental significance both for thermonuclear fusion research and for the transport of energy across vast reaches of space inhabited by the interstellar plasmas. To my knowledge this is the first manifestation of such a high electron thermal diffusivity which does not invoke either instabilities or non-linear turbulence.

Apparently previous attempts at determining radiative contribution to $\chi$ have tended to underestimate its importance. Several reasons may be cited for this oversight. Bernstein waves are internally trapped within the plasma (with the exception of a narrow window near the upper-hybrid resonance) and lack the ability to communicate with launching/receiving antennas situated outside in the vacuum region. As such they are of no importance for either electron-cyclotron heating or for plasma diagnostics which are the two principal motivations for ray-tracing studies. Thus their potential as

instigators of electron thermal diffusivity has evaded detection. Much work, however, has been dedicated to the radiation and transport caused by the electromagnetic branch of the ordinary and extraordinary waves. The net transport due to these waves is found to be insignificant in the context of thermonuclear fusion [2], since the radiation from these waves originates from a comparatively sparse $k$-space volume.

Experimentally, the electrostatic-electron-Bernstein wave radiation with normalized energy density of

$$u_\varepsilon = \frac{2}{3n_e}\frac{1}{(2\pi)^3}\int_{\mathbf{k}} d\mathbf{k} \sim \mathcal{O}(10^{-6}) \,, \tag{9}$$

would escape observation with the current diagnostic techniques.

The difficulties encountered in carrying out ray tracing using the full hot-plasma dielectric tensor are severe indeed. The choice of the rather restrictive set of parameters in this paper is due to the somewhat fragile constitution of the computational code. The origin of the rays has been confined to the torus axis because the absence of sharp gradients in density and temperature allows computations with larger step sizes. The program is being improved to enable ray tracing in the outer plasma region to facilitate study of the variation of $\chi$ with plasma radius. A more ambitious undertaking that includes rotational transform effects is also being pursued.

The physical picture of electrostatic rays leaving the resonance, getting reflected in the region of zero group velocity (upper-hybrid resonance in the present case) and finally being reabsorbed at the resonant layer, albeit at a different vertical location, is instructive. The largest contribution to $\chi$ comes from the weakly damped components having $2 \lesssim \varsigma = (\omega - n\omega_c)/k_z v_\perp \lesssim 4$ since these rays traverse great distances. The stronger radiation arising near the resonance with $\varsigma \lesssim 2$ makes only a small contribution, since the waves are absorbed almost immediately after they are emitted. Thus the effective value of $< r^2 >$ for the spectrum pertinent in the present context far exceeds its average value. The important implication is that radiation contributing strongly to $\chi$ is carried over large distances. In fact, from every point in the plasma there is a well-directed stream of radiation aimed at precise locations well away from the point of emission. For the case of radiation originating from points other than the median plane, the contributions to $< r^2 >$ are not likely to be symmetrical in the vertical displacement. Thus it may be improper to treat radiative transport as a diffusive process. It has aspects that resemble convection; as such, the energy containment time could be significantly less than that indicated by the diffusivity $\chi$.

Only the fundamental cyclotron emission with the upper-hybrid resonance situated between the fundamental and the first harmonic cyclotron frequency is considered in this paper. Higher harmonics, no doubt, also have their part to play.

To summarize, the radiative transport of electrostatic Bernstein wave emission may hold important clues to the understanding of anomalous thermal transport in magnetoplasmas both in the laboratory and in space.

I am grateful to Prof. R. Wilhelm for his helpful comments.

## REFERENCES

[1] G. Bekefi, in *Radiation Processes in Plasmas*, John Wiley, New York (1966).
[2] M. Bornatici et al., Nuclear Fusion **9**, (1983)1153.
[3] I. B. Bernstein, Phys. Rev. **109**, (1958)10.
[4] S. Weinberg, Phys. Rev. **126**, (1962)1899.
[5] N. I. Grishanov and F. M. Nekrasov, Sov. Phys. Plasma Phys. **16** (1990)230.

# NONLINEAR EXCITATION OF P-POLARIZED SURFACE WAVE IN ANISOTROPIC PLASMA LAYER

Sh. M. Khalil and B. F. Mohamed

Atomic Energy Authority, N.R.C., Plasma Physics Dept.
Cairo - Egypt

Recently, investigation of surface waves and its properties has been a subject of great interest either from the theoretical point of view /1-3/ or in connection with some experiments and applications of plasma devices /4,5/, In addition, to understand the physics of plasma-wall interaction, laser plasma in vicinity of the critical density surface, particle acceleration, determination of the optical characteristics of the medium, some phenomena in space and solar plasmas, we have to deal with surface waves /6,7/.

In case of excitation of surface waves by electromagnetic wave packet /1/, it is shown that, in the linear stage, independent of its polarization, a wave packet propagating along a plasma-vacuum boundary can excite surface waves associated with the boundary in the presence of static magnetic field. If the magnetic field is absence /8/, only P-polarized electromagnetic wave can excite a surface waves.

In the present work, we show that S-polarized electromagnetic waves can also excite surface waves in the presence or absence of magnetic field. In fact, the excitation of surface wave in our case is due to nonlinear interaction of two incident S-polarized electromagnetic waves onto a thin plasma layer and we study the effect of an external time-dependent magnetic field on these surface waves.

Let us assume that waves propagates in the x-y plan and the fields does not depend on coordinate z. The external magnetic field is directed along z-direction and oscillates with frequency equal to the sum of interacting waves frequencies $\omega_1$ and $\omega_2$

$$\vec{\mathcal{H}} = H_{ext.} e^{-i\omega_m t} \vec{e}_z \quad , \qquad \omega_m = \omega_1 + \omega_2 \qquad (1)$$

We shall consider a thin plasma layer satisfy that the unperturbed plasma density $n_o(x)$ equal to zero in the region $x \leq 0$ , a linear function of $x$ ($n_o(x) = N_o \frac{x}{d}$ ) in the region $0 \leq x \leq d$ , and independent of $x$ ($n_o(x) = N_o = Const.$) in the region $x \geq d$ . Ion motion is neglected.

We can write the equation of motion for waves oscillates with combined frequencies $\omega_g = \omega_1 + \omega_2$ and wave number $K_g = K_1 + K_2$ as:

$$\frac{\partial \vec{U}^G}{\partial t} + \sum_{\substack{\alpha,\beta \\ \alpha \neq \beta}}^{1,2} (\vec{U}_\alpha \cdot \vec{\nabla}) \vec{U}_\beta = -\frac{e}{m} \left[ \vec{E}^G + \frac{1}{c} \sum_{\substack{\alpha,\beta \\ \alpha \neq \beta}}^{1,2} \vec{U}_\alpha \times \vec{H}_\beta \right], \quad (2)$$

where, $\vec{U}^G$ and $\vec{E}^G$ are the velocity and electric field components of the generated waves. $\vec{U}_{\alpha,\beta}$ and $\vec{H}_\beta$ are the velocity and magnetic field components of the fundamental S-polarized waves in the linear approximation. It is in agreement with that for unmagnetized plasma /9/, since the magnetic field has no effect on the S-polarized waves in the linear stage. The only change is that we have the exact solution for the electric field components in the inhomogeneous plasma region $0 \leq x \leq d$ when considering a linear density profile, as:

$$E_{lz} = E_{od} \sqrt{\xi}\, J_{1/3}\left(\frac{2}{3}\xi^{3/2}\right), \quad \xi = \left(\frac{K_l^2}{N_l^2 \chi_0}\right)^{1/3} \left[(1-N_l^2)\chi_0 - x\right], \quad (3)$$

$$N_l = \frac{K_l c}{\omega_l}; \quad \chi_0 = \frac{\omega_l^2}{\omega_0^2}; \quad \omega_0^2 = \frac{4\pi e^2 N_0}{m_e}; \quad l = (1,2)$$

Also, reflection coefficient from the plasma layer is:

$$\Gamma_l = \frac{A - i\varkappa_{l0} B}{A + i\varkappa_{l0} B}; \quad A = \left|\frac{\partial}{\partial \xi}\sqrt{\xi}\, J_{1/3}\left(\frac{2}{3}\xi^{3/2}\right)\right|_{\xi=\xi_0}; \quad B = \sqrt{\xi_0}\, J_{1/3}\left(\frac{2}{3}\xi_0^{3/2}\right), \quad (4)$$

$$\xi_0 = (K_l \chi_0 / N_l)^{2/3} (1 - N_l^2); \quad \varkappa_{l0}^2 = K_l^2 \left(\frac{1}{N_l^2} - 1\right).$$

Now, we can derive the following expressions for the generated current density components:

$$J_x^G = i \frac{\omega_{pe}^2}{4\pi\omega_g} \left(E_x^G - J_y'\right); \quad J_y^G = i \frac{\omega_{pe}^2}{4\pi\omega_g} \left(E_y^G + J_x'\right), \quad J_z^G = 0 \quad (5)$$

where,

$$J'_{(x,y)} = \frac{1}{c} \sum_{\substack{\alpha,\beta \\ \alpha \neq \beta}}^{1,2} U_{\alpha z} H_{\beta(x,y)}, \quad \omega_{pe}^2 = \frac{4\pi e^2 n_0(x)}{m_e}$$

It is clear from (5) that the generated waves are of P-polarization. From Maxwell's equations we can obtain the generated electric field components in terms of $H_z^G$ as:

$$E_x^G = -\frac{1}{\epsilon_g}\left(N_g H_z^G + \frac{\omega_{pe}^2}{\omega_g^2} J_y'\right); \quad E_y^G = -\frac{i}{\epsilon_g}\left(\frac{N_g}{K_g}\frac{\partial H_z^G}{\partial x} + i\frac{\omega_{pe}^2}{\omega_g^2} J_x'\right); \quad E_z^G = 0 \quad (6)$$

$$\epsilon_g = 1 - \frac{\omega_{pe}^2}{\omega_g^2}; \quad N_g = \frac{K_g c}{\omega_g}$$

The generated magnetic field $H_z^G$ can be calculated by solving the inhomogeneous differential equation

$$\epsilon_g \frac{\partial}{\partial x}\left(\frac{1}{\epsilon_g}\frac{\partial H_z^G}{\partial x}\right) - \varkappa_g^2 H_z^G = \epsilon_g R(x), \quad (7)$$

$\varkappa_g^2 = k_g^2\left(1-\frac{\epsilon_g}{N_g^2}\right) > 0$ ; $R(x) = -i\frac{2}{\partial x}\left(\frac{\omega_{pe}^2 J_x'}{c\omega_g \epsilon_g}\right) + \frac{\omega_{pe}^2 k_g J_y'}{c\omega_g \epsilon_g} - \left(\frac{\omega_g}{c}\right)^2 H_{ext.}$

$R(x)$ represents a source term due to: (i) nonlinear effects, (ii) presence of the external magnetic field. Even for $H_{ext.}=0$ ; $R(x)\neq 0$ . At $x\leqslant 0$ and $x\geqslant d$ equation (7) has the following solutions:

$$H_z^G = H_0 e^{\varkappa_{0g} x} + \frac{R_0}{\varkappa_{0g}^2} \quad , \quad x\leqslant 0 \qquad (8)$$

$$H_z^G = H_d e^{-\varkappa_{dg}(x-d)} + e^{-\varkappa_{dg}(x-d)} \int_0^x e^{2\varkappa_{dg}x'} dx' \int_0^{x'} e^{-\varkappa_{dg}x''} R_d(x'')\, dx'' \quad , \quad x\geqslant d \qquad (9)$$

$H_0$ and $H_d$ the amplitudes of the generated magnetic field components at the boundaries, and

$\varkappa_{dg}^2 = k_g^2\left(1-\frac{\epsilon_{0g}}{N_g^2}\right)$ ; $\varkappa_{0g}^2 = k_g^2\left(1-\frac{1}{N_g^2}\right)$ ; $\epsilon_{0g} = 1-\frac{\omega_0^2}{\omega_g^2} = Const.$ ;

$R_0 = \left(\frac{\omega_g}{c}\right)^2 H_{ext.}$ ; $R_d = -i\frac{\omega_0^2}{c\omega_g}\left(\frac{2}{\partial x} J_x' + i k_g J_y'\right) - \epsilon_{0g} R_0$

It is clear from (8) and (9) that we obtained solutions describing a surface waves that decay on both sides of the boundaries (i.e., at $x=0$ and $x=d$ ). The first terms on the R.H.S. of (8) and (9) are in agreement with that obtained for unmagnetized plasma /9/, while second terms are due to the effect of the time dependent magnetic field, which leads in this case to the amplification of the generated surface waves.

Let us substitute in (7):

$$H_z^G = \eta Y(\eta) \quad ; \qquad \eta = \epsilon_g x_0' \qquad (10)$$

where, $\epsilon_g = 1-\frac{x}{x_0'}$ ; $x_0' = \left(\frac{\omega_g}{\omega_0}\right)^2 d$ .

If we look for solution near the cutt-off layer, i.e., at $\eta\to 0$ ($x\to x_0'$), we can put equation (7) in the form:

$$\frac{d^2Y(\eta)}{d\eta^2} + \frac{1}{\eta}\frac{dY(\eta)}{d\eta} - \left(k_g^2+\frac{1}{\eta^2}\right)Y(\eta) = \frac{R(\eta)}{\eta} \qquad (11)$$

Accordingly, the exact solution for the magnetic field components of the generated surface wave in the inhomogeneous plasma region $0\leqslant x\leqslant d$ is:

$$H_z^G = k_g\eta \int_0^{k_g\eta} \left[I_1(k_g\eta)\cdot K_1(k_g\eta') - I_1(k_g\eta')\cdot K_1(k_g\eta)\right] R(k_g\eta')\, d\eta' , \qquad (12)$$

$I_1$ and $K_1$ are the modified Bessel functions of the first and second type, and solution (12) is valid for $x_o' - d \leq \eta \leq x_o'$.

In conclusion, nonlinear interaction of S-polarized waves in the presence or absence of external time-dependent magnetic field leads to the generation of P-polarized surface waves. The magnetic field has an amplification effect. It is also clear from (8), at $x \leq 0$, the generated surface wave is associated with P-polarized electromagnetic wave oscillates as $\exp.(ik_y y - i\omega_g t)$ with amplitude $R_o / \alpha_{og}^2$. In addition, we obtained an exact solution for the fields of the generated surface (12) which different from previous works (e.g., /3,9/) where the small parameters $|\alpha_o d| \ll d$ and $|\alpha_g d| \ll 1$ are used to solve equations similar to (7) by the method of successive approximation. In our case, the obtained solutions are general, i.e., it is independent of the relation between the wavelengths of waves and the plasma layer width.

References:


/1/ R. Dragila and S. Vukovic, J. Opt. Soc. Am. (B), 5, 789 (1988).
/2/ L. Stenflo and M.Y. Yu, J. Plasma Physics, 41, 239 (1989).
/3/ Sh.M. Khalil and B.F. Mohamed, International Conference on Phenomena in Ionized Gases (ICPIG XIX), 10-14 July, Belgrade, Yugoslavia, PS/G, 4, 842 (1989).
/4/ R.P.H. Chang and B. Abeles, Plasma Synthesis and Etching of Electronic Materials, Material Research Society (1985).
/5/ R.D. Jones, Surface Waves in Plasma and Solids (ed. S. Vukovic), World Scientific, P. 198 (1986).
/6/ B. Buti, Advances in Space Plasma Physics, World Scientific (1985).
/7/ M.I. Bakunov, V.D. Pikulin and N.S. Stepanov, Soviet J. Plasma Phys., 13, 35 (1987).
/8/ R. Dragila and S. Vukovic, Phys. Rev. Lett., 61, 2759 (1988).
/9/ V.V. Dolgopolov, N.M. El-Siragy and Y.A. Sayed, J. Plasma Physics, 12, 15 (1973).

# NON-LINEAR COUPLING OF DRIFT MODES IN A QUADRUPOLE

J A Elliott, J C Sandeman and G Y Tessema

Department of Pure and Applied Physics, UMIST, Manchester M60 1QD, UK

**ABSTRACT:** We report continuing experimental studies of non-linear interactions of drift waves, with direct evidence of a growth saturation mechanism by transfer of energy to lower frequency modes. Wave launching experiments show that the decay rate of drift waves can be strongly amplitude dependent.

## 1. INTRODUCTION

The UMIST linear quadrupole is a steady-state device in which Hydrogen plasma is continuously injected axially, at one end, from an external duoplasmatron source. The system has been described by Phillips et al (1978) and Daly and Elliott (1982), and consists essentially of two parallel conductors carrying 19,500 A-turns, with current centroids separated by 0.31m. The quadrupole is 2m in length. A cross-section of the magnetic field configuration is shown in Figure.1. The system manifests a range of plasma micro-instabilities, and of these the drift waves particularly have been studied in some detail (Carter et al.,1981). They occur in the shared-flux region, between the separatrix and the critical surface. In this region $T_e$= 0.5 eV and n=$10^{15}m^{-3}$.

The spontaneously excited drift waves are driven by the `dissipative trapped particle' mechanism, and appear in the frequency band 40 - 60 kHz. They are weakly unstable, with $\gamma/\omega$ measured to be ~0.1. They propagate parallel to the machine axis, away from the plasma source, with a phase velocity of ~3 km/s; along the closed magnetic field lines they form standing waves with nodes at the field maxima. The growth rate is a sensitive function of the plasma parameters (Hastie and Taylor 1971), and the drift modes only appear spontaneously when plasma density, collision rates, density and temperature gradients are in appropriate ranges.

Also in this region is found a low frequency band (1 - 5 kHz) of flute-like modes. They are fluid-unstable, with $\gamma/\omega$ ~1, and wavelength 0.2 - 1 m. These modes have been shown (Crossley et al 1989a) to play an important role in the non-linear interaction of the drift modes.

Previous studies (Greb and Rusbridge 1988a,b, Crossley et al 1989a,b) of non-linear interactions between drift modes in this system were performed by measuring the bi-spectra of the intrinsic modes. We have shown (Tessema et al 1989) that drift waves can be launched from antennae in the plasma over a much wider frequency range (20 - 70 kHz) than covered by the intrinsic modes. The coherence of the launched waves makes their study much easier than for the intrinsic modes. Non-linear effects are readily observable, and measurable with accuracy, which should greatly facilitate the testing of theoretical models. The studies give a valuable insight into the manner in which such drift modes contribute to the dissipation of the free energy of confinement, and clearly show that energy loss is initially by a cascade downwards in frequency among drift modes, mediated by

coupling with the low frequency flutes. We postulate that the energy is then dissipated by ion Landau damping, which increases with decreasing frequency until the drift mode cut-off is reached at about 15 kHz, the ion bounce frequency.

## 2. THE WAVE-LAUNCHING SYSTEM

The observed frequency of the intrinsic drift waves is between 40 and 60 kHz, and the wavelength along the direction of propagation is about 60 mm. A launching system has been constructed using two flag probes, each 30 x 20 mm, aligned with the long dimension along the radius of the vessel, and the short dimension parallel to the field. The flags are placed at the minimum field points, on opposite sides of the system, and lying on the same flux tube. The system draws no net current from the plasma; current is passed from one flag to the other through the plasma by means of an isolating transformer. In the experiments described, the voltage applied between the flags was sinusoidal, and typically 0 - 5 V peak-to-peak. The corresponding current was 0 - 3 mA. The launching mechanism has been discussed in a previous report (Tessema et al 1989).

The launched waves were detected using a small cylindrical Langmuir probe, 1mm in diameter and 1mm in length, and biassed to -60 V. The signal from the probe, essentially proportional to the plasma density, was fed to a lock-in amplifier, the launching signal being used as the reference. The lock-in amplifier yielded the wave amplitude and phase relative to the launcher, as a function of distance. In this way a plot of the spatial wave in the z-direction was obtained.

If non-linear interactions are occurring in the system, we expect that the decay/growth rate will be a function of the launching amplitude as well as the frequency, and measurements have confirmed this.

## 3. DRIFT WAVE BLOCKING

We have observed that the presence of the two 3 x 2 cm floating flag probes in the drift wave region completely prevents the propagation of the intrinsic waves past the flags. Immediately downstream of the flags, the plasma is quiescent for about 3 cm, and then the drift modes begin to reappear. The reason for this stabilising effect is not understood, but it offers a very powerful means of studying drift wave growth in an unstable but quiescent plasma. Waves may also be launched into such plasma, from the blocking flags. Figure [2] shows one observation of the spatial re-development of the intrinsic power spectrum. This may be interpreted as the time development.

The drift peak appears after about 17 $\mu$s (i.e.3 cm), and grows to a very sharp peak initially. It subsequently broadens, but only in the direction of decreasing frequency. This is consistent with the model being developed, in which the drift wave at frequency $\omega_1$ couples non-linearly with a low frequency flute mode at frequency $\omega_2$ giving rise to a drift mode at the lower frequency $\omega_1 - \omega_2$.

The drift instability thus appears, as suggested, to saturate by transfering energy to lower frequencies by coupling with flute modes. The

rate of re-growth of the drift modes varies markedly with plasma conditions, and is the subject of further study.

## 4. MEASUREMENT OF THE DECAY RATE

Typical wave traces are shown in figure [3]: the "near field" within one wavelength of the antennae behaves in a complex manner, and we have taken our data only from the "far field" region. Growth is never observed, even when a wave is launched in the presence of a high amplitude of intrinsic drift modes. The reason is not yet understood. The decay constant is shown in figure [4] as a function of launching current, for three different frequencies. For small currents, when non-linear effects should be negligible, the data is not precise enough to reveal any marked dependence on frequency or amplitude. Above ~0.8 mA, the decay constant begins to increase with frequency, showing a marked increase at 60 kHz, the upper limit of the intrinsic drift modes. These results suggest therefore that the upper cut-off is due to strong damping through some non-linear process not yet identified, but which may be the cascade process of Crossley et al (1989a).

The decay rate curves for higher frequencies show evidence of saturation: as the launching current increases, $\gamma$ increases to a saturation value which depends on frequency. At 30 kHz, the data indicates that the damping decreases with increasing amplitude, a result consistent with a non-linear ion Landau damping mechanism.

## 5. MEASUREMENT OF LAUNCHING EFFICIENCY

Knowing the decay rate, it is possible to project the launched wave back to the origin assuming exponential decay, and calculate the effective amplitude at the launching flags. Figure [5] shows the results. For launching currents below 1.7 mA the amplitude is a linear function of launching current for all frequencies; the availability of a linear launching mechanism is important for the study of non-linear effects in the wave phenomena. Above 1.7 mA, the efficiency falls off. The reason for this is not yet clear, but may reflect the bulk disturbance of plasma properties by the injection of the drift wave.

## 6. REFERENCES


Carter P S, Edwards D N, Mossack P R, Rusbridge M G and Hastie R J, (1981) Plasma Physics 23, 819.

Crossley F J, Rusbridge M G and Uddholm P (1989), "Non-linear Vlasov Plasmas" ed. Doveil (proceedings of Cargese workshop 1988) p.327

Crossley F J, Duncan P, Elliott J A, Khalid M, Rusbridge M G, Tessema G Y and Uddholm P (1989), Proc. of Cadarache Workshop on Electrostatic Turbulence p.39

Daly E J and Elliott J A (1982) Plasma Physics 24, 923.

Greb U and Rusbridge M G (1988), Plasma Phys. Cont. Fus. 30, 537

Greb U and Rusbridge M G (1988), Plasma Phys. Cont. Fus. 30, 551

Hastie R J and Taylor J B (1971) Plasma Physics 13, 265.

Phillips K, Rusbridge M G, and Young K M (1978) Plasma Physics 20, 653.

Tessema G Y, Elliott J A and Rusbridge M G (1989), Plasma Phys. Cont. Fus. 31, 2177

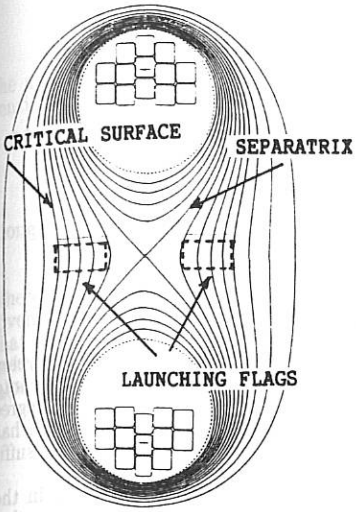


Fig 1: The quadrupole field

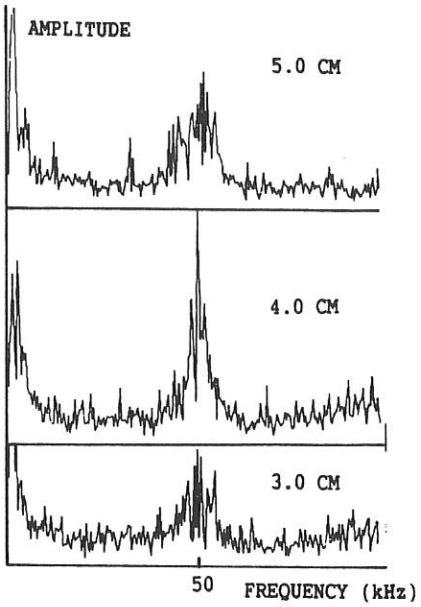


Fig 2: Re-growth of the drift wave

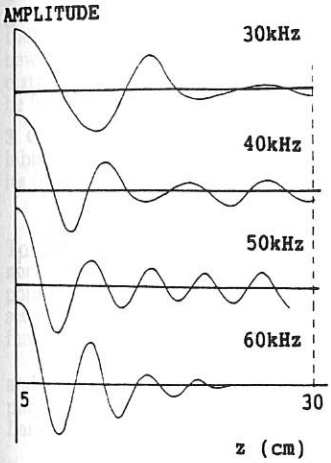


Fig 3: Typical wave traces

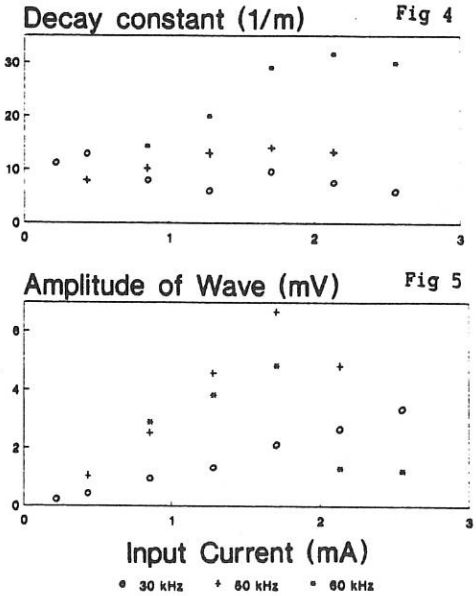

# A TWO–DIMENSIONAL COLLISIONLESS MODEL OF THE SINGLE–ENDED Q–MACHINE

H. Pedit and S. Kuhn

*Institute for Theoretical Physics, University of Innsbruck*
*Technikerstrasse 25, A–6020 Innsbruck, Austria*

**1. Introduction and summary.** Q–Machines have been around for almost thirty years /1,2/, but it appears that there exist no comprehensive theoretical models taking into account their considerable geometrical and physical complexity with a reasonable degree of self–consistency. The (one–dimensional) "collisionless plane–diode model", e.g., has proved useful but its validity is restricted to certain *longitudinal* phenomena in "sufficiently" *low–density* machines /3/.

Accordingly, to make progress in the understanding of Q–machines (and, in the longer run, of bounded plasma systems in general), we find it indispensable to develop and study models that are more realistic with respect to (i) the geometry, (ii) the physics, and (iii) the dynamics of these devices. In view of the obvious complexity of such an undertaking, we believe that the most promising strategy is that of limited but still substantial steps of improvement.

In the present work, we develop a two–dimensional slab model for the dc states of the low–density single–ended Q–machine /4/ by adding to the (axial) x–coordinate /3/ a y–coordinate that is still cartesian but simulates the radial coordinate of the cylindrical Q–machine geometry, cf. Fig. 1. A uniform magnetic field B is applied in the x–direction, and the plasma is assumed to be sufficiently rarefied ($n_P \leq 10^8$ cm$^{-3}$ for typical Q–machines) to be tractable as collisionless. Both the ions and the electrons leave the emitter with half Maxwellian distribution functions corresponding to the hot–plate temperature T, but their emission densities may be different. All particles reaching either the emitter ("hot plate") or the collector ("cold plate") are absorbed. The system is specified by prescribing the following parameters: axial length L, emitter "radius" $R_e$, collector "radius" $R_c$, wall "radius" $R_w$; emitter potential $\Phi_e \equiv 0$, collector potential $\Phi_c$, wall potential $\Phi_w$; emitter temperature T, electron emission density $n_{e0}^+$, ion emission density $n_{i0}^+$ (or, equivalently, the "neutralization parameter" $\alpha \equiv n_{i0}^+/n_{e0}^+$).

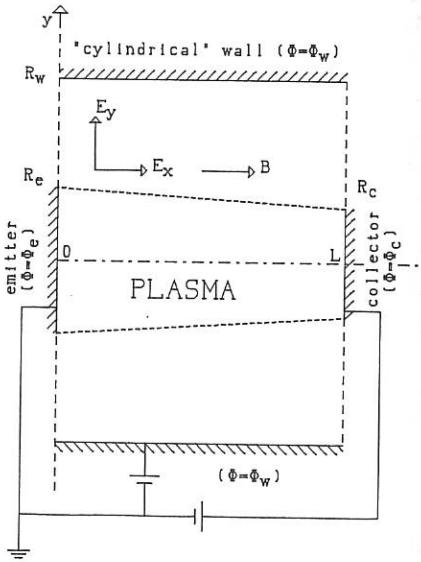


Fig. 1

In what follows, our method of calculating self–consistent collisionless dc states of the above configuration is described, and first numerical results on axial and radial potential distributions are presented.

**2. Method of solution.** By integrating the Vlasov equation

$$\left[\frac{\partial}{\partial t} + \mathbf{v}\cdot\nabla_r + \frac{q_a}{m_a}\mathbf{E}(\mathbf{x},t)\cdot\nabla_v\right] f_a(\mathbf{x},\mathbf{v},t) \equiv \frac{d_a}{dt} f_a(\mathbf{x},\mathbf{v},t) = 0 \qquad (1)$$

along the species–a particle trajectory passing through the point $(\mathbf{x},\mathbf{v},t)$, we obtain

$$f_a(\mathbf{x},\mathbf{v},t) = f_{a0}(\mathbf{x}_{a0},\mathbf{v}_{a0},t_{a0}) , \qquad (2)$$

where $(\mathbf{x}_{a0},\mathbf{v}_{a0},t_{a0})$ is some previous point on the trajectory, at which $f_a$ is assumed to be given in the form $f_{a0}$. Tracing the trajectory back in time and defining $(\mathbf{x}_{a0},\mathbf{v}_{a0},t_{a0})$ as that point where it first intersects the emitter or some other material boundary (where f is known to be half Maxwellian or zero, respectively), Eq. (2) enables us to determine $f_a(\mathbf{x},\mathbf{v},t)$. From this and Poisson's equation we obtain the system of equations

$$n_a(x,y) = n_{a0}^{+}\int d^3v\, f_a(x,y,\mathbf{v}) = n_{a0}^{+}\int d^3v\, f_{a0}(x_0,y_0,\mathbf{v}_0) \qquad (a = e,i) \qquad (3a,b)$$

$$\nabla^2\Phi(\mathbf{x}) = -\frac{\rho(\mathbf{x})}{\epsilon_0} = \frac{e}{\epsilon_0}[n_e(\mathbf{x}) - \alpha n_i(\mathbf{x})] \qquad (4)$$

with the boundary conditions

$$\Phi(0,0\le|y|\le R_e) = 0 , \quad \Phi(0,R_e<|y|\le R_w) = \Phi_e + (\Phi_w-\Phi_e)\,(|y|-R_e)/(R_w-R_e)$$
$$\Phi(L,0\le|y|\le R_c) = \Phi_c , \quad \Phi(L,R_c<|y|\le R_w) = \Phi_c + (\Phi_w-\Phi_c)\,(|y|-R_c)/(R_w-R_c) \qquad (5)$$
$$\frac{\partial\Phi}{\partial y}(x,0) = 0 , \qquad \Phi(x,R_w) = \Phi_w .$$

This system is solved numerically by the following iterative scheme: Given an initial guess for the potential distribution, the particle densities are calculated according to (3), then from solving (4) a new potential consistent with these densities is obtained, with it new particle densities are found via (3), etc., until self–consistent potential and density distributions are reached. Due to the y–symmetry of the problem, the solution need to be found only in the upper half ($y \ge 0$).

**3. Calculating the electron and ion densities.** Due to their large mass, ions typically exhibit small velocities and large Larmor radii, so that each ion trajectory is traced back to its point of emission by *direct* numerical backward integration of the equation of motion

$$m_i\frac{d\mathbf{v}}{dt} = q_i[\mathbf{E}(\mathbf{x}) + \mathbf{v}\times\mathbf{B})] . \qquad (6)$$

To this end, velocity space (parametrized by the parallel velocity component $v_p$, the normal velocity component $v_n$, and the polar angle $\vartheta$) is discretized. If for some phase point $(\mathbf{x},v_p,v_n,\vartheta)$ the emission point is located outside the emitter, the ion distribution is set equal to zero; otherwise, it is set equal to the half Maxwellian emission distribution function. Summing up over velocity space yields $n_i(\mathbf{x})$.

For the electron trajectories, which are typically characterized by fast gyrations and small Larmor radii, direct trajectory integration would be inappropriate so we simplify matters by using a guiding–center approach. Electron motion is decomposed into a Larmor gyration and a guiding–center component:

$$\mathbf{x} = \boldsymbol{\rho} + \mathbf{R} , \qquad \mathbf{v} = \mathbf{v}_l + \mathbf{v}_{gc} . \qquad (7a,b)$$

Inserting this into the electon equation of motion, expanding the guiding–center velocity in the form

$$\mathbf{v}_{gc} = \mathbf{v}_p + \frac{\mathbf{E}_n\times\mathbf{B}}{B^2} - \frac{1}{\Omega}\frac{d}{dt}\frac{(\mathbf{E}_n\times\mathbf{B})\times\mathbf{B}}{B^3} - \frac{1}{\Omega^2}\frac{d^2}{dt^2}\frac{\mathbf{E}_n\times\mathbf{B}}{B^2} - \frac{1}{\Omega^3}\frac{d^3}{dt^3}\frac{(\mathbf{E}_n\times\mathbf{B})\times\mathbf{B}}{B^3} - O(\frac{1}{\Omega^4}) \qquad (8)$$

(where $\Omega \equiv -eB/m_e$), and averaging over the gyrophase we obtain

$$\left\langle \frac{dv_{gc1}}{dt} \right\rangle \equiv \frac{dV_1}{dt} = -\frac{\Omega}{B}\frac{\partial\tilde{\Phi}}{\partial R_1} \tag{9a}$$

$$\langle v_{gc2}\rangle \equiv V_2 = -\frac{1}{\Omega B}(\mathbf{R}\cdot\nabla_r)\frac{\partial\tilde{\Phi}}{\partial R_2} - \frac{1}{\Omega^3 B}\left[(\frac{d^3\mathbf{R}}{dt^3}\cdot\nabla_r)\frac{\partial\tilde{\Phi}}{\partial R_2} + 3(\frac{d^2\mathbf{R}}{dt^2}\cdot\nabla_r)(\frac{d\mathbf{R}}{dt}\cdot\nabla_r)\frac{\partial\tilde{\Phi}}{\partial R_2} + (\frac{d\mathbf{R}}{dt}\cdot\nabla_r)(\frac{d\mathbf{R}}{dt}\cdot\nabla_r)(\frac{d\mathbf{R}}{dt}\cdot\nabla_r)\frac{\partial\tilde{\Phi}}{\partial R_2}\right] \tag{9b}$$

$$\langle v_{gc3}\rangle \equiv V_3 = \frac{1}{B}\frac{\partial\tilde{\Phi}}{\partial R_2} - \frac{1}{\Omega^2 B}\left[(\frac{d^2\mathbf{R}}{dt^2}\cdot\nabla_r)\frac{\partial\tilde{\Phi}}{\partial R_2} + (\frac{d\mathbf{R}}{dt}\cdot\nabla_r)(\frac{d\mathbf{R}}{dt}\cdot\nabla_r)\frac{\partial\tilde{\Phi}}{\partial R_2}\right], \tag{9c}$$

where

$$\tilde{\Phi}(\mathbf{R}) \equiv \langle\Phi(\mathbf{x})\rangle = \frac{1}{2\pi}\int_0^{2\pi} d\vartheta\,\Phi(\mathbf{R}+\rho) = \Phi(\mathbf{R}) + \frac{\rho_1^2}{4}\left[\frac{\partial^2}{\partial R_2^2} + \frac{\partial^2}{\partial R_3^2}\right]\Phi(\mathbf{R}) \tag{10}$$

denotes the gyrophase average of $\Phi(\mathbf{x})$. On neglecting terms containing $V_2$ oder derivatives thereof we obtain the following three equations governing the guiding–center motion:

$$\frac{dV_1}{dt} = -\frac{\Omega}{B}\frac{\partial\tilde{\Phi}}{\partial R_1} \tag{11a}$$

$$V_2 = V_1\left[-\frac{\partial^2\tilde{\Phi}}{\partial R_1\partial R_2} + \frac{1}{\Omega B}\frac{\partial^2\tilde{\Phi}}{\partial R_1^2}\frac{\partial^2\tilde{\Phi}}{\partial R_1\partial R_2} + \frac{3}{\Omega B}\frac{\partial\tilde{\Phi}}{\partial R_1}\frac{\partial^3\tilde{\Phi}}{\partial R_1^2\partial R_2} - \frac{V_1^2}{\Omega^2}\frac{\partial^4\tilde{\Phi}}{\partial R_1^3\partial R_2}\right]\times\left[\Omega B + \frac{\partial^2\tilde{\Phi}}{\partial R_2^2} - \frac{1}{\Omega B}\left[\frac{\partial^2\tilde{\Phi}}{\partial R_1\partial R_2}\right]^2\right]^{-1} \tag{11b}$$

$$V_3 = \frac{1}{B}\frac{\partial\tilde{\Phi}}{\partial R_2} - \frac{1}{\Omega^2 B}\left[\dot{V}_1\frac{\partial^2\tilde{\Phi}}{\partial R_1\partial R_2} + V_1^2\frac{\partial^3\tilde{\Phi}}{\partial R_1^2\partial R_2}\right]. \tag{11c}$$

These simplifications are realistic because the main portion of the velocity perpendicular to the magnetic field is already contained in the Larmor motion. Therefore, the normal component of the guiding–center velocity is small as compared to the parallel component.

Now the electron density at some position $\mathbf{x}$ can be obtained from (2) by numerically integrating Eqs. (11), superimposing the Larmor motion, and finally summing up over velocity space.

**4. Relaxation scheme for solving Poisson's equation.** Discretizing Poisson's equation (4) on a two–dimensional grid with variable meshwidths and introducing a relaxation parameter $\omega$ (with $0 < \omega < 2$), whose proper choice will accelerate convergence, we obtain

$$\Phi_{ij}{}^n = (1-\omega)\Phi_{ij}{}^a + \frac{\omega}{a_{i+1}a_i + b_{j+1}b_j}\left[\frac{b_{j+1}b_j}{a_{i+1}+a_i}(a_i\Phi_{i+1j}{}^a + a_{i+1}\Phi_{i-1j}{}^n) + \frac{a_{j+1}a_i}{b_{j+1}+b_j}(b_j\Phi_{ij+1}{}^a + b_{j+1}\Phi_{ij-1}{}^n) + \frac{a_{i+1}a_j b_{j+1}b_j}{2\epsilon_0}\rho_{ij}\right], \tag{12}$$

where $a_i$ and $b_j$ are the meshwidths in the x– and y–directions, respectively, and $\Phi_{ij}{}^a$ and $\Phi_{ij}{}^n$ are the potential values before and after some iteration step. After several sweeps, Eq. (12) yields a potential distribution consistent with the given charge distribution.

**5. Results and discussion.** In Figs. 2(a) and 2(b), axial and radial potential distributions are shown for a configuration characterized by the following parameters: $L = 5$ mm, $R_e = R_c = 1.5$ cm, $R_w = 6.5$ cm; $\Phi_e = 0$, $\Phi_c = -3$ V, $\Phi_w = 0$; $T = 2000$ K, $n_{e0}{}^+ = 5.12\times10^8$ cm$^{-3}$, and $\alpha = 0.1$. For the numerical calculations, the relevant (x,y)–region ($0 \le x \le L$, $0 \le y \le R_w$) was discretized by a 17×22 mesh with enhanced x–resolution near the emitter and enhanced y–resolution in the plasma–vacuum transition region. Velocity space was discretized by a 8×9×11 grid for $v_P$, $v_n$ and $\vartheta$, respectively.

Since the particular system presented here is among the first ones we have con–

sidered in detail, we have chosen it extremely short (L = 5 mm is unrealistic for existing Q–machines but still realizable in principle) so as to minimize computational expense and concentrate on getting our – rather complex – method working properly. Starting out from a bilinear initial approximation to the potential distribution, the results shown here are typically obtained after 6 iterations. Each iteration required about 80 minutes of CPU time on the Innsbruck University Cyber 840 mainframe computer (electron–density distribution 35 min, ion–density distribution 45 min, potential distribution 2 min).

The axial potential distribution in the center of the plasma (y = 0) exhibits a point of inflection at x ≃ 1.5 mm. The related potential value ("plasma potential") is $\Phi_P = -0.76$ V, in good agreement with one–dimensional theory /3/. Radially, the potential is practically constant near y = 0 but jumps at the plasma–vacuum transition (y ≃ $R_e$), where a radial space–charge double layer exists due to the combined effects of electron drift and the vastly different electron and ion Larmor radii ($\rho_e \simeq 7$ μm, $\rho_i \simeq 1.87$ mm, hence $\rho_i/\rho_e \simeq 270$). Near the emitter, where most ions have performed only a fraction of a Larmor gyration, the plasma–vacuum transition is sharpest. Far from the emitter, where most electrons cannot get due to the negative potential, the potential distribution is solely determined by the ion–density distribution and the boundary conditions.

Similar computations for longer systems and various wall potentials are now under way. We believe that the method outlined here is open to various generalizations (e.g., to collisional plasmas or truly cylindrical geometry) and, with appropriate modifications, applicable to many bounded–plasma configurations of interest, such as fusion plasmas near limiters or first walls.

**Acknowledgment**. This work was partly supported by Austrian Research Fund project No. P7005.

/1/ N. Rynn and N.D. D'Angelo, Rev. Sci. Instr. **31**, 1326 (1960).

/2/ R.W. Motley, *Q Machines* (Academic Press, New York, 1975).

/3/ S. Kuhn, Plasma Phys. **23**, 881 (1981).

/4/ J.M. Buzzi, H.J. Doucet, and D. Grésillon, Phys. Fluids **13**, 3041 (1970).

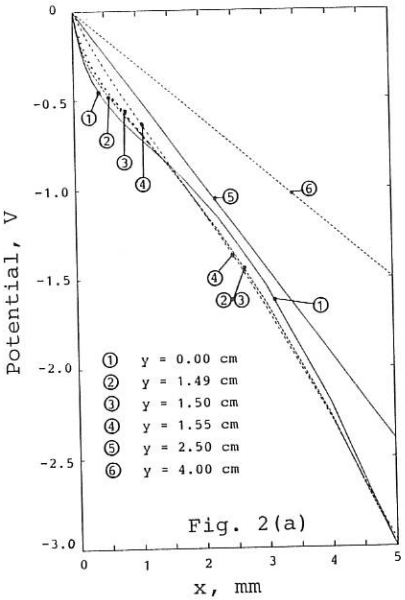


Fig. 2(a)

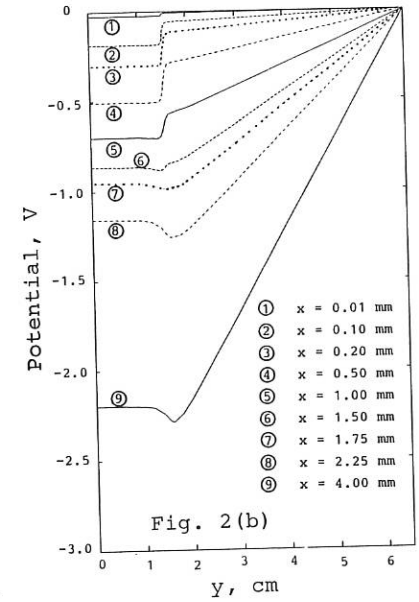


Fig. 2(b)

# ION–ACOUSTIC EIGENMODES IN A COLLISIONLESS BOUNDED PLASMA

S. Kuhn, N. Schupfer, M.A.M. Santiago,* and A.S. de Assis*

Institute for Theoretical Physics, University of Innsbruck
A–6020 Innsbruck, Austria

*Instituto de Física, Universidade Federal Fluminense
24020 Niterói, RJ, Brazil

**1. Introduction and summary.** This work is based on the integral–equation method proposed in Ref. /1/ for solving the general linearized perturbation problem for a one–dimensional, uniform collisionless plasma with thin sheaths, bounded by two planar electrodes. In a first, predominantly analytical application /2/, this method was used to analyze the Pierce diode with a non–trivial external circuit. Here, on the other hand, we apply the method to *ion–acoustic* eigenmodes in a one–dimensional, collisionless bounded plasma consisting of non–drifting thermal electrons and a cold ion beam propagating through them. This case is of relevance in the context of both Q– and DP–machines. First numerical results include eigenfrequencies and related eigenmode profiles. For the specific situation considered, these modes turn out to be unstable, but it is concluded that more investigations are needed to substantiate this finding. A more detailed account will be given elsewhere /3/.

**2. The collisionless plane–diode model; linearized basic equations.** We consider a one–dimensional diode as shown in Fig. 1, where the surfaces of the (ideally conducting) electrodes are located at x = 0 ("left–hand electrode") and x = L ("right– hand electrode"), and the far ends of the electrodes are connected through an external circuit with specified properties. The intervening space ("interelectrode region", "diode gap") is filled with a collisionless plasma consisting of $n_s$ particle species. The particle charge and mass of species $\sigma$ ($\sigma = 1, \ldots, n_s$) are denoted by $e^\sigma$ and $m^\sigma$, respectively. Figure 1. shows the model geometry, with a monotonically decreasing equilibrium potential distribution as an example.

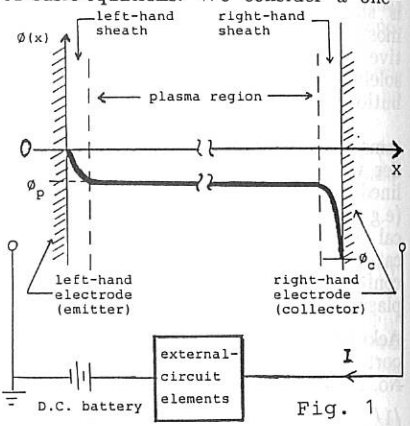

Fig. 1

Each physical quantity Q involved is decomposed in the form

$$Q(x,v,t) = \bar{Q}(v) + \tilde{Q}(x,v,t) , \quad (2.1)$$

where $\bar{Q}$ is the (given) time–independent, or "equilibrium" part, and $\tilde{Q}$ is the small–amplitude perturbation, which is to be calculated. For the equilibrium state we assume a uniform plasma with two "thin" sheaths adjacent to the electrodes. This "uniform–plasma, thin–sheath approximation" is of relevance, e.g., for longitudinal modes in a single–ended Q–machine at "moderate" values of the interelectrode bias, whereas for "very high" values the sheath widths may no longer be negligible /4,5/.

The small–amplitude longitudinal perturbations in the collisionless plane diode are governed by the following set of equations /1/:

$$\frac{\partial \tilde{f}^{\sigma}}{\partial t} + v\frac{\partial \tilde{f}^{\sigma}}{\partial x} = -\frac{e^{\sigma}}{m^{\sigma}} \bar{f}_v^{\sigma} \tilde{E} \qquad \left[\begin{array}{l}\text{linearized Vlasov equa-}\\ \text{tions } (\sigma = 1, \ldots, n_s)\end{array}\right] \qquad (2.2)$$

$$\frac{\partial \tilde{E}}{\partial x} = 4\pi \sum_{\sigma=1}^{n_s} e^{\sigma} \int_{-\infty}^{\infty} dv\, \tilde{f}^{\sigma} \qquad [\text{Poisson's equation}] \qquad (2.3)$$

$$\frac{1}{4\pi}\frac{\partial \tilde{E}(x,t)}{\partial t} + \sum_{\sigma=1}^{n_s} e^{\sigma} \int_{-\infty}^{\infty} dv\, v\, \tilde{f}^{\sigma} = \tilde{j}_e(t)\,, \qquad \left[\begin{array}{l}\text{equation of total-}\\ \text{current conservation}\end{array}\right] \qquad (2.4)$$

$$-\int_{0_+}^{L_-} dx\, \tilde{E}(x,t) = \hat{Z}\{\tilde{j}_e(t)\}\,, \qquad [\text{external–circuit equation}] \qquad (2.5)$$

$$\tilde{f}_l^{\sigma}(v>0,t) = \tilde{f}_{lg}^{\sigma}(v,t) + \sum_{\sigma'=1}^{n_s} \int_{-\infty}^{0} dv'\, b_l^{\sigma\sigma'}(v,v')\, \tilde{f}_l^{\sigma'}(v',t) \qquad \left[\begin{array}{l}\text{left–hand particle}\\ \text{boundary condition}\end{array}\right] \qquad (2.6)$$

$$\tilde{f}_r^{\sigma}(v<0,t) = \tilde{f}_{rg}^{\sigma}(v,t) + \sum_{\sigma'=1}^{n_s} \int_{0}^{\infty} dv'\, b_r^{\sigma\sigma'}(v,v')\, \tilde{f}_r^{\sigma'}(v',t) \qquad \left[\begin{array}{l}\text{right–hand particle}\\ \text{boundary condition}\end{array}\right] \qquad (2.7)$$

where $E(x,t) = \bar{E}(x,t) + \tilde{E}(x,t)$ is the electrostatic field, $f^{\sigma}(x,v,t) = \bar{f}^{\sigma}(v) + \tilde{f}^{\sigma}(x,v,t)$ is the velocity distribution function of species $\sigma$, $\bar{f}_v^{\sigma}(v) \equiv d\bar{f}^{\sigma}(v)/dv$; $\tilde{j}_e(t)$ is the perturbation of the external–circuit current density (i.e., of the external–circuit current per unit electrode area), $\hat{Z}$ is the (linear) "impedance operator" of the "extended external circuit" (by which we mean the "real" external circuit plus the two electrode sheaths); $\tilde{f}_{lg}^{\sigma}$ and $\tilde{f}_{rg}^{\sigma}$ are externally generated (and, hence, explicitly given) perturbations, and the "generalized reflection–coefficient functions" $b_l^{\sigma\sigma'}(v>0,v'<0)$ and $b_r^{\sigma\sigma'}(v<0,v'>0)$ essentially represent the probabilities for a sheath–bound particle of species $\sigma'$ with velocity $v'$ to "produce" a plasma–bound particle of species $\sigma$ with velocity $v$. Clearly, $\tilde{f}_l^{\sigma}(v>0,t)$ and $\tilde{f}_r^{\sigma}(v<0,t)$ are the perturbations of the distribution functions of the *plasma–bound* particles at the sheath–plasma boundaries, and hence may be sloppily referred to as "injection distribution functions".

Equations (2.2) to (2.7) constitute a complete system of evolution equations (including boundary conditions) for the perturbations. In /1/ they have been transformed into $(2+2n_s)$ coupled linear integral equations for the $(2+2n_s)$ time Laplace transforms $\tilde{j}(\omega)$, $\tilde{E}(x,\omega)$, $\tilde{f}_l^{\sigma}(v>0,\omega)$, and $\tilde{f}_r^{\sigma}(v<0,\omega)$. These "Laplace–transformed integral equations" [Eqs. (37)–(40) of Ref. /1/] are the basis of our analysis, and their specific form appropriate to the physical situation considered here (Sec. 3) will be given in Sec. 4.

**3. Special case: ion–acoustic oscillations in the negatively biased single–ended Q–machine.** For Q–machines under a wide range of operating conditions, the sheath regions are usually far less extended than the plasma region, so that the uniform–plasma, thin–sheath approximation is applicable. Assuming half–Maxwellian emission from the hot plate (whose temperature is T), the injection distribution functions at the left–hand plasma boundary are cut–off Maxwellians for both the electrons and the ions /5/. At the right–hand boundary plane ($x = L_-$), on the other hand, all ions are absorbed, while all electrons are specularly reflected due to the cold–plate sheath, cf. Fig. 1. A quantitative analysis of this model has been given in Ref. /5/.

In this first approach to the problem, we try to simplify our model as much as possible, while still keeping the essential physics. In particular, we approximate the electron velocity distribution function by the "waterbag"

$$\bar{f}^{e}(v) = \bar{n}_p[U(v+\bar{v}_{cw}^{e}) - U(v-\bar{v}_{cw}^{e})] \,/\, (2\bar{v}_{cw}^{e}) \qquad (3.1)$$

with $n_p$ the equilibrium plasma density and $\bar{v}_{cw}^{e} = \sqrt{(3kT/m)}$ the waterbag cutoff

velocity, and the ion distribution by the cold beam

$$\bar{f}^i(v) = \bar{n}_P\, \delta(v-\bar{v}^i)\,, \tag{3.2}$$

with $\bar{v}^i$ the ion average velocity. For the initial perturbations of the distribution functions we assume

$$\tilde{f}^e_i(x,v) = 0 \quad \text{and} \quad \tilde{f}^i_i(x,v) = \delta(x-\xi)\,\delta(v-\bar{v}^i)\,, \tag{3.3a,b}$$

which, although the simplest possible perturbation, is sufficient to excite all eigenmodes of the system. Since we do not allow for any *externally imposed* modulation of particle injection through the boundary planes, we have that $\tilde{f}^e_{lg} = \tilde{f}^i_{lg} = \tilde{f}^e_{rg} = \tilde{f}^i_{rg} \equiv 0$. Most of the *generalized reflection–coefficient functions* introduced in Eqs. (2.6) and (2.7) vanish ($b_l^{ei} = b_l^{ie} = b_r^{ei} = b_r^{ie} = b_l^{ee} = b_l^{ii} = b_r^{ii} \equiv 0$), and the only nontrivial one is

$$b_r^{ee}(v<0,v'>0) = \delta(v+v')\,. \tag{3.4}$$

Finally, the external circuit is taken to be a *short–circuit*, which corresponds to $\hat{Z} \equiv 0$.

**4. Solving the eigenmode problem by means of the integral–equation method.** With the specifications of Sec. 3, the Laplace–transformed integral equations yield the explicit relations

$$\tilde{f}^e_l(v>0,\omega) = \tilde{f}^i_l(v>0,\omega) = \tilde{f}^i_r(v<0,\omega) = 0\,. \tag{4.1a–c}$$

and the "reduced" system of coupled integral equations

$$\int_{0_+}^{L_-} dx'\,\tilde{E}(x',\omega) = 0\,, \qquad \text{[external–circuit equation]} \tag{4.2}$$

$$-k_5(x,\omega)\tilde{j}_e(\omega) + \tilde{E}(x,\omega) + \mathscr{S}_0(x,[x'],\omega)\,\tilde{E}([x'],\omega) + \mathscr{V}^e_{0r}(x,[v<0],\omega)\,\tilde{f}^e_r(v,\omega) = \tilde{k}_8(x,\omega)\,, \qquad \text{[Poisson's equation]} \tag{4.3}$$

$$\mathscr{S}^e_r(v<0,[x'],\omega)\,\tilde{E}([x'],\omega) + \tilde{f}^e_r(v,\omega) = 0\,, \qquad \begin{bmatrix}\text{right–hand electron}\\ \text{boundary condition}\end{bmatrix} \tag{4.4}$$

from which the remaining unknowns $\tilde{j}_e(\omega)$, $\tilde{E}(x,\omega)$ and $\tilde{f}^e_r(v,\omega)$ must be determined. Here, $k_5$ and $\tilde{k}_8$ are known functions, $\mathscr{S}_0$ and $\mathscr{S}^e_r$ are known x–space operators, and $\mathscr{V}^e_{0r}$ is a known v–space operator. While for the full details of these functions and operators the reader has to be referred to Refs. /1/ and /3/, we present here, as an example, only the operator $\mathscr{S}^e_r$:

$$\mathscr{S}^e_r(v<0,[x'],\omega)\,\tilde{E}([x'],\omega) = \frac{en_P}{2m^e(\bar{v}^e_{cw})^2}\,\delta(v+\bar{v}^e_{cw})\int_{0_+}^{L_-} dx'\,\exp\left[i\omega\frac{L-x'}{\bar{v}^e_{cw}}\right]\tilde{E}(x',\omega)\,. \tag{4.5}$$

Via appropriate basis–set expansions of all functions and operators involved, Eqs. (4.2–4) are then transformed into a system of linear algebraic equations for the $\omega$–dependent expansion coefficients, which can be written as the matrix equation

$$\mathscr{D}(\omega)\cdot\tilde{u}(\omega) = \tilde{k}(\omega),\ \text{with}\ \mathscr{D}(\omega) \equiv \begin{bmatrix} 0 & L\bar{\varphi}^T & 0^T \\ -k_5 & 1+\mathscr{S}_0 & \mathscr{V}^e_{0r} \\ 0 & \mathscr{S}^e_r & 1 \end{bmatrix},\ \tilde{k}(\omega) \equiv \begin{bmatrix} 0 \\ \tilde{k}_8 \\ 0 \end{bmatrix},\ \tilde{u}(\omega) \equiv \begin{bmatrix} \tilde{j}_e \\ \tilde{E} \\ \tilde{f}^e_r \end{bmatrix}. \tag{4.6a–d}$$

Here, $\mathscr{D}(\omega)$ is the "system matrix", $\tilde{k}(\omega)$ is the vector of known expansion coefficients, and $\tilde{u}(\omega)$ is the vector of unknown expansion coefficients. The formal solution to our perturbation problem is obtained by inverting Eq. (4.6a) and performing the inverse Laplace transformation:

$$\tilde{u}(t) = \int\frac{d\omega}{2\pi}\,e^{-i\omega t}\,\tilde{u}(\omega) = \int\frac{d\omega}{2\pi}\,e^{-i\omega t}\,\mathscr{D}^{-1}(\omega)\cdot\tilde{k}(\omega) = \int\frac{d\omega}{2\pi}\,e^{-i\omega t}\,\frac{\mathscr{A}(\omega)}{D(\omega)}\cdot\tilde{k}(\omega)\,, \tag{4.7}$$

where $\mathscr{D}^{-1}$ is the inverse matrix, $\mathscr{A}(\omega)$ is the adjoint matrix, and $D(\omega)$ is the

determinant of $\mathscr{D}(\omega)$. More specifically, one can show that the n–th eigenmode is defined by

$$\tilde{u}_n(t) = -i\,\mathrm{Res}_n[\mathscr{D}^{-1}(\omega)\cdot\tilde{k}(\omega)\,e^{-i\omega t}] = -i\,[\mathscr{A}(\omega_n)/D'(\omega_n)]\cdot\tilde{k}(\omega_n)\,e^{-i\omega_n t} \qquad (4.8)$$

where $\omega_n$ is the n–th solution of the "eigenfrequency equation"

$$D(\omega_n) = 0\,, \qquad (4.9)$$

$\mathrm{Res}_n$ denotes the residue at the pole $\omega = \omega_n$, and $D'(\omega) \equiv \mathrm{d}D(\omega)/\mathrm{d}\omega$.

**5. Results and discussion.** Figure 2 shows the first and second eigenmodes for a negatively biased single–ended Q–machine characterized by the following parameters: electron–$K^+$ plasma; interelectrode distance L = 30cm; hot–plate temperature T = 2200 K, electron emission density $n_{e0^+} = 10^{10}$ cm$^{-3}$, ion emission density $n_{i0^+} = 10^8$ cm$^{-3}$ (hence neutralization parameter $\alpha \equiv n_{i0^+}/n_{e0^+} = 10^{-2}$), plasma density $n_p = 2\times10^7$ cm$^{-3}$, plasma potential $\Phi_p = -1.3$ V, electron waterbag cutoff velocity $v_{cw}^e = 2.7\times10^5$ cm/s, electron plasma frequency $\omega_p^e = 2.5\times10^8$ s$^{-1}$, ion–beam velocity $v^i = 2.7\times10^5$ cm/s, ion plasma frequency $9.4\times10^5$ s$^{-1}$, external short–circuit. Each of the relevant variable spaces ($0 \le x \le L$, $0 \le v \le v_{max}$, and $v_{min} \le v \le 0$) was discretized by a one–dimensional mesh consisting of 21 gridpoints, and the basis functions were chosen to be square functions whose localization interval essentially coincides with one meshwidth.

The eigenfrequencies corresponding to the first and second eigenmodes shown in Fig. 2 have been found to be $\omega_1 = (3.2204\times10^4 + 1.5235\times10^3 i)\,s^{-1}$ and $\omega_2 = (6.2512\times10^4 + 6.6399\times10^2 i)\,s^{-1}$, respectively. The positive imaginary parts mean that these modes are unstable, so that ion– acoustic turbulence should be expected in the negatively biased single–ended Q–machine for the parameters considered here. However, we wish to point out that these results are still of a preliminary character and hence will have to be checked carefully before definite conclusions can be drawn. Forthcoming numerical results will include studies on how the eigenfrequencies depend on plasma, boundary, and external–circuit parameters /3/.

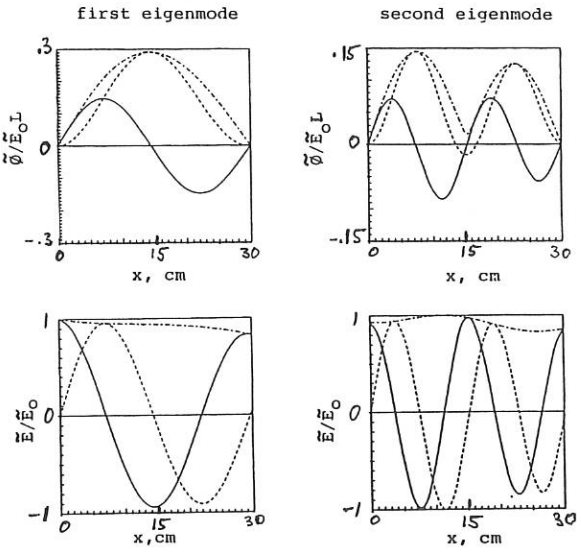


Fig. 2

**Acknowledgment.** This work was supported by the Austrian Research Fund (projects P5178 and P7005), the Austrian Foreign Student Service, and the Conselho Nacional de Pesquisas (Brazil).

/1/ S. Kuhn, Phys. Fluids **27**, 1821 (1984).
/2/ S. Kuhn, Phys. Fluids **27**, 1834 (1984).
/3/ S. Kuhn et al., to be published (1990).
/4/ G. Popa, et al., Phys. Lett. **87A**, 175 (1982).
/5/ S. Kuhn, Plasma Phys. **23**, 881 (1981).

# PLASMA HEATING BY A STRONG MULTIMODE LASER FIELD

R. Daniele°, G. Messina* and G. Ferrante§

° Istituto di Fisica, via Archirafi 36, 90123 Palermo, Italy.
* Istituto di Fisica di Ingegneria, via E. Cuzzocrea, 89100 Reggio Calabria,Italy.
§ Istituto di Fisica Teorica, P.O.Box 50, Sant'Agata di Messina, 98100 Messina, and Dipartimento di Energetica ed Applicazioni di Fisica, viale delle Scienze, Parco d'Orleans, 90128 Palermo, Italy.

The energy absorption rate by a classical plasma irradiated by a strong fluctuating laser field via stimulated bremsstrahlung is considered. In the first step of the laser plasma interaction, when collective instabilities have not yet developed, the main mechanism of heating is the inverse bremsstrahlung, where electrons absorb energy from the electromagnetic field when they collide with ions. The theory of this phenomenon is fully developed in the case of low radiation intensity, where the main process is one-photon absorption and the result is given by a simple analitycal formula[1]. Rather complete calculations are also available[1] for high radiation intensity for the case when the laser field is described by the ideal model of a single-mode (SM), purely coherent field. It amounts to say that the field fills all the space and that its parameters have well-fixed values. It is by now well known that very strong fields are never purely coherent and that fluctuations of the electromagnetic field, space and/or time inhomogeneities may affect significantly the elementary processes of radiation-matter interaction. A chaotic field is used here and a comparison is carried out with the purely coherent field. In the present analysis, the emphasis is put on the interplay between the laser field statistics and the plasma electron energy distribution. We shall calculate the energy absorption rate in collisions of electrons and ions in a fully ionized plasma. Numerical calculations are concerned with the dependence of the energy absorption rate on laser intensity, frequency, and statistics. The multiphoton structure of the energy absorption is analyzed as well. The approach used here has two steps: first, we calculate the transition probability for the elementary process of inverse bremsstrahlung in electron-ion collision in the presence of a radiation field and then one takes both a statistical average over all the electron momenta and over the fluctuations of the radiation field. It is assumed that the electron of mass m and charge -e interacts with infinitely heavy ions via a static potential $V(r)$; the radiation field is taken in the dipole approximation and it is described by its vector potential $A(t)$. For strong assisting fields, it is appropriate to assume the potential V as a perturbation causing the transition, as in the conventional scattering theory[2]. The unperturbed initial and final states are states embedded in the field, that is, the nonrelativistic Volkov waves

$$X_k(r,t)=\exp\{i\,k\cdot r\}\,\exp\{(-i/2m\hbar)\int^t dr\,[\hbar k+\frac{e}{c}A(r)]^2\} \qquad (1)$$

labelled by $\hbar k$, the particle momentum averaged over the field period or statistics, as required, and normalized in a box of unit volume. The first order[2] S-Matrix for the transition from the initial momentum $\hbar k_i$ to the final momentum $\hbar k_f$ is

$$S_{fi}^{(1)}=(-i/\hbar)\lim_{T\to\infty}\int_{-T}^{T}dt\int dr\,X^*_{k_f}(r,t)\,V(r)\,X_{k_i} \qquad (2)$$

with $X_{k_f}$ and $X_{k_i}$ Volkov waves. At any order in the scattering potential, the radiation field is included exactly. The first order transition probability per unit time is

$$P(p_i\to p_f)=\lim_{T\to\infty}\frac{1}{T}\,|\,S_{fi}^{(1)}\,|^2=\lim_{T\to\infty}\frac{1}{T}\int_{-T}^{T}dt\int_{-T}^{T}dt'\,|\,\tilde V(Q)\,|^2\times$$

$$\times\,\exp\{-i\alpha_{fi}\int_{-t}^{t'}dr\,A(r)\}\,\exp\{(i/\hbar)(\epsilon_f-\epsilon_i)(t-t')\} \qquad (3)$$

being

$$\epsilon_\gamma=\hbar^2k_\gamma^2/2m,\ \gamma=i,f;\quad \hat e_L=A(t)/A(t);\quad Q=k_i-k_f;\quad p_\gamma=\hbar k_\gamma;$$

$$\tilde V(Q)=(1/\hbar)\int dr\,V(r)\,\exp\{-iQ\cdot r\};\quad \alpha_{fi}=(e/mc)\hat e_L\cdot Q.$$

In the process of plasma heating the physical quantity of interest is the energy absorption rate $d\epsilon/dt$, i.e., the energy absorbed per unit volume and unit time. The ions are assumed to be at rest and randomly distributed. If the field is fluctuating, what is physically meaningful is the average over all the possible realizations of the absorption rate. In the present approach the radiation field is treated exactly, whatever its time dependence (deterministic or stochastics). In the case of a purely coherent field (i.e. a field with well-stabilized parameters) no average operations are needed. The energy absorption rate with the appropriate average over all the possible realizations of the fluctuating assisting field is:

$$<\frac{d\epsilon}{dt}>_{FL}=<\frac{1}{2}N_i\sum_{p,p'}[f(p)-f(p')]\,(\epsilon'-\epsilon)\,P(p\to p')>_{FL} \qquad (4)$$

with the maxwellian distribution function f(p) given as

$$f(p)=N_e\,(2\pi mkT)^{-3/2}\,\exp\{-p^2/2mkT\};\quad \int f(p)\,d^3p=N_e.$$

We compare our results with those of a monoenergetic and spatially collimated beam via the $\delta$-function distribution. The used plasma parameters are: the electron and ion density $N_e=N_i=10^{19}\ cm^{-3}$; the plasma temperature $T=10^5\ ^oK$. A $Ne^{+++}$ glass laser is used with photon energy $\hbar\omega=1.17$ eV. The laser is linearly polarized. The laser intensity I, in the coherent field case, or the mean intensity in the chaotic field one, is chosen in the range: $2\cdot10^7\le I\le 4\cdot10^{16}\ W/cm^2$.

The Figure shows the total energy absorption rates for both the electrons distribution functions (curves 1 and 3, or 2 and 4) and for both the radiation field models (curves 1 and 2, or 3 and 4)as a function of the ratio R of the oscillatory velocity of the electrons in

the field and the mean thermal electron velocity in the plasma

$$R=v_{osc}/v_T, \qquad 10^{-3}\leq R\leq 15.$$

In particular the sums over the first 100 contributions are performed and these are found to give a good representation of the whole absorption rate. For $R\leq 1$ in the case of a monoenergetic beam, the Marcuse effect (negative absorption) is still present (although less pronounced) also in the chaotic field case. This effects occurs when the electron oscillatory velocity imparted by the field is lower than the electron beam velocity, so that the electrons tend to emit photons to reach the oscillatory velocity of electrons in the laser wave. In the monoenergetic and spatially collimated beam model, the SM field results (curve 1) show the typical oscillatory behaviour after the perturbative intensity region with the position of the maximum situated at oscillatory velocity values $v_{osc}\sim v_i$, being $v_i$ the incident velocity, while for velocity $v_{osc}>>v_i$ the energy absorption rate is lower than the corresponding CH field result (curve 2). Comparing curves 1 and 3 or curves 2 and 4, it can be noted that the δ-distribution results are, in general, higher than those corresponding to the Maxwellian distribution function. This is due to the well known fact that a monoenergetic electron beam in the parallel direction of the laser electric field, realizes the most effective interaction with the field.

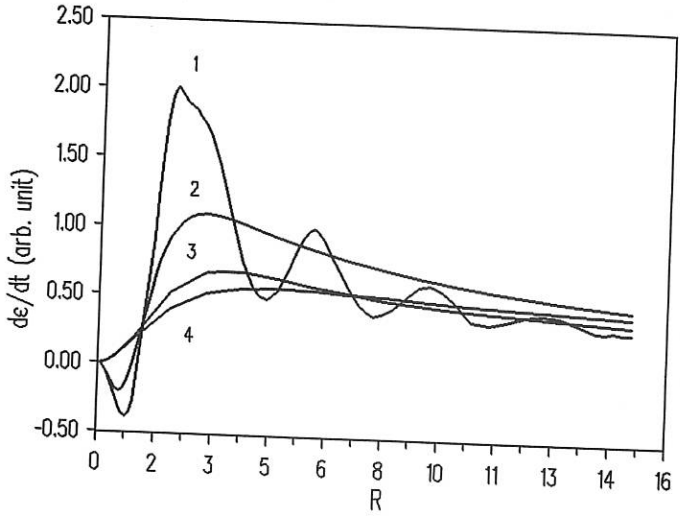

Concerning the joint influence of the radiation field and particle statistics on the absorption rate, the basic result may be stated as follows. For situations when the particle thermal velocity $v_T$ is longer than the oscillatory velocity $v_{osc}$ imparted by the field ($v_T \geq v_{osc}$, relatively weak fields), the absorption rate is only weakly dependent on the radiation statistics. For situations, instead, when $v_{osc} \gg v_T$, which occurs for very high intensities, the reverse becomes true: now the initial particle velocity distribution plays the modest role of a velocity spread of an electron beam oscillating at $v_{osc}$. In general, however, for very high intensities ($v_{osc} \ll v_T$), the energy absorption via bremsstrahlung becomes less effective because the high oscillatory velocity $v_{osc}$ reduces the time available to the electrons for the interaction with the ions, the "third body" which makes possible the exchange of energy between the plasma electrons and the radiation field. Finally, the relevant physical quantities as functions of field intensity exhibit in realistic cases, as a rule, a rather smooth behaviour, which could be easily fitted to be incorporated in more realistic modelling of many-particle process.

References

1. Y.Shima and H. Yatom, Phys. Rev. A12, 2106 (1975).
2. For a more detailed information on particle-atom collisions in strong laser fields and the related literature see, for instance, G. Ferrante in : **Fundamental Processes in Atomic Collision Physics** Ed. H. Kleinpoppen, J.S. Briggs and H.O. Lutz, pp. 343-395, (New York: Plenum Press, 1985).

# TURBULENCE AND FLUCTUATION INDUCED TRANSPORT IN A DOUBLE PLASMA DEVICE

M.J. Alport, R. Gaunt and G. Wintermeyer

Plasma Physics Research Institute, Department of Physics,
University of Natal, Durban, South Africa.

## Introduction

The use of the fixed double probe method[1] to obtain the spectral power density $S(\omega, k)$ is well known and has been used widely to study edge plasma turbulence in tokamaks for example. We have used this technique to analyse the ion beam turbulence in a Double Plasma (DP) device. The implicit assumption when using a double probe with fixed separation to determine the complete $k$-spectrum is that a single $\vec{k}$ is present for each frequency. We have demonstrated that this limitation can be relaxed by translating one probe relative to the other. As an application of this technique, we have constructed the $S(\omega, k)$ diagram for an ion-beam geometry where more than one mode is present.

## Experimental Results

We have used an experimental configuration in which an ion beam of energy 1-60 eV is injected into a background argon plasma parallel to the axis of the DP device. It is well known[2] that for a beam velocity $v_b > 2c_s$, ($c_s$ = ion acoustic velocity), such a configuration is unstable and the slow beam mode has a positive growth rate as it propagates down the axis of the device. In addition to the slow beam mode, if a test wave is launched, two other damped modes (the fast mode and the normal acoustic mode) can also be seen. We thus have a situation in which more than one mode ($k$ vector) is present at a particular frequency. This is of particular relevance to tokamak edge plasma turbulence measurements where it is very likely that more than one $k$ may be present at each frequency. A further problem inherent in the two-probe technique is that it is sensitive to differences (phase, amplitude) in the transfer functions of the two probe circuits and hence distorts the perceived propagation characteristics of the waves.

With a view to overcoming these limitations of the fixed two-probe technique, a new method has been developed which utilises a number of two-probe measurements taken at regularly increasing spatial separations. The separation is varied by placing a reference probe at a fixed axial position, and incrementally moving a second probe in the axial direction. The frequency spectra obtained from each two-probe measurement are cross-correlated, effectively producing a resultant spectrum $S(\omega, x)$ which is

independent of the characteristics of the two probes. Following this, the $k$-components are obtained by taking the FFT with respect to $x$ for each $\omega$ to obtain the full discrete wavenumber-frequency power spectrum, $S(\omega, k)$. Assuming time stationary data, this process is analogous to using a $n$-probe array, without the latter technique's intrusiveness or the associated duplication of probes, digitisers etc.

A result obtained in the manner described is shown in the axiometric plot in Figure 1 with a 220 kHz injected wave. Frequencies below 120 kHz have been zeroed for clarity. The fast and slow modes are clearly seen at $k \sim 2.7$, 5.1 cm$^{-1}$. The ion acoustic mode is not visible since it is strongly damped. Repeating such measurements for different injected wave frequencies, and combining the results in a single contour diagram gives the plot shown in Figure 2. The solid lines which have been computed from the theoretical dispersion relation with $E_b \sim 4.2$ eV, $n_e = 5.7 \times 10^8$ cm$^{-3}$, $n_b/n_e = 0.5$ and $T_e = 1.5$ eV agree fairly closely with the fast and slow modes. This technique may be easily modified to include complex $k$ to describe the growth or damping of the waves as they propagate down the axis by analysing the spatial growth of the various k-components.

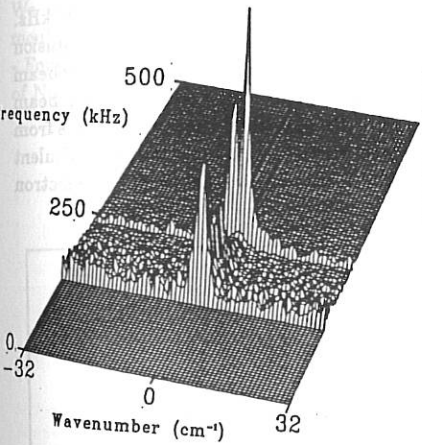


Figure 1: Axiometric plot of $S(\omega, k)$ with a 220kHz test wave.

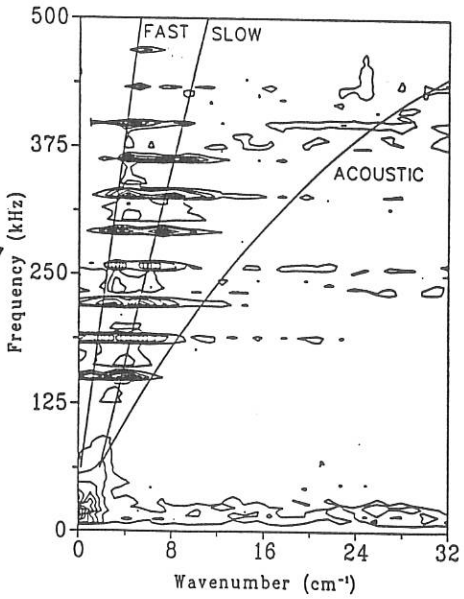


Figure 2: Composite contour plot of $S(\omega, k)$ with injected frequencies of 150, 185, 220, 255, 289 325, 360, 394, 429 and 465 kHz.

We have also used the standard fixed double probe method to calculate the fluctuation induced cross field transport driven by electrostatic cross field ion acoustic turbulence[3]. If the beam energy is increased to $\sim$ 40 eV and a perpendicular B-field (1-20G) applied, there is a rather sharp onset of a fairly broad band fluctuation spectrum. Figure 3 shows the $\tilde{n}(\omega)$ power spectrum and the coherency $\gamma(\omega)$. Measurement of the two dimensional $S(\omega, k)$ indicate that the turbulence is propagating predominantly in the axial direction resulting in fluctuation induced transport in the $k \times B$ direction.

The (spectrally resolved) fluctuation induced particle flux $\Gamma$ may be measured directly by calculating the ensemble average $< \tilde{n}\tilde{v} > = < \tilde{n}\tilde{E} > /B = < \tilde{n}k\tilde{\phi} > /B$. This requires the simultaneous measurement of $\tilde{n}$ and $\tilde{\phi}$ at the same physical location in addition to $\alpha$, the phase angle between $\tilde{n}$ and $\tilde{\phi}$. This can be achieved to a good approximation by performing two measurements to separate the inherent phase difference $\alpha(\omega)$ and $k(\omega)d$ due to the propagation from probe 1 to probe 2. $d$ is the probe separation. Firstly, probe 1 measuring $\tilde{\phi}$ is placed downstream from probe 2 measuring $\tilde{n}$. The phase difference between these two signals is $\Delta\phi_1 = \alpha(\omega) + k(\omega)d$. Next, the probes are exchanged and now the phase difference is $\Delta\phi_2 = -\alpha(\omega) + k(\omega)d$. The dispersion is then given by $k(\omega) = (\Delta\phi_1 + \Delta\phi_2)/2d$ and $\alpha(\omega) = (\Delta\phi_1 - \Delta\phi_2)/2d$. The flux $\Gamma$ is then calculated[4] from

$$\Gamma(\omega) = 2\frac{k(\omega)}{B}\sqrt{\tilde{n}(\omega)}\sqrt{\tilde{\phi}(\omega)}\gamma(\omega)\sin(\alpha(\omega)) \qquad (1)$$

Figure 4 shows a plot of $\Gamma(\omega)$ indicating transport in a band between 30 and 100 kHz.

The relative importance of classical and anomalous fluctuation driven diffusion in a magnetic field can be accessed using the test particle method[5], in which a slow beam of electrons is injected parallel to the weak magnetic field. By modulating the beam and employing lockin amplifier techniques, we have distinguished the test particles from the background electrons. The diffusion of charged particles produced by the turbulent electrostatic fluctuations may then be calculated from the spreading of the electron beam.

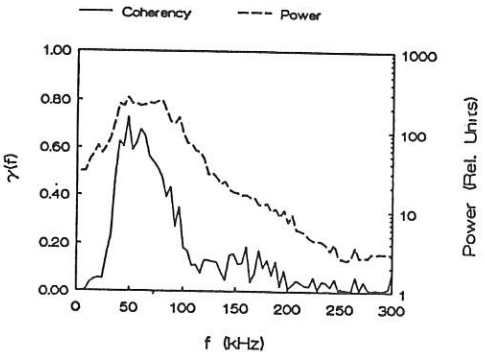


Figure 3: Power spectrum and coherency as a function of frequency.

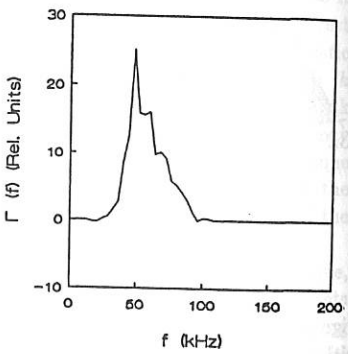


Figure 4: Fluctuation driven flux calculated from Equation 1.

## Conclusion

We have used a moveable Langmuir probe to obtain the spectral power density $S(\omega, k)$ of plasma fluctuations for a configuration in which more than one mode is present at a particular frequency. This overcomes the limitations of the fixed 2-probe method as well as the interferometer method where beating between modes can mask the wave number and growth rate. We have also directly measured the fluctuation induced $\tilde{E} \times B$ transport due to cross-field ion acoustic turbulence.

## References

1. J.M. Beall, Y.C. Kim and E.J. Powers, *J. Appl. Phys.* **53**, 3933, (1982).

2. D. Gresillon and F. Doveil, *Phys. Rev. Lett.* **34**, 77, (1975).

3. R.G. Greaves and P.J. Barrett, *Plasma Physics and Contr. Fusion* **31**, 76 (1989).

4. E.J. Powers, *Nucl. Fusion* **14**, 794, (1974).

5. R.L. Stenzel and W. Gekelman, *Phys. Rev. Lett.* **40** 550 (1978).

*Acknowledgements*
We are grateful for financial support from the Foundation for Research and Development and one of us (G.W.) would like to acknowledge the support of the A. v. Humboldt - Foundation for providing a Feodor Lynen Scholarship for his stay at the University of Natal.

# RESONANT FOUR-WAVE MIXING AND PHASE CONJUGATION IN AN UNMAGNETIZED PLASMA

C.W. DOMIER, N.C. LUHMANN, JR., W.A. PEEBLES

Institute of Plasma and Fusion Research, UCLA
Los Angeles, California 90024 U.S.A.

## INTRODUCTION:

In recent years, there has been renewed interest in generating phase conjugate reflections via resonant four-wave mixing (FWM) in plasmas. There have been several theoretical treatises published on the subject[1-4], but little in the way of experimental results[4]. We wish to present here a brief review of the relevant optical mixing and resonant (FWM) formulae, followed by the first detailed measurements of resonant FWM in an unmagnetized plasma.

## OPTICAL MIXING THEORY:

A simple two-fluid description suffices to calculate the steady-state density response of the plasma to the beating of two electromagnetic waves. The continuity and momentum equations for the two fluid species $\alpha = (i,e)$ are

$$\frac{\partial n_\alpha}{\partial t} + \nabla\cdot(n_\alpha v_\alpha) = 0, \tag{1}$$

and

$$m_\alpha\left(\frac{\partial}{\partial t} + v_\alpha\cdot\nabla\right)v_\alpha = \frac{T_\alpha}{n_\alpha}\nabla n_\alpha + m_\alpha\nu_\alpha v_\alpha + q_\alpha\left(E + \frac{1}{c}\nabla\times B\right), \tag{2}$$

where $q_\alpha$, $m_\alpha$, $T_\alpha$, $n_\alpha$ and $v_\alpha$ are the charge, mass, temperature, density and velocity respectively. Here, $\nu_\alpha$ is a phenomenological damping constant. These equations are to be solved in the presence of two external transverse EM waves

$$E^{ext}(r,t) = \sum_{j=1}^{2} E_j\cos(k_j\cdot r - \omega_j t), \tag{3}$$

where $k_j$ and $\omega_j$ are the wave vector and frequency.

We are looking for a low frequency plasma response to the beating of waves 1 and 2, in which $k = k_1 - k_2$ and $\omega = \omega_1 - \omega_2$. We linearize Eqs. (1) and (2) and retain only terms to second order, giving

$$\frac{\partial\tilde{n}_\alpha}{\partial t} + n_\alpha\nabla\cdot U + n_0\nabla\cdot\tilde{v}_\alpha = 0, \tag{4}$$

and

$$\frac{\partial\tilde{v}_\alpha}{\partial t} + U\cdot\nabla\tilde{v}_\alpha - \nu_\alpha\tilde{v}_\alpha + \frac{T_\alpha}{m_\alpha n_0}\nabla\tilde{n}_\alpha - \frac{q_\alpha}{m_\alpha}\tilde{E} = -\left\langle\nabla(\tilde{v}_\alpha^{(1)}\cdot\tilde{v}_\alpha^{(2)})\right\rangle_t, \tag{5}$$

where $\langle\ \rangle_t$ denotes a time average over high frequency oscillations, U is the plasma drift velocity and $\tilde{v}_\alpha^{(j)}$ is the linear plasma response to the external field $E^{(j)}$ given by

$$\tilde{v}_\alpha^{(j)} = \frac{q_\alpha}{m_\alpha c}E_j\sin(k_j\cdot r - \omega_j t). \tag{6}$$

Equations (4) and (5) may then be Fourier transformed in both space and time. Solving for a quasi-neutral response $\tilde{n}_i \simeq \tilde{n}_e \simeq \tilde{n}$ we find, in the small m/M limit, the fractional density response to be given by

$$\frac{\tilde{n}}{n_0} = \frac{(1/2)(m/M)k^2 v_1\cdot v_2^*}{(\omega - k\cdot U)(\omega - k\cdot U - i\nu_i) - k^2 c_s^2}, \tag{7}$$

where $v_j = eE_j/m\omega_j$ and $c_s = [(T_e + T_i)/M]^{1/2}$ is the ion acoustic speed. Note

that at resonance, $(\omega - k\cdot U)^2 = k^2c_s^2$, the fluctuation amplitude reaches a maximum of

$$\frac{\tilde{n}_{res}}{n_0} = \frac{im\omega}{2M\nu_i}\left(\frac{e}{m\omega_o c_s}\right)^2 E_1\cdot E_2^*, \tag{8}$$

and lies 90° out of phase with the beating of waves 1 and 2.

The predictions of Eqs. (7) and (8) have been quantitively verified by experiments done at UCLA involving the optical mixing of two anti-parallel microwave beams[5]. Detailed studies were made of the growth and saturation of the ion acoustic waves driven by this three-wave mixing process. As expected, the interaction was found to be greatly enhanced when the difference frequency is tuned to match ion acoustic resonances in the plasma.

FOUR-WAVE MIXING THEORY:

In four-wave mixing, a strong pump wave mixes with a weak signal (or probe) wave in a nonlinear medium to generate a density modulation or "grating". A second strong pump wave scatters from this grating to generate a fourth wave. If the two pump waves are antiparallel, then the fourth wave is phase conjugate to the signal wave. Following the approach laid out in [6,7], the equations governing resonant FWM can be found from the wave equation

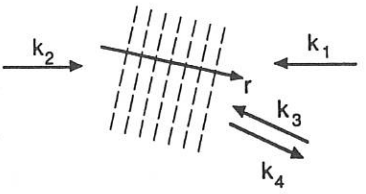


Figure 1. Four wave mixing geometry.

$$\left[\frac{\partial^2}{\partial t^2} + c^2\nabla^2 + \omega_p^2\left(1 + \frac{\tilde{n}}{n_0}\sin(k\cdot r - \omega t)\right)\right]E = 0, \tag{9}$$

where $E = E^{(1)} + E^{(2)} + E^{(3)} + E^{(4)}$. We assume that all EM waves are approximated by plane waves polarized perpendicular to the intersection plane. We let the signal frequency $\omega_3 = \omega_0 + \Delta\omega$, and assume an anti-Stokes shifted signal (i.e. $\Delta\omega$ positive). The conjugate beam will then have a frequency $\omega_4 = \omega_0 - \Delta\omega$ and wave vector $k_4 \simeq (k_1 + k_2 - k_3)(1 + 2\Delta\omega/\omega_0)$. We note that the phase mismatch $\Delta k = k_1 + k_2 - k_3 - k_4$ between the four waves is often sufficiently large that it may not be neglected.

We consider the case where the grating formed by pump 2 and signal wave 3 (and hence also pump 1 and conjugate wave 4) is resonant. We assume the pump beam intensities to be much stronger than that of the signal and conjugate beams, so that we may neglect pump depletion. Making the usual slowly-varying approximations, the steady-state solutions of Eq. (9) are

$$\frac{\partial E_3}{\partial r} = \frac{g}{2}E_2\left(E_2^*E_3 + E_1E_4^*\exp(i\Delta kr)\right), \tag{10a}$$

$$\frac{\partial E_4}{\partial r} = \frac{g}{2}E_1\left(E_2E_3^*\exp(i\Delta kr) + E_1^*E_4\right), \tag{10b}$$

where

$$g = \frac{k_0}{4}\frac{n_0}{n_c}\frac{m}{M}\frac{\Delta\omega}{\nu_i}\left(\frac{e}{m\omega_o c_s}\right)^2. \tag{11}$$

Note that if the signal wave is Stokes shifted ($\Delta\omega$ negative), then the gain parameter g is replaced with -g.

We consider a uniform plasma extending from 0 to L (or alternatively a larger plasma within which the pump and signal beams overlap from 0 to L). Using the boundary condition $E_4(0) = 0$, the reflectivity is given by

$$R \equiv \frac{I_4(L)}{I_3(L)} = \frac{M_1M_2}{|A - 2B\coth B|^2}, \tag{12}$$

where $M_j = g|E_j|^2L = gI_jL$, $A = (M_1 + M_2)/2 + i\Delta kL$, and $B = 1/2(A^2 + M_1M_2)^{1/2}$. In the short interaction length limit, $\Delta kL \ll (M_1 - M_2)/2$, and this simplifies to

$$R = I_1I_2 \left[\frac{\exp(M_1 + M_2) - 1}{I_1 + I_2\exp(M_1 + M_2)}\right]^2 . \quad (13)$$

**EXPERIMENTAL RESULTS:**

The experimental studies are performed in a cylindrical plasma chamber (75 cm in diameter by 200 cm long). Inside the chamber are three microwave horns. Horns 1 and 2 are large aperture horns centered along the chamber axis providing the two anti-parallel pump beams ($\leq$ 30 kW/beam) for the experiment. A third horn (signal horn) launches the signal beam ($\leq$ 1.7 kW) at a 40° tilt with respect to the pump beams, and collects the conjugate beam. The pump wave frequency is 3.24 GHz, and the signal wave frequency can be offset from that of the pump wave over a ± 20 MHz range to within ± 500 Hz. The pulse duration of each input wave (pump and signal) can be adjusted up to 60 μsec, with controlled rise- and fall-times from 0.1–10 μsec.

Much of the power collected by the signal horn is pickup of the signal and pump beams, arising from beam-spreading effects and reflections from the chamber walls. In order to select the desired phase conjugate reflected (PCR) signal, a microwave source whose frequency lies half-way between that of the pump and signal waves is used for mixing down the signals picked up by the signal horn. The pump and signal power now at a frequency $0.5\Delta f$ can then be filtered out, allowing the PCR power at a frequency $1.5\Delta f$ to be measured. Shown below are sample data taken at resonance ($\Delta f$ = 200 kHz) in a Hydrogen plasma. The ringing in the PCR signal seen at t = 0 μsec arises from the filtering out of fast risetime pump wave signals.

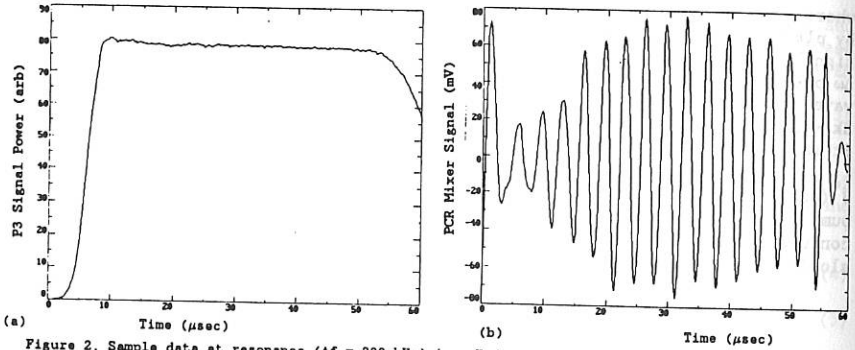


Figure 2. Sample data at resonance ($\Delta f$ = 200 kHz) in a Hydrogen plasma of (a) input signal waveform, and (b) PCR mixer output signal after high-pass filtering.

At resonance, the momentum of the ion wave must be matched to the momentum difference between the two optically mixed waves. For any non-zero tilt between the signal and the two anti-parallel pump beams, there are 4 possible resonances. Figure 3 displays the resonances which exist for a 40° tilt angle, showing the wavefronts and propagation directions of the corresponding ion waves. Figure 4 shows the results of difference frequency scans performed to determine the ion acoustic resonances in (a) Helium and (b) Hydrogen plasmas. Notice that in both cases all 4 resonances can be clearly seen. Note also the shift in resonant frequency between +'ve and −'ve frequency space due to a plasma drift along the chamber axis.

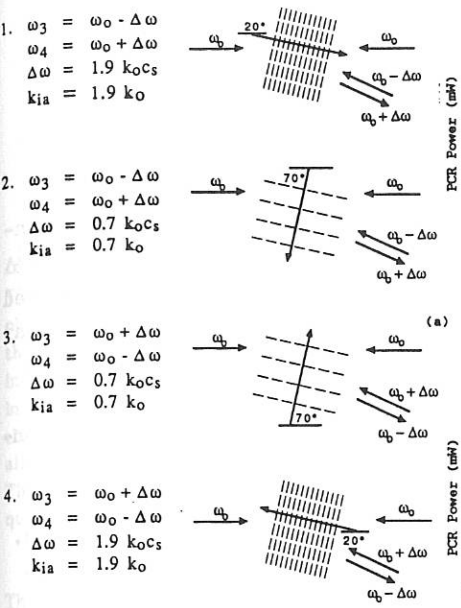


Figure 3. Ion acoustic resonances which exist for a 40° tilt angle.

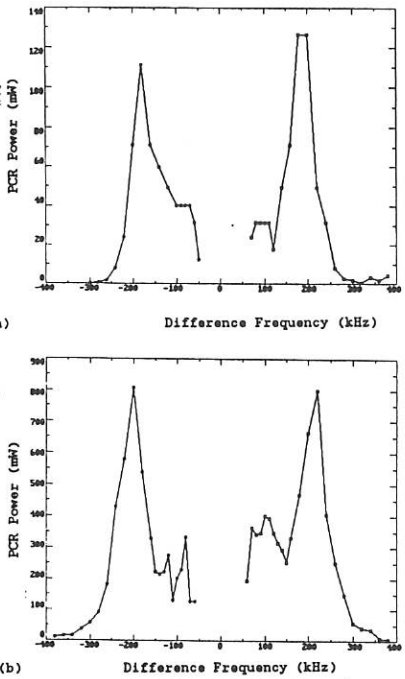


Figure 4. Difference frequency scan of ion acoustic resonances in a (a) Helium, and (b) Hydrogen plasma.

DISCUSSION:

Direct measurements of phase conjugate reflected power have been made in a resonant FWM microwave-plasma experiment. Work is still ongoing to study the effects that beam-spreading and beam curvature have on the physics of resonant FWM, as well as studying ion-wave saturation and plasma heating effects which occur under high power conditions.

ACKNOWLEDGEMENTS:

This work was supported by the Laser Fusion Program of the Lawrence Livermore National Laboratory.

REFERENCES:

[1]J. Federici, and D. Mansfield, J. Opt. Soc. Am. B 3, 1588 (1986).
[2]I. Nebezahl, A. Ron, and N. Rostoker, Phys. Rev. Lett. 60, 1030 (1988);
I. Nebezahl, A. Ron, D. Tzach, and N. Rostoker, Phys. Fluids 31, 2144 (1988).
[3]E. Williams, D. Lininger, and M. Goldman, Phys. Fluids B 1, 1561 (1989).
[4]T. Lehner, Physica Scripta, 39, 595 (1989).
[5]C. Pawley, H. Huey, and N. Luhmann, Jr., Phys. Rev. Lett. 49, 877 (1982).
[6]A. Scott and M. Hazell, IEEE J. Quantum Elect. 22, 1248 (1986).
[7]A. Scott and K. Ridley, IEEE J. Quantum Elect. 25, 438 (1988).

# KINETIC VORTICES IN MAGNETIZED PLASMAS

A.G.Sitenko, P.P.Sosenko

Earlier [1,2] the quadratic polarization approximation (QPA) has been suggested for the description of strongly nonlinear low-frequency motions in a magnetized plasma. The essence of this approach is in introduction of the renormalized equations for the nonlinear plasma polarization (or nonlinear charge density) implying the renormalization of the second-order nonlinear electric susceptibility. The renormalized equations make it possible to describe the low-frequency nonlinear oscillations in the broad range of wavelengths and phase velocities, which includes the kinetic scales of the order of particle gyroradii and parallel thermal velocities.

We demonstrate within the context of the QPA the existance of nonlinear structures possessing kinetic characteristic scales. The vortex-like solutions of the renormalized equations are found, and the crucial role of the finite-gyroradius effects is established.

1. Sitenko A.G., Sosenko P.P. Aspects of the renormalized statistical theory of plasma turbulence//Sov.-Ital. Symp. on Math. Problems of Stat. Physics: Abstr. of Contr. (Lviv, Sept.30-Oct.11, 1985). Kiev: ITP, 1985.P.105-106.

2. Sitenko A.G., Sosenko P.P. Kinetic theory of low-frequency nonlinear structures in magnetized plasmas// 1987 ICPP Inv. papers, v.1.P.486-524. Singapore, World Scientific, 1987.

# ELEKTRON - CYCLOTRON - WAVES IN NON - MAXWELLIAN, RELATIVISTIC PLASMAS

E. Borie, Kernforschungszentrum Karlsruhe, I.T.P., Fed. Rep. Germany
F. Moser, E. Räuchle, Institut für Plasmaforschung der Universität Stuttgart
7000 Stuttgart 80, Pfaffenwaldring 31, Fed. Rep. Germany

Abstract:

The dispersion relation for electromagnetic and electrostatic waves propagating obliquely to the magnetic field is derived for weakly relativistic plasma using the dielectric tensor due to Orefice (1 ). Numerical examples for the complex index of refraction are shown for a propagation oblique to the magnetic field in the frequency range of the first harmonic. For perpendicular propagation there exist differences in comparison with the results of Robinson (2) especially in the damping rates of the waves.
The dependence of the dispersion and absorption of temperature, density, frequency and angle of propagation is shown.

## The dielectric tensor, dispersion relation:

Electromagnetic and electrostatic waves are investigated in the frequency range of the electron - cyclotron resonance and harmonics. The plasma is described by the relativistic dielectric tensor due to Orefice (1) for plasmas with relativistic Maxwellian, drifting relativistic Maxwellian or Loss - Cone electron distribution functions. The Loss - Cone distribution functions

$$f(p_\perp, p_\parallel) = n_0 p_\parallel^{2m_\parallel} p_\perp^{2m_\perp} \exp\left[-\frac{1}{2}\mu_2 (p_\perp^2 + p_\parallel^2)\right] \qquad (1)$$

are characterized by the Loss - Cone - index $m_\perp$ and Anti - Loss - Cone - index $m_\parallel$.
There is:

$$n_0 = \frac{1}{m_\perp!}\left(\frac{\mu_2}{2\pi}\right)^{\frac{3}{2}}\left(\frac{\mu_2}{2}\right)^{m_\perp + m_\parallel}\frac{\sqrt{\pi}}{\Gamma(m_\parallel + \frac{1}{2})}, \qquad \mu_2 = \frac{m_{eo}c^2}{kT_{e_2}}. \qquad (2)$$

$\Gamma$ is the Gamma - function, $m_{eo}$ the electron rest mass, $T_{e_2}$ the electron temperature and the indices $\perp$ and $\parallel$ refer to the directions perpendicular and parallel to the external magnetic field.

In the dielectric tensor

$$\varepsilon_{ij} = \delta_{ij} + \left(\frac{\omega_{pe}}{\omega}\right)^2 \left\{ \tilde{H}_{ij}\left[\frac{L_1(f)}{p_\perp}\right] - \Gamma_{ij}\left(w_2 - w_1\mu_1 p_0^2\right)\right\} \qquad (3)$$

$w_1$ and $w_2$ are the weights of the drifting Maxwellian and the Loss-Cone-distribution functions with $w_1 + w_2 = 1$, $\mu_{1/2} = m_{eo}c^2/kT_{e_{1/2}}$ with $T_{e_{1/2}}$ the electron temperatures, p is the electron momentum in $m_{eo}$ c units, $\omega_{pe}$ the electron plasma frequency, $\Gamma_{ij} = \delta_{i3}\delta_{3j}$, $p_0$ is the electron drift momentum parallel to the magnetic field. The operator $\tilde{H}_{ij}$ and further details are described in (1) and (3). In $\varepsilon_{ij}$ the Shkarofsky-functions are expressed by the plasma dispersion function Z using the recursion relations due to Shkarofsky (4).

The finite Larmor radius expansion is considered to arbitrary order.

Different solutions of the dispersion relation correspond to different wave modes.

Numerical results:

Ordinary and extraordinary electromagnetic waves and electrostatic Bernstein waves are investigated for a propagation perpendicular and oblique to the external magnetic field. By relativistic effects the dispersion is greatly influenced in the frequency range of the electron-cyclotron-resonance and their harmonics, additionally new modes appear. Such a new mode of ordinary wave polarisation is shown in figs. 1 and 2 with the real part of the index of refraction Re(n) versus the normalized electron-cyclotron frequency $\bar{\omega}_{ce} = \frac{\omega_{ce}}{\omega}$ ($\omega_{ce}$ = electron-cyclotron-frequency and $\omega$ = frequency of the wave).

Two characteristic examples of the dispersion for ordinary waves are shown in fig. 1 (low density, $\bar{\omega}_{pe}^2 = (\omega_{pe}/\omega)^2 = 0.8$) and in fig. 2 (high density, $\bar{\omega}_{pe}^2 = 100$) for perpendicular propagation ($\Theta = 90^0$). Values for Im(n) are indicated. The slow relativistic ordinary wave is weakly damped especially in the frequency range $\omega \gg \omega_{ce}$.

For different angles of propagation $\Theta$ the wave characteristics Re(n) and Im(n) are given in figs. 3 and 4. Values for Re(n) obtained by Robinson (2) are indicated in fig. 3. Robinson obtained his results using an approximation to the dispersion relation.

Electrostatic Bernstein waves are influenced by relativistic effects in the dispersion as well as in the polarisation.

In the results described above relativistic Maxwellian distribution functions were used. Similar investigations with Loss-Cone or Anti-Loss-Cone relativistic distribution functions show a large influence of the Loss-Cone or Anti-Loss-Cone index on the absorption of the waves.

Therefore the knowledge of the electron distribution function is necessary to obtain a good agreement between theory and experimental results.

Figure captions:

Fig. 1: Real part of the index of refraction $n_r = \mathrm{Re}(n)$ versus the electron cyclotron frequency $\bar{\omega}_{ce} = \frac{\omega_{ce}}{\omega}$ of the slow and fast ordinary wave (O.W.). Maxwellian distribution function, low density case.
(parameters: $\bar{\omega}_{pe}^2 = \omega_{pe}^2 / \omega^2 = 0.8$, $T_e = 5$ keV, $\Theta = 90^0$)

Fig. 2: Real part of the index of refraction $n_r = \mathrm{Re}(n)$ versus the electron cyclotron frequency $\bar{\omega}_{ce} = \frac{\omega_{ce}}{\omega}$ of the slow and fast ordinary wave (O.W.). Maxwellian distribution function, high density case.
(parameters: $\bar{\omega}_{pe}^2 = \omega_{pe}^2 / \omega^2 = 100$, $T_e = 5$ keV, $\Theta = 90^0$)

Fig. 3: Real part of the index of refraction $n_r = \mathrm{Re}(n)$ versus the normalized frequency $\omega / \omega_{ce}$ for three angles of propagation $\Theta = 86^0, 88^0, 90^0$, compared with Robinsons results for $\Theta = 90^0$ for the fast ordinary wave. Maxwellian distribution function, high density case.
(parameters as in fig. 2)

Fig. 4: Damping rate $n_i = \mathrm{Im}(n)$ versus $\omega / \omega_{ce}$ for three angles of propagation $\Theta = 86^0, 88^0, 90^0$ of the fast ordinary wave.
Maxwellian distribution function, high density case.
(parameters as in fig. 2)

References:

(1) A. Orefice, J. Plasma Physics 39, (1988) 61.
(2) P. A. Robinson, J. Plasma Physics 37, (1987) 435.
(3) F. Moser et al., Proc. 16 th Europ. Conf. on Contolled Fusion and Plasma Physics, Venice, 1989, Vol. III. 1147.
(4) I. P. Shkarofsky, J. Plasma Physics 35, (1986) 319.

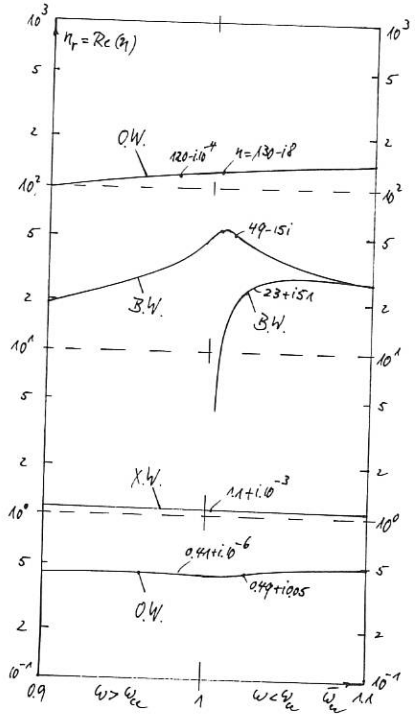


Fig. 1

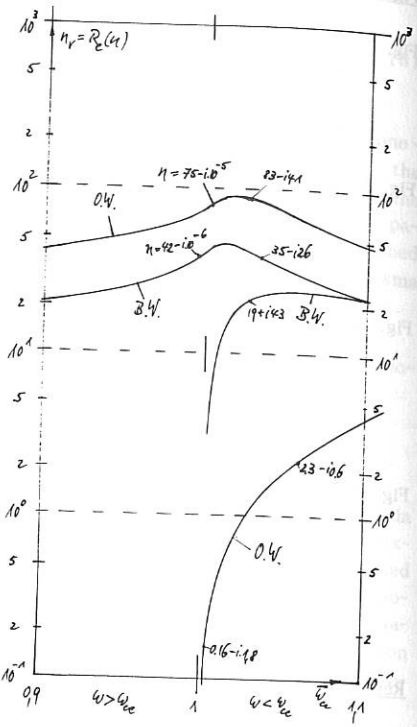


Fig. 2

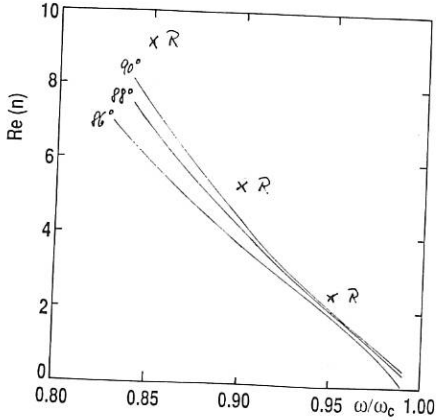


Fig. 3

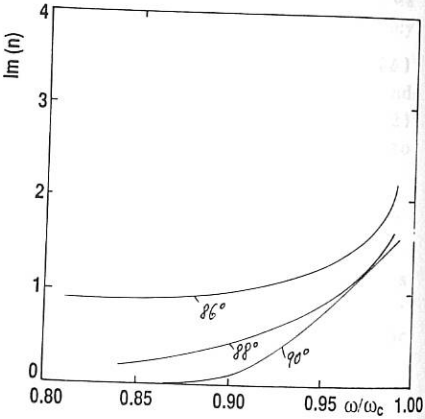


Fig. 4

# ION CYCLOTRON WAVE EXCITATION BY DOUBLE RESONANCE PARAMETRIC COUPLING

A. Fasoli, T.N. Good, P.J. Paris, F. Skiff+, M. Q. Tran

Centre de Recherches en Physique des Plasmas
Association Euratom - Confédération Suisse
Ecole Polytechnique Fédérale de Lausanne
21, Av. des Bains - CH-1007 Lausanne - Switzerland

## Introduction.

The term Double Resonance indicates generally a non-linear coupling between an electron plasma resonance (in our case, the Upper Hybrid,UH) and a low frequency eigenmode (typically, in a magnetized plasma, the ion cyclotron mode) [1]. The modulated parametric decay has been investigated in the past, both in theory [2] and in experiments [3], mostly in the context of plasma heating, in order to decrease the power threshold required in the case of a monochromatic pump wave. More recently, renewed interest has been shown in connection with experiments on large scale modification of the ionosphere [4].

In the experiment reported herein, we studied the modulated UH resonance as an *internal* antenna for Electrostatic Ion Cyclotron (EIC) waves. A method for a selective excitation of the Bernstein mode, based on the choice of the modulation excursion, is proposed.

## 1.Experimental set-up and diagnostic apparatus.

The experiment has been performed on the Linear Magnetized Plasma (LMP) Q-machine [5]. The plasma column has a length of about 470 cm and a diameter of 5 cm. The axial B-field is of the order of 0.3 T ($f_{ce}\simeq 8$ GHz, $f_{ci}\simeq 30$ kHz). Densities are of the order of $10^9$-$10^{10}$ $cm^{-3}$; $T_e \equiv T_{i\perp} \equiv 2T_{i\parallel} \equiv 0.2$eV. Sheath acceleration at the hot plate causes a supersonic ion drift $v_D \equiv 1.2\times10^5$ cm/s.

The RF launching system is composed of a high frequency (7-12 GHz) generator, a Traveling Wave Tube amplifier (20W), and an open waveguide disposed in the extraordinary mode inside the vacuum chamber and facing the plasma at a distance of about one cm. The maximum power flux to the plasma is of the order of 1 $W/cm^2$. A lay-out of the LMP device, with the geometry of the launching and detection systems, is shown in fig.1.

The diagnostic apparatus, mainly devoted to the study of the ion features, is based on the technique of Laser Induced Fluorescence (LIF) [6]. Direct information on the ion distribution function and the related moments (density, ion temperature, drift velocity, etc.) can be obtained. In the case of collisional pumping of the quantum states, a measurement of the line intensity ratio for two different transitions enables one to infer the electron temperature.

## 2.The monochromatic wave.

We considered an electromagnetic (e.m.) wave in the UH frequency regime: $f_{UH}(r) \equiv (f_{ce}^2+f_{pe}^2(r))^{1/2}$ $(\simeq f_{ce})$. When the e.m. wave propagating in the X-mode across the density profile encounters the UH resonance, its E-

field enhances in amplitude and tends to become parallel to the wave vector. An efficient conversion to the electrostatic Electron Bernstein Wave (EBW) can then take place. Radial probe measurements confirmed the presence of these e.s. oscillations ($k_\perp \rho_e^{exp} \cong 2\times10^{-4}$). Strong local electron heating is produced by the enhanced field at resonance.

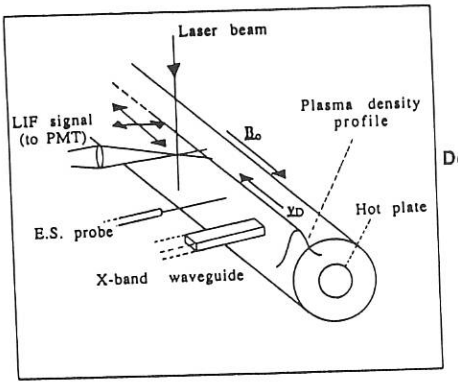


Fig.1:LMP experimental set-up

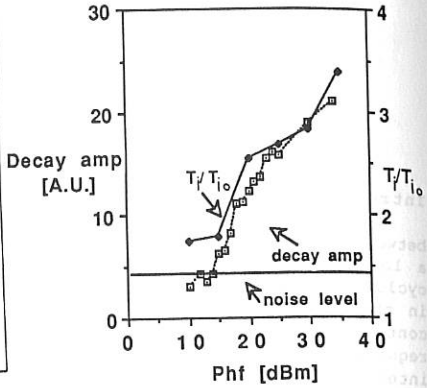


Fig.2:Decay amplitude and ion heating effects vs. RF pump power at resonance (r/a=0).

Along with the linear conversion, non linear parametric effects occur. When the driving wave is kept at resonance, a signal around $f_{ci}$ and its harmonics is seen on the low frequency fluctuation spectrum. By scaling the frequency of this signal with the B-field ($f^{decay} \approx (1+\delta)\times f_{ci}$, with $\delta$=0.2), and by measuring perpendicular and parallel wavenumbers, we identified the decay product to belong to the forward branch of the EICW dispersion relation. Ion heating has been observed in correspondence to the parametric decay; the decay amplitude and the increase in $T_i$ are represented as a function of the RF power in fig.2. A relatively low level for the instability threshold, buried into the background noise, has to be noticed.

**3.Ion wave excitation by modulation of the h.f. resonance.**

The central part of our experiment was the study of the effects of the modulation of the h.f. field, primarily in relation to the possible excitation of ion oscillations over an extended frequency domain.

When the e.m. wave is frequency modulated ($f^{FM}$) in the $f_{ci}$ range, an enhancement in the level of the low frequency oscillation (≈+15 dB) with respect to the monochromatic case is observed for different pump powers. A reduction in the instability threshold can be inferred indirectly.

A first indication of ion wave propagation can be obtained from the probe signal locked to the FM driver. This signal, reported in fig.3a as a function of $f^{FM}$, shows, along with low frequency (drift or "edge") modes around 10 kHZ, a clear response over an entire portion of the first ion cyclotron harmonic band. To prove that this signal derives effectively from the h.f. resonance, we fixed $f^{FM}=1.2f_{ci}$ and swept the pump frequency. The

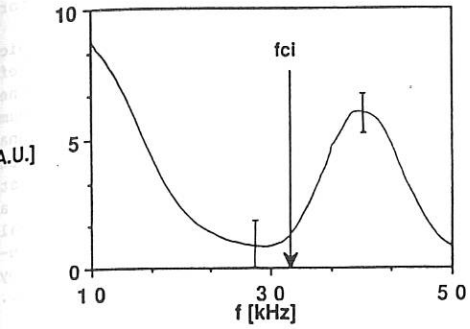


Fig.3a

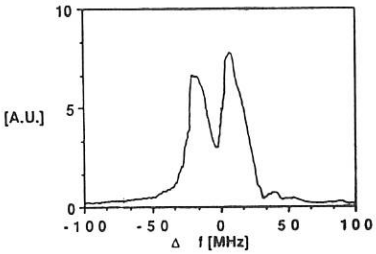


Fig.3b

ig.3:Probe response locked to the M driving signal: a)vs. the odulation frequency, for pump wave t resonance (≈1 W; r/a=-0.5). b)vs. he h.f. resonance detuning (Δf), for $f^{FM}=1.2f_{ci}$.

ig.4:Perturbed perp ion istribution function; $f^{FM}=1.3f_{ci}$, ≅0.3W at resonance, r/a=-0.5, mod. xcursion≅15 MHz.

ig.5:Dependence of the measured λ n the modulation excursion translated into the radial scillation of the resonant layer); $f^{FM}=1.1f_{ci}$, P≅0.3W, r/a=-0.5.

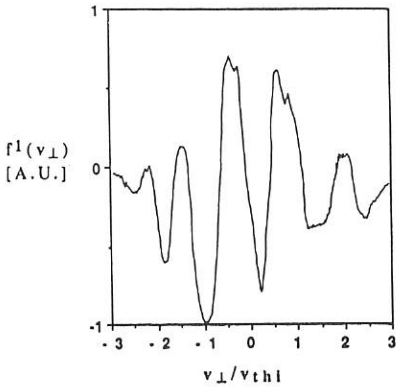


Fig.4

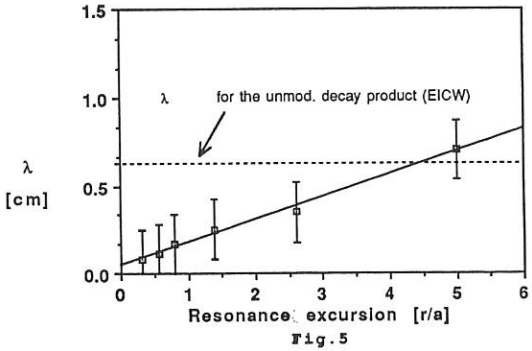


Fig.5

result is displayed in fig.3b; the signal at $f^{FM}$ is present only for resonant pump frequencies ($\Delta f \equiv f_{UH} - f_{ce} \approx 50$ MHz).

The ion wave characteristics are investigated via LIF. The macroscopic interferograms at different modulation frequencies reveal the presence of both the forward and the backward (or Ion Bernstein, IB) branches in the EIC range. The two modes have comparable amplitudes, for the maximum modulation excursion, in contrast to the usual case of capacitive-antenna excited ion waves, where the coupling efficiency for the IBW is much smaller than for the fast mode [7]. On a kinetic level, the clearest signature of an ion wave propagating in a plasma is the presence of a perturbed ion distribution $f^1(v_\perp, v_{||})$. In fig.4 we show a typical measurement of $f^1(v_\perp)$, for an IBW driven at $f^{FM}=1.3f_{ci}$. Ballistic and free-streaming effects, which characterize the plasma perturbation induced by antennas in contact with the plasma [8], are not observable in this case. The excitation seems to occur only through collective field interaction.

Another important feature of this launching scheme, concerning the character of the excited e.s. waves, is suggested by simple theoretical considerations. In the Vlasov equation for ions, a source term can be introduced in the form of a pressure-gradient driven electric field. The pressure perturbation can be represented as $p_1(r,t)=p_1\delta(r-r_0+\Delta\cos\omega_2 t)$, where $r_0$ is the resonance location, $\omega_2$ the modulation frequency (FM), and $\Delta$ the radial excursion of the resonant layer; $\Delta \equiv [d\omega_{UH}(r)/dr]^{-1} \times \omega_1$ ($\omega_1$ is the modulation excursion). The Fourier analysis of such a field term will give a series like $\Sigma_n J_n(k_\perp \Delta)\exp(in\omega_2 t)$. The term of interest is $J_1(k_\perp\Delta)$; maximum efficiency will manifest for a fixed value of the product $k_\perp\Delta$. So, when varying $\Delta$, the corresponding wavenumber should be determined (or "influenced") consequently. A linear dependence of $\lambda_\perp = 2\pi k_\perp^{-1}$ on the resonance excursion $\Delta$ is indeed observed in the experiment (fig.5).

**Conclusions.**

A localized virtual antenna for the excitation of electrostatic waves is created inside the plasma by modulating a resonant e.m. wave in the Upper Hybrid frequency regime. Wavelength and distribution function measurements identified the launched modes as EIC waves. A control on perpendicular wavelengths and a selective excitation of the IB wave can be achieved experimentally by acting on the FM modulation parameters.

***

[+]Permanent address: Laboratory of Plasma Research, University of Maryland, College Park, MD 20742.

The authors would like to express their gratitude to Dr.A.Wong for having inspired the experiment. This work was partly supported by the Fonds National Suisse pour la Recherche Scientifique under Grant No.20-25526.88.

**References.**

[1]-A.Y.Wong, D.R.Baker and N.Booth, *Phys. Rev. Lett.* **24**, 805 (1970).
[2]-D.Arnush et al., *Phys. Fluids* **16**, 2270 (1973).
[3]-K.Matsumoto and M.Sato, *Pl. Phys. and Controlled Fus.* **26**, 935 (1984).
[4]-A.Y.Wong et al., *Phys. Rev. Lett.* **63**, 271 (1989).
[5]-M.Q.Tran et al., *CRPP Laboratory Report* No. LRP 205/82 (1982).
[6]-R.A.Stern, D.N.Hill and N.Rynn, *Phys. Rev. Lett.* **37**, 833 (1981).
[7]-J.Goree, M.Ono and K.L.Wong, *Phys. Fluids* **28**, 2845 (1987).
[8]-T.N.Good et al., *this conference*.

# ION WAVE EXCITATION FOR THE STUDY OF WAVE-INDUCED TRANSPORT

T.N. Good, A. Fasoli, F. Skiff*, F. Anderegg**, P.J. Paris, M.Q. Tran, N. Rynn+, R. Stern++, and M. Yamada+++.

Centre de Recherches en Physique des Plasmas
Association Euratom - Confédération Suisse
Ecole Polytechnique Fédérale de Lausanne
21, Av. des Bains - CH-1007 Lausanne - Switzerland

## Introduction

A general program to study wave-particle interactions and wave-induced transport in a low temperature, low density, collisionless plasma has led to the application of an assortment of ion wave launching schemes. These wave launching techniques include the use of: capacitively coupled rings at the plasma periphery, inductive coils, grids immersed in the plasma, and ion wave excitation by modulation of microwaves (double resonance- see paper presented at this meeting by A. Fasoli et al). The generated ion waves are either ion acoustic, the forward and backward (neutralized ion Bernstein) branches of electrostatic ion cyclotron, and/or ballistic modes.

Our earlier studies have addressed the ion interaction with a single monochromatic wave, such as ion acceleration by intrinsic stochasticity induced by interaction with an ion Bernstein mode [1], and ion coordinate space diffusion constrained by conservation of integrals of the motion in this deterministic system [2]. In the case of linear ion acoustic wave-particle interaction, an experimental test ion approach has yielded direct evidence of phase space orbit perturbations for ions resonant with the wave phase velocity, demonstrating on the kinetic level the essence of ion Landau damping [3,4].

We are now turning our attention to the problem of stochastic interaction with two ion cyclotron modes. A detailed knowledge of the waves excited by the antenna will allow a selection of mode phase velocities such that the seperation of wave-particle resonances can be controlled. In this way, the wave field amplitudes necessary for reaching the stochasticity threshold can be reduced, in comparison to the situation with one wave [5].

This paper reviews the wave dispersion characteristics compiled during the aforementioned wave-particle interaction studies. It will be seen that the plasma dispersion relation universally determines the wave response, quite independent of the antenna configuration.

## Experimental Apparatus and Methods

The experiments have been conducted in the Linear Magnetized Plasma [6] device arranged as a 470 cm long Q-machine with variable magnetostatic field of 0.1-0.3 Tesla. The 5 cm diameter barium plasma can be described by the following parameters: density:$10^9$-$10^{10}$ $cm^{-3}$, temperatures: $T_e \cong T_{i\perp} \cong 2T_{i\parallel} \cong 0.2$ eV, ion drift velocity: $v_D/v_{th} \cong 4$, and with ion-ion collision length greater than the plasma length.

Wave features were measured optically via laser induced fluorescence (LIF), by analysis of the ion dielectric response [7,8]. Through the use of phase-lock techniques, or spatially localized measurements of the ion velocity distribution function synchronous with the wave field, a component of the perturbed distribution is observed that oscillates coherently with the wave. Single point detection of the perturbed distribution, or spatial scanning of the velocity moments of this distribution yield measurements of wave vector and amplitude. The superb velocity, spatial, and temporal resolution ($\Delta v/v_{th} < 1\%$, $\Delta x^3 \approx 1mm^3$, $\Delta t \cong$ 1 μsec) complement the nonperturbative nature of this diagnostic.

The electrostatic antenna consists of 1 to 4 insulated metal rings of length ≈ 5 mm, maintained in contact with the plasma edge, and with variable spacing and phasing to allow an antenna wavelength from 3-18 cm. The electromagnetic antenna is an inductive coil of 3 cm length and situated outside the plasma radial boundary with diameter 7 cm. The planar grid (grid spacing ≈ 2 mm) was kept normal to the plasma column axis and covered the plasma cross section to ensure plane wave propagation parallel to the magnetic field.

**Experimental Results**

The measured wave dispersion relations for propagation perpendicular and parallel to the magnetic field are summarized in Figs. 1 and 2. A composite of data points from all wave launching structures is presented to underline the primacy of the role of the plasma in determining the wave response. In Fig. 1, one can recognize the resonant feature of the wave near the cyclotron harmonic frequencies. By comparison with the theoretical dispersion relation derived for these plasma parameters (displayed with constant $k_{\parallel}$ for aiding identification), one identifies the fast, backward branch and slow, forward branch of the electrostatic ion cyclotron mode.

The parallel dispersion of Fig. 2 shows two readily identifiable curves. The ion acoustic mode (with theoretical prediction) propagates with phase velocity equal to the sum of the ion drift and sound speeds. The fast wave is most likely the electrostatic ion cyclotron mode, since it exhibits a cutoff at the fundamental cyclotron frequency. Note also the convergence of the two dispersion curves for large $f_{RF}/f_{ci} \approx 4\text{-}5$, where the ion cyclotron frequency is indicated in the figure. A few points showing propagation at low frequency and slower phase velocity than the ion acoustic wave remain as yet unidentified.

By observing the ion density response locally as the excitation frequency is slowly swept, a coupling efficiency curve is determined for each antenna configuration as in Fig. 3. In this case, we show the peaked response at the ion cyclotron frequency and its first harmonic, as well as a non-zero response for nonresonant frequencies below and between these values. Our results indicate that there is an evident optimum spacing for most efficient coupling at each frequency. Still, for a given frequency, we have observed no wavelength dependence on the type of antenna or on the electrostatic antenna ring spacing.

The ions responded to grid excitation in two modes: the ion acoustic waves shown in Fig. 2, and ballistic pseudowaves. The presence of the pseudowave depended on large excitation amplitude ($eV_{grid}/T_e > 1$), and could be avoided by limitation of the fluctuating grid voltage. The spatial evolution of the total time-resolved ion velocity distribution is presented in Fig. 4, under conditions where the pseudowave response

dominates. In this 3-D plot, one clearly sees the velocity space propagation characteristic of ballistic ion bursts accelerated locally at the grid.

The investigation of two wave launching has been initiated as we have evaluated the importance of wave-wave interactions on the particle dynamics. Employing two electrostatic antennas, beat waves have been observed that obey the conservation laws for matching parallel wave numbers and frequencies. The waves beating at the difference frequency also follow the ion acoustic dispersion relation, as seen in Fig. 2.

In the context of utilizing two antennas to reach stochasticity conditions, it is important to mention some adverse effects of large amplitude excitation. For continuous wave operation in this regime, the electrostatic antenna cuts off the plasma flow beyond it, by some mechanism not yet well understood. Ions are even reflected axially and carry a ballistic perturbation upstream, like in the case with the grid. With only partial plasma cutoff, the downstream plasma profile is modified, pinching the plasma radially, and enhancing the static radial electric field and resultant plasma rotation. In a gated RF operation, a severe transient response reduces the plasma density to zero upstream too, before a new quasi-equilibrium is restored in an ion transit time.

**Conclusions**

A proper theoretical investigation in support of our data would involve a two dimensional analysis of the plasma dispersion function. As shown above, both wavenumbers are changing with frequency. In contrast to standard assumptions, the parallel wavelength is not fixed by the antenna structure, and the perpendicular wavelength is not fixed (but probably influenced by) radial boundary conditions. Thus the dispersion relation must be solved simultaneously for $k_\perp$ and $k_\parallel$, with frequency as the independent variable.

The problem of plasma cutoff presents an obvious impediment to coupling from two antennas seperated axially. Achieving sufficient wave amplitude for stochasticity studies will isolate the downstream antenna from the plasma. These adverse effects have motivated a search for other wave-launching schemes that minimize plasma contact with strong local antenna electrostatic fields, such as double resonance techniques [9].

Permanent addresses:
* Laboratory of Plasma Research, U. Maryland, College Park MD 20742.
** Dept. of Physics, U.California San Diego, La Jolla, CA 92093.
\+ Dept. of Physics, U.California Irvine, Irvine, CA 92717.
++ University of Colorado, Boulder, CO 80309.
+++ Plasma Physics Lab., Princeton U., Princeton, NJ 08543.

This work was partly supported by the Fonds National Suisse pour la Recherche Scientifique under Grant No. 20-25526.88.

**References**

[1]--F.Skiff, F.Anderegg, M.Q.Tran, Phys. Rev. Lett. **58**, 1430 (1987).
[2]--F.Skiff *et al.*, Phys. Rev. Lett. **61**, 2034 (1988).
[3]--A.Fasoli *et al.*, Phys. Rev. Lett. **63**, 2052 (1989).
[4]--A.Y.Wong, R.W.Motley, and N.D'Angelo, Phys. Rev.**133**, A436 (1964).
[5]--D.F.Escande, Phys. Rep. **121**, Nos. 3 and 4 (1985).
[6]--M.Q.Tran *et al.*, CRPP Laboratory Report No. LRP 205/82 (1982).
[7]--F.Skiff and F. Anderegg, Phys. Rev. Lett. **59**, 896 (1987).
[8]--T.N.Good *et al.*, in *Nonlinear Phenomena in Vlasov Plasmas*, edited by F. Doveil (Editions de Physique, Orsaz, 1989), p. 255.
[9]-A.Fasoli *et al.*, this conference.

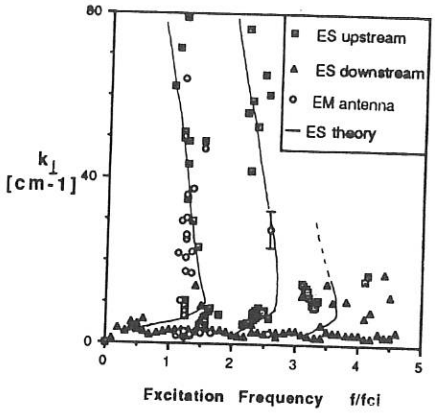


Fig.1: Perpendicular dispersion

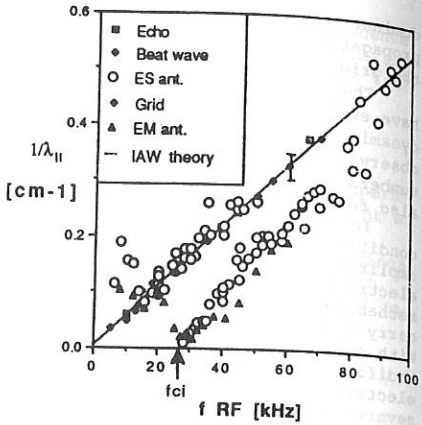


Fig.2: Parallel dispersion

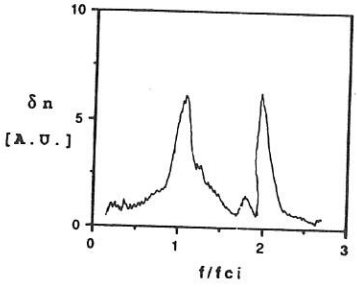


Fig.3: Ion response vs. frequency

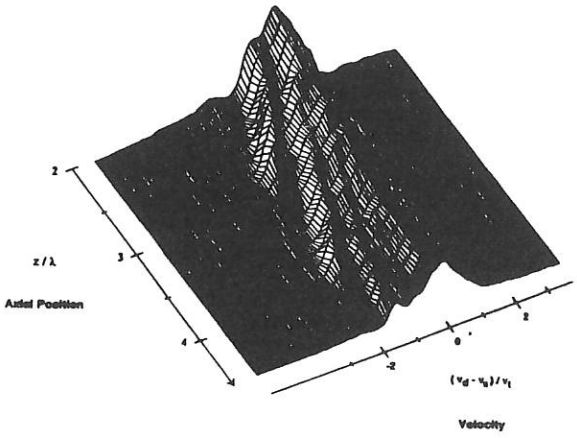


Fig.4:Spatial evolution of time-resolved $f(v_{||})$

# THE SHEATH FORMATION NEAR AN ELECTRON ABSORBING BOUNDARY

Nikola Jelić, Milan Čerček and Tomaž Gyergyek
*J.Stefan Institute, E. Kardelj University of Ljubljana,*
*Jamova 39, 61000 Ljubljana, Yugoslavia*

## INTRODUCTION

The conditions for an ion-rich sheath formation near a negatively biased or floating object representing a boundary for a plasma were widely investigated from the early days of plasma physics [1]. However there are less works reported about the conditions for the electron-reach sheaths forming near an electron drawing boundary. The both cases are important for the edge plasma investigations in front of a limiter or divertor plate in fusion mashines, as well as in the probe diagnostics. In our experiments on double layers [2] this problem arises in the context of a (monotonic) double layer existence conditions as well as for the plasma existence conditions in the presence of such a double layer or a positively biased anode. In the probe theory it is convenient to make an analogy between the cases of positive and negative sheath. Such an analogy implies the critical electron velocity at the plasma electron-reach sheath boundary to be less then the ion acoustic speed for the finite electron temperature plasma (e.g. [3]). In the literature concerning the double layers it was recognized that the average electron velocity for such a case must be larger than the sum of ion acoustic and electron thermal velocity [4]. However, no matter if the distinction between the two cases was made, a common questionable analogy about the mechanism for the electron drift, being represented by an electron accelerating electric field in a "preasheath" region, still remains (e.g.[5]).

The measurements of the drift electron velocity $u_d$ in the presence of a double layer show that the minimum electron velocity required at the low potential side of the double layer could vary depending on the experimental conditions from $u_d \sim 0.3 v_{th}$ [6] to $u_d \sim 1.0 v_{th}$ [7] (where $v_{th} = \sqrt{kT_e/m_e}$). In the presence of an anode at different potentials the measurements were performed far from the plasma sheath boundary where the electron drift velocity saturates at $u_d \sim 0.4 v_{th}$ when the anode becomes positively biased [8]. Due to importance of the value for the electron drift velocity for the investigations of the of the plasma turbulence observed under conditions similar to those in our experiments, we try to measure this velocity with and without the presence of a double layer. Furthermore, we were interested in the origin of such a drift and so the detailed shape of the electron velocity distribution was investigated.

## EXPERIMENTAL CONDITIONS

All measurements were performed in a collisionless cylindrical plasma in a homogeneous magnetic field $B_o = 70 \times 10^{-4}\,T$. (A detailed description of the experimental conditions could be found elsewhere [2].) Plasma created by a hot filament source flowed from the source region along weakly converging magnetic field lines into stainless steel tube region (length $1.20\,m$, diameter $0.18\,m$ ) making a plasma column (diameter $2\,cm$) terminated by an end plate (anode of the radius $R = 1\,cm$). The plasma density, electron and ion temperature and plasma potential were $n_1 \sim 2 \times 10^{15}\,m^{-3}$, $T_{e1} \sim 2\,eV$, $T_{i1} \sim 0.1\,eV$ and $\phi_p \sim 2\,V$, respectively. The neutral gas (argon) pressure ranged from $p = 4 \times 10^{-2}\,Pa$ to $1\,Pa$.

Increasing the anode bias potential led to an anode current-voltage characteristic which is plane probe-like up to some critical anode potential where a sharp increase in the anode current

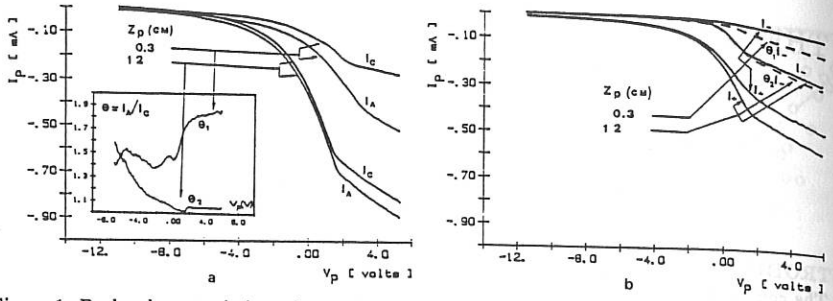


Figure 1: Probe characteristics taken at different distances from the anode for the floating anode potential with (inserted) the current ratio $\theta(V_p) \equiv I_A/I_C$ $(a)$, and in the current saturation regime $(b)$. The indexes "$A$" and "$+$" correspond to the positive, and "$C$" and "$-$" to the negative electron velocity orientations.

is observed, corresponding a new plasma formation. The new (anode) plasma at high plasma potential was separated from the basic (cathode) plasma by a strong double layer. The position of the double layer could be controlled by the external bias voltage, i.e. changing the total anode current [2]. The electron velocity distributions were investigated by the help of an onesided plane probe. An emissive probe was used for the plasma potential profile measurements.

## EXPERIMENTAL RESULTS

The first set of measurements was performed for the case when the anode was at the floating potential ($\Phi_a = -12V$). The measurements were performed for different axial distances ($0.3 - 12\,cm$) from the anode. The typical probe traces taken at the positions $0.3$ and $12\,cm$ from the anode, are given in the Figure 1-$a$. Under these conditions the electron distribution, and therefore also the probe traces for the probe orientations corresponding the positive and negative electron velocities ( $I_a$ and $I_c$) should be identical. The difference in the probe traces $I_a$ and $I_c$ could be interpreted in terms of the shadow effect. This behaviour is more pronounced and complicated at smaller distances $z$ from the anode due to plasma inhomogeneity near boundaries. We characterized this effect by the electron currents ratio $\theta(V_p, z) \equiv I_A/I_C$ (inserted in Figure 1-a). The investigations of the shape of the velocity distribution in the floating anode regime were performed by fitting straight lines to the experimental probe traces in the semilog plot. This method showed that the electron distributions were maxwellian with a small contribution due to the primary electrons.

Under the current carrying conditions ($\phi_a \sim 10V$) the functions $\theta$ obtained in the anode floating regime were taken into account as the corrections to probe traces $I_-$ obtained for the negative velocity orientations. To investigate the shape of the velocity distribution under these conditions a more general method of fitting straight lines to the experimental curves $ln(I_+ I_-) = -2e/kT_e V_p$ is shown to be applicable in the range of the probe currents $I_\pm$, collected far from the plasma potential. This method is valuable in the cases when there are reasons to expect shifted (or nonshifted) maxwellian distributions [9]. Under current-carrying conditions good agreement of the experimental curves with straight lines confirmed the assumption of the nearly shifted maxwellian distributions.

A comparison of the distributions obtained experimentally by differentiating the previously corrected probe traces, and by fitting to it the shifted maxwellian, is shown in Figure 2 in velocity space, for the cases when anode was floating and in the current carrying conditions . The results of the axial dependence of the velocity distributions corresponding to these conditions are given in the Figure 3. When a double layer was formed the observed behaviour with respect to the

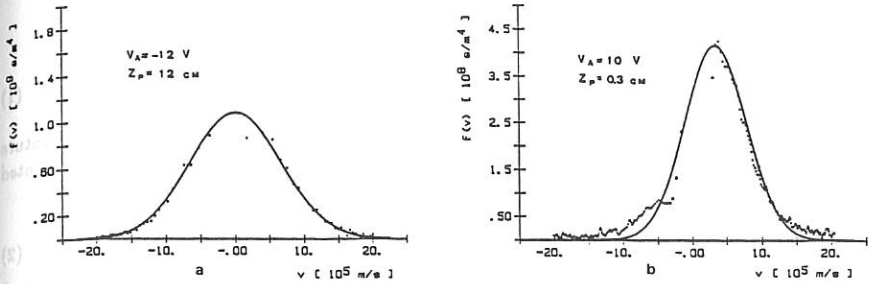


Figure 2: Comparison of the experimental (dotted lines) and fitted (full lines) velocity distributions for the floating anode potential (a) and in the current saturation regime (b)

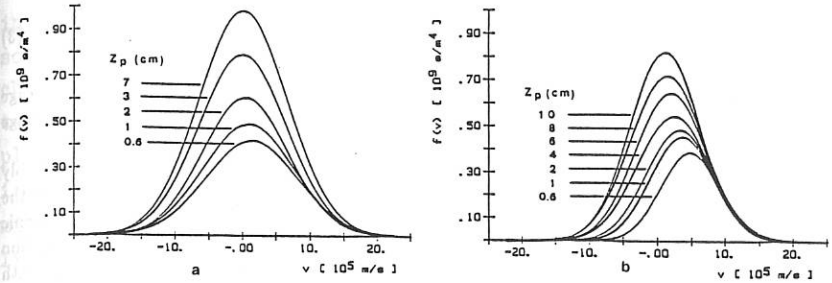


Figure 3: Axial dependence of the electron velocity distributions for the floating anode potential (a) and in the current saturation regime (b)

double layer position was the same as presented for current saturation regime. The calculations of the electron drift were performed using direct integration method of the experimental velocity distributions. However for such calculations very close to the anode or the double layer the electron density was normalized to the ion density as it was confirmed not to suffer of the shadow effect up to the plasma sheath boundary. We chequed out the results obtained from the electron velocity distributions at the plasma sheath boundary by the electron drift calculation based on the electron current continuity with a good agreement. At the distance 3 $mm$ from the anode we measured $u_d \sim 0.85 v_{th}$ while on the low potential side of the double layer (identified at the point where the ion density has a minimum) it was $u_d \sim 1.0 v_{th}$.

## DISCUSSION

From Figure 3 it is clear that there are no electrons accelerated towards the anode. The emitting probe measurements have not given any indication about an electron accelerating stationary electric field. Therefore we conclude that an electron accelerating preasheath can not ensure fulfillment of the theoretical requirement for the minimum electron velocity necessary for a monotonic negative sheath or a double layer formation, at least in the cases when the ion temperature is much less from that of the electrons. Instead of that an electron drift could be provided by the mechanism of the electron absorption at the anode (or high potential plasma when a double layer is present). To shed more light on the nature of such a drift we performed the standard analysis for the formation of a monotonic negative sheath. The generalized Bohm

criterion for this case must hold at the plasma-sheath boundary:

$$\frac{d}{d\Phi}(n_i - n_e) \leq 0 \tag{1}$$

If the electron velocity distribution is supposed as a nonshifted maxwellian with a temperature $T_e$ and the electron mass $m_e$, truncated at some finite velocity $u_{tr}$, and the ions are represented as a fluid with finite temperature $T_i \ll T_e$, the criterion 1 becomes:

$$\frac{u_{tr}}{\sqrt{2kT_e/m_e}} \exp\left(\frac{m_e u_{tr}^2}{kT_e}\right)\left[1 - erf\left(\frac{u_{tr}}{\sqrt{2kT_e/m_e}}\right)\right] \geq \frac{1}{\sqrt{\pi}}\frac{\kappa_i T_i}{T_e} \tag{2}$$

(providing the anode potential is sufficiently high to reflect all ions). Here $\kappa_i$ represents the adiabatic constant for ions. Due to small temperature ratio this expression could be reduced to:

$$u_{tr} \geq \sqrt{\frac{2}{\pi}}\frac{\kappa_i T_i}{T_e}\sqrt{\frac{kT_e}{m_e}} \tag{3}$$

For such a nearly half-maxwellian distribution it is straightforward to show that the average electron velocity must satisfy the condition $u_d > 1.32 v_{th}$ where these velocities are the average of a half-maxwellian.

However, our experimental distributions are not truncated but rather relaxed, probably due to streaming instabilities which could be excited by such distributions [10]. Therefore the truncated velocity distribution could be treated only as an initial condition for the monotonic sheath formation. To obtain a criterion applicable to more realistic conditions the assumption about the truncated distribution as well as about the laminar nature of the negative sheath and double layer must be relaxed. This could be done, supposing that in this situation a non-stationary velocity distribution in a fluctuating electric field establishes and which preserves the current continuity and the total particle energy of the initial distribution. Then the generalized Bohm criterion must be modified to include the time-averaged fluctuating electric field pressure at plasma sheath boundary, calculated as a free energy released in the transition from half-maxwellian to the shifted maxwellian. Such a model is expected to give the somewhat less severe requirements for the electron drift at the plasma sheath boundary, in better agreement with experimental results. This work is in progress.

## REFERENCES


[1] L.Tonks and I.Langmuir, *Phys.Rev.* **34**, 876 (1929)

[2] N.Jelić, M.Čerček and T.Gyergyek, *Contributed papers of the 1989 International Conference on Plasma Physics* - New Delhi, India, 689 (1989)

[3] F.F.Chen, in *Plasma Diagnostic Techniques*, ed. R.H. Huddlestone and S.L.Leonard, Academic Press, 113 (1965)

[4] J.G.Andrews and J.E.Allen *Proc.Roy.Soc.Lond*, A. **320** 459 (1971)

[5] L.Block, *Cosmic Electrodyn.* **3**, 349 (1972)

[6] M.Guyot and Ch.Hollenstein, *Phys.Fluids*, **26**, 1596 (1983)

[7] P.Leung A.Y.Wong and B.H.Quon, *Phys.Fluids*, **23**, 992 (1980)

[8] W.Gekelman and R.L.Stenzel *Phys.Fluids*, **21**, 2014, (1978)

[9] N.Jelić, M.Čerček and T.Gyergyek, *to be published*

[10] M.A.Raadu and J.J.Rasmunssen, *Proc.Second Symp. on Plasma Double Layers and Related Topics*, Innsbruck, Ed.by R.Schrittwiesser and G. Eder, 334 (1984)

# KINETIC DESCRIPTION OF NONEQUILIBRIUM PLASMA FLUCTUATIONS

O.D.Kocherga
Institute for Theoretical Physics, Kiev, USSR

The general statistical approach is applide to derive a nonlinear equation for the stationary spectra of electromagnetic field fluctuations in a nonequilibrium plasma including third-order terms with respect to the field intensity. The collision term and incoherent fluctuation sources associated with the stochastic motion of individual charged particles are involved into consideration consistently. A nonlinear dispersion equation for nonequilibrium plasmas is obtained and the nonlinear eigenfrequency shift is expressed in terms of the renormalized dielectric permittivity. This allows one to take into account both quasilinear diffusion and particle collisions. The nonlinear shift of one-dimensional Langmuir oscillations in a strongly nonequilibrium cold plasma is shown to be not equal to zero.

The formalism of multiple time scale approximations enables one to consider time evolution of fluctuation spectra. Kinetic equations for waves are derived for the cases of three- and four-wave resonances. These are suitable for the study of the mutual effect of resonant and nonresonant phenomena.

Resonance wave interactions are shown to be influenced by nonresonant wave processes as well as by wave-particle interactions and particle collisions. The nonlinear wave damping and cross-sections of wave scattering and transformation by plasma fluctuations are shown to be different under the conditions of three- and four-wave resonances.

# ON THE ROLE OF ANOMALOUS RESISTIVITY IN A DYNAMICS OF PLASMA SWITCHING

J.L.Kalda, A.S.Kingsep, A.A.Sevastyanov
I.V.Kurchatov Institute of Atomic Energy,
123182, Moscow, USSR

High-current plasma diodes are considered now in a problem of plasma switching [1-3]. The switching scenario admits the MHD framework if the space scale $a \gg c/\omega_{pi}$. The most popular erosion model [4] corresponds to the vacuum diode approximation $a \ll c/\omega_{pe}$. Some intermediate region in a broad range of parameters

$$c/\omega_{pi} \gg a \gg c/\omega_{pe}$$
$$v_A, c_s \ll j/ne \ll v_{Te}, v_{Ae} \qquad (1)$$

is adequate to the limits of applicability of EMH i.e. electron magnetohydrodynamics [5]. In a plasma diode EMH describes so-called conductivity phase [1]. The real physical switching may be achieved already at this stage, at any rate, it corresponds to the magnetic field penetration into a gap.

The model of the diode geometry is presented in Fig 1. The mechanism of the field penetration was proposed in [5,6]. It turns out to be non-diffusional, based on the Bürgers equation

$$\partial B/\partial t + (\varkappa/2)\partial B^2/\partial z = D\partial^2 B/\partial z^2 \qquad (2)$$

$B(z,t)_{z=0}=B_0$, $B(z,t)_{t=0}=B_0[1-\theta(z)]$, $D=c^2/4\pi\sigma$, $\varkappa=(c/4\pi e)\nabla n^{-1}$

Its solution looks like the shock wave:

$$B=(B_0/2)[1-\mathrm{th}(\varkappa B_0/4D)(z-Vt)],\ V=\varkappa B_0/2 \qquad (3)$$

The result (3) has been obtained in the assumptions $\sigma$ =const and $P=P(n)$. Let us note however that condition (1) just corresponds to the excitation of the ion-acoustic instability providing the anomalous resistivity. It may be taken into account within the framework of hydrodynamics in Sagdeev's form:

$$\sigma_{an}=(\omega_{pe}/4\pi)(\nu_{Te}/u),\ u=j/ne \qquad (4)$$

Assume the diode plasma to be cold (e.g., due to the thermal losses). Instead of Eq.(2) one can obtain using (4):

$$\partial B/\partial t + \varkappa B\partial B/\partial z = \lambda|\partial B/\partial z|\partial B/\partial z$$
$$\lambda=(4\pi)^{3/2}\, mc^3/ne^2P^{1/2}$$

The result looks simple enough:

$$B = (B_o/2)[1 - \sin\pi(z - Vt)\delta^{-1}],\ \delta = \pi(\lambda/\varkappa)^{1/2},\ V = \varkappa B_o/2 \qquad (5)$$

$$\arg(\sin\phi) \in [-\pi/2, +\pi/2]$$

The width of the "shock" front (5) exceeds those for the case of Coulomb resistance $\delta_q$:

$$\delta_q/\delta = 270\pi^{3/2}\Lambda e^{7/2}|n/\nabla n|^{1/2} n^{5/2} B_o^{-7/2} \qquad (6)$$

E.g., taking $n \sim 10^{13}\,cm^{-3}$, $|n/\nabla n| \sim 1$cm, $B_o \sim$ 20KGs, one has $\delta \sim 0.5cm \gg \delta_q$ and only by $B_o \sim$ 20 Gs $\delta \sim \delta_q \sim 10^{-2}$cm. Then assume plasma to be hot taking into account the turbulent heating. So the field dynamics is conditioned by the effect $\nabla n \times \nabla(P + B^2/8\pi)$. Respectively, the fundamental system of equations is the following

$$\partial\vec{B}/\partial t + (c/e)[\nabla(P + B^2/8\pi), \nabla n^{-1}] = -\mathrm{rot}\vec{j}/\sigma$$

$$\partial(c_v P + B^2/8\pi) = \mathrm{div}(c_p P\vec{v}_e + \vec{S}) \qquad (7)$$

$$\vec{S} = (c/4\pi\sigma) j_x B_y \vec{e}_z + (c/4\pi e)(\partial P/\partial z) B_y \vec{e}_x + (4\pi)^{-1} B^2 \vec{v}_e$$

Two first integrals result from the system (7): $V = \gamma\varkappa B_o/2$ and $P(z) = B^2(z)/8\pi c_v$. As for the width of the front, it may be described by the formula (6) again. The shape of the front turns out to coinside with the KDV soliton (or, more exactly, one half of it):

If $z \le Vt$, $B = B_o$

If $z \ge Vt$, $B = B_o \mathrm{ch}^{-2}[(\omega_{pe}/c)(V/c)^{1/2}(2c_v)^{1/4}(z - Vt)]$

If however the diode gap $d \le \delta$, the penetration of the magnetic field is purely diffusional.

Anomalous resistivity is allowed to be the main reason of switching by itself. The condition (1) shows that, while decreasing of plasma density, the "vacuum" limit is being achieved simultaneously with the threshold of the Buneman instability $j \sim nev_{Te}$. The latter at the non-linear stage leads to the formation of double sheets. This critical point may have been coming in owing to both EMH dynamics and/or overheating (when the magnetic field does not play any essential role). Assume formula (4) to remain still valid, but the external magnetic field to be applied to the diode strong enough for the crossing the electrodes by the net field line. The basic system of equations

$$nM\vec{dv}/dt + \nabla nT_e = 0$$
$$\partial n/\partial t + \mathrm{div}\,(n\vec{v}) = 0 \qquad (8)$$
$$n(\vec{u}\nabla)T - (\gamma - 1)T(\vec{u}\nabla)n = j^2 4\pi u/\omega_{pe}\nu_{Te}$$

may be reduced in this case to the 1-d:

$$n(M/m)(\partial v/\partial t + v\partial v/\partial x) + \partial(n\nu_{Te}^2)/\partial x = 0$$
$$\partial n/\partial t + \partial(nv)/\partial x = 0 \qquad (9)$$
$$n\nu_{Te}^2 = [n^{3\gamma/2} n_o^{3(1-\gamma)/2} \nu_o^3 + (3/2)(\gamma-1)(4\pi/m)^{1/2}(j^2/e)n^{3\gamma/2} \times \int_o^x n(\xi)^{-3\gamma/2} d\xi]^{2/3}$$

$$n_o = n(x)_{x=0}, \quad \nu_o = \nu_{Te}(x)_{x=0}$$

The stationary solution of (9)

$$n = n_o \exp[(j/n_o\nu_o)^2 (x/r_{De}(0))(1-\gamma)/\gamma]$$

cannot be realised within a reasonable range of parameters because condition (1) breaks and Buneman instability joins the game. The time-dependent solution of the linearized system (9)

$$\delta n(t) = -0.67\,(m/M)[(\gamma-1)m^{-1/2} j^2/e]^{2/3} x^{-4/3} t^2$$
$$x > r_{De}(0)(\nu_o/u)^2$$

reveals the swift decrease of plasma density close to the cathode (Fig.2). During the time interval $\tau \sim (M/m)^{1/2}\omega_{pi}^{-1}$ the system penetrates the Buneman threshold and then formation of the double sheet occurs in a time $\tau \sim \omega_{pi}^{-1}$. This sheet turns out to be located in a cathode region, its space scale is of the order of $c/\omega_{pe}$.

Thus we can see the anomalous resistivity in a broad range of plasma density and/or current velocity values does condition both current penetration into the PEOS gap and probably the mechanism of the switching.

## References


1.P.F.Ottinger et al.Int.Workshop on Physics and Technique of High Power Opening Switches.Novosibirsk,1989,I.1

2.L.P.Zakatov et al.Ibid,III.2

3.R.J.Comisso et al.Ibid,II.1

4.P.F.Ottinger et al.J.Appl.Phys.,1984,V.56,p.774

5.A.S.Kingsep,K.V.Chukbar,V.V.Yan'kov.Voprosy teorii plasmy (Problems of Plasma Theory),ed.by B.B.Kadomtsev,1987,V.16

6.A.S.Kingsep et al.Sov.J.of Plasma Physics,1984,V.10,p.854.

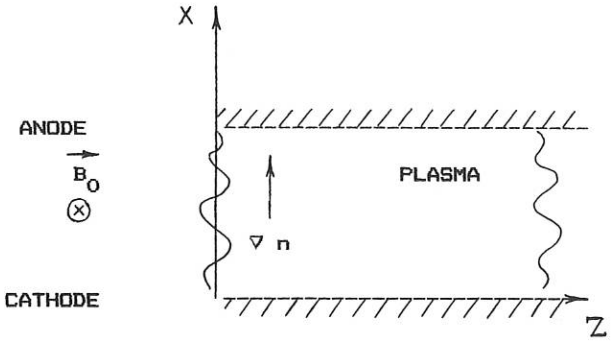


Fig.1

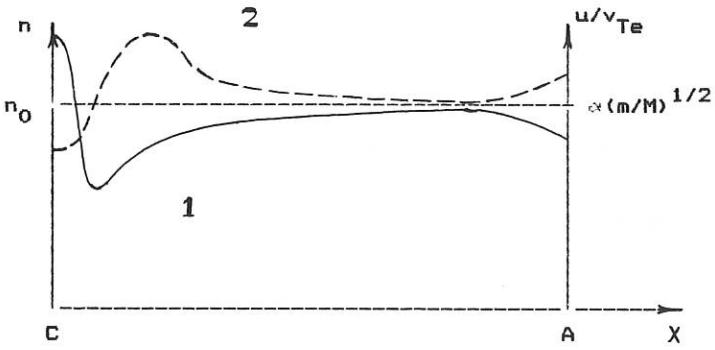


1 - n, 2 - $u/v_{Te}$

Fig.2

# KINETIC THEORY ON ALFVEN SOLITIONS IN COLLISIONAL PLASMAS

PAN Chuan-Hong QIU Xiao-Ming JAN Guang-De
(Southwestern Institute of Physics, P.O.Box 15, Leshan, Sichuan, P.R.China)

ABSTRACT In kinetic theory frame we have studied numerically the Alfven wave nonlinear propagation in collisional plasmas, and observed that an initial solitary wave packet undergoes viscosity and damps because of both the collision effect and nonlinear Landau damping.

1. BASIC EQUATIONS We are now dealing with the following system, the plasma is homogeneous and includes only two components, electron and ion; the d.c. magnetic field, $\vec{B}_0$, is constant and directs along z axis; a parallel Alfven wave propagetes in the direction of $\vec{B}_0$. Under the conditions considered here, we have $\partial/\partial x = \partial/\partial y = 0$ and $\partial/\partial z \neq 0$ when spatial differential operator acts on the wave field-quantities.

Each component of the plasma is described by its own Boltzmann's equation. We take the form of

$$f = f_g + f_\xi \,, \tag{1}$$

to express the distribution function. Where $f_g$ is the part independent on $\xi$, and $f_\xi$ the oscillations on $\xi$. Substituting expression (1) into Boltzmann's equation, we obtain

$$\frac{d_0}{dt} f_g + S_g = \left(\frac{\partial f}{\partial t}\right)_g \tag{2}$$

$$\frac{\partial f_\xi}{\partial \xi} = \frac{1}{\Omega}\{\Omega v_\perp (b_y \cos\xi - b_x \sin\xi)\frac{\partial f_g}{\partial v_z} + [(\frac{q\tilde{E}_x}{m} - \Omega v_z b_y)\cos\xi + (\frac{q\tilde{E}_y}{m} + \Omega v_z b_x)\sin\xi]\frac{\partial f_g}{\partial v_\perp} + \frac{d_0}{dt} f_\xi + S_\xi - (\frac{\partial f}{\partial t})_\xi\} \tag{3}$$

where we have dropped the subscript indicating particle species and written the velocity variable as $\vec{v} = v_z\hat{z} + v_\perp(\hat{x}\cos\xi + \hat{y}\sin\xi)$, $\xi$ is the angle in the transversal velocity space. $\Omega \equiv qB_0/mc$ the gyro-frequency, q and m are the electric charge and mass respectively, $\vec{\tilde{E}} = \tilde{E}_x\hat{x} + \tilde{E}_y\hat{y}$ the wave electric field. $\vec{\tilde{B}} = \tilde{B}_x\hat{x} + \tilde{B}_y\hat{y} = B_0(b_x\hat{x} + b_y\hat{y})$ the wave magnetic field, $S_g$ and $S_\xi$ have the same

meaning as $f_g$ and $f_\xi$ for the quantity

$$S \equiv \Omega v_\perp (b_y \cos\xi - b_x \sin\xi)\frac{\partial f_\xi}{\partial v_z} + \left[\left(\frac{q\tilde{E}_x}{m} - \Omega v_z b_y\right)\cos\xi + \left(\frac{q\tilde{E}_y}{m} + \Omega v_z b_x\right)\sin\xi\right]\frac{\partial f_\xi}{\partial v_\perp}$$

$$- \frac{1}{v_\perp}\left[\left(\frac{q\tilde{E}_x}{m} - \Omega v_z b_y\right)\sin\xi - \left(\frac{q\tilde{E}_y}{m} + \Omega v_z b_x\right)\cos\xi\right]\frac{\partial f_\xi}{\partial \xi} . \qquad (4)$$

Similarly, $(\partial f/\partial t) = (\partial f/\partial t)_g + (\partial f/\partial t)_\xi$ the collision term. In this paper we take a Fokker-Planck aperator, which conserves momentum and energy.

In fact, Both $f_g$ and $f_\xi$ include two parts, one is the pure response to the incident wave (without a collision term) and the other is related to collision. Taking the equilibrum distribution to be a Maxwellian, we have $f_g = f_g^w + f_m + \tilde{f}_g$ , $f_\xi = f_\xi^w + \tilde{f}_\xi$ , Here $f_m$ indicates Maxwellian, $f^w = f_g^w + f_\xi^w$ the response to the incident wave, and

$$\tilde{f} = \tilde{f}_g + \tilde{f}_\xi \qquad (5)$$

the perturbation distribution function due to collision.

Making use of the Fourier series expansion for $f_\xi^w$ , $\tilde{f}_\xi$ and $(\partial f/\partial t)_\xi$ , $f_\xi^w = \sum (A_n^w \cos n\xi + B_n^w \sin n\xi)$ , $\tilde{f}_\xi = \sum (\tilde{A}_n \cos n\xi + \tilde{B}_n \sin n\xi)$ , $(\partial f/\partial t)_\xi = \sum (C_n \cos n\xi + D_n \sin n\xi)$ , we found that only the first order of oscillations on $\xi$ are essential to our problem. Integrating over $\xi$ by parts, the current components, $j_x$ and $j_y$ , can be reduced to

$$j_x = -\frac{1}{2}\sum q \int dv\, v_\perp (B_1^w + \tilde{B}_1), \qquad j_y = \frac{1}{2}\sum q \int dv\, v_\perp (A_1^w + \tilde{A}_1) . \qquad (6)$$

In which the collisional contribution has been taken into account, and the conservation relations have beenused here.

Using the Fourier series expansion, $S_g$ can be found from Eq. (4) . We can also calculate $(\partial f/\partial t)_g$ and $C_1$, $D_1$ , by Sustituting $f_0 = f_m$ and $\tilde{f} = \tilde{f}_g + \sum (\tilde{A}_n \cos n\xi + \tilde{B}_n \sin n\xi)$ into the Fokker-Planck operator. After that the functions $f_g^w$ and $\tilde{f}_g$ are determined. Both $A_1 \equiv A_1^w + \tilde{A}_1$ and $B_1 \equiv B_1^w + \tilde{B}_1$ can be finally obtained from Eq.(3). Finishing the integrating over velocity space and neglicting the displaeement current, we obtain from Ampere's law that

$$\begin{cases} \dfrac{\partial b_y}{\partial \tau} + \bar{\nu} b_y + \dfrac{\partial}{\partial \eta}\{b_y + b_y(b_x^2+b_y^2)(1-\beta+\beta_d)\} + \mu \dfrac{\partial^2}{\partial \eta^2} b_x = 0 \\ \dfrac{\partial b_x}{\partial \tau} + \bar{\nu} b_x + \dfrac{\partial}{\partial \eta}\{b_x + b_x(b_x^2+b_y^2)(1-\beta+\beta_d)\} - \mu \dfrac{\partial^2}{\partial \eta^2} b_y = 0 \end{cases} \tag{7}$$

Here we have token the approximations $\tilde{E}_x = v/c\tilde{B}_y$ and $\tilde{E}_y = -v/c\tilde{B}_x$, $V$ is the characteristic speed of Alfven wave $v^2 = B_0^2/4\pi n_0 (m_i+m_e)$. $\eta$ is the dimensionless distance along the d.e.magnetic field, and $\tau$ the dimensionless time variable. They are introduced by means of $\partial/\partial z \to 1/L\ \partial/\partial\eta$, $\partial/\partial t \to \omega\partial/\partial\tau$, where L and $\omega$ are, respetively, the Characteristic length and frequency of Alfven wave, $\beta$ the ratio of plasma pressure to magnetic pressure, $\mu \equiv 1/2\ (1/R_i - 1/R_e)\ \beta$, $1/R_j \equiv \omega/\Omega_j$ the ratio of Alfven wave characteristic frequency to particle gyro-frequency and

$$\bar{\nu} \equiv (m_i \nu_i \alpha_i/\Omega_i + m_e \nu_e \alpha_e/\Omega_e)/(m_i+m_e)$$

$$\beta_d \equiv 4\pi n_0/B_0^2 [T_i W(\xi_i) + T_e W(\xi_e)],$$

$\alpha_j \equiv R_j/n_0 \int dv\ [1 + (v_\perp^2/2 - v_z^2)/v^2]\ \tilde{f}_{j0}$, $W(\xi_j) \equiv (2\pi)^{-1/2} \int_{-\infty}^{\infty} dx \times \exp(-x^2/2)/(x-\xi_j)$ the dispersion function, $\xi_j \equiv v/\sqrt{T/m_j}$ the ratio of Alfven wave characteristic velocity to particle thermal speed. Other quantities are conventional.

From Eqs. (7), we get

$$i\left(\frac{\partial}{\partial\tau} + \nu\right)\phi_\pm + i\frac{\partial}{\partial\eta}\{\phi_\pm [1 + |\phi_\pm|^2 (g - i\,\mathrm{Im}\,\beta_d)]\} \pm \mu \frac{\partial^2}{\partial\eta^2}\phi_\pm = 0 \tag{8}$$

Where $\phi_\pm \equiv b_y \pm i b_x$, $g \equiv 1 + \beta - \mathrm{Re}\,\beta_d$.

In Eq. (8) the terms including $\bar{\nu}$ and $\mathrm{Im}\,\beta_d$ indicate the collision viscosity and the nonlinear Landau damping respectively. This shows us that the system here is dissipative. So that it is no longer to find a stationary soliton-like solution.

## 2. DISCUSSION AND CONCLUSION

Dropping the collisional term and the nonlinear Landau demping, we can reduce equation (8) to that Spangler et al. studied in Ref. [1] as long as replacing g by $1/4(1-\beta)$. In Ref. [1] Spangler et al. adopt the pseudo-potential method[2] and found the solution in the form of $\phi = u(\eta, \tau)\, e^{i\theta(\eta,\tau)}$. They pointed out that both $\phi_+$ and $\phi_-$ have two

solitons, a super-Alfvenic soliton, and the one with $v_E<1$ ($v_E$ is envelope speed of Alfven wave-packet). From Ref. [1], the super-Alfvenic soliton can be reduced to a simple form

$$\phi_{\pm}^{super}=\sqrt{\frac{v_E-1}{g}}(\sqrt{5}\mathrm{ch}x+1)^{-1/2}\exp\{\pm i[\frac{x}{2}+\frac{T}{2}-3\mathrm{tg}^{-1}(\frac{\sqrt{5}-1}{2}\mathrm{th}\frac{x}{2})]\}$$

Here $v_E$ is the envelope speed. $X\equiv (v_E-1)/\mu\ [\eta-v_E\tau)]$. $T\equiv [(v_E-1)^2/\mu]\tau'$, $\tau'$ is the time measured in the frame moving with the wave-packet.

We now consider that a wave-packet shown above exists initially in the plasma at t=0, and investigate numerically its time evolution for non-zero values of $\bar{\nu}$ and $I_m\beta_d$. To do this, we adopt the variables X and T instead of $\eta$ and $\tau$, and make a tranform $\phi_{\pm}(\eta,\tau)\rightarrow[(v_E-1)/g]^{1/2}\phi_{\pm}(X,T)$. Equation (8) can be rewritten as

$$i(\frac{\partial}{\partial T}+C)\phi_{\pm}+i\frac{\partial}{\partial X}\{\phi_{\pm}[1+|\phi_{\pm}|^2(1-iD)]\}\pm\frac{\partial^2}{\partial X^2}\phi_{\pm}=0$$

where $C\equiv\bar{\nu}\mu/(v_E-1)^2$, $D\equiv I_m\beta_d/g$.

The equation was discretized according to Grank-Nicholson schem. The numerical results show us that the initial wave-packet uncergoes viscosity and damps because of both the collision effect and nonlinear Landau damping. Our numerical results include both the $\phi_+$ and $\phi_-$. We illustrate here the time evolution of $|\phi_-|$ in the figure for C=0.08 and D=0 we see that the envelope damps obviously as T increases. We have also obtained the results for C=0 and D=0.08, and found that the envelope can exist for a longer time than the preceding case. So we can conclude that nonlinear Landau damping is a weak demping-effect comparing with the collision one.

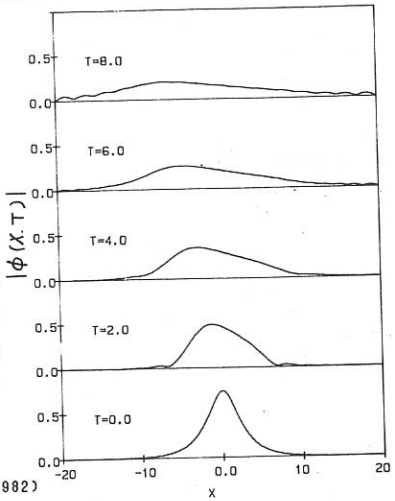


[1.] S.R. Spangler et al., J. Plasma Phys. 27, 193(1982)

[2.] P.J. Hansen and D.R. Nicholson, Am. J. Phys. 47, 769(1979).

# ION-ACOUSTIC RAREFACTIVE SOLITON IN TWO-ELECTRON TEMPERATURE PLASMA

V.K. Sayal and S.R. Sharma

Department of Physics, University of Rajasthan,
Jaipur - 302004 (INDIA)

## 1. Introduction

The Ion-acoustic rarefactive soliton (IARS) in a two-electron temperature plasma with cold ions has been investigated theoretically using fluid model [1,2]. It has been found that only for certain temperature and density ratios of the cold and hot electron components IARS exists. However, experimental study of IARS showes that there is a discrepancy between theoretical predictions and experimental observations. Specifically experimental results show that the relationship between Mach number and amplitude of the IARS is not a linear one. Experimentally observed width of the IARS is much smaller than that predicted by theory. It seems that the fluid mldel is not suitable to explain quantitatively the propagation characteristics of the IARS.

In this paper we have tried to explain the propagation characteristics of the IARS assuming that reflected electrons also play the crucial role. Section 2 deals with the formulation of the problem. Conclusions are drawn in section 3.

## 2. Formulation of the Problem

We consider a plasma consisting of cold ions, two electron components having different temperatures $T_c$ and $T_h$. Since ions are cold therefore the dynamics of the ions is determined by fluid equations i.e.

$$\frac{\partial N}{\partial t} + \frac{\partial}{\partial x}(Nu) = 0 \qquad (1)$$

$$\frac{\partial u}{\partial t} + u\frac{\partial u}{\partial t} = -\frac{e}{m_i}\frac{\partial \varphi}{\partial x} \qquad (2)$$

The distribution function for free and refleced cold (hot) electrons can be described in the following form which are the steady state solution of Vlasov equation [4].

for free electrons i.e. $v^2 > 2\frac{e}{m_e}(\psi + \varphi)$

$$F_{sf} = A_s n_{os} \left(\frac{m_e}{2\pi T_s}\right)^{1/2} \exp\left(-\frac{m_e}{2T_s}\left(V_o \pm \left(v^2 - 2\frac{e}{m_e}(\psi+\varphi)\right)^{1/2}\right)^2\right) \qquad (3.a)$$

for reflected electrons i.e. $v^2 \leq 2\frac{e}{m_e}(\psi + \varphi)$

$$F_{st} = A_s\, n_{os}\, \left(\frac{m_e}{2\pi T_s}\right)^{1/2} \exp\left(-\frac{m_e}{2T_s}\left(V_o^2 + \beta_s\left(v^2 - 2\frac{e}{m_e}(\psi+\varphi)\right)\right)\right) \tag{3.b}$$

where s = c (h) corresponds to cold (hot) component. $n_{os}, T_s$ are unperturbed density, temperature of the electrons, $\beta_s$ is an arbitrary number ($\geq 0$) associated with reflected electrons. $A_s$ is normalization fator. $V_o$ is the velocity of perturbation. $\psi$ is amplitude of the potential $\varphi$ , $-\psi \leq \varphi \leq 0$.

Since $V_o$ is of the order of ion-acoustic speed and is much less than electron thermal speedtherefore it can be neglected in (3). Hence the density of the electrons, obtained by integrating the distribution function (3) over velocity space, is

$$n_s = \alpha_s A_s \left(\exp(\theta_s\phi)\,(1-\mathrm{erf}(\sqrt{\theta_s\phi})) + \frac{1}{\sqrt{\beta_s}}\exp(\beta_s\theta_s\phi)\,\mathrm{erf}(\sqrt{\beta_s\theta_s\phi})\right) \tag{4}$$

where $\alpha_s = n_{os}/n_o$, $\theta_s = T_{eff}/T_s$, $\phi = \psi + \varphi$ is normalized with $T_{eff}/e$, $T_{eff} = T_h T_c/(\alpha_c T_h + \alpha_h T_c)$

$$A_s = \left(\exp(\theta_s\psi)\,(1-\mathrm{erf}(\sqrt{\theta_s\psi})) + \frac{1}{\sqrt{\beta_s}}\exp(\beta_s\theta_s\psi)\,\mathrm{erf}(\sqrt{\beta_s\theta_s\psi})\right)^{-1} \tag{5}$$

For the steady state solution of (1) and (2), we use the transformation $\xi = x - V_o t$ and get,

$$N = M/(M^2 - 2\varphi)^{1/2} \tag{6}$$

where $M = V_o/\sqrt{(T_{eff}/m_i)}$. N, $\varphi$ are normalized by $n_o$ and $T_{eff}/e$ respectively.

Ions and electrons densities are coupled with the normalized Poisson's equation

$$\frac{\partial^2\varphi}{\partial\xi^2} = n_c + n_h - N \tag{7}$$

Using the conditions that as $\xi \to \infty$, $\varphi$ and $\varphi' \to 0$ we get from (4), (6) and (7)

$$\frac{1}{2}\left(\frac{d\varphi}{d\xi}\right)^2 = -V(\varphi) \tag{8}$$

where

$$V(\varphi) = M^2 - M(M^2 - 2\varphi)^{1/2} - \alpha_c A_c/\theta_c\, f_c(\varphi) - \alpha_h A_h/\theta_h\, f_h(\varphi) \tag{9}$$

$$f_s(\varphi) = \exp(\theta_s(\psi+\varphi))\,(1-\mathrm{erf}(\sqrt{\theta_s(\psi+\varphi)})) - \exp(\theta_s\psi)\,(1-\mathrm{erf}(\sqrt{\theta_s\psi})) + \frac{2}{\sqrt{\pi}}(1-1/\beta_s)\sqrt{\theta_s}\,(\sqrt{(\psi+\varphi)} - \sqrt{\psi}) + 1/\beta_s^{3/2}\,(\exp(\beta_s\theta_s(\psi+\varphi))\,\mathrm{erf}(\sqrt{\beta_s\theta_s(\psi+\varphi)}) - \exp(\beta_s\theta_s\psi)\,\mathrm{erf}(\sqrt{\beta_s\theta_s\psi}))$$

In order to get rarefactive solitary solution of (8), Sagdeev potential (9) must satisfied following conditions

at $\varphi=0$, $V''(0) = 1/M^2 - n_c'(0) - n_h'(0) \leq 0$ (10.a)

at $\varphi = -\psi$, $V'(-\psi) = M/(M^2+2\psi)^{1/2} - \alpha_c A_c - \alpha_h A_h \leq 0$ (10.b)

and $V(-\psi) = 0$ (10.c)

where $n_s'(0)$ =

$$\alpha_s A_s \theta_s \left(\exp(\theta_s\psi)\,(1-\mathrm{erf}(\sqrt{\theta_s\psi})) + \sqrt{\beta_s}\,\exp(\beta_s\theta_s\psi)\,\mathrm{erf}(\sqrt{\beta_s\theta_s\psi})\right)$$

The nonlinear dispersion relation for IARS obtained from (9) using condition (10.c) is

$$M^2 = A^2 \,/\, 2(\psi+A) \qquad (11)$$

where $A = \alpha_c A_c/\theta_c\, f_c(-\psi) + \alpha_h A_h/\theta_h\, f_h(-\psi)$

Perturbation in ion density at $\xi = 0$ i.e. at $\varphi = -\psi$ is

$$\delta N = M/(M^2 + 2\psi)^{1/2} - 1 \qquad (12)$$

From (6) and (8) we can define the width of the soliton as follows

$$D = \int_{N_o/2}^{N_o} \frac{M^2}{N^3}\,\frac{dN}{\sqrt{(-2V(\varphi))}} \qquad (13)$$

In order to get numerical value of D we rewwrite (13) as

$$D = \frac{M}{4\sqrt{(-2V'(-\psi))}}\left(\frac{(2N_o+3N_1)\sqrt{(N_1-N_o)}}{N_1^2\sqrt{N_o}} + \frac{3}{N_o}\tan^{-1}\left(\frac{N_1}{N_o}-1\right)\right)$$
$$\int_{N_o/2}^{N_1} \frac{M^2}{N^3}\,\frac{dN}{\sqrt{(-2V(\varphi))}} \qquad (14)$$

where $N_o = 1+\delta N = M/(M^2+2\psi)^{1/2}$ and $N_1 = 1+0.99\,\delta N$

## 3. Discussion and Results

One can see that for $\beta_c = \beta_h = 1$ the nonlinear dispersion relation for the IARS (11) reduced to that derived with fulid model for electrons. Numerical analysis is performed with (11), (12) and (14) along with the conditions (10.a&b) for different values of $\beta_c$ and $\beta_h$ keeping $T_h/T_c = 14$, $\alpha_h/\alpha_c = 12.6$ as in experiment [3].

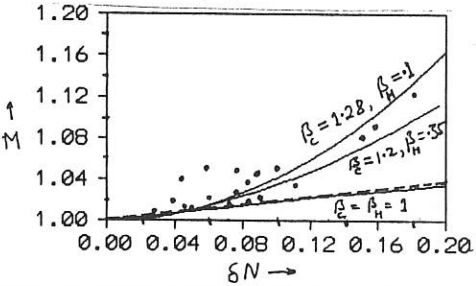


Fig.1: Variation of Mach number with the amplitude ($\delta N$) of the IARS, given by relation (11 & 12), for $\alpha_h/\alpha_c$=12.6 and $T_h/_c$=14. line (---) refers to Kdv solution. Dots (●) are experimental values [3].

Fig.(1) shows the variation of Mach number with the amplitude ($\delta N$) of the IARS with three sets of $\beta_c$ and $\beta_h$. We have choosen suitable values of $\beta_c$ and $\beta_h$ and compare with the experimental values as obtained by Nishida and Nagasawa [3]. In fig.(2) the variation of square of width with the inverse of the amplitude is shown. For the same values of $\beta_c$ and $\beta_h$ we find that the curves are closer to the experimental values as compared to the

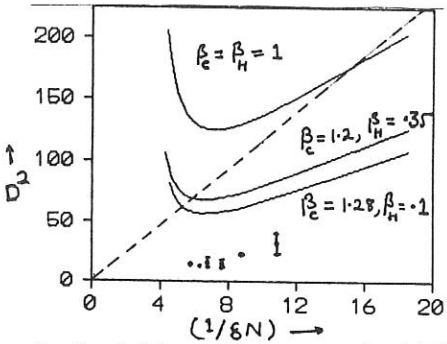


Fig.2: Variation of square of width ($D^2$) with the inverse of amplitude ($1/\delta N$), given by relation (14), for $\alpha_h/\alpha_c = 12.6$ and $T_h/T_c = 14$. Line (---) refers to Kdv solution. Dots (•) are experimental values [3].

Kdv solution. Thuse we see that instead of fluid model for electrons the kinetic model is a better representative of the experimenal finding.

References

1. B.N Goswami and B. Buti, Phys. Lett. 57A (1976) 149.
2. B. Buti, Phys. Lett. 76A (1980) 251.
3. Y. Nishida and T. Nagasawa, Phys. Fluid 29 (1986) 345.
4. H. Schamel, Plasma Phys. 13 (1971) 491.

# RELATIVISTIC DISPERSION FUNCTIONS FOR ANISOTROPIC PLASMAS

M. Bornatici

Physics Department, University of Ferrara, Ferrara, Italy
Physics Department "A.Volta", University of Pavia, Pavia, Italy

A general class of weakly relativistic plasma dispersion functions (PDF's) relevant to describing the dielectric properties of a plasma with temperature (and loss-cone) anisotropy is discussed. Series representations of the new PDF's in terms of standard trascendental functions are obtained and a number of relevant limiting cases are discussed.

Introduction. The presence of a low-density population of superthermal particles is a common feature of plasmas with significant additional heating and/or current drive. Whereas a detailed knowledge of non-thermal velocity distribution requires the use of a Fokker-Planck code, to get a first insight into the main physics of a non-thermal plasma it is often useful to adopt a model distribution function suited to describing the salient characteristics envisaged for the plasma under consideration.

For the specific case in which the particle distribution is a bi-Maxwellian ($T_\parallel \neq T_\perp$, with $T_\parallel$ and $T_\perp$, respectively, the temperature parallel and perpendicular to the external magnetic field), the case of a loss-cone anisotropy in the form of a Dory-Guest-Harris distribution being formally the same, the plasma dielectric properties are described by the following class of weakly relativistic plasma dispersion functions (PDF's) /1/

$$R^{(n)}_{q,\ell}\left[z_n(T_\parallel), a_\parallel, \lambda_\perp; T_\perp/T_\parallel\right] \equiv -i\int_0^\infty d\tau \, \frac{e^{iz_n(T_\parallel)\tau - a_\parallel \tau^2/(1-i\tau)}}{(1-i\tau)^q (1-i\tau\, T_\perp/T_\parallel)^\ell} \, \Gamma_n\left(\frac{\lambda_\perp}{1-i\tau T_\perp/T_\parallel}\right)$$

$$= \sum_{k=0}^{\infty} a_{k,|n|}\, \lambda_\perp^{k+|n|}\, W_{q,k+\ell+|n|} \,. \qquad (1)$$

with q and $\ell$, respectively, semi-integer and integer positive numbers,

$$z_n(T_\parallel) \equiv \mu_\parallel (1 - n\omega_c/\omega), \quad a_\parallel \equiv \mu_\parallel N_\parallel^2/2, \quad \mu_{\parallel(\perp)} \equiv mc^2/T_{\parallel(\perp)} \quad (>> 1)$$

$$\Gamma_n(x) \equiv e^{-x} I_n(x), \quad \lambda_\perp \equiv (\omega/\omega_c)^2 N_\perp^2/\mu_\perp$$

AS

being a modified Bessel function, with $N_{\parallel}$ and $N_{\perp}$ , respectively, the llel and perpendicular wave refractive index . Furthermore,

$$\equiv \frac{(-1)^k[2(|n|+k)]!}{(|n|+k)!(2|n|+k)!k!} \quad 2^{-(k+|n|)}, \quad \text{and}$$

$$z_n(T_{\parallel}),a_{\parallel};T_{\perp}/T_{\parallel}) \equiv -i\int_0^{\infty} d\tau \frac{e^{iz_n(T_{\parallel})\tau - a_{\parallel}\tau^2/(1-i\tau)}}{(1-i\tau)^q(1-i\tau T_{\perp}/T_{\parallel})^p} \qquad (2)$$

ction he effect of the temperature anisotropy can be delt with by applying asma inomial expansion to the $(1-i\tau T_{\perp}/T_{\parallel})^{-p}$-factor of the integrand of (2), esent the result that the $W_{q,p}$ -functions can be expressed in terms of the e obt index) Shkarofsky functions /2/ for which several analytical proper- are known /3/ .

herma weakly relativistic anisotropic PDF's. Depending upon whether the l hea erature-anisotropy is such that $|1-T_{\parallel}/T_{\perp}| < 1$, or $T_{\perp} < T_{\parallel}$, or $T_{\parallel} < T_{\perp}$, the l velo owing series representations of the $W_{q,p}$ -functions (2) are obtained,

first useful ient c $= \left(\frac{T_{\parallel}}{T_{\perp}}\right)^p \sum_{k=0}^{\infty} \frac{(p)_k}{k!} \left(1 - \frac{T_{\parallel}}{T_{\perp}}\right)^k W_{q+p+k}(z_n(T_{\parallel}),a_{\parallel}), \quad \left|1 - \frac{T_{\parallel}}{T_{\perp}}\right| < 1 \qquad (3a)$

a bi- ure pa of a l $= \sum_{k=0}^{\infty} (p)_k \left(\frac{T_{\perp}}{T_{\parallel}}\right)^k \sum_{j=0}^{k} \frac{(-1)^j}{j!(k-j)!} W_{q-j}(z_n(T_{\parallel}),a_{\parallel}), \quad T_{\perp} < T_{\parallel} \qquad (3b)$

being d by t s (PD

$= \frac{T_{\parallel}}{T_{\perp}} e^{-a_{\parallel}} \sum_{k=0}^{\infty} (q)_k M(q+k,q,a_{\parallel}) \left(\frac{T_{\parallel}}{T_{\perp}}\right)^k \sum_{j=0}^{k} \frac{(-1)^j}{j!(k-j)!} F_{p-j}(x_n(T_{\perp},N_{\parallel}^2)),$

$T_{\parallel} < T_{\perp} \qquad (3c)$

e $(b)_k = b(b+1)\ldots(b+k-1)$, $(b)_0 = 1$; the $W_q$ -functions are the Shkarofsky tions /2/ which are defined by (2) with $T_{\perp}^q = T_{\parallel}$ in the denominator of bers, integrand; the $F_p$ -functions are the Dnestrovskii functions of integer x /3/ and are defined by (2) with $a_{\parallel} = 0$ and $T_{\perp} = T_{\parallel}$, the argument of s $x_n(T_{\perp},N_{\parallel}^2) \equiv \mathcal{M}_{\perp}[(N_{\parallel}^2/2)+(n\omega_c/\omega)-1]$ ; $M(a,b,x)$ is the confluent hypergeome- (Kummer's) function /4/ , also referred to as a degenerate hypergeo- ic function /5/ . A few relevant limiting cases can be obtained from

(3). In particular, i) from (3a), $W_{q,p} = W_{q+p,n}(z_n(T_\parallel), a_\parallel)$ to lowest order in $|1 - T_\parallel/T_\perp|$, with $a_\parallel = \mu_\parallel N_\parallel^2/2$; ii) from (3b), to lowest order in $T_\perp/T_\parallel$, $W_{q,p} = W_{q,n}(z_n(T_\parallel), a_\parallel)$, which is independent of the index p; iii) to lowest significant order in $(T_\parallel/T_\perp)$, from (3c) one obtains $W_{q,p} = (T_\parallel/T_\perp) F_p(zn(T_\perp))$, which is independent of the index q; on the other hand, for perpendicular ($N_\parallel = a_\parallel = 0$) propagation, (3c) yields, (M(a,b,o)=1),

$$W_{q,p}(N_\parallel=0) = \frac{T_\parallel}{T_\perp} \sum_{k=0}^{\infty} (q)_k \left(\frac{T_\parallel}{T_\perp}\right)^k \sum_{j=0}^{k} \frac{(-1)^j}{j!(k-j)!} F_{p-j}\left[\mu_\perp\left(\frac{n\omega_c}{\omega} - 1\right)\right] \qquad (3d)$$

For the case in which the density of the non-thermal population is small with respect to the density of the bulk, the non-thermal plasma component contributes mainly to the anti-Hermitian part of the dielectric tensor. It is thus of particular relevance to evaluate the imaginary (Im) part of the PDF's (3). From (3a) we get

$$\mathrm{Im}W_{q,p} = -\pi \left(\frac{T_\parallel}{T_\perp}\right)^p \left[x_n(T_\parallel, N_\parallel^2)\right]^{q+p-1} e^{-a_\parallel - x_n(T_\parallel, N_\parallel^2)} g_{q,p}(x_n(T_\parallel, N_\parallel^2), a_\parallel, T_\parallel/T_\perp) \qquad (4)$$

with

$$g_{q,p} = \sum_{k=0}^{\infty} \frac{\left[a_\parallel x_n(T_\parallel, N_\parallel^2)\right]^k}{k!(q+p+k-1)!} M\left(p, q+p+k, \left(1 - \frac{T_\parallel}{T_\perp}\right) x_n(T_\parallel, N_\parallel^2)\right) \qquad (5a)$$

or, alternatively,

$$g_{q,p} = \left[\frac{1}{a_\parallel x_n(T_\parallel, N_\parallel^2)}\right]^{\frac{q+p-1}{2}} \sum_{k=0}^{\infty} \frac{(p)_k}{k!} \left[\left(1 - \frac{T_\parallel}{T_\perp}\right)\left(\frac{x_n(T_\parallel, N_\parallel^2)}{a_\parallel}\right)^{1/2}\right]^k \cdot$$

$$\cdot I_{q+p+k-1}\left(2\sqrt{a_\parallel x_n(T_\parallel N_\parallel^2)}\right) \qquad (5b)$$

the profile variable $x_n(T_\parallel, N_\parallel^2) (\equiv \mu_\parallel [(N_\parallel^2/2) + (n\omega_c/\omega) - 1]) > 0$ ($\mathrm{Im}W_{q,p} = 0$ for $x_n(T_\parallel, N_\parallel^2) \leqslant 0$). By noting that $\int_0^\infty t^{b-1} M(a,b,t) e^{-st}\, dt = (b-1)! \cdot s^{-b}(1-s^{-1})^{-a}$, Reb > 0, Res > 1, cf. Ref. 5, from (5a) one finds $\int_0^\infty (-\mathrm{Im}W_{q,p})\, dx_n = \pi$. For perpendicular ($N_\parallel = a_\parallel = 0$) propagation,

$$\mathrm{q,p}(N_{\parallel}=0) = \frac{1}{(q+p-1)!}\ M\left(p,q+p,\left(1-\frac{T_{\parallel}}{T_{\perp}}\right)\left|z_n(T_{\parallel})\right|\right) \qquad (6)$$

The limits of strong temperature anisotropy can be obtained from (5a) by using the asymptotic expansion of the hypergeometric function M(a,b,z)/4/. To lowest order in $(T_{\perp}/T_{//}) \ll 1$, one has

$$\mathrm{mW}_{q,p} = -\pi e^{-\frac{\mu_{\parallel}N_{\parallel}^2}{2}-x_n(T_{\parallel},N_{\parallel}^2)}\left[\frac{2x_n(T_{\parallel},N_{\parallel}^2)}{\mu_{\parallel}N_{\parallel}^2}\right]^{\frac{q-1}{2}} I_{q-1}\left(\sqrt{2\mu_{\parallel}N_{\parallel}^2 x_n(T_{\parallel},N_{\parallel}^2)}\right) \qquad (7)$$

i.e., $\mathrm{ImW}_{q,p} = \mathrm{ImW}_{q}$, a result which follows immediately from (3b). On the other hand, to lowest significant order in $(T_{\parallel}/T_{\perp}) \ll 1$, it is

$$\mathrm{mW}_{q,p} = -\frac{\pi}{(p-1)!}\ \frac{T_{\parallel}}{T_{\perp}}\ \left|z_n(T_{\perp})\right|^{p-1} e^{-\left|z_n(T_{\perp})\right|},\quad z_n(T_{\perp}) \equiv \mu_{\perp}\left(1-\frac{n\omega_c}{\omega}\right) < 0 \qquad (8)$$

a result which can also be obtained directly from (3c).

Acknowledgement: This work was supported by the Ministero della Pubblica Istruzione of Italy.

References

/1/ M.Bornatici, G.Chiozzi and P.De Chiara, J. Plasma Phys. (submitted).

/2/ I.P. Shkarofsky, Phys. Fluids 9, 561 (1966).

/3/ P.A.Robinson, J.Math. Phys. 27, 1206 (1986); 28, 1203 (1987); 30, 2484 (1989).

/4/ L.J. Slater, in Handbook of Mathematical Functions, M. Abramowitz and J.A. Stegun (Ed.s), National Bureau of Standards, 1972, p. 504.

/5/ I.S. Gradshteyn and I.M. Ryzhik, Table of Integrals, Series, and Products, Academic Press, New York, 1980, p. 860.

# Boundary Larmor Radius Effects

Jin Li and Jan Scheffel

*Plasma Physics and Fusion Research*
*Royal Institute of Technology, S-100 44, Stockholm, SWEDEN*

## Introduction

The Vlasov-Poisson system for a plasma slab of width $L$ with a homogeneous Maxwellian equilibrium is considered. The purpose is to try to understand how stability is affected by Large Larmor Radius effects when the Larmor radius is comparable to the characteristic dimensions of the plasma. Basically there are only two kinds of inhomogeneity: inhomogeneous equilibrium (e.g. non-constant magnetic field or density) or the inhomogeneity due to finite dimensions of the plasma (a boundary prevents a complete gyromotion and therefore destroys homogeneity). Most of the published works concerning Vlasov stability deal only with the first kind of inhomogeneity, and kinetic boundary conditions are usually not considered. In the present paper we show a method of treating the kinetic boundary conditions when deriving the dispersion relation. Under a specific boundary condition the dispersion relation takes the form of an integro-differential equation, and it is solved numerically.

## Formulation

We consider Vlasov-Poisson equations in a homogeneous, Maxwellian plasma

$$\frac{df_{\alpha 1}}{dt} \equiv \frac{\partial f_{\alpha 1}}{\partial t} + \boldsymbol{v}\cdot\frac{\partial f_{\alpha 1}}{\partial \boldsymbol{x}} + \frac{q_\alpha}{m_\alpha}\boldsymbol{v}\times\boldsymbol{B}_0\cdot\frac{\partial f_{\alpha 1}}{\partial \boldsymbol{v}} = -\frac{q_\alpha f_{\alpha 0}}{k_B T_\alpha}\boldsymbol{v}\cdot\nabla\phi_1, \tag{1}$$

$$-\varepsilon_0\nabla^2\phi_1 = \Sigma_\alpha q_\alpha\int f_{\alpha 1}d\boldsymbol{v}. \tag{2}$$

Here, $f_{\alpha 1}$ is the perturbed distribution function of particles of species $\alpha$, $f_{\alpha 0}$ is the Maxwellian distribution function of species $\alpha$, $\boldsymbol{v}$ the particle velocity, $\boldsymbol{x}$ the spatial coordinate vector, $q_\alpha$ and $m_\alpha$ the charge and the mass of species $\alpha$ respectively, $\boldsymbol{B}_0$ the equilibrium magnetic field in the $z$-direction, $\phi_1$ the perturbed electric potential, $k_B$ the Boltzmann constant, and $\varepsilon_0$ the vacuum dielectric constant. Integrating Eq.(1) along the unperturbed orbits, and noticing that $f_{\alpha 0}$ is the orbital invariant, we obtain a formal solution for $f_{\alpha 1}$

$$f_{\alpha 1}(\boldsymbol{x},\boldsymbol{v},t) = -\frac{q_\alpha f_{\alpha 0}}{k_B T_\alpha}\int_{t_b}^{t}\boldsymbol{v}'\cdot\nabla\phi_1(\boldsymbol{x}',t')dt' + f_{\alpha 1}(\boldsymbol{x}_b,\boldsymbol{v}_b,t_b), \tag{3}$$

where $\boldsymbol{x}'(t')$ and $\boldsymbol{v}'(t')$ are the coordinate of the particle orbits with initial conditions $\boldsymbol{x}'(t'=t) = \boldsymbol{x}$ and $\boldsymbol{v}'(t'=t) = \boldsymbol{v}$. The subscript '$_b$' stands for boundary values. Using the relation $d\phi/dt = \partial\phi/\partial t + \boldsymbol{v}\cdot\nabla\phi$, we obtain from Eq.(3)

$$f_{\alpha 1}(\boldsymbol{x},\boldsymbol{v},t) = -\frac{q_\alpha f_{\alpha 0}}{k_B T_\alpha}\left[\phi_1(\boldsymbol{x},t) - \int_{t_b}^{t}\frac{\partial\phi_1}{\partial t'}dt'\right] + f_{\alpha 1}(\boldsymbol{x}_b,\boldsymbol{v}_b,t_b) + \frac{q_\alpha\phi_1(\boldsymbol{x}_b,t_b)f_{\alpha 0}}{k_B T_\alpha}. \tag{4}$$

ote here that the lower time limit of the orbital integral is not necessarily minus infinity if e orbit comes from a wall, which must happen for some particles in a finite plasma. This rmula suggests also that the boundary conditions of the perturbed distribution function ould be properly given only for the in-coming velocities which direct into the plasma re- on in the velocity space. The boundary values of the perturbed distribution function for the t-going velocities are in general determined through the orbital integral by the values for in- ming velocities at some other places and should not be given again. In this paper, we con- ler only one specific boundary condition which simplifies the formulation

$$f_{\alpha 1}(\boldsymbol{x}_b,\boldsymbol{v}_b,t_b) + \frac{q_\alpha \phi_1(x_b,t_b)}{k_B T_\alpha} f_{\alpha 0} = 0. \tag{5}$$

this case we obtain a simple formula for the initial value problem:

$$f_{\alpha 1}(\boldsymbol{x},\boldsymbol{v},t) = -\frac{q_\alpha f_{\alpha 0}}{k_B T_\alpha}\left[\phi_1(\boldsymbol{x},t) - \int_{t_b}^{t} \frac{\partial \phi_1}{\partial t'}\, dt'\right]. \tag{6}$$

e apply normal mode analysis in order to derive a dispersion relation, i.e., we perform a urier transform in the $y$- and the $z$-directions and a Laplace transform in time:

$$f_{\alpha 1}(\boldsymbol{x},\boldsymbol{v},t) = f_{\alpha k}(x,\boldsymbol{v}) e^{\,i(\boldsymbol{k}\cdot\boldsymbol{x}-\omega t)}, \quad \phi_1(\boldsymbol{x},t) = \phi_k(x) e^{\,i(\boldsymbol{k}\cdot\boldsymbol{x}-\omega t)}, \tag{7}$$

ere $\boldsymbol{k} = k_y \boldsymbol{e}_y + k_z \boldsymbol{e}_z$. Making use of these in Eq.(6) we have

$$f_{\alpha k}(x,\boldsymbol{v}) = -\frac{q_\alpha f_{\alpha 0}}{k_B T_\alpha}\left(\phi_k(x) + i\omega \int_{\tau_b}^{0} \phi_k(x') e^{i(\boldsymbol{k}\cdot\boldsymbol{X}-\omega\tau)} d\tau\right), \tag{8}$$

ere $\tau_b = t_b - t < 0$; its absolute value is the time taken for a particle to travel from the undary to the phase point $(x,\boldsymbol{v})$. So $\tau_b$ is a function of $(x,\boldsymbol{v})$. Here $\boldsymbol{X} = X\boldsymbol{e}_x + Y\boldsymbol{e}_y + Z\boldsymbol{e}_z$, $= \boldsymbol{x}+\boldsymbol{X}$ and the relative orbital position $\boldsymbol{X}$ in a homogeneous field are given by

$$X = \frac{v_\perp}{\omega_{c\alpha}}[\sin(\omega_{c\alpha}\tau - \varphi) + \sin\varphi], \tag{9}$$

$$Y = \frac{v_\perp}{\omega_{c\alpha}}[\cos(\omega_{c\alpha}\tau - \varphi) - \cos\varphi], \tag{10}$$

$$Z = v_{//}\tau, \tag{11}$$

ere $(v_\perp,\varphi,v_{//})$ are the cylindrical coordinates of the velocity space. The indices $\perp$ and $//$ are ferred to the direction of the equilibrium magnetic field. Using Eq.(8) in Eq.(2) we obtain e eigen equation

$$\frac{d^2\phi_k}{dx^2} - k^2\phi_k = \sum_{\alpha=e,i} \frac{1}{\lambda_{D\alpha}^2}\left(\phi_k + i\omega \int F_{\alpha 0}\, d\boldsymbol{v} \int_{\tau_b}^{0} \phi_k(x') e^{i(\boldsymbol{k}\cdot\boldsymbol{X}-\omega\tau)} d\tau\right), \tag{12}$$

ere $F_{\alpha 0} = (2\pi v_\alpha^2)^{-3/2} \exp(-v^2/2v_\alpha^2)$ is the Maxwellian distribution, $v_\alpha = \sqrt{k_B T_\alpha / m_\alpha}$ is the ermal velocity, and $\lambda_{D\alpha} = \sqrt{\varepsilon_0 k_B T_\alpha / (q_\alpha^2 n)}$ is the Debye length of $\alpha$ species particles.

## Numerical Method

The eigen equation (12) is an integro-diffrential equation. For this type of equation very little is known about the well-posedness of the problem. In the following, however, we assume that the problem is well-posed. Galerkin method is applied to solve Eq.(12), following Davidson (1976, Phys. of Fluids **19**, 1189). In a preliminary study, we adopt periodical boundary conditions, i.e., expanding $\phi_k(x)$ in terms of periodical, exponential functions

$$\phi_k(x) = \sum_{n=-\infty}^{\infty} \phi_n e^{ik_n x}, \quad k_n = 2n\pi/L, \quad n = 0,\pm1,\pm2,\ldots . \tag{13}$$

Using this in Eq.(12) and integrating with a weight function $e^{-ik_m x}$ we obtain, after some manipulation, we obtain a matrix eigenequation for the vector $\{\phi_n\}$:

$$\sum_{n=-\infty}^{\infty} \phi_n D_{mn} = 0, \quad m = 0,\pm1,\pm2,\pm3,..., \tag{14}$$

$$D_{mn} = \delta_{mn}(k_m^2+k^2) + \sum_{\alpha=e,i} \frac{1}{\lambda_{D\alpha}^2}(\delta_{mn} + S_{\alpha,mn}). \tag{15}$$

$$S_{\alpha,mn} = \frac{1}{2\pi v_\alpha^2} \int_0^1 e^{i2\pi(n-m)\eta} d\eta \int_0^\infty v_\perp \exp(-\frac{v_\perp^2}{2v_\alpha^2}) dv_\perp \int_{-\pi/2}^{3\pi/2} e^{i\lambda_{n\perp}\sin\varphi_n} d\varphi$$

$$\cdot \zeta_{0\alpha} \sum_{l=-\infty}^{\infty} J_l(\lambda_{n\perp}) e^{-il\varphi_n} \left[ Z_p(\zeta_{l\alpha}) - Z_p(\zeta_{l\alpha} - \frac{i\tau_b k_{//} v_\alpha}{\sqrt{2}}) e^{i(l\omega_{c\alpha}-\omega)\tau_b - k_{//}^2 \tau_b^2 v_\alpha^2/2} \right], \tag{16}$$

where $\lambda_{n\perp} = v_\perp \omega_{c\alpha}^{-1}(k_n^2+k_y^2)^{1/2}$, $\varphi_n = \varphi - \cos^{-1}(k_n(k_n^2+k_y^2)^{-1/2})$, $\zeta_{l\alpha} = (\omega - l\omega_{c\alpha})/(\sqrt{2}k_{//}v_\alpha)$, $\eta = x/L$, $\omega_{c\alpha}$ is the gyrofrequency and $Z_p(\zeta)$ is the plasma dispersion function. The dispersion relation then takes a form

$$\det |D_{mn}(\omega,k)| = 0. \tag{17}$$

From Eq.(17) the eigenvalues $\omega$ are determined, and from Eq.(14) the eigenvectors $\{\phi_n\}$ are determined for given $k$ and mode number in the $x$-direction $n_x$. In the calculation a $5\times5$ matrix is used.

## Results and Discussions

Some preliminary results have been obtained for the pure ion Bernstein waves. Figures 1 and 2 show the scalings of the eigen frequency to $k_y r_L$ and $L/r_L$, which reflects the boundary effects, respectively. Some phenomena in these scalings have not been well understood. Four eigen-modes in the $x$-direction are recognized according to the shape of the eigenfunction, as shown in Figs. 3. The assumption of the periodical boundary condition $\phi_k(x) = \phi_k(x+L)$ can be seen clearly in these figures. It seems that the Bernstein waves are seriously influenced for $L/r_L < 10$ and the damping usually reaches maximum for $L/r_L$ between 3 and 7 depending on $k_y r_L$ and the $x$-mode number $n_x$. A possible physical reason for the damping is that the boundary inhomogeneity prevents regular cyclotron motion for a fraction of ions and causes phase mixing.

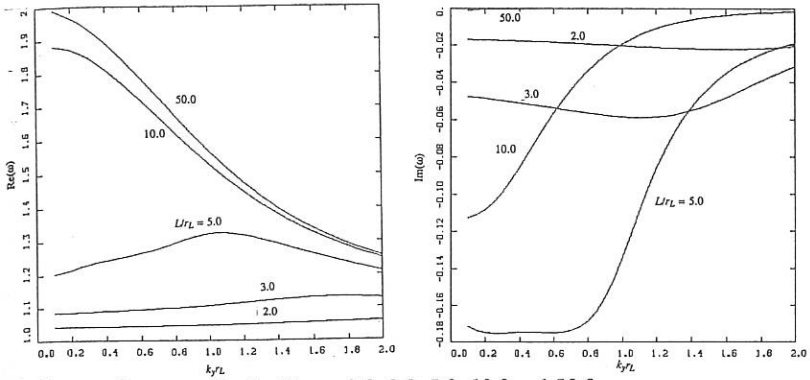


Fig. 1 $\omega$ vs $k_y r_L$, $n_x = 1$, for $L/r_L = 2.0, 3.0, 5.0, 10.0$ and $50.0$

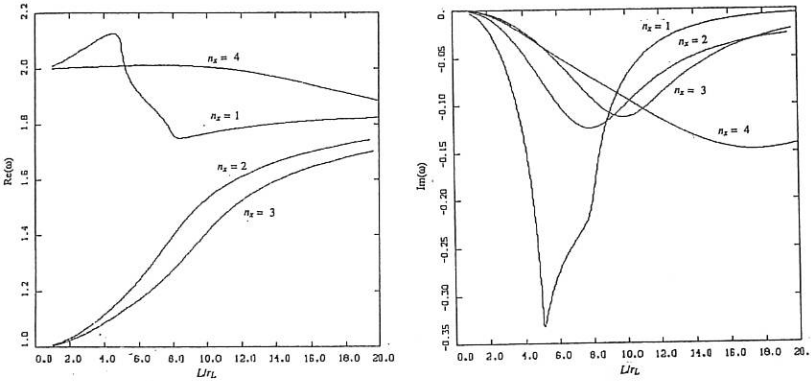


Fig. 2 $\omega$ vs $L/r_L$, $k_y r_L = 0.5$, for $n_x = 1, 2, 3$ and $4$

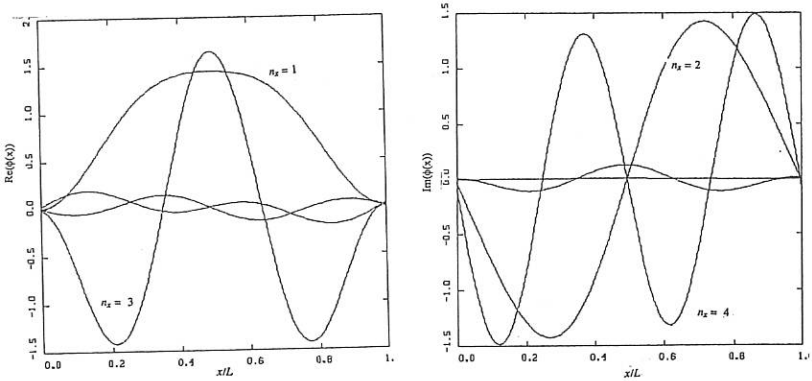


Fig. 3 Eigen functions $\phi(x)$, for $n_x = 1, 2, 3$ and $4$. $L/r_L = 100$, $k_y r_L = 2.0$.

# NUMERICAL SOLUTION OF THE VLASOV-MAXWELL SYSTEM IN THE HEAVY-ION FUSION PROBLEMS.

Batishchev O.V., Karas' V.I.*, Sigov Yu.S., Silaev I.I.

M.V.Keldysh Institute of Applied Mathematics, USSR Academy of Sciences, 125047, Miusskaya sq.4, Moscow, USSR.

*Kharkov Physical Technical Institute, Ukrainian Academy of Sciences, 310108, Akademicheskaya st.1, Kharkov, USSR.

The development of linear induction accelerators with spatial charge compensation and magnetic isolation of boosting intervals is one of the perspective trends to obtain a high current beam of heavy ions for inertial controlled fusion problem. Two main ideas, underlying this system, are to the first glance contrary to each other. First, for the ion beam propagation throughout the system without retaining it must be accompanied by the electron one. From the other hand, the isolating magnetic field cusp structure

$$\mathbf{H} = H_0/k\ \mathbf{rot}\,(\theta\, I_0(kr)\sin(kz)),$$

($I_0$ being modified Bessel function of the zeroth order, L being the cusp length, $k=\pi/L$ ) should evacuate electrons from the working region. Fortunately Karas' et al. [1] showed mechanism, which allows to avoid difficulties, mentioned above: electron beam will cross the region with the strong transverse magnetic field due to the $[\mathbf{E}\times\mathbf{B}]$ drift, provided by the radial polarization electrostatic field and the self-consistent azimuthal magnetic field components, if following conditions are met:

$$n_1 > \frac{H^2}{4\pi m_e c^2}, \qquad \Delta \geq c\,\frac{\Omega_e}{\omega_e^2} \qquad (1)$$

where $n_1$ is the ion beam density, H is an external magnetic field amplitude, c is the speed of light, $\Omega_e$ and $\omega_e$ are cyclotron and plasma electron frequencies.

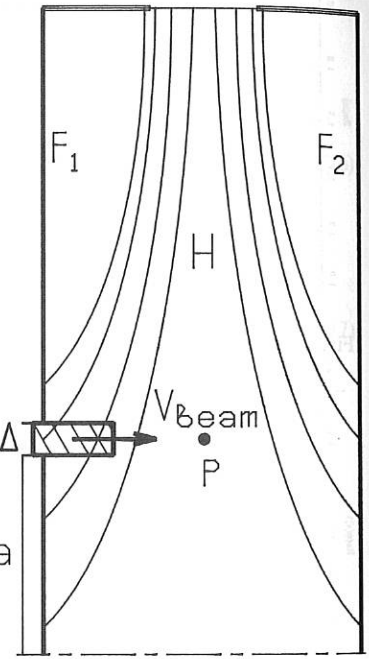


Fig.1

The self-consistent plasma dynamics in a linear induction

accelerator is described by the relativistic Vlasov equations for the electron and ion distribution functions coupled with the Maxwell equations. Numerical simulation of physical processes in such a system may be performed with the use of two-dimensional discrete kinetic model based on particle method for open plasma configurations [2], in which charged particles injection in and exit from a bounded computational domain are essential. In cylindrical frame the problem is a spatially two-dimensional one due to the assumption, that all the functions do not depend on azimuthal angle $\varphi$ (while the velocity space still has all three dimensions), and is formulated as follows. The tubular ion and electron beams are injected into the rectangular vacuum domain $0 < r < R$, $0 < z < L$ (see Fig.1). All geometrical parameters are the same for both beams: the beam radius is $a=R/3$, its thickness $\Delta \ll a$. Initial ion and electron temperatures are $T_i = T_e = 0$, the injecting velocities are of the order $V_{beam}/c \simeq 0.2 \div 0.8$, with current compensating condition being $q_e n_e V_e = q_i n_i V_i$. In the region involved the cusp magnetic field configuration and ion accelerating potential difference $\Delta F = F_2 - F_1$ are imposed. The similar problem was considered in the Cartesian geometry as well, with the beams being planar and infinite along ignorable z- coordinate. Cylindrical and Cartesian spatially two-dimensional computations, from our point of view, mutually complement each other and enable comprehensive study of 3-D physical processes in the system.

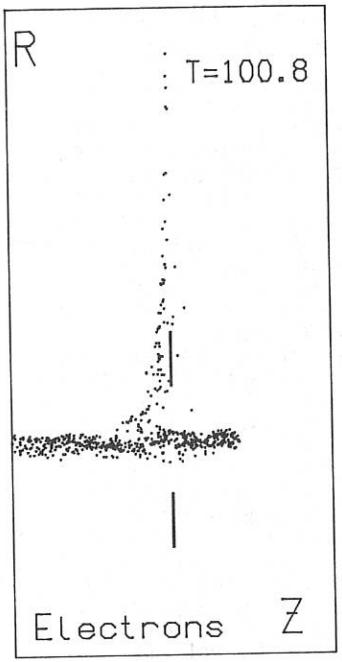


Fig.2

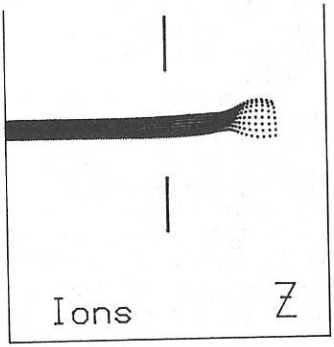


Fig.3

2.5-D particle simulations were performed on the grid (256x128), the typical number of model particles was $\simeq 10^4$, mass ratio was $m_i/m_e = 1840$. The boundary conditions for the EM field were symmetry at the axis and metallic at the outer surface. Those for the particles were symmetry at the axis as well and free exit from the working region through the external

contour (in practice, most of the beam electrons are reflected by the magnetic field and only few of them actually reach the boundary r = R). Explicit integrating schemes were used for solving both the Maxwellian system and relativistic particle dynamics equations (similar to those used by Boris [3]). The cell dimensions were $\Delta r = \Delta z = 1\, c/w_{pe}$, time step $\Delta t$ was $\simeq 0.1\, w_{pe}^{-1}$, the typical run of some thousand steps, corresponding to several ion transition times $T_{TR}^{1}$ $(= L/V_1 \simeq 100\, w_{pe}^{-1})$ takes a few hours of CPU time at IBM- AT/386 personal computer in standard configuration. The developed system enables to compute dynamics of up to 1 million particles of dozens of sorts at computational grids as large as (1024x1024) and requires 2 Mb of RAM and 40 Mb hard disk. Interactive regime and rich graphical support make it possible for physicist to start simulation with desired parameters and to get any diagnostics in a simple manner. A specially designed technique implemented in our code was successfully applied to numerical experiments on interactions of plasma potential solitary vortices [4], plasma electron injectors [5] and large-scale astrophysical problems (to be published).

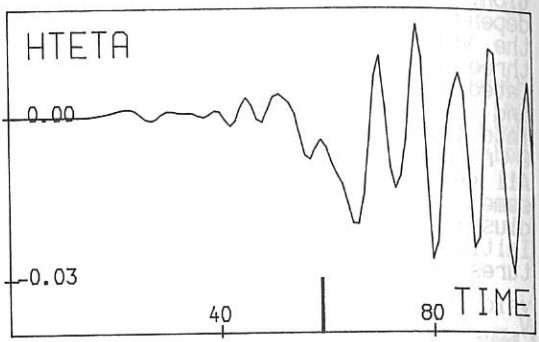


Fig. 4

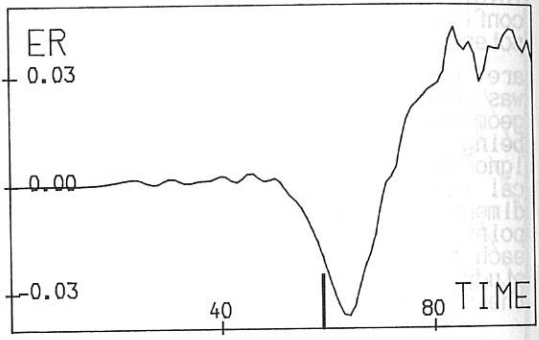


Fig. 5

Numerical simulations were mainly intended to prove the validity of the charge compensation mechanism mentioned above. Electron spatial distribution, obtained during the simulation with magnetic field H, satisfying (1) and $F_1 = F_2 = 0$, is presented at Fig. 2. It is seen, that the main portion of the electron beam is passing through the middle of the cusp, marked by two vertical lines, due to the drift mechanism. The main contribution to the drift velocity is given by the product of azimuthal magnetic $H_{TETA}$ and radial

polarization $E_R$ fields. Fig.4,5 present time dependence of these field components, measured at the point P (see Fig.1). A vertical dash on the time axis indicates ion half- transition time $T^i_{TR}/2$. As can be seen from the pictures positive z-drift in the middle of the cusp is provided by increasing negative values of the fields involved up to the electron half-transition time. Note, that the electrons exit cusp center with the velocity of about ion beam speed. The last circumstance is important for ion beam further compensation. Approximately at $t > 2/3\,T^i_{TR}$ a quasi- stationary regime is settled. The ion beam propagation is shown at Fig.3. Being unmagnetized and more inertial ions have straight trajectories, except the small front part of them expanding in the absence of charge compensation.

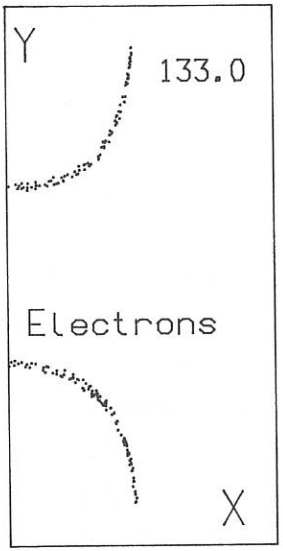

Fig.6

When an external magnetic field is stronger than condition (1) prescribes, the electrons trace magnetic lines, because they can't be pulled through the cusp. An example of Cartesian simulation for this case is shown at Fig.6.

So the simulations performed confirm the principal possibility of heavy ions acceleration with the use of the technique described above. Studying of the beam-plasma instabilities plausible here must be an object of further investigations. Regular full-scale qauntitive simulation on heavy ion beam propagation, stability and optimization are to be fulfilled. The authors have developed implicit relativistic particle method, which enables stable computation for hundreds of the ion transition times $T^i_{TR}$.

[1] Karas' V.I., Mukhin V.V., Novikov V.E., Naboka A.M. The Soviet Journal of Plasma Physics, 1987, 13, 494-496.

[2] Bakai A.S., Batishchev O.V., Sigov Yu.S. Proc. Int. Workshop on Nonlinear Phenomena in Vlasov Plasmas. Cargese, France, 1988, pp.163-192.

[3] Boris J.P. Proc. Forth Conf. Num. Sim. Plasmas, Naval Res.Lab., Wash.D.C., pp.3-67, 2-3 November, 1970.

[4] Batishchev O.V., Sigov Yu.S., Silaev I.I., Petviashvili V.I. Proc. XII Europ. Conf. Controlled Fusion and Plasma Phys. Budapest, 1985, v.9F, part 2, p.350.

[5] Batishchev O.V., Sigov Yu.S. Preprint, Keldysh Inst. Appl. Math. Acad. Sci. USSR, 1988, N87.

# NONSTATIONARY SELF-ACTION OF ELECTROMAGNETIC WAVE BEAMS IN THE BEAT ACCELERATOR

L.A.Abramyan, A.G.Litvak, V.A.Mironov

The resonance excitation of a plasma wave in a modified accelerator using the beats of two electromagnetic waves [1] permits to increase considerably the intensity of the accelerating field and, consequently, the rate of the accumulation of the energy by charged particles. The efficiency of the electromagnetic radiation conversion to the longitudinal wave is defined by nonlinear processes. The saturation of the accelerating field is considered which is due to the appearance of multiflux motion of electrons oscillating in the wave field with overturn of waves [2], due to the development of parametric instabilities [3, 4] and due to the change of natural frequency of plasma oscillations caused by the relativistic increase of electron mass [2]. The effects of self-action which change the form of the electromagnetic radiation pulse and the wave beam structure play a significant role in the most promising laser plasma beat accelerator [5]. We consider dynamics of space distribution of the plasma wave in a self-consistent field of the wave beam.

To describe the evolution of the transverse distribution of the field of two collinear wave beams

$$\vec{E}_{1,2} = E_{1,2}(\vec{r}_\perp, z, t)\,\vec{y}_0\, \exp i\omega_{1,2}(t - z/c)$$

during the generation of a longitudinal wave at the frequency of beats in a homogeneous plasma $\omega_p = \omega_2 - \omega_1$ $(\omega_p \ll \omega_{1,2})$

$$\vec{E}_p = \vec{z}_0\, E_p(\vec{r}_\perp, z, t)\, \exp i\omega_p(t - z/c)$$

we use the following set of equations

$$-2ik_{1,2}\frac{\partial \ell_{1,2}}{\partial z}+\Delta_\perp \ell_{1,2}+\frac{3}{2}|\ell_p|^2 k_{1,2}\frac{\omega_p^2}{\omega_{1,2}^2}\ell_{1,2}=0 \quad (1)$$

$$+2i\omega_p^{-1}\frac{\partial \ell_p}{\partial t}-3|e_p|^2 e_p=-2i\frac{\omega_p^2}{\omega_1\omega_2}\ell_1^*\ell_2 \quad (2)$$

Here it is assumed that wave beams are wide on a scale of the electromagnetic wave wavelength, plasma nonlinearity is associated with the dependences of electron mass on the rate of oscillations in the plasma wave field, the group velocity of a plasma wave is equal to zero. It is supposed that relativity is weak. Fields are normalized to the fields which are characteristic to relativistic nonlinear effects $E_z=2m\omega_p c/e$ $(\ell=E/E_z)$. The saturation of the amplitude of plasma oscillations is defined by a nonlinear frequency shift.

Further we shall consider a more simple situation when the intensities and forms of wave beams are equal. Now the initial set of equations assumes the form which is standard for studying nonstationary self-action.

$$-i\frac{\partial \ell}{\partial z}+\Delta_\perp \ell+|n|^2\ell=0 \quad (3)$$

$$\frac{\partial n}{\partial t}+i|n|^2 n=|\ell|^2 \quad (4)$$

where $z_H=\left(\frac{\omega_p}{\omega}\right)^{10/3}kz/2\cdot 6^{2/3}$, $t_H=6^{3/2}\left(\frac{\omega_p}{\omega}\right)^{4/3}\omega_p t/4$,

$r_H=(kr_\perp)(\omega_p/\omega)^{5/3}/6^{3/2}$, $n=\left(6\omega^2/\omega_p^2\right)^{1/3}\ell_p$

The study of the stability of a plane wave in a nonstationary regime shows that the increment of instability does not depend on the wave number of disturbance. Owing to the absence of the optimal scale of instability at the initial stage of the plasma wave excitation ( $\frac{\partial n}{\partial t} \gg |h|^2 n$ , a homogeneous wave beam collapse can take place and self-similar distribution forms

$$\ell = \frac{1}{t_0 - t} \mathcal{E}\left(r/(t_0-t)\right) \exp i A r/(t_0-t)$$

$$n = \frac{1}{t_0-t} N\left(r/(t_0-t)\right)$$

The structure of the field of homogeneous waveguide channels which collapse during the finite time $t_0$, is described by a localized solution of the equations

$$\Delta_\perp \mathcal{E} + (N^2 - A)\mathcal{E} = 0 \qquad (5)$$

$$\tau \frac{\partial N}{\partial \tau} + N = \mathcal{E}^2, \quad \tau = r/(t_0-t) \qquad (6)$$

As the stationary distribution establishes ( $\frac{\partial n}{\partial t} = 0$) a wide wave beam is expected to be divided into a number of narrow ones with a characteristic size $L_\perp = 6^{3/2}\left(\frac{\omega}{\omega_p}\right)^{5/3} \lambda/2\, \ell_0^{2/3}$ ($\lambda$ is the wavelength, $\ell_0$ is the dimensionless field amplitude). Since the nonlinearity ( $|n|^2 \simeq |\ell|^{4/3}$ ) is "weaker" than a cubic one, peculiarities do not appear ( the fields remain finite) and there forms the succession of quasiwaveguide structures.

The results of the numerical calculation of the set of equations (3), (4) for the two-dimensional case are given in

Fig. 1, 2. It is seen that at $t \lesssim 1$ according to quantitative analysis, the excitation of a plasma wave leads to the focusing of the electromagnetic radiation. Then ($t > 1$) the plasma wave field distribution becomes strongly inhomogeneous and results in the defocusing of the wave beam.

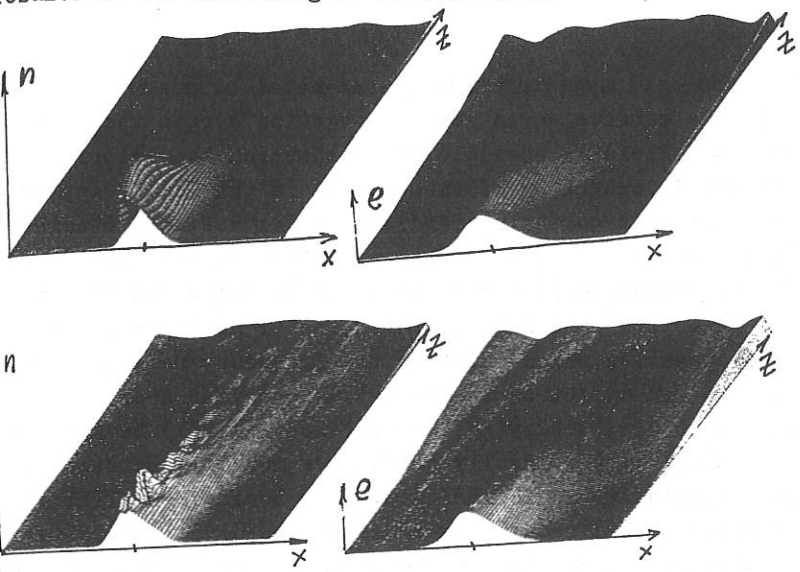


REFERENCES

1. Dawson J.M. Proc. of the ICPP, Lausanne 1984, v.11, p.837.
2. Fainberg Ya.B. Fizika plazma 1987, v.13, vyp.5, p.607.
3. Bogomolov Ya.L., Litvak A.G., Feigin A.M. Pis'ma v ZhETF 1987, v.45, vyp.1, p.12.
4. Salomas R.R.E., Karttunen S.J. Phys.Scripta 1986, v.33, p.370.
5. Mori W.B., Joshi C., Dawson J.M. et al. Phys.Rev.Lett. 1988, v.60, N13, p.1298.

# SELF-INTERACTION OF THE MAGNETOHYDRODYNAMIC SURFACE WAVES AT THE PLASMA-METAL BOUNDARY

N.A.Azarenkov , K.N.Ostrikov

Kharkov State University , 310077 , Kharkov , USSR

At the cold magnetoactive plasma-metal boundary the existence of the surface waves (SW),propagating across the external magnetic field is possible.The dispersion characteristics and the field topography of these waves in the linear approximation in respect to their field amplitudes are well studied [1,2].The results of these works are valid for the small amplitude waves,when nonlinear effects can be neglected.In the present report we consider the influence of nonlinearity for the SW propagation,which exist in the frequency range $\omega < \omega_i$ ($\omega_i$ is the ion cyclotron frequency).We consider a cold and homogeneous plasma occupying the half-space $X > 0$ bounded at the plane $X = 0$ by the ideally conductive metallic surface.The external stationary magnetic field $\vec{H}_0$ is applied parallel to the boundary at Z direction.We consider the wave perturbations propagating at Y direction at the plasma-metal boundary.In the frequency range $\omega^2 \ll \omega_i^2$ ,in the linear approximation,the dispersion of these waves is described by the following expression :

$$\omega = \kappa_2 V_A \left(1 - \kappa_2^2 V_A^2 / 2\omega_i^2\right) , \qquad (1)$$

where $V_A$ , $\kappa_2$ are the Alfven velocity and the Wavenumber.

We study the nonlinear properties of the SW in the weak nonlinearity approximation,when the electron and ion oscillation velocities are much less than the wave phase velocity.In our case the nonlinear effects clear up in the second harmonic generation of the SW and in the appearence of the drift of charged particles across the external field with the second order nonlinearity taken into account,and in the self-interaction of waves - with the third order nonlinearity considera-

tion.The estimates show that the dynamics of the SW is defined by both ion and electron nonlinearities in the frequency range of our interest.Using the method,presented in[3],in the third approximation in respect to the SW field it is possible to obtain the following dispersion equation :

$$\omega = \omega_0 + Q|E|^2, \qquad (2)$$

where $Q = -\frac{1}{128}\frac{e^2}{m_i^2 c^2}\frac{\omega_i^7}{\Omega_0^4 \omega_0^4} B(\omega_0)$,

$B(\omega_0) = 18 - 45\frac{\omega_0}{\omega_i} - 256\frac{\omega_0^2}{\omega_i^2} + 270\frac{\omega_0^3}{\omega_i^3} + 896\frac{\omega_0^4}{\omega_i^4} + 360\frac{\omega_0^5}{\omega_i^5}$,

$\Omega_0^2 = 4\omega_0^2 - \omega_i^2$ , $\omega_0$ is defined by expression (I).Our consideration is valid in the frequency range $0{,}25\omega_i < \omega < 0{,}45\omega_i$ , where together with the fulfillment of the inequality $\omega^2\omega_i^{-2} \ll 1$ the second harmonic is not the eigenwave of the system,but is the forced perturbation,disappearing with fundamental wave ( sinus first harmonic signal)switch off.This fact gave us a possibility not to consider the resonant first harmonic interaction with the second one(when the conditions $\omega+\omega=2\omega$ and $2k_2(\omega)=k_2(2\omega)$ are satisfied)and effects associated with higher harmonics generation.

When calculating the nonlinear frequency shift $\delta\omega_{NL}=Q|E|^2$ both self-interaction channels $2\omega-\omega=\omega$ (through the second harmonic generation) and $0+\omega=\omega$ (through the ponderomotive force action) are taken into account,and the corresponding frequency shifts $\Delta^{(2\omega)}=Q^{(2\omega)}|E|^2$ and $\Delta^{(0)}=Q^{(0)}|E|^2$ are calculated.It can be shown that in the frequency range $0{,}27\omega_i<\omega<0{,}33\omega_i$ the inequality $|\Delta^{(2\omega)}| \gg |\Delta^{(0)}|$ is valid.When $0{,}25\omega_i<\omega<0{,}38\omega_i$ and $0{,}4\omega_i<\omega<0{,}45\omega_i$ $|\Delta^{(2\omega)}|>|\Delta^{(0)}|$ .When $0{,}25\omega_i<\omega<0{,}38\omega_i$ the signs of $\Delta^{(2\omega)}$ and $\Delta^{(0)}$ are the opposite,and when $0{,}38\omega_i<\omega<0{,}45\omega_i$ -are the same.In the whole frequency range of our interest $\Delta^{(0)}<0$ .This means that the self-interaction channel $0+\omega=\omega$ taking into account leads to a decrease of the wave phase velocity.If the channel $2\omega-\omega=\omega$ is considered only,the SW phase velocity increases in the frequency range $0{,}25\omega_i<\omega<0{,}38\omega_i$ and decreases when $0{,}38\omega_i<\omega<0{,}45\omega_i$ In the first frequency range both processes lead to the opposite results,and in the second one lead to the wave phase ve-

locity decrease. The resulting nonlinear frequency shift is positive when $\omega<0{,}37\omega_i$ and is negative when $\omega>0{,}37\omega_i$.

With nonlinear dispersion equation (2) in mind, one can derive the nonlinear Shrödinger equation for the envelope amplitude [4]:

$$i\left(\frac{\partial E}{\partial t}+V_g\frac{\partial E}{\partial y}\right)+i\nu E+P_{\parallel}\frac{\partial^2 E}{\partial y^2}+P_{\perp}\frac{\partial^2 E}{\partial z^2}=Q|E|^2E, \qquad (3)$$

where $V_g\simeq V_A$ is the SW group velocity,

$$P_{\parallel}=\frac{1}{2}\frac{\partial V_g}{\partial k_2}\Big|_{k_2=k_{20}}=-\frac{3V_A^2\omega_0}{2\omega_i^2},\quad P_{\perp}=\frac{V_g}{2k_{20}}=\frac{V_A^2}{2\omega_0},$$

$\nu$ is the linear decrement of the collisional damping. Because $Q$ changes its sign in the range $0{,}25\omega_i<\omega<0{,}45\omega_i$ in the vicinity of the frequency $\omega_0\approx 0{,}37\omega_i$ we can make the following conclusions about the stability of the SW.

I. In the frequency range $0{,}25\omega_i<\omega_0<0{,}37\omega_i$ $(Q>0)$ the stationary waves of the SW envelope considered are unstable in respect to longitudinal perturbations. The greatest instability increment is reached when $\varkappa_{\parallel}^2=-E_0^2QP_{\parallel}^{-1}$, $\varkappa_{\perp}=0$ and is equal to $(\mathrm{Im}\,\Omega)_{max}=-\nu/2+(E_0^4Q^2+\nu^2/4)^{1/2}$. The greatest increment in a lossless medium is $(\mathrm{Im}\,\Omega)_{max}=E_0^2Q$. In this frequency range, assuming $P_{\perp}\partial^2E/\partial z^2$ and $\nu$ to be equal to zero in (3), one can obtain the soliton type solution for the SW field envelope:

$$A=A_1\exp(i\varphi_1)\exp(-\varkappa_1 x) \qquad (4)$$

Here $A_1=\sqrt{2}B_1\,\mathrm{ch}^{-1}[\sqrt{\gamma_1}B_1(\xi-\xi_0)]$, $\varphi_1=-QB_1^2t$, $\gamma_1=-Q/2P_{\parallel}$, $\xi=y-V_gt$, $\xi_0=\xi(t=0)$.

When $P_{\parallel}\partial^2E/\partial y^2=\nu=0$, the antisoliton solution for the steady state spatial distribution of the SW field envelope can be realized as a result of the evolution of stable transverse perturbations:

$$A=A_2\exp(i\varphi_2)\exp(-\varkappa_1 x) \qquad (5)$$

where $A_2=B_2|\mathrm{th}[\sqrt{\gamma_2}(z-z_0)B_2]|$, $\varphi_2=\gamma_2B_2^2(y-y_0)/2k_{20}$, $\gamma_2=k_{20}Q/V_g$, $z_0=z(t=0)$, $y_0=y(t=0)$.

2. In the frequency range $0{,}37\omega_i<\omega_0<0{,}45\omega_i$ an instability in respect to transverse perturbations occurs. The greatest increment $(\mathrm{Im}\,\Omega)_{max}=-\nu/2+(E_0^4Q^2+\nu^2/4)^{1/2}$ is reached when $\varkappa_{\perp}^2=-E_0^2QP_{\perp}^{-1}$ and $\varkappa_{\parallel}=0$. When $\nu=0$ $(\mathrm{Im}\,\Omega)_{max}=E_0^2|Q|$.

s a result of the instability in respect to transverse per-
rbations ( $P_{\parallel} \partial^2 E/\partial y^2 = 0$ ) the stationary solution in the
orm of the wave with the soliton profile of its intensity
hich does not depend on the Y coordinate,can be realized in
he collisionless case.It is given as

$$A = A_3 \exp(i\varphi_3) \exp(-\mathcal{H}_1 x), \qquad (6)$$

here $A_3 = B_3 \operatorname{ch}^{-1}[\sqrt{\gamma_3} B_3 (z - z_0)]$, $\varphi_3 = \gamma_3 B_3^2 (y - y_0)/2\kappa_{20}$,
$\gamma_3 = -\kappa_{20} Q / V_g$ .

olution (6) describes the steady-state spatial distribution
f the SW field envelope.

In the same range of frequencies in collisionless plasma
he solution in the form of the antisoliton of the SW field
nvelope can be realized.Neglecting $P_{\perp} \partial^2 E/\partial z^2$ and $i\nu E$ in
3), and following [5], we get :

$$A = A_4 \exp(i\varphi_4) \exp(-\mathcal{H}_1 x), \qquad (7)$$

here $A_4 = B_4 \left| \operatorname{th}[\sqrt{\gamma_4} B_4 (\xi - \xi_0)] \right|$, $\varphi_4 = -Q B_4^2 t$, $\gamma_4 = Q/4P_{\parallel}$.

The account of a damping effect in (3) leads as in the
ork [5] to a decrease of the amplitude in solutions (4) and
7) $\sim \exp[-c|Q|E_0^2 \nu t / V_A \omega_i]$.

## REFERENCES


. Azarenkov N.A. et.al. I985.Radiotekhnika i electronika. V. 30 . P. 2I95.

. Kondratenko A.N. I985. Surface and volume waves in bounded plasmas. Energoatomizdat.

. Kondratenko A.N. I976. Plasma waveguides. Atomizdat.

. Karpman V.I. I975. Nonlinear waves in dispersive media. Pergamon Press.

. Boardman A.D.,Grosev D.,Shivarova A. I987. J. Plasma Physics. V. 38(3) . P. 427.

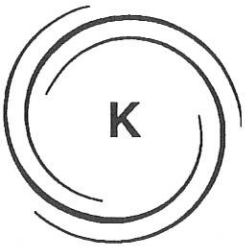


# INERTIAL CONFINEMENT FUSION

# DETECTION OF SRS PRODUCED ELECTRON PLASMA WAVES BY THE USE OF ENHANCED THOMSON SCATTERING.

E.J. LEENSTRA

AERP, University of Washington, Seattle WA 98195.

Fast electrons have been observed to eject from a preformed plasma during laser-plasma interactions and have been measured[1] to be Maxwellian with a temperature ranging from 29keV to 105keV. The laser-plasma interaction is conducted in a preformed plasma, generated by two opposing shock tubes (figure 1), at densities well below the quarter critical density of the laser driver. In this situation the only two parametric decay processes allowed are the stimulated Brillouin scattering (SBS) process and the stimulated Raman scattering (SRS) process. This leaves the electron plasma wave (EPW) as the most likely candidate for generating the fast electrons, since it is the only electrostatic wave in both decay processes. Simple trapping of the electrons into the EPW at wave matching conditions in the SRS process, predicts that the

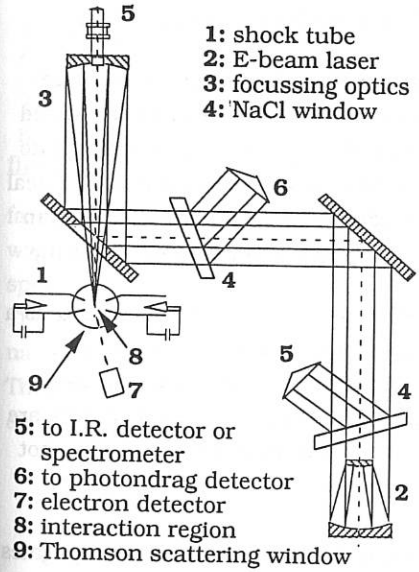


**figure 1** Experimental setup

electrons are ejected out of the plasma with energies of 5keV corresponding to the phase velocity of the wave. Therefore the observed fast electrons cannot be explained by simple trapping of the electrons into the electrostatic daughter wave of the SRS process.

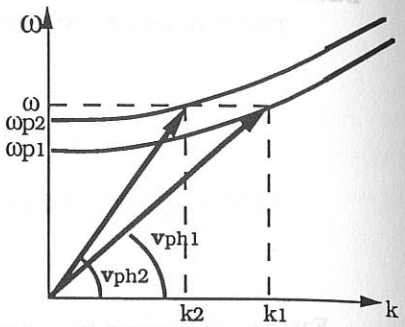


**figure 2** EPW dispersion relation plotted for two densities.

Brooks & Pietrzyk[2] have proposed that the electrons can gain significantly more energy if the EPW in which they are trapped itself accelerates while the trapped electrons remained trapped. This process can be readily seen in the dispersion relation for an EPW in a uniform isotropic unmagnetized plasma (figure 2), i.e. $\omega^2=\omega_p^2 + k^2v_{th}^2$. Since the wave will propagate at constant $\omega$, an increase in density (i.e. $\omega_p$) will require the wavevector to decrease and thus the phase velocity to increase if the temperature is assumed to remain constant. Thus the wave "accelerates" as it propagates into regions of increasing density. For densities well below quarter critical density, as in our experiment, the second term is much smaller than the first term, i.e. $\omega_{pe}^2 \gg k^2v_{th}^2$. Consequently, a small increase in the plasma density will require a large decrease in the wavevector and as a result a large increase in phase velocity of the wave. For typical experimental conditions, a density increase of a mere 2% will force the wavevector to become very small (~0). Density gradient EPW's are in a sense unavoidable in our experiment, because the density cannot be controlled to such an accurate degree for any reasonable propagation length.

This process of accelerating electrons in an EPW that propagates into a region of increasing density (density gradient acceleration

mechanism) has been modeled by the authors in ref. [2]. Thermal electrons are trapped into the density gradient EPW at the low density side of the wave and can gain ten to a thousand time its initial kinetic energy by the time it detraps from the wave. The energy gain depends on the electric field strength of the wave, the amount of damping of the wave, the density gradient and the plasma temperature. The density gradient acceleration mechanism therefore can account for the unexpected higher energies observed in the experiment.

There are of course other processes that may generate higher than expected electrons energies and the likely candidates are Langmuir wave collapse, wave breaking and two plasmon decay. An Enhanced Thomson scattering diagnostic (figure 3) has been added to the experiment and will be able to discriminate against the above mentioned alternative processes. This Enhanced Thomson scattering diagnostic will reveal the wavevector spectrum of the probed waves in the interaction region in a time resolved fashion. The density gradient EPW is expected to exhibit a broadened wavevector spectrum compared to the uniform EPW wavevector spectrum, as can be seen in the calculated case depicted in figure 4. The frequency spectrum on the other hand is expected to remain narrow as is the case with the uniform EPW frequency spectrum. These features of the density gradient EPW will allow for the discrimination against the above mentioned alternative processes.

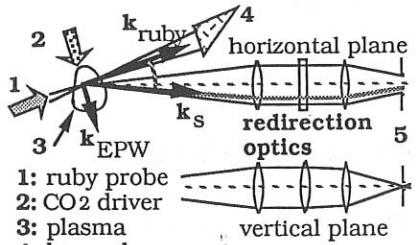


**figure 3** Thomson scattering setup

Time correlation of the density gradient wavevector spectra with the detection of fast electrons will support the conjecture that the fast electrons are accelerated in the density gradient acceleration mechanism. Data is expected to be presented using this diagnostic.

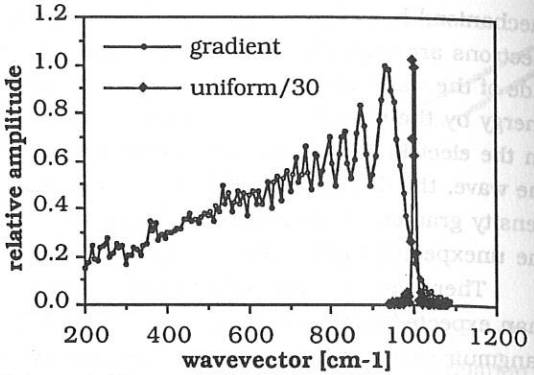


**figure 4** The expected wavevector spectrum of the density gradient EPW.

References:

1 R.G. Berger, R.D. Brooks & Z.A. Pietrzyk, Phys. Fluids **26**, 354 (1983).

2 R.D. Brooks & Z.A. Pietrzyk, Phys. Fluids **30**, 3600 (1987).

# MEASUREMENTS OF MASS ABLATION RATE AND ABLATION PRESSURE IN PLANAR LAYERED TARGETS

F. DAHMANI and T. KERDJA

HCR/CDTA, Laboratoire de Fusion, 2, Bd Frantz Fanon
PB 1017 Alger-Gare Algiers, Algeria

## I. INTRODUCTION

Here we report the layered targets experiments at 1.06-$\mu$m laser light in order to measure mass-ablation rate $\dot{m}$ and ablation pressure Pa as a function of absorbed laser flux Ia and laser wavelength $\lambda_L$ .

## II. EXPERIMENT CONDITIONS

Planar targets were irradiated with 3-ns pulse of 1.06-$\mu$m at laser intensities of $10^{11}$ - $4.5 \times 10^{12}$ W/cm2. The experiments were carried out with a Nd-glass laser. Typical laser energies were upto 5 J focused onto spot of 96 $\mu$m diameter using an f/10 quartz lens.

The targets were massive polyethylene (CH2) foils with over-coatings of 0.2-0.9 $\mu$m Al, in order to observe the burn-through of the overlayer as a function of laser intensity. The experimental set up included a Faraday cup, anx-ray yield detectors, and a time of flight spectrometer (LTOFS).

## III. EXPERIMENTAL RESULTS

In table I we give an example of the characteristic over-layer thicknesses $d_t$ ablated experimentally by using the ion analysis diagnostic for 1.06-$\mu$m laser light as a function of the absorbed laser flux Ia. The last column of table I repre-sents the value of B defined as $B = \dfrac{\rho d_t}{Ia^{5/9} \quad \lambda_L^{-4/9} \quad \tau_a}$ .

If we define the experimentally ablation rate $\dot{m}_{exp}$ as

$\dot{m}_{exp} = \frac{\rho_o d_t}{\tau_a}$ , $\rho_o$ being the solid density of the overlayer material, $\tau_a = c\,\tau_L$ the time duration for the ablation, where c is a factor close to unity ($c \approx 1.1$) (Goldsack et al.1982), we can write B as :

$$B = \frac{\dot{m}_{exp}\ (kg/cm^2\ sec)}{\left[\frac{I_a\ (W/cm^2)}{10^{14}}\right]^{5/9} \lambda_L^{-4/9}} \qquad (1)$$

TABLE I. Experimental values of characteristic overlayer $d_t$

| $\lambda_L$ ($\mu m$) | $\tau_L$ (nS) | $I_a$ ($W/cm^2$) | $d_t$ ($\mu m$) | B |
|---|---|---|---|---|
| | | $3 \times 10^{11}$ | 0.2 | 423 |
| | | $1.2 \times 10^{12}$ | 0.4 | 395 |
| 1.06 | 3 | $4 \times 10^{12}$ | 0.78 | 386 |
| | | $4.5 \times 10^{12}$ | 0.9 | 413 |
| 0.27[a] | 2 | $10^{12}$ | 0.63 | 454 |
| | | $1.4 \times 10^{12}$ | 0.8 | 462 |

[a] Reported by Ng et al.(1986)

One can see that, for our various experimental conditions, B is constant with value of 425 ± 55. Taking into account the definition of B, we obtain the experimental mass ablation rate :

$$\dot{m}_{exp}\ (Kg/cm^2 sec) \approx 425 \left[\frac{I_a(W/cm^2)}{10^{14}}\right]^{5/9} \cdot \left[\frac{1\mu m}{\lambda_L}\right]^{4/9} \qquad (2)$$

and taking the ablation pressure from the self-regulatored model (Fabbro et al.(1985) as $Pa = (Ia.\dot{m})\ 1/2$, we obtain the experimental ablation pressure :

$$Pa(Mbar) \approx 20 \left[\frac{Ia(W/cm^2)}{10^{14}}\right]^{7/9} \cdot \left[\frac{1\mu m}{\lambda_L}\right]^{2/9} \qquad (3)$$

## IV. COMPARISON WITH NUMERICAL SIMULATIONS

We have used the Lagrangian hydrodynamics code MEDUSA to check the validity of the principal results in our experimental work, and to evaluate the range of applicability of our experimental relations (Eqs.2 and 3).

The numerical simulations show that approximately

$$n_1 \propto nc^{1/3} I_a^{1/3} \tag{4}$$

where $n_1 \leqslant n_c$ ($n_c$ is the critical density) (Mora. 1982). This result is valided by the code calculated mass-ablation rate $\dot{m}$ and ablation pressure $P_a$ which are found to scale as :

$$\dot{m} \propto I_a^{5/9} \lambda_L^{-4/9} \tag{5}$$

$$P_a \propto I_a^{7/9} \lambda_L^{-2/9} \tag{6}$$

To illustrate the laser-wavelength dependences, fluid code calculations and values from Eqs.(2) and (3) of $\dot{m}$ and $P_a$ are plotted against $\lambda_L$ at absorbed laser fluxes of $3\times10^{11}$, $1.2\times10^{12}$, and $4\times10^{12}$ W/cm$^2$ (Figs. 1 and 2).

## V. DISCUSSION

These results are in good agreement with the published experimental measurements reported by Gupta et al. 1984 at 1.06-$\mu$m, by Ng et al. 1986 at 0.53-, 0.35-, and 0.27-$\mu$m, and by Meyer et al. 1984 at 0.35-$\mu$m.

Several authors reported the wavelength scalings close to $\lambda_L^{-4/3}$ for $\dot{m}$ and $\lambda_L^{-2/3}$ for $P_a$. This is true because of their laser intensities range which are close to $10^{13}$ W/cm$^2$ and well beyond this value. At these intensities a steepening of the density gradient for decreasing wavelength occurs. This is due to the fact that laser energy is deposited at the critical density which means that the reflection rate becomes important and leads to important ponderomotrice forces or to thermal inhibition as is the case in the paper by Fabbro et al.1982, and by Dahmani.1989. That's why these authors asked themselves about the discrepancy for the wavelength dependence of $P_a$ between low - and high-intensities. In fact, the steepening of the density gradient for decreasing wavelength occurs even at lower intensities.

## VI. CONCLUSIONS

We have measured the rate in planar targets irradiated by 1.06-$\mu$m laser light. The results which were presented were found to agree with previous data. These results are also in good agreement with simulation results.

## REFERENCES

Dahmani, F. 1989, Thèse de Magister (unpublished)
Fabbro, R. et al. 1985, Phys. Fluids 28, 1463.
Fabbro, R. et al. 1982, Phys. Rev. A26, 2289.
Goldsack, T.J et al. 1982, Phys. Fluids 25, 1634.
Gupta, P.D. et al. 1982, J.Appl. Phys. 53, 2956.
Meyer, B. et al. 1984, Phys. Fluids, 27, 302
Ng. A. et al. 1986, Appl. Phys. Lett. 45, 1046.

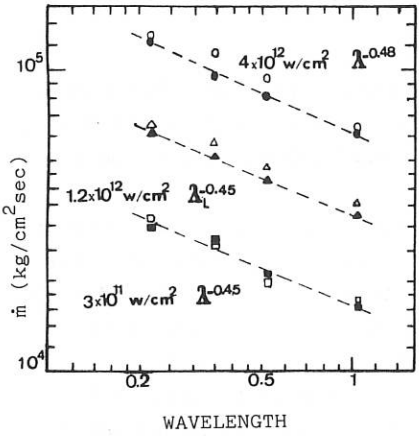


FIG.1. Mass ablation rate Vs laser wavelength. Closed points : Simulation, open points : from Eq.2.

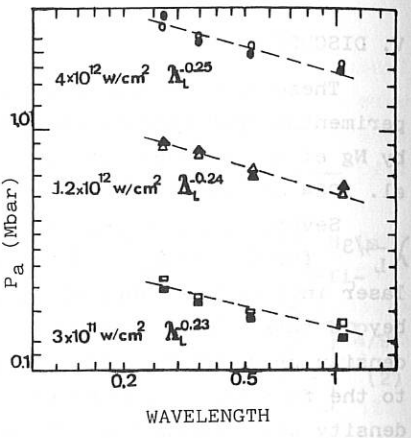


FIG.2. Ablation pressure Vs laser wavelength. Closed points : Simulation, open points : from Eq. 3.

# Heavy-Ion Driver Design for Indirect-Drive Implosion Experiments

R.C. Arnold

Theoretische Quantenelektronik, Institut für Angewandte Physik

Technische Hochschule Darmstadt, 6100 Darmstadt, FRG

and

R.W. Müller

Gesellschaft für Schwerionenforschung, 6100 Darmstadt, FRG

Design issues are presented for a heavy-ion driver suitable for pellet implosion research with indirect-drive targets. A low repetition rate and low efficiency driver using synchrotron acceleration with non-Liouville final bunch stacking is described. The goal is to design an intermediate facility an order of magnitude less costly than the HIBALL fusion reactor driver. We find this is reasonable if molecular-ion photodissociation can be used in final stacking. Pellet gains of order unity or more would be expected from a driver which produces at least 100 kJ of thermal radiation in a few ns, inside a high-Z hohlraum which contains a fusion pellet. This radiation would be generated by a solid converter heated by an intense pulse of high-energy heavy ions. Such a pulse, of several MJ energy, could be produced by a heavy-ion accelerator with two rings of 1000 Tm magnetic rigidity, one for acceleration and one for pulse stacking. Only one beam is required. Utilization of rings designed for relativistic heavy-ion colliders may be possible.

# NOVA PROGRAM AT LLNL*

C. Bibeau, M. Cable, M. Campbell, L. Coleman, D. Correll, C. Darrow, J. I. Davis, R. Ehrlich, G. Glendinning, B. Hammel, W. Hatcher, B. Haendler, M. Henesian, D. Kania, R. Kauffman, C. Keane, J. Kilkenny, H. Kornblum, D. Kyrazis, N. Landen, S. Lane, C. Laumann, J. Lawson, R. Lerche, D. Montgomery, D. Phillion, D. Ress, R. Speck, E. Storm, R. Thoe, J. Trebes, R. Turner, P. Young, R. Wallace, P. Wegner, F. Ze

University of California
Lawrence Livermore National Laboratory
P.O. Box 808, Livermore, California 94550

At LLNL, successful experimental work is being performed with the Nova laser facility (Fig. 1), a solid state laser system using neodymium-doped glass (ND:glass) laser technology. Nova is the primary U.S. facility devoted to the study of the indirect drive approach to inertial fusion. In this concept, energy from a laboratory driver is converted to radiation that is used to implode and heat the fusion fuel in an inertial fusion capsule. Nova's principal objective is to demonstrate that laser-driven hohlraums (chambers that trap electromagnetic radiation) can meet the conditions of driver/target coupling efficiency, driver irradiation symmetry, driver pulse-shaping, target preheat, and hydrodynamic stability required by hot spot ignition and by fuel compression in order to realize net fusion gain (fusion energy released/driver energy delivered). Major results within the Nova Program fall within the areas of laser performance, target diagnostics, and implosion experiments.

Completion of the Nova laser amplifier glass replacement with platinum free material has resulted in reliable laser performance at a level exceeding the originally specified performance. The ten beamlines of Nova have produced 125 kJ (2.5 ns) 83 TW (1.0 ns), and 125 TW (0.1 ns) pulses at 1.05 μm with no system damage. With this demonstrated performance at 1.05 μm it is now possible to irradiate targets with over 45 kJ of 0.35 μm light in a 2 ns pulse. Over 5 TW (1 ns) and 8 kJ (2.5 ns) of 0.35 μm light has been demonstrated on a single beamline.

*Work performed under the auspices of the U.S. Department of Energy by the Lawrence Livermore National Laboratory under contract number W-7405-ENG-48.

Progress in target diagnostics has led to multiple frame (>10) x-ray and optical gating cameras with effective shutter times <100 ps. Prototype x-ray cameras have demonstrated 50 ps shutter times, and we expect to achieve ≤ 30 ps in the near future. LLNL is actively developing neutron spectroscopy, imaging and time-resolving diagnostics that rival those based on x-ray detection. The diagnostics on Nova allow for an unprecedented study of implosion experiments.

Implosion experiments continue to address the target physics issues of radiatively driven targets: laser-plasma interaction physics, the efficiency of laser light conversion to x-rays, hohlraum characterization and design, hydrodynamic stability, and implosion physics. For example, hydrodynamic experiments, including Rayleigh-Taylor instability studies, have led to a better understanding of single-mode perturbations in ablatively driven planar samples. As predicted by computational simulation, using shaped laser pulses having increasing energy versus time led to higher capsule volume compression when the same target capsule was compared to experiments with unshaped (square) pulse laser energy. With unshaped pulses, we demonstrated the successful implosion of capsules with a uniform volume compression that exceeds the value of 30,000 required for the success of ICF. This performance is critical for ICF, and achieving it meets a major program objective. In these experiments, the fuel pellet performance essentially matched one-dimensional computer predictions of implosion values when degradation due to present laser beam asymmetry was included. This is the first time that ICF theory and experiments have agreed so closely, indicating that our ability to predict and understand results has greatly improved. These experimental results were achieved both through improved theoretical understanding and computational modeling and through the use of ultraviolet (0.35 μm) light from the Nova laser. The experiments also demonstrated control of the hohlraum environment—in particular, achieving the radiation flux uniformity required for gain.

As shown by the solid Nova point in Fig. 2, a combination of confinement time and fuel temperature has been achieved that is less than a factor of 10 away from the value needed to meet the criterion for fusion ignition. With experiments at high driver energies, using the sophisticated temporal pulse-shaping capability of Nova and advances in diagnostic capability, our future work will refine target designs and is expected to improve results to the regimes indicated by the open circles in Fig. 2. Successfully executing these physics and implosion experiments will confirm that fuel pellets indirectly driven with a 1–2 MJ driver will achieve the conditions required for ignition.

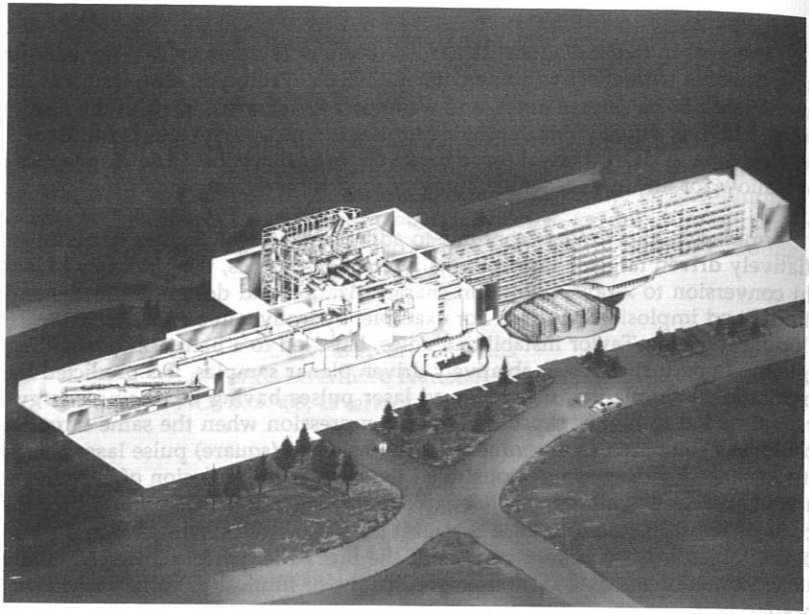

Figure 1

A rendering of the 100-kJ, 100-TW Nova laser facility now in operation at LLNL

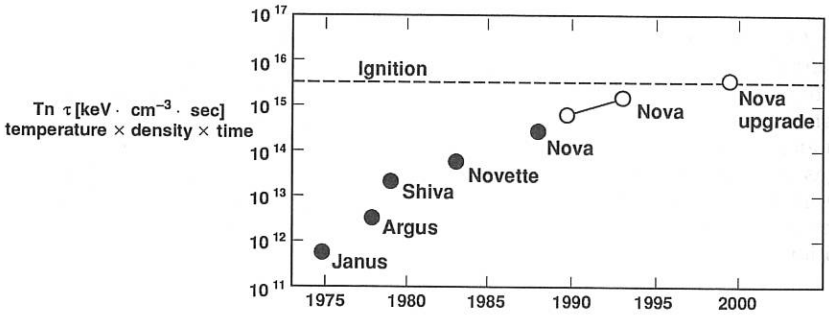


Figure 2

Successive ICF facilities at LLNL have made progress toward achieving the conditions required for laboratory ignition. The filled circle for Nova indicates the combination of confinement time and fuel temperature that has already been achieved; future Nova work is expected to lead to the regimes indicated by the open circles.

# STUDY OF INSTABILITIES IN LONG SCALELENGTH PLASMAS WITH AND WITHOUT LASER BEAM SMOOTHING TECHNIQUES

T. Afshar-rad, M. Desselberger, S. Coe, F. Khattak, L. Gizzi and O. Willi

The Blackett Laboratory, Imperial College of Science, Technology and Medicine, London SW7 2BZ, U.K.

A. Giulietti

Istituto di Fisica Atomica e Molecolare del C.N.R., 56100 Pisa, Italy

The interaction of intense laser light with large underdense plasmas is of great interest for inertial confinement fusion since fusion pellets will be surrounded by large plasma coronas. Under these conditions various parametric instabilities such as Stimulated Brillouin Scattering (SBS), Stimulated Raman Scattering (SRS) and laser beam filamentation may be very effective in reducing the laser-plasma coupling efficiency, in the production of high energy electrons and in the nonuniform heating of the plasma corona. To simulate fusion conditions, plasmas with scalelengths of up to a mm were produced by focussing four green laser beams of the Rutherford Appleton Laboratory high power laser system onto thin foil targets in a line focus configuration. A delayed green laser beam was focussed axially into the preformed underdense plasma with an electron temperature and density of about 0.5 keV and 0.1 $n_c$ respectively. The levels of SRS and SBS generated were recorded [1]. Laser beam filamentation and whole beam self-focusing was clearly observed [2,3]. Further, direct experimental observations showed that a significant level of the SRS and SBS were being generated in the filamentory structures [4,5]. When the incident laser beam was smoothed either by Random Phase Plate Arrays (RPPA) or Induced Spatial Incoherence (ISI) a significant reduction in the absolute levels and the virtual suppression of filamentation was observed [5-7].

In this paper experimental results of a recent investigation are reported. The preformed plasma was again formed by a line focus configuration using four heating beams irradiating a thin aluminium foil target (700nm thick, 0.7mm long, 0.3mm wide). However, in this experiment the heating beams were also smoothed by ISI in contrast to previous measurements in order to produce a more uniform preformed plasma. The two pairs of oppossing green laser beams were smoothed using an ISI and RPPA combination and superimposed in a line focus configuration. Typical irradiances of $10^{14}$W/cm$^2$ were used. Either an ISI smoothed infrared (1.05 $\mu$m) laser beam or a broadband beam (the ISI beam with the echelons removed ) delayed by 2.2 ns was focussed axially into the plasma. An extensive set of diagnostics was used to investigate the plasma conditions of the preformed plasma and the nonlinear interaction of the laser beam with the plasma.

Measurements were made of the absolute levels of SBS backscattering with the

broadband beam ($\Delta\omega/\omega \simeq 0.1\%$) or with an ISI laser beam to study the effect that spatial incoherence played in the reduction of the backscattered instabilities. At the time of interaction the nominal electron density was about 0.3 $n_c$ ($n_c$ is critical density for the infrared laser light) and the electron temperature was about 500 eV of the preformed plasma. The uniformity of the preformed plasma was investigated transversely to the exploding foil target by using optical Moire deflectometry techniques with a probe wavelength of 350 nm. The density profile was also measured interferometrically with 350 nm probe beam propagating along the axis of the preformed plasma. The electron temperature of the plasma was obtained from time resolved x−ray streak spectroscopy. The backscattered Brillouin signal generated by the interaction beam was imaged out via the incident focussing lens onto a calibrated photodiode. In addition, time resolved SBS spectra were recorded with a S1 optical streak camera. A four frame x−ray pinhole camera with a gating time of about 150 ps was used to observe the x−ray emission of the preformed plasma and of the interaction beam.

Figure 1 shows the absolute levels of SBS backscattering for the ISI and broadband interaction beams as a function of the incident irradiance.

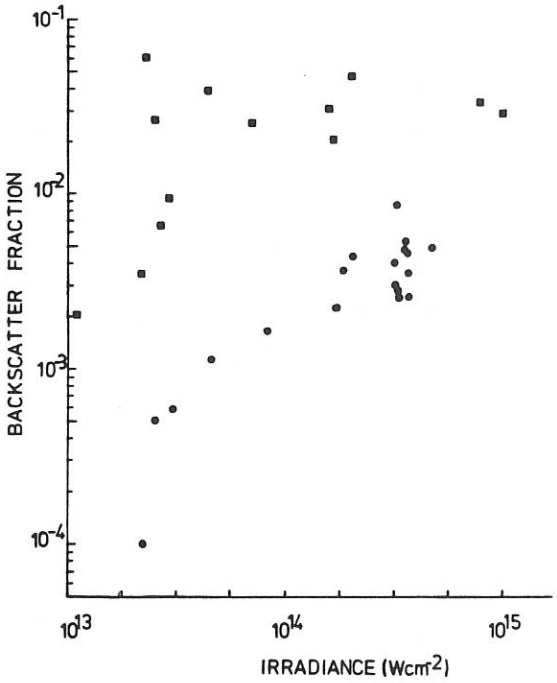


Fig. 1. Variation of SBS backscatter fraction with average irradiance for an ISI (illustrated by the solid circles) and broadband (squares) interaction beam.

The focal spot of the interaction beam was 140 $\mu$m in diameter and was kept constant for all the data shots. For the broadband laser beam a threshold at an irradiance of about $3x10^{13}$ $Wcm^{-2}$ is observed with a saturation level between 2 to 6% of the incident laser energy. For the ISI interaction beam an exponential behaviour is seen with an average SBS value of 0.5% at an irradiance of $7x10^{14}$ $Wcm^{-2}$. The SBS backscattering levels are significantly higher than observed in a previous experiment [4,5] in which a green interaction beam was used, the plasma was less uniform and the electron density was lower (by about a factor of 3) during interaction. However, SBS levels were also recorded in the present experiment for thinner targets (500nm thick). For these targets a similar electron density ( $0.1n_c$) as used previously is expected. However, the level of SBS did not vary significantly when compared with thicker targets. The estimated electron density is consistent with backscattered Simulated Raman Scattering (SRS) which was detected by diodes filtered with narrowband interference filters. For the 700nm targets virtually no SRS backscatter is observed. On the other hand, clear SRS signals (at a wavelength of about 1.5 $\mu$m) are seen with the 500 nm. These results indicate that the electron density was below 0.25 $n_c$ during interaction.

For some of the data shots anomolously high levels of SBS (larger by about a factor of 8 compared to the data shown in fig.1) were observed when an ISI interaction beam was used. On these shots the x− ray framing camera images as well as the optical probing diagnostic indicated that whole beam self−focusing may have occurred. A channel like structure was observed in the x−ray emission with a diameter of about 40 $\mu$m. In addition, a substantially higher transmitted laser energy was measured at the output plane of the the preformed plasma.

In conclusion the absolute levels of SBS in long scalelength underdense homogenous preformed plasmas were measured for a broadband laser beam and a beam smoothed by ISI which interacted axially with the preformed plasma. Whole beam self−focusing of the ISI interaction beam may have been observed for some of the shots.

References

1. O. Willi, D. Bassett, A. Giulietti and S. Karttunen, Opt. Commun. 70, 487 (1989).

2. S. Coe, T. Afshar−rad and O. Willi, Opt. Commun. 73, 299 (1989).

3. S. Coe, T. Afshar−rad and O. Willi, submitted to Europhys. Lett.

4. T. Afshar−rad, O. Willi, S. Coe, To be published.

5. O. Willi, T. Afshar−rad, S. Coe and A. Giulietti, Phys. Fluids, accepted.

6. S. Coe, T. Afshar−rad, M. Desselberger, F. Khattak, O. Willi, A. Giulietti, Z. Q. Lin, W. Yu and C. Danson, Europhys. Lett. 10, 31 (1989).

7. C. Danson, R. Bann, D. Pepler, N. Rizvi, I. Ross, P. Rumsby, R. Jackson, S. Coe, T. Afshar−rad, M. Desselberber and O. Willi, LFC Annual Report RAL−89−045, 141 (1989).

# HYDRODYNAMIC BEHAVIOR OF THE PLASMA ABLATION IN LASER-IRRADIATED PLANAR TARGETS

D.P. Singh, V.Palleschi and M.Vaselli
Istituto di Fisica Atomica e Molecolare del C.N.R.
Via del Giardino 7- 56127 Pisa (ITALY)

Using local flux-limited model for thermal flux transport, the dynamics of steady state planar ablative front is studied in details. A set of nonlinear fluid equations corresponding to the conservation of mass, momentum and energy is solved self-consistently to investigate the spatial profiles of plasma density, temperature and the flow velocity. The flux-transport inhibition on these profiles are studied and some results are also compared with the differential representation of the heat flux formula obtained from Fokker-Planck equation.

## 1. INTRODUCTION

Thermal conduction plays an important role in the energy transport process, as it drives the ablative compression of the interior of the plasma target necessary for the eventual success of laser-fusion[1-2 ]. The use of planar targets has the practical advantages such as ease of diagnostic access and the experimental design. In the present paper, we study the hydrodynamic behavior of plasma flow in laser-irradiated planar targets. The plasma flow beyond the plasma resonance layer may be assumed in steady state, but on the other hand, the underdense plasma is non-stationary due to its free expansion in vacuum.

Here we study the hydrodynamics of plasma ablation through local flux-limited formula. Though the formula is valid for the whole plasma region, we will confine our attention to the supercritical zone. In Sec. 2 the hydrodynamic equations governing the plasma flow are solved in a self-consistent manner by using local flux-limited formula and the differential representation of heat flux obtained from FP equation. A brief discussion of the relevant results is given in Sec. 3.

## 2. HYDRODYNAMICS OF PLASMA FLOW

We assume that the laser-energy is deposited at the plasma critical surface through collective processes such as resonance absorption. The electron and ion temperatures are considered to be equal. The justification of the above-mentioned assumptions is given elsewhere[2].

The steady state equations governing the plasma flow in slab geometry are:

$$\frac{\partial(\rho v)}{\partial x} = 0 \quad , \tag{1}$$

$$\frac{\partial(p + \rho v^2)}{\partial x} = \mu_o \rho \frac{\partial E_o^2}{\partial x} \quad , \tag{2}$$

$$\frac{5}{2}\rho v c^2\left(1+\frac{v^2}{5c^2}\right) = q \quad , \tag{3}$$

where $\rho$, v, x, $E_o$ and p ($=\rho c^2$) are the fluid density, fluid velocity, flow position, laser field and the pressure respectively. c ($=\sqrt{\frac{k_B T}{\mu}}$) is the isothermal sound speed and $\mu_o$ ($=\frac{Ze^2}{4m_e m_i \omega^2}$) and $\mu$ ($=\frac{Am_i}{Z+1}$) are constants. T is the plasma temperature. e, $m_e$, $m_i$, $k_B$ and $\omega$ are the electronic charge, electronic mass, ion mass, Boltzman constant and laser-frequency, respectively. q represents the heat flux . Using harmonic average between Spitzer's classical heat flux ($q_{cl}$) and the reduced free-streaming flux ($q_{fs}$) for effective heat flux, q may be written as

$$q = \left(q_{cl}^{-1} + q_{fs}^{-1}\right)^{-1} \tag{4}$$

where

$$q_{cl} = -K_{cl}\nabla T \qquad q_{fs} = -f\, n\, k_B\, T\, v_{th}\frac{\nabla T}{|\nabla T|} = -5\,\Phi\,\rho\, c^3\frac{\nabla T}{|\nabla T|} \quad . \tag{5}$$

$K_{cl}$ is Spitzer's classical conductivity[3]. Flux-limits f and $\Phi$ are inter related [2]

The second formula incorporating the non-local properties of the distribution function in FP equation may be written as

$$q = -K_{cl}\frac{dT}{dx}\left[1+\delta_1\left(\frac{\lambda_e}{T}\frac{dT}{dx}\right)^2 + \delta_2\left(\frac{\lambda_e^2}{T}\frac{d^2T}{dx^2}\right)+\delta_3\left(\lambda_e^2\left(\frac{dT}{dx}\right)^{-1}\frac{d^3T}{dx^3}\right)\right] \quad , \tag{6}$$

where $\lambda_e$ is the electron-mean free path. $\delta_1$, $\delta_2$ and $\delta_3$ are constants. The derivation of expression (6) and the numerical values of $\delta_1$, $\delta_2$ and $\delta_3$ can be found elsewhere[4].

Inserting expression (4) into eq. (3), the energy equation reveals as

$$T^*\frac{dT^*}{dx^*} = \frac{Nr}{Dr} \quad , \tag{7}$$

where

$$Nr = \frac{x_c}{k_c T_c}\frac{5}{2}\dot{m}c^2\left(1+\frac{M^{*2}}{5}\right) \quad , \quad Dr = 1-\frac{5}{2}\frac{\dot{m}}{5\Phi\rho_c}\left(1+\frac{M^{*2}}{5}\right) \quad .$$

where $T^*$ and $x^*$ are the variables dimensionalised with respect to their values at plasma critical layer. M=v/c and $M_c$ is the mach number of plasma flow at the critical layer. $T_c$ and $K_c$ are plasma temperature and Spitzer's conductivity at the plasma critical layer ($x_c$) and $\dot{m}$ ($=\rho v$) the mass flow rate. R.H.S. in eq. (2) representing the ponderomotive force is quite small and evanescent in the conduction zone, hence we will neglect it in the calculations. Eqs. (1), (2) and (7)( or eq .6 instead of (7)) have been solved simultaneously to determine the dimensionalised variables $\rho^*$ ($\rho/\rho_c$), $M^*$ and $T^*$.

The numerical calculations have been made for DT slab target for the following set of parameters:
$T_c$=2 KeV, $x_c$=200 μm, λ= 1 μm, $M_c$=1.

## 3. DISCUSSION

Figures 1 and 2 show the spatial profiles of the mach number of the plasma flow ($M^*$) and the plasma density ($\rho^*$) using local flux-limited formula for different values of flux-limit. It can be seen that the increase of flux limit enhances the plasma flow velocity and consequently reduces the plasma density.

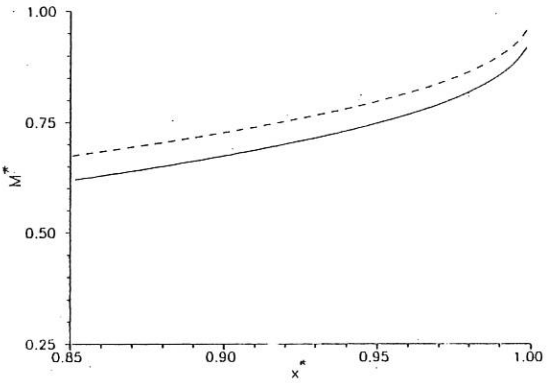


Fig. 1 - Spatial profiles of mach number ($M^*$) of plasma flow using local-flux limited formula. Continuous (--------) and dashed (- - - - ) curves correspond to f=0.3 and 0.5 respectively.

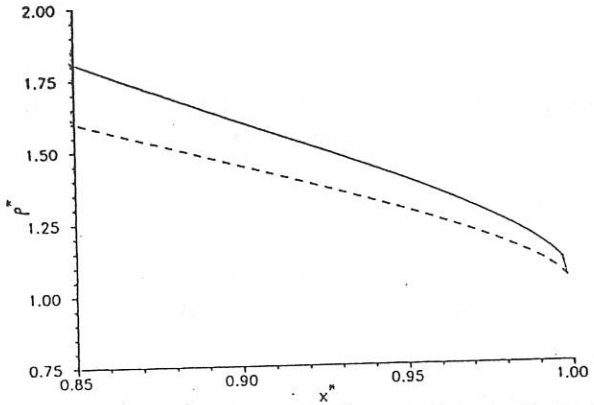


Fig. 2 - Spatial profiles of plasma density ($\rho^*$) using local-flux limited formula. Continuous (--------) and dashed (- - - - - ) curves correspond to f=0.3 and 0.5 respectively.

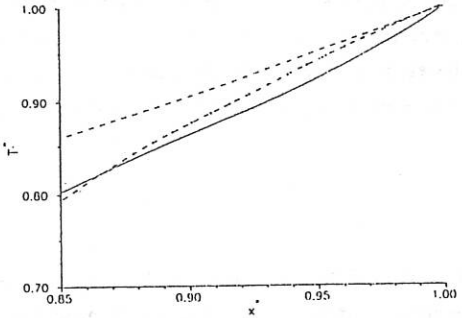


Fig. 3 - Spatial profiles of plasma temperature using local-flux limited formula (-------- for f=0.3 and - - - - - for f=0.5) and the differential representation of heat flux from FP equation (- · - · - ·).

In fig. 3, a comparison of the spatial plasma temperature gradients is made by using local flux-limited formula with different flux-limits and from the differential representation of heat flux derived by Kishimoto and Mima[4]. It is found that the latter thermal gradient profile resembles with the former one with flux -limit f (0.3 - 0.5).

REFERENCES

[1] A. Raven and O. Willi, *Phys. Rev. Lett.* 43 (4), 278 (1978).
[2] R. Fabbro, C. Max and E. Fabre, *Phys. Fluids* 28 (5), 1463 (1985).
[3] L. Spitzer Jr., *'Physics of Fully Ionised Gases'* 2nd Interscience (1962).
[4] Y. Kishimoto and K. Mima, *J. Phys. Soc. of Japan* 52, no. 10, 3389 (1983).

# EXPERIMENTAL STUDIES ON THE MECHANISM OF MACH WAVE GENERATION

M. De Rosa, F.Famà, V.Palleschi, A.Salvetti, D.P. Singh and M.Vaselli

Istituto di Fisica Atomica e Molecolare del C.N.R.,
Via del Giardino, 7 - 56127 Pisa(ITALY)

## 1. Introduction

In the process of interaction of shock waves the mechanism of Mach wave generation allows the smoothening and stability of the resulting shock fronts. Such a mechanism has practical application in inertial confinement fusion. The present paper reports some experimental studies on Mach wave generation in air in almost plane geometry. The experimental results are theoretically interpreted using the hydrodynamic equations of a perfect gas and the self-similar model of strong explosion [1].

## 2. Analysis

Analytical description of the fluid perturbed by a shock wave (SW) makes use of the oblique SW relations, namely conservation equations across the SW front and appropriate boundary conditions [2, 3].

The $(p,\theta)$-polar [4] is a graphical representation of the relation between the pressure across the SW front and the deflection angle for a fixed value of the SW Mach number $M_1=u_1/c$, where $u_1$ is the velocity of the shock wave and c is the speed of sound in the unperturbed gas.

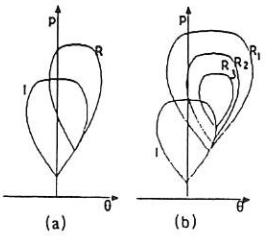


Fig. 1 - Shock polars in the p-θ plane for regular (a) and Mach (b) reflection.

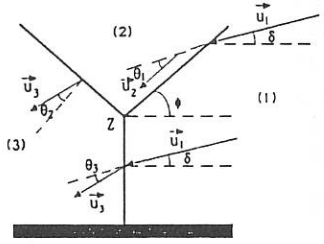


Fig. 2 - Fluid velocities for Mach reflection, in a frame of reference at rest with the triple point Z.

The boundary condition for SW reflection is that the velocity must be tangential near the reflecting surface , because the fluid can not penetrate the surface. Therefore a graphical representation of the SW reflection may be given in terms of two (p,θ)-polars, related to the incident (I) and reflected (R) SWs respectively. Two general cases can be considered:

1.) For regular reflection (fig. 1a) the boundary condition $\theta_1=\theta_2$ is met by the intersection of the R-polar with $\theta=0$ axis and two solutions are allowed, although only the 'weak' (low pressure) solution has been observed in most of the laboratory experiments.

2.) For Mach reflection (fig. 1b) the boundary condition $\theta_1 - \theta_2 = \theta_3$ is satisfied by the intersection of the R-polar with the I-polar, and three different net reflections of the flow in region 3 of fig. 2 are possible.

In the non-stationary case the Mach wave front travels parallel to the reflection plane, while the triple point Z (see fig. 2) detaches from the plane along an almost straight line making an angle δ with the reflection plane. The velocity of the Z point along the trajectory is predicted to be [2] :

$$|v_Z| = \frac{u_1}{\sin(\phi - \delta)} \qquad (1)$$

where $\phi$ is the angle of incidence.

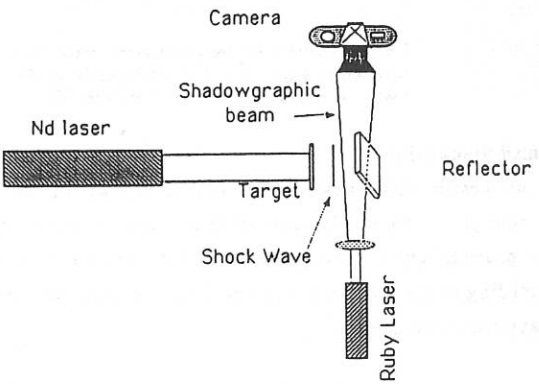


Fig. 3 - Experimental set-up for plane shock wave reflection.

### 3. Experimental set up

In order to produce shock waves an unfocussed Nd-laser beam ( $\lambda$=1.06 $\mu$m, 5 J in 20 ns (FWHM)) was shot onto a plastic film coated with a thin layer of aluminium. The fast absorption of the laser energy by the aluminium coating produces a strong explosion of the layer which, in turns, generates an almost plane shock wave. The resulting shock wave was then forced to interact with a rigid reflector, whose surface makes an angle $\alpha$ with the direction of the incident shock wave ( fig. 3).

We used a shadowgraphic method for the detection of the shock wave front. A 30 mJ, 20 ns [FHWM] beam, produced by a Ruby laser was properly synchronized with the Nd laser pulse.

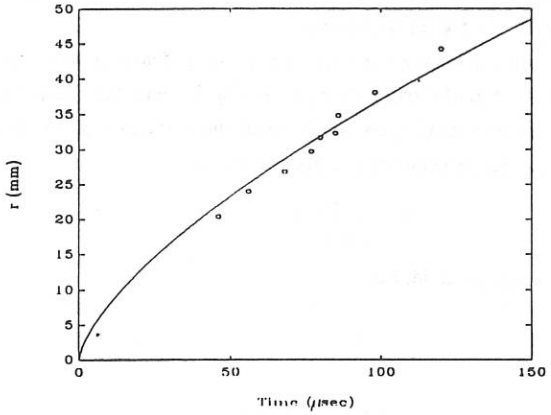


**Fig. 4 - Position of the plane shock wave as a function of time. Full line corresponds to the best fit of the experimental data with eq. (2).**

### 3. Results and discussion

The conversion efficiency of the optical energy of the laser into the mechanical energy of the shock wave, in the plane geometry, can be estimated following the propagation of the unperturbed shock wave before its reflection by the obstacle. According to the self-similar model of strong explosion, the propagation of the shock wave front results as [1]:

$$R = \left(\frac{E}{\beta \rho}\right)^{1/3} t^{2/3} \qquad (2)$$

in which R, E, $\rho$ and t represent the shock wave position, energy of the SW, the unperturbed gas density and time respectively. The parameter $\beta$ is a numerically determined constant, which in the case of air is about 0.8. From the best fit of the experimental data (fig. 4) with eq. (2) a conversion efficiency about the order of 1% can be estimated, which is quite plausible due to the large difference between the acoustic impedances of the target (plastic film) and the material in which the shock wave propagates (air). Because of the relatively low efficiency of the process, the velocity of the shock wave on the target is slightly supersonic ($u_1$ = 350 m/sec.). In these conditions, the critical angle above which the Mach reflection occurs is theoretically estimated as $(\phi_{cr})^{th}$ = 74°. This value well agrees with the experimental data: the transition between normal and Mach reflection regimes was, indeed, experimentally found around a critical angle $(\phi_{cr})^{ex} = 75° \pm 1°$. In figures (5a-5d) some shadowgrams are shown, referring to the onset of Mach reflection ($\phi$=77° > $\phi_{cr}$). The trajectory of the triple point makes an angle $\delta$=8.2° with the surface of the reflector; its velocity along the trajectory, as determined experimentally, is $(v_Z)^{ex}$= 377 ± 1 m/sec. This value has to be compared with the theoretical prediction of eq. (2), $(v_Z)^{th}$= 375 m/sec. In this case, too, the experimental results agree extremely well with the predictions of the theory.

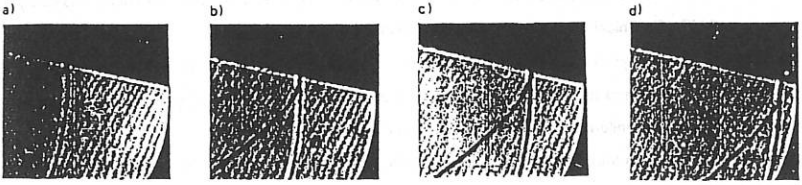


Fig.5 - Mach reflection of the incident shock wave at different times ($\phi$=77°).

## References

[1] L.Sedov, *Similarity and Dimensional Methods in Mechanics*, (Mir Publisher, Moscow,1982).

[2] R.Courant and K.O.Friedrichs, *Supersonic Flow and Shock Waves* (Springer-Verlag, New York, 1976).

[3] L.D.Landau and E.M.Lifshitz, *Hydrodynamics* (in Russian) ( Nauka, 1986).

[4] R.Kawamura and H.Saito, *J. Phys. Soc. Japan*, **11**, (1956) 584.

# EVALUATING KrF LASERS FOR ICF APPLICATIONS

*David C. Cartwright*
*Joseph F. Figueira*
*Thomas E. McDonald*
*David B. Harris*
*Allan Hauer*

*Los Alamos National Laboratory*

Characteristics of the KrF laser that make it a very promising driver for inertial confinement fusion (ICF) are that it operates naturally at a near-optimum wavelength (248 nm) for efficient conversion of laser energy into target compression, can achieve bandwidths approaching 1%, and will produce precise temporal pulse shapes with high contrast ratio. KrF also holds the promise for a system efficiency (wall plug to laser light) of greater than 5%, and can be operated at a pulse repetition rate appropriate for an ICF electric power plant (estimated to fall within the range of 1 to 10 pulses per second).

The KrF Laser-Fusion Program has three elements:

- Operation and performance of experiments on the Aurora laser system,
- Demonstration of advanced technology development, and
- Advanced KrF laser system design.

A major effort in the KrF laser technology area of the Los Alamos program is the development of AURORA, a nominal 10 kJ KrF laser. AURORA is a prototype of a KrF driver and is being used to develop technology and designs appropriate to an LMF. Technical issues being addressed include beam control, ability to focus, and contrast for target experiments. Target physics experiments on AURORA will address studies of stimulated Raman and Brillouin scattering; x-ray conversion and other indirect-drive target performance issues; hydrodynamic instability growth; mix; and drive symmetry and uniformity for both indirect and direct drive.

Aurora has achieved more than 100 TW/cm$^2$ on target with > 1 kJ of energy. The facility is designed to deliver 5 kJ to the target with a 5-ns pulse length and spot size ~200 μm. The system employs angular multiplexing, in which 96 beam pulses are overlapped into a single, 500-ns beam train. The 96 paths are offset and staggered through the amplifier chain to provide spatial and temporal separation of the individual beams and the energy from each amplifier is extracted continuously over the 500-ns electron beam pumping duration. The appropriate time delay is then removed from each beam segment so that they are simultaneously recombined at the target plane.

In the Advanced Technology Development Program, we are actively working to advance the state of the art in the areas of optics, pulse power, and laser kinetics. In particular, we are examining new manufacturing techniques for optics, working to increase the optical damage thresholds, examining new pulsed power techniques that will result in lower costs and higher efficiency, and performing laser kinetics experiments to better understand the laser.

# SECOND HARMONIC: A VERSATILE DIAGNOSTIC FOR LASER INTERACTION WITH UNDERDENSE PLASMAS

D. Giulietti*, D. Batani, V. Biancalana, F. Bianconi, I. Deha, and A. Giulietti

Istituto di Fisica Atomica e Molecolare, CNR,
Via del Giardino, 7, 56100, Pisa, Italy
*Dipartimento di Fisica, Universita' di Pisa, Italy

**1. Introduction.** In the ICF scheme, laser radiation has to propagate in a few millimeter underdense plasma (corona): instabilities arising in this region can greatly affect the laser energy deposition and the uniformity of compression. Second harmonic of the laser ligth can be generated in the corona from zones affected by density gradients. Time resolved imaging of these structures in second harmonic light can give useful information on the "quality" of the interaction.

An experimental campaign is in progress at IFAM in order to optimize the diagnostic use of second harmonic. Experiments are performed at 1.064 μm laser wavelength and nominal intensity of the order of $10^{13}$ W/cm$^2$. The evolution of filamentary regions has been studied with this method[1]. Time resolved spectroscopy of $2\omega$ emitted at $90^0$ allowed to evidence for the first time the contribution of Brillouin backscatter to second harmonic generation[2]. It seems possible to use second harmonic emitted at different angles not only to observe the localization and evolution of density gradients, but also to provide an additional tool to evaluate the local plasma temperature and to get a deeper knowledge of filamentation and stimulated Brillouin instabilities.

In the following we introduce the theoretical background of the problem and the main experimental results obtained so far. The underdense plasma was obtained in two different ways:optical gas breakdown and exploding thin foils.

**2.Second harmonic generation in underdense plasma.** A simple way to introduce second harmonic generation in a plasma is the equation of motion for electrons,taking into account the spatial variations of electron density (n) and velocity (**v**), but neglecting collisions responsible for damping

$$d\mathbf{v}/dt + (\mathbf{v}\cdot\nabla)\mathbf{v} = -e/m \quad (\mathbf{E} + \mathbf{v}/c \times \mathbf{B}) \qquad (1)$$

$$dn/dt + \nabla (n\mathbf{v}) = 0 \qquad (2)$$

where T is the plasma temperature, and **E** and **B** the electric and magnetic fields of the impinging radiation.

The optical nonlinearity in the plasma can be treated as a perturbation in the successive approximation method, finding for the equations (1) and (2), coupled with Maxwell's equations, the solutions

$$n = n_0 + n_1 = n_0 - e/m\omega^2 \nabla(n_0 \mathbf{E}) \quad (3)$$

$$\mathbf{v} = \mathbf{v}_1 + \mathbf{v}_2 = - ie/m\omega \mathbf{E} + ie^2/4m^2\omega^3 \nabla(\mathbf{E}\cdot\mathbf{E}) \quad (4)$$

from which we easily obtain the current densities:

$$\mathbf{j}_1 = n_0 e\mathbf{v}_1 = - in_0e^2/m\omega \mathbf{E} \quad (5)$$

$$\mathbf{j}_2 = n_0 e\mathbf{v}_2 + n_1 e\mathbf{v}_1 = ie^3/m^2\omega^3 [ \varepsilon_\omega^{-1} (\nabla n_0 \cdot \mathbf{E}) \mathbf{E} + n_0/4 \nabla(\mathbf{E}\cdot\mathbf{E}) ] \quad (6)$$

where $\omega$ is the laser pulsation, and $\varepsilon_\omega$ the dielectric constant of the plasma. Equation (6) shows that from an uniform plasma ($\nabla n_0 = 0$) second harmonic radiation can't be emitted. In fact the first term vanishes, while the second being irrotational can't radiate.

Considering now $\mathbf{j}_2$ as a source for second harmonic generation in the plasma and using again Maxwell's equations, we obtain:

$$\nabla^2 \mathbf{B}_{2\omega} + (2\omega/c)^2 \varepsilon_{2\omega} \mathbf{B}_{2\omega} = - 4\pi/c \nabla \times \mathbf{j}_{2\omega} \quad (7)$$

and developing the source term:

$$\nabla \times \mathbf{j}_{2\omega} = ie^3/m^2\omega^3 [ \varepsilon_\omega^{-1} (\nabla n_0 \cdot \mathbf{E}) \nabla \times \mathbf{E} + \varepsilon_\omega^{-1} \nabla(\nabla n_0 \cdot \mathbf{E}) \times \mathbf{E} - (\varepsilon_\omega^2 n_c)^{-1} (\nabla n_0 \cdot \mathbf{E}) \nabla n_0 \times \mathbf{E} + \nabla n_0 \times \nabla(\mathbf{E}\cdot\mathbf{E})/4 ] \quad (8)$$

For density gradients with cylindrical symmetry, as expected for a beam-plasma interaction, $\nabla n_0 = F(r)\mathbf{r}$, we find that almost all the second harmonic emission is forwards; in particular the contribution normal to the laser beam is several orders of magnitude lower.

**3. Second harmonic emission from laser produced plasmas in gases.** We have studied second harmonic emission from laser interaction with a fully ionized helium plasma whose density was much lower than the critical ( $n \approx n_c/100$ ). The density scale length was much larger than in usual solid target experiments. Plasma temperature was measured to be $T_e \approx 50$ eV [3]. Second harmonic was studied forward. It is relevant that no second harmonic was detectable sideward in agreement with the equation (8) of the previous section. The same equation shows that side $2\omega$ emission is possible in presence of a relevant reflection or backscattering, as experimentally verified with denser plasmas (see next section).

Both reflection and backscattering were negligible in our experiment in gas. The conditions of maximum $\omega$ to $2\omega$ conversion efficiency were 150 Torr and 400 MW for the gas pressure and laser power respectively and it resulted, in agreement with theoretical evaluation, $\eta = P_{2\omega}/P_{\omega} \approx 5\times10^{-12}$ [1]. The laser operated with 20 ns FWHM pulses. We had previously found that in these conditions both whole beam self focusing and filamentation occurred. The former was evidenced through beam recollimation and using interferometric methods to show the formation of a low density plasma channel. The second looking at diffraction at large angles of part of the laser $\omega$ light. The observed spreading (up to $14^0$) is consistent with saturated plasma filaments of diameter $d \approx 5.4\mu m$ [4]. For what concerns the second harmonic angular distribution, the observed patterns showed two ring shaped maxima and a minimum near the axis. Rings correspond to about $2^0$ from the beam axis. This angular distribution also agrees with a diameter of the emitting region $d \approx 5.5$ $\mu$m. Despite to the very low conversion efficiency, we were able to obtain time resolved images of the cross section of the interaction region. Using a streak camera we collected front images in which the $2\omega$ source is clearly distinct from the background plasma, and filaments appear as "$2\omega$ hot spots". Second harmonic sources were localized in the laser beam which focuses and defocuses in time in agreement with other experiments on non steady state self focusing. Micron sized sub-structures ($d \leq 10$ $\mu$m), with a mean lifetime of a few ns, were identified as filaments generated by non linear interactions.

To check the validity of our model we also calculated the expected $2\omega$ polarization and compared it with data. Firstly we used laser light linearly polarized as in all other measurements of the experiment. For the second harmonic we found a quasi linear polarization, with the same polarization axis and a ratio $P_{2\omega}^{(x)}/P_{2\omega}^{(y)} \approx 10 \pm 2$ in agreement with theoretical expectations. Subsequently the laser light was circularly polarized and we found, both theoretically and experimentally, that the $2\omega$ light has no net polarization, that is $P_{2\omega}^{(x)}/P_{2\omega}^{(y)} \approx 1$.

Obsevations and measurements performed in gas clearly showed the diagnostic potentiality of the $2\omega$ detection, but the interest of this study is limited by the peculiarity of gas breakdown and hydrodynamics as well as the lower temperature obtainable in this way, if compared with that of fusion target corona.

**4. Second harmonic emission from thin foil laser produced plasmas.** In a subsequent experimental campaign the second harmonic from a plasma produced by laser irradiation of thin plastic foils was studied. The plastic used for thin-target preparation was polyvinyl formal and the target thickness used in the experiment was in the range 0.3-1.8 $\mu$m. The thin foil was irradiated at 1.064 $\mu$m laser wavelength with a pulse of 3 ns FWHM at irradiance up to $5\times10^{13}$ W/cm$^2$.

The laser beam was focused perpendicularly to the target plane with an f/8 optics. The laser bandwidth was 0.7 Å. Second harmonic emission at $90^0$ (parallel to the target plane) was observed in a wide range of target thickness, down to 0.5μm. The radiation emitted at $90^0$ was collected with an f/7 optics, time resolved with an intensified optical streak camera, and analyzed by time-resolved spectra and images.

According to theory [5] the $2\omega$ emission at $90^0$ in an underdense plasma originates from the source term (8) in the presence of the incident and reflected electromagnetic waves. The spectroscopic data were consistent with second harmonic emission resulting from the sum $\omega_0 + \omega_B$ of the laser frequency with the frequency of the backscattered light. The signature of this process came from the red shift of the backscattered light as expected from the Stimulated Brillouin Scattering which in turn gave a red shift of the second harmonic light. Other spectroscopic features were explainable in terms of the plasma motion. In addition, the measured threshold $\approx 10^{12}$ W/cm$^2$ of the $2\omega$ emission agreed with the expected Brillouin threshold in our experimental conditions.

The frequency sum process, postulated by Stamper et al. [5] was experimentally confirmed as a non linear process occurring in laser produced plasmas as well as already observed in crystals [6]. The emission detected in this experiment can be used, in principle, as a diagnostic in place of direct measurements on stimulated Brillouin backscattered light. A disadvantage is given by equality $(\Delta\omega/\omega)_{2\omega} = 1/2\ (\Delta\omega/\omega)_{\omega}$ making the spectroscopic analysis less sensitive. However, this method could be convenient because $2\omega$ light is spectroscopically well separated from the fundamental $\omega_0$ much better than $\omega_B$. Moreover, the experimental detection is generally more suitable at $90^0$ than backward. At the present time measurements are in progress to analyze the forward emitted second harmonic, which results, as expected from the equation (8), orders of magnitude more intense than side emitted one.

In conclusion we belive that $2\omega$ detection techniques have to be developed as diagnostic tools for laser fusion in order to control the formation of unstable regions in the corona, signed by strong density gradients. At the same time more experiments are necessary to well understand the limits and possible contradictions of this method [7].

[1] D. Batani et al., Opt. Comm. **70**, 38, (1989).
[2] A. Giulietti et al., Phys.Rev.Lett., **63**, 524, (1989).
[3] A. Giulietti et al., Proceedings of XVIII ICPIG , Swansea, U.K., (1987).
[4] D. Giulietti et al., J.Appl.Phys. **58**, 2916, (1985).
[5] J.A. Stamper et al., Phys.Fluids, **28**, 2563, (1985).
[6] Y.R. Shen, The principles of nonlinear optics, Willey, New York, 1984.
[7] P. E. Young et al, Phys.Rev.Lett., **63**, 2812, (1989).

# EXCITATION OF SOUND BY ELECTROMAGNETIC PULSE IN A DENSE SEMI-INFINITE NON-ISOTERMAL COLLISIONAL PLASMA

V.I.Muratov , A.P.Shuklin

Kharkov State University , Kharkov ,3I0077,USSR

Resently,the problem of the sound excitation when an electromagnetic pulse is incident on a non isotermal collisionless plasma,the latter being nontransparent at the carrier frequency,has been solved [I].Neglect of electron-ion collisions sets limits on the field of application of the results, obtained in [I].The most important is the requirement on smal lness of the parameter $\nu_{ei}\tau \ll 1$ ( $\nu_{ei}$ -the rate of electron -ion collisions , $\tau$ - the characteristic pulse time ).In this paper we propose the solution of one-dimensional problem of the sound excitation by electromagnetic pulse in a nonisothermal collisional plasma with the requirement that $\nu_{ei}\cdot\tau \ll \ll (m_i/m_e)^{1/2}$ ,where $m_e$ and $m_i$ - electron and ion masses, respectively.We assume that a plasma bounded by a nonconducting medium fills the half-space $z \geqslant 0$ .Starting from $t=0$ ,an electromagnetic radiation of frequency $\omega_0$ and slowly variable amplitude $E_0(t)$ actson plasma.The electric field of the radiation is directed normally to the $z$ axis.The plasma is nontransparent for an external radiation at $\omega_0$ .

To present the low-frequency plasma oscillations we use the system of transfer equations for the electron-ion plasma corresponding to Grad five-moment approximation [2] :

$$\frac{\partial^2 \overline{\delta n}}{\partial t^2} - \frac{T_e}{m_i}\frac{\partial^2}{\partial z^2}\left(\overline{\delta n} + \overline{\delta T}\right) = -\frac{T_e}{2m_i}\frac{\partial^2}{\partial z^2} V^2(t,z) \qquad (I)$$

$$\frac{\partial \overline{\delta T}}{\partial t} = \frac{2}{3}\frac{\partial \overline{\delta n}}{\partial t} + \frac{2}{3}\nu_{ei} V^2(t,z) \qquad (2)$$

where $\overline{\delta n} = \delta n / n_0$ , $\overline{\delta T} = \delta T / T_e$ are the temperature and density dimensionless variations, respectively, and

$$V^2(t,z) = \frac{E_0^2(t)}{2\pi n_0 T_e} \exp(-\varkappa_0 z) = V_0^2(t)\exp(-\varkappa_0 z)$$

$(\varkappa_0/2) = (\omega_0/c)\sqrt{-\varepsilon_0}$ -the electromagnetic wave skinning reverse depth, $\varepsilon_0 = 1 - (\omega_{pe}/\omega_0)^2$. The system (I)-(2) must be supplemented with boundary ( initial and terminal ) conditions :

$$\frac{\partial}{\partial z}\left(\overline{\delta n}(t,z) + \overline{\delta T}(t,z) + \frac{1}{2}V^2(t,z)\right)\Big|_{z=+0} = 0 \qquad (3)$$

$$\overline{\delta n}(0,z) = \overline{\delta T}(0,z) = 0 \qquad (4)$$

We assume that the boundary of the plasma is fixed ( terminal condition ), the initial condition is evident. Integrating ( 2 ) and taking ( 4 ) into account we find :

$$\overline{\delta T}(t,z) = \frac{2}{3}\overline{\delta n}(t,z) + \frac{2}{3}\nu_{ei}\int_0^t V^2(t',z)\,dt' \qquad (5)$$

After substitution (5) into (I) and (3) we obtain :

$$\frac{\partial^2 \overline{\delta n}}{\partial t^2} - c_s^2\frac{\partial^2 \overline{\delta n}}{\partial z^2} = \frac{3}{10}\varkappa_0^2 c_s^2 Q(t,z) \qquad (6)$$

$$\frac{\partial \overline{\delta n}}{\partial z}\Big|_{z=+0} = \frac{3}{10}\varkappa_0 Q(t,0), \quad \overline{\delta n}(0,z) = 0 \qquad (7)$$

where

$$Q(t,z) = \left[V_0^2(t) + \frac{4}{3}\nu_{ei}\int_0^t V_0^2(t')dt'\right]\exp(-\varkappa_0 z) \qquad (8)$$

Hereinafter, it is assumed that $V_0(0) = V_0(\infty) = 0$ and the integral in (8) converges at $t \to \infty$. We seek the solution of (6) as approximated by the form :

$$\overline{\delta n}(t,z) = \overline{\delta n}_1\left(t - \frac{z}{c_s}\right) + \overline{\delta n}_2\left(t + \frac{z}{c_s}\right) + W(t)\exp(-\varkappa_0 z) \qquad (9)$$

Then using the boundary conditions (7), we find the following set of equations :

$$\overline{\delta n}(t,z) = -\frac{W(0)}{2}\left[\exp\left(-\omega_s\left(t + \frac{z}{c_s}\right)\right) + \exp\left(-\omega_s\left|t - \frac{z}{c_s}\right|\right)\right] +$$

$$+ \frac{1}{2\omega_s}\frac{\partial W(t')}{\partial t'}\Big|_{t'=t+\frac{z}{c_s}} - \frac{1}{2\omega_s}\frac{\partial W(t')}{\partial t'}\Big|_{t'=\left|t-\frac{z}{c_s}\right|} + W(t)\exp(-\varkappa_0 z) \qquad (10)$$

$$\frac{\partial^2 W(t)}{\partial t^2} - \omega_s^2 W(t) = \frac{3}{10}\omega_s^2 Q(t,0), \quad \omega_s = C_s \varkappa_0 \qquad (II)$$

We remind that the temperature variation is related to the density variation by (5).The complete system of partial differential equations (I)-(2) and boundary conditions (3)-(4) is thus reduced to an ordinary differential equation.We did not mean to dwell on the analyses of the system (I0)-(II) in great detail,we only report on some quality results. At $t \to \infty$ ( of course,the presented results hold for a situation when $t$ is well below the temperature relaxation time ),in the region near the plasma boundary, $\overline{\delta n}$ and $\overline{\delta T}$ are :

$$\overline{\delta n}(t,z) \simeq -\frac{2}{5}\nu_{ei} \int_0^\infty V_0^2(t)dt \cdot \exp(-\varkappa_0 z)$$

$$\overline{\delta T}(t,z) = \frac{2}{5}\nu_{ei} \int_0^\infty V_0^2(t)dt \cdot \exp(-\varkappa_0 z)$$

For $V_0^2(t) = (t/a)^2 \exp[-(t-a)^2/a^2]$ , at $a\nu_{ei} = 5$ equations (I0)-(II) were computer analysed.The results of the computer analysis are shown below .

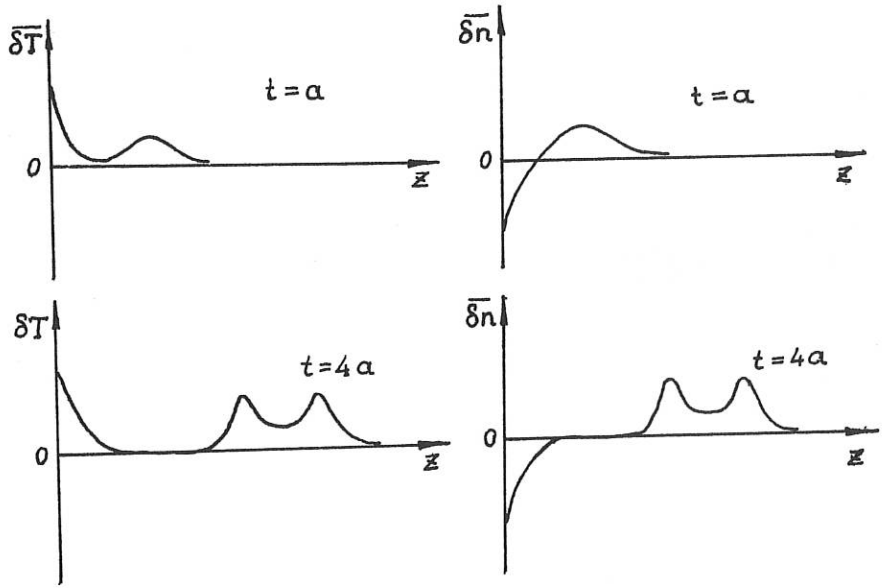

It is clear from the pictures that the density and temperature waves travel from the boundary deep into the plasma.

REFERENCES

I D.O.Livdan , V.I.Muratov , A.P.Shuklin . Sov. Phys. JETP , V. 67 (6), I988, P. II40 .

2 V.P.Silin. Introduction in gas-kinetic theory. Moscow, Nauka publ., I97I , 33I p.

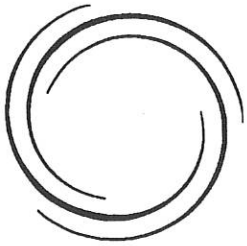

# INDEX OF ALL AUTHORS

INDEX